Beam Simulation Studies of Plasma-Surface Interactions in Fluorocarbon Etching of Si and SiO_2

by

David Charles Gray

B.S. Chemical Engineering
Carnegie Mellon University, 1987

M.S. Chemical Engineering Practice
Massachusetts Institute of Technology, 1989

Submitted to the Department of Chemical Engineering in partial fulfillment of the requirements for the degree of

Doctor of Philosophy
in
Chemical Engineering

at the
Massachusetts Institute of Technology
April, 1992

Signature of Author_____
Department of Chemical Engineering

Certified by_____
Prof. Herbert H. Sawin, Thesis Advisor
Departments of Chemical Engineering and Electrical Engineering and Computer Science

Accepted by_____
Prof. William M. Deen
Department of Chemical Engineering
Chairman, Graduate Student Committee

Beam Simulation Studies of Plasma-Surface Interactions in Fluorocarbon Etching of Si and SiO_2

by

David C. Gray

Submitted to the Department of Chemical Engineering
on April 27, 1992, in partial fulfillment of the requirements
for the degree of Doctor of Philosophy in Chemical Engineering.

Abstract

A molecular beam apparatus has been constructed which allows the synthesis of dominant species fluxes to a wafer surface during fluorocarbon plasma etching. These species include atomic F as the primary etchant, CF_2 as a potential polymer forming precursor, and Ar^+ or CF_x^+ type ions. Ionic and neutral fluxes employed are within an order of magnitude of those typical of fluorocarbon plasmas and are well characterized through the use of in-situ probes. Etching yields and product distributions have been measured through the use of in-situ laser interferometry and line-of-sight mass spectrometry. XPS studies of etched surfaces were performed to assess surface chemical bonding states and average surface stoichiometry. A useful design guide was developed which allows optimal design of straight-tube molecular beam dosers in the collisionally-opaque regime.

Ion-enhanced surface reaction kinetics have been studied as a function of the independently variable fluxes of free radicals and ions, as well as ion energy and substrate temperature. We have investigated the role of Ar^+ ions in enhancing the chemistries of F and CF_2 separately, and in combination on undoped silicon and silicon dioxide surfaces. We have employed both reactive and inert ions in the energy range most relevant to plasma etching processes, 20-500 eV, through the use of Kaufman and ECR type ion sources. The effect of increasing ion energy on the etching of fluorine saturated silicon and silicon dioxide surfaces was quantified through extensions of available low energy physical sputtering theory. The ability of CF_2 to enhance the Ar^+ etching of silicon dioxide and to suppress the ion-enhanced etching of silicon was measured. Ar^+/F chemistry was found to dominate the overall etching rates in Ar^+/F/CF_2 etching of silicon and silicon dioxide. CF_2 radicals were rapidly lost due to F-CF_2 surface recombination and enhanced SiO_2-to-Si selectivity only slightly at Ar^+ bombardment energies above 250 eV. High energy CF_x^+ ions appear to be the important species in obtaining large SiO_2-to-Si selectivities representative of fluorocarbon oxide etching processes.

Simple "site"-occupation models were developed for the quantification of the ion-enhanced fluorine etching kinetics in these systems. These models are suitable for use in topography evolution simulators (e.g. SAMPLE) for the predictive modeling of profile evolution in non-depositing fluorine-based plasmas such as NF_3 and SF_6. With this addition, the advancement of the surface will no longer be arbitrary but will depend on the relative species fluxes and energies to each surface element.

Thesis Supervisor: Prof. Herbert H. Sawin
MIT Professor of Chemical and Electrical Engineering

...to my parents ...for believing in and supporting me every day.

Acknowledgments

Ahhh...Finally! Time to bid my thanks to all those who have contributed to this thesis work and permitted me to retain some semblance of sanity (?) during my stay at MIT. First and foremost I am eternally grateful to the Big Three for giving me the talent and opportunity to be here at MIT, and blessing me with more than my share of good friends to see me through this program. I offer my most sincere gratitude, love, and respect to my parents; to my mother for teaching me to mind my phrasology and keep my ducks in a row, and to my father for cultivating my interest in the sciences. This degree is yours as much as it is mine. Also, I thank all my family for supporting me during this work and seeing me through good times and bad. Finally, to Dipa I offer my love and appreciation for letting me be myself, putting up with the long hours and bad jokes, and for "perking" up the gloomiest of days.

Next, I extend my heartfelt thanks to Prof. Herb Sawin for acting at various times as my thesis advisor, fellow commiserant, and friend-in-need during my tenure at MIT, and for sparking my interest in engineering science through his commitment and enthusiasm toward this project. I also offer thanks to the members of my thesis committee; Prof. Bob Brown, Prof. Karen Gleason, Prof. Sylvia Ceyer, and Prof. Rafael Reif.

I am indebted to everyone associated with the METL group for providing moral and intellectual support and camaraderie during my stay here. I gratefully acknowledge the contributions of my friends:

-Dr. Jeffery Butterbaugh, Igor "Fishy" Tepermeister, and Vivek "Mr. Control" Mohindra in the construction and implementation of the "3-beam" reactor

-"Gib" Gibson for sharing my enthusiasm for "the science" and helping me destroy vital liver cells at the Muddy with Ted Layman et al.

-To Tim "Squawk" Dalton, John "who?" Arnold, Gavin "Vacation" Zau, and Gil "IHTFMC" Huppert for compromising the moral standards of the METL group just enough to make life amusing.

-To Joanne Liu and Dr. Linda Kiss for subsequently raising the moral standards of the group when necessary and maintaining their professionalism in the face of buffoonery.

-And to Dr's Kulkarni, Gogolides, Nicolai, Connors and the rest of "those who made it out" for showing me the way.

Special thanks also to John Cremin and the "shop guys", and all the other MIT staff members who facilitated this thesis work on a daily basis.

I also offer special thanks to my good friends in the MIT Korean Karate Club for helping me to keep body and mind together during the past few years, and for teaching me that "pain is my friend...it is just weakness leaving my body."

Financial support for this project was provided by SEMATECH, through the Massachusetts Center of Excellence. The interdisciplinary environment created at MIT by the Massachusetts SCOE was a critical element in the success of this project, and I would like to thank Kate Paterson and the SCOE administrators for their efforts in coordinating this program.

Table of Contents

Abstract 2
Acknowledgements 4
List of Figures 7
List of Tables 17

1. Introduction 18

1.1 Surface Interactions and "Microscopic Non-Uniformity" in Plasma Etching ... 18
1.2 Studies of Ion-enhanced Fluorine Etching of Si and SiO_2 24
1.3 Role of Carbonaceous Radicals and Ions in Etching Selectivity 26
1.4 Quantitative Modeling of Ion-Enhanced Surface Reaction Kinetics 29

2. Experimental System 33

2.1 The "3-Beam" Reactor 35
2.2 Sample Mounting Assembly 38
2.3 Diagnostics and Data Acquisition System 42
2.4 XPS and Sample Transfer System 54
2.5 Gas Delivery and Pumping Systems 57
2.6 Summary 60

3. Characterization of Free Radical Beams 61

3.1 Design Considerations for Collisionally-Opaque Effusive Beams 62
3.2 Operating Principles of the Impact Tube 89
3.3 Characterization of the CF_2 Radical Beam 101
3.4 Characterization of the F Atom Beam 118
3.5 Estimation of Errors in Radical Flux and Etching Yield Measurement 130
3.6 Summary 131

4. Ion Production Techniques 133

4.1 Operating Principles of the Retarding Grid Ion Analyzer 134
4.2 Characterization of the Kaufman Ion Source 138
4.3 Characterization of the CECR Ion Source 149
4.4 Summary 155

5. Ion-Enhanced F Etching of Si and SiO_2 156

5.1 Ar^+ Sputtering of Si and SiO_2 157
5.2 Thermal F Etching of Si and SiO_2 163
5.3 Yield Studies of Ar^+/F Etching 168
5.4 Mass Spectrometric Studies of Product Distributions 188

5.5 XPS Studies of Ar^+/F Etched Surfaces 218
5.6 "Site" Models of Ion-Enhanced Etching 229
5.7 Summary 256

6. CF_2 Radical Interactions with Si and SiO_2 257

6.1 Spontaneous Interaction of CF_2 with Si and SiO_2 257
6.2 Yield Studies of Ar^+/CF_2 Etching of Si and SiO_2 273
6.3 XPS Studies of Fluorocarbon Films 286
6.4 "Site" Models of CF_2 Radical Interactions 300
6.5 Summary 309

7. Plasma-Surface Interactions in Fluorocarbon Etching 310

7.1 Influence of CF_2 radicals on Ar^+/F etching 310
7.2 F-CF_2 Surface Recombination Kinetics 316
7.3 XPS Studies of $Ar^+/F/CF_2$ Etched Surfaces 319
7.4 CF_x^+/F Etching of Si and SiO_2 322
7.5 Summary 328

8. Redeposition Processes in Fluorocarbon Plasmas 329

8.1 Redeposition in Ar^+ Sputtering of Si and SiO_2 331
8.2 Redeposition in Ar^+/F Etching 342
8.3 Influence of CF_2 Radicals on Redeposition Rates. 361
8.4 Summary 375

References 376

Appendices 385

A. Reactor Machine Drawings 385
B. Reactor Electrical Systems 479
B.1 Chamber Connectors 480
B.2 Ion Analyzer Power Supply 484
B.3 Kaufman Gun Power Supplies 490
B.4 Data Acquisition Interface 495
C. Acquisition Code 501
D. Doser Design Code 595

List of Figures

Figure 1-1 Schematic description of a parallel plate plasma etching process. Reactive free radicals species and ions are generated in the "glow" region. Ions are accelerated by the plasma sheath fall to produce anisotropic etching.

Figure 2-1 "Cartoon" schematic of the multibeam apparatus and XPS system utilized in this thesis work.

Figure 2-2 Profile cross sectional view of the multibeam etching apparatus.

Figure 2-3 Beam plane cross sectional view of the multibeam apparatus.

Figure 2-4 Summary views of the multibeam chamber port locations and usages.

Figure 2-5 Sample die mounting assembly.

Figure 2-6 UTI-100C mass spectrometer installed on the side flange adapter to allow characterization of source beams.

Figure 2-7 Impact probe system.

Figure 2-8 Probe for ion flux and energy distribution analysis.

Figure 2-9 Geometry of the quartz crystal microbalance (QCM) system used to measure redeposition rate kinetics.

Figure 2-10 XPS chamber constructed by Tepermeister [1992].

Figure 2-11 Multibeam apparatus gas delivery manifold.

Figure 2-12 Surface table pumping schematic.

Figure 3-1 Schematic description of the co-axial flux interception problem

Figure 3-2 Experimental system for in situ beam flux measurement. The impact probe rotates directly into the sample-face position and senses the pressure differential between the molecular beam and chamber background.

Figure 3-3 Relationship of impact tube geometry and beam incidence angle to measured impact pressure.

Figure 3-4 Flux intensity variation $J(\theta)$ of an opaque regime point source versus distance across a 1cm sample, d=1 cm, for various values of the dimensionless parameter η.

Figure 3-5 Fraction of total flux intercepted by a 1cm diameter sample as a function of distance from an opaque regime point source ($a/2R_t$=0.05) for various η values.

Figure 3-6 Fractional interception versus tube-to-target diameter ratio, $a/2R_t$ for various η values.

Figure 3-7 Flux intensity variation of a 0.2 cm i.d. opaque regime source versus radial distance across a 1 cm sample, d=1.0cm, for various values of N_{tot}. Fractional interception versus angle subtended are provided on the opposite axes.

Figure 3-8 Flux intensity variation of a 0.4 cm i.d. opaque regime source at the same values of N_{tot} presented in Figure 3-7.

Figure 3-9 Sensitivity of opaque regime intensity distribution to gas temperature and molecular mass and size, for constant N_{tot}.

Figure 3-10 Comparison of Giordmaine-Wang theory to experimentally measured Ar beam shapes.

Figure 3-11 Comparison of Giordmaine-Wang theory to experimentally measured HFPO beam shapes.

Figure 3-12 Measured peak beam enhancement factors versus HFPO flux. Ionization gauge sensitivity for HFPO is estimated a factor of three greater that N_2. Data taken at normal incidence is uncorrected for beam incidence angle factor of 0.51.

Figure 3-13 Enhancement factors for N_2 flowing through a 1/4" o.d. stainless steel tube (L>40 cm) measured mass spectrometrically over the 1 cm^2 ionizer orifice.

Figure 3-14 Enhancement factors for N_2 flowing through a 1/8" o.d. tube (L>40 cm) measured mass spectrometrically over the 1 cm^2 ionizer orifice.

Figure 3-15 HFPO pyrolysis doser geometry.

Figure 3-16 Variation in amu 50 (CF_2^+) peak height with pyrolysis tube tip temperature.

Figure 3-17 Variation in CF_2^+/CF_3^+ peak ratio with pyrolysis tube tip temperature.

Figure 3-18 Variation in $CF_2^+/C_2F_3O^+$ peak ratio with pyrolysis tube tip temperature.

Figure 3-19 Variation in CF_2^+/CF_3^+ peak ratio with HFPO flow rate at 460°C.

Figure 3-20 Effect of HFPO flow on Ar+ sputtering yields of polysilicon.

Figure 3-21 Effect of HFPO flow on Ar+ sputtering yields of silicon dioxide.

Figure 3-22 Teflon-lined doser assembly used in attempts to produce a CF_3 beam via the H abstraction pathway described by Plumb and Ryan [1984].

Figure 3-23 All alumina ceramic doser design for F atom production.

Figure 3-24 Effect of microwave discharge "on" and "off" states on F beam production.

Figure 3-25 F production efficiency at microwave powers of 70 watts and 90 watts at various F_2 throughputs.

Figure 3-26 Measured XeF_2 enhancement factors from the F discharge source tube, d=1.0 cm.

Figure 3-27 Measured versus predicted beam pressure rise for F atom production from XeF_2.

Figure 3-28 Measured versus predicted beam pressure rise for F atom production from F_2/Xe.

Figure 3-29 Apparent attenuation of F_2 enhancement factors due to sorption on impact tube surfaces.

Figure 4-1 Ion flux probe geometric details.

Figure 4-2 Kaufman Gun schematic showing power supply interconnections.

Figure 4-3 Measured ion beam current versus main chamber pressure for the 1-cm Kaufman gun.

Figure 4-4 Measured ion beam current versus ion energy at constant chamber pressure.

Figure 4-5 Measured ion beam current versus neutralization filament voltage at various probe distances.

Figure 4-6 Predicted neutral-to-ion flux ratio variations from the 1/8" HFPO pyrolysis doser and the 1-cm Kaufman gun.

Figure 4-7 Ion energy distribution developed in the 1-cm Kaufman gun as measured with the gridded probe.

Figure 4-8 Extension mount for usage of the Kaufman ion source with the differential pumping system.

Figure 4-9 CECR source schematic and power supply interconnections.

Figure 4-10 CECR Ar^+ ion beam current versus microwave power without differential pumping.

Figure 5-1 Comparison of the a) Sigmund [1969] and b) Steinbrükel [1989] models for the low energy Ar^+ sputtering of silicon.

Figure 5-2 Comparison of the a) Sigmund [1969] and b) Steinbrükel [1989] models for the low energy Ar^+ sputtering of SiO_2.

Figure 5-3 Schematic description of the "ion-mixing" zone created at the near-surface due to the ballistic mixing action of the bombarding ions.

Figure 5-4 Silicon etching yield (Si removed per Ar^+) versus F/Ar^+ ratio in the mass-transfer-limited etching regime.

Figure 5-5 Silicon etching yield versus F/Ar^+ ratio showing the ion-flux-limited etching regime at large F/Ar^+. Lines shown are the fits of surface kinetic models discussed in Section 5.6.

Figure 5-6 The "Chemical Enhancement Factor" for Ar^+/F etching of silicon relative to Ar^+ physical sputtering. Saturation Ar^+/F etching yields were used in the ratio.

Figure 5-7 Ar^+/XeF_2 versus Ar^+/F etching of silicon at 150 eV and 350 eV ion energy levels.

Figure 5-8 Comparison of 250 eV Ar^+-enhanced etching of silicon by F, XeF_2, and F_2.

Figure 5-9 Comparison of Ar^+/F versus Ar^+/F_2 etching of silicon at 20 eV.

Figure 5-10 Effect of surface temperature, T_s, on Ar^+/F etching of Si and SiO_2.

Figure 5-11 Dependence of silicon Ar^+/F etching yield on absolute Ar^+ ion flux at constant F/Ar^+.

Figure 5-12 SiO_2 etching yield (SiO_2 removed per Ar^+) versus F/Ar^+ ratio in the mass-transfer-limited etching regime.

Figure 5-13 SiO_2 etching yield versus F/Ar^+ ratio showing the ion-flux-limited etching regime at large F/Ar^+. Lines shown are the fits of surface kinetic models discussed in Section 5.6.

Figure 5-14 The "Chemical Enhancement Factor" for Ar^+/F etching of SiO_2 relative to Ar^+ physical sputtering. Saturation Ar^+/F etching yields were used in the ratio.

Figure 5-15 Ar^+/XeF_2 versus Ar^+/F etching of SiO_2 and 150 eV and 350 eV ion energy levels.

Figure 5-16 Comparison of 250 eV Ar^+-enhanced etching of SiO_2 by F, XeF_2, and F_2.

Figure 5-17 Dependence of SiO_2 Ar^+/F etching yield on absolute Ar^+ ion flux at constant F/Ar^+.

Figure 5-18 SiF_4 cracking patterns at 70 eV electron impact energy.

Figure 5-19 F-Si etching product cracking patterns at 70 eV electron impact energy.

Figure 5-20 Identification of an Si_2F_6 product in F-Si etching via observation of the $Si_2F_5^+$ peak with the line-of-sight shutter a) open and b) closed.

Figure 5-21 F-Si etching product cracking patterns at 30 eV electron impact energy.

Figure 5-22 Increase in the SiF^+ (AMU 47) peak versus F flux in room temperature F etching of silicon.

Figure 5-23 Behavior of the $Si_2F_5^+$-to-SiF_3^+ peak ratio versus F flux in F etching of silicon.

Figure 5-24 Comparison of Ar^+/F-Si versus F-Si etching products at 70 eV electron impact energy.

Figure 5-25 Enhancement in $Si_2F_5^+$ fragment production in Ar^+/F etching of silicon for a) open and b) closed shutter positions.

Figure 5-26 Comparison of Ar^+/F-Si versus F-Si etching product cracking patterns at 30 eV electron impact energy.

Figure 5-27 SiF^+-to-SiF_3^+ and SiF_2^+-to-SiF_3^+ peak ratios versus ion energy in Ar^+/F etching of silicon.

Figure 5-28 SiF^+-to-SiF_3^+ and SiF_2^+-to-SiF_3^+ peak ratio versus F/Ar^+ ratio in Ar^+/F etching of silicon.

Figure 5-29 Hypothetical dependence on the product branching parameter $b=\sum SiF_x/SiF_4$ (x=1-3), versus $\sqrt{E_i}$ for Ar_x/F etching of silicon. Semi-quantitative results from various literature studies are shown.

Figure 5-30 Hypothetical dependence on the product branching parameter $b=\sum SiF_x/SiF_4$ (x=1-3), versus $\sqrt{E_i}$ for Ar^+/F etching of SiO_2. Semi-quantitative results from various literature studies are shown.

Figure 5-31 Behavior of the Si(2p) XPS peak versus F/Ar+ ratio in 150 eV Ar^+/F etching of silicon.

Figure 5-32 Behavior of the F(1s) XPS peak versus F/Ar^+ ratio in the 150 eV Ar^+/F etching of silicon. Peak areas are corrected and normalized by total Si(2p) intensity.

Figure 5-33 Behavior of the O(1s) XPS peak versus F/Ar^+ ratio in the 150eV Ar^+/F etching of silicon. Peak areas are corrected and normalized by total Si(2p) intensity.

Figure 5-34 Comparison of the F(1s) peak growth versus F/Ar^+ ratio at 150 eV and 500 eV ion bombardment energy. Solid lines represent model predictions for near-surface fluorination.

Figure 5-35 Behavior of the F(1s) peak versus ion energy at constant F/Ar^+ for Ar^+/F etching of silicon. Solid line represent predictions of models.

Figure 5-36 F(1s)-to-Si(2p) elemental ratios from corrected XPS data for Ar^+/F etched silicon at 150 and 500 eV bombardment energies.

Figure 5-37 Behavior of the F(1s) XPS peak versus F/Ar^+ ratio in the 250 eV Ar^+/F etching of SiO_2.

Figure 5-38 Si(2p) XPS spectra for Ar^+/F etched SiO_2 showing low binding energy tail due to $Si-F_x$ bonding.

Figure 5-39 F(1s)-to-Si(2p) elemental ratios from corrected XPS data for Ar^+/F etched SiO_2 at 250 eV ion bombardment energy.

Figure 5-40 Behavior of the F(1s) peak versus ion energy at constant F/Ar^+ for Ar^+/F etching of SiO_2. O(1s) peak behavior is also shown.

Figure 5-41 Conceptual comparison between a) mechanistic Ar^+/F surface kinetic model and b) the CSTR-"site" model.

Figure 5-42 Mechanistic model of Ar^+/F etching of silicon showing hypothetical reaction pathways to volatile products.

Figure 5-43 Graphical decomposition of Ar^+/F etching yield data for the a) 150 eV etching of SiO_2, and b) the 20 eV etching of silicon showing the relative contributions of physical sputtering, thermal etching, and ion-enhanced etching to the total measured yields.

Figure 5-44 Behavior of the fitted β_2 parameter versus $\sqrt{E_i}$ for the Ar^+/F etching of silicon.

Figure 5-45 Behavior of the fitted β_2 parameter versus $\sqrt{E_i}$ for the Ar^+/F etching of SiO_2.

Figure 5-46 Predicted behavior of the near-surface fluorination, θ_F and the relative F atom sticking coefficient, s_F/s_o, versus F/Ar^+ ratio for the 150 eV Ar^+/F etching of silicon.

Figure 5-47 Predicted product distribution behavior in the Ar^+/F etching of silicon as a function of F/Ar^+ ratio at 200 eV.

Figure 5-48 Predicted product distribution behavior in the Ar^+/F etching of SiO_2 as a function of F/Ar^+ ratio at 200 eV.

Figure 6-1 Laser interferometry signals during exposure of Ar^+ sputter cleaned a) polysilicon and b) SiO_2 films to a CF_2 flux of 5.6×10^{15} $cm^{-2}\text{-}s^{-1}$, major chart divisions are 4 minutes. Initial cycle shown is during Ar^+ sputter cleaning.

Figure 6-2 Variation of apparent CF_2 sticking coefficient, γ_{CF2}, on the non-bombarded QCM surface with total CF_2 exposure.

Figure 6-3 Calculated C-to-Si and F-to-Si elemental ratios from XPS studies of CF_2 exposed Si and SiO_2 surfaces.

Figure 6-4 Comparison of Si(2p) XPS spectra of a) "clean" Ar^+ sputtered silicon with b) silicon exposed to a CF_2 flux of $3.0x10^{16}$ for 5 minutes (>1000L).

Figure 6-5 Comparison of C(1s) XPS spectra of a) "clean" Ar^+ sputtered silicon with b) silicon exposed to a CF_2 flux of $3.0x10^{16}$ for 5 minutes (>1000L).

Figure 6-6 Comparison of F(1s) XPS spectra of a) "clean" Ar^+ sputtered silicon with b) silicon exposed to a CF_2 flux of $3.0x10^{16}$ for 5 minutes (>1000L).

Figure 6-7 Comparison of Si(2p) XPS spectra of a) "clean" Ar^+ sputtered SiO_2 with b) SiO_2 exposed to a CF_2 flux of $3.0x10^{16}$ for 5 minutes (>1000L).

Figure 6-8 Comparison of C(1s) XPS spectra of a) "clean" Ar^+ sputtered SiO_2 with b) SiO_2 exposed to a CF_2 flux of $3.0x10^{16}$ for 5 minutes (>1000L).

Figure 6-9 Comparison of F(1s) XPS spectra of a) "clean" Ar^+ sputtered SiO_2 with b) SiO_2 exposed to a CF_2 flux of $3.0x10^{16}$ for 5 minutes (>1000L).

Figure 6-10 Measured silicon etching yield versus CF_2/Ar^+ flux ratio. Solid lines represent model results.

Figure 6-11 Measured silicon etching yield versus absolute Ar^+ flux, at constant CF_2/Ar^+.

Figure 6-12 Effect of substrate temperature on CF_2/Ar^+ silicon etching yields.

Figure 6-13 Mass spectral comparison of AMU 85 (SiF_3^+) to fluorocarbon background AMU 81 ($C_2F_3^+$) in a) Ar^+/CF_2 etching of silicon versus b) CF_2 exposure only.

Figure 6-14 Measured SiO_2 etching yield versus CF_2/Ar^+ ratio. Solid lines represent model results.

Figure 6-15 Measured SiO_2 etching yield versus absolute Ar^+ flux, at constant CF_2/Ar^+.

Figure 6-16 Effect of CF_2/Ar^+ ratio on SiO_2-to-Si etching rate selectivity.

Figure 6-17 C(1s) peak intensity of silicon exposed to increasing CF_2/Ar^+ flux ratio. C(1s) peak area is corrected and normalized by total Si(2p).

Figure 6-18 Comparison of Si(2p) spectra of silicon exposed to increasing CF_2/Ar^+ flux ratio.

Figure 6-19 Calculated C-to-Si elemental ratios from XPS studies of Ar^+/CF_2 exposed silicon.

Figure 6-20 Comparison of F(1s) spectra of silicon exposed to increasing CF_2/Ar^+ flux ratio.

Figure 6-21 Calculated F-to-Si elemental ratios from XPS studies of Ar^+/CF_2 exposed silicon.

Figure 6-22 Comparison of Si(2p) spectra of silicon with increasing Ar^+ energy, at constant $CF_2/Ar^+ = 50$.

Figure 6-23 Calculated C-to-Si and F-to-Si elemental ratios from XPS studies of Ar^+/CF_2 exposed silicon with increasing Ar^+ energy, at constant $CF_2/Ar^+ = 50$.

Figure 6-24 C(1s) peak intensity of SiO_2 exposed to increasing CF_2/Ar^+ flux ratio.

Figure 6-25 Comparison of C(1s) spectra of SiO_2 exposed to increasing CF_2/Ar^+ flux ratio.

Figure 6-26 Calculated C-to-Si elemental ratios from XPS studies of Ar^+/CF_2 exposed SiO_2.

Figure 6-27 Calculated F-to-Si elemental ratios from XPS studies of Ar^+/CF_2 exposed SiO_2.

Figure 6-28 Comparison of C(1s) spectra of SiO_2 with increasing Ar^+ energy, at constant CF_2/Ar^+.

Figure 6-29 Calculated C-to-Si and F-to-Si elemental ratios from XPS studies of Ar^+/CF_2 exposed SiO_2 with in increasing Ar^+ energy, at constant CF_2/Ar^+.

Figure 7-1 Three beam studies of $Ar^+/F/CF_2$ interactions on silicon at 250 eV bombardment energy.

Figure 7-2 Three beam studies of $Ar^+/F/CF_2$ interactions on silicon at 20 eV bombardment energy.

Figure 7-3 Effect of ion bombardment energy on Ar+/F silicon etching rate suppression by CF_2.

Figure 7-4 Three beam studies of $Ar^+/F/CF_2$ interactions on SiO_2 at 250 eV bombardment energy.

Figure 7-5 QCM studies showing the a) initial rate removal of F via F-CF_2 recombination and b) the eventual net deposition of CF_2.

Figure 7-6 Comparison of an a) Ar^+/CF_2 etched silicon Si(2p) XPS spectra to b) $Ar^+/F/CF_2$ etched silicon at 150 eV, CF_2/Ar^+ ~50 and F/Ar^+ ~400 .

Figure 7-7 Comparison of Ar^+/CF_2 etched SiO_2 a) Si(2p), b) C(1s) and c) F(1s) XPS spectra to $Ar^+/F/CF_2$ etched SiO_2 surfaces d)-f) at 150 eV, CF_2/Ar^+ ~50 and F/Ar^+ ~400.

Figure 7-8 CF_x^+ etching of silicon and SiO_2 using a CF_4 CECR plasma beam.

Figure 7-9 CF_x^+/F versus Ar^+/F etching of silicon at 20 eV.

Figure 7-10 CF_x^+/F versus Ar^+/F etching of SiO_2 at 20 eV.

Figure 7-11 Comparison of SiO_2-to-Si etching selectivity in 20 eV a) $Ar^+/F/CF_2$ etching and b) CF_x^+/F etching.

Figure 8-1 Schematic representation of the redeposition experiments showing the analogy to trench sidewall deposition in plasma etching.

Figure 8-2 Redeposition rates measured during the sputtering of silicon and SiO_2 as a function of Ar^+ ion flux at 500 eV.

Figure 8-3 Redeposition rates measured during the sputtering of silicon and SiO_2 as a function of $\sqrt{E_i}$.

Figure 8-4 Apparent sticking coefficient for sputtered silicon and SiO_2 redepositing of the QCM surface as calculated from equation (5-7) as a function of ion flux.

Figure 8-5 Apparent sticking coefficient for sputtered silicon and SiO_2 redepositing of the QCM surface as calculated from equation (5-7) as a function of ion energy.

Figure 8-6 Angular characteristics of sputtered silicon redeposition.

Figure 8-7 Angular characteristics of sputtered SiO_2 redeposition.

Figure 8-8 Redeposition rates measured during Ar^+/F etching of silicon as a function of F/Ar^+ flux ratio.

Figure 8-9 Redeposition rates measured during Ar^+/F etching of SiO_2 as a function of F/Ar^+ flux ratio.

Figure 8-10 Predicted production rates for Ar^+/F etching of silicon as a function of F/Ar^+ ratio at a) 200 eV and b) 500 eV ion energy.

Figure 8-11 Predicted production rates for Ar^+/F etching of SiO_2 as a function of F/Ar^+ ratio at a) 200 eV and b) 500 eV ion energy.

Figure 8-12 Predicted trends in product redeposition for 200 eV Ar^+/F etching of silicon given $\gamma_{Si}=0.15$ and $\gamma_{SiF_x}=0.01$.

Figure 8-13 Predicted trends in product redeposition for 500 eV Ar^+/F etching of silicon given $\gamma_{Si}=0.15$ and $\gamma_{SiF_x}=0.01$.

Figure 8-14 Predicted trends in product redeposition for 200 eV Ar^+/F etching of SiO_2.

Figure 8-15 Predicted trends in product redeposition for 500 eV Ar^+/F etching of SiO_2.

Figure 8-16 Redeposition rates measured during Ar^+/F etching of silicon as a function of $\sqrt{E_i}$.

Figure 8-17 Redeposition rates measured during Ar^+/F etching of SiO_2 as a function of $\sqrt{E_i}$.

Figure 8-18 Predicted production rates for Ar^+/F etching of silicon as a function of $\sqrt{E_i}$ at F/Ar^+ ratios of a) 50 and b) 500.

Figure 8-19 Predicted production rates for Ar^+/F etching of SiO_2 as a function of $\sqrt{E_i}$ at F/Ar^+ ratios of a) 50 and b) 500.

Figure 8-20 Predicted trends in product redeposition versus $\sqrt{E_i}$ for Ar^+/F etching of silicon at F/Ar^+ ratios of a) 50 and b) 500.

Figure 8-21 Predicted trends in product redeposition versus $\sqrt{E_i}$ for Ar^+/F etching of SiO_2 at F/Ar^+ ratios of a) 50 and b) 500.

Figure 8-22 Angular characteristics for redeposition in Ar^+/F etching of silicon.

Figure 8-23 Redeposition rates measured during Ar^+/CF_2 etching of silicon as a function of CF_2/Ar flux ratio.

Figure 8-24 Redeposition rates measured during Ar^+/CF_2 etching of SiO_2 as a function of CF_2/Ar^+ flux ratio.

Figure 8-25 Relative contributions of silicon and CF_x fragment redeposition in the Ar^+/CF_2 etching of silicon at 500 eV.

Figure 8-26 Apparent sticking coefficient for CF_x fragments in Ar^+/CF_2 etching of silicon and SiO_2.

Figure 8-27 Relative contributions of Si, O, and CF_x fragment redeposition in the Ar^+/CF_2 etching of SiO_2 at 500 eV.

Figure 8-28 Measured redeposition rates in Ar^+/CF_2 etching of silicon versus $\sqrt{E_i}$.

Figure 8-29 Measured redeposition rates in Ar^+/CF_2 etching of SiO_2 versus $\sqrt{E_i}$.

Figure 8-30 Apparent sticking coefficient for CF_x fragments in Ar^+/CF_2 etching of silicon and SiO_2 versus ion energy.

Figure 8-31 Angular characteristics for redeposition in Ar^+/CF_2 etching of silicon at 500 eV.

Figure 8-32 Angular characteristics for redeposition in Ar^+/CF_2 etching of SiO_2 at 500 eV.

List of Tables

Table 3-1 Nomenclature for Chapter 3.

Table 3-2 Typical values of the critical length parameter, Λ, for 300 K argon.

Table 3-3 HFPO Cracking Patterns.

Table 5-1 Si and SiO_2 Low Energy Sputtering Model Parameters

Table 5-2 Arrhenius Rate Parameters for F Etching of Si and SiO_2

Table 5-3 Mass Peaks Observed in the F-Si System

Table 5-4 F-Si System 70 eV Product Cracking Patterns

Table 5-5 Ar+/F-Si System 70 eV Product Cracking Patterns

Table 5-6 Ar+/F-Si, SiO_2 Systems 30 eV Product Cracking Patterns

Table 5-7 Ar+/F-Si Phenomenological Surface Kinetic Model

Table 5-8 Ar+/F-SiO_2 Phenomenological Surface Kinetic Model

Table 5-9 Ar+/F-Si Model Parameters

Table 5-10 Ar+/F-SiO_2 Model Parameters

Table 6-1 Ar^+/CF_2 SiO_2 Etching Model Parameters

Table 6-2 Ar^+/CF_2 Si Etching Model Parameters

Chapter 1

Introduction

In the previous decade, plasma etching was firmly established as a standard "unit operation" in microfabrication for the transfer of fine line lithographic patterns into thin films [Wolf and Tauber, 1986], and will continue to play a vital role in submicron device fabrication processes in the 1990's. However, much more basic research is necessary in the area of plasma-surface interactions to reliably etch submicron features, especially in low pressure processes where the geometric length scales are on the order of the plasma gas mean free path. Etching profile control under these conditions becomes problematic due to a broad class of aspect-ratio-dependent etching phenomenon which are generally described as "microscopic non-uniformities" [Gottscho et al., 1992]. From the viewpoint of a surface scientist, a "plasma" or "glow discharge" is simply a method to generate large surface fluxes of reactive radicals (e.g. F, CF_x) and directed energetic ions (e.g CF_x^+) as shown in Figure 1-1. The synergistic effect of the directed ions in combination with absorbed neutrals results in the rapid production of volatile substrate products when the correct gas chemistry is chosen, and gives plasma processes the ability to remove material in an anisotropic manner [Coburn and Winters, 1979]. Although the "de-coupling" of the plasma gas-phase chemistry and physics from the etching surface is conceptually useful in understanding the results presented herein, one should be aware that this is an artificial separation. Comprehensive plasma processes models must incorporate the interplay between the gas-phase and surface chemistries.

1.1 Surface Interactions and "Microscopic Non-Uniformity" in Plasma Etching

A mechanistic understanding of plasma-surface interactions in the etching of silicon and

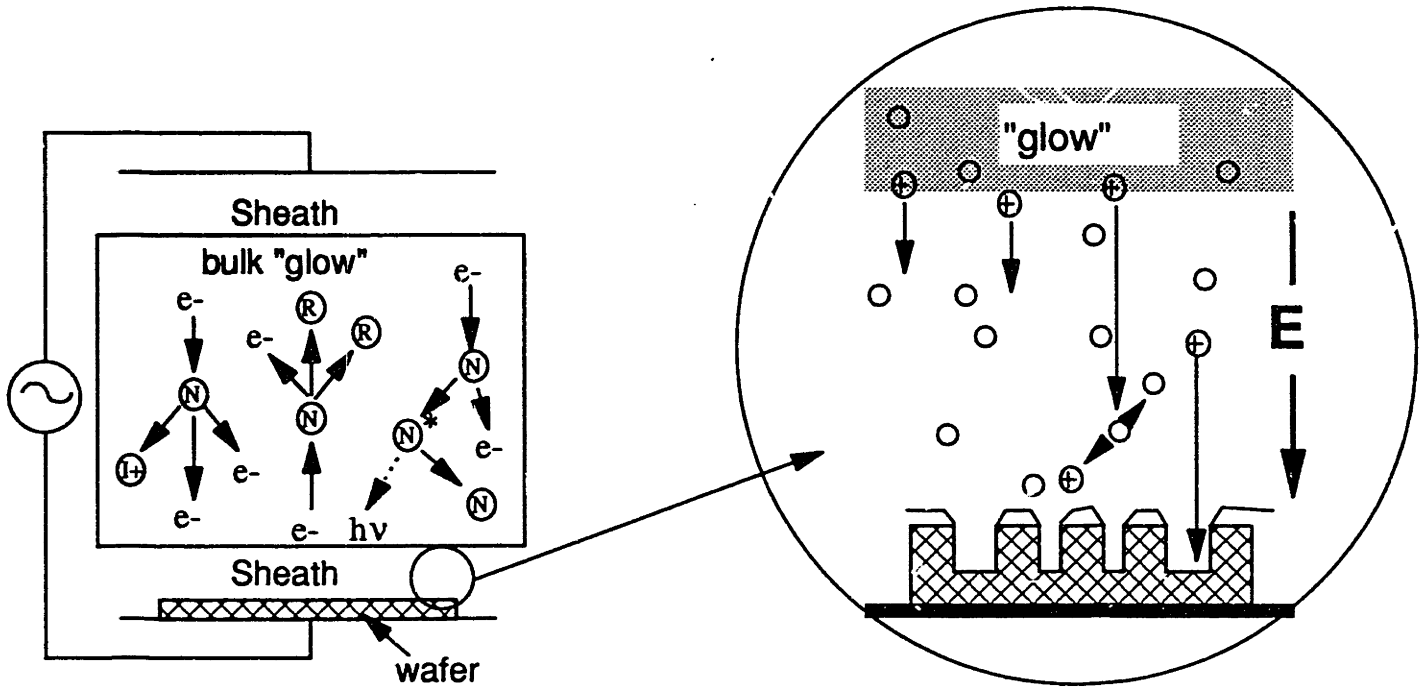

Bulk "glow" region

- pressure 10^{-3} to 1 torr
- 10^{8} to 10^{12} e^{-}/cm^{3}
- 10^{-4} to 10^{-7} ion fraction
- free radicals 10-30 %

Sheath Region

- directed energetic ions
  <Ei> 50-500 eV
- narrow angular dispersion

Figure 1-1. Schematic description of a parallel plate plasma etching process. Reactive free radical species and ions are generated in the "glow" region. Ions are accelerated by the plasma sheath fall to produce anisotropic etching.

silicon dioxide by fluorocarbon plasmas is critical to the development of predictive models for plasma process design. Currently, there are several efforts underway to develop numerical models of etching profile evolution [Shaqfeh et al., 1989; Jackson et al., 1989; McVittie et al., 1990] during plasma etching, but they have no predictive value because the surface etching kinetics have not been quantified as a function of neutral-to-ion flux ratios, ion energies and incidence angles, and substrate temperature. Due to the relatively high pressures and harsh chemical environments involved in commercial etching processes, detailed in-situ studies of plasma-surface interactions are very difficult. In addition, neutral and ion fluxes to the wafer surface are highly correlated with the discharge physics in the plasma environment, making it difficult to independently assess the role of individual species fluxes on the surface chemistry. In an effort to gain insight into the dominant surface processes occurring during plasma etching, molecular beam studies of ion-enhanced and reactive ion etching have frequently been described in the literature over the past decade [Winters et al., 1983; Mayer et al., 1982; Harper et al., 1981]. Using this technique, system base pressures can be maintained in the high vacuum range, allowing the application of *in situ* surface analytical techniques such as line-of-sight mass spectrometry, XPS, and AES. However, due to experimental limitations, the neutral and ion flux and energy regimes studied to date have not been representative of the plasma environment, and early studies which employed single reactive beams such Cl_2 or XeF_2 could not represent the chemical complexity of the ion and radical surface interactions.

We have constructed a molecular beam apparatus which allows the synthesis of dominant species fluxes impinging upon a wafer during fluorocarbon plasma etching. These include CF_2 as a polymer forming precursor, atomic fluorine as the primary etchant, and Ar^+ or CF_x^+ ion bombardment. Generation of this "synthetic" plasma allows the decoupling of plasma-surface interactions from the plasma gas-phase chemistry and transport effects so that etching yields may

be systematically studied as a function of neutral-to-ion flux ratios. Our work represents an advancement in the application of molecular beams to the study of plasma surface interactions through the use of multiple reactive beams with well characterized fluxes at the sample surface. These fluxes are within an order of magnitude of those achieved in low pressure fluorocarbon plasma processing.

The down-scaling of LSI feature sizes into the submicron regime in the last decade, and the need to etch large aspect ratio trench structures, has revealed a number of effects which make profile control in plasma etching a difficult task. These aspect-ratio-dependent etching phenomenon, which have been broadly characterized as "microscopic non-uniformities" [Gottcho et al. 1992] or "pattern-dependent etching effects" [Sawin et al., 1989], make profile control especially problematic when it is necessary to etch features of large aspect ratio next to much wider features or open areas. The term "microscopic non-uniformity" has been generically applied to describe many aspect-ratio-related changes in etching characteristics to include: variations in total etch rate (RIE lag), variation in profile shapes (dovetailing, bowing, faceting, mousebites), variations in selectivity to the underlying film (trenching), and variations in film morphology. It is obvious that a detailed understanding of the near-surface ion/neutral transport and reaction effects in plasma processing is necessary to understand the physical basis behind these phenomenon.

Since the surface chemistry involved in parallel plate plasma etching tools is dominantly ion-driven, physical processes which result in the modification of total ion flux, or ion trajectories into features of differing aspect ratio will produce different etching profiles and depths. For instance, the ion angular distribution which develops due to collisional phenomenon in the plasma sheath, results in a decreased "view factor" of the off-angle ions into narrow (large aspect ratio) versus wide trenches. This view factor effect has been shown in experiments [Chin et al., 1985]

and simulations [Pelka et al., 1989] to result in trench bowing and RIE lag. Distortion of ion trajectories via feature charging may also lead to aspect-ratio-dependent profile development when insulating surfaces are present [Arnold et al., 1991]. Ion scattering from photoresist sidewalls may lead to mousebites and bowing in narrow features, while trenches and dovetails may result in wider features or at the end of line sets where the scattered ions eventually reach the bottom [Dalton et al., 1992].

While the bombarding ions supply the energy to activate surface reactions, net etching/deposition rates in plasma processes as well as the etching product distributions are determined by the relative arrival ratios of neutral-to-ionic species at the various feature surfaces. As a result, aspect-ratio related phenomenon which change the relative flux of neutral-to-ionic species into features, or the flux of etching products out of features may also result in microscopic non-uniformities. Coburn and Winters [1989] recognized that the conductance limitations of large aspect ratio features will attenuate the flux of randomly directed atomic etchants to the bottom of large aspect ratio features, due to the significant probability of reaction, or re-emission in the wrong direction after wall collisions. This same conductance limitation will result in a reduced probability of 1) depositing fragments from the plasma reaching the trench bottom, and 2) of "sticky" products resulting from etching at the trench bottom leaving the trench without redepositing. These two processes have been shown in simulations to result in bottle-necking and V-shaped trenches [Lii and Jorne, 1990]

In this thesis, we use the term "redeposition" in reference to the second process noted above; that of etching product species and/or resputtered fragments from the trench or mask surfaces permanently sticking to feature sidewalls. Other authors [Lii and Jorne, 1990] have extended application of the term "redeposition" to the process whereby etching products which have re-entered or been scattered from the gas-phase subsequently deposit on the wafer surface.

We prefer to refer to this process as "plasma deposition" and reserve the term "redeposition" to refer to the line-of-sight effect only. The probability of redeposition occurring during plasma etching of a given feature is a function of the:

i) product-type evolved (e.g. its sticking coefficient and subsequent volatility),

ii) product evolution mechanism (e.g. the energy and directionality of the product), and

iii) probability of collision with at feature sidewall before re-entering the gas-phase.

Accordingly, redeposition effects are by nature very aspect-ratio dependent, since modification of neutral-to-ion ratios at the trench bottom will effect the etching mechanism and product distribution, and the probability of sidewall collisions increases with aspect ratio.

Several researchers have recognized the importance of redeposition processes in the modification of trench shapes during plasma etching, RIE, or sputtering processes, and several efforts have been made to qualitatively understand this effect through the use of profile simulation tools such as SAMPLE [Lii and Jorne, 1990; Lehmann et al. 1977]. The problem becomes especially important in the etching of deep narrow trenches e.g. for storage capacitors, or in subtractive processing via sputter etching where the products evolved may be very "sticky" pure metals and unsaturated fragments [Gloersen, 1976]. The combination of fragment redeposition and facet formation in sputter etching results in the formation of V-shaped trenches at large aspect ratios [Lehmann et al. 1977; Gloersen, 1975], and is also observed under certain conditions to cause surface roughening in the form of "cones" [Solberg and Spain, 1990]. In plasma etching processes, however, Lii and Jorne [1990] point out that the combination of lower ion energies, and redeposition of carbonaceous, halide, and/or oxide fragments is an important anisotropy mechanism. In their simulations, sidewall deposits were shown to reduce the net etching rates of the sidewalls by off-normal ions, thus reducing sidewall "bowing" effects. Sidewall deposits may also enhance anisotropy by passivating the surface toward thermal attack by sorbed free radicals

such as F or Cl, effectively presenting a diffusion barrier [Mogab and Levinstein, 1980]. While several researchers have discussed the importance of masking polymer redeposition in achieving anisotropy in plasma etching processes, Alfred et al. [1989] found that Si and oxygen residues were present in sidewall films as well, in Cl-based etching of polysilicon and TaSi. They attributed this material to redeposition of sputter etched material from trench bottoms once the polysilicon or nitride layers were cleared. Although no compositional analysis was performed on the redeposited films in this work, the chemical constituency of sidewall deposits formed in the fluorocarbon environment has been studied in detail by Oehrlein et al. [1989]. Despite the consensus concerning the importance of redeposition in pattern dependency effects, little experimental work has been conducted concerning the redeposition rate kinetics in halocarbon etching environment. In Chapter 8 we present measurements of redeposition rate kinetics representative of fluorocarbon plasma processes.

1.2 Studies of Ion-Enhanced Fluorine Etching of Si and SiO_2

In the literature, it is established that atomic fluorine is a primary etchant in fluorocarbon plasma etching of both silicon and silicon dioxide, resulting in the production of volatile SiF_x products. Flamm et al. [1979; 1981] provide rate expressions and a plausible kinetic mechanism for the spontaneous thermal etching of both Si and SiO_2, where SiF_4 and SiF_2 have been suggested as the dominant and secondary reaction products, respectively. Winters and Plumb [1991] have recently shown that Si_2F_6 and higher fluorosilanes are significant secondary Si etching products near room temperature, and that SiF_2 production is small until surface temperatures reach 600K. Thermal etching of silicon by fluorine atoms proceeds slowly (~0.1 nm/min @ 25°C and 0.1 mTorr F), and large F partial pressures are required in barrel type etchers to achieve reasonable silicon etch rates in the absence of ion bombardment. The thermal etching rate of

silicon dioxide by F atoms is over an order of magnitude slower.

The etching of Si and SiO_2 by fluorine is greatly enhanced when the surface is simultaneously exposed to a flux of energetic ions, as is the case in parallel plate (diode configuration) plasma etching. In addition, the production of unsaturated products (SiF_x, x=1-3) via collision cascade becomes important, and may constitute over to 50% of the product stream at 3 keV ion energies when fluorine surface coverages are low [Haring et al., 1982]. Coburn and Winters [1979] initially revealed a synergism between the ions and neutral etchant in which the composite etching rate is much higher than the sum of the spontaneous etching rate and ion physical sputtering rate. Several researchers have since studied ion-enhanced fluorine etching of silicon through the use of XeF_2, a convenient precursor which apparently dissociates upon impact with the surface, providing a source of atomic fluorine. Tu et al. [1981] recognized that increased fluorine (XeF_2) uptake by a silicon surface under ion bombardment was a critical step in the ion-enhanced etching mechanism due to simple mass balance considerations e.g. more reactant must adhere to the surface as the steady-state evolution of etching products increases. Ion bombardment increases the apparent sticking coefficient for F on the etching surface due to creation of free valences (dangling bonds) through several mechanisms including lattice damage, chemical assisted physical sputtering of SiF_x fragments, and direct promotion of SiF_4 formation, which volatilizes and exposes virgin silicon. Winters [1988] emphasizes that ion-mixing of surface fluorine into an amorphized near surface region (typically 1-5 nm depending on ion energy) is required for the formation of fully saturated volatile products, and the continual exposure of new silicon surface sites.

Studies of ion-enhanced fluorine etching of silicon and silicon dioxide done in the past typically employed much higher ion energies and lower ion fluxes than are typical of commercial plasma processes. We felt at the start of this thesis work that the state of understanding did not

necessarily allow the extrapolation of this data into higher flux and lower energy regimes. In addition, some controversy has evolved concerning the ability of XeF_2 to emulate the surface flux of atomic fluorine generated in a plasma etching process. We have avoided this issue by using a well characterized flux of microwave-discharge-produced atomic fluorine. In the work described in Chapter 5, inert Ar^+ ions in the energy range of 20-500 eV were using in conjunction with this F atom source to study ion-enhanced F-Si and F-SiO_2 surface chemistries in the energy and flux regimes typical of fluorine-based plasma processes

1.3 Role of Carbonaceous Radicals and Ions in Etching Selectivity

There are several fluorocarbon radical species present in the fluorocarbon plasma environment including CF_3, CF_2, and CF, where CF_2 is typically the most plentiful by over an order of magnitude due to its gas-phase stability [Kiss, 1991]. It has been suggested that CF_2 and CF_3 may be active participants in the fluorocarbon plasma etching of SiO_2 [Heinecke, 1975; Flamm and Donnelly, 1981]. Selectivity of SiO_2 etching over silicon etching in fluorocarbon plasmas is attributed to carbonaceous film formation on the silicon surface [Jaso and Oehrlein, 1988], while the highly anisotropic nature of SiO_2 etching is attributed to the strongly ion-enhanced nature of the etching process. Previous research into these mechanisms has included post-process surface analysis with X-ray photoelectron spectroscopy (XPS), Auger electron spectroscopy (AES), and ellipsometry. Other research efforts have focused on the relative importance of the radical and ionic species by isolating these species outside of the plasma environment in "beam" studies. In the studies presented in Chapters 6 and 7, a beam of CF_2 was used to represent the effect of fluorocarbon radicals, and their ability to enhance the etching of SiO_2 and suppress the etching of silicon under ion bombardment were investigated. To our knowledge, our work is the first to employ a "clean" high flux source of carbonaceous free

radicals for the study of competitive interactions with F in the ion-enhanced etching of silicon.

Researchers have recognized the importance of carbonaceous surface films in suppressing silicon etching for well over a decade. In the course of early efforts to develop a selective plasma chemistry for the etching of contact windows in SiO_2 films on silicon substrates, Heinecke [1975] found SiO_2:Si selectivities up to 15 in CF_4/H_2 mixtures. He suggested that scavenging of gas-phase fluorine and adsorption of fluorocarbon free radicals on the silicon surface were the operative mechanisms. Coburn and Winters [1979] point out that these passivating fluorocarbon residues may form as the result of ion impact dissociation of physisorbed species and surface bombardment by carbonaceous ions as well as through dissociative chemisorption of free radicals. Other researchers have pointed to the importance of redeposition of sputtered polymeric fragments in achieving sidewall passivation in silicon trench etching [Lehmann, 1977]. A number of investigators have applied surface diagnostic tools such as XPS and AES to the compositional analysis of these surface films on post-etched wafers. The general conclusion of the post-process surface studies is that while carbonaceous films form on the surface of silicon, little carbonaceous residue is found on the surface of SiO_2 [Oshima, 1979; Jaso and Oehrlein, 1988]. The probable explanation for the absence of a carbon layer on the SiO_2 surface is the availability of oxygen to form volatile carbon-fluorine-oxygen species. *Ab initio* calculations [Jenichen and Johansen, 1988] show COF_2 to be very weakly bound on SiO_2 surfaces making it a likely product of the etching process. In contrast, Thomas et al. [1987] found Teflon-like polymeric deposits with CF_2, CHF, and C-C functionalities in XPS studies of films formed in CF_4/H_2 plasmas with complete silicon etching suppression. Oehrlein and co-workers [1989] have suggested that thick passivating fluorocarbon polymers may propagate once a Si-C "bridging" layer is established. Conditions under which finite silicon etching rates are observed require a thin enough film to allow "ion-mixing" of silicon into an amorphized $Si_xC_yF_z$ layer, and the net removal of silicon containing

fragments.

Several papers have appeared in which reactive independent radical sources were employed to study surface interactions in carbonaceous free radicals outside of the discharge environment. Joyce et al. [1988] and Robertson et al. [1988] both confirm chemisorption of CF_3 and initial etching of clean silicon which is suppressed below measurable levels upon formation of a carbon overlayer. CF_2 was also found to dissociatively chemisorb on clean silicon, but no spontaneous steady-state etching was maintained [Langan et al., 1989]. The reactivity of CF_2 with SiO_2 has been studied by several researchers. Selamoglu et al. [1986] reported that SiO_2 does not etch in the presence of CF_2 without simultaneous irradiation of the surface. Langan et al. [1989] performed XPS analysis of SiO_2 surfaces exposed to CF_2 radicals and found that CF_2 adsorbs on the SiO_2 surface, but does not dissociate or react with the surface. After bombardment of the surface with energetic ions, the CF_2 adsorption probability increased, but there was still negligible dissociation. These studies suggest that while CF_2 does not spontaneously etch silicon or SiO_2, CF_2 will etch SiO_2 when the surface is under simultaneous energy irradiation (e.g. ion bombardment).

In addition to the flux of neutral radical species, there is significant ion bombardment of the wafer surface in a parallel-plate plasma reactor, which "drives" the neutral-surface chemistry by supplying the activation energy for reaction. In a fluorocarbon plasma these ions are mainly CF_3^+, CF_2^+, and CF^+ [Butterbaugh, 1990]. Due to difficulties in making a clean, high flux beam of CF_3^+, inert Ar^+ ions of similar mass have been substituted in past studies of the ion-enhanced etching of silicon and SiO_2 as to decouple the effects of ion inertia and ion chemistry. Efforts have been made to more closely simulate the fluorocarbon plasma chemistry in beam studies through the use of CF_x^+ ions mixtures produced in a CF_4 DC discharge source [Harper, 1981; Mayer, 1982]. The results of these studies are, however, difficult to interpret quantitatively due

to the production of multiple ionic and free radical species. Fluorocarbon ion interactions with silicon surfaces have been the focus of a number of papers attempting to describe the tradeoff between carbon deposition and etching in fluorocarbon plasmas. Coburn et al. [1977] have shown that Ar^+ ions etch silicon more rapidly than CF_3^+ at low ion energies, but that CF_3^+ etching yields are nearly twice as high in the keV range where the carbon deposits are easily cleared. Harper et al. [1981] used a CF_4 DC discharge source to show that low energy CF_x^+ ions etched silicon at the same rate as Ar^+, while SiO_2 etching rates were greatly enhanced by the reactive ions. It has been demonstrated in several studies that these molecular ions, which supply chemical reactants to the surface as well as energy, remove a larger number of SiO_2 molecules than the noble gas ion of similar mass. For example, the etching yield (number of SiO_2 molecules removed per incoming ion) has been measured at an ion energy of 500 eV to be 0.2 for Ar^+ and 0.5 for CF_x^+ by Tu et al. [1981]. The observed SiO_2 rate enhancement observed for CF_x^+ versus Ar^+ ions, and the subsequent silicon etching rate suppression observed in low energy CF_x^+ ion bombardment, allow large SiO_2-to-Si etching selectivities to be observed in fluorocarbon ion etching [Mayer, 1982; Heath, 1982].

In most of our work, we have similarly separated the ion mass and chemistry effects which make interpretation of previous studies difficult, and instead focused on the interaction between neutral chemistry and ion energetics. Some studies using a CF_x^+ ion mixture at near-threshold energies are reported in Chapter 7.

1.4 Quantitative Modeling of Ion-Enhanced Surface Reaction Kinetics

Comprehensive models of the ion-enhanced surface kinetics described above require complete knowledge of product distributions, surface bonding states and radical sticking coefficients in the presence of energetic ion bombardment. *In situ* information at this level of

detail is, however, not currently available. In addition, the continuous mixing of the surface adsorbates into the near-surface bulk region, complicates the kinetic treatment of this problem beyond the scope of classical treatises on gas-solid reactions at well-defined surfaces.

Winters and Coburn [1985] have pointed out that the basic steps for a chemical etching process parallel those in many heterogeneous catalysis mechanisms. These steps include 1) adsorption of reactive gas species on the surface, 2) chemical reaction to produce a product molecule, and 3) desorption of the product molecule into the gas phase, liberating a clean adsorption site. Depending on the specific etchant-substrate system, ion-bombardment may enhance (or impede) any or all of these steps. At steady-state, all steps proceed at the same rate, but one is rate-limiting; our data indicates both neutral-adsorption limited and ion-flux limited etching regimes as a function of the neutral-to-ion flux ratio and the ion energy. The ion-enhanced etching of Si and SiO_2 by XeF_2 has been studied extensively; several of the proposed ion-enhanced etching models based on these studies have been summarized by Coburn and Winters [1985], who present data which discredits a number of them. Serious controversy has evolved concerning the suggestion that ion bombardment enhances the adsorption of fluorine which is subsequently involved in a rapid, thermally-driven reaction with the damaged lattice [Flamm and Donnelly, 1981]. Winters [1988] has shown that XeF_2 does not spontaneously etch an ion-damaged lattice at significantly increased rates and that continuous ion-mixing of the surface adsorbates into the lattice is necessary to accelerate the reaction.

A rigorous consideration of ion-induced surface reaction pathways suggests application of Monte Carlo type models to this problem to capture the random nature of this process, since it is unlikely that a simple analytical theory of chemical sputtering will be found to parallel Sigmund's [1969] classical treatment of physical sputtering. Nevertheless, a few researchers have attempted to model ion-enhanced surface kinetics on the basis of steady-state etching yield data,

and as a function of neutral-to-ion flux ratios. Gerlach-Meyer [1981] first modeled ion-enhanced etching of silicon by XeF_2 and Cl_2 with noble gas ions of various mass, using etching yield information and neutral-to-ion flux ratios as we present here. In her model of ion-enhanced XeF_2 etching of silicon, and excited SiF_2^* surface species was created as a result of the bombardment, which subsequently reacted to form SiF_4 with a high probability. Although the physical interpretations given to this model do not appear to be valid, we have derived similar mathematical functionalities in our work revealing great similarity between the effect of increasing ion energy and the effect of increasing ion mass modeled by Gerlach-Meyer. Barker et al. [1983] and McNevin and Becker [1985] have both proposed adsorption/reaction models for the Ar^+ ion-induced reaction of Cl_2 with silicon. Barker proposed that the operative ion-enhancement mechanism was collision-cascade induced desorption of $SiCl_x$ species to produce clean sorption sites for Cl_2, while McNevin invoked a mechanism similar to Gerlach-Meyer. Allen and Sawin [1986] developed an empirical surface kinetic model in CF_3Cl etching of silicon in which the total etching rate was taken as the sum of a isotropic component and an ion-enhanced anisotropic component. In this work they recognized the importance of incorporating a threshold energy in the ion-enhanced etching expression. Tachi and Okudaira [1986] proposed a "hot spot" model for the reactive ion etching where the reactions between implanted halogen species and the substrate lattice occur during the picosecond ion collision spike of an incoming ion. This model is mechanistically inconsistent with much longer reaction time constants measured modulated reactive beam scattering experiments [Rossen, 1986]. However, the authors recognized the importance of ion energy and reactant flux in determining mass-transfer-limited versus reaction-rate-limited etching regimes. Pelletier [1987] has proposed an adsorption/ reaction surface kinetic model in which parallel diffusion-controlled thermal etching and ion-enhanced etching are operative. However, his model implies that the reaction occurs at a well defined surface, which

is clearly incorrect on a physical basis given the ballistic mixing action of the incoming ions.

Recently, Manenschijn et al. [1991] have developed an integral surface kinetic model which accounts for the effects of reaction threshold energy, ion angular distribution, ion energy distribution, and "hot" neutrals in the Cl_2 reactive ion etching of silicon in a Cl_2 discharge. This type of integral approach will be necessary for incorporation of surface kinetic data such as is presented in this thesis into topography evolution simulators. We have constructed a simplified mechanistic model which decouples radical adsorption/recombination effects from the ion-driven reaction and mixing steps. We acknowledge that the exact ion-enhanced chemical pathways are unknown and involve multiple surface layers, where SiF_x type species become fully fluorinated as the near surface region is "mixed" by the ballistic effect of the ions. We have therefore represented this process with global reaction steps which attempt to capture the correct overall stoichiometry as discussed in Chapter 5, but should not be taken as elementary surface reaction steps.

Chapter 2

Experimental System

A detailed description of the experimental hardware utilized in this thesis is presented below. The primary apparatus constructed for these surface kinetic studies has been coined the "3-beam" reactor since it allows the simultaneous impingement of up to three molecular, free radical, or ionic beams on a sample located at the reactor center. A large (4000 l/s) cryogenic pump evacuates the main reaction chamber, allowing us to employ high beam impingement fluxes representative of the plasma environment, while still maintaining operating pressure in the 10^{-5} torr region. Since gas mean free paths are typically on the order of 100 cm in the main chamber, neither reactant beams or product species are effected by gas-phase interactions which would convolute measurement of the surface reaction kinetics. While this thesis focuses on a fluorocarbon etching system, the multibeam reactor was designed with the goal of creating a flexible research tool to which several types of beam sources could be easily "bolted" on and off to allow study of a wide range of chemical-substrate systems. The experimental concept and associated diagnostics are presented in "cartoon" form in Figure 2-1, and are detailed below. Description of beam production hardware has been relegated to separate chapters on free radical beam production and characterization (Chapter 3), and on ion production techniques (Chapter 4).

In addition to the diagnostic capabilities of the beam apparatus, we have also added a vacuum pathway into an adjoining XPS facility [Tepermeister, 1992], to allow transfer and surface chemical analysis of samples etched in the multi-beam apparatus. While this technique is not as powerful as full in-situ XPS studies of the etching surfaces, it allows us to evaluate surface bonding states and species coverages shortly after etching (5-15 minutes) without exposure of the surfaces to atmosphere.

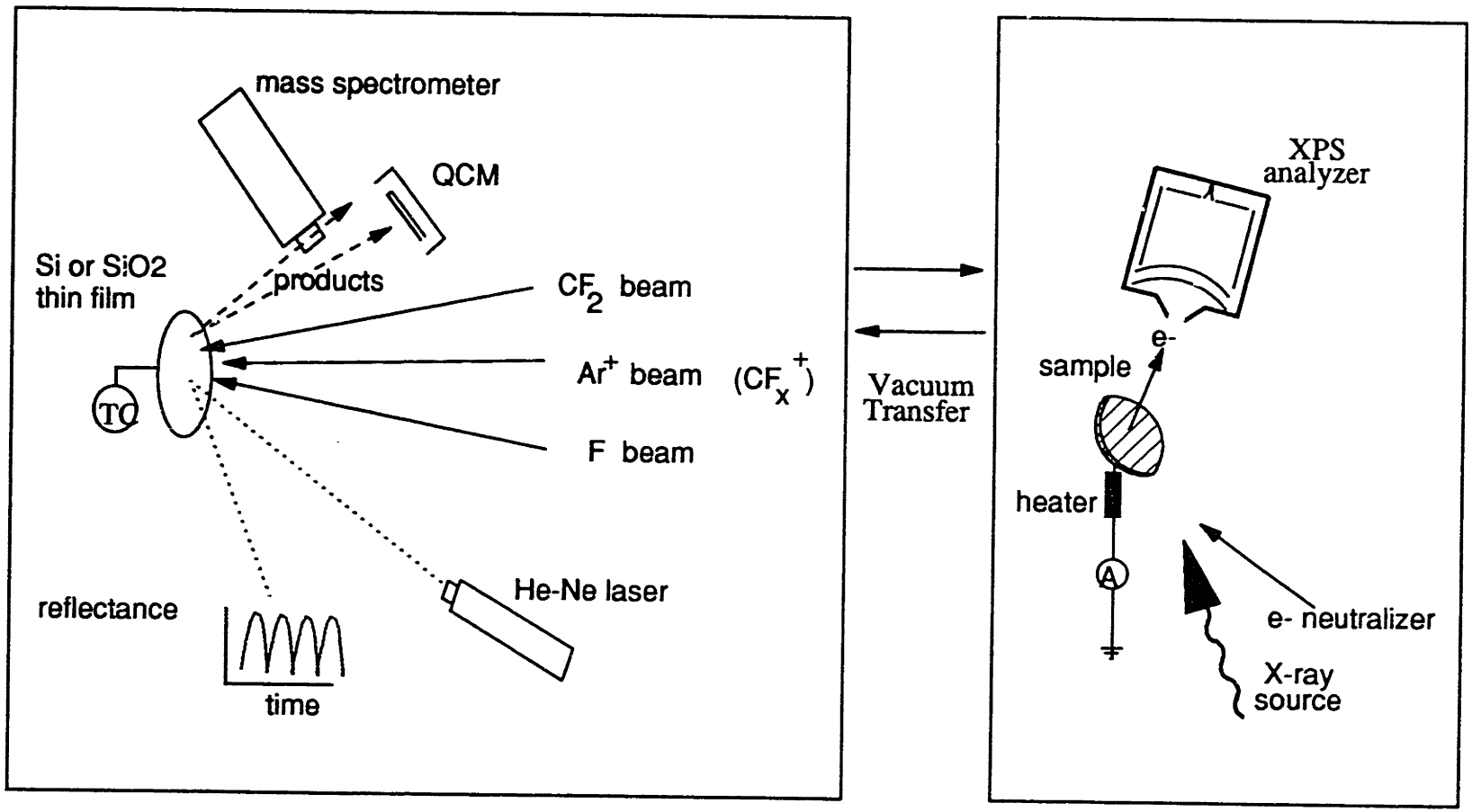

Figure 2-1. "Cartoon" schematic of the multibeam apparatus and XPS system utilized in this thesis work.

2.1 The "3-beam" reactor

The main reaction chamber built for these "beam simulation studies" consists of an 8" diameter stainless steel reaction vessel evacuated by a 4000 l/s cryogenic pump (CTI Cryogenics Cryo-torr 8). Schematic diagrams showing mechanical details of this apparatus are provided in Figures 2-2 and 2-3. Complete machine drawings for this apparatus and its ancillary systems are included in Appendix A. A load-lock assembly is available for rapid introduction of thin film samples into the main vacuum vessel. The load-lock consists of a 4.62" conflat six-way cross which is evacuated by a 110 l/s turbo pump (Balzers TPU 110), and isolated from the main chamber with at viton-seal gate valve. Opposite the load-lock, the main chamber is equipped with three 4.62" conflat nipples which define the molecular beam plane, the center port being concentric with the load-lock. Molecular, free radical, and ionic source beam hardware has been constructed directly on 4.62" conflat flanges to facilitate mounting and removal of various sources on the beam chamber. A differential pumping system has been added to reduce the background gas load of the ion guns (typically 1-5 sccm) employed in these studies as shown Figure 2-2. Using a 1 cm i.d. collimating cap and a 1000 l/s cryo pump (CTI Cryogenics Cryo-Torr 1000) gives an order of magnitude reduction in operating base pressure, and reduces back-mixing effects in the ion sources, allowing greater free radical fluxes to be utilized in the main chamber. The details of this system are presented in Chapter 4. Opposite the ion source is a 10" conflat flange adapter to which the load-lock is attached, as well as the internal sample mounting platen. The sample mount assembly (Section 2.2) is introduced into the main chamber on a differentially pumped slide rod, and mates to a pair of alignment pins, placing the substrate face at the reactor center and ensuring reliable electrical contact. Beam diagnostic probes are also mounted on this side flange adapter as discussed in Section 2.3.

The top flange assembly allows rotation of the mass spectrometer or quartz crystal

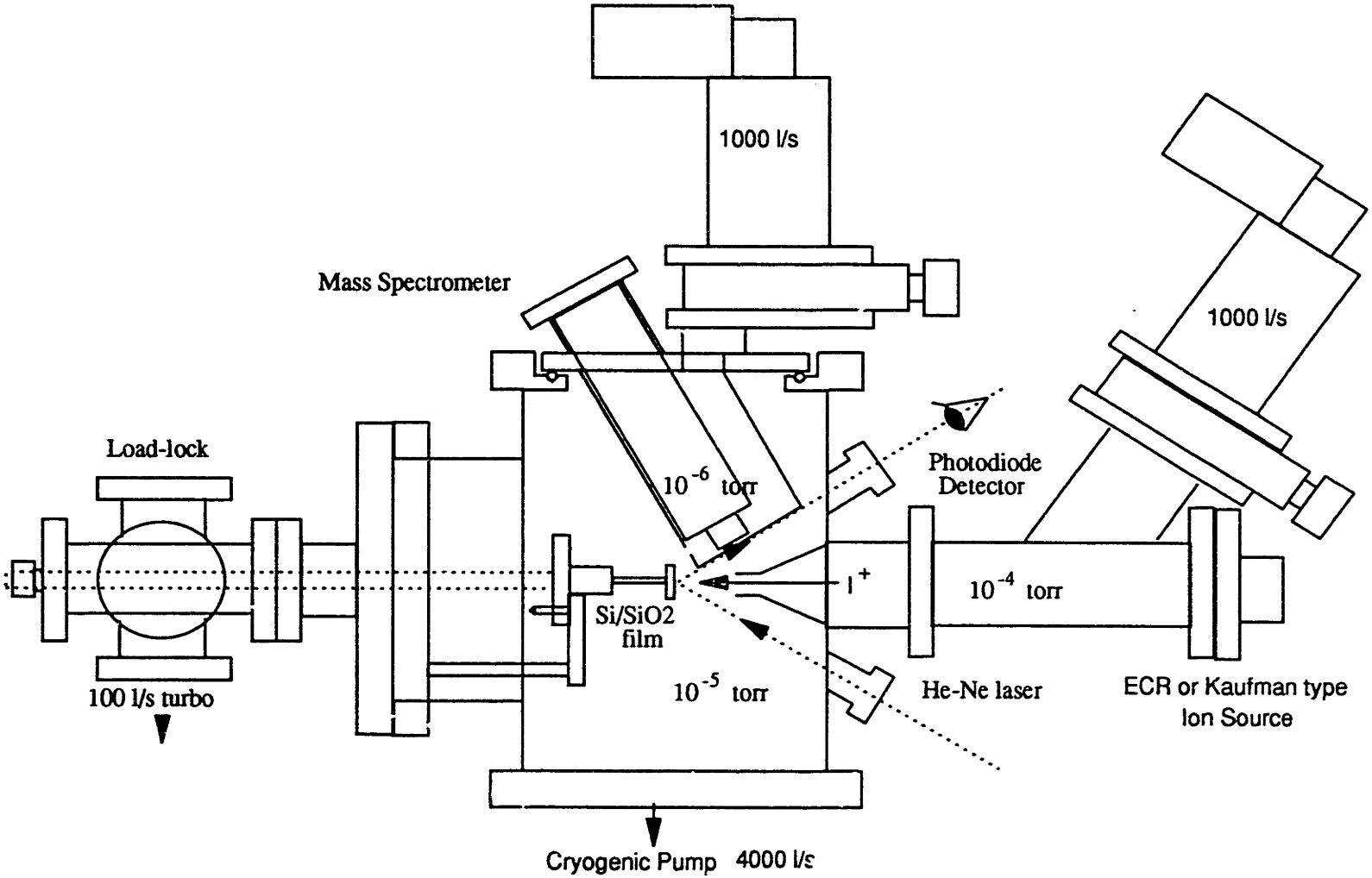

Figure 2-2. Profile cross sectional view of the multibeam etching apparatus.

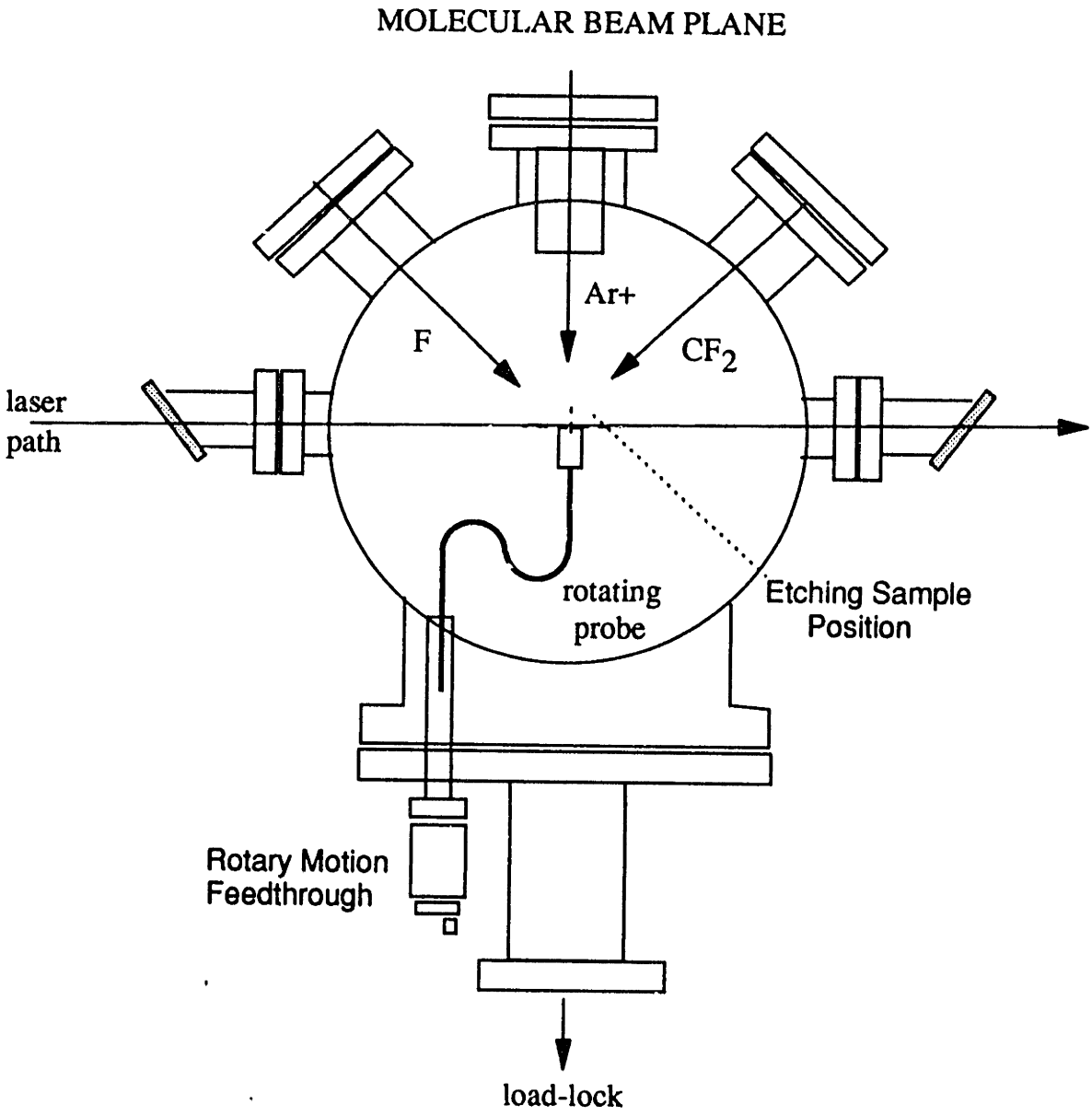

Figure 2-3. Beam plane cross sectional view of the multibeam apparatus.

microbalance (QCM) assembly (see Figure 2-1) around the sample face for angular resolution of product distributions. Two top flange assemblies are currently available, including one which allows differential pumping of the UTI-100C mass spectrometer as shown in Figure 2-2, and a second on which the QCM hardware is mounted. The rotating assemblies sit on a ball bearing ring, and a vacuum seal is made on the plate face by a set of greased viton O-rings. A port is available to allow differential pumping of the bearing groove, reducing pressure transients during flange rotation into the 10^{-10} torr regime.

Several 2.75" conflat ports are available on the main chamber body. Shown in Figure 2-2 are two 40° optical ports which allow in-situ interferometric measurement of thin film etch rates. A 0.25 W He-Ne (632 nm, Uniphase 1508-P) polarized laser beam is introduced through the lower port, striking the sample at the chamber center, and reflecting through the upper port where the interferometric signal is measured with a photometer. A laser beam can also be directed in front of the sample face through side Brewster's windows as shown in Figures 2-3 and 2-4, so that LIF studies may be performed, or for the application of REMPI in mass spectral characterization of the source beams. Fluorescence signals may be collected and focused using an adjustable parabolic mirror, which is mounted in the chamber below the beam plane. Chamber base pressure is monitored with a Bayard-Alpert type ionization gauge (Perkin Elmer DGC III) and is typically 5.0×10^{-8} torr after 10 hours of pumping. Numerous viton gaskets and compression-type seals are included in the apparatus at present so the system is not bakeable above 100°C. The remaining port allows main chamber roughing via a 16 CFM oil sealed roughing pump (Leybold Trivac D16-AC) and the introduction of N_2 to bring the system up to air.

2.2 Sample mounting assembly

For the purpose of this work, 2 μm undoped films of steam grown thermal oxide and

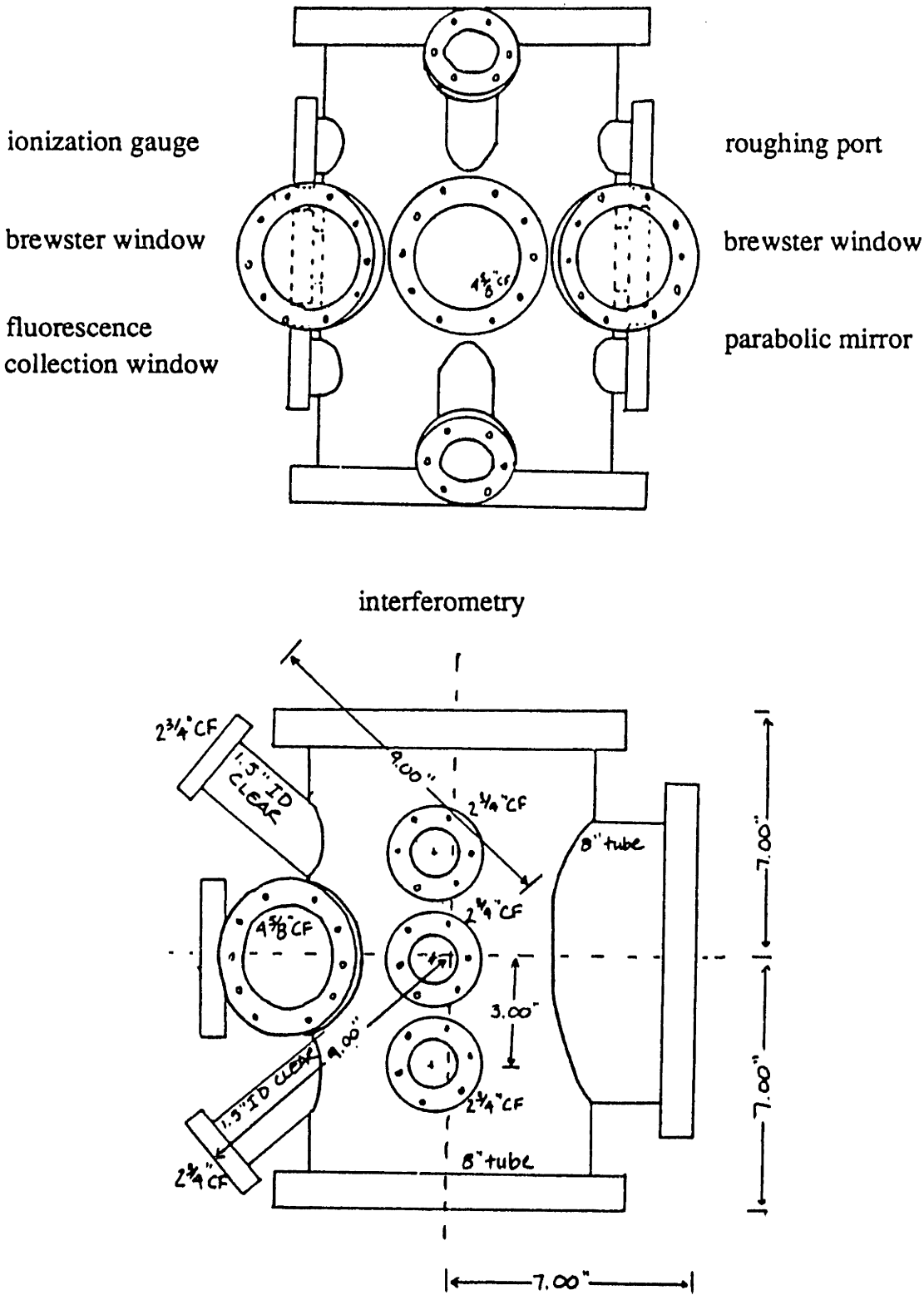

Figure 2-4. Summary views of the multibeam chamber port locations and usages.

polysilicon over (over LTO) were prepared by the MIT ICL on undoped silicon <100> wafers. The wafers were sawed or cleaved into 1-cm square dies and mounted onto modified Be-Cu wire connectors (ISI #9924003; Appendix A 3B.47) using Torr-Seal resin and a silver paint solution to achieve thermal contact. The face of the Be-Cu wire connectors was turned down by 0.1" to allow a sufficient mounting surface for the dies that they could be pressed firmly against the clip face. The dies must lie flat on the sample clip face to ensure that the interferometry laser beam may be reflected out of the 40° optical ports. Three 1-72 threaded holes were fabricated in the sample clips to be transferred into the XPS system; two on opposite sides at 90° with respect to the face normal, with the final hole at 60° with respect to the sample face normal to allow mounting on the XPS sample manipulator (see Appendix A 3B.47). Sample transfers are described in Section 2-4. The Torr-seal die mounting technique is reliable for sample temperatures below 400°C, above which a silver epoxy resin solution (Dupont 6838) may be used. The epoxy must be baked at 300°C in the vacuum oven for several hours to cure completely. However, after etching the dies, the Torr-seal-mounted samples may be removed using a heat gun while the epoxied samples must be turned down on a lathe to fully remove sample fragments and recover a flat face.

The sample clip is press fit onto a sample mounting assembly which includes a resistive sample heater and K thermocouple to measure temperature at the back of the Be-Cu clip. The resistive heater is comprised of 12 gauge stainless steel wire mounted in ceramic paste (Coultronics #903) on piece of alumina tubing to provide electrical isolation. Based on the large thermal conductivity of the clip, this measurement should represent the sample face temperature to within 5°C at steady-state. A schematic of the sample mounting assembly is shown in Figure 2-5. The entire sample mounting assembly is introduced into vacuum through the load-lock on the tip of a 5/8" Teflon-sealed slide rod. A set of two spring-loaded telflon rod seals (Furon

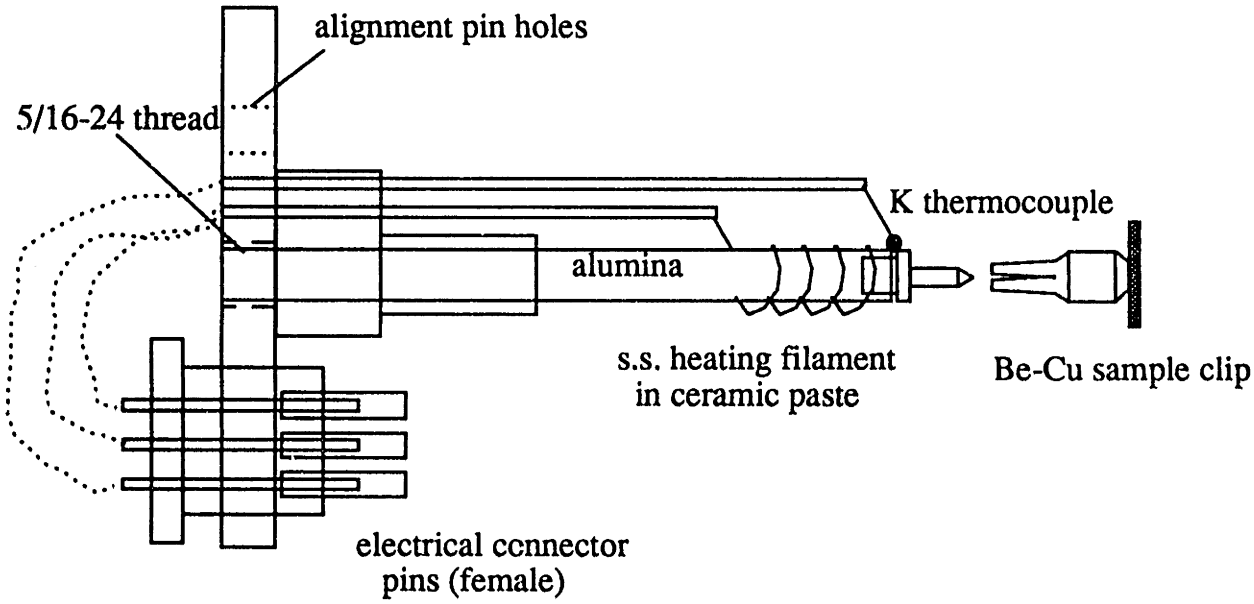

Figure 2-5. Sample die mounting assembly.

Omniseals #230-208-0107) with an intermediate stage of differential pumping were employed to seal the slide rod, elimination the necessity of using a vacuum grease seals. The slide seal design is detailed in Appendix A drawing 3B.36. The seals work reliably for a finite number of rod transfers (500-1000) but require replacement at regular intervals due to erosion of the teflon liners. The sample mount assembly is threaded on the end of the transfer rod and introduced into the main chamber where it slides over a set of alignment pins and plugs into a mating electrical connector mounted near the chamber center. Samples can be repeatedly withdrawn for beam flux measurements and reconnected with no detectable positioning error over long intervals. Electrical schematics for the sample mount electrical connector are provided in Appendix B. During most experiments, the sample temperature was held at 80°C by controlling heater power with a proportional feedback controller. Temperature readings were found to stabilize within approximately 2 minutes after electrical contact was made, depending on the starting temperature.

2.3 Diagnostics and Data Acquisition System

Mass Spectrometry

A UTI-100C mass spectrometer system was used for mass analysis of neutral beams and characterization of etching products. A conflat adapter was designed for mounting the mass spectrometer head on the back flange in place of the load-lock assembly. This places axial-cross beam ionizer (modified EAI QUAD 2100) on the UTI head directly at the sample position for analysis of beam composition and radical production efficiency as shown in Figure 2-6. Production of CF_2 and F has been optimized using this technique as discussed in Chapter 3. For analysis of etching products, the mass spectrometer is positioned on a rotatable face-sealed assembly mounted on the chamber top flange. The mass spectrometer head is angled at 25° to allow a direct line-of-sight from the etching sample face into the ionizer region for analysis of

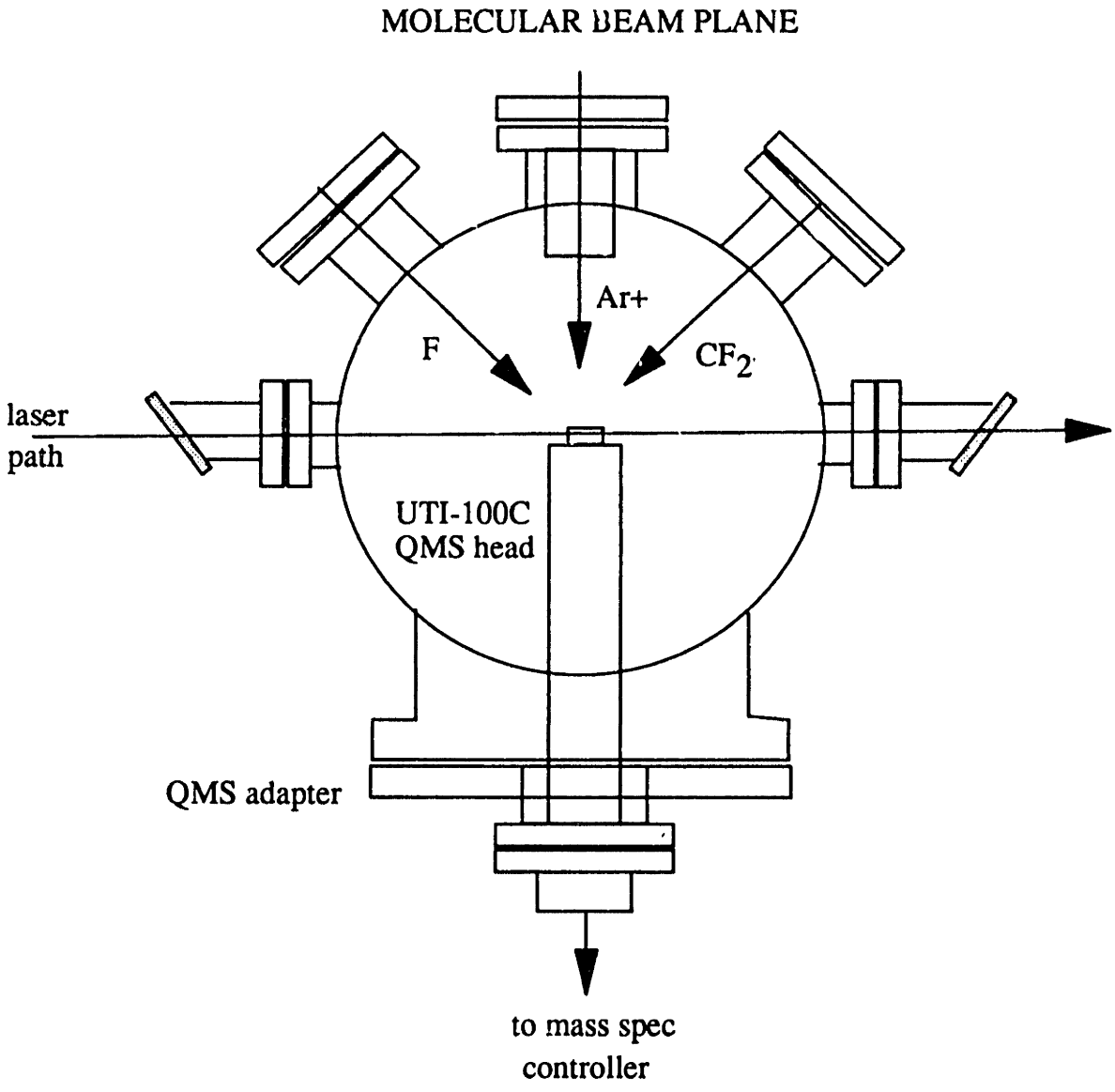

Figure 2-6. UTI-100C mass spectrometer installed on the side flange adapter to allow characterization of source beams.

thermally desorbing or sputtered products. Rotation of the mass spectrometer assembly allows angular resolution of etching products in a 180° arc above the sample, which allows access to polar angles of approximately 15° to 90° relative to the sample face normal vector. It should be noted that the beam flux probes normally interfere with the mass spectrometer rotation at angles larger than 60° and must be moved back or removed to access the complete range of angles. The end cap on the mass spec differential pumping shroud currently has a 1/8" diameter orifice, and background pressure in the mass spec is reduced over an order of magnitude while cryo pumping, relative to the main chamber pressure. A flag is available to block the line-of-sight product beam to the mass spectrometer which enables us to distinguish surface products from background signals. A mechanical beam chopping system was constructed to enable modulation of the source beams, but was not utilized in this thesis work. Details of a digital sine wave generator constructed to power the chopper motors are included the thesis work of Ai [1989].

Mass scans are currently taken via an 8088-PC based data acquisition system which utilizes a Data Translations DT2811 card to drive the mass spectrometer scan ramp while reading ion current signals. Some mass spectral data presented in this thesis was taken before the automated data acquisition system was completed, using an HP 7044B X-Y recorder. A data acquisition interface (DAI) was constructed to allow connection of the DT2811 card with the UTI-100C mass spectrometer controller, the interferometry photometer output, and the QCM frequency output. Voltage divisions and multiplications necessary to match the DT2811 card voltage levels with the various diagnostic equipment were performed using 725 op amp filter circuits in the DAI as detailed in Appendix B. The mass spectrometer data acquisition code (3BACQ.EXE) was implemented in Turbopascal version 4.0 as detailed in Appendix C. The mass spectral experimental parameters and scan data were stored in separate turbopascal records and later massaged using the 3BMS.EXE program which allows automated mass peak detection and data

output in the form of postscript files.

Beam Flux Probes

The load-lock flange adapter was designed with several mini-conflat feedthrough ports to allow the mounting of beam flux probes. The beam flux probes are mounted on rotary feedthroughs on opposite sides of this flange, allowing them to rotate directly into the sample position at the reactor center as shown in Figure 2-3. Ion and neutral beam fluxes can thus be measured in-situ at the sample face position, directly preceding and following each etching rate measurement.

The neutral flux probe (Figure 2-7) consists of an impact tube which is designed to sense the differential pressure between a radical or molecular beam impinging upon the probe face, and the chamber base pressure. This pressure differential is measured by a capacitance manometer (MKS Baratron 315B) with the reference leg at the base chamber pressure. The gas leak path through the impact tubing to the pressure transducer represents a small flow resistance, such that a steady-state is rapidly established (<10 sec) at the impact tube sample orifice. Flow through the 1/16" OD thin wall orifice is molecular in nature at all but the highest beam fluxes employed. The impact tube theory and working assumptions are discussed in Chapter 3, and mechanical drawings for the system are included in Appendix A. The beam equivalent pressure measured by the impact probe at the sample position may be converted directly to a number flux as a function of the species mass. An MKS 170M-6B high accuracy controller enabled beam pressures as low as 10^{-6} torr to be sensed by the probe. Although the probe head itself was insulated, it was not temperature compensated so long term stability was poor due to thermal drift. Thermal drift was not problematic for the instantaneous beam pressure measurements made during the experiments in this thesis work. A valve was available to short circuit the pressure differential between the

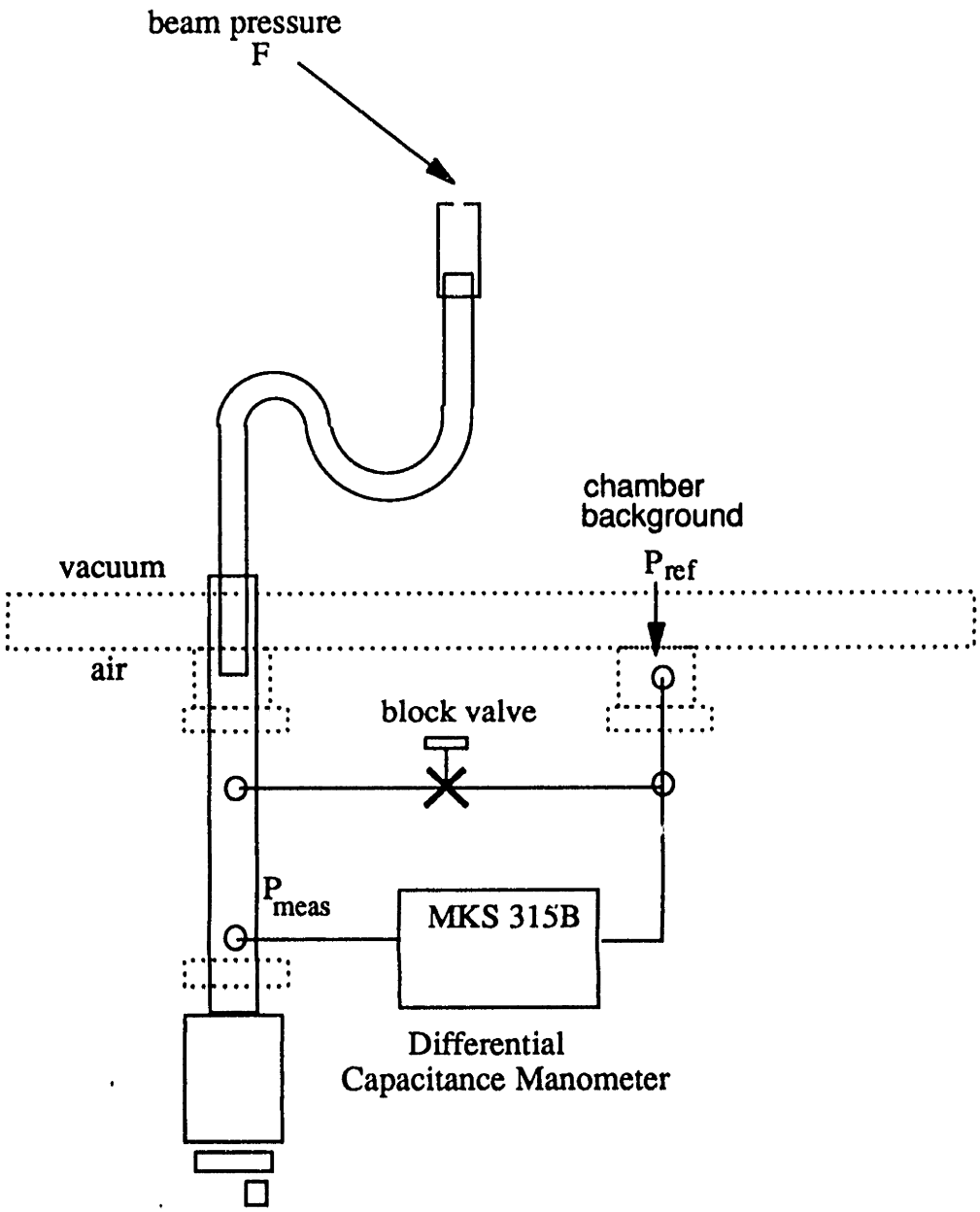

Figure 2-7. Impact probe system

capacitance manometer head and the chamber background in order to rapidly equilibrate the system, and to prevent overpressuring of the differential manometer head when the chamber is brought up to air. Beam pressures were acquired manually from a digital panel display.

The ion flux probe consists of a Faraday cup and retarding grid system (Figure 2-8) which allows energy analysis of the incoming ion flux. The energy analyzer is a triple grid design which includes a negative bias on the first and third grids, while the second grid is biased at the ion retarding potential. The first grid serves to repel neutralizing beam electrons (2-5 eV) generated by the Kaufman ion source to prevent "blooming" of the ion beam, or to exclude electrons generated in the CECR plasma stream (<20 eV). The third grid prevents the escape of secondary electrons from the Faraday plate as a result of ion impact events. During ion flux measurements with the Kaufman ion source, the retarding grid bias was held constant at +40V to eliminate any low energy charge exchange ions from the incoming beam, while the first grid was held at -10V and the third at -90 V. The probe grid potentials are set by the ion beam energy analyzer (IBEA) which allow G1 and G3 potentials of 0 to -250v, and an ion retarding potential of 0-250V. The ion retarding potential may be ramped manually, internally, or via PC computer control. Details of the IBEA construction are included in Appendix B. Ion currents were acquired manually using a Keithley 485 autoranging picoammeter. The flux probe was originally designed for characterization of the Kaufman ion source, and a 100x100 lpi tungsten mesh (Unique Wire Weaving) was employed in grid assemblies. The 0.005" spacing of this grid is, however, large compared to the Debye length in the CECR plasma, making the probe ineffectual for ion energy profiling with this ion source, although it can still be used as a current probe. These issues are discussed in Chapter 4. The entire ion flux probe assembly was enclosed by a ground shield in order to emulate the presence of a grounded wafer sample in the ion beam, and avoid perturbations of the ion beam. The construction of the probe is detailed in Appendix A drawing

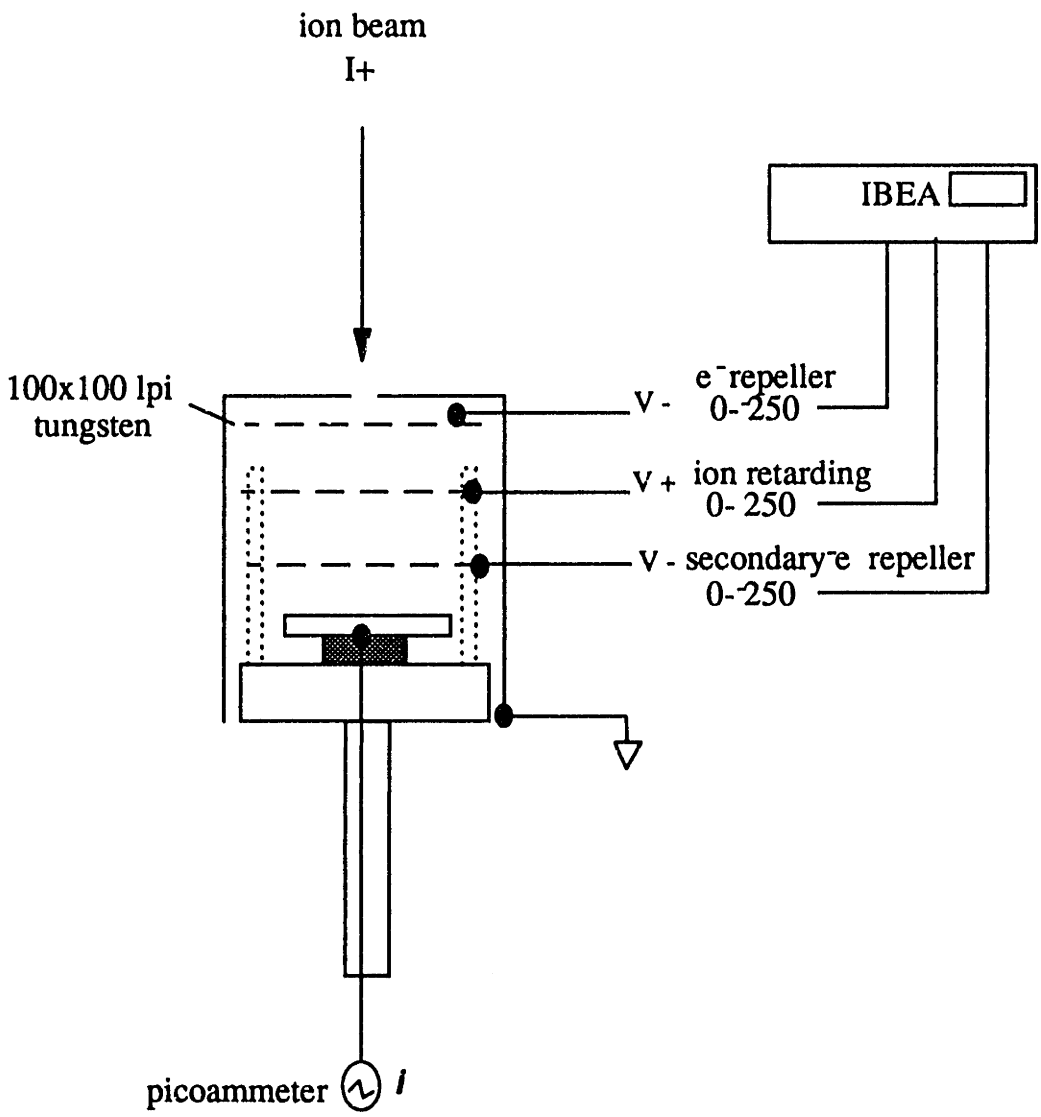

Figure 2-8. Probe for ion flux and energy distribution analysis.

3B.17. A 1/16" OD sampling orifice was used in order to characterize a "point" ion flux on the length scale of the interferometry laser spot.

Laser Interferometry

Etching rates of undoped polysilicon and silicon dioxide films may be measured in-situ in the multibeam apparatus through application of laser interferometry [Maissel and Glang, 1970]. Single and multipoint laser interferometry is widely applied in research and industrial etching tools to measure instantaneous etching rates and uniformities, and to aid in end point detection. Application of this technique requires an abrupt change in refractive index at the thin film/ substrate interface, given by significant differences in doping level or material type, and a sufficiently thin film (<5μm) that laser beams may be transmitted through the film with adequate intensity to enable photo-detection. The physical basis of the laser interferometry technique involves the impingement of a coherent light source on an etching thin film, and the subsequent measurement of the time periodicity in the interference patterns of the reflected light. The interference is created between the light beam reflected from the film vacuum interface, and that which is reflected from the thin film-substrate interface due to the refractive index gradient. The optical path length traversed by the later beam in the etching film is directly related to the phase relationship of the two beams. In the case of a normally incident light source, the film thickness change between any two interference minima and maxima is given by the simple formula,

$$\Delta d = \frac{\lambda/2}{n_2} \qquad (2\text{-}1)$$

where λ is the wavelength of the light source (632.6nm for He-Ne), Δd is the change in film thickness, and n_2 is the refractive index of the etching film. In the case of the multibeam

apparatus, the laser light is incident at 40° so a more general form must be applied [Maissel and Glang, 1970],

$$\Delta d = \frac{\lambda/2}{[n_2^2 + \sin^2\theta_1]^{1/2}} \qquad (2\text{-}2)$$

where θ_1 is the incidence angle of the laser with respect to the sample face normal vector. Given refractive indices, n_2, of 3.42 and 1.45 for undoped polysilicon (over LTO) and silicon dioxide films (over Si<100>) gives respective thickness changes between maxima of 940 Å (Si) and 2431 Å (SiO_2). With 2μm films of each of these materials we may therefore make about 20 etching rate measurements with polysilicon and about 10 with silicon dioxide.

A 4mW polarized He-Ne (Uniphase 1508-P) laser was utilized in the interferometry setup to prevent the development of multiple maxima and minima due to beams of multiple polarization interacting with the etching substrate, as is the case in ellipsometry. An Edmunds Scientific Metrologic photometer was used for detection of the reflected light intensity. The output voltage signal may be sent to either a strip chart recorder, or the DAI box for automatic scan acquisition. The photometer circuitry and signal lines must be well shielded due to noise introduced when the microwave discharge source and CECR source are running. Currently, scans acquired by the PCXT are stored in Turbo Pascal 4.0 as linked-lists such that the list length is subject to Turbo's 640 K memory limitation. This feature is very limiting since it is often desirable to leave the interferometry scans run for hours during a set of experiments, without having to save and restart multiple scan files. For this reason, most scans were taken manually using a strip chart recorder. Future acquisition code should incorporate direct write of interferometry data to hard disk to circumvent this digital memory limitation.

Quartz Crystal Microbalance

A quartz crystal holder (modified Leybold Inficon compact sensor) has been placed with the crystal face within 2.2 cm of the etching sample face (Figure 2-9); the crystal holder is above the beam plane at an angle of 27° with respect to the sample face normal. The holder is water-cooled and is mounted on a rotatable flange which allows the crystal face to be moved in a 180° arc around the etching sample face, allowing us to measure redeposition rates over polar angles of 27° to 90°. The remainder of the QCM system is comprised of a Leybold Inficon oscillator (ISPN 013-001), a 5V power supply, and a Hewlett Packard 5384A frequency counter for monitoring of the oscillation frequency. The frequency counter is interfaced to the PC XT computer via an IEEE GPIB card (IO Tech Personal 488) for acquisition of raw data in the form of oscillator frequency as a function of redeposition time.

The operation principle of the QCM has been discussed in detail elsewhere [Pulker et al., 1976]. Briefly, an AT-cut quartz crystal is excited into oscillation in the thickness shear mode by applying a small potential (5V) across the crystal in a direct application of the piezoelectric effect. The crystal thickness and cut are initially selected to give stable oscillation at 6MHz. The deposition of material on the exposed crystal face results in an oscillation frequency decrease in direct response to the foreign mass, m_f,

$$\frac{\Delta \nu}{\nu} \approx -\frac{m_f}{m_q} \qquad (2\text{-}3)$$

This approximation is valid for a film-to-quartz mass ratio (m_f/m_q) of about 2%. For thicker deposits, is it necessary to make a correction for the acoustic impedance difference (e.g. relative "stiffness") between the depositing film and the quartz crystal, through application of the Z-matching technique [Wajid, 1991]. The QCM oscillation frequency is very susceptible to

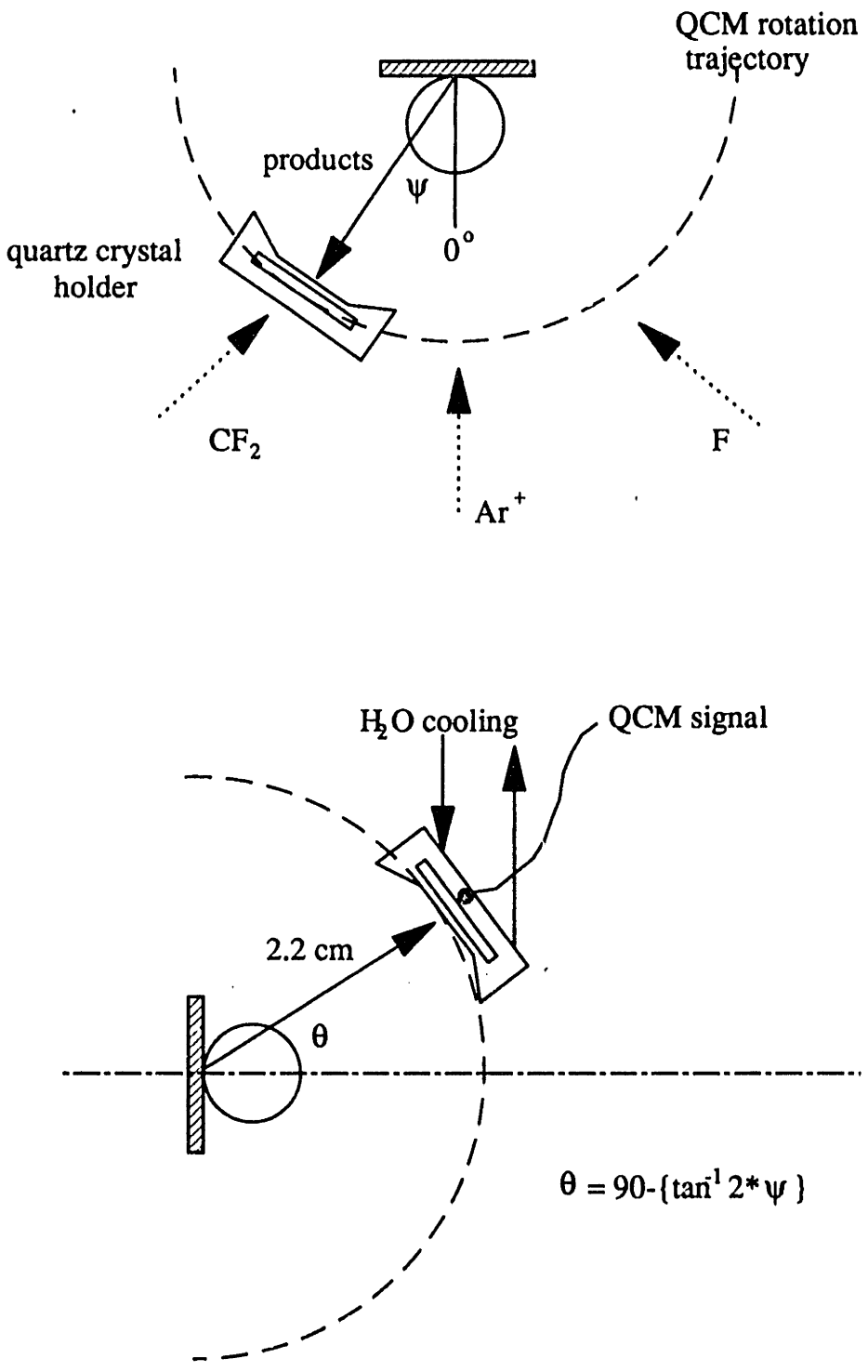

Figure 2-9. Geometry of the quartz crystal microbalance (QCM) system used to measure redeposition kinetics.

temperature variations in the crystal, on the order of .1 HZ/°C. However, once the system is temperature stabilized the QCM is sensitive to coverages as low as fractions of a monolayer. For these studies standard gold-coated AT-cut 6 MHz crystals were employed (Filtech #QI8010), which were subsequently coated with redepositing material during etching so that "self-sticking" coefficients are being measured. The crystals maintain adequate stability with up to about 0.01 MHz worth of frequency shift of deposited material in our system (about 5000 Å Si). The calibration constant for the 6 MHZ AT-cut quartz crystals used was calculated as 12.1 ng/Hz for both Si and SiO_2, using the Z-matching technique suggested by the manufacturer. Using this value gives a limiting sensitivity of $2.6x10^{14}$ Si atoms or $1.2x10^{14}$ SiO_2 molecules.

A jig has been constructed to allow the quartz crystal microbalance to be mounted on the sample holder in place of a sample die clip (Appendix A, drawing 3B.72-74). The QCM may be used in place of laser interferometry as an in situ etch rate measurement technique for bulk material (versus thin films). The jig also allows rotation of the QCM crystal holder in the sample position for measurement of angular dependencies in ion-enhanced etching. The QCM currently may not be cooled in this position so care must be taken to temperature stabilize the system after ion current changes. 1μm Si and SiO_2 films were sputter deposited onto gold-coated quartz crystals to allow etching rate measurements using this technique. Problems were encountered in achieving stable resonant oscillation of the loaded crystals due to the fact the that current QCM power supply (Kronos QM-311) and crystal oscillator (Inficon) are incompatible and do not facilitate resonant tuning modifications to stabilize oscillation of heavily loaded crystals. This problem can be eliminated in the future by purchasing the appropriate Inficon controller for future experiments.

2.4 XPS and sample transfer system

An adjoining surface analysis chamber has been constructed which allows XPS analysis of samples etched in the multibeam chamber (See Figure 2-10). The two chambers are interconnected by a 3" o.d. vacuum transfer tube assembly which is evacuated by the 110 l/s Balzers turbo pump, achieving a base pressure in the 10^{-7} range in several minutes.

A schematic drawing of the chamber interconnection assembly is provided in Appendix A (drawing surftab.1). The XPS system has been custom built to include a high throughput spherical retarding grid/post monochromator electron energy analyzer [Tepermeister, 1992], which allows us to perform rapid scans on a series of etched dies with acceptable resolution. For the purpose of this thesis work, a 1.25 keV Mg Kα x-ray source was used. Although the FWHM of this radiation source is 0.8eV, resolution of the energy analyzer was at best 1.5-2 eV. The energy analyzer orifice (Figure 2-10) in the XPS system is positioned at a large angle with respect to the sample face normal, making the system surface sensitive to the first 1-2 monolayers, since photoelectron escape paths are limited to 10-20 Å. Details of the XPS system construction are presented in the work of Tepermeister [1992].

A set of teflon-sealed slide rods was installed to facilitate transfer of the etched sample dies into the XPS chamber. All slide seals were made using dual spring-loaded teflon Omniseals (Furon #230-208-0107 and #230-204-0107) with an intermediate stage of differential pumping on either 5/8" nominal or 3/8" nominal precision ground rod stock. The addition of a roughing pump port between the seals reduced pressure transients during rod motion into the 10^{-6} torr region. However, it is important to keep the rod surfaces clean of contaminants during transfer by wiping them down with ethanol, and handling them only with gloved hands. 5/8" slide rod assemblies were designed for the transfer of samples into the multibeam and XPS chambers where alignment is critical. 3/8" slide rods are used for the main transfer of samples along the vacuum tube

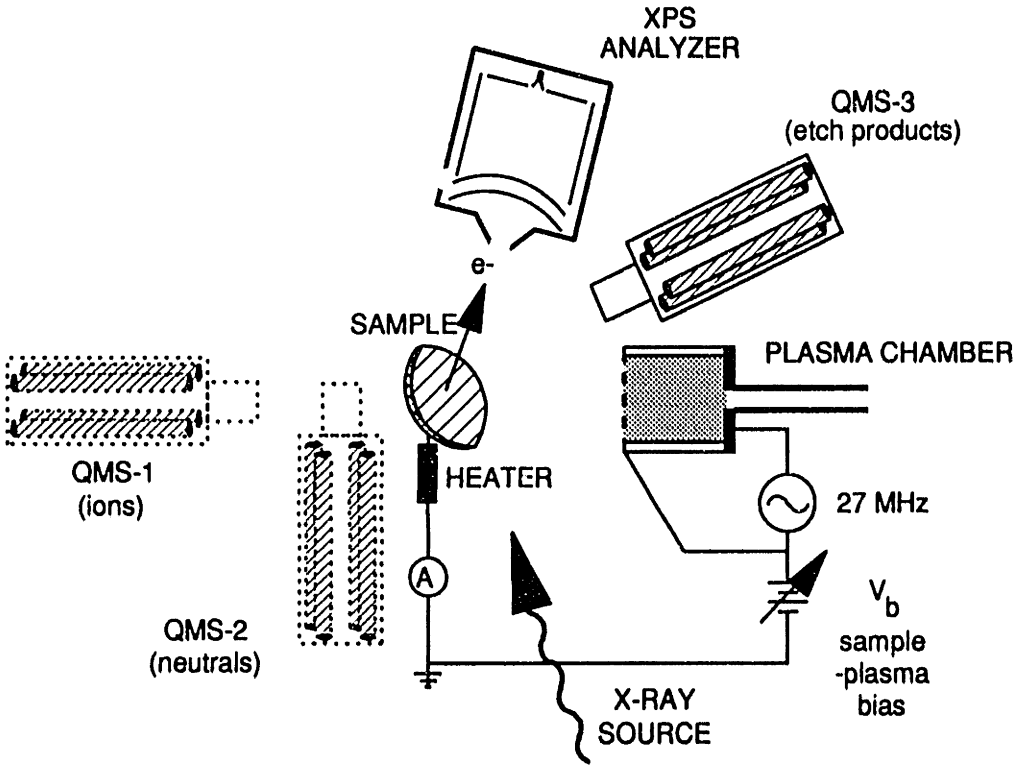

Figure 2-10. XPS chamber constructed by Tepermeister [1992].

between the two chambers, and in a wobble stick assembly mounted on the XPS load-lock. Sample transfers are initiated by fully withdrawing the multibeam sample mount assembly into the multibeam load-lock such that the sample clip is centered under the viewport. The main transfer rod is equipped with a 1-72 threaded tip which is then screwed into the appropriate side hole of the Be-Cu sample clip, allowing the clip to be slid off the sample mounting pin. The sample clip is then transferred to the XPS loadlock where it is slid onto a heater stage, which allows volatilization of adsorbates on the sample, and facilitates transfer of the clip to the wobble stick. In practice, the transfer rod is locked in place with the sample faced upwards, such that the heater stage may be moved up into the clip via a threaded rod. The sample clip may be pulled off the heater stage by threading into the opposite 1-72 hole with the wobble stick. The clip is then turned on the wobble stick so that the sample face is at an angle of 60° with respect to the main XPS transfer rod, which is threaded into the 60° 1-72 holed in the clip, and the wobble stick is threaded out. An alignment cone was machined into the 1-72 clip holes, and the rod tips have ground into a conical shape to help the rods pick up alignment. The clip is finally moved on the XPS slide rod into the XPS chamber where the sample clip is visually aligned with the sample manipulator pin in the XPS chamber. This alignment process currently requires two persons; one to watch the alignment process in the XPS chamber viewport, and a second to manipulate the transfer rod and the XPS sample mount. The entire process can be performed in 5-15 minutes by a facile operator.

Finally, it should be noted that extra care must be taken in the mounting of sample dies to be transferred to the XPS system after etching. It was found that XPS signal intensity is optimized by shifting the dies slightly off center toward the top of the XPS chamber. Oxide dies must be well contacted to the sample clip using the silver paint solution. The Be-Cu clips themselves must be properly maintained and replaced after several transfers due to stripping of

the soft Be-Cu threads by the stainless steel transfer rod tips.

2.5 Gas delivery and pumping systems

The gas handling and delivery system is currently a weak point in the construction of the multibeam apparatus due to the unavailability of economical corrosive service leak valves or mass flow controllers in the low flow ranges (<1 sccm) utilized in this work. A small gas manifold was developed to allow operation of up to 3 independent beam sources, with the facility to introduce gas mixtures into the microwave discharge source, and/or the ion source as shown in Figure 2-11. Nupro SS-4BK metal bellows block valves and SS-SS4 fine metering needles valves were used to control gas flow on each line. Metering at <1 sccm flow rates using these components is possible if cylinder backing pressures are maintained below 5 psig, but the needle valves cannot be reproducibly calibrated. Several failures of both valves types occurred during the course of this work due to corrosion, and overtightening of valves to achieve low flows. High density polyethylene and teflon lines with swadgelock fittings were utilized in the manifold design, adding to background contamination levels due to gas permeation and out-gassing. The manifold currently can only be "roughed" through the chamber, which is problematic in clearing large volumes of gas from the lines. Although this manifold is not "clean" in the UHV sense, contamination levels are representative of those found in commercial plasma tools, such that the surface kinetics are measured in a true "process" environment.

The multibeam pumping system is quite complex due to the large number and types of pumps employed. Figure 2-12 is a schematic representation of the current pumping configuration included for reference.

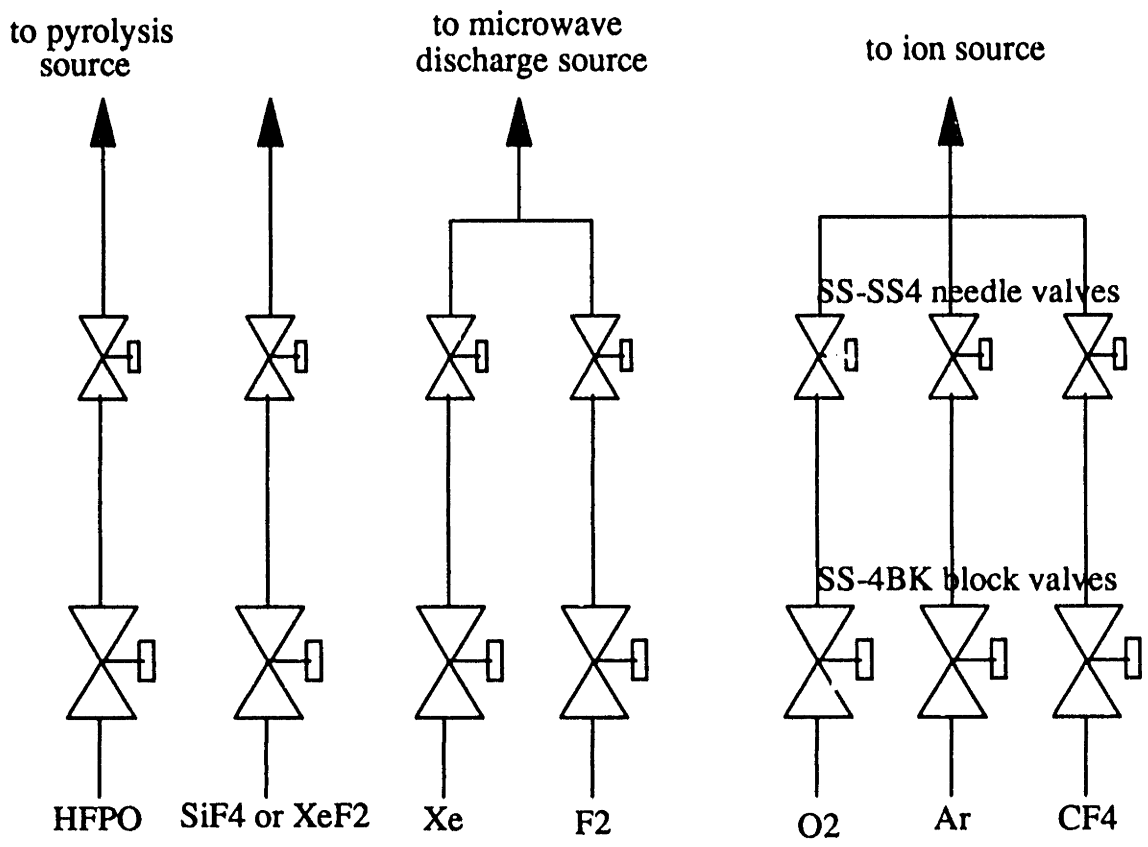

Figure 2-11. Multibeam apparatus gas delivery manifold.

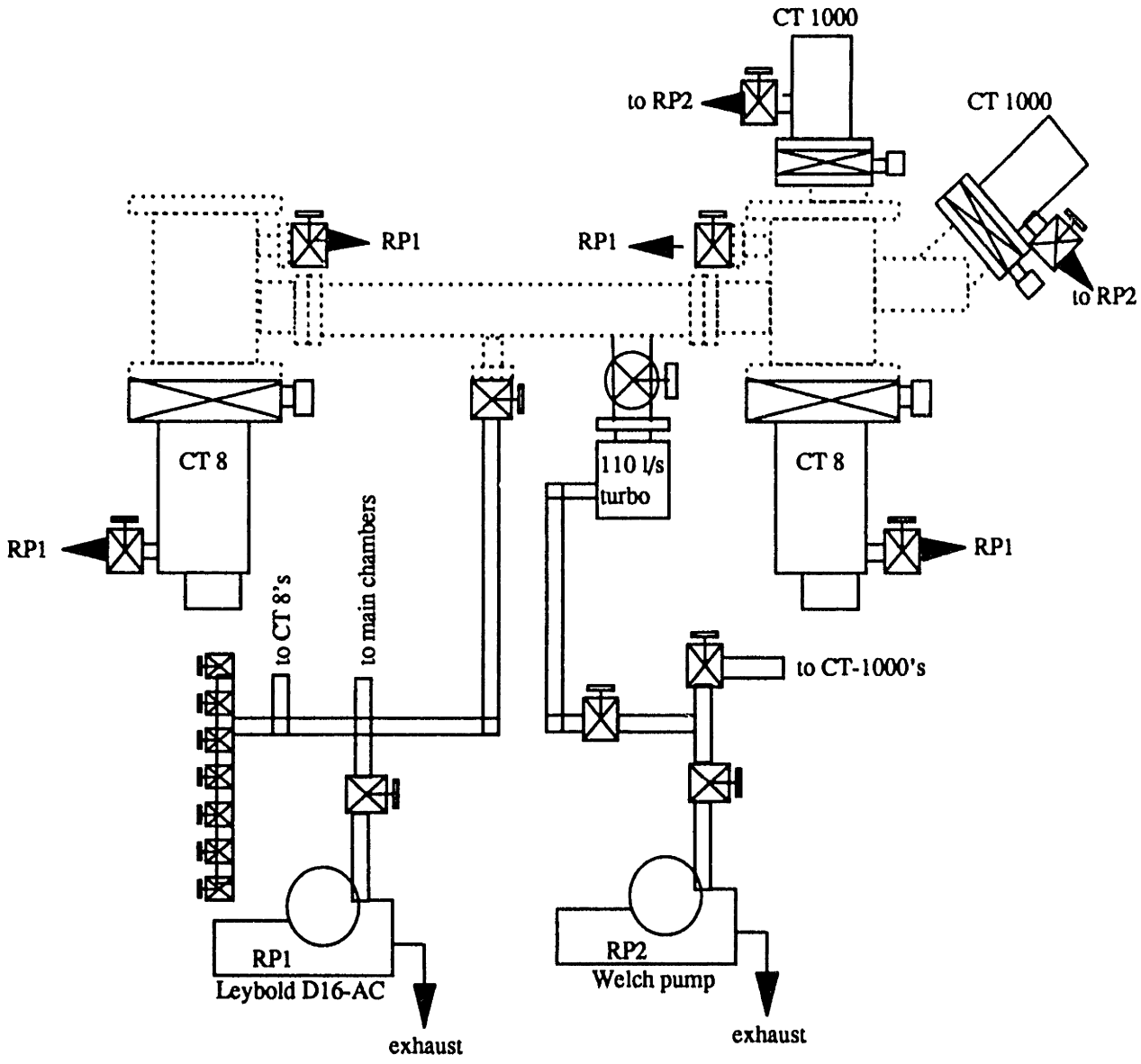

Figure 2-12. Surface table pumping schematic.

2.6 Summary

A flexible multibeam etching tool was designed an constructed to facilitate the study of ion-enhanced surface kinetics through the simultaneous impingement of up to three beams on a sample substrate. This facility allows us to independently vary the fluxes of incoming ion and free radical species, and to measure the beam fluxes at the sample face in situ using a set of probes which rotate directly into the sample face position. Diagnostic capabilities of the system include laser interferometry for the in situ measurement of etch rates, mass spectrometry for the assessment of reaction products, and a quartz crystal microbalance for the measurement of product redeposition rates. A sample transfer facility was constructed to allow transfer of the etched samples to an adjoining XPS facility for surface chemical analysis.

Chapter 3

Characterization of Free Radical Beams

A large portion of this thesis work was dedicated to the characterization of free radical beam sources which were utilized in the simulation of plasma fluxes. In order to make accurate surface kinetic measurements in plasma processes, as in any other chemical process, it is essential to quantify the chemical natures, total fluxes, and total energies (e.g. quantum state) of reactant species impinging on the wafer surfaces. While these quantities are difficult to measure and control in the plasma environment, reactant energies and fluxes were well defined in the controlled environment of the multibeam apparatus. The F and CF_2 radicals utilized in these beam-simulation studies were generated in source "tubes" which allowed the collimation and transport of these species to a sample (die) surface in the form of radical "beams". Since the maximum chamber pressures attained during these studies were limited to $<10^{-4}$ torr, gas mean free paths were at worst on the order of 10 cm, such that the radical beams were "non-collisional" on the length scales of these experiments, and radical fluxes were not modified by gas-phase interactions.

In order to fully quantify radical fluxes at the die surface, it was necessary to address the following issues:

i) Production efficiency of the radical species from parent gases

ii) Attenuation of radical concentrations due to tube wall effects

iii) Chemical state of the radical species produced

iv) Flow dynamics (e.g. peak fluxes and angular dispersions) of straight-tube doser designs

Production and transport efficiency of various free radical doser designs were investigated early in this thesis and are described in detail below. Free radical concentrations at the sample face

position were characterized and optimized mass spectrometrically using the UTI-100C mass spectrometer in the beam characterization position as depicted in Figure 2-6. This setup allowed us to assess the effect of different doser designs and tube wall materials on free radical production and transport efficiency. The chemical "state" (e.g. translation, rotational, and vibrational state populations) of the radical sources used in this thesis were not measured directly, however, limited information was available in the literature. The impact tube system described in Chapter 2 was characterized and utilized in the measurement of radical "beam pressures" at the sample face. In order to generate the high radical fluxes characteristic of fluorocarbon plasma processes, high driving pressures were utilized behind the doser tubes, such that gas mean free paths in the tubes were smaller than the tube lengths and inner diameters ($Kn_a<1$, $Kn_L<<1$), except for a short transition regime near the doser tip. This flow regime is described as "collisionally opaque" since very few gas molecules traverse the entire tube length without a gas-phase collision. This is in contrast to operation of doser tubes in the transparent regime where low driving pressures allow $Kn_a>1$, and gas phase collisions may be neglected, greatly simplifying analysis of gas flow dynamics. Very little information was available at the start of this thesis regarding the characteristics and optimal design of opaque-regime straight tube sources. We have assimilated available information in this area from the literature, and applied the information to characterization and optimal design of our radical sources as detailed below.

3.1 Design Considerations for Collisionally Opaque Effusive Beams

Design of molecular beam sources has long been of interest to investigators in the areas of chemical physics and surface science. Highly directed beams of reactive radical and molecular species are widely used to probe reaction mechanisms in the gas phase and at gas-solid interfaces. Several early treatises in this area describe the theoretical basis for the formation of directed

molecular beams in capillaries and capillary arrays [Giordmaine and Wang, 1960; Jones et al., 1968]. Design of effusive molecular sources in the transparent regime ($Kn_L>1$; where Kn_L, the Knudsen number, is the dimensionless ratio of gas mean-free-path to the tube length) has reached a high level of development and several recent works serve as useful design guides in this regime [Campbell and Valone, 1985; Winkler and Yates, 1988; Murphy, 1989]. However, there is a dearth of such information for the design of collisionally-opaque molecular beam sources where $Kn_L<1$.

Within the past decade, molecular beams have found extensive use in the area of microelectronics fabrication. Generally, low flux sources are required in the fields of molecular and chemical beam epitaxy (MBE/CBE) for the slow growth of single crystalline films. However, recent interest in the use of directional molecular beams as an etching tool requires much larger fluxes to achieve practical etching rates [Suzuki et al., 1988]. The potential exists for development of highly selective dry etching processes using vibrationally hot molecular beams alone or in combination with low energy ion beams. There is interest in development of such a process for the removal of surface layers damaged by reactive ion etching, which can be implemented in a vacuum environment, eliminating a wet etching step in wafer fabrication. Due to pumping speed and beam uniformity limitations, efficient design of these high flux beam sources is critical but is not well understood because the beam formation is affected by gas-phase collision events and the theory becomes less tractable. The goal of this paper is to assimilate previous theoretical work in this area to present a useful design guide.

For the purposes of this work, we have limited our design analysis to straight-tube sources of circular cross section. This limitation precludes the formation of supersonic beams at high source pressures ($Kn_a<<1$) since a converging tip section is typically required for the mach number to exceed unity. Some of the results of this work may be extended to molecular beam

sources of arbitrary cross section by application of the concept of hydrodynamic radius. There has been much confusion in the literature concerning nomenclature of molecular beam sources. One must be careful when assigning descriptors to specific source designs which make presumptions about the flow regime in which the source is operating. In our analysis we refer to high efflux beam formation in cylindrical tubes as a straight-tube source since the nomenclature "capillary" or "channel" source is widely applied to operation in the effusive (low pressure) regime where $\mathbf{Kn_L}>1$.

Mathematical Description of Co-Axial Flux Interception

The design rules for constructing straight-tube molecular sources are dependent on the flow regime in which the source is operating and upon its particular geometry. To complete a quantitative design of a molecular beam system, we need a mathematical description of total molecular throughput ($\mathbf{N_{tot}}$ [=] mols/s) and a normalized angular intensity distribution ($\mathbf{J(\theta)}$ [=] sr^{-1}) at the source tip in the flow regime of interest. These functions allow calculation of total molecular flux intercepted by a target area, and flux uniformity across a sample surface through appropriate integrations. The problem we focus on is shown schematically in Figure 3-1. Here a single straight-tube source of radius $\mathbf{R_s}$ (diameter **a**), with a backing reservoir pressure $\mathbf{P_s}$ is used to dose a target of radius $\mathbf{R_t}$ at a distance **d**. We consider the co-axial case only. It should be noted that for long straight-tube source, the distinction between the gas reservoir and the "source tube" is arbitrary and depends on the length over which useful beam collimation occurs.

Invariably, the goal in designing a molecular beam source is to obtain an enhanced directional flux of some chemical species over a limited target area. This target may be a real surface such as single crystalline substrate sample or a detector area, or an area projected in space where multiple beams are to intersect. Winkler and Yates [1988] have recently reviewed the

Table 3-1 Nomenclature

a	= source tube inner diameter	[=]	cm
L	= source tube length	[=]	cm
d	= source-to-target co-axial distance	[=]	cm
R_t	= beam target radius	[=]	cm
R_s	= source inner radius	[=]	cm
P_s	= gas reservoir pressure	[=]	dyne/cm^2
N_{tot}	= total molecular flow	[=]	mols/s
$J(\theta)$	= integral normalized angular flux distrib.	[=]	sr^{-1}
$I(\theta)$	= angular flux distribution	[=]	mols/cm^2-s
N	= molecular flow hitting target area	[=]	mols/s
f	= fractional interception by target	[=]	1
P	= chamber background pressure	[=]	dyne/cm^2
P_{meas}	= measured impact pressure	[=]	dyne/cm^2
P_{beam}	= beam equivalent pressure	[=]	dyne/cm$_2$
E	= beam enhancement factor	[=]	1
m	= molecular mass	[=]	g
n	= gas molecular density	[=]	mol/cm^3
v	= mean molecular speed	[=]	cm/s
λ	= molecular mean free path	[=]	cm
Kn_a	= diameter Knudsen number, λ/a	[=]	1
Kn_L	= length Knudsen number, λ/L	[=]	1
Λ	= critical tube length	[=]	cm
σ	= mean molecular collision diameter	[=]	cm
k_b	= Boltzman Constant 1.38e-16	[=]	ergs/K
T	= gas temperature	[=]	K
K	= Clausing factor	[=]	1
γ	= tube diameter-to-length ratio	[=]	1
η	= tube diameter-to-tip mean free path ratio	[=]	1
θ	= polar angle referenced to sample center	[=]	rad
θ_{max}	= maximum polar angle subtended by sample	[=]	rad
A_o	= impact probe orifice area	[=]	cm^2

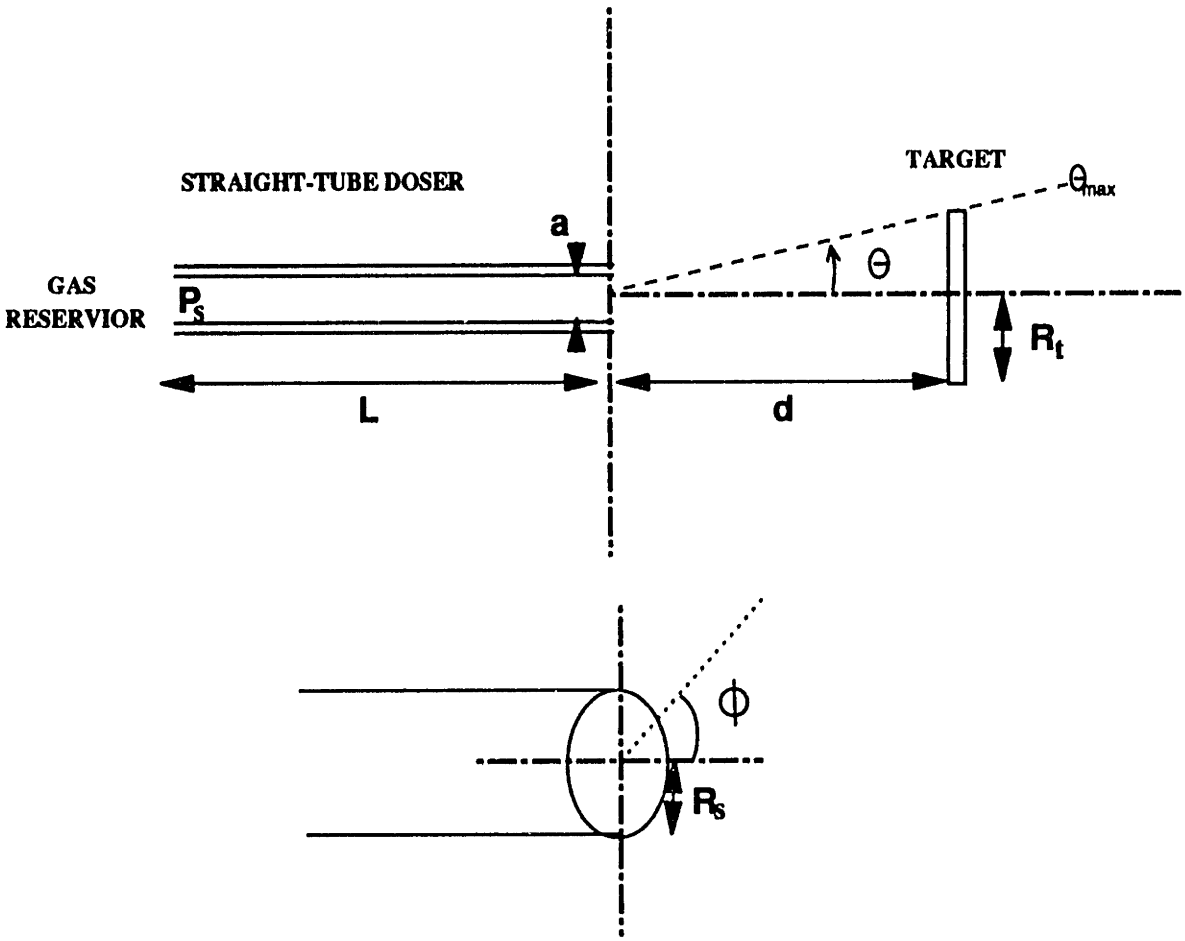

Figure 3-1. Schematic description of the coaxial flux interception problem.

general mathematical formalism for this calculation in the simple case of a cylindrical co-axial system as shown in Figure 3-1. Given a source of N_{tot} mols/sec emitting with an angular distribution function $J(\theta)$, the total molecular flow, N, intercepted by the target at distance d is

$$N = 2\pi S \int_0^{R_t} \int_0^{R_s} \int_0^{2\pi} \frac{J(\theta)\, d\, r_s\, r_t}{Y^3}\, d\phi\, dr_s\, dr_t \quad , \tag{3-1}$$

where

$$Y = [d^2+r_t^2+r_s^2-2r_t r_s \cos(\phi)]^{1/2} \quad , \tag{3-2}$$

$$\theta = \cos^{-1}\left[\frac{d}{Y}\right] \quad , \tag{3-3}$$

and

$$S = \frac{N_{tot}}{\pi R_s^2} \quad . \tag{3-4}$$

Note that N involves integration of the angular distribution function $J(\theta)$ over the range of polar angles, θ to θ_{max}, subtended by the target. The fraction of total gas issuing from the source and intercepted by the target area is simply the ratio

$$f = \frac{N}{N_{tot}} \quad . \tag{3-5}$$

Analysis of flux enhancement of the molecular beam over that of background gas, and of flux uniformity across a sample surface was cast in a useful form for transparent regime beam

sources by Campbell and Valone [1985]. The enhancement factor, E, was defined as a measure of the integral average flux enhancement over a given target surface of radius R_t as

$$E = \frac{Pv_c + \frac{fN_{tot}}{\pi R_t^2}}{Pv_c} \quad ,$$

where flux due to the chamber background pressure, P, is given by

$$background\ flux = Pv_c = P\,(2\pi mk_bT)^{-1/2} \quad . \tag{3-7}$$

In the multi-beam experimental system we have designed, the molecular or atomic beam pressure is measured by a small impact probe, allowing us an experimental measurement of the enhancement factor over the probe orifice area (see Figure 3-2) in the form

$$E = \frac{P+P_{beam}}{P} \tag{3-8}$$

where P_{beam} is the "beam equivalent pressure" of the directed flux at the sample face. The enhancement factor is a measure of the average efficiency of the source in generating a directional flux of molecules to the surface, and is thus dependent on the source geometry and flow regime as well as a source-to-target distance, the target area, and the pumping speed of the chamber. Also of great importance is the variation of flux across a sample surface. This information is most usefully cast as plots of relative flux intensity $I(\theta)/I(0)$ versus fractional distance across a target sample, at a given distance from the beam source (i.e at a given θ_{max} subtended by the target). In the limit where the tube diameter, a, is small compared to the target radius ($a/2R_t<0.05$) and appears as a point source, the relative flux distribution is closely approximated by $J(\theta)$. We have chosen to extend the efforts of Campbell and Valone [1985] to the collisionally opaque regime for straight-tube sources where design information is most required for etching studies.

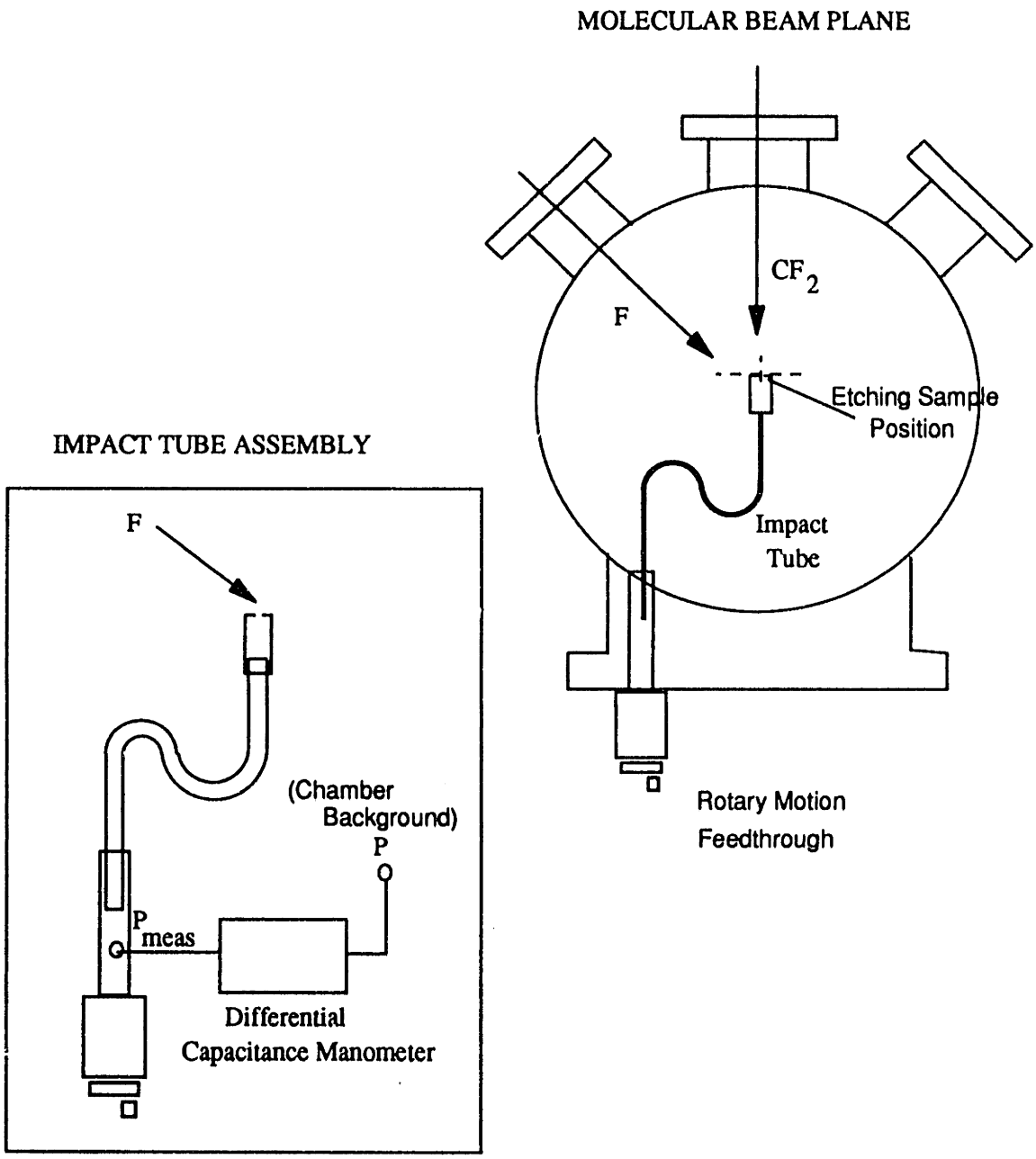

Figure 3-2. Experimental system for in situ beam flux measurement.
The impact probe rotates directly into the sample face position and senses the pressure differential between the molecular beam and chamber background.

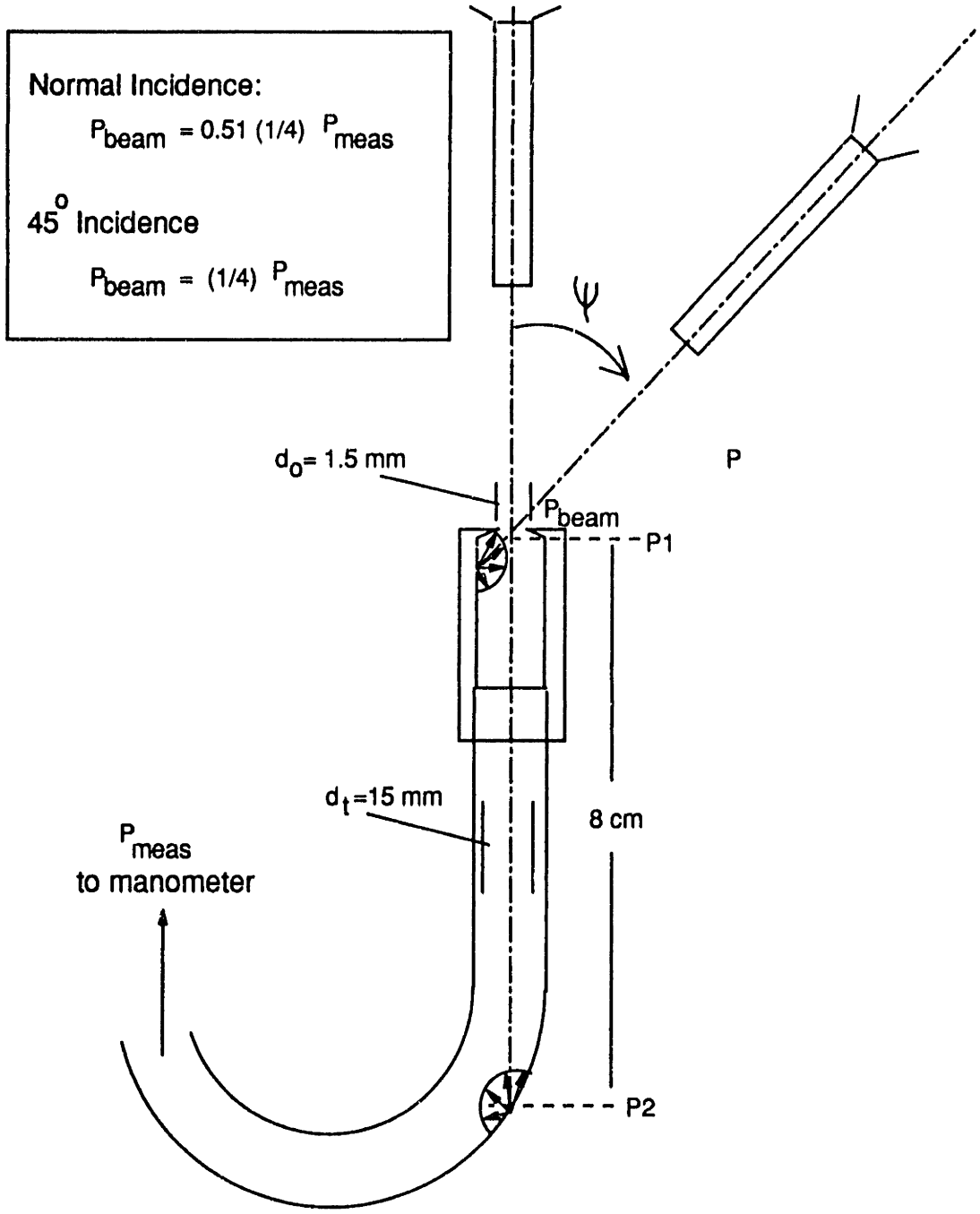

Figure 3-3. Relationship of impact tube geometry and beam incidence angle to measured impact pressure.

It should be noted that for some applications it may be more useful to know the "peaking factor", χ, as defined by Jones et al. [1969], where χ represents a ratio of the peak beam flux to that of a point cosine source with the same total efflux. This concept is useful in "skimmed" molecular beam systems were only the peak beam flux impinges upon a target area, the remainder of the gas being skimmed off and differentially pumped.

Gas Flow Regimes in Straight Tubes

Transparent Flow Regime

When conditions are such that the molecular mean free path, λ, of the gas at all points is larger than both the diameter and length of the capillary tube ($\mathbf{Kn_a}>1$ and $\mathbf{Kn_L}>1$), the gas flow regime is described as "transparent" in that the total gas fluence and angular distribution are dominated by gas-wall interactions inside the capillary, gas-phase collisions being unimportant. In transparent flow, the total flux through the capillary is described simply by the impingement flux on a thin walled orifice of equal area, multiplied by the appropriate Clausing factor, K, which accounts for flow attenuation due to molecules which interact with the inner tube wall and are isotropically scattered

$$N_{tot}\ (Kn>1) = \mathrm{K}\ P_s\ \frac{\pi R_s^2}{[2\pi m k_b T]^{1/2}} \quad . \tag{3-9}$$

Both "short tube" and "long tube" Clausing factors are tabulated in the literature depending on the aspect ratio, **L/a**, of the source [O'hanlon, 1980]. An approximate form is given by the expression

$$\mathrm{K} = \left[1+\frac{3L}{8a}\right]^{-1} \quad . \tag{3-10}$$

The integral normalized angular flux distribution for this regime was derived by Olander and

Kruger as described by the following expressions [Olander et al., 1970]:

$$\begin{aligned} &\tan(\theta)<\gamma \\ &J(\theta) = \xi\cos(\theta) + (2/\pi)\cos(\theta)\,[(1-\xi)\,R(p) + 2/3\,(1-\xi)\,(1-(1-p^2)^{3/2})/p] \\ &\tan(\theta)\geq\gamma \\ &\qquad J(\theta) = \xi\cos(\theta) + (4\gamma/3\pi)\,(1-\xi)\,\left(\frac{\cos^2(\theta)}{\sin(\theta)}\right) \quad , \end{aligned} \tag{3-11}$$

where

$$\gamma = \frac{a}{L} \quad , \tag{3-12}$$

$$\xi = \frac{2\gamma}{3} \quad , \tag{3-13}$$

$$p = \frac{\tan(\theta)}{\gamma} \quad , \tag{3-14}$$

and

$$R(p) = \cos^{-1}(p) - p(1-p^2)^{1/2} \quad . \tag{3-15}$$

By substituting these expressions into the flux integral (3-1), we can calculate the fraction of total gas issuing from a tube of arbitrary dimensions which is intercepted by the target area. Any molecular beam design involves a tradeoff between beam directionality (e.g. total flux intercepted) and flux uniformity across the sample in locating the best source-sample geometry. The work of Campbell and Valone [1985] serves as a useful design guide in this Kn>1 regime. For more

complete design information in this regime including characteristics of multichannel arrays and cosine emitters, one may refer to this reference.

Note that in the set of equations presented above, the gas mean free path does not appear in the flux distribution expression, since beam collimation occurs over the entire tube length. Accordingly, the effects of tube geometry on the transparent regime angular distribution are fully contained in the dimensionless ratio of capillary diameter-to-length, γ, and the angular flux distribution function $J(\theta)$ in this regime is more appropriately written $J(\theta,\gamma)$. As the gas throughput is increased and the tube flow becomes collisionally-opaque (i.e. $Kn_L<1$, so few molecules pass through the tube without a gas-phase collision), γ is no longer the valid group for characterizing the beam directionality. Instead we might intuitively introduce the dimensionless group $\eta = a/\lambda_{tip}$, the ratio of the source radius-to-mean free path at the source tip, since useful beam formation can occur only on the length scale of the gas mean free path, regardless of the tube length. A simple first order estimate of η may be made by assuming the gas mean speed at the source tip for a tube of set diameter, **a**, and desired total flow, N_{tot}. The exit gas density and mean velocity determine the throughput via

$$N_{tot} = n_{tip} v \frac{\pi a^2}{4} \tag{3-16}$$

where

$$v = \sqrt{\frac{8k_b T}{\pi m}} \tag{3-17}$$

assuming the gas is in approximate thermal equilibrium at the tube wall temperature T and the beam is highly directed. Application of the ideal gas law for the transparent tip region yields

$$P_{tip} = \frac{N_{tot}\, 4k_bT}{\pi a^2 v} \quad , \tag{3-18}$$

which allows calculation of η using the definition of mean free path from kinetic theory

$$\eta = \frac{a}{\lambda_{tip}} = \frac{\sqrt{2}\pi\sigma^2 a P_{tip}}{k_bT} = \frac{4\sqrt{2}\sigma^2 N_{tot}}{av} \quad . \tag{3-19}$$

Directionality is greatest when η is small (i.e. as λ_{tip} approaches L), while angular dispersion of the source increases as η increases. It should be apparent that the ratio η allows dynamic similarity between straight-tube sources of arbitrary diameter such that identical angular flux distributions may be attained from different sized tubes simply by adjusting the total gas throughput or equivalently the tube backing pressure.

Opaque Flow Regimes

The opaque flow regime is defined by the criterion that for most of the straight tube length $\lambda << L$, until some point sufficiently near the tube end that the gas experiences a transition to Knudsen type flow. In the limit of extremely high flow rates, the total gas flow into the low pressure chamber becomes a pure Pousille type flow and eventually reaches the thermodynamic limit of an isentropic expansion into vacuum. Total gas flow through straight tubes over the entire flow regime from Knudsen to Pousille flow may be computed by a universal form summarized by Jones et al. [1968]:

$$N_{tot} = K\, l^*\, f(p_r) \quad , \tag{3-20}$$

$$l^* = \left(\frac{n\nu}{4}\right) \pi R_s^2 \quad , \tag{3-21}$$

$$p_r = \frac{\sqrt{2}\ \pi\ \sigma^2\ a\ P_s}{k_b T} \quad , \tag{3-22}$$

$$f(p_r) = p_r^{-1}\left[\frac{\pi}{4}\ p_r + (1-\pi/4)\ \ln(p_r+1) + \frac{\pi}{128}\left[\frac{3}{2}\ p_r^2 + p_r^3 - (p_r^2 + 1)^{3/2} + 1\right]\right] \tag{3-23}$$

where K is the Clausing factor given in equation (3-10), and ν and σ are the molecular mean speed and mean collision diameter of the gas respectively. p_r represents a reduced pressure in which the reservoir source pressure, P_s, is ratioed to the pressure at which λ=a. Note the similarity between this dimensionless parameter, p_r, which characterizes total throughput, and our dimensionless parameter η (equation (3-19)) which characterizes the angular flux dispersion. This form displays the limits f=1 at p_r=0 yielding the Knudsen flow expression (3-9), and reduces to pure pousille (viscous) flow at p_r=large where

$$f(p_r) = \frac{3\pi}{256} p_r \quad . \tag{3-24}$$

At extremely high source pressures the total straight-tube flow becomes an isentropic expansion into vacuum and is thermodynamically limited by specific heat capacity ratio of the expanding gas. Typically, the maximum chamber gas loading would be exceeded before this limit. For the purposes of our work, equations (3-20 to 3-23) provide a good estimate of the total source strength when the backing pressure is known. However, it is common that the source backing

pressure is not a measured variable, in which case the total molecular flow through the tube must be related to the measured beam peak intensity and the system geometry, or to total chamber pressure rise at a given pumping speed.

Approximate peak intensity and angular flux distribution functions for long straight-tube sources in the opaque flow regime were derived by Giordmaine and Wang [1960]. Peak intensity, I(0) [=] mols/cm^2-s, is related to total efflux through the approximation

$$I(0) \sim \frac{0.103\sqrt{vR_s}}{\sigma}\sqrt{N_{tot}} \quad . \tag{3-25}$$

This form is valid for gas-phase collisionally dominated opaque flow where the tube length is greater than a critical length parameter, Λ, defined by

$$\Lambda = \frac{2.427\sqrt{vR_s^3}}{\sigma\sqrt{N_{tot}}} \quad . \tag{3-26}$$

This critical length, which physically defines the transition from Knudsen to opaque regime gas flow, is a useful design parameter for straight-tube sources. Increases in tube length beyond Λ attenuate total molecular flow without changing the directionality of the source. This implies that straight-tube sources may be most efficiently constructed using Λ length tube appended to a larger reservoir tube to achieve both maximum directionality and maximum transmittance. Typical values of Λ for 300K Argon flowing through large straight-tube sources are provided in Table 3-2, along with values for the parameter η which characterizes our opaque regime angular dispersion. In practice, Λ contains the same information as our tip-mean-free-path estimate, λ_{tip}, (equation (19)) and could also have been used to form our dimensionless grouping η, described in the order

Table 3-2. Typical values of the critical length parameter, Λ for 300K argon.

a (cm)	N_{tot} (mol/sec)	Λ (cm)	η
0.1	1E+15	5.71	1.7e-3
	1E+16	1.81	1.7e-2
	1E+17	.571	0.17
	1E+18	.181	1.7
0.2	1E+15	16.1	8.7e-4
	1E+16	5.11	8.7e-3
	1E+17	1.61	0.09
	1E+18	.511	0.9
0.4	1E+15	45.7	4.4e-4
	1E+16	14.4	4.4e-3
	1E+17	4.57	0.04
	1E+18	.144	0.4

of magnitude calculation in equations (3-16 to 3-19).

Jones et al. [1968] noted that for a single capillary source, equation (3-25) begins to underpredict the beam peak intensity at high total flow rates, N_{tot}, where the reduced source pressure p_r approaches a value of 10. We have noted this flaw experimentally, where at high molecular flow rates calculation of N_{tot} based on measured peak beam intensities I(0) in equation (3-25) begins to exceed estimates made based on total chamber pressure rise and reasonable pumping speeds. Jones et al. [1968] offer several corrections to this simple theory which may be applied if high driving pressures are employed. It should also be noted at this point that opaque regime theories developed thus far have assumed that gas molecules interact via hard sphere collisions described by the single parameter σ, so application to large interactive molecular systems is tenuous.

The angular intensity distribution in the opaque regime as derived by Giordmaine and Wang [1960] may be expressed as:

$$I(\theta) \sim \alpha \sqrt{N_{tot}} \cos^{3/2}(\theta) \int_0^1 (1 - \zeta^2)^{1/2} \, erf(2\, k\, \zeta)\, d\zeta \quad , \tag{3-27}$$

$$\alpha = \frac{0.148 \sqrt{R_s\, v\, \pi}}{2\sigma} \quad , \tag{3-28}$$

$$\zeta = \frac{z \tan(\theta)}{a} \quad , \tag{3-29}$$

$$k = \frac{a}{\tan(\theta)} \left[\frac{\pi \sigma^2 r}{\sqrt{2} \cos(\theta)} \right]^{1/2} , \qquad (3\text{-}30)$$

and

$$r = \frac{d(n)}{d(z)} \qquad (3\text{-}31)$$

where z is the tube length coordinate and r is the axial gas density gradient. In order to transform this distribution into the dimensionless form, $J(\theta)$, required for integration in equation (3-1), it was necessary to perform the integral normalization of the distribution in the form:

$$J(\theta) = \frac{I(\theta)}{\beta} \qquad (3\text{-}32)$$

where

$$\beta = 2\pi \int_0^{\pi/2} I(\theta) \sin(\theta)\, d(\theta) \quad . \qquad (3\text{-}33)$$

Calculation of these distributions requires knowledge of the molecular density profile in the tubes as well as physical gas constants and geometric parameters. The density gradient, r, after the viscous-knudsen transition near the tube end is largely unknown, so we have taken the first-order expression suggested by Giordmaine and Wang [1960],

$$r = \frac{3 N_{\infty}}{2 \pi \nu R_s^3} \quad . \qquad (3\text{-}34)$$

Given this approximation for the density gradient, what is most interesting to note is that the parameter **k** (equation (3-30)) which mathematically controls the beam shapes, may be rewritten in terms of our dimensionless grouping η in the form

$$k = \frac{1}{\tan\theta}\left[\frac{3\eta}{2\cos\theta}\right]^{1/2} \quad . \tag{3-35}$$

Physically this tells us that to the extent that a source tube appears as a point source to a distant target, it is not the absolute tube dimensions which determine the angular dispersion but the dimensionless ratio of the tube diameter-to-mean free path at the tube end. Constants in equation (3-27) cancel in calculation of $J(\theta)$, which in the context of this opaque regime theory becomes an explicit function of the gas collision diameter and η i.e. $J(\theta,\sigma,\eta)$.

The opaque regime intensity distributions described above closely approximate experimental beam shapes over a wide range of flow rates and source pressures. At low source pressures, the distributions are highly peaked and very similar in shape to those described by equation (11). As the source backing pressure is increased, the distributions flatten and appear more "cosine-like". Olander and Kruger [1970] have noted minor discrepancy between the opaque regime flux distributions measured by Giordmaine and Wang and their simple theory. They attribute this discrepancy to the assumption of zero exit density and have derived a corrected form of the flux distribution based upon more realistic exit density conditions. The magnitude of this correction was found to be insignificant for our purposes, however.

Flux intensity variations across a 1 cm diameter sample, at d=1.0 cm, as calculated from the opaque regime flow theory of Giordmaine and Wang [1960] (equations (3-27) to (3-33)) are shown in Figures 3-4, 3-6, 3-7, and 3-8 for a variety of conditions, where physical properties of Ar at 300K were nominally employed (M=40 amu, $\sigma=5.0x^{-8}$cm). A FORTRAN code entitled

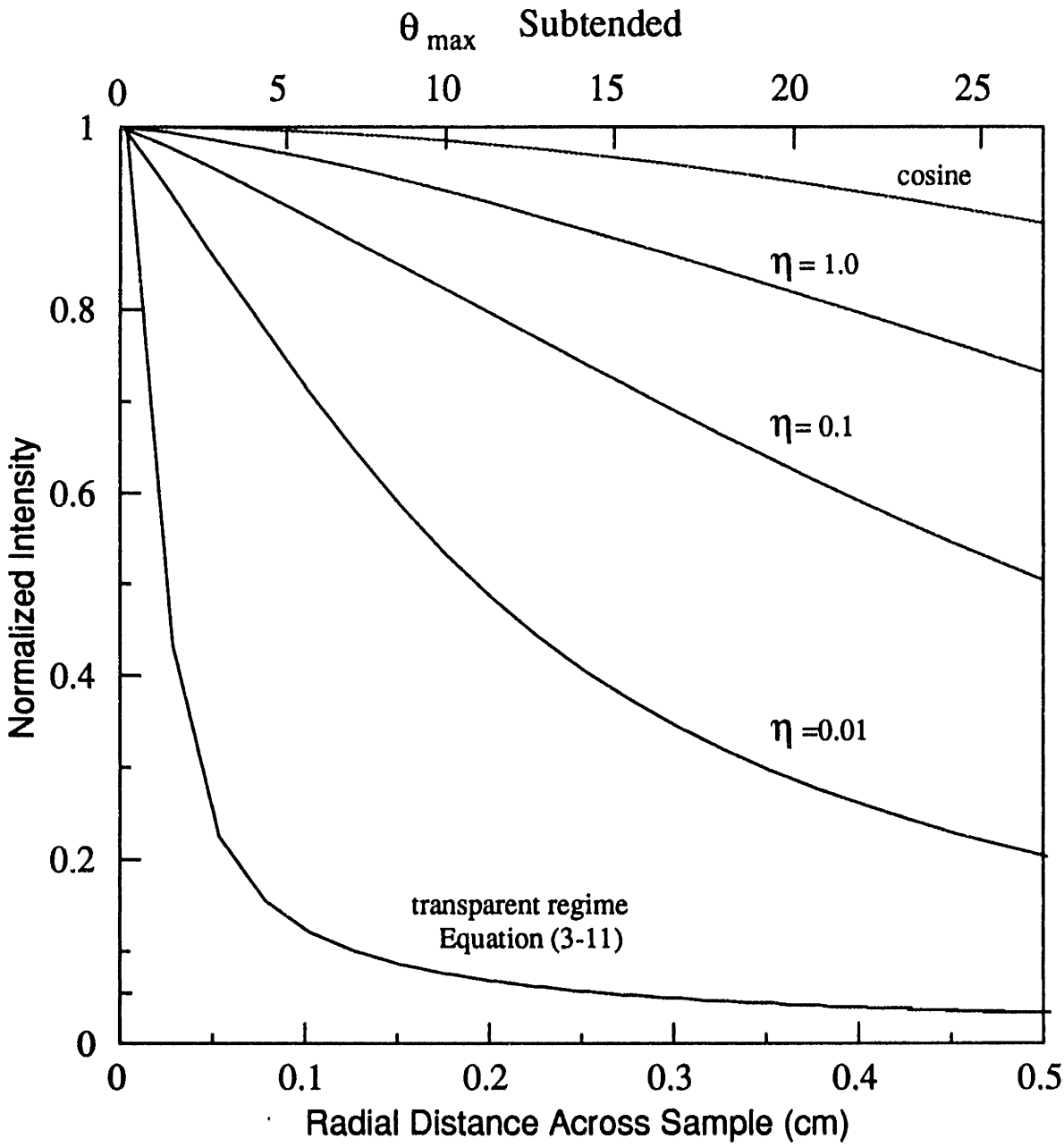

Figure 3-4. Flux intensity variation J(θ) of and opaque regime point source versus distance across a 1cm sample, d=1cm, for various values of the dimensionless parameter η .

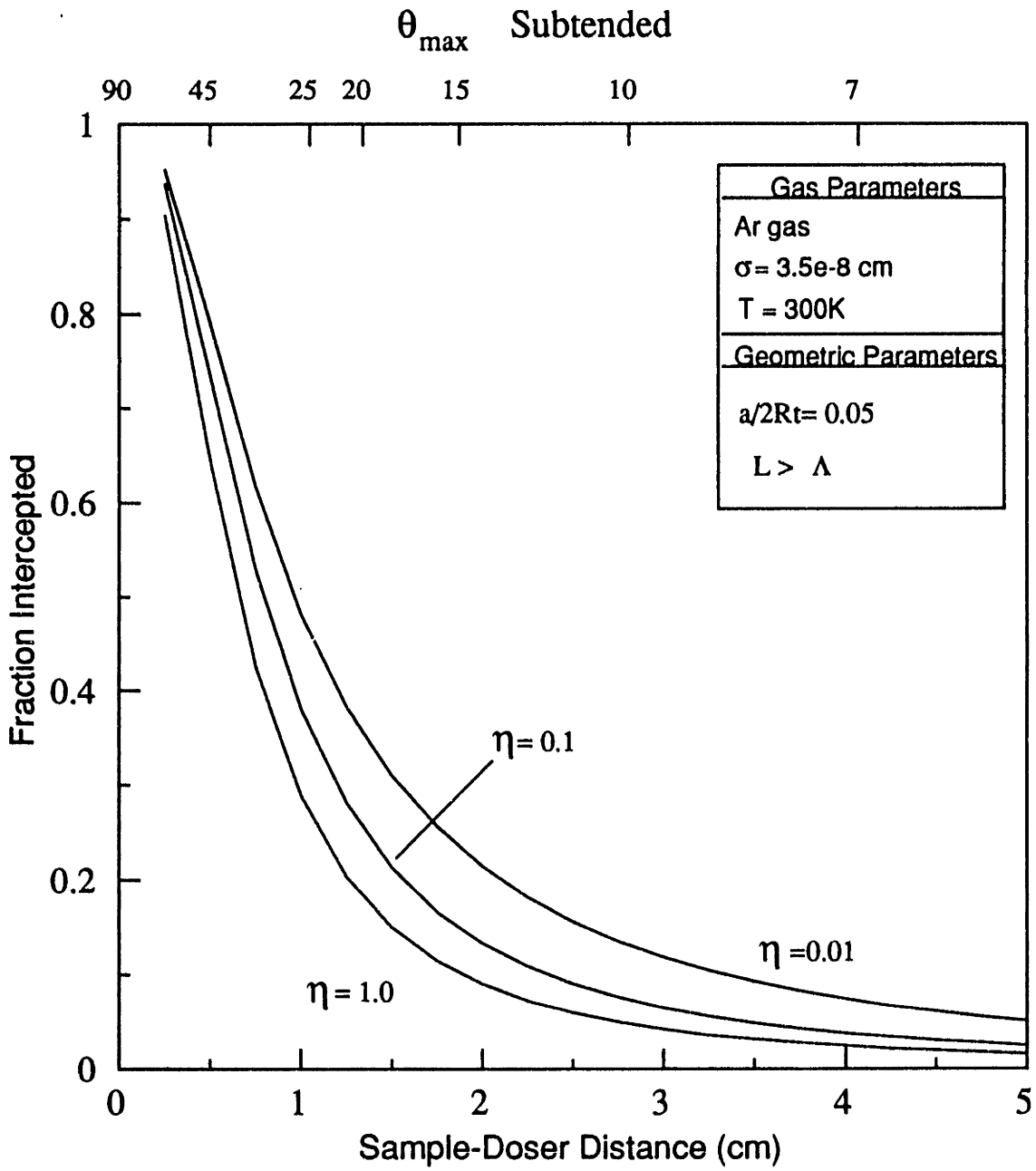

Figure 3-5. Fraction of total flux intercepted by a 1 cm diameter sample as a function of distance from an opaque regime point source (a/2Rt=0.05) for various η values.

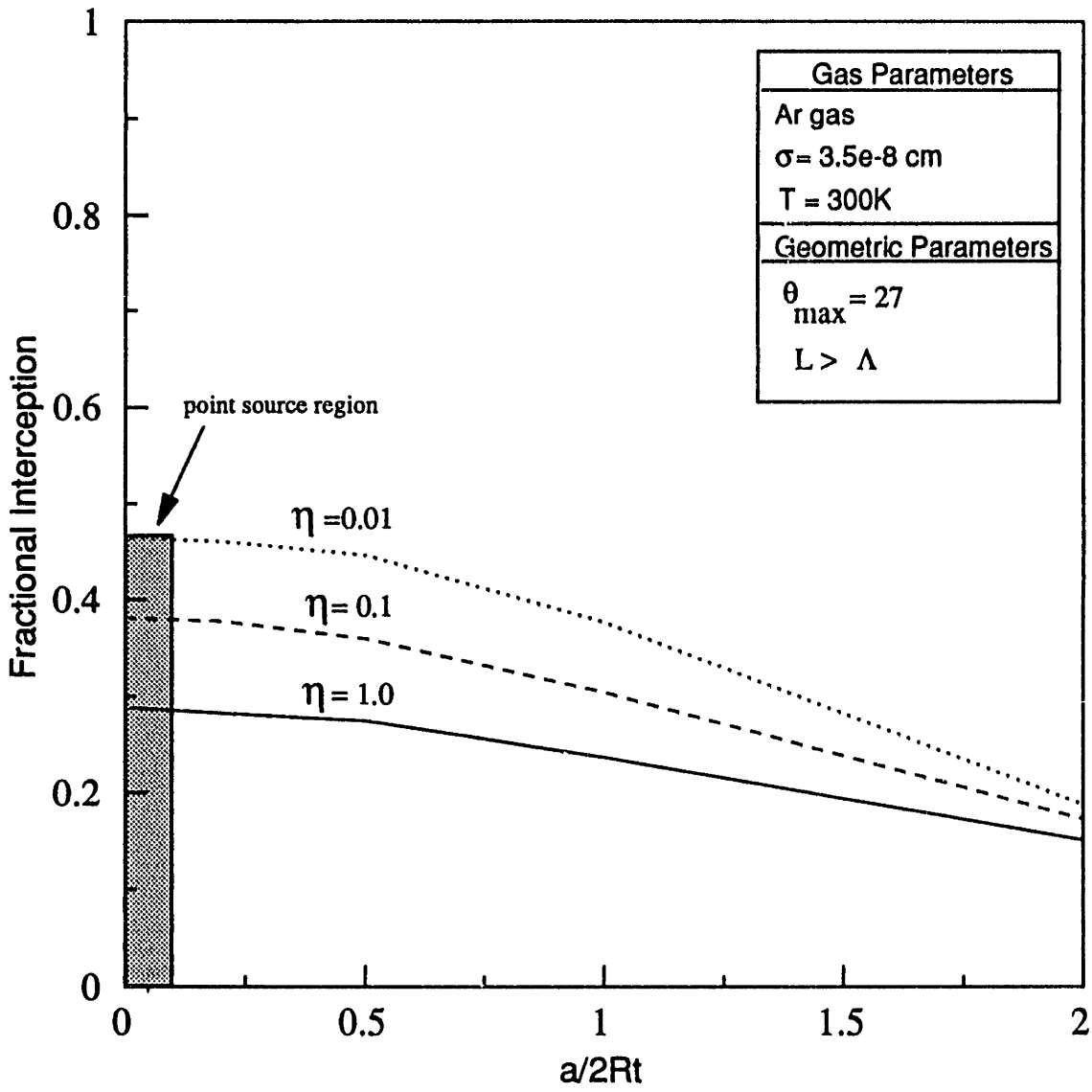

Figure 3-6. Fractional interception versus tube-to-target diameter ratio, a/2Rt, for various ηvalues.

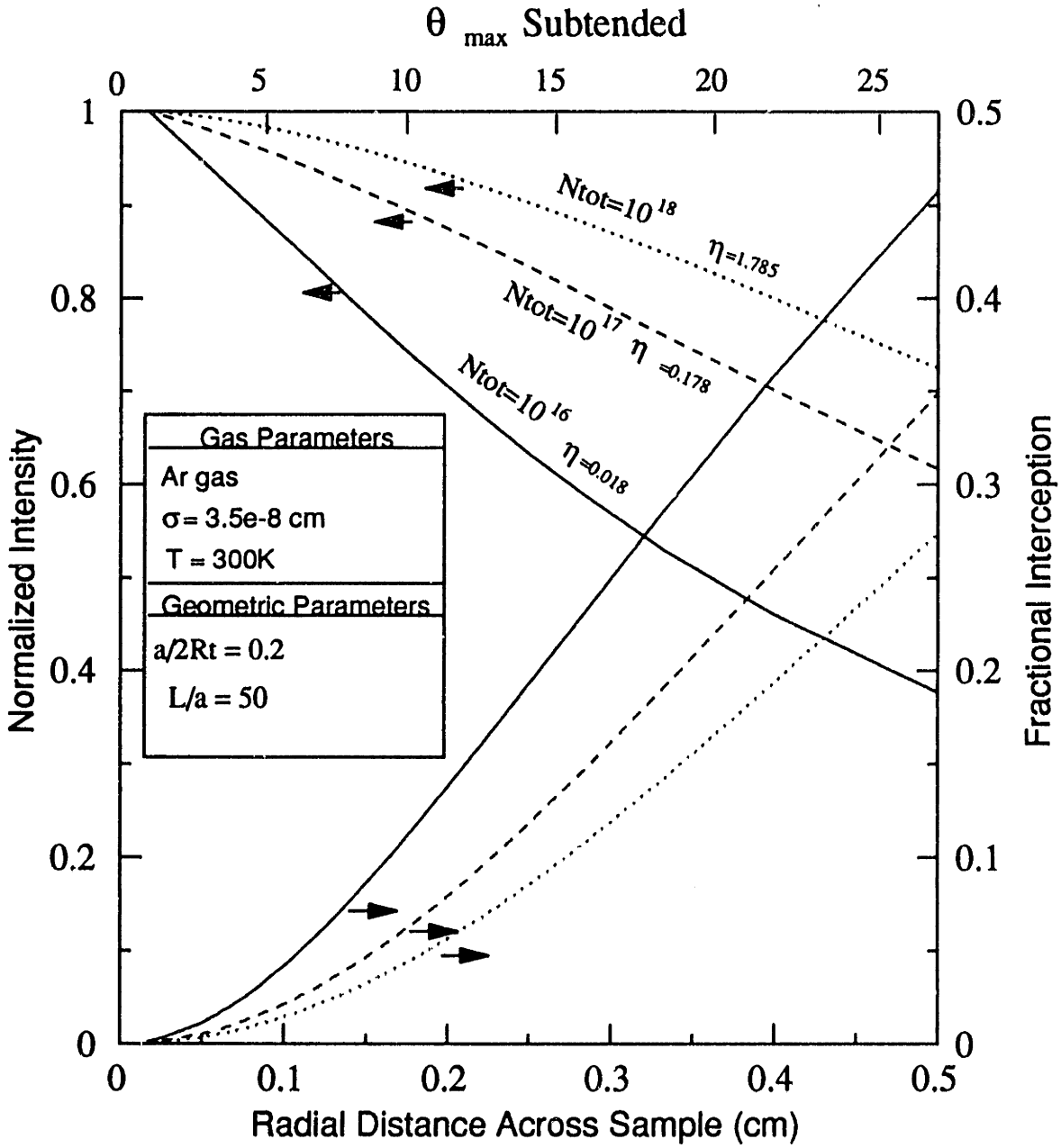

Figure 3-7. Flux intensity variation of a 0.2 cm i.d. opaque regime source versus radial distance across a 1 cm sample, d=1.0 cm, for various values of Ntot. Fractional interception versus angle subtended are provided on the opposite axes.

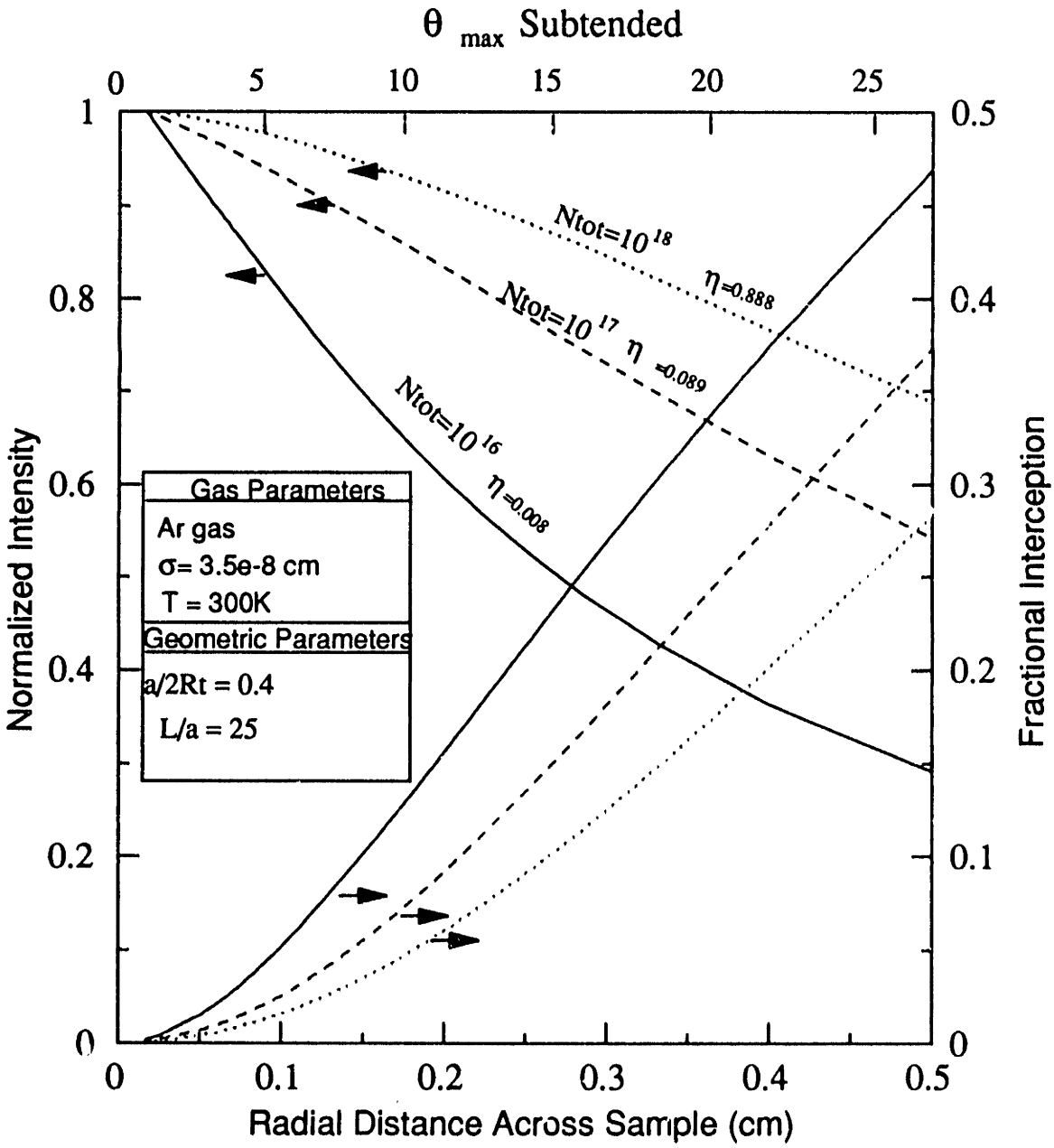

Figure 3-8. Flux intensity variation of a 0.4 cm i.d. opaque regime source at the same values of Ntot presented in Figure 3-7.

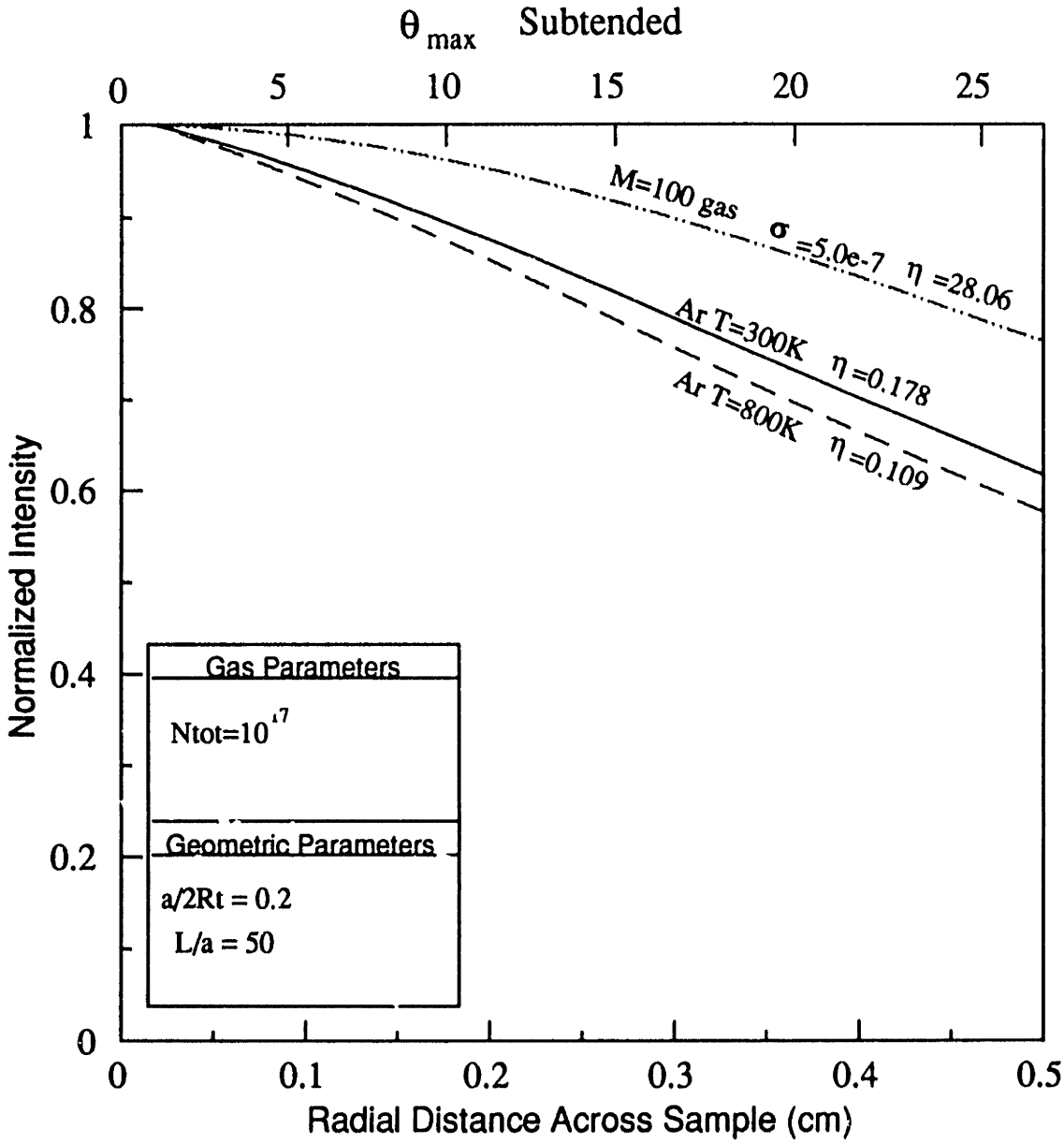

Figure 3-9. Sensitivity of opaque regime intensity distribution to gas temperature and molecular mass and size for constant Ntot.

"Flowtype" was written to allow calculation of intercepted flux (equation (3-1)) for a coaxial tube-sample geometry. Nested Gaussian quadratures were employed to solve the integrations to three significant figures. Details of this program are relegated to Appendix D. Figure 3-4 shows the broadening of the angular flux dispersion, $J(\theta)$, for an opaque regime point source ($a/2R_t<0.05$), 1.0 cm from the sample face, as the dimensionless parameter η is increased over three orders of magnitude. Because the beam molecules do not experience gas-phase collisions outside the tube, the fractional interception of a given co-axial target is a function of only of solid angle (θ_{max}) subtended by a given target. To the extent that the tube looks like a point source to the target area, the flux gradient across the target area may also be plotted as a function of θ_{max} subtended as shown in Figure 3-4. For comparison, the intensity variation of a transparent regime point source (equation (3-11), $L/a>40$) and a cosine emitter are shown. Figure 3-4 demonstrates the decrease in beam directionality with increasing η; at $\eta<0.01$ the beam shapes become very similar to those described by the transparent regime theory (equation (3-11)), while as $\eta>1.0$ the intensity distribution looks like that of the cosine emitter. Physically, as the opaque source throughput is increased, the viscous-Knudsen flow transition approaches the tube end (λ_{vip} becomes very small relative to a and very few molecules traverse the entire tube length without a gas phase collision. The beam peak intensity is thus decreased while the flux of non-directed molecules is increased. Figure 3-5 shows the fractional interception of an opaque regime point source as the source distance from the 1cm diameter sample is increased, which effectively decreases the maximum angle subtended as shown on the alternate x-axis of this plot. Fractional interceptions for $\eta\leq0.01$ are very similar to those plotted by Campbell and Valone [1985] for a transparent regime needle doser, but decrease significantly as η is increased and the beam losses directionality. We have noted that factional interceptions for $\eta\leq0.01$ opaque regime sources may exceed those calculated using equation (3-11). Mathematically this is due to the fact that the transparent regime

distribution, although highly peaked on axis, also has a very broad and slowly decaying tail at large angles which miss the target, while the opaque regime distributions are more heavily weighted at medium dispersion angles. For source tube diameters which can not be approximated as a point, fractional interception and target flux gradients are a function of the ratio of the tube-to-target diameter $a/2R_t$ as well as the solid angle subtended as shown in Figure 3-6. The relative decrease in factional interception for constant η as $a/2R_t$ is increased is largest for low η, or highly collimated beams, where large fractions of the total flux are intercepted in the point source region. The relative decrease in fractional interception with $a/2R_t$ is small ($\leq 2\%$) in the range $a/2R_t$=0-0.5, however, the sample flux gradients change much more rapidly on a percentage basis with $a/2R_t$ as demonstrated by comparison of Figure 3-7 ($a/2R_t$=0.2) to Figure 3-4 (point source).

For large $a/2R_t$ the sample flux gradient cannot be approximated by the normalized intensity function $J(\theta)$, but must be calculated as the ratio $I(\theta)/I(0)$ through full integration across the target surface as,

$$I(\theta) = f(\theta)\, N_{tot}/\Omega(\theta) \qquad (3\text{-}36)$$

where $\Omega(\theta)$ is the total solid angle subtended by the target at position θ. $I(0)$ is mathematically defined as the source intensity over the first degree of beam divergence (θ=1°). This normalized intensity is plotted as a function of radial distance across the 1cm diameter sample as a function of total throughput in Figure 3-7, where a=0.2 (1/8" nominal o.d. doser) and L=10 cm. Fractional interception versus θ_{max} is shown on the alternate axes. For comparison, we calculated flux gradients for a 1/4 nominal doser (a=0.4) with the same tube length and total throughput values as in Figure 3-8. Although the ratio $a/2R_t$ has increased, the value of η obtained in the 1/4" doser at the same total flow decreases so that the flux becomes more directed and the sample flux

gradients actually increase. It should be noted that L>Λ for all conditions in Figures 3-7 and 3-8. Sensitivities of beam directionality at a given throughput to gas temperature and molecular size were investigated in Figure 3-9 for $N_{tot}=10^{17}$. Increasing Ar gas temperature to 800K increases beam directionality slightly due to the decrease in gas density and collisionality. Increasing the collision diameter of the gas by and order of magnitude, and the molecular weight to 100 amu i.e. to simulate the flow characteristics of a medium size organic molecule, decreases the directionality of the flux significantly at the same total flow, due to the increase in η.

3.2 Operating Principles of the Impact Tube

Peak beam intensities were accurately measured in situ using an impact tube system described in Chapter 2 in which the probe face was rotated directly into the sample position (Figure 3-2). This facility allowed beam flux levels to be set directly preceding etching rate measurements. The etching rates of thin films were measured via laser interferometry in this apparatus, so the He-Ne laser spot was used to align the impact probe orifice exactly on the spot of etching rate measurement. The methodology described in Section 3.1 was employed for calculation of beam intensity variations and enhancement factors over sample areas (1 cm dies), since the beam profiling capabilities of the impact probe were limited. The probe was not designed for accurate radial positioning, however, flux fall-off from the sample center-to-edge was measured in 0.5 cm increments with reasonable accuracy through visual alignment of the probe, allowing us a measure of comparison between experiment and theory. The enhanced or "beam equivalent pressure" at the impact probe face was sensed using an MKS Baritron 170M-6B differential pressure transducer with its reference leg at the chamber base pressure. System base pressures were monitored with a Bayert-Alpert type ionization gauge. A 1.5mm diameter orifice was used in the probe face such that flow through the orifice was molecular, or at worst

transitional in nature. The flow path from the probe face to the capacitance manometer was of sufficiently large conductance and small volume that a stable beam pressure was attained in a few seconds. Since beam pressure measurements are made rapidly, thermal drift due to temperature fluctuations in the pressure transducer was not an issue. The transducer head was insulated but not heated, thus avoiding the effects of thermal transpiration on the pressure equilibrium. The measured impact pressure is directly related to the "beam equivalent pressure" which is employed in equation (3-8) to yield an experimental beam enhancement factor over the probe orifice area. Since probe orifice area is small compared to the sample die area, this is essentially a measure of the peak enhancement factor if the system is well aligned. Enhancement factors over the entire 1 cm^2 sample area are numerically estimated using the experimentally measured peak enhancement factor, and the opaque regime flux distributions.

This impact probe technique has been successfully employed for measurement of molecular, free radical, and atomic beam pressures. Some difficulty was encountered in reproducibly measuring beam pressures of atomic species such as F which stick readily to the inner walls of the impact tubing as discussed in Section 3.4. This problem may be alleviated through use of a less reactive probe material such as Al_2O_3, or in the case of atomic F and stainless steel, through a sufficient period of wall passivation before pressure readings are made. Alternately the measured impact pressure must be corrected by the apparent surface loss coefficient. A beam pressure correction is also necessary for accurate comparison of flows impinging on the probe face at various angles. At 45° incidence angles, measured beam pressures are attenuated by a factor of 2 below the expected cosine factor, versus those measured at normal incidence. Beam pressures measured at normal incidence, in fact, overpredict the molecular flux to the probe unless the pressure gradient associated with the flow of non-directed gas exiting the probe is considered. This effect is illustrated in Figure 3-3, where the relationship between the

incoming beams and the impact probe geometry are considered in more detail. First let us consider the working assumptions for the impact probe system. Since the impact probe is a stagnation tube, there should be no net gas flow into the probe orifice when the system pressure comes to steady-state. We can thus equate the net flow of directed flux into the probe orifice and the gas flux out of the probe,

$$m_{beam} = m_{out} \tag{3-37}$$

here we have neglected the flux of background gas into the probe since it is typically <1% of the beam flux. At the highest beam fluxes employed, beam pressures are on the order of 10^{-2} torr, resulting in $\mathbf{Kn}_a$=1-5 at the probe orifice. Although we are bordering on the transitional regime here, we assume that the beam flux into the orifice is not influenced by gas-phase collisions, multiple scattering events from the probe face, or scattering from the orifice lip. Under these assumptions the mass flux into the probe is given by,

$$m_{beam} = f_{beam} A_o \cos(\psi) = \left(\frac{P_{beam}}{k_b T_{beam}}\right) v \cos(\psi) \tag{3-38}$$

where introduction of beam velocity, v, allows us to write the directed flux in terms of an equivalent beam pressure. Although the gas flux out of the orifice in steady-state must be equal to the flux in, the measured beam pressure depends on the impingement angle of the beam. A normally directed beam is collimated by the probe orifice and impinges on the interior tube wall approximately 8 cm from the orifice entrance at the tube elbow (see Figure 3-3). If we assume that diffuse emission of gas from this point represents our major exit gas source, we must consider that a pressure gradient develops between this source point and the orifice due to the tube flow

resistance. Since there is no net gas flow from the high pressure point, P_2, and the manometer head, P_2 is the measured pressure. Gas flow out of the probe is given by the pressure behind the probe face, P_1, which we assume is an isotropic source, and the probe orifice conductance. If we consider the tube and orifice conductances in series, the system pressures are related by the following equation,

$$m_{out} = C_{total} \frac{(P_2 - P)}{k_b T} = C_{total} \frac{(P_{meas} - P)}{k_b T} \tag{3-39}$$

where the total series conductance may be written in terms of the Clausing factor, K [8],

$$C_{total} = \left(\frac{1}{C_o} + \frac{1}{C_t}\right)^{-1} = \left(\frac{K d_t^2}{d_o^2 + K d_t^2}\right) \frac{v A_o}{4} \tag{3-40}$$

Note here that we have again assumed that the gas flow dynamics at the orifice are non-collisional, such that the exiting gas experiences a pressure drop down to the chamber base pressure. Given the probe orifice diameter, d_o=1.5mm, the tube inner diameter, d_t=5mm, and the tube length:diameter ratio of 16 gives a Clausing factor of about 0.1, making the bracketed term in equation (3-39) 0.51. The conductance through an orifice in the molecular flow regime is given by $vA_o/4$, so the net effect of the series conductance is to increase in measured beam pressure by a factor of two, which is observed experimentally (see Figure 3-12). Equating the right hand sides of (3-37) and (3-38) allows a calculation of the beam flux, f_{beam}, once the measured pressure, P_{meas}, is known. The correction factor of 0.51 is not necessary for beams entering the probe orifice at 45° since the directed beam impacts the tube wall near the orifice (Figure 3-3), thus the flow resistance of the tube is unimportant and the measured pressure is the pressure P_1. All data

presented herein is taken at normal beam incidence angles, and the enhancement factor data has been corrected for the tube conductance effect. Under typical operating conditions, the background flux entering the impact tube was <1% of the beam flux, so the enhancement factor could be approximated as the ratio P_{beam}/P. From the mass balance around the impact orifice, the measured impact pressure can be directly related to the peak enhancement factor in the form

$$E = \frac{P_{meas}}{(4*P)} \qquad 45°\textit{incidence}$$
$$E = \frac{P_{meas}}{(8*P)} \qquad \textit{normal incidence} \tag{3-41}$$

Finally, it is important to consider that in addition to the flux of background gas into the impact tube, in the experiments where multiple beams are employed, several directed gas fluxes are impinging on the impact orifice simultaneously. Since the ion sources employed in this work were broad beam sources (see Chapter 4), the directed flux from the ion beam was typically low even though the background pressure increase due to the ion source throughput was very large, typically 10^{-5} torr. Beam pressures on the order of $1x10^{-6}$ to $5x10^{-6}$ torr were typical for the ion beam without differential pumping; with the differential pumping system beam pressures decrease only slightly, while the background pressure decreases by an order of magnitude. Since the multiple beams are non-collisional, we may assume the various gases are non-interacting, allowing us to extend equation (3-38) in the form

$$m_{beam} = \left(\frac{P_{beam}^{tot}}{k_b}\right)*\left[x_1\left(\frac{v_1}{T_1}\right)\cos(\psi_1) + x_2\left(\frac{v_2}{T_2}\right)\cos(\psi_2) + \ldots x_n\left(\frac{v_n}{T_n}\right)\cos(\psi_n)\right] \tag{3-42}$$

where $x_1..x_n$ denote the mole fractions of the various n gases in the mixture of beams. Since we are interested in the measured flux at the sample face and not the beam flux normal to the doser

tubes, we absorb the cos(ψ) term. Substituting the formula for mean velocity from kinetic theory, and assuming similar beam temperatures, we can write the total beam pressure in terms of an effective mass which represents the RMS mass of the gas mixture,

$$m_{beam} = \left(\frac{P_{beam}^{tot}}{k_b T}\right)\left(\frac{8k_b T}{\pi}\right)^{1/2}\left[\frac{x_1}{\sqrt{(m_1)}} + \frac{x_2}{\sqrt{(m_2)}} + \ldots \frac{x_n}{\sqrt{(m_n)}}\right] = \left(\frac{P_{beam}^{tot}}{k_b T}\right)\left(\frac{8k_b T}{\pi}\right)^{1/2}\left[1/\sqrt{m_{rms}}\right] \quad (3\text{-}43)$$

This method was employed to calculate the flux of CF_2 from the pyrolysis of HFPO which results in a 50:50 molar mixture of CF_2 and CF_3CF_2O if the reaction is 100% efficient.

Typically during experimentation, we incrementally increase the flux of one of the beam sources while holding the others constant. When this is the case, the beam pressure reading may be zeroed at the capacitance manometer controller before increasing the beam pressure. The subsequent incremental increase in the total measured impact pressure due to that individual beam may be calculated according to equation (3-37) where the beam species mass is the appropriate mass for calculation of the incremental pressure rise.

Although our ability to characterize beam flux distributions experimentally is limited, Figures 3-10 and 3-11 demonstrate a reasonable agreement between data and the theoretical predictions of Giordmaine and Wang [1960]. The data shown in Figures 3-10 and 3-11 respectively are beam profile measurements for argon and the fluorocarbon compound hexafluoropropylene oxide (HFPO) through a 0.2 cm i.d. source and with a 1.0 cm source-sample distance. HFPO has a molecular weight of 166 amu and a collision diameter which we estimated at order 10^{-8} cm through linear addition of bond lengths along the carbon backbone. The solid lines in these figures represent theoretical predictions at similar values of η, and the relative

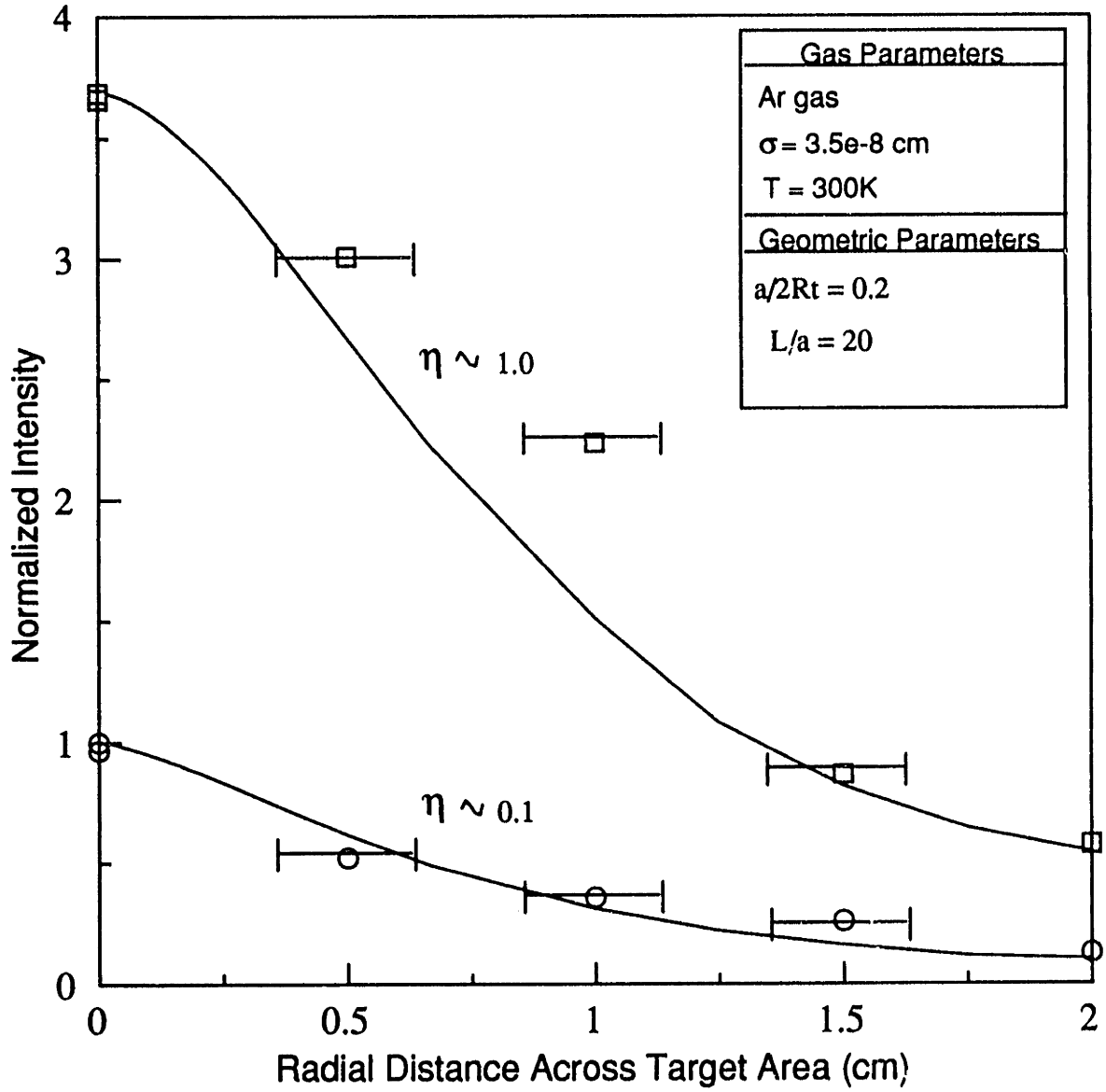

Figure 3-10. Comparision of Giordmaine-Wang theory to experimentally measured Ar beam shapes.

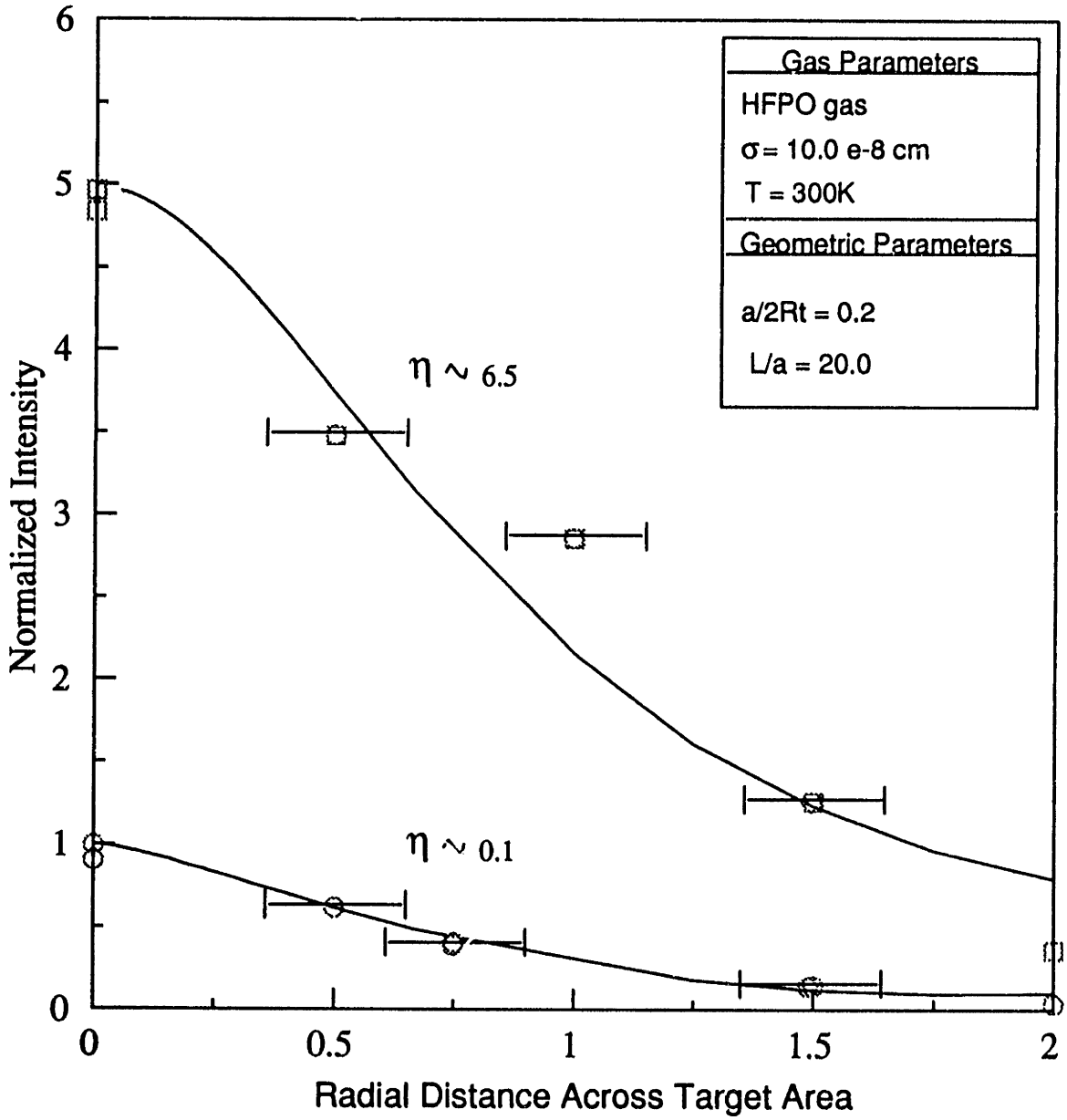

Figure 3-11. Comparision of Giordmaine-Wang theory to experimentally measured HFPO beam shapes.

scaling between curves demonstrates the difference in peak intensity at the two η values. Error bars on the probe positioning accuracy are rather large, but the flux measurement repeatability is very good as demonstrated by the duplicate data taken at the target center. The beam shapes and peak intensities predicted via this simple theory are well within the experimental uncertainty of our measurements for both argon and the larger molecular gas, HFPO. Figure 3-12 shows peak enhancement factors measured for the 0.2 cm HFPO source at 1.0 cm from the sample (probe) face, as a function of total throughput. Peak enhancement factors were calculated according to equation (3-8) where the HFPO base pressure has been corrected using an estimated ion gauge sensitivity of 3.0 [O'Hanlon,1980] which was found to agree with the expected pumping speed. Several sets of data are presented, one of which was taken with the beam at normal incidence to the probe (squares) to demonstrate the beam impingement angle effect which must be corrected by a factor of 0.51 (see Figure 3-3). Due to the decrease in beam directionality (increase in η) with throughput, our simulations predict large peak enhancement factors at low HFPO flux, which subsequently fall off with increasing throughput. This trend was verified experimentally in the data taken with a 45° beam impingement angle. At medium to high HFPO fluxes, peak enhancement factors around 6 were measured in our system where the HFPO pumping speed was on the order of 800 l/s. At the lowest throughputs, peak enhancement factors up to 10 were measured in good agreement with the data of Campbell and Valone [1985] for transparent regime dosers. Integrated enhancement factors over the entire 1 cm diameter sample area can be significantly lower than this measured peak value when flux intensity gradients are large.

While the impact tube allowed us a method to measure beam profiles and enhancement factors in situ, it is also possible to measure beam enhancement factors mass spectrometrically with the UTI-100C in the beam characterization position (Figure 2-6). The axial-cross beam ionizer (modified EAI QUAD 2100) mounted on this head has an approximate 1 cm^2 orifice on

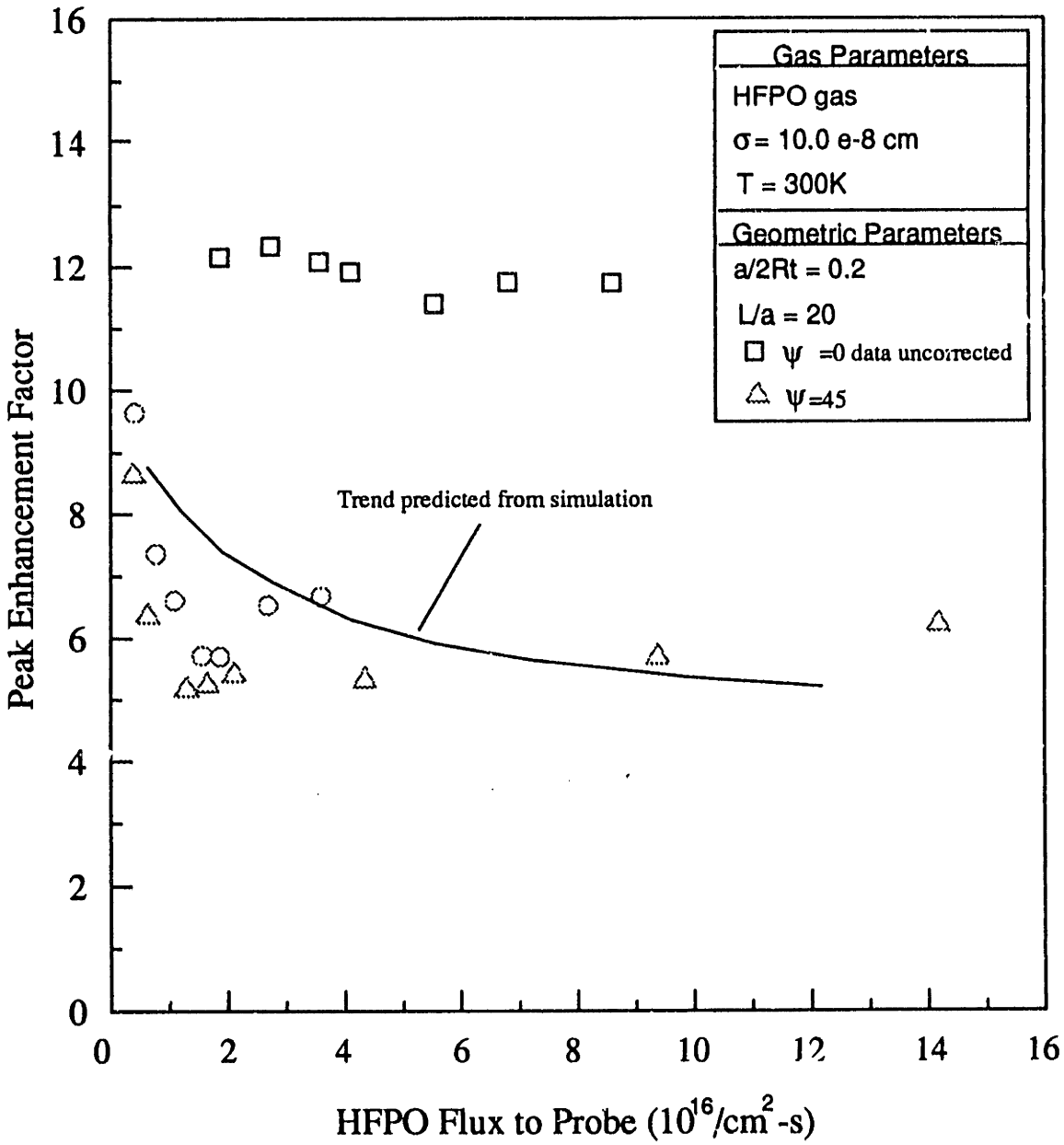

Figure 3-12. Measured peak beam enhancement factors versus HFPO flux. Ionization gauge sensitivity for HFPO is estimated a factor of three greater than N2. Data taken at normal incidence is uncorrected for beam incidence angle factor of 0.51.

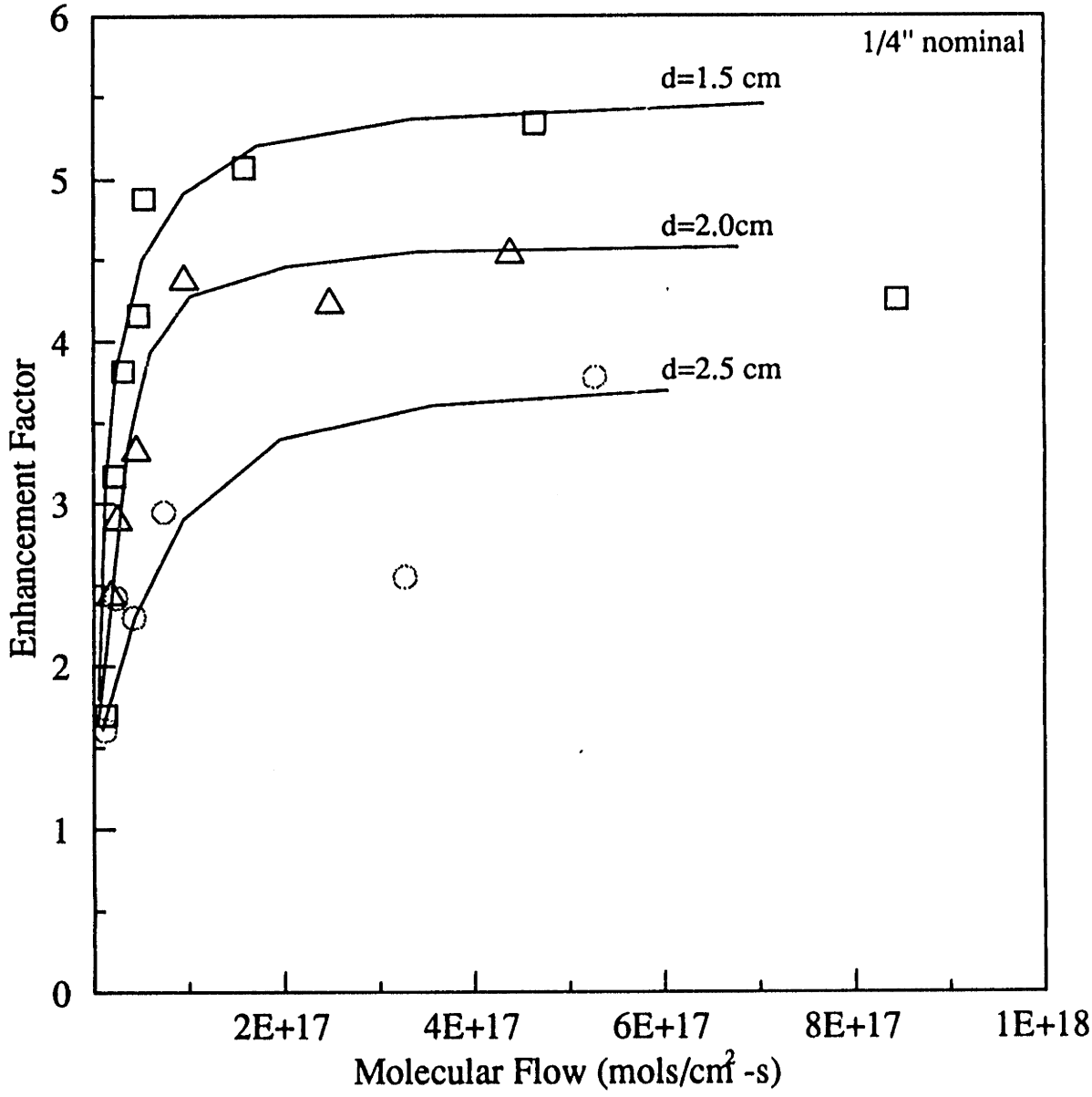

Figure 3-13. Enhancement factors for N2 flowing through 1/4" stainless steel tubing (L>40 cm) measured mass spectrometrically over the 1 cm^2 ionizer orifice.

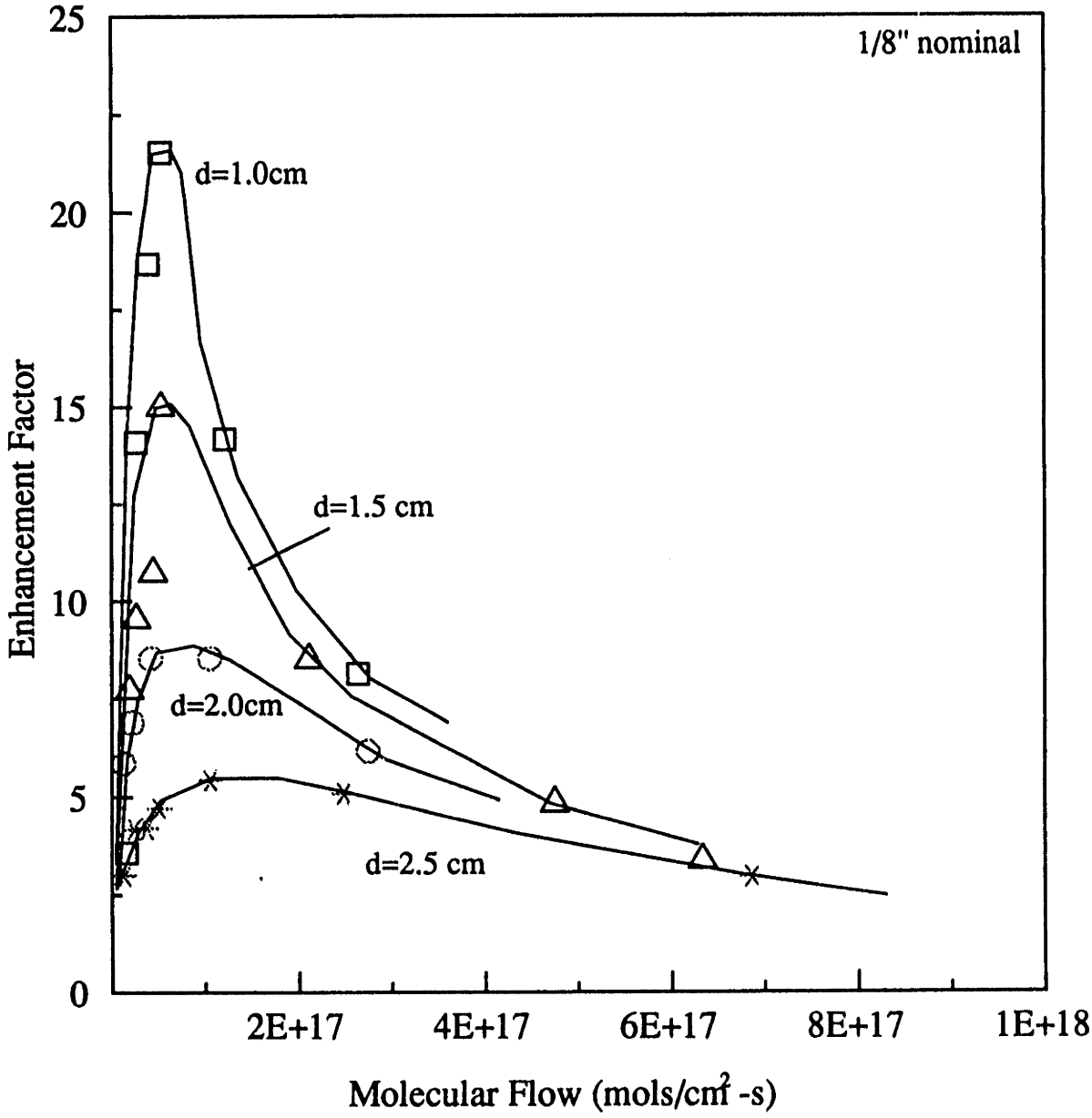

Figure 3-14. Enhancement factors for N2 flowing through 1/8" o.d. tubing (L>40 cm) measured mass spectrometrically over the 1 cm^2 ionizer orifice.

the probe axis. Beam enhancement factors over this 1 cm^2 orifice may be estimated by simultaneously measuring the sum of the beam pressure and background pressure at the mass spec ionizer, and the chamber base pressure using the Bayert-Alpert ionization gauge. A sensitivity calibration curve for the beam gas must be constructed before such an experiment to allow accurate conversion of ion current signal from the UTI-100C to absolute pressure. The procedure is described in the UTI-100C operator's manual. N_2 enhancement factors were measured as a function of total molecular flow, and doser-to-ionizer distance for 1/4" (nominal stainless steel o.d.) and 1/8" straight tubes respectively as presented in Figures 3-13 and 3-14. The data demonstrates the fall-off in enhancement factor and the smoothing of flux gradients as the doser-sample distance is increased, or the total flow is increased. The enhancement factors measured via this technique are in good agreement with the impact tube method when the mass spectrometer sensitivity is carefully calibrated.

3.3 Characterization of the CF_2 radical beam

CF_2 radicals were produced through a pyrolytic technique characterized by Knickelbein et al. [1985] which allows the economical generation of large radical fluxes not possible with laser generated sources utilized by other researchers [Langan et al., 1988]. This technique involves the unimolecular decomposition of hexafluoropropylene oxide (HFPO) at moderate temperatures (350°-450°C) to produce CF_2 and a stable molecular by-product (CF_3COF) with a low sticking probability [Winters, 1978] according to,

$$CF_3O\text{-}CF\text{-}CF_2 \text{ ---> } CF_3\text{-}CF{=}O + CF_2$$

(the oxygen in HFPO is bonded to both the second and third carbon). Knickelbein found complete saturation of this pyrolysis for tube wall temperatures above 450°C with a hot zone

residence time of ~10 msec using LIF for CF_2 species detection. Further analysis showed vibrational state population in pyrolytically produced CF_2 to be similar to that generated in a pulsed DC discharge. With estimated tube wall temperatures of 800K, $0_0/2_1$ vibrational temperature of the pyrolytic CF_2 was estimated at 360 K.

Since our doser design differs from that of Knickelbein et al. [1985], we have fully characterized pyrolysis and residence time effects in our source tube mass spectrometrically as detailed below, to assure performance in or near the saturation regime. Our doser configuration consists of a resistively heated 0.2 cm ID pyrex tube with a 2-3 cm hot zone (Figure 3-15), resulting apparently in complete decomposition of HFPO above 450°C. A typical chamber pressure rise due to HFPO flow was $3x10^{-6}$ torr. This corresponded to an HFPO flow rate of about 0.2 sccm, giving a 10 millisecond residence time in the 2 cm hot zone of the pyrolysis tube, similar to that of Knickelbein et al. Consequently, we observed onset and saturation of CF_2 production at similar temperatures, and have operated the doser at 460°C throughout these studies where near 100% production efficiency from the parent gas is expected. The flux range used in these studies extends from zero to $5x10^{17}$ mols/cm^2-s (2.5 mTorr). Lower fluxes were employed when the ion source was not differentially pumped to avoid back-mixing effects in the Kaufman gun discharge chamber. The upper CF_2 flux limit is representative of fluorocarbon radical fluxes estimated by modeling of fluorocarbon plasma kinetics [Butterbaugh, 1990] and via LIF studies of real plasmas [Buchmann et al., 1990; Baston, 1991]. The effect of HFPO fluence on CF_2 production efficiency is discussed below. HFPO used in these studies was a Dupont technical grade (98+%) with hexafluoropropylene (<1%) and solubilized air(<0.3% N_2/O_2) being the major impurities.

Flow dynamics of an opaque regime 0.2 cm i.d. tube were discussed in Section 3.1 above. The pyrolysis tube was designed with a 4 cm tip length fed by a larger 1/4" o.d. tube gas reservoir

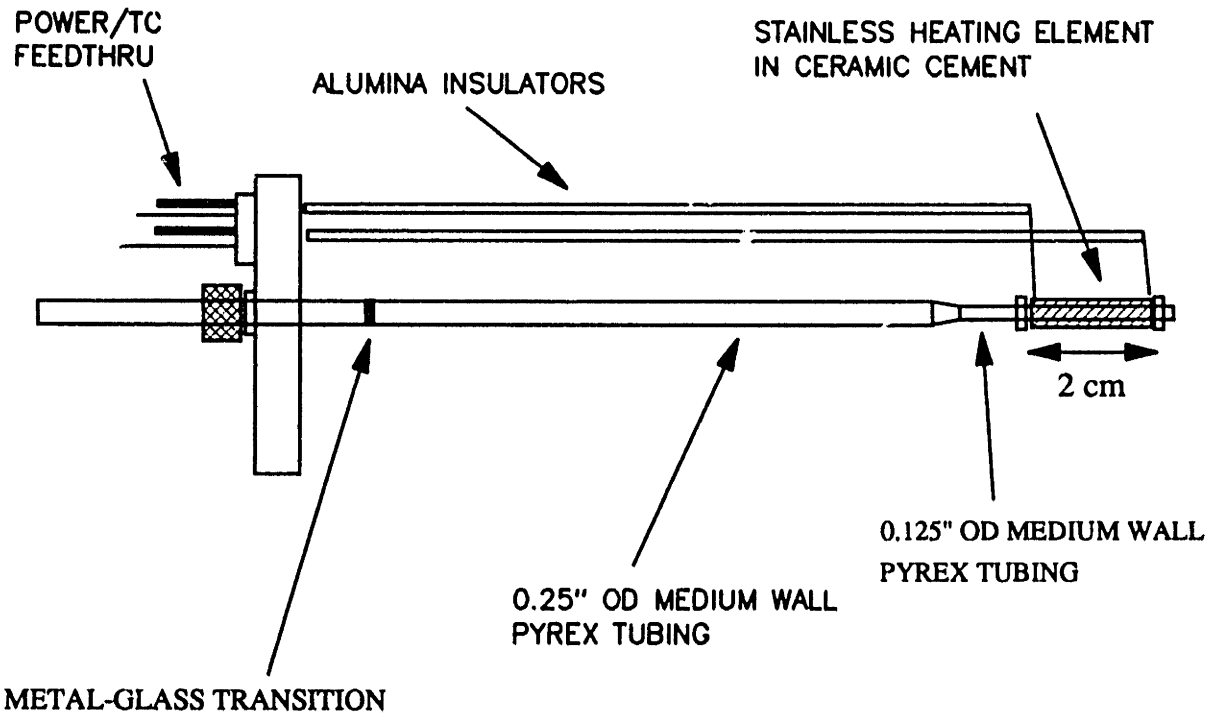

Figure 3-15. HFPO pyrolysis doser geometry.

to maximize gas collimation and throughput. This tip length is greater that the tube critical length for the CF_2 flux range of interest. CF_2 flux gradients expected over the 1-cm sample die for the range of fluxes employed are represented in Figure 3-7, varying from 20% to 60% in the flux range of 10^{18} to 10^{16}. When the laser interferometer spot is well aligned with the flux probe orifi, the flux gradients are not an issue since etch rates are measured only at the point of flux measurement. The flux gradients are more of a concern when it is necessary to uniformly etch entire sample dies, or in the line-of-site mass spectral characterization of etching products, where variations of radical coverage over the die surface may give different product emission characteristics. This issue is discussed in more detail in Chapter 4.

Mass Spectral Characterization of HFPO Pyrolysis

The pyrolysis of HFPO was characterized as a function of tube wall temperature by monitoring the mass spectrum of the products flowing out of the tube, and into the UTI-100C mass spectrometer in the beam characterization position. Room temperature HFPO cracking patterns have not been previously reported to our knowledge, but are summarized for electron impact energies of 70 eV and 20 eV, respectively, in Table 3-3. Dominant mass peaks in the 0-150 amu region include 31 (CF^+). 47 (COF^+), 50 (CF_2^+) and 69 (CF_3^+). Relative peak heights indicate that CF_2^+ is the dominant cracking product at 20 eV while CF^+ is the dominant product at 70 eV. The behavior of major peaks in the mass spectrum of room temperature HFPO with increasing electron impact energy has been characterized in the range of 20 eV to 70 eV [Gray and Butterbaugh, 1989].

In the pyrolysis mixture, because CF_2^+ is a product of the electron impact of HFPO and CF_3CFO, as well as CF_2, at high ionizer energies, it is advantageous to choose an electron energy which ionizes the CF_2 radical, but which produces as little dissociation as possible of higher

molecular weight species. Therefore, the ionizer electron energy was held at 20 eV (the minimum for the mass spectrometer) for the HFPO pyrolysis characterization to increase sensitivity to the free radical CF_2. Cracking patterns of the HFPO pyrolysis stream at 70 eV and 20 eV are provided in Table 3-3 for comparison to cold HFPO cracking patterns. The appearance potential for the process

$$CF_2 + e^- \text{----> } CF_2^+ + 2e^-$$

has been measured at 13.3 eV [Lossing, 1963]. Appearance potentials for the dissociative processes are unknown, but are expected to be several eV larger, and may be estimated through the bond addition method suggested by Lossing [1963]. For instance, production of a CF_2^+ ion from the CF_3COF byproduct involves the net breakage of one additional C-C bond at approximately 3.6 eV [Dickerson et al.,1979], so we estimate an appearance potential of about 17 eV for the process,

$$CF_3COF + e^- \text{ ----> } CF_2^+ + COF_2 + 2e^-$$

Similarly the lowest energy electron impact process for the production of CF_2^+ from the parent HFPO gas involves the net breakage of one additional C-C bond and should have a comparable appearance potential. Unfortunately, the minimum electron impact energy attainable with the UTI-100C system is 20 eV such operation near the CF_2 radical appearance potential was not possible.

Lossing [1963] also summarizes a form for the increase in mass spectrometric detection sensitivity to the free radical via a direct ionization process versus the dissociative ionization of a molecular gas bearing the same ion,

Table 3-3 HFPO Cracking Patterns

AMU	Probable Fragment	T = 25°C V_{ee} = 20 eV	T = 25°C V_{ee} = 70 eV	T = 460°C V_{ee} = 20 eV	T = 460°C V_{ee} = 70 eV
low AMU					
12	(C+)	nm	0.23	nm	0.38
19	(HF+)	0.03	0.09	nm	nm
24	(C2+)	nm	0.05	nm	nm
31	(CF+)	0.39	6.5	.27	2.96
44	(CO2+)	0.04	0.05	nm	nm
47	(COF+)	0.07	0.63	.08	0.60
50	(CF2+)	1.0	1.0	1.0	1.0
69	(CF3+)	0.48	0.32	.29	0.68
high AMU					
78	(C2F20+)	nm	0.1	0.53	nm
81	(C2F3+)	0.1	1.0	0.90	nm
97	(C2F30+)	0.82	0.07	0.64	nm
100	(C2F4+)	1.0	0.17	1.0	nm
119	(C2F5+)	0.15	0.03	0.02	nm

$$\frac{C_r}{C_m} = \frac{2k_b^3T^3 + (V-E)k_b^2T^2}{2k_b^3T^3 + (E-I)k_b^2T^2}\exp\frac{-[V-E]}{k_bT} \qquad (3\text{-}44)$$

Here, T is the electron emitting filament temperature (2000K), E is the electron impact energy, I is the radical ionization potential, and V is the appearance potential of the radical ion from the molecular species. Using the values quoted above for the free radical and dissociative ionization process thresholds indicates that the sensitivity to free radical detection is increase by a factor of 10^4 by working at 20 eV versus 70 eV electron impact energies, thus greatly increase our sensitivity to CF_2 radicals versus other components of the pyrolysis mixture.

Behaviors of the primary mass peaks in this system were studied as a function of tube wall temperature in the range of 300 K to 800 K at a 20 eV electron impact energy. Figure 3-16 shows the behavior of the mass 50 (CF_2^+) peak versus tube wall temperature. The rapid onset of the HFPO pyrolysis to form CF_2 occurs at approximately 720 K, in good agreement with tube wall temperatures estimated in the experiments of Knickebein et al. [1985], and saturation of the CF_2 production occurs near 800 K. Figure 3-17 is a plot of the ratio of the CF_2 peak to the CF_3 peak versus temperature. Plotting mass ratios eliminates noise due to variations in the flow rate and base pressure during the series of readings, and allows us follow the CF_2^+ peak growth by comparison to parent gas peaks. The CF_2^+/CF_3^+ ratio starts increasing at about 500 K, which corresponds to the minimum temperature at which Knickelbein et al. could detect CF_2 radicals by LIF, and has a sigmoidal shape with a knee in the range of 750 K to 800K. Plotting the ratio of CF_2 to higher amu peaks such as 97 ($C_2F_3O^+$) (Figure 3-18) show a similar sigmoidal behavior, indicating reduction in the parent gas peak and increase of the CF_2^+ peak due to CF_2 radical production. It should be noted that the mass spectral intensity ratios CF_2^+/CF_3^+ and $CF_2^+/C_2F_3O^+$

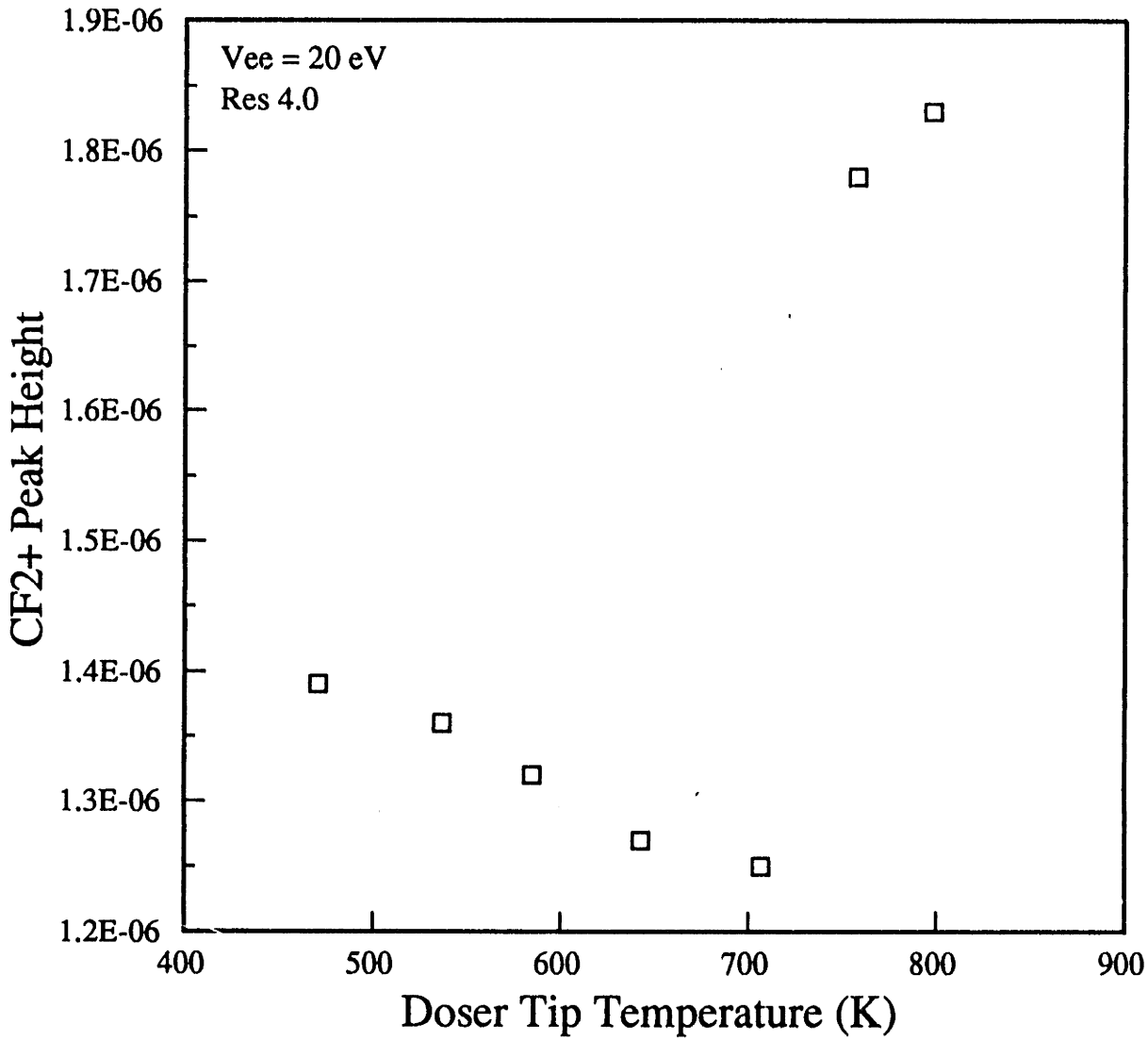

Figure 3-16. Variation in amu 50 (CF2+) peak height with pyrolysis tube tip temperature.

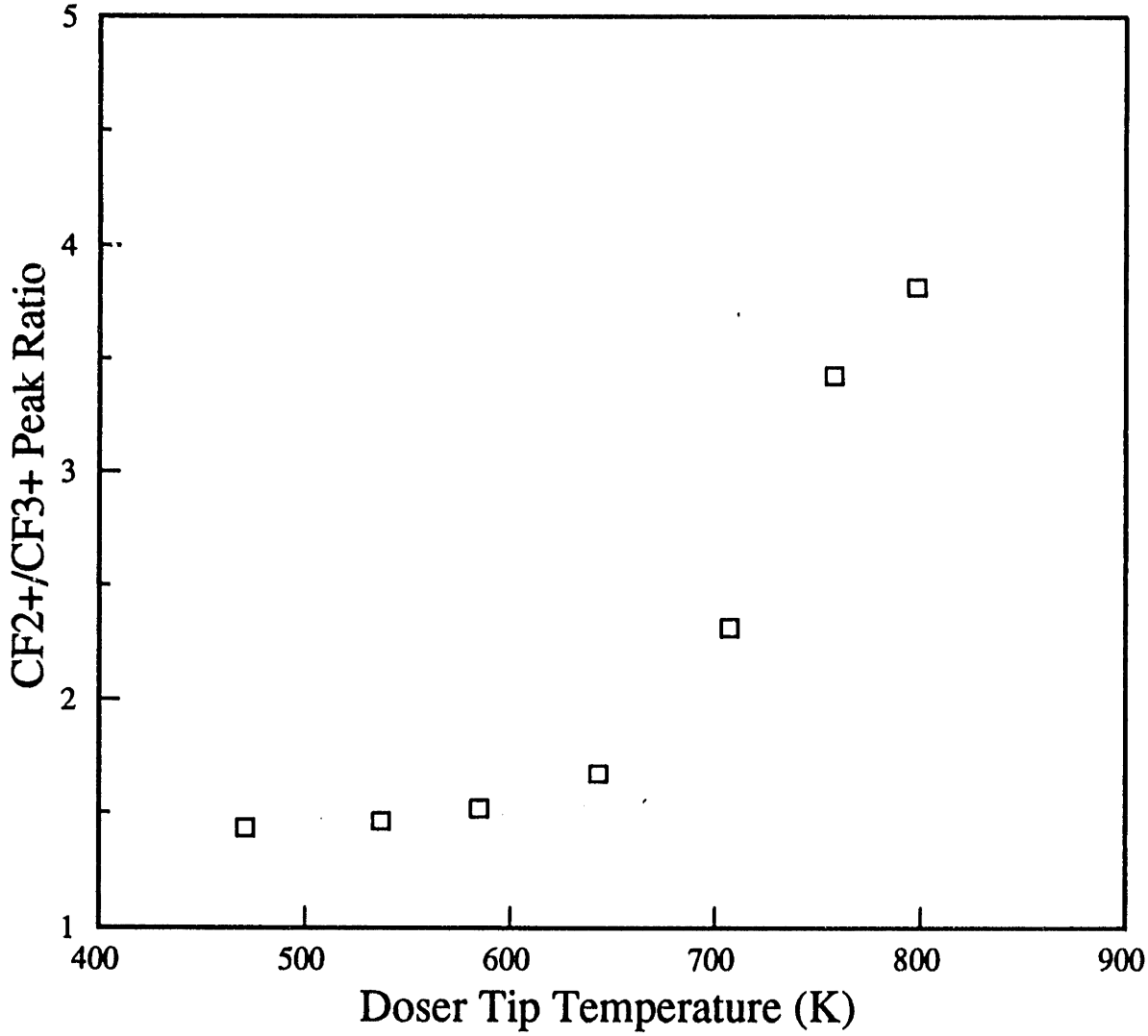

Figure 3-17. Variation in CF2+/CF3+ peak ratio with pyrolysis tube tip temperature.

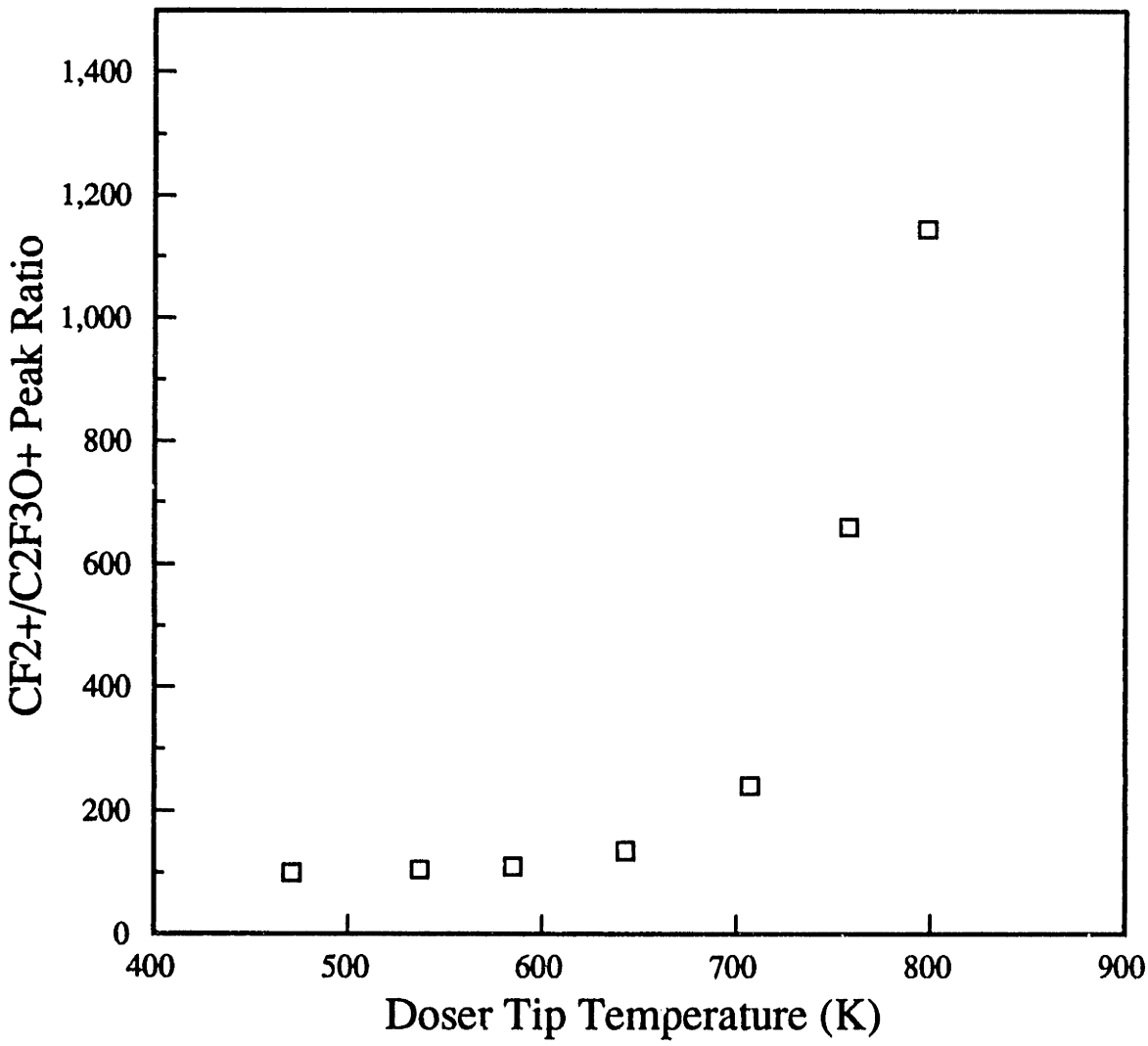

Figure 3-18. Variation in CF2+/C2F3O+ peak ratio with pyrolysis tube tip temperature.

do not completely "flatten" as shown in the LIF work of Knickelbein et al. due to the effect of vibrational heating on the dissociative ionization probability of the molecular byproduct e.g. the production of CF_2^+ from electron impact cracking of CF_3COF is more likely as the gas becomes hotter. For this reason, we have chosen the "knee" or break-point as indicated in Figure 3-17 as the doser operating temperature, and have held the tip temperature at 740-760 K during experimentation. The saturation behavior observed in our mass spectrometric characterization of the pyrolysis of HFPO in this apparatus supports the work of Knickelbein et al. and indicates that pyrolysis was occurring with an efficiency close to 100% The dependence of the pyrolysis on the flow rate of HFPO was also investigated at 740 K as shown in Figure 3-19. It was found that there is no significant change in the CF_2^+-to-CF_3^+ signal ratio over a flow range of 0.2 sccm to 0.6 sccm, indicating that the CF_2 production was well within saturation with a tube wall temperature of >460°C.

Finally, one must also be concerned with the effect of the CF_3CFO and any unreacted HFPO on the etching reaction investigated in this thesis. The rates of physical sputtering of polysilicon and SiO_2 by Ar^+ were not measurably affected by the presence of the "cold" HFPO beam as show in Figures 3-20 and 3-21, indicating that neither unreacted HFPO nor the O_2 impurity confounded the yield measurements presented in this thesis. This is not surprising as Winters [1978] determined that the sticking probability of molecular species like CF_4, CF_3H, and CF_3Cl is less than 10^{-7}. It was expected that the sticking probability of CF_3CFO is also negligible since it is a stable molecular species. Given a reasonable estimate of 3-5 Kcal/mole for the adsorption energy of HFPO on silicon or silicon dioxide, order of magnitude estimates would place HFPO steady-state fractional coverage in the range of 10^{-8} to 10^{-10} monolayer for the fluxes employed [Adamson, 1982]. Thus, it was reasonable to assume that the only species in the pyrolyzed HFPO beam which can affect the etching of the SiO_2 was the CF_2 radical. XPS studies

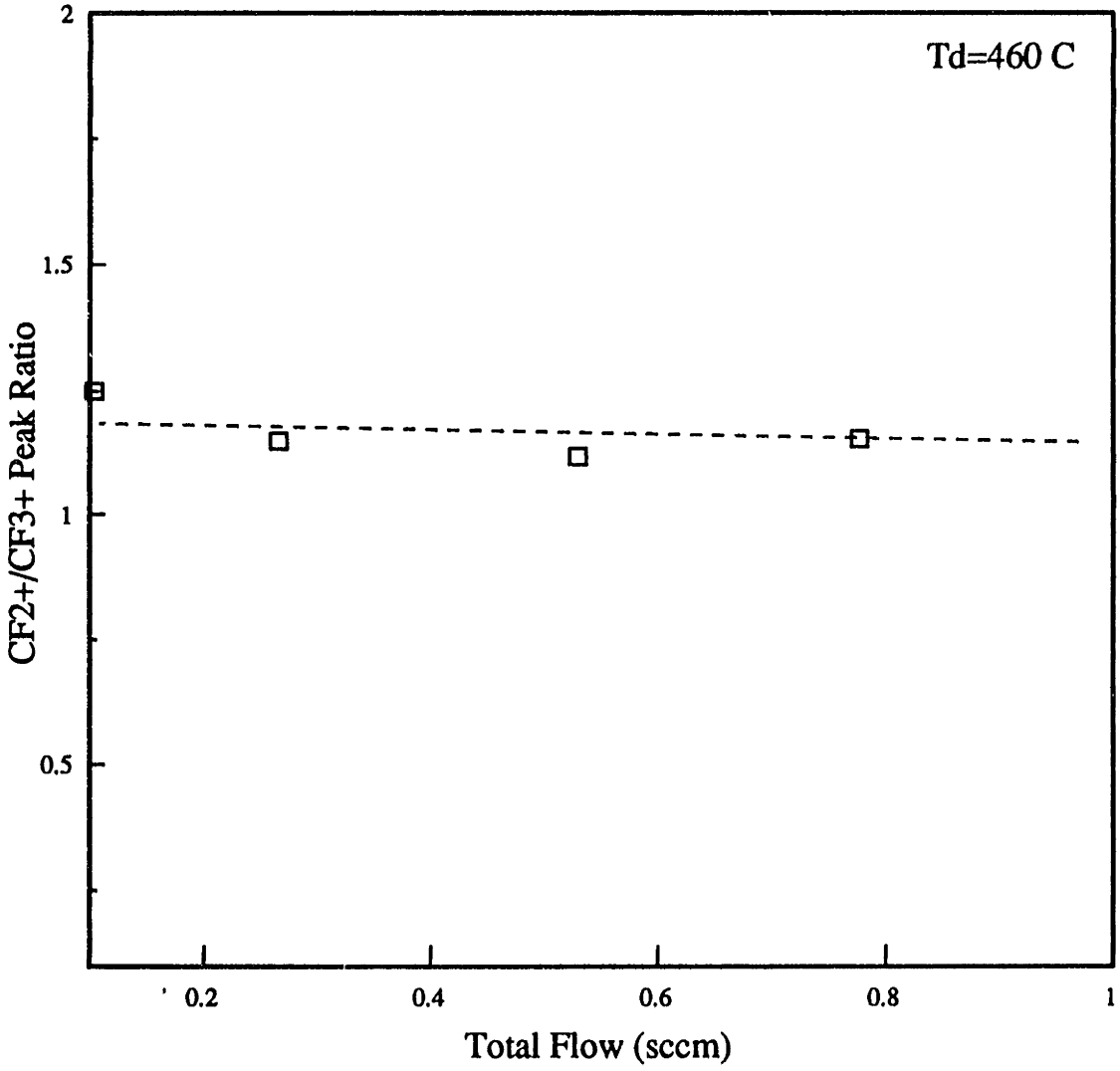

Figure 3-19. Variation in CF2+/CF3+ peak ratio with HFPO flow rate at 460 C.

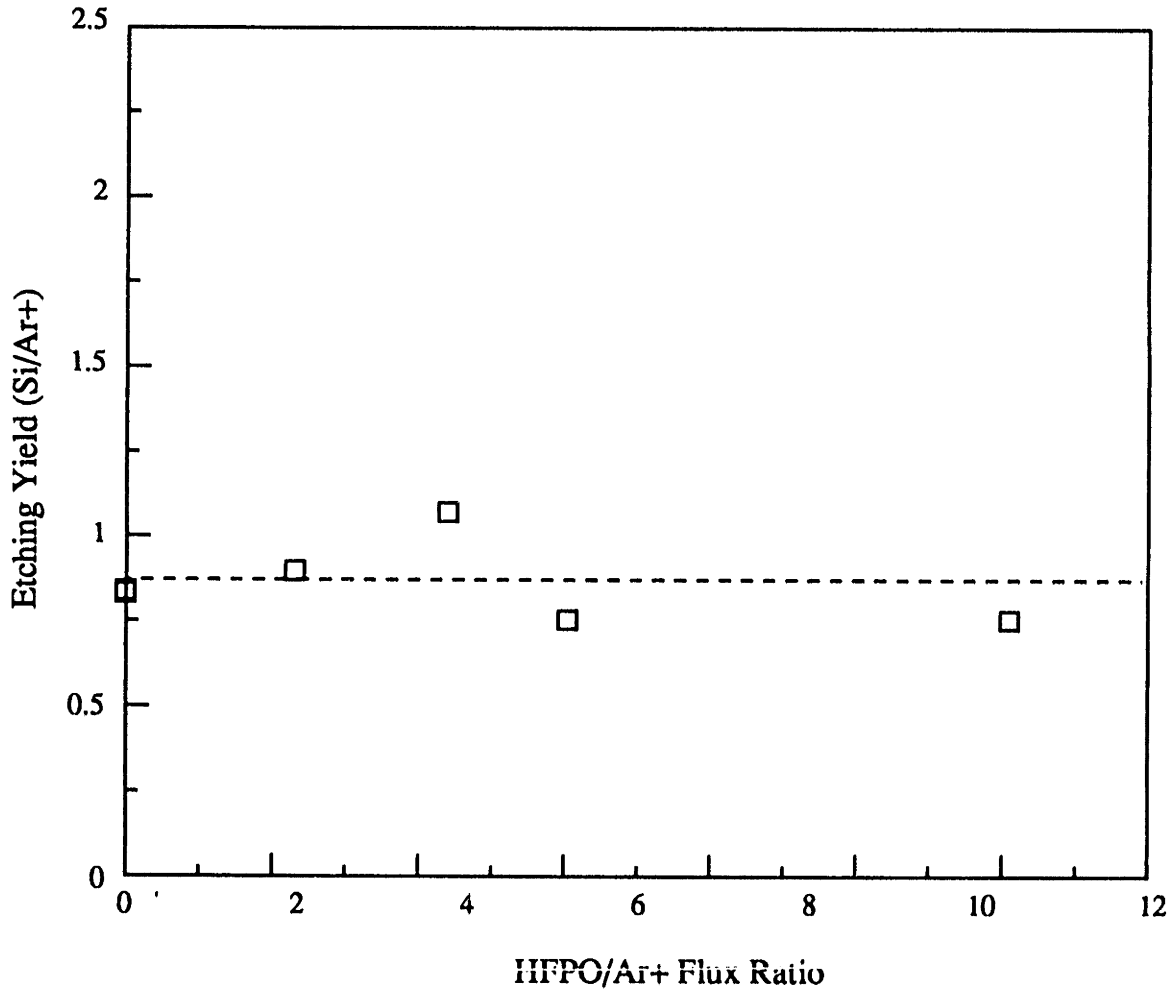

Figure 3-20. Effect of HFPO flow on Ar+ sputtering yields of polysilicon.

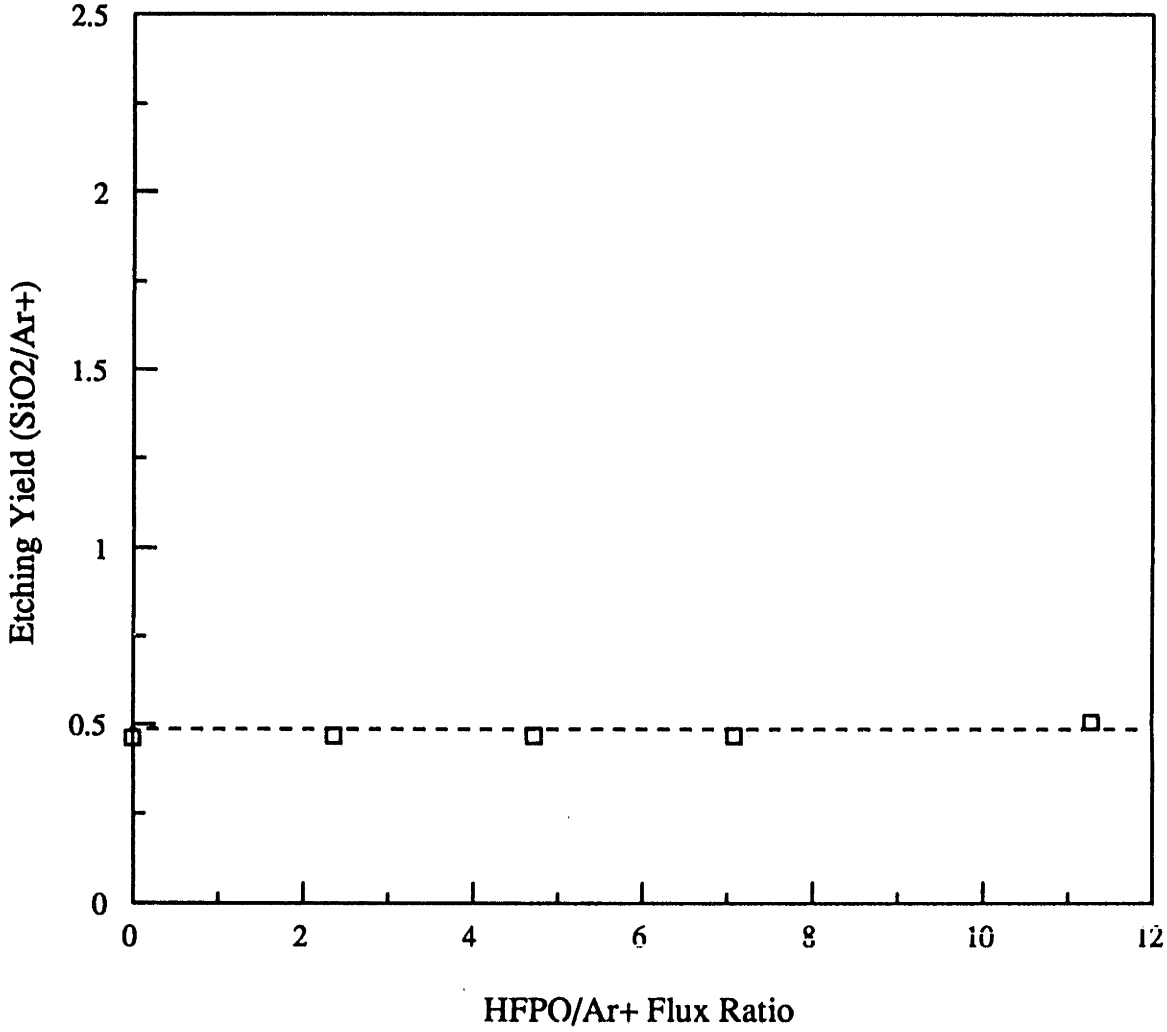

Figure 3-21. Effect of HFPO flow on Ar+ sputtering yields of silicon dioxide.

of HFPO exposed silicon and SiO_2 surfaces also showed no significant carbon uptake above background levels of adventitious carbon.

CF_3 Beam source

While the CF_2 beam source detailed above allowed us to explore the role of the most plentiful potential polymer forming radicals in the fluorocarbon etching environment, we cannot rule out the possibility that CF_3 or CF radicals may exhibit different behaviors. For instance, because the CF_2 species is sp^2 hybridized, it is not a "true" free radical in the sense that a vacant sp^3 orbital or "dangling bond" is available. Consequently, the adsorption of CF_2 on surface sites may exhibit an activation barrier, whereas the sticking of CF_3 and CF is expected to be non-activated on clean surfaces. In addition, CF radicals may exhibit much higher self-sticking probabilities than does CF_2, facilitating more rapid growth of surface films than does CF_2, or CF_3 which would act as a chain terminator.

Early in this thesis work we considered several methods for production of a high fluence CF_3 radical source [McFeely et al., 1988; Joyce et al., 1988; Robertson et al., 1988; Ryan and Plumb, 1984], which would allow us to compare and contrast the role of a potential polymer chain propagating (CF_2) versus a chain terminating radical species. The most viable of these methods were the thermal pyrolysis or UV-photolysis of the compound $(CF_3)_2N_2$ [McFeely et al.,1988] which results in decomposition according to,

$$(CF_3)_2N_2 \text{ ----> } 2\ CF_3 + N_2,$$

and the hydrogen abstraction reaction described by Ryan and Plumb [1984],

$$CHF_3 + F \text{ ----> } CF_3 + HF.$$

The $(CF_3)_2N_2$ precursor provides the "cleaner" CF_3 source since the byproduct is molecular nitrogen. However, this diazide species is reportedly unstable and not commercially available.

We therefore pursued the hydrogen abstraction pathway described above, which is reportedly characterized by a forward rate constant of $k_f^{298}= 1.5x10^{-13}$ cm^3/s [Clyne and Hodgson, 1983]. A source tube was designed as shown in Figure 3-24 which included an upstream microwave discharge for production of F atoms from an XeF_2 parent, and a down-stream mixing tee where CHF_3 was introduced at 100 mtorr, giving a pseudo first order reaction time constant $\tau=\{k_f^{298}[CHF3]\}^{-1}$ = 7 msec. At typical throughputs, a 10 cm tube tip region gave 4τ gas residence times. The discharge region of the tube was sapphire lined, while the remainder was teflon lined to limit radical surface recombination. The UTI-100C mass spectrometer head was used for CF_3 species detection, where both electron impact ionization and a 3+1 REMPI (resonance enhanced multi-photon ionization) process using a 480 nm dye laser (Coumarin 480) [Dulgnan et al., 1982] were attempted. Order of magnitude calculations indicated that the detection limit of the REMPI experiments was better than 10^{12} CF_3/cm^3 given 10^6 ion current gain, and a 10^{-5} REMPI probability in a 10^{-5} cc focal volume, and signal averaging of the current pulses. Given this limit, CF_3 fluxes of 10^{16} $mols/cm^2$-s or greater should have been detectable. However, no consistent mass spectral evidence of CF_3 product was found using either ionization technique. Further studies showed that the use of teflon liners, and the high surface area to volume ratio of the doser shown in Figure 3-22 resulted high F surface loss coefficients, leading to very inefficient CF_3 production. Much better F production efficiencies were later obtained using large i.d. alumina (Al_2O_3) ceramic tubing in the discharge region, and along the flow path as discussed in Section 3.4. Although attempts to produce CF_3 were abandoned, it is likely that a very efficient source could be constructed using an all-alumina design with smaller surface area to volume ratio to exploit the H abstraction pathway described above.

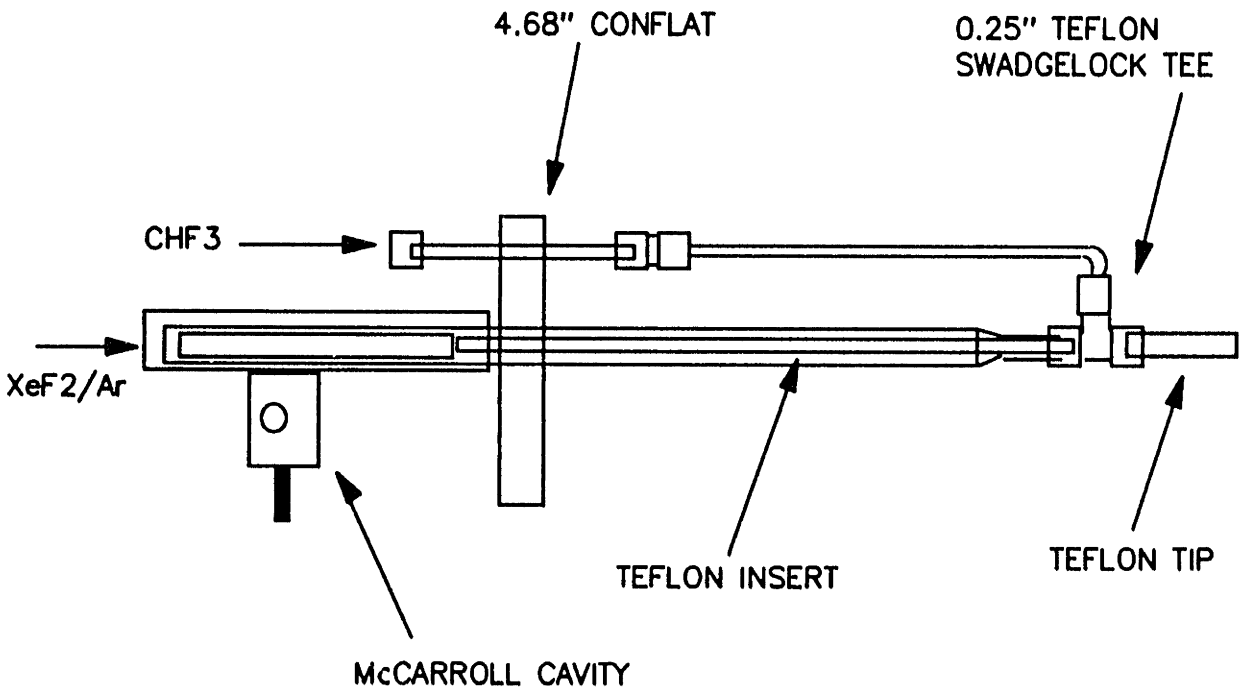

Figure 3-22. Teflon-lined doser assembly used in attempts to produce a CF3 beam via the H abstraction pathway described by Plumb and Ryan [1984].

3.4 Characterization of the F atom beam

Atomic fluorine was generated in a flow-through microwave (2.45 GHz) cavity through the dissociation of molecular fluorine slightly diluted with xenon to improve discharge stability. The experimental setup is shown schematically in Figure 3-27. The optimal configuration consisted of 0.5" o.d. Al_2O_3 (99+%) in the discharge region and extending into the main chamber (30 cm), coupled to a 0.25" o.d. tip of length 7.0cm. A teflon coupler is used to mate the two ceramic tubes but does not contact the gas stream. All Al_2O_3 construction of the doser allowed transport of the F species over large distances without severe wall recombination losses, in agreement with the observations of other researchers [Coburn and Winters, 1990; Nordine and LeGrange, 1976]. Other investigators have successfully produced F atom discharge sources in pyrex [Clyne et al., 1973] and teflon-lined tubing [Clyne and Hodgson, 1983] where surface area-to-volume ratios were sufficiently large, and F atom transport distances were not great. However, SiF_4 is seen as a byproduct of F production in pyrex-type discharge tubes, confounding the study of F-Si surface kinetics. A teflon- lined doser tube of the geometry shown in Figure 3-22 was evaluated, but was found to give low F yields due to a high surface area to volume ratio.

A McCarrol cavity (Opthos Instruments) was utilized to couple microwave (2.45 GHz) power to the flow tube and to generate a discharge a the flowing F_2/Xe mixture. The amount of Xe employed in the discharge was typically < 0.1 sccm, and represented a small fraction of the total doser throughput at all but the lowest F fluxes employed. A Tesla coil was utilized to break down a pure Xe discharge, after which F_2 was added to the discharge incrementally to prevent it from extinguishing. Breakdown of a pure F_2 gas flow in the McCarrol cavity was found to be difficult in the allowable tube pressure regime.

Near quantitative production of atomic fluorine was achieved at 75 watts total power with only slight losses (<2%) most likely due to HF formation via hydrogen abstraction from reactor

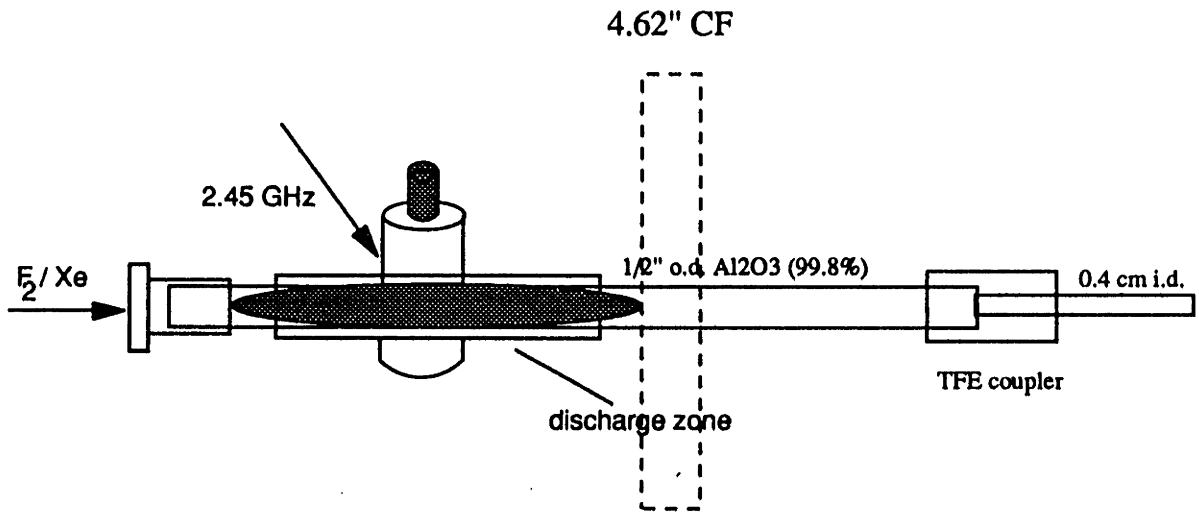

Figure 3-23. All alumina ceramic doser design for F atom production.

surfaces. Reflected microwave power in this system is typically 30%-50% of the forward power. All data taken in this thesis employed a 75 watt forward power level to the McCarrol cavity, of which about 40 watts was effectively coupled to the discharge. Coburn and Winters [1990] have previously reported near quantitative production of F using the doser geometry described above. Figure 3-24 compares mass scans of the F beam with the discharge "on" and "off" at a 70 eV electron impact energy. With the discharge "on" we observed complete disappearance of the mass 38 (F_2^+) peak, and a significant increase in the mass 19 (F^+) peak. The mass 20 (HF^+) peak was also found to increase slightly with the discharge on. Vasile and Stevie [1982] provide ionization cross sections and relative extraction efficiencies for the production of F_2^+ and F^+ from F_2. Total ionization cross sections for F and F_2 are approximately $1.0x10^{-16}$, however, the relative collection efficiencies $F_2^+/F^+=0.71$. Although these values may include some equipment specific uncertainties, they allow us to complete a F atom balance and to estimate a dissociation efficiency for the beam source. From Figure 3-24 the heights of the F_2^+ (38) peak and F^+ (19) peak are 1.1 and 1.4 in arbitrary units, respectively with the discharge "off". With the discharge "on" the F^+ peak grows to 4.5, a net growth of 3.1, and the F_2^+ peak disappears. If all F^+ measured in the "on" state were the result of F_2 dissociation, the original F_2 peak height should be 3.1/2*0.781 = 1.2 (accounting for the increased collection efficiency of F^+) in close agreement with the measured value of 1.1. This observation suggests near 100% efficiency of the doser design for F atom production. The slight growth in the mass 20 (HF^+) peak may be due to F abstraction of H from the reactor chamber walls or the mass spectrometer surfaces.

F production from F_2/Xe discharge was studied mass spectrometrically as a function of total throughput and input (forward) microwave power to the discharge. Near 100% production efficiencies were found for all stable operating conditions tested, from 50 to 100 watt forward powers, and calculated throughputs of 0.1-0.3 sccm as shown in Figure 3-25. Evaluation at higher

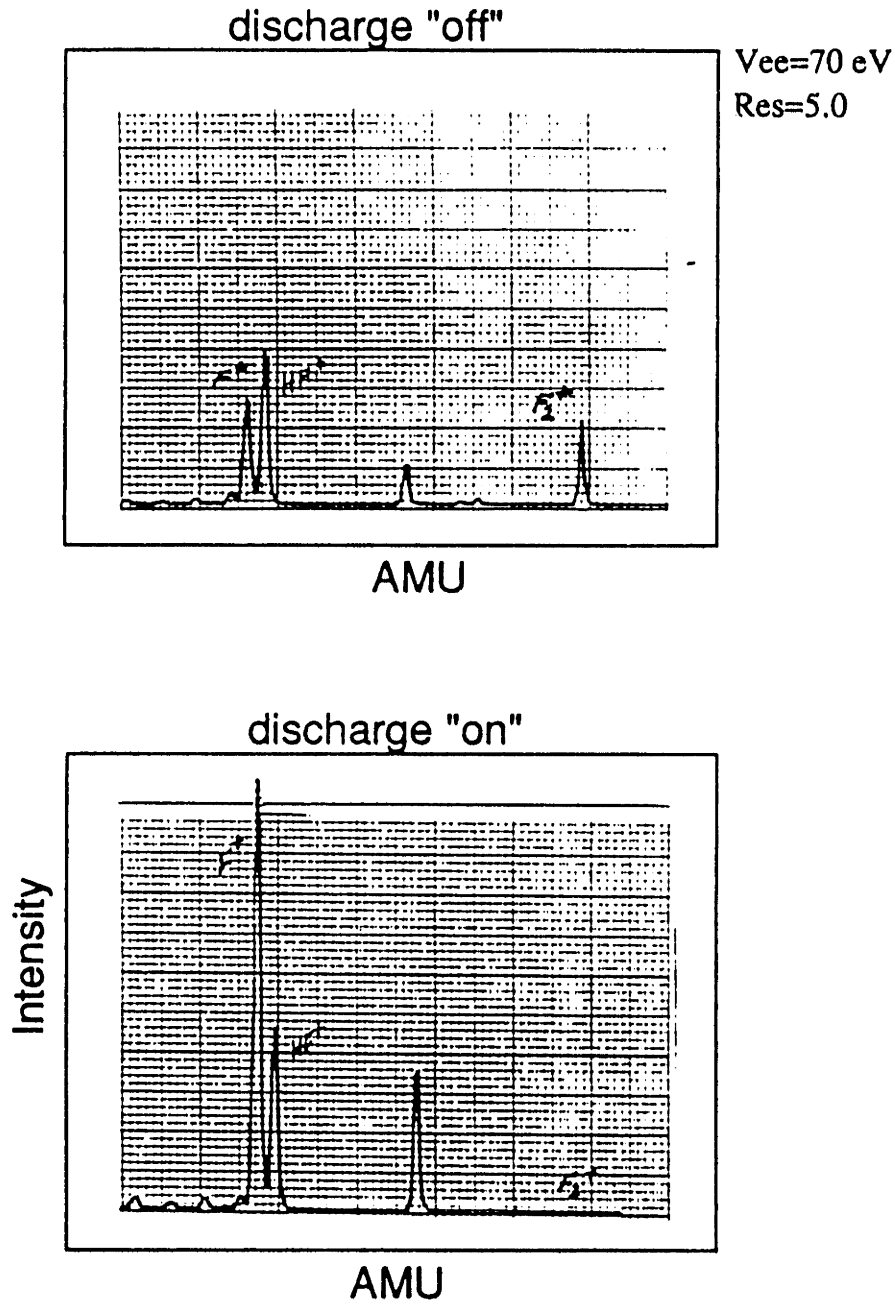

Figure 3-24. Effect of microwave discharge "on" and "off" states on F beam production.

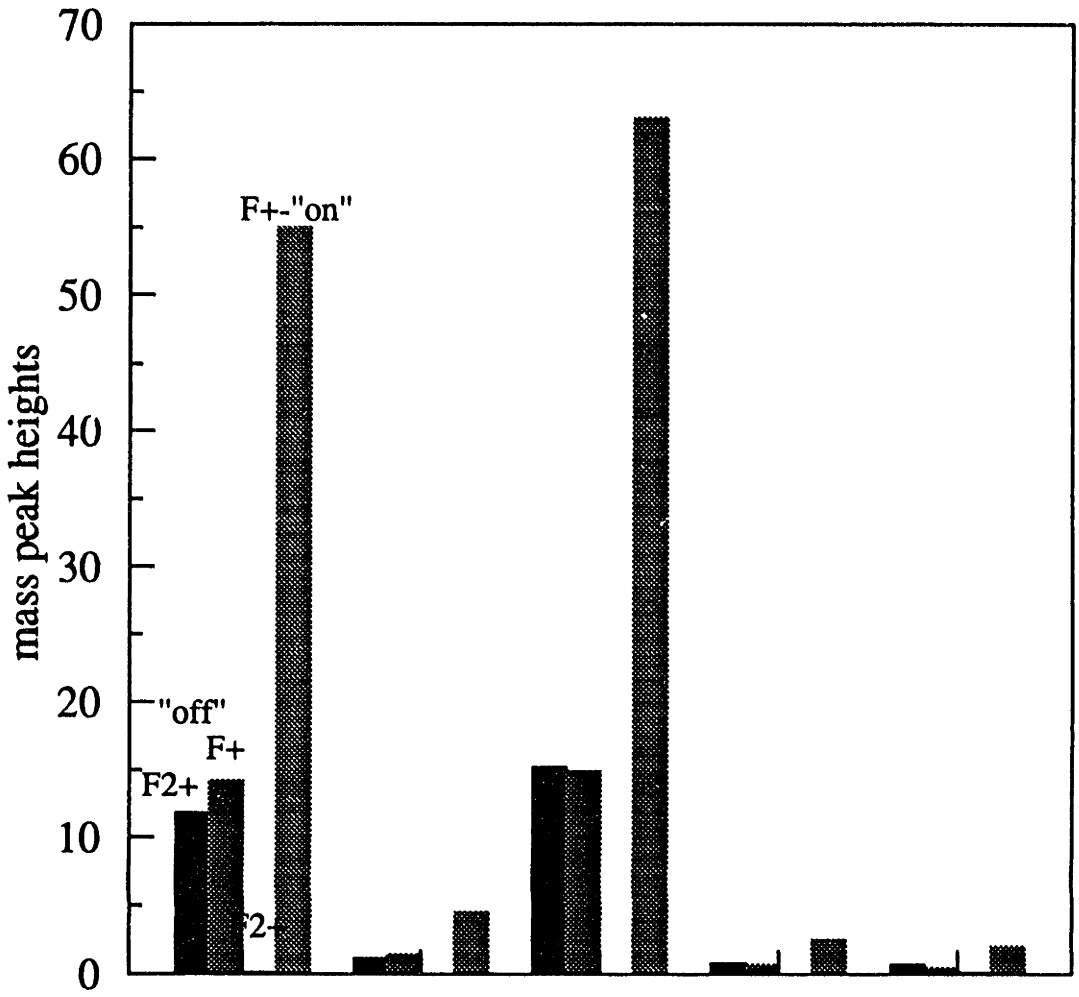

	70w	70w	90w	90w	90w
F2+ off	11.80	1.10	15.20	0.80	0.67
F+ off	14.20	1.40	14.90	0.70	0.45
F2+ on	0.1	0.0	0.0	0.0	0.1
F+ on	55.0	4.5	63.0	2.5	2.0

Figure 3-25. F production efficiency at microwave powers of 70 watts and 90 watts at various F2 throughputs.

flows was not possible due to the "overpressuring" of the mass spectrometer. Nordine and Rosner [1976] have shown near 100% F atom production for microwave powers above 40 watts for throughputs under 10 sccm, using an alumina flow tube arrangement nearly identical to ours. Nordine and Legrange [1976] has also shown that F surface loss coefficients on high purity Al_2O_3 are on the order 10^{-4}, which explains the very high efficiency of our source. We did not spectroscopically characterize the state distribution of F from the microwave discharge. However, Clyne et al. [1973] indicate that such a microwave discharge source is primarily a source of ground state $F(^2P)$ atoms, where the relative ratio of $^2P_{3/2}$ to $^2P_{1/2}$ J-excited atoms (>10:1 at 300 K) is unknown to us.

Flux gradients to be expected from the F discharge tube (0.4 cm i.d.) over a $1cm^2$ die area are shown in Figure 3-8, decreasing from 85% to 25% over a flow range of 10^{16} to 10^{18}. Although F/Ar^+ flux ratios over the die area are much smaller, the variation in the absolute magnitude of etchant fluxes resulted in large non-uniformities in the etching of patterned dies [Gray, 1990]. Experimentally measured enhancement factors for this doser geometry are shown in Figure 3-26 for the compound XeF_2 which has also been used as a F atom source in surface kinetic studies. Measured XeF_2 enhancement factors using the impact probe are in good agreement with the N_2 enhancement factor data for 1/4" o.d. nominal tubing shown in Figure 3-14. Care must be taken in the quantitative measurement of F atom fluxes using the impact probe technique. We have found that without an extended period of passivation of the impact tube assembly inner surfaces with F, the impact tube system acted as a "sink" for F atoms via sorption and or recombination with surface impurities. This effect resulted in the reduction of instantaneously measured F atom fluxes by a factor of ~2 (see Figure 3-28) over that expected based on the total flux of the F_2 parent gas, and a 100% dissociation efficiency.

Impact tube measurements of F atoms versus XeF_2 molecules from a XeF_2 source with

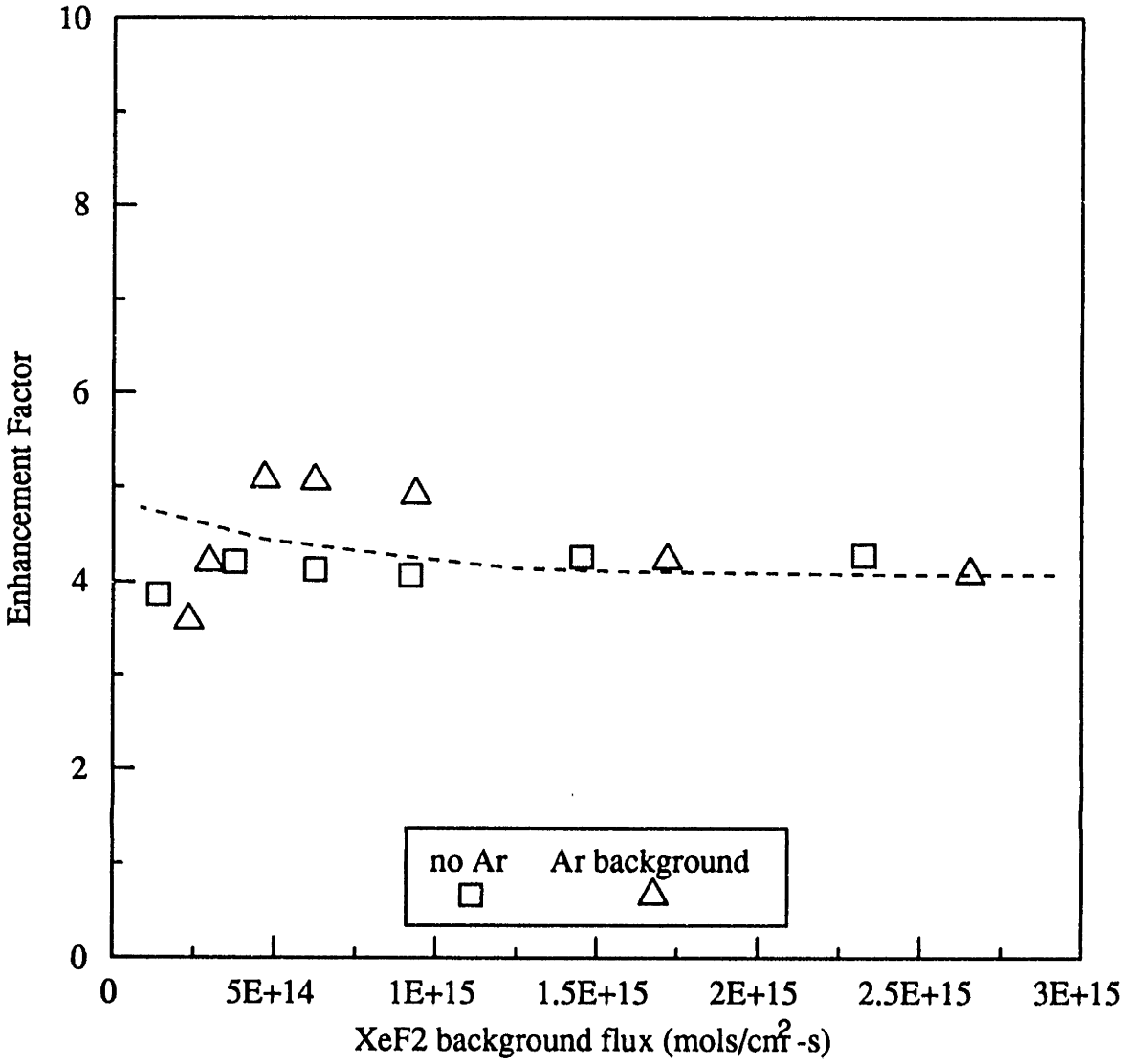

Figure 3-26. Measured XeF2 enhancement factors from the F discharge source tube, d=1.0 cm.

the discharge "on" and "off" , respectively, are shown in Figure 3-27. Increase in measured beam pressure of the XeF_2 parent with doser throughput is given by the solid line (rectangles are data points). The expected beam pressure rise due to the complete dissociation of XeF_2 into Xe + 2F was calculated according to equation (3-43) and is given by the dotted line, while the measured pressure rise with the XeF_2 discharge "on" is given by the asterisks. Agreement between the measured and predicted pressure rise is well within a factor of 2 in this low throughput regime. This data was taken after a significant period of "passivation" of the impact tube surfaces with fluorine. Data could not be taken at higher F atom fluxes using XeF_2 without heating the source cylinder since the room temperature vapor pressure of this waxy solid is only about 5 torr. XeF_2 has been evaluated as an alternate F atom source in Chapter 6 to allow comparison of this thesis work to literature references which employ XeF_2 as an F atom source.

Larger F atom fluxes where generated by usage of a F_2/Xe mixture as described above, and data analogous to that shown in Figure 3-27 is presented in 3-28 for the F_2 discharge source. The significant offset between measured and predicted F production was inconsistent with the mass spectral data presented above, and was assumed to be the result of F atom sorption/recombination in the impact tube system. This hypothesis was supported by the observation that impact tube measurements of F atom fluxes are initially low but increase in time, ostensibly due to the passivation of the impact tubing and manometer surfaces. The parent F_2 gas is also very "sticky" and will adhere to non-passivated surfaces. This effect is demonstrated in Figure 3-29 where the F_2 enhancement factor from the discharge tube is measured as a function of total throughput. The flux readings, which were taken in sequence, appear to have an isothermic form, suggesting the sorption and saturation of F_2 in the impact system as fluxes are increased. This is in contrast to XeF_2 studies in which enhancement factors measured after passivation showed slightly higher E factors a low fluxes. Maximum enhancement factors

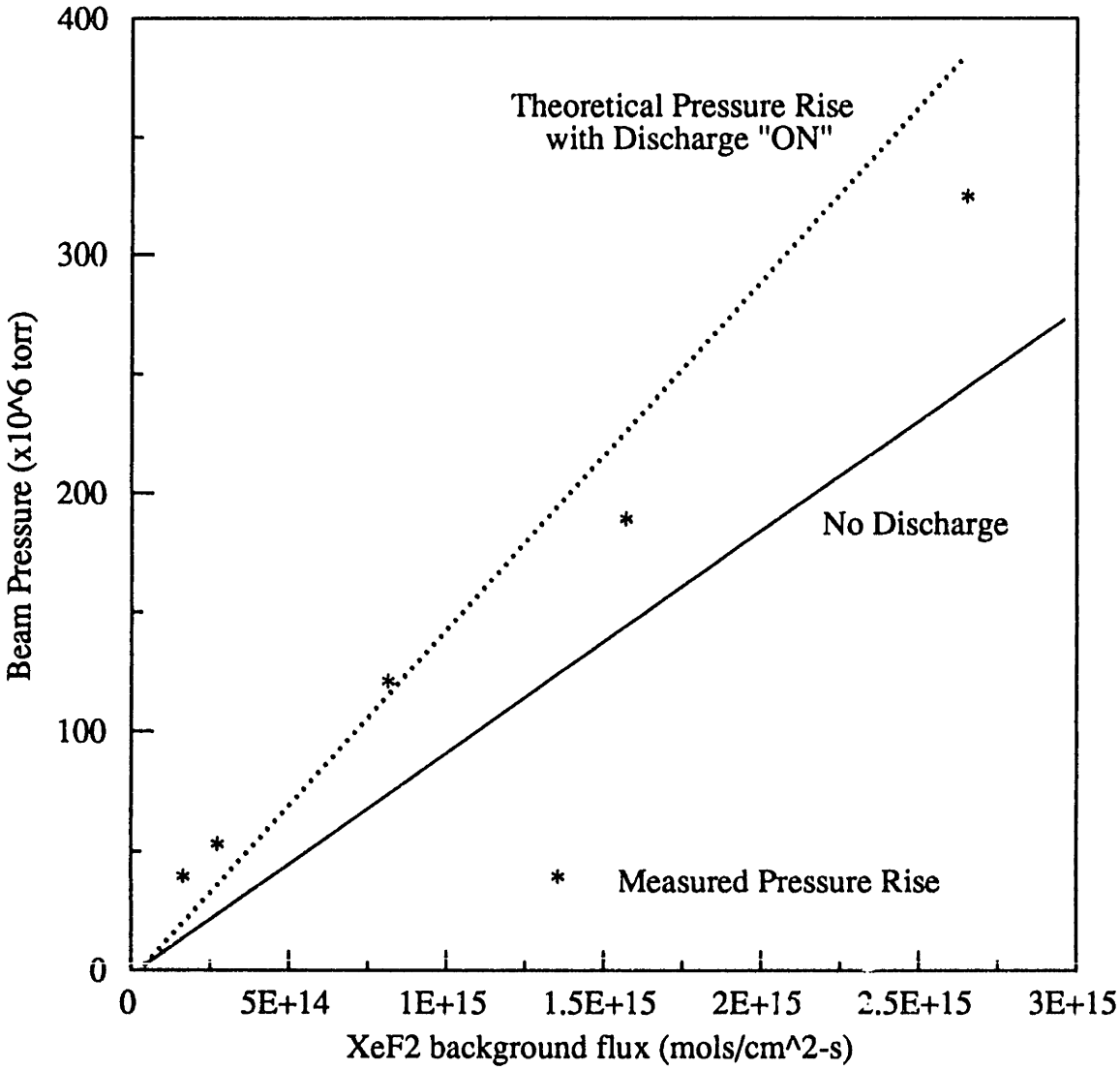

Figure 3-27. Measured versus predicted beam pressure rise for F atom from XeF2.

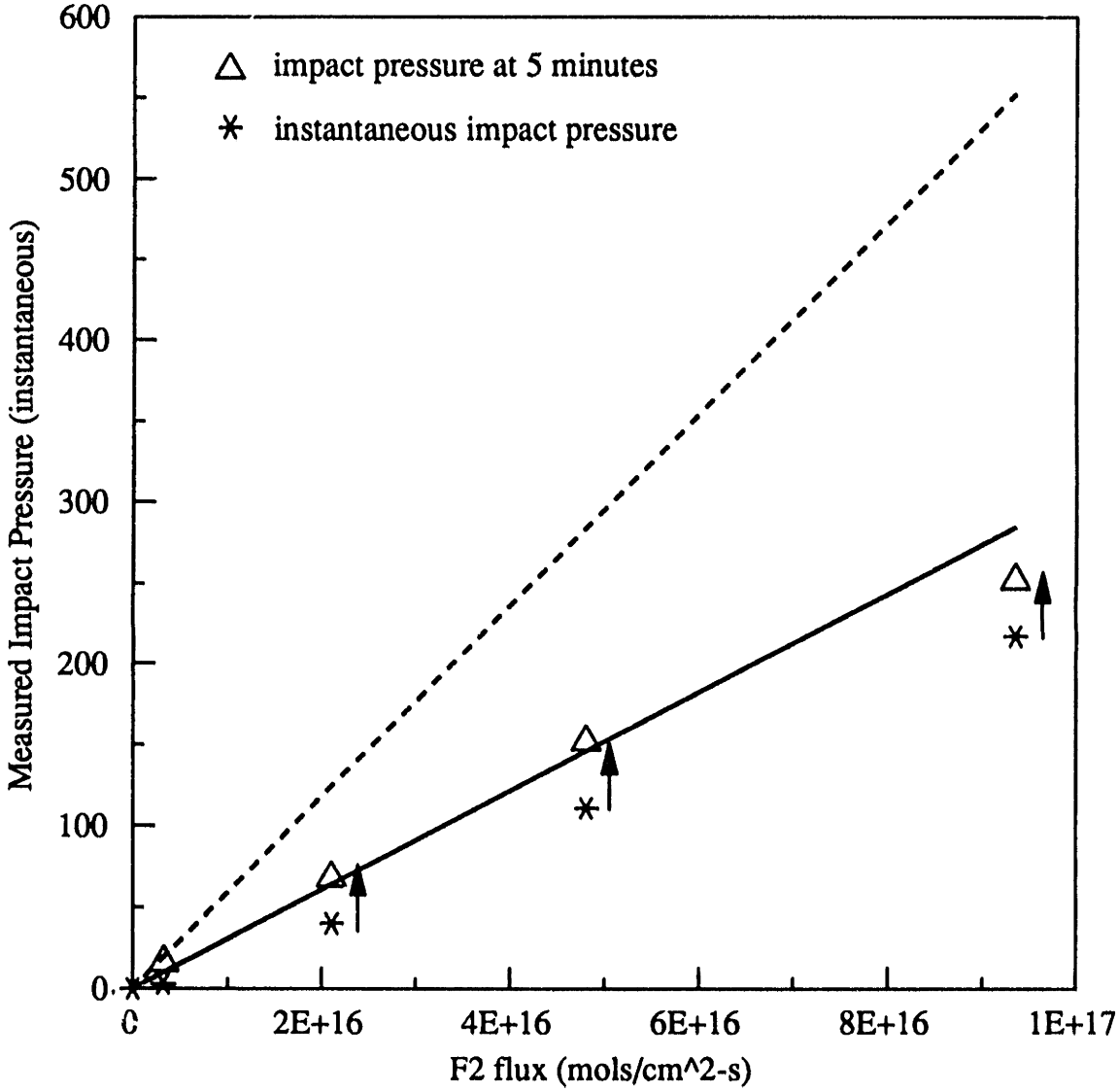

Figure 3-28. Measured versus predicted beam pressure rise for F atom production from F2/Xe.

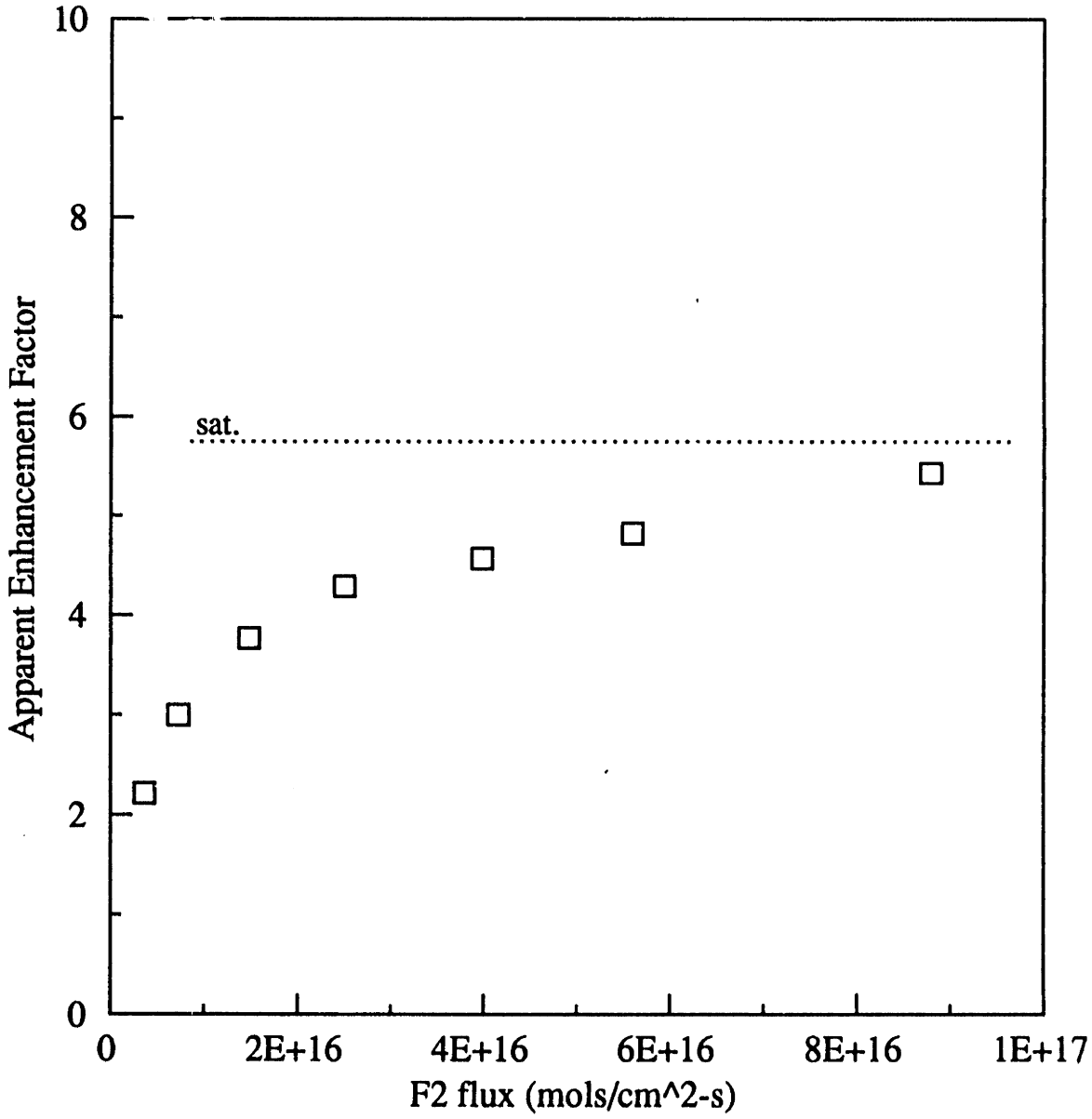

Figure 3-29. Apparent attenuation of F2 enhancement factors due to sorption on impact tube surfaces.

measured in Figures 3-26 and 3-29 are identical as expected.

Because it was nearly impossible to initiate an F_2/Xe discharge at large F_2 fluxes, we were unable to use parent gas flux as a measure of F atom flux. Instead, a pure Xe discharge was first initiated, and F_2 was added incrementally to the mixture, being careful not to cause rapid flow perturbations which extinguish the discharge. F_2 flux was increased with the impact tube in place, giving an instantaneous measure of F atom flux increase. A correction factor of 2.0 was added to account for effect of free radical consumption in the impact system. Using this incremental addition method in the F experiments greatly increase the integrity of the data, since errors in the F flux measurements appear only as a offset of measured rate curves on the F/Ar^+ axis and not as random noise.

The beam flux range investigated in this work extended from zero to about 10^{18} mols/cm^2-s. Maximum fluxes employed when the ion source was not differentially pumped were an order of magnitude lower to restrict back-mixing effects in the ion gun, and avoid production of reactive ions. The maximum fluxes employed were representative of fluorine surface fluxes in low pressure fluorocarbon plasmas [Butterbaugh, 1990]. Air products technical grade fluorine (98%) and Spectra gases research grade Xe were used for this work, the major F_2 impurity being HF. XeF_2 was purchased from PCR research chemicals, and was packed into a source cylinder under N_2 purge in a fume hood, resulting in some exposure to atmospheric contaminants. The cylinder was chilled in liquid nitrogen and pumped to 10^{-4} torr before utilizing the source in order to remove the atmospheric gases. A slight increase in the amu 16 (O^+) and 32 (O_2^+) peaks were noted while running the microwave discharge in the alumina tubing, whereas usage of a pyrex tube resulted in significant oxygen production. Measurements of baseline silicon sputtering rates were not affected by the while running a Xe microwave discharge, indicating that competitive oxidation of the Si was not significant. Additionally, F-Si bond formation is both

kinetically and thermodynamically favored over Si-O bonding, such that F surface kinetics are expected to dominate. Zau et al. [1990] have shown that the addition of O_2 impurity during CF_4 plasma etching of polysilicon does not effect etch rates until the 10,000 ppm level is reached, at which point the etch rates increase due to increases in gas phase F atoms. This study suggest that competitive surface oxidation effects are not prevalent even with significant oxygen backgrounds.

3.5 Estimation of Errors in Radical Flux and Etching Yield Measurement

It was difficult to confirm the accuracy of our radical flux measurements since no absolute calibration technique such as gas-phase titration was attempted. However, based on the agreement between theoretical work and the mass spectrometric characterization of the CF_2 and F radical source presented above, we believe our absolute flux measurements to be within ± 25%. Errors in the absolute accuracy of our radical flux measurement technique would result in a constant offset shift on the reported etching yield data, while the relative behavior would remain the same. The precision (repeatability) of our etching yield measurements was determined by the repeatability and stability of the impact tube measurements, the ion flux stability, and the accuracy with which interferometry peaks could be located in the chart traces. Repeatability in the species flux measurements were estimated at,

$$\Delta F = \pm 20 \times 10^{-6} \text{ torr}$$

$$\Delta CF_2 = \pm 2 \times 10^{-6} \text{ torr}$$

$$\Delta I^+ = 0.05 * I^+$$

The effect propagation of these errors on the precision of flux ratios was calculated according to the sum of squares formula

$$\frac{\Delta(N/I^+)}{(N/I^+)} = \left[\left(\frac{\Delta N}{N}\right)^2 + \left(\frac{\Delta I^+}{I^+}\right)^2\right]^{1/2} \tag{3-45}$$

which was used for determination of error bars on neutral-to-ion flux ratios presented in this thesis. The error bars on yield measurements were similarly calculated,

$$\frac{\Delta Y}{Y} = \left[\left(\frac{\Delta C}{C}\right)^2 + \left(\frac{\Delta I^+}{I^+}\right)^2\right]^{1/2} \tag{3-46}$$

where ΔC is the error in interferometry chart readings of the $\tau/2$ etching cycle estimated at half a block at a given chart speed.

3.6 Summary

Flux distributions and fractional interceptions for large straight-tube sources in the collisionally- opaque regime have been calculated and compared to experiment. The angular flux distribution in this regime is shown to be an explicit function of the gas collision diameter, σ, and the dimensionless parameter η, which is the doser diameter-to-mean free path at the doser tip. Useful beam collimation occurs only over the limited region of non-collisional flow near the doser tip, as characterized by Giordmaine and Wang's [1960] critical length parameter. This is in contrast to the transparent flow regime in which the beam directionality is determined solely by the tube aspect ratio, and collimation occurs over the entire tube length. A multi-beam etching system operating in the opaque regime was constructed, and beam fluxes were characterized using a novel impact tube system. Beam directionality and enhancement factor behavior was found to be well represented, within experimental error, by the available theory. The data contained herein should provide a useful guide for the design of molecular sources in the collisionally opaque gas flow regime.

The production of CF_2 via pyrolysis of hexafluoroprolylene oxide has been characterized mass spectrometrically, and appears to saturate at tube wall temperatures >460°C. Cold HFPO was shown not to effect the Ar^+ sputtering rates of Si or SiO_2, nor is the molecular by-product of the pyrolysis expected to influence etching. Near quantitative production and transport of F atoms was achieved using an large i.d. alumina discharge tube, coupled to a smaller alumina tip near the etching sample. Quantitative production of F from a discharge in flowing F_2/Xe was demonstrated mass spectrometrically at powers of 50-90 watts, and over a wide range of throughputs. The impact tube probe technique was employed for measurement of molecular and radical beam pressures, but a factor of 2 correction was required to account for F radical sorption in the impact assembly.

Chapter 4

Ion Production Techniques

It was essential to the goals of this thesis that we be able to produce a broad, high current ion beam over the wide range of energies, 10-500 eV, important in commercial plasma and RIE processes. Currents on the order of 0.1-1 mA/cm^2 were required at the sample face in order that we be able to measure reasonable etch rates interferometrically, and so that ion fluxes employed were representative of real plasma processes. A broad beam was necessary to avoid the ambiguities associated with sharp ion flux gradients across the 1 cm sample dies in the measurement of etch rates and product distributions. While mean ion energies in plasma processes are typically 50-100 eV, a wide distribution of energies develops in commercial plasmas where the sheath region is highly collisional [Lui et al., 1990]. Knowledge of the etching yield of each ion of a given energy striking the wafer surface is essential for the development of quantitative topography evolution simulations. The near threshold energy regime (10-50 eV) is very much of interest in the areas of ECR, RFI, and helicon plasma etching, in which plasma densities are high but mean ion energies are very low.

We were, however, unable to find one commercial ion source which met all of our criteria. Initial experiments were conducted using a compact Kaufman-type ion source, which is essentially a DC discharge source sustained by a hot tungsten filament. The dual grid ion optics available with the Kaufman gun restricted the usable energy range to 100-500 eV as discussed in Section 4.2. In addition, the usage of reactive gases in the Kaufman gun was impractical due to short filament lifetimes, and ion flux instability. Backmixing of reactive gases from the beam chamber into the Kaufman gun under conditions of high F atom flux also reduced filament lifetimes and flux stability. A differential pumping system was constructed to alleviate this

problem and to reduce the large chamber gas load resulting from operation of the ion gun (1-2 sccm). A compact ECR plasma source was characterized and used for production of large fluxes of low energy (25 eV nominal) ions for near threshold studies, and for production of carbonaceous ions (Section 4.3). Several modifications are necessary to allow the CECR source to function in the differential pumping system, and over a broad range of ion energies.

4.1 Operating Principles of the Retarding Grid Ion Analyzer

The construction and usage of the ion flux probe was discussed briefly in Chapter 2. Here we discuss in detail design considerations in construction of the probe, and limitations in its application and energy resolution. Geometric details of the current probe construction are summarized in Figure 4-1. The primary purpose of the gridded probe is to allow accurate in situ measurement of ion beam currents at the sample face i.e. it is primarily used as a "Faraday cup". In its simplest implementation, a Faraday cup does not require a grid system at all; one may simply bias the collection plate negatively to repel incoming electrons, using a "floatable" picoammeter for current measurement. This type of probe suffers from two major sources error. First, secondary electrons emitted during the ion bombardment of the collection plate escape and contribute to the measured ion current. Given a typical secondary electron emission coefficient for 500 eV Ar^+ on stainless steel of 0.1 [Chapman, 1980], this results in a +10% error in the measured ion current. Secondly, low energy ions which are generated via charge exchange collisions of the beam ions and the chamber background cannot be distinguished from the primary beam ions. This process is generally only important in gases with large resonant charge exchange cross sections, such as argon, where chamber base pressures are high and ion beam transport distances are large. In the case of the multibeam apparatus, argon background pressures are typically 10^{-5} torr, which results in less than 0.01% fall off in ion beam current due to resonant

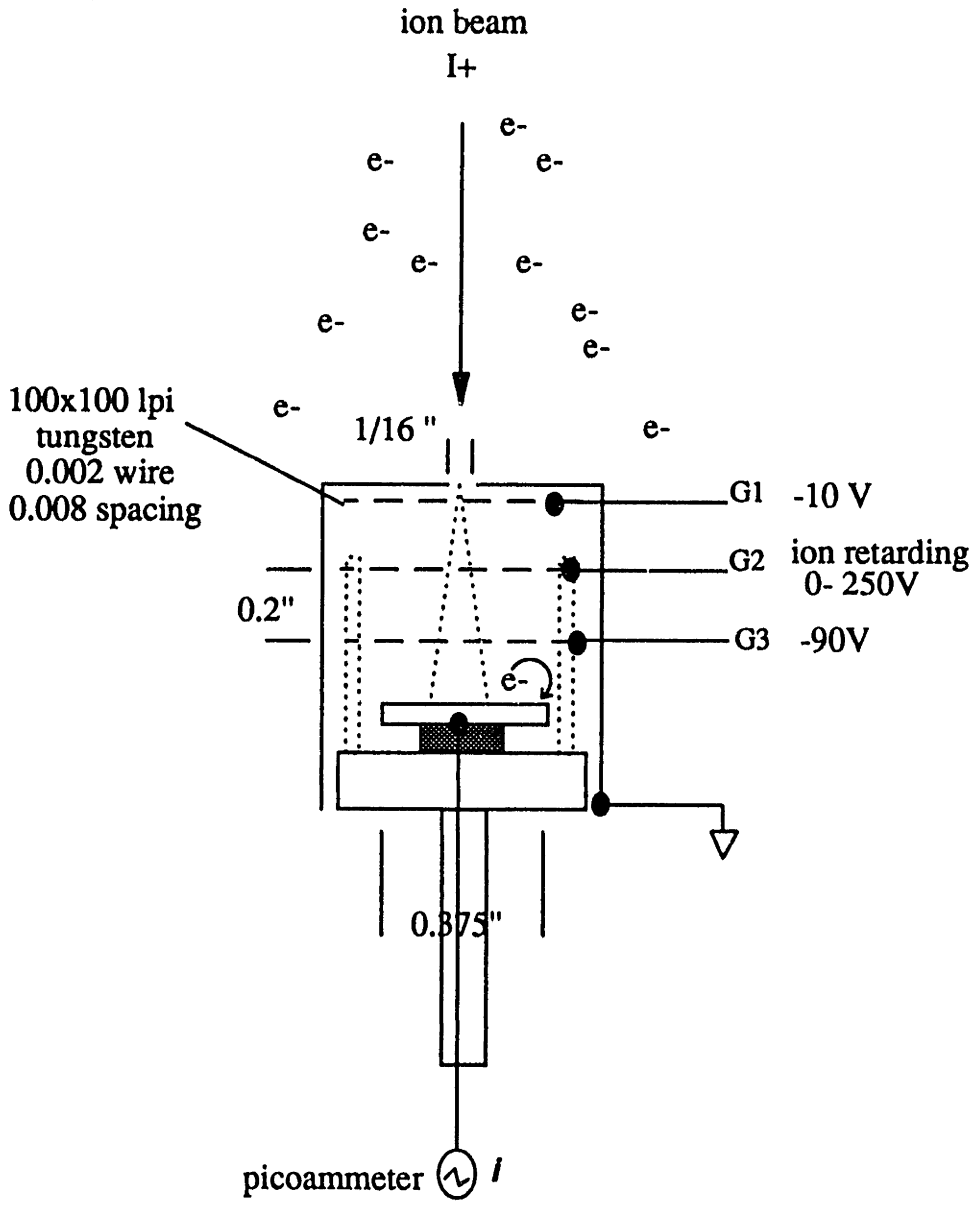

Figure 4-1. Ion flux probe geometric details.

charge exchange collisions (σ=10mtorr-cm @ 200eV) [Kaufman, 1984] over a 10 cm beam path.

The addition of the grid system to the current probe serves several purposes. The first grid (G1), when biased negatively on the order of -10V, serves to repel the primary neutralizing beam electrons, thus eliminating the necessity of biasing the collection plate. It is critically important that all other accesses of chamber electrons into the probe be sealed off by enclosing the entire structure in a well grounded shield, and insulating all electrical connectors and wires. The third grid (G3, closest to the ion collection plate), when biased negatively on the order of -100V, serves to repel secondary electrons generated during ion bombardment back onto the collection plate. The intermediate grid (G2) may be biased positively to repel charge exchange electrons, or to allow energy profiling of the incoming beam. Assuming that all primary beam electrons are stripped by the first grid, all secondaries are repelled and recollected, and that all ions arrive at the collection plate, the beam current is directly related to the measured current (I^+_{meas}), the probe orifice area (A_o), and grid transmission (t) in the form,

$$I^+ = I^+_{meas} \left[\frac{1}{A_o}\right] \left[\frac{1}{t^3}\right] \qquad (4\text{-}1)$$

We have employed 100x100 lpi tungsten mesh (0.002" wire, Unique Wire Weaving) with a 64% transmitivity in the current probe construction, such that the measured beam currents are on the order of μA, or a factor of 200 lower than the actual beam current densities.

There are several potential sources of error which we considered in the operation of this probe. To begin with, once the primary neutralizing electrons are stripped from the incoming ion beam, the ion beam is not longer "net neutral" and will begin to bloom due to coulombic forces between the like charged particles. For the geometry shown in Figure 4-1, and beam current densities on the order of 1 mA/cm^2, beam blooming should be < 5°, whereas the collector-to-

orifice area ratio allows 15° divergence. Perturbation of the incoming beam due to insulator charging is also of concern. However, in the current design two very small (1/16" o.d.) alumina posts are used for grid mounting, giving an insulator surface area-to-volume ratio between grids of about 0.05, hopefully negating the influence of charging effects. In order for the probe to be effective in energy profiling of the ion beam, the grid spacing must be on the order of, or smaller than the charge neutral beam Debye length. If this is not the case (i.e. the beam density is very large), the plasma will appreciably attenuate the grid potential toward the center of the mesh holes and both ions and low energy electrons will stream through the mesh. The quasi-neutral ion beam density can be related to the Debye length in the form,

$$\lambda_D = \left(\frac{k_b T_e e_o}{n_e q_e^2}\right)^{1/2} \tag{4-2}$$

where n_e and T_e are the electron temperature and density respectively, q_e is the electron charge, and e_o is the permitivity of free space. In the Kaufman ion beam plasma densities are on the order of 10^9-10^{10}/cm^3, and electron temperatures are at most 2 eV, giving a Debye length of about 0.005", which is similar to the present grid half spacing of 0.004". Ion energy distributions in the Kaufman ion beams have been successfully profiled as discussed in Section 4.2. However, plasma electron densities in the CECR plasma beam are 1-2 orders of magnitude greater, rendering the probe ineffectual for energy profiling of the ECR source beam. Gibson [1993] has developed a probe which achieves energy profiling in the ECR density regime with good resolution, and his design should be employed in future studies. A worst case estimate of the energy resolution offered by the gridded probe can be obtained by calculating the electric field generated between the ion retarding grid (G2) and G3, and assuming that this field is perturbed over the length scale

of the inter-wire spacing. For typical grid voltages of +100V (G2) and -100V (G3), we obtain a field of 1000V/in, and an voltage perturbation of about 4V, suggesting a resolution on the order of 5% of the measured ion energy. Finally, in the flux measurement of high current ion beams, one must consider the possibility of a space charge limitation to ion transport developing inside the probe. Hutchinson [1987] suggests that the electron repeller (G1)-ion repeller (G2) distance should be no more that 4 λ_D to avoid this limit, based on a 1 dimensional order-of-magnitude calculation. Our spacing is an order of magnitude greater that this, however, space charge limitations can be avoided since the beam can spread laterally. A full three dimensional simulation of the probe structure would be necessary to clarify the beam density limit in which space charge transport limitations become important.

4.2 Characterization of the Kaufman Ion Source

Most of the work presented in this thesis was conducted using a Commonwealth Scientific 1-cm Kaufman source for production of the ion beam. A schematic diagram of this device is presented in Figure 4-2 in which the power supply interconnections are also shown. An electrical interface box which allowed interconnection of the various KEPCO power supplies, and provided DC power to the Kaufman gun filaments, was constructed as detailed in Appendix B. The basic operating principle of the Kaufman gun is as follows. A DC discharge is created in the anode cavity due to the potential difference between the anode and the cathode filament (V_d), which is heated to sustain the plasma via thermionic emission. The entire assembly is floated at a potential, V_b, above ground which basically determines the ion potential relative to a grounded target. A small permanent magnet is situated under the anode in this particular source to aid in electron confinement, densifying the plasma and allowing operation at lower pressures. Ions are extracted from the 1-cm Kaufman source via a dual grid optics assembly in which the first grid

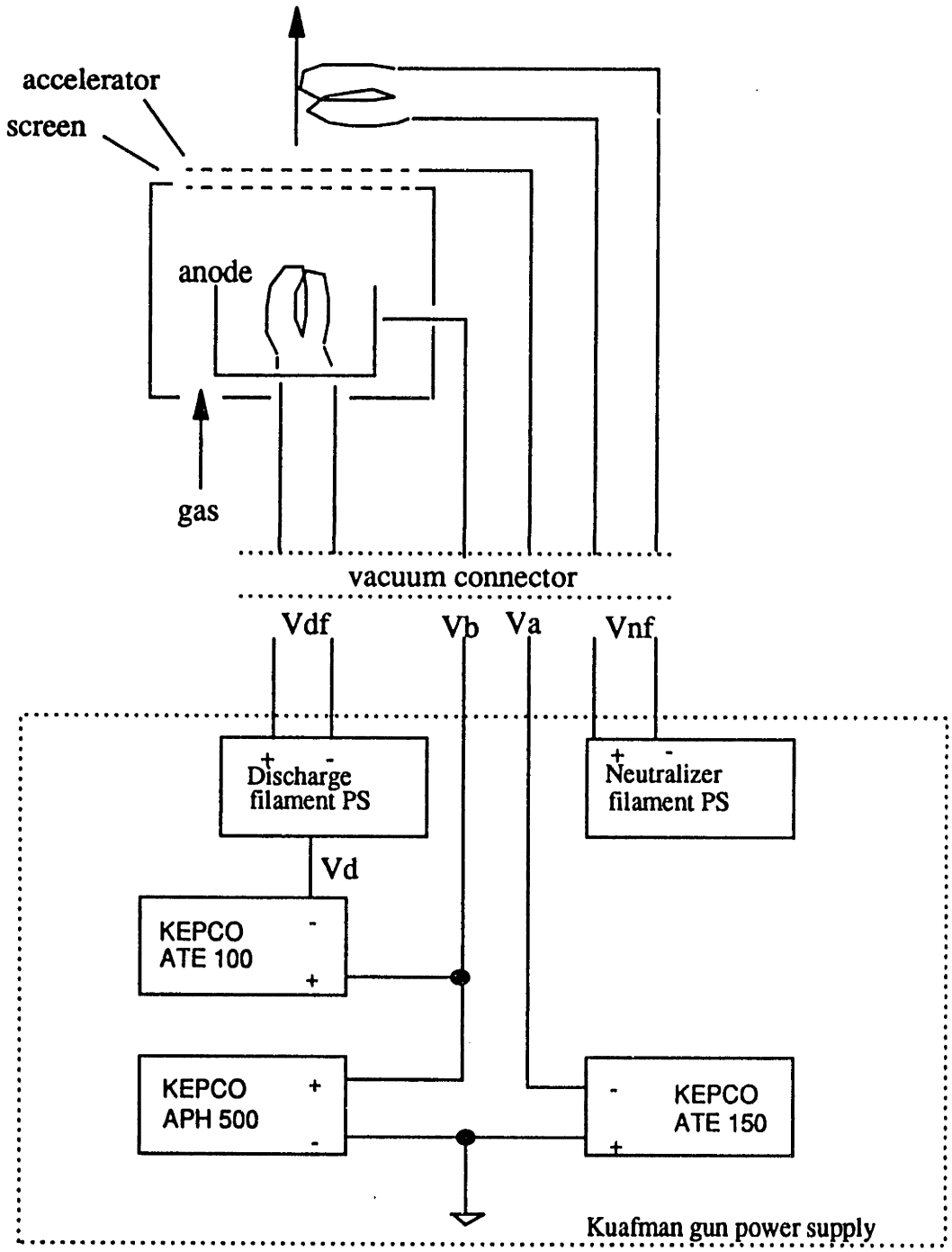

Figure 4-2. Kaufman gun schematic showing power supply interconnections.

(screen) serves to confine the plasma, and charges to approximately the cathode potential to equalize the ion and electron fluxes to its surface. The second grid (accelerator) is precisely aligned with the hole pattern in the first grid, and is biased negatively to enhance the extraction and focusing of ions effusing through the screen. The intergrid spacing must be extremely small ($<10\ \lambda_D$) to prevent space charge limitations to the ion transport. Ion extraction from the discharge region is governed by sum of the beam potential, V_b, and the magnitude of the accelerator grid potential, V_a. The accelerator grid, in addition, serves to prevent the backstreaming of neutralizing electrons produced outside the discharge back through the grid assembly. The neutralizing electrons are produced via an external hot filament and are necessary to achieve a "net neutral" beam to prevent beam "blooming" and surface charging during insulator etching. The beam is "neutral" only in the sense that the electron gas through which the beam is transported neutralizes coulombic interactions in the beam column and prevents surface charging. No substantial ion-electron recombination takes place.

The maximum extractable ion flux available from the Kaufman source, and the tunable range of beam divergence (i.e angular flux dispersion) is limited by the dual grid optics assembly. Of specific interest to us in selecting this source, were the allowable range of operating pressures and the maximum ion flux achievable by the gun. The lower limit on operating pressure in the anode chamber is in the range of 10^{-3} to 10^{-4} torr, giving a minimum flow requirement of about 1 sccm (argon) through the gun. The graphite grid optics consist of two hexagonal arrays of about 200 by 0.5 mm holes, putting the conductance of the optics assembly in the range of 1-10 l/s. Given this lower limit on argon throughput for stable ion gun operation puts main chamber base pressure in the $7x10^{-6}$ to 10^{-5} torr range. Figure 4-3 shows the fall-off in measured Ar^+ beam current with the decrease in main chamber base pressure. Without the differential pumping of the ion source, we of necessity must operate in a regime of large ion current variation with gas flow,

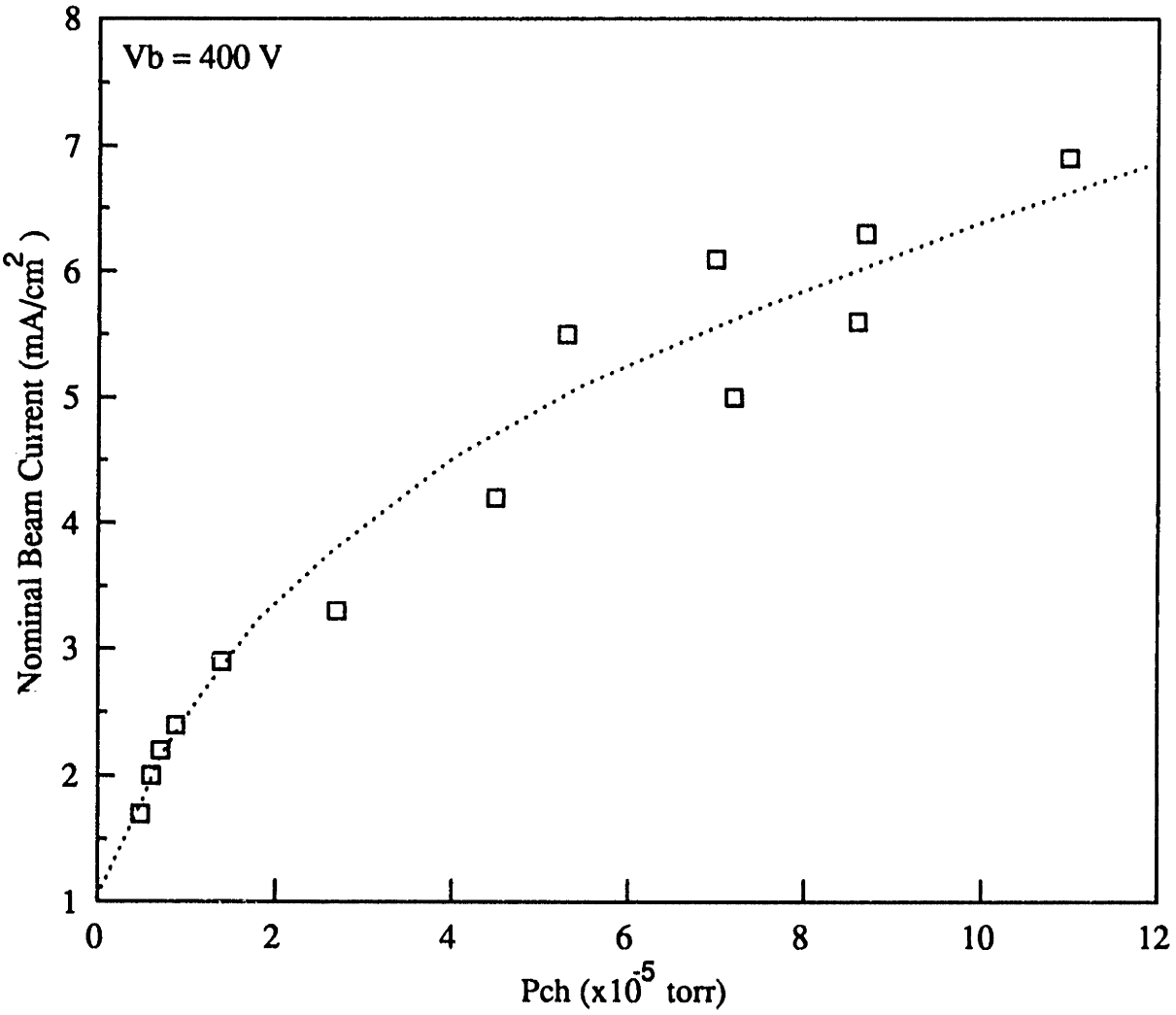

Figure 4-3. Measured ion beam current versus main chamber for the 1-cm Kaufman gun.

in order to limit the chamber base pressure rise. Accordingly, instabilities in argon gas metering contributed to the experimental limitations on ion flux stability. The maximum ion flux which can be obtained using the dual grid optics is governed by Child's law as applied between the screen and the accelerator grid, i.e. the current is space charge limited. Accordingly the maximum extractable current varies as $V_t^{3/2}$, where V_t is the sum of the beam potential, V_b, and the magnitude of the accelerator potential, V_a, as,

$$j_{max} \propto \frac{V_t^{3/2}}{l_g^2} \tag{4-3}$$

where l_g is the inter-grid spacing. This space charge limitation results in rapid fall-off of the maximum beam flux with ion energy as shown in Figure 4-4, at a chamber base pressure of about 10^{-5} torr. Given this limitation, the usable energy range of the Kaufman gun extends down to about 100 eV, below which currents were too low to get reasonable etch rates over the lifetime of the Kaufman gun filaments. Kaufman et al. [1982] describe the usage of three grid and single grid optics in this type of ion source, which allow the production of large fluxes of low energy ions not allowed in the two grid system. However, the three grid system suffers from the added complexity of accurately aligning a third grid, while the single grid optics require frequent replacement due to grid sputtering by directly impinging ions. Neither of these options was commercially available for the 1-cm Kaufman source employed at the time of this thesis work.

Several other performance issues were considered in the use of the Kaufman gun. While it is possible to achieve reasonable ion fluxes and to etch conducting films without adding the neutralizing electrons, operation of the neutralizer filament was essential for the etching of silicon dioxide and was found to increase beam collimation substantially. Figure 4-5 shows the increase

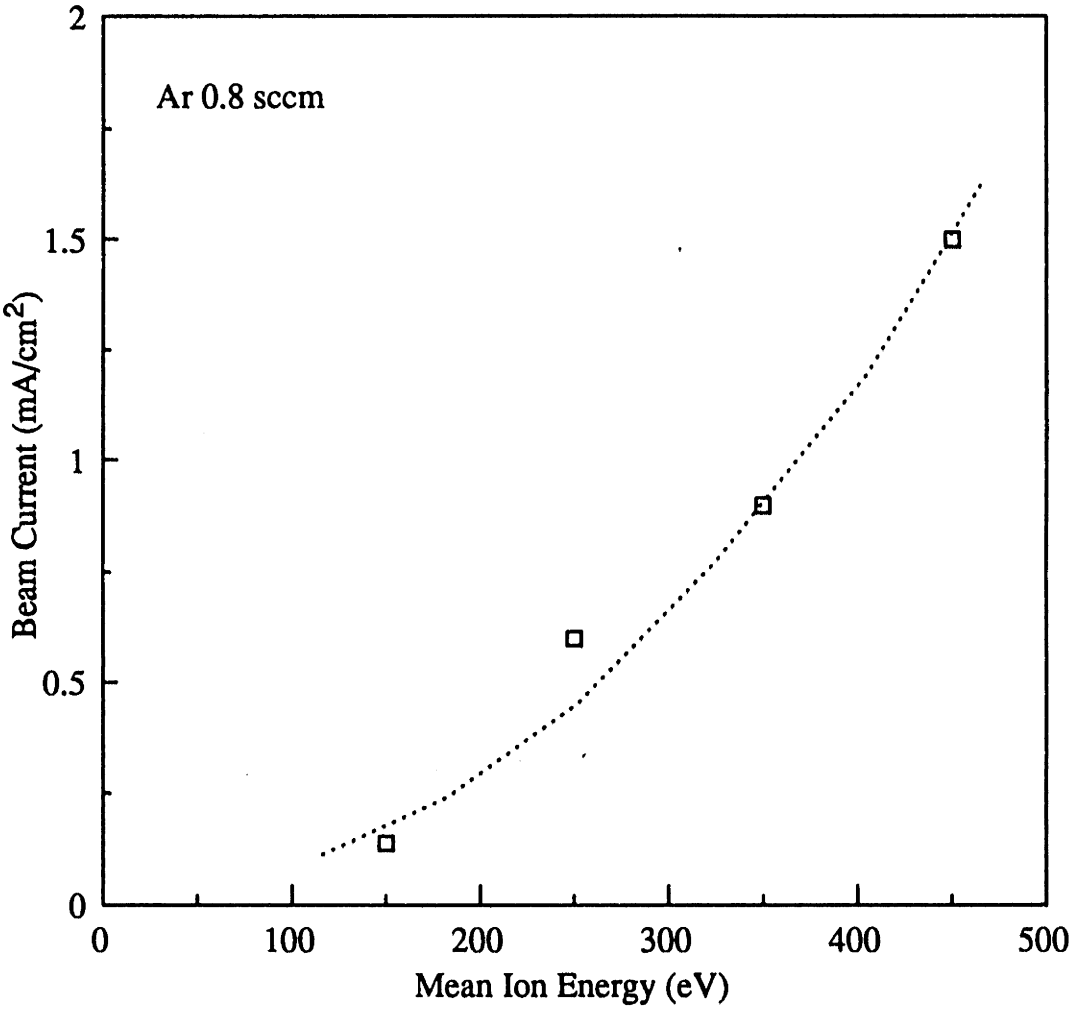

Figure 4-4. Measured ion beam current versus ion energy at constant chamber pressure.

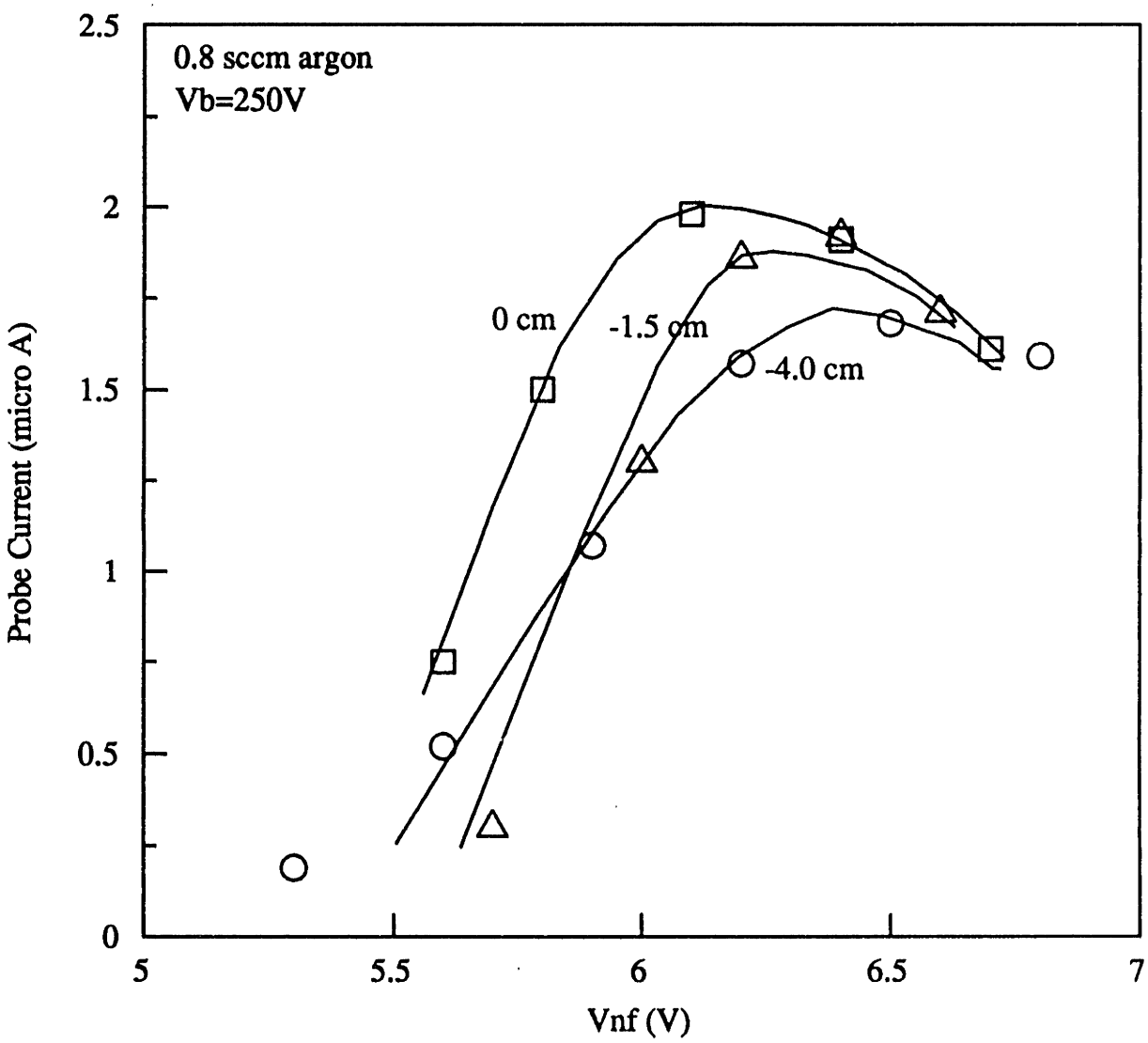

Figure 4-5. Measured ion beam current versus neutralization filament voltage at various probe distances.

in the measured beam current as a function of potential across the neutralization filament (5 mil tungsten wire). The point of maximum beam current occurs near the condition where the neutralizing electron current is equal to the total beam current. In certain experiments it was necessary to move the ion flux probe back several centimeters to allow full rotation of the top flange assembly. Under these conditions the ion beam current at the sample face was not measured directly by the flux probe, and a small correction factor was necessary due to beam current attenuation with distance, also shown by the separate curves in Figure 4-5. Given optimal neutralization conditions for maximum current at the sample face, a correction factor of +25% was required to relate sample-face current to that measured by the probe 4 cm further down stream. The angular divergence, or focusing, of the ion beam is determined roughly by the ratio of the accelerator voltage to beam voltage in the two grid optics; small accelerator potentials (magnitudes) result in highly collimated beams while large accelerator potentials result in broader beams at the expense of beam current density. This behavior is illustrated in the inset to Figure 4-6 which appears in the users manual for the Commonwealth Scientific 1-cm Kaufman source. We have operated under conditions where $V_a \approx 25\%$ of V_b in order to achieve maximal current densities at the sample die. Based on Figure 4-6, ion flux variation over the 1-cm dies was expected to be <15%. Although the absolute flux of both the neutral and ion beams vary over the sample die, the variation of the neutral-to-ion flux ratios is fairly small since the fluxes fall off in a similar manner. Figure 4-6 shows the expected variation in neutral-to-ion flux ratios for a neutral beam produced in the HFPO pyrolysis tube (Chapter 3) over the 1-cm sample die. This information suggests that we do not have large variations in the relative surface coverages of neutral adsorbates over the die surface since relative ion and neutral arrival rates are similar everywhere. From an energetics viewpoint the Kaufman gun was ideal since it generates ions of a given energy with a very peaked distribution, allowing us to clearly assess the effect of ion

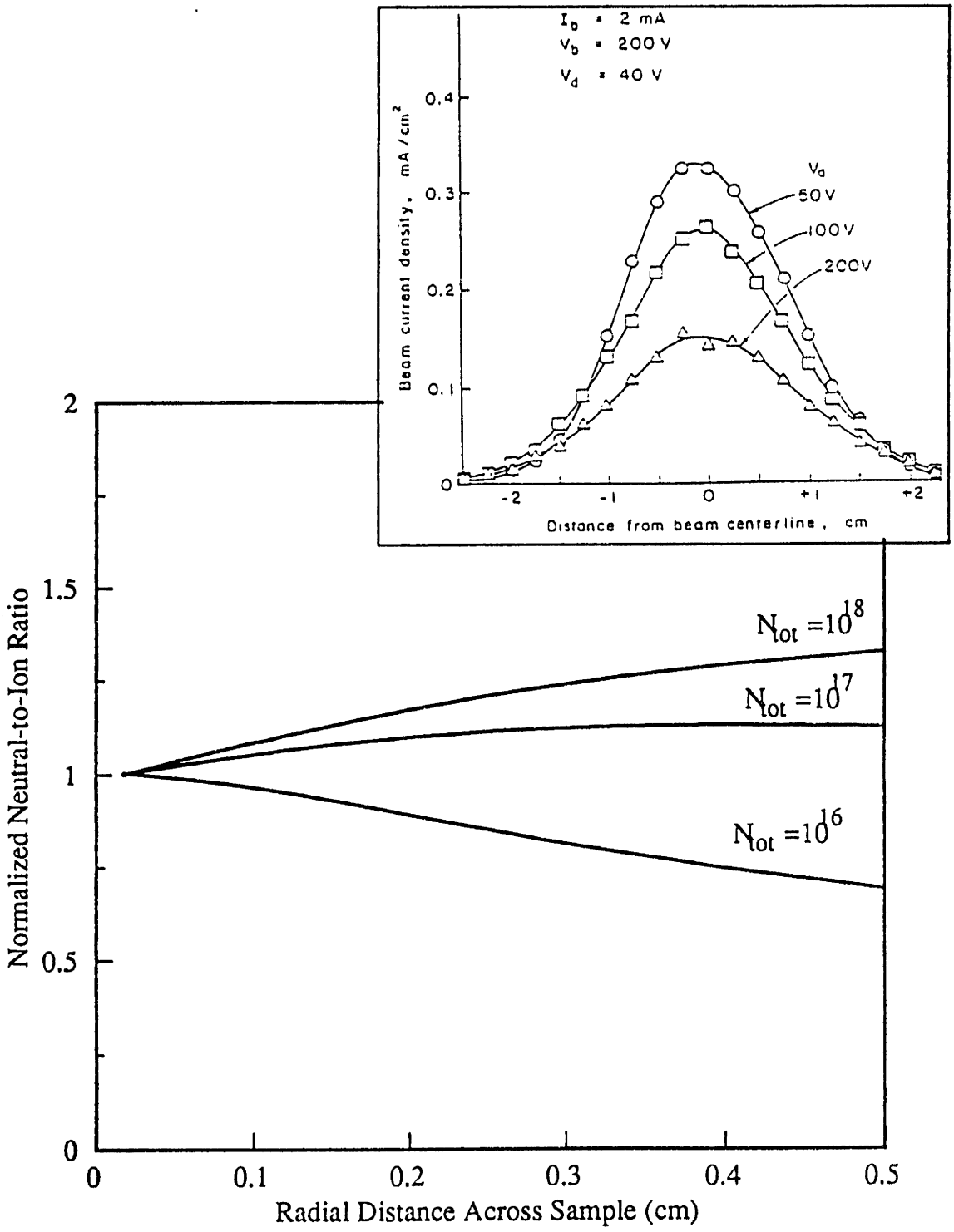

Figure 4-6. Predicted neutral-to-ion flux ratio variation from the 1/8" HFPO pyrolysis tube and the 1-cm Kaufman gun.

energy on etching yield. Figure 4-7 presents a measurement of the ion energy distribution for a 250V nominal ion beam, in which the energy spread is within +/- 5V and the measured peak energy is within about 4V of the nominal beam potential, demonstrating acceptable energy resolution in the gridded analyzer.

By far the largest disadvantage to the use of the Kaufman ion source was the limited filament lifetimes obtained as the result of impingement erosion and reactive etching. The use of 5 mil tungsten filaments in argon gas for both the neutralizer and discharge filaments resulted in typical lifetimes of 6-10 hours. Practically, once an argon discharge is run for an extended period, the filaments sag and no longer make solid electrical contact with their mounting posts, such that the discharge cannot be restarted. As a result, it was found that both filaments required replacing after every experimental set to achieve consistent operation and reasonable flux stability. Cleaning of the filament mounting posts after every run with a mild abrasive was also necessary to remove deposits which prevented the filaments from making good electrical contact. Both the total filament lifetime, and the overall ion flux stability were greatly reduced when large chamber pressures of reactive gases such as HFPO and fluorine were present. Operation of the Kaufman gun inside of a vented shroud (Appendix A, drawings 3B.50-51) improved the operation stability somewhat, but attenuated measured beam fluxes by approximately 50%. Without differential pumping on the Kaufman ion source, the maximum F fluxes employed where limited to about 10^{18} mols/cm^2-s (at the doser tip), in order to limit reactive gas backmixing rates into the Kaufman source to < 1% of the total argon throughput. This limit was set to prevent production of reactive F ions, to preserve reasonable filament lifetimes, and to keep the total chamber background pressure < 10^{-4} torr where collisional effects could become important. Large HFPO background pressures were also problematic in that carbon deposits began to form on the Kaufman gun optics assembly, and in the gun interior, degrading performance. The deposits were cleaned by running

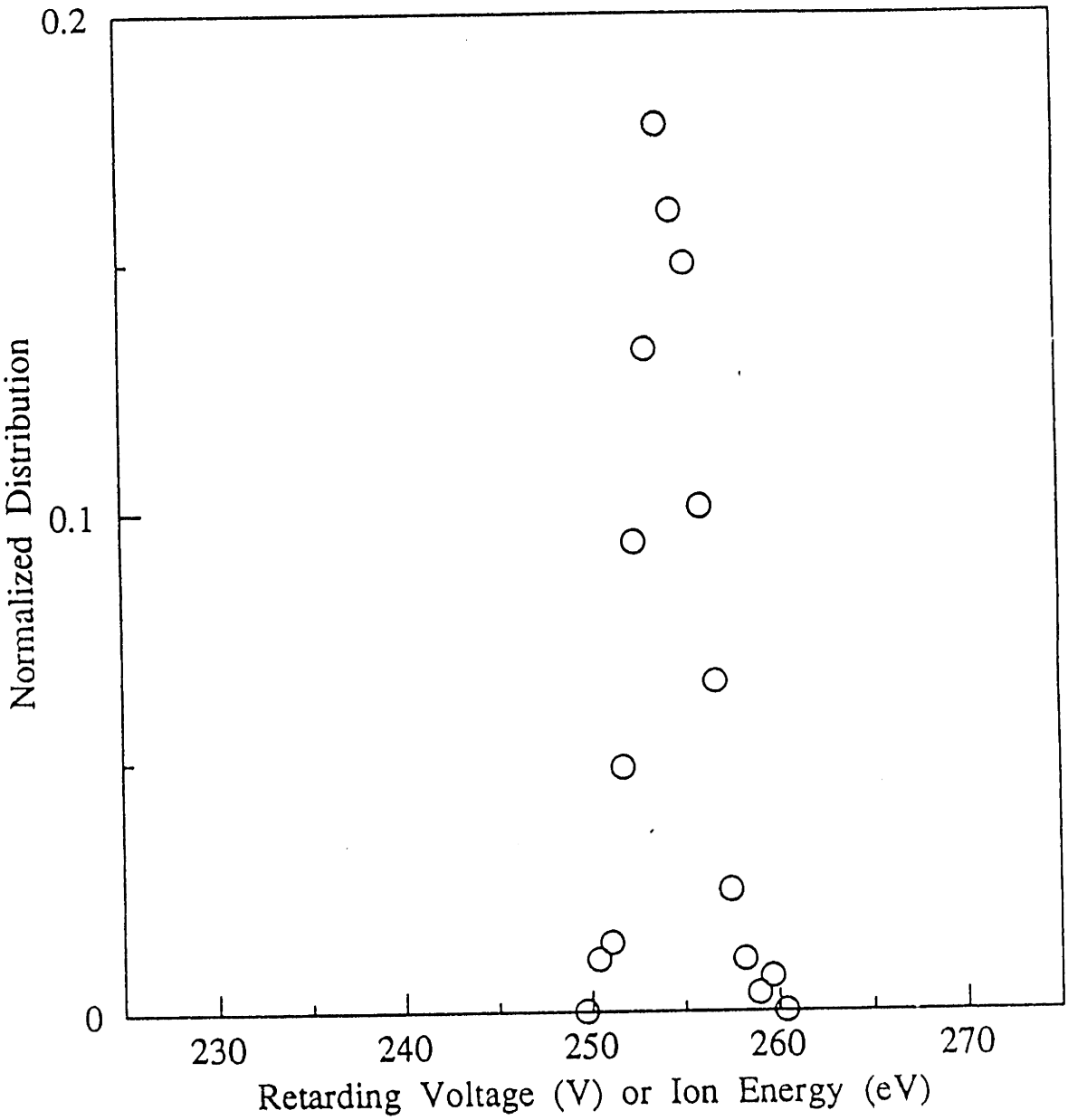

Figure 4-7. Ion energy distribution developed in the 1-cm Kaufman gun as measured with the gridded probe.

oxygen discharges after experimental sets, and by manually cleaning the gun interior with a mild abrasive and acetone. Usage of CF_4 gas in the Kaufman gun for the production of CF_x^+ ions was found to be destructive as well as impractical due to rapid filament erosion and unstable beam currents, and rapid etching of the graphite grid assembly.

A differential pumping system was added to the multibeam apparatus to reduce the large chamber gas load resulting from ion source operation, thus allowing larger radical fluxes to be employed in the main chamber. The system is shown schematically in Figure 2-2, and facilitates cryogenic pumping of the ion source gas load at an effective rate of about 100 l/s, reducing the main chamber gas load by an order of magnitude. A 1-cm diameter orifice was used on the ion collimating cap, giving a conductance of about 10 l/s between the chambers. This system was constructed to allow use of either the Kaufman ion source, or the AsTex CECR source described below. In order to obtain the maximum possible ion fluxes from the Kaufman ion source inside the differentially pumped chamber, and extension assembly was constructed to place the mouth of the Kaufman gun as close as was practical to the collimating cap. A schematic diagram of the Kaufman gun extension mount is shown in Figure 4-8. Maximum ion fluxes obtainable with the operation of the Kaufman gun in the differential pumping shroud are about 60% lower that those obtained with direct insertion of the source in the main chamber.

4.3 Characterization of the CECR Ion Source

A compact ECR plasma source (ASTEX CECR) was purchased to enable production of near-threshold energy ions in this thesis, and to allow the production of reactive gas ions without the problems of filament replacement and grid erosion associated with the Kaufman ion source. A schematic diagram of the CECR source and major system components is shown in Figure 4-9. In the CECR source, a 2.45 GHz whister wave is launched into a resonant cavity which is

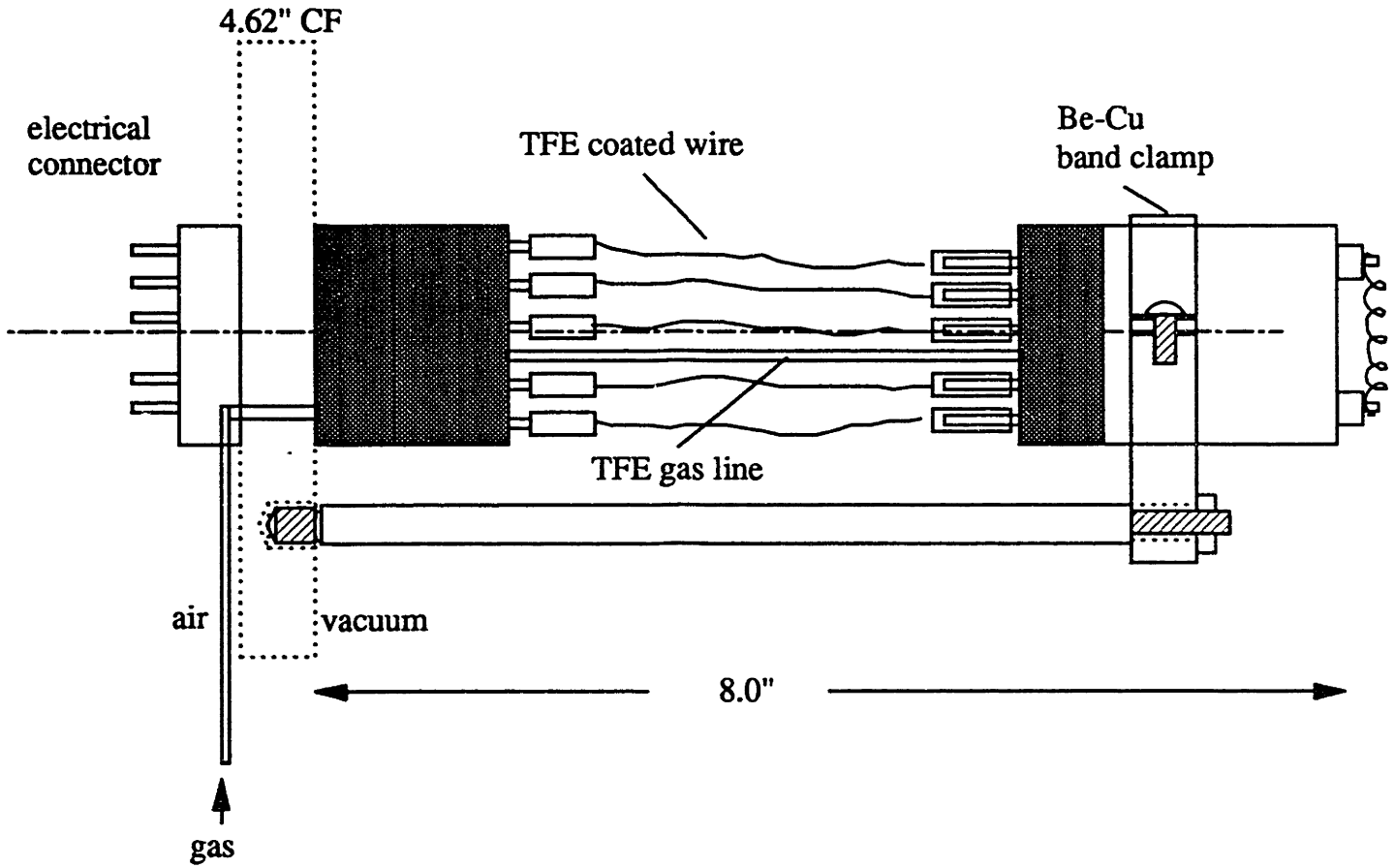

Figure 4-8. Extension mount for usage of Kaufman ion source with the differential pumping system.

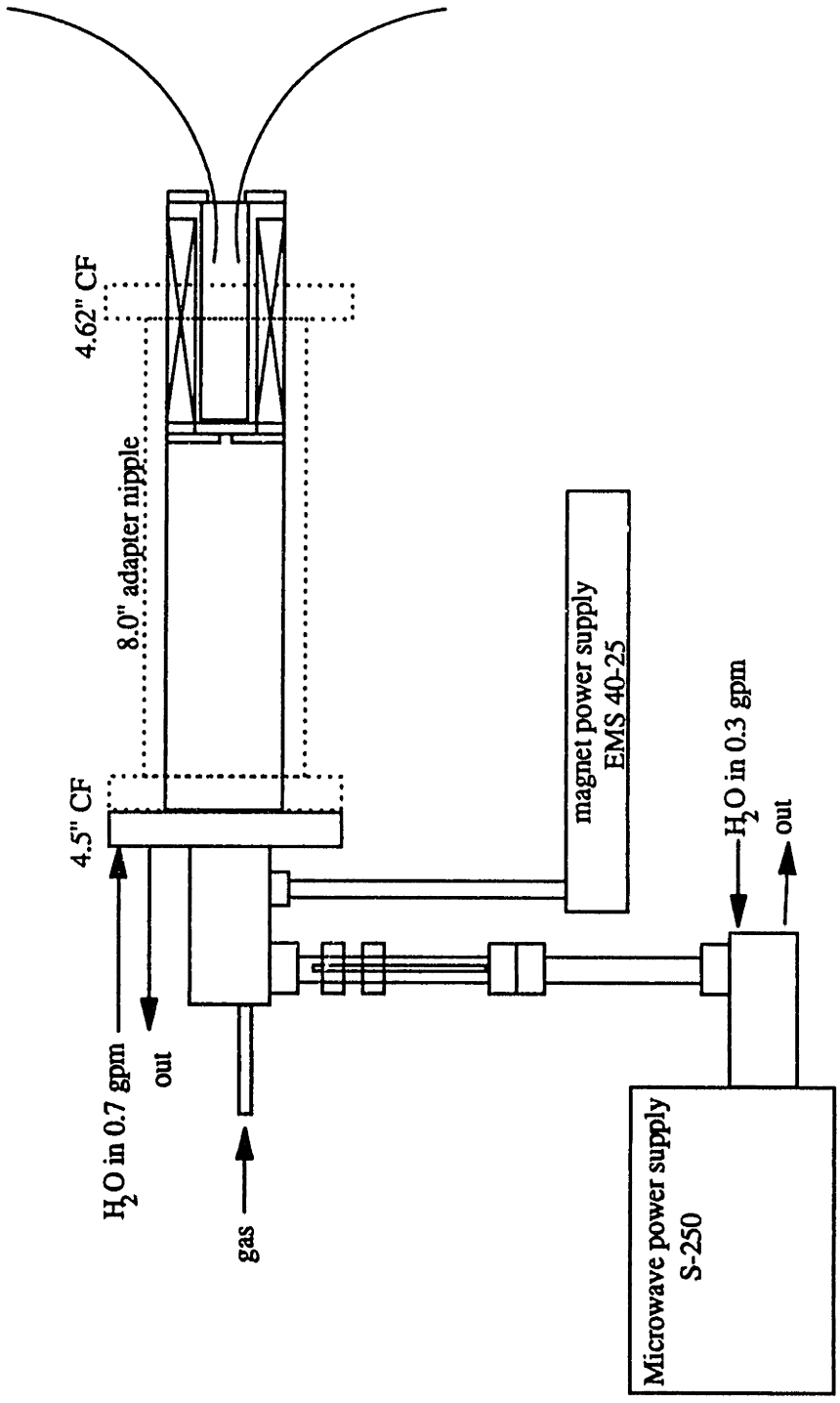

Figure 4-9. CECR source schematic and power supply interconnections.

surrounded by a set of solenoid magnets (streaming field configuration) capable of producing local magnetic fields in excess of 875 Gauss. Electron cyclotron resonance (ECR) occurs where the local magnetic field attains the value of 875 Gauss, and the electron cyclotron frequency (eB/m) equals the excitation frequency (2.45 GHz). In this local region, electron trajectories are confined to tight spirals due to the axial magnetic field, but can very effectively absorb power from the local electric field, in the form of increased electron velocities (resonant heating) and Larmar radii. The magnetic confinement of these hot electrons results in very efficient ion and free radical production in the source via electron-neutral collisional processes, and allows stable operation at plasma pressures well below the mTorr range without the use of hot filaments. ECR sources are capable of producing plasma densities on the order of 10^{11}-10^{12}/cm^3, while the mean ion energies are in the range of 10-30V (i.e. the plasma floating potential) [Asmussen, 1989]. Electrons produced are much hotter than those obtained in DC or RF plasma sources, on the order of 5-10 eV, due to the highly efficient ECR heating mechanism.

At the time of this thesis work, the CECR had not been well characterized for use as an ion source due to its recent introduction, and because its major application is in the production of free radicals to stimulate film deposition processes. Use of the CECR as an ion source suffers from the problem that the magnetic fields outside of the source mouth diverge rapidly, causing rapid divergence of the plasma beam since the electrons are fully magnetized and the ions follow by ambipolar diffusion. This feature aids in ion flux uniformity over large areas, but results in rapid attenuation of ion flux as a function of distance from the CECR mouth. However, based on preliminary data provided by ASTEX, ion fluxes on the order of 1 mA/cm^2 are achievable at a distance of 10 inches from the source, at 250 watts microwave power and argon gas throughputs on the order of 10 sccm. We found that the CECR source could be operated at much lower gas throughputs and powers if a 1-cm diameter quartz orifice plate was used at the source mouth,

effectively increasing the source backing pressure at low flow rates. Stable operation of the CECR was achieved at argon flows of about 2 sccm over a wide range of operating powers as shown in Figure 4-10. At these low flow rates, the CECR could be operated while directly inserted into the main chamber (i.e without the differential pumping system). For the purposes of experimentation, microwave power was set at 250 Watts, and ion current was controlled by adjusting the magnet current. The behavior of the measured ion current with CECR magnet current is highly non-linear, and not all magnet current settings allow stable operation. Ion flux gradients across the sample face under CECR operation are essentially flat, increasing the variation in neutral-ion flux ratios across the die. Backmixing of main chamber gases into the ECR source is problematic without differential pumping, due to the relatively large conductance of the mouth orifice plate (> 10 l/s). CF_x^+ ion production in the CECR source was achieved, but resulted in rapid etching of the internal quartz liners. Alumina liners are being designed to alleviate this problem and allow usage of a wide range of reactive gases.

Operation of the CECR source inside the differential pumping assembly allowed reduction of the main chamber pressure by an order of magnitude. A single stainless steel grid with 0.002 mil holes and 27% open area (Buckbee-Mears Co.) was added to the source to enhance the extraction and collimation of the low energy ions. In addition, a stainless-steel liner was inserted into the discharge cavity liner to allow the CECR source to be biased above its natural floating potential. Independent control of the bias potential and the extraction grid potential allows large currents (order mA/cm^2) to be extracted over a range of energies from 20-500 eV. A neutralization filament is required under some bias conditions to keep the ion beam net neutral and allow transport to the sample face. The neutralizing filament is also required in insulator etching to prevent charging of the sample. Further details of this source design are reported by Zau [1993].

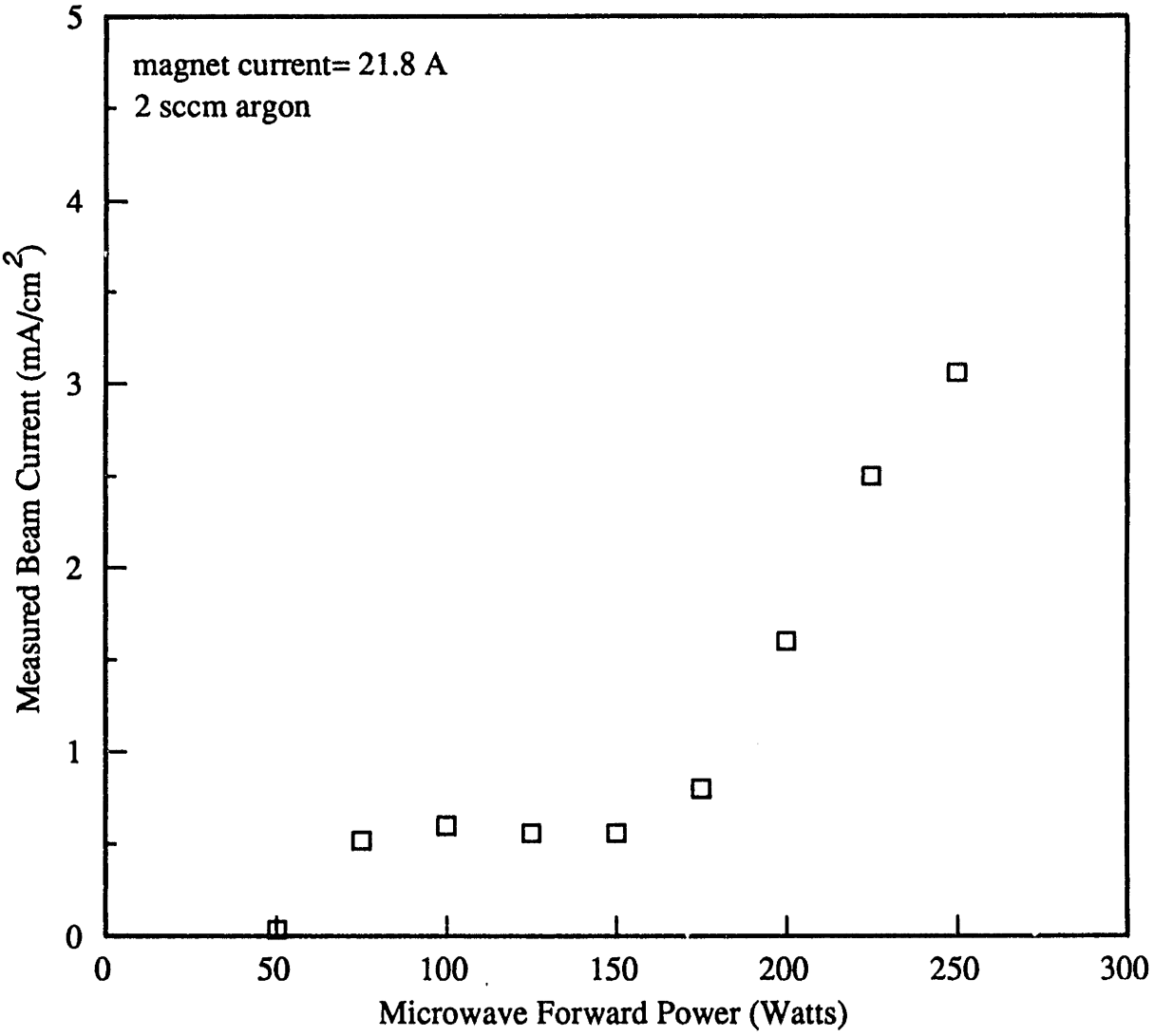

Figure 4-10. CECR Ar+ ion beam current versus microwave power without differential pumping.

4.4 Summary

Two ion sources were characterized and utilized in this thesis work for the production of high current, broad ion beams over an energy range of 20-500 eV. A 1-cm Kaufman ion source was employed for most of this thesis work, but was unable to produce reasonable ion fluxes at energies below 100 eV. Filaments in the Kaufman source required replacement after every experimental set, greatly limiting the amount of data which could be taken. A CECR source was used for production of 20 eV ions for near-threshold etching studies, and for the production of CF_x^+ ions from a CF_4 discharge. A differential pumping system was constructed to reduce main chamber gas loads due to these ion sources, either of which is compatible for use in the differentially pumped mode. Difficulty was encountered in transporting CECR ions out of the collimating orifice.

Chapter 5

Ion-Enhanced F Etching of Si and SiO_2

In the set of experiments discussed in this chapter, we have studied the Ar^+ ion-enhanced etching of Si and SiO_2 by atomic fluorine (F), as a function of the relative fluxes of neutral-to-ionic species, and the incident ion energy. Although it is well established that atomic fluorine is the primary etchant species in the fluorocarbon etching of silicon, F interactions with SiO_2 surfaces have been less well studied, and some researchers have contended that CF_x type radicals are the dominant etchants for SiO_2 in fluorocarbon plasma processes (see Chapter 7). Coburn and Winters [1979, 1985, 1987] have conducted a number of studies of inert ion-enhanced XeF_2 etching of Si and SiO_2 in an effort to understand the fundamental mechanisms by which high energy ions (>500 eV) enhance F-surface chemistry, and the types of products which are evolved. Other studies of this system [Haring et al., 1982; Houle, 1987] have sought to measure the energy distribution of products evolved at KeV ion bombardment energies. At the start of this thesis work, very little information was available concerning ion-enhanced surface kinetics at low ion bombardment (20-500 eV) energies representative of plasma processes. Harper et al. [1981] and Steinbrukel [1989] have made observations of surface etching kinetics of low energy reactive ions such as CF_3^+ and F^+, but these studies do not allow deconvolution of the neutral flux effects from the ion bombardment effects. The goal of this thesis work was to measure Ar^+ enhanced F-Si and F-SiO_2 steady-state surface kinetics using F and ion fluxes representative of the plasma processing environment and in the energy range of interest to plasma processing (20-500 eV). This kinetic data, together with studies reported in the literature, were used to construct simple models of the ion-enhanced F chemistry which capture the functional dependence of the major variables. Models of physical sputtering and thermal F etching of Si and SiO_2 available in the literature were

incorporated self-consistently, to capture the correct limiting behaviors. Product distributions in these systems were studied mass spectrometrically, to determine the qualitative effect of relative species fluxes and energies on the product spectrum. XPS studies were conducted to determine the chemical nature of the etching surfaces, and to allow model verification.

5.1 Ar^+ Sputtering of Si and SiO_2

In the effort to develop quantitative models of ion-enhanced F etching, it was necessary to incorporate models for the limiting processes of F atoms alone, or Ar^+ ions alone impinging on the Si and SiO_2 surfaces. We first consider the case of Ar^+ ion etching alone ($F/Ar^+ \dashrightarrow 0$), or "physical sputtering", of the substrate material. Sigmund [1969] has developed analytical solutions to the problem of sputtering of amorphous or polycrystalline homogeneous materials in the medium (0.1-1 KeV) and high (>1 KeV) energy ranges through approximate solution to the Boltzmann equation. In this theory, the binary collision cascade which results from a high energy particle (ion) impinging upon the surface results in the momentum transfer back toward the surface, and the "sputter removal" of particles which can overcome their local binding energies. When the incoming particle energies are ≤1 KeV, the binary particle interactions are well described by a Born-Mayer potential, and sputtering yield is found to be linear in the incoming particle energy, E_i. In this "linear cascade regime", the sputtering yield, S, is most simply expressed as:

$$S(E) = C_{pt}\, S_n(E) \qquad (5\text{-}1)$$

where C_{pt} is a constant which depends on the relative masses of the projectile (**p**) and target (**t**) and is inversely proportional to the surface binding energy, U_o, according to,

$$C_{pt} = \frac{3\alpha}{4\pi^2 U_o} \tag{5-2}$$

α is determined as a function of the relative masses as summarized by Winters [1976]. $S_n(E)$ is the nuclear stopping power as determined from the Born-Mayer interaction potential,

$$S_n(E) = \frac{4M_p M_t E}{(M_p+M_t)^2} \tag{5-3}$$

It is common to express the nuclear stopping potential in terms of a reduced bombardment energy, $\varepsilon=E/E_{pt}$, as described by Zalm [1984]. Details concerning the linear-cascade regime theory may be found in several sputtering treatises [Winters, 1976; Behrisch, 1981]. In regards to this thesis work, what is most important to note is that the linear cascade theory does not accurately reflect measured physical sputtering yields when the incoming ion energies fall below 200 eV or so. This shortcoming is due to the lack of treatment of sputtering "threshold" effects when the incoming particle energies become comparable to target-surface binding energies.

In the regime of interest to plasma processing, the physical sputtering yield of polysilicon is observed to be linear in Ar^+ flux, and the energy scaling has been predicted through extension of the Sigmund model to the low energy regime as suggested by Steinbrukel [1989],

$$Y_p(E_i) = C_{pt}\, S_n\left(\frac{E}{E_{pt}}\right) f(E_{th},E_i) \tag{5-4}$$

In this expression, the parameter C_{pt} is the same function of the ion mass and incidence angle, and of target physical parameters such as atomic density, target atom mass, and surface binding

energy. Steinbrukel recognized that using the approximations for $S_n(E/E_{pt})$ and $f(E_{th}, E)$ suggested by Wilson et al.[22] and Mitsunami et al.[23] respectively for low energy sputtering, gives a linear proportional relationship between ion flux and Si etching rate,

$$S_n(\frac{E_i}{E_{pt}}) \propto E_i^{0.5} \tag{5-5}$$

$$f(E_{th},E_i) = 1 - (\frac{E_{th}}{E_i})^{0.5} \tag{5-6}$$

$$R_{Si} = Y_{p,si}\, I^+ = A\,(E_i^{0.5} - E_{th}^{0.5})\, I^+ \tag{5-7}$$

This expression describes our total sputtering rate of silicon by normally incident Ar^+ ions as a function of ion flux, ion energy, and the sputtering threshold energy. In the case of amorphous and polysilicon etching, available data is well fit by the parameters shown in Table 5-1. Zalm

Table 5.1 Si and SiO_2 Low Energy Sputtering Model Parameters

	A	E_{th}
Si	0.0337	~20 eV
SiO_2	0.0139	~18 eV [ref. Chapman, 1980]

[1984] has derived a similar expression for the low energy sputtering regime, and notes that sputtering yield in this regime is to within 20% a function of particle energy only, and not particle type (i.e. atomic number, Z). Comparison of several recent sets of data for Ar^+ sputtering of polysilicon are compared to the functionalities predicted by equation (5-7) versus the linear cascade theory of Sigmund [1969] in Figure 5-1. It is readily apparent that the available data is

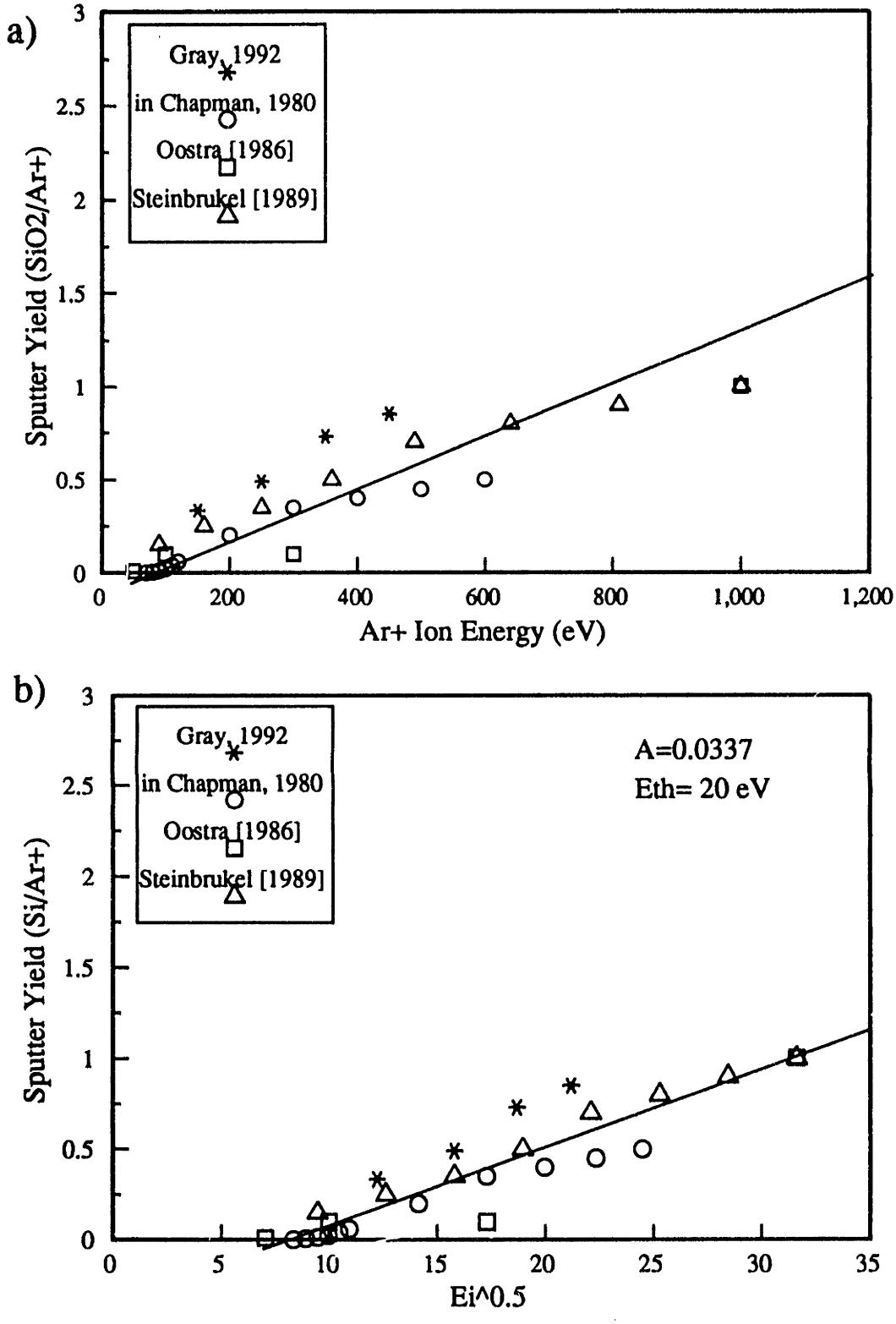

Figure 5-1. Comparison of the a) Sigmund [1969] and b) Steinbrukel [1989] models for the low energy Ar+ sputtering of silicon.

more accurately represented by equation (5-7), although the experimental spread is still appreciable due to inaccuracies in the various sputtering yield measurement methods. Some data points from our experiments are shown for comparison, where the measurement of reasonable sputter yields demonstrates the accuracy of our ion flux measurement technique.

Variations in sputtering yield or reactivity of single crystal Si <100> versus polysilicon were not measurable within the sensitivity of our methods, and are generally important only in high energy sputtering with light ions where channeling and implantation effects become important. In our sputtering regime ($>10^{15}$ $cm^{-2}s^{-1}$) we expect rapid amorphization of the single crystal under ion bombardment, washing out the crystallographic effects. Extension of the Sigmund theory to the physical sputtering of composite materials such as SiO_2 is not rigorous. However, for lack of a better model, we have applied an expression analogous to equation (5-7) to describe SiO_2 etching yield as a function of Ar^+ ion flux and energy over the limited range studied, as described by the parameters in Table 5-1. As demonstrated in Figure 5-2, equation (5-7) was again found to give a much more accurate representation of SiO_2 sputtering yields as a function of incoming Ar^+ ion energy. Agreement of our sputtering data with that found in the literature is excellent. Based on these observations, equation (5-7) was employed as our working model for the physical sputtering component of Ar^+ enhanced F etching, where the appropriate parameters in Table 5-1 were employed for the silicon and SiO_2 systems.

Even in the relatively low ion energy regime investigated in this thesis work, 20-500 eV, the bombardment energies are 1-2 orders of magnitude larger than the thermal activation barrier to Si-F_x bond formation, typically 0.1-1eV. Consequently, it is appropriate to think of the incoming ions as providing the "activation energy" which promote surface bond formation, and drive the etching chemistry. Mechanistically, the bombarding ions are thought to enhance Si-F bond formation through the ballistic "mixing" action of the collision cascade induced by the

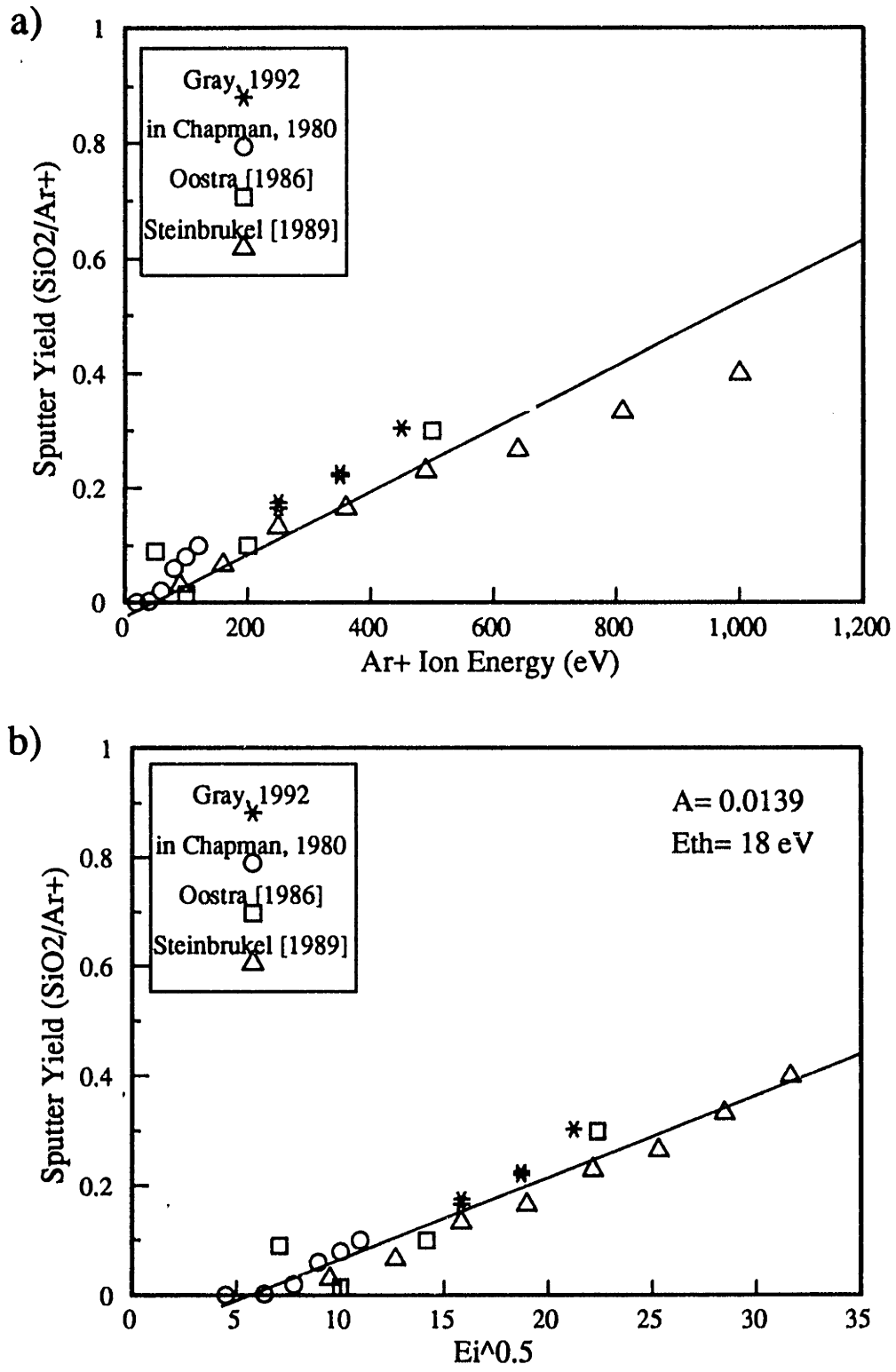

Figure 5-2. Comparison of the a) Sigmund [1969] and b) Steinbrukel [1989] models for the low energy Ar+ sputtering of SiO_2.

bombarding ions as suggested by Winters [1988]. This "ion mixing" action prevents the formation of a thick SiF_x overlayer on the substrate surfaces, and facilitates the rapid transport of surface F into the lattice via direct knock-on collisions, or damage-enhanced diffusion [Mitzutani et al., 1985]. The depth over which 200-1000 eV ion bombardment can cause appreciable lattice disturbance, or substrate damage, has been empirically correlated by Kaufman et al. [1982],

$$l = 1.1\frac{W_t}{\rho_t}E^{2/3}(Z_p^{1/4} + Z_t^{1/4})^2 \qquad (5\text{-}8)$$

where E is the ion energy in eV, W_t and ρ_t are the atomic weight and specific gravity of the target, and Z represents the atomic numbers. This length scale, l, roughly defines the "ion mixing zone" as shown schematically in Figure 5-3, and determines the length scale over which the ion-enhanced chemistry is operative. For Ar^+ bombardment of silicon and SiO_2 in the energy range of 20-500 eV, damage depth estimates range from 1 to 15 Å, and 5 to 35 Å respectively. Mitzutani [1985] has shown that 1 keV Ar^+/Cl_2 etching of Si<100> results in significant Ar and Cl incorporation ($>10^{14}$ mols/cm^2) up to about 100 Å in depth. Based in these observations, a good rule of thumb is that the "mixing zone" depth increases about 1 monolayer (~5 Å) per 50 eV increase in ion energy in this regime. At ECR ion energies of ≈20 eV, application of the "ion-mixing" concept is tenuous since the ion energies are on the order of the Si lattice displacement energy (≈13 eV), and little lattice displacement damage is expected. Ion-enhancement mechanisms in this regime have not yet been investigated.

5.2 Thermal F Etching of Si and SiO_2

The second limiting process we must consider is that of F atoms alone impinging on a silicon or SiO_2 substrate (F/Ar+ -->∞), where only thermal or "spontaneous" etching by fluorine

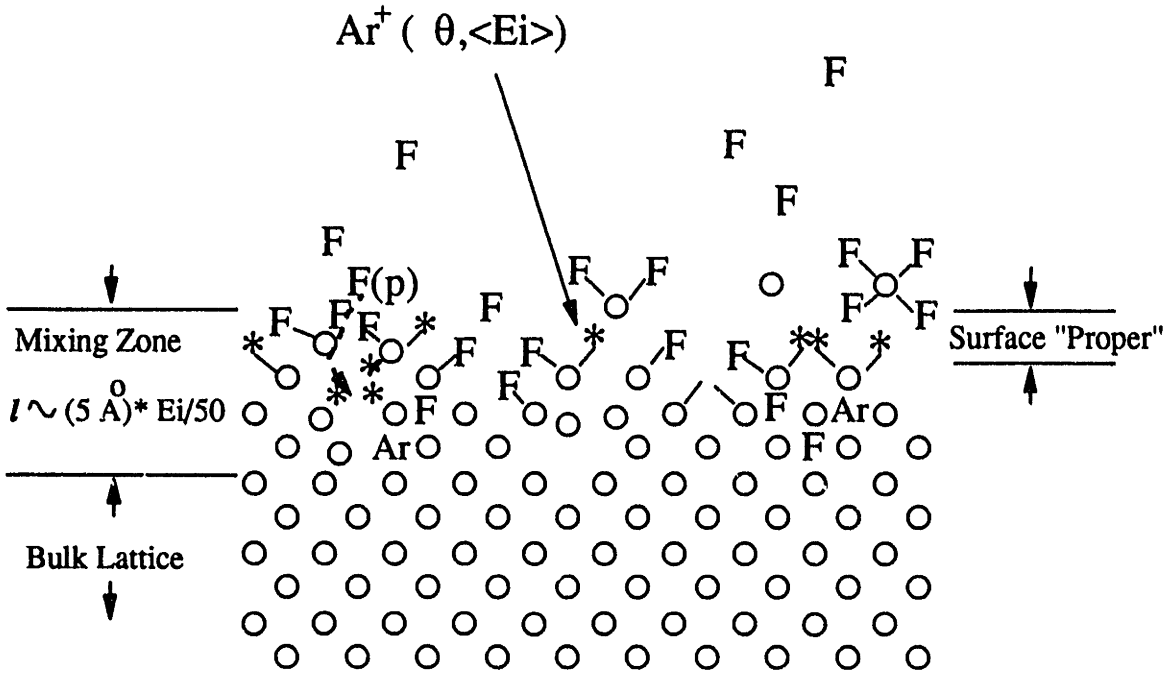

(*): Si* dangling bond

F: gas phase atomic F

F(p): physisorbed F

Ar+: bombarding Ar ions

Ar: implanted argon

O: silicon lattice atom

Figure 5-3. Schematic description of the "ion-mixing zone" created at the near-surface due to the ballistic mixing action of the bombarding ions.

atoms can occur. Several groups have measured reaction rates of atomic ground state (^{2}P) F atoms with silicon [Flamm et al., 1981; Vasile and Stevie, 1982, Ninomiya et al., 1985], but the measured reaction probabilities vary due to inaccuracies in etching rate measurement and calculation of F atom fluxes at the sample surfaces. As recently reviewed by Kojima et al. [1991], the etching rate of lightly doped silicon ($<10^{19}$ dopant atoms/cm^3) is well described by the Arrhenius form

$$R_s = k_o T^n Q_F \exp(\frac{-E_a}{k_b T}) \qquad (5\text{-}9)$$

where Q_F is the atomic fluorine flux (mols/cm^2-s) at the substrate surface. Neither the range of data nor the resolution of available measurements is sufficient to determine the exponent, **n**, which is taken as zero for our purposes. It is also important to note that atomic F etching shows no preference to crystallographic orientation since the mechanism involves the formation of a thick SiF_x overlayer (5-10 monolayers), which obscures the crystallographic planes on single crystal Si. The Arrhenius rate parameters extracted from the three major studies cited are given in Table 5-2, where the F flux range investigated is also cited. Within the accuracy of the methods employed,

Table 5.2 Arrhenius Rate Parameters for F Etching of Si and SiO_2

Reference	Q_F range reported	k_o	E_a
Flamm et al. [1981]	2.3×10^{19}-1.1×10^{22}	3.59×10^{-15}	-0.108±0.005
Vasile et al. [1982]	2.5×10^{14}-5.0×10^{14}	1.65×10^{-15}	-0.09 to -0.15
Ninomiya et al. [1985]	1.6×10^{16}-5.2×10^{18}	2.01×10^{-14}	not measured

an activation energy of 0.1 eV is observed in the F-Si etching rate expression. Kojima [1991]

points out that this activation energy is probably indicative of the barrier to F diffusion through the SiF_x overlayer. Houle [1983, 1984] has shown that F diffusion through the SiF_x layer may be driven by Coulombic forces on F^- anions work which described the influence of large n^+ and p^+ dopant concentrations, and the effects of UV-light stimulation.

The pre-exponential factors reported in Table 5-2 vary over an order of magnitude, and reflect uncertainties in measured F atom fluxes and etching rates. The pre-exponential factor reported from the studies of Ninomiya et al. [1985] was back-calculated from a plot of measured silicon etching yield versus F atom flux using the activation energy reported by Flamm et al. [1981], and is subject to large uncertainty. It is important to consider that measurement of F atom reaction probabilities on silicon involve the convolution of the F atom physisorption/desorption problem with the F-Si reaction chemistry. It is typical in these reaction rate studies to define an apparent Si-F reaction probability, η, assuming the production of SiF_4 as,

$$\eta_{SiF4} = 4\frac{n_{si}}{Q_F} \tag{5-10}$$

where n_{SiF4} is the observed silicon etching rate in mols/cm^2-s. The actual surface physisorption concentration, $n_F(p)$, on the SiF_x surface can be estimated using the Langmuir form to relate the coverage fraction to the impingement flux, J_F,

$$\frac{n_F(p)}{n_m} = \frac{b'Q_F}{1 + b'Q_F} \tag{5-11}$$

where n_m is the monolayer saturation coverage, and b' is determined by the F physisorption energy [Adamson, 1982]. The F physisorption energy on an SiF_x surface is expected to be very

low (≤5 kcal/mole), such that the parameter **b'** is on the order of 10^{-24} cm^2-s/mol. As a result, surface F physisorption coverages are expected <10% at $Q_F \leq 10^{23}$ mols/cm^2-s, under which conditions we are in the low pressure limit and $n_F(p) \approx n_m b' Q_F$. Substituting into equation (5-10), we find that the apparent Si-F reaction probability and F surface coverage are related by

$$\eta_{SiF4} = 4\frac{n_s n_m b'}{n_F(p)} \qquad (5\text{-}12)$$

In this low pressure limit, Arrhenius parameters can be safely regressed from the apparent reaction probability data without the convolution of surface coverage effects. However, it is obvious that at high Q_F fluxes, $n_F(p)$ and Q_F are not longer linearly related, such that surface coverage effects and possible F atom recombination reactions will convolute the apparent reaction probability calculated according to equation (5-10). In the extreme limit of near saturation F(p) coverage, the apparent reaction probability with appear to fall-off as $1/Q_F$ since increasing F impingement flux can no longer increase surface coverage. Such effects could explain the discrepancy in pre-exponential factors reported by Vasile and Stevie [1982] versus Flamm et al. [1981] who worked at much higher F concentrations, and need to be considered in future studies. For lack of better information, we have used the Arrhenius parameters reported by Flamm et al. [1981] for calculation of spontaneous F-Si etching rates in our work, since the flux range studied was representative of plasma processing conditions. Product distributions observed in the thermal etching of silicon by F are discussed in Section 5.4.

Little information was available concerning the spontaneous interaction of atomic F with SiO_2. Flamm et al. [1979] also performed studies of spontaneous interaction of F with SiO_2, and found an activation energy of 0.163 eV, and a pre-exponential factor of 7.4×10^{-16}. No other

quantitative studies of the F-SiO_2 reaction system are known to us, so the data of Flamm was employed for calculation of F-SiO_2 spontaneous etching rates. Nordine and LeGrange [1976] measured F atom loss coefficients on F-passivated SiO_2 surfaces from which the importance of F atom desorption versus recombination may be assessed.

5.3 Yield Studies of Ar^+/F Etching

Ar^+/F Etching of Polysilicon

Studies of ion-enhanced etching of silicon and silicon dioxide by fluorine have been examined in the past with XeF_2 as a fluorine source, but at much higher ion energies and lower ion fluxes than are typical of commercial plasma processes as discussed in Chapter 1. At the start of this thesis work, the necessary scaling information to allow the extrapolation of this data into higher flux and lower energy regimes was not available. In addition, some controversy has evolved concerning the ability of XeF_2 to emulate the surface flux of atomic fluorine generated in a plasma etching process as discussed below. We have avoided this issue by using a well characterized flux of microwave-discharge-produced atomic fluorine. Simple two beam experiments have been conducted where the F and Ar^+ fluxes, as well as the ion bombardment energy were varied to ascertain their effects on silicon and SiO_2 etching yield. For the experiments described herein, the Ar^+ ions were always normally incident upon the sample face, with the radical beams incident at a 45° angle.

Experimental results concerning the Ar^+/F etching of polysilicon are summarized in Figures 5-4 and 5-5, where solid lines represent the results of kinetic models discussed in Section 5.6. The low flux ratio regime, F/Ar^+=0 to 200, is first considered in Figure 5-4 where the experimental yield curves show an initial sharp rise in etching yield with the F/Ar^+ flux ratio. In this regime, the Ar^+/F etching of silicon is essentially mass-transfer-limited, in the sense that the

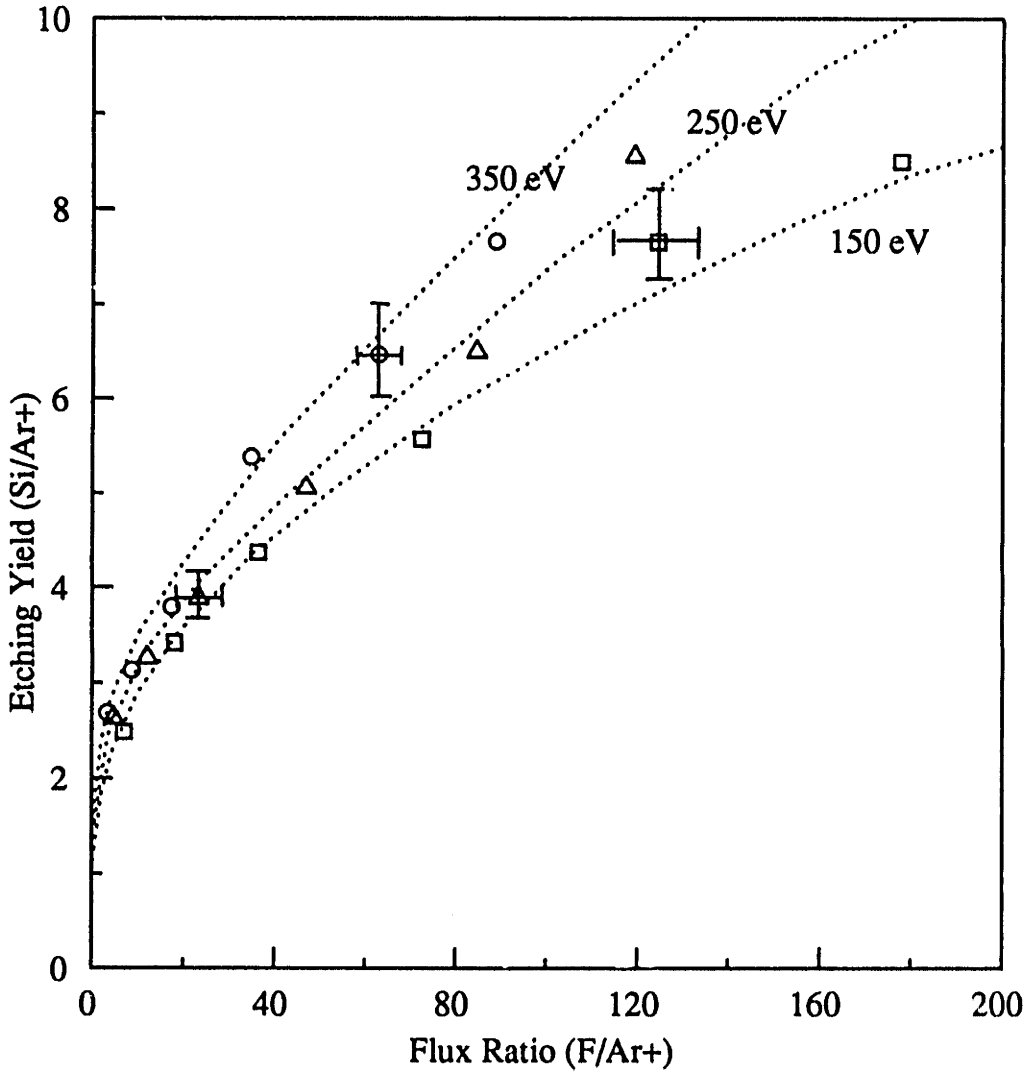

Figure 5-4. Silicon etching yield (Si removed per Ar+) versus F/Ar+ ratio in the mass-transfer-limited etching regime.

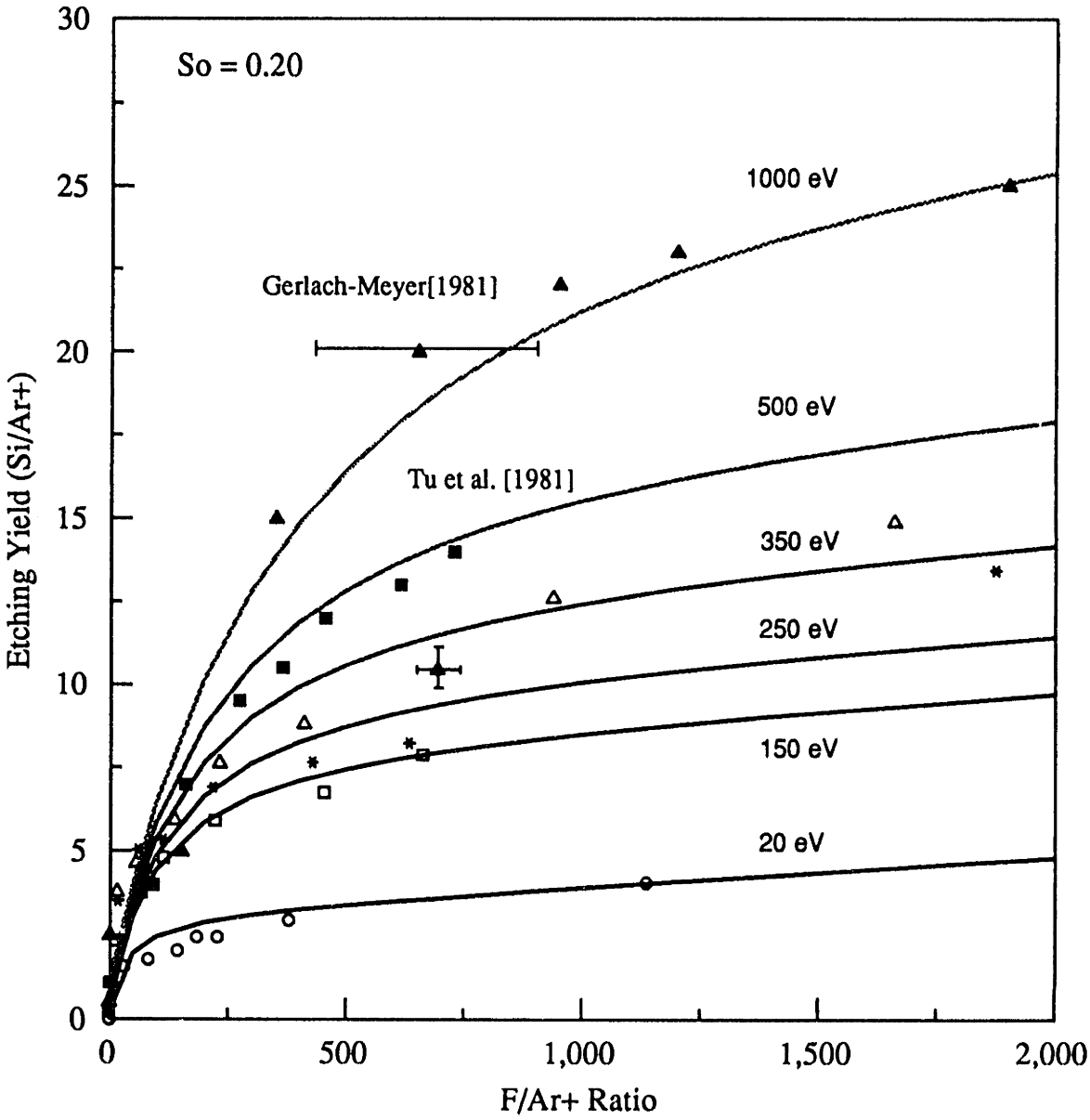

Figure 5-5. Silicon etching yield versus F/Ar+ ratio showing the ion-flux-limited etching regime at large F/Ar+. Lines shown are fits of the surface kinetic model discussed in Section 5.6.

rate of F atom transport to the substrate is limiting the etching yield per ion. In the fluorocarbon plasma processing environment, operation in this regime would be characterized by observation of rapid increase in film etching rates with plasma (e.g. CF_4) pressure at constant power input. As is shown in Figure 5-4, etching yield increase per 100 eV increase in incoming ion energy in this regime is insignificant due to the fact that excess surface fluorine is not available to participate in ion-enhanced etching reactions. Increase in the yield of physically sputtered silicon per 100 eV increase in ion energy is insignificant on this scale. The pure Ar^+-silicon physical sputtering yields are indicated by the regression of the yield curves to $F/Ar^+=0$, and are in the range of 0.1 to 0.4 (Si/Ar^+) in the 150 eV to 350 eV energy range.

At sufficiently high F/Ar^+ ratio, a discrete saturation level is expected for all ion energy levels since the number of etching reactions induced by a single ion impacting a fluorine saturated surface is finite. The high F/Ar^+ flux ratio regime ($F/Ar^+=0$-2000) is considered in Figure 5-5, where the results of Ar^+/XeF_2 yield studies reported in the literature are shown for comparison. XeF_2, as discussed below, acts as an equivalent source of 2 F atoms in Ar^+/XeF_2 silicon etching. However, the XeF_2/Ar^+ ratios reported by Tu et al. [1981] and Gerlach-Meyer [1981] were not corrected by this factor in Figure 5-5 because of the large uncertainty in their XeF_2 flux measurements. At sufficiently high F/Ar^+, the etching yield curves saturate in what we have termed the ion-flux-limited regime. Since the ions are providing the activating energy which drives the F-Si etching chemistry, this is essentially a reaction-rate-limited regime by analogy to the well known Langmuir-Hinshelwood surface kinetic model, where the reaction chemistry is thermally driven. The data presented in Figure 5-5 suggests that the transition between the mass-transfer-limited and ion-flux-limited regime is a strong function of ion energy due to the increased ability of high energy ions to promote surface reactions and enhance F chemisorption through the creation of Si^* dangling bonds. At high F/Ar^+, each 100 eV increment in ion energy greatly

influences the number of etching reactions induced by a single ion because the near-surface region is highly fluorinated, allowing the excess bombardment energy to be translated directly into F-Si bond formation events. It is also interesting to note that in the 20-1000 eV energy range, saturation yields (Si per incoming Ar^+) are at least an order of magnitude higher than the baseline Ar^+ sputtering yields at a given energy. This information is plotted in Figure 5-6, where some early researchers in the field defined this ratio as the "chemical enhancement factor". This ratio essentially goes to infinity at 20 eV bombardment energies, which is near the silicon physical sputtering threshold.

In the fluorocarbon plasma processing environment, operation in the ion-flux-limited regime would be characterized by insensitivity of film etching rates to plasma pressure increase at constant power input. Conversely, sharp increase in substrate etching rates would be expected with increasing input power. The determination of conditions under which these ion-enhanced etching systems are mass-transfer versus ion-flux-limited is extremely important to matching the appropriate control and response variables in plasma process modeling. In addition, due to the wide distribution of ion energies developed in RF diode reactors [Lui et al.,1990], topography evolution simulators must incorporate accurate models of F surface coverage effects to ascertain whether an incoming ion of given energy can achieve its saturation yield.

A limited number of experiments were performed using XeF_2 as a fluorine source rather than microwave generated atomic F, in order to compare the relative reactivity of these two species. The main question was whether XeF_2 is stoichiometrically equivalent to 2 F atoms impinging upon a substrate surface, or is more or less reactive than the stoichiometric equivalent F atom flux. This information was necessary to allow comparison to older literature studies of Ar^+/XeF_2 etching. Some studies have suggested that XeF_2 is more reactive than the equivalent 2 F atoms on clean silicon surfaces due possibly to long surface residence time of an $XeF_2(p)$

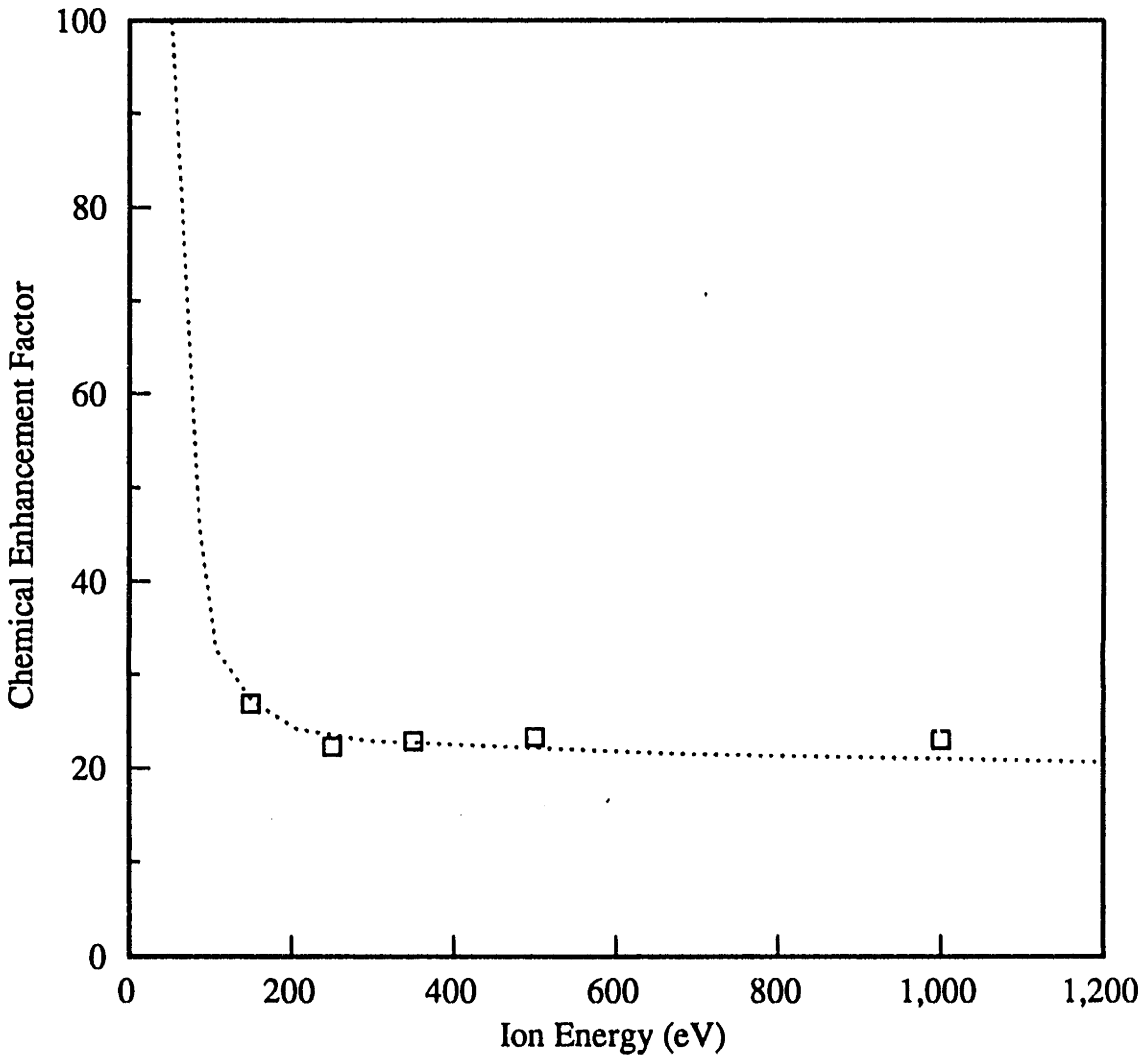

Figure 5-6. The "Chemical Enhancement Factor" for Ar+/F etching of silicon relative to Ar+ physical sputtering. Saturation Ar+/F etching yields were used in the ratio.

physisorbed precursor [Joyce, 1987]. Comparison of Ar^+/F and Ar^+/XeF_2 etching of silicon are shown in Figure 5-7 for 150 eV and 350 eV energy levels, where XeF_2 has been assumed to be the stoichiometric equivalent of 2 F atoms impinging on the substrate. Within the error bars on our yield measurements, this stoichiometric equivalent representation of XeF_2 is found to be valid. Higher flux ratios could not be easily obtained with the solid XeF_2 source since the room temperature vapor pressure is only 4 torr, and the effect of cylinder heating on XeF_2 stability is unknown to us. Figure 5-8 shows another interesting comparison between Ar^+/F, Ar^+/XeF_2, and Ar^+/F_2 etching of silicon at 250 eV, demonstrating that the XeF_2 is much more representative of the ion-enhanced atomic chemistry than the parent molecular chemistry. The work of Engstrom et al. [1988] suggests that the chemisorption of F_2 on silicon is second order with respect to Si^* sites, whereas the F chemisorption is obviously first order. As a result, the Ar^+/F_2 etching yields at a given energy saturate very rapidly as the availability of adjacent Si^* "sites" falls off with fluorine surface coverage. The wide separation between the Ar^+/F and Ar^+/F_2 yield curves at high flux ratios allows us to neglect the parent molecular chemistry in the modeling of fluorocarbon plasma processes, where the effective free radical sticking coefficients at high fluorine coverages are orders of magnitude higher than those of the parent molecular species. This effect is observed all the way down to ECR (≈20 eV) energies as shown in Figure 5-9.

We also studied the effect of substrate temperature and absolute ion flux (at constant F/Ar^+ ratios) in this system. Varying substrate temperature from 25 to 200°C (Figure 5-10) revealed no changes in the ion-enhanced silicon etching yield, as expected. The enhancement in spontaneous etch rate is too small to be seen in the resolution of this data and the surface Si-F bond (~150 kcal/mole) is too strong to allow coverage variations in this temperature range. The ion flux dependency experiments (Figure 5-11) also showed no effect on etching yield over a 3x increase in ion flux at constant F/Ar^+ ratios, validating the use of this ratio as dimensionless

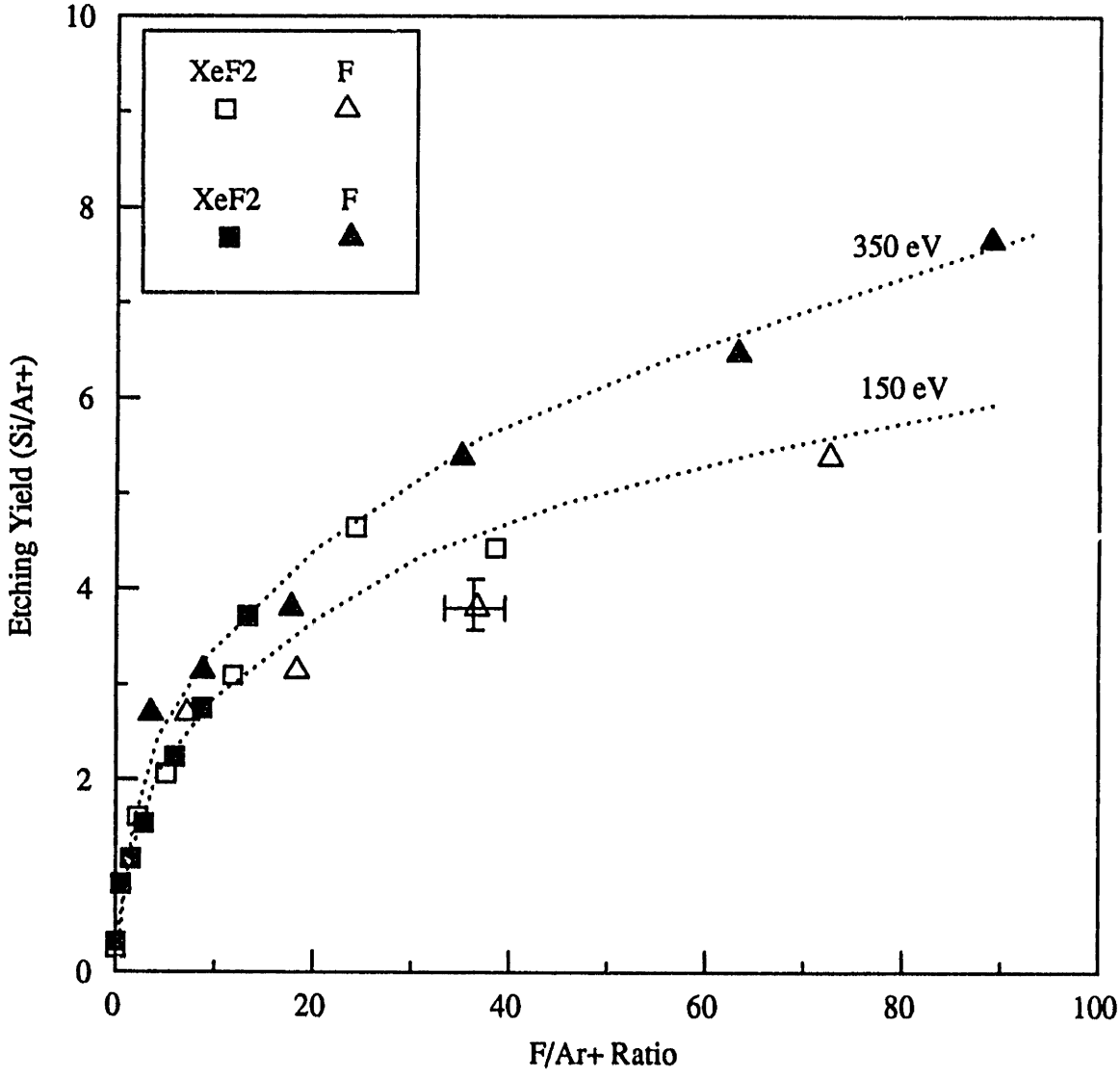

Figure 5-7. Ar+/XeF2 versus Ar+/F etching of silicon at 150 eV and 350 eV ion energy levels.

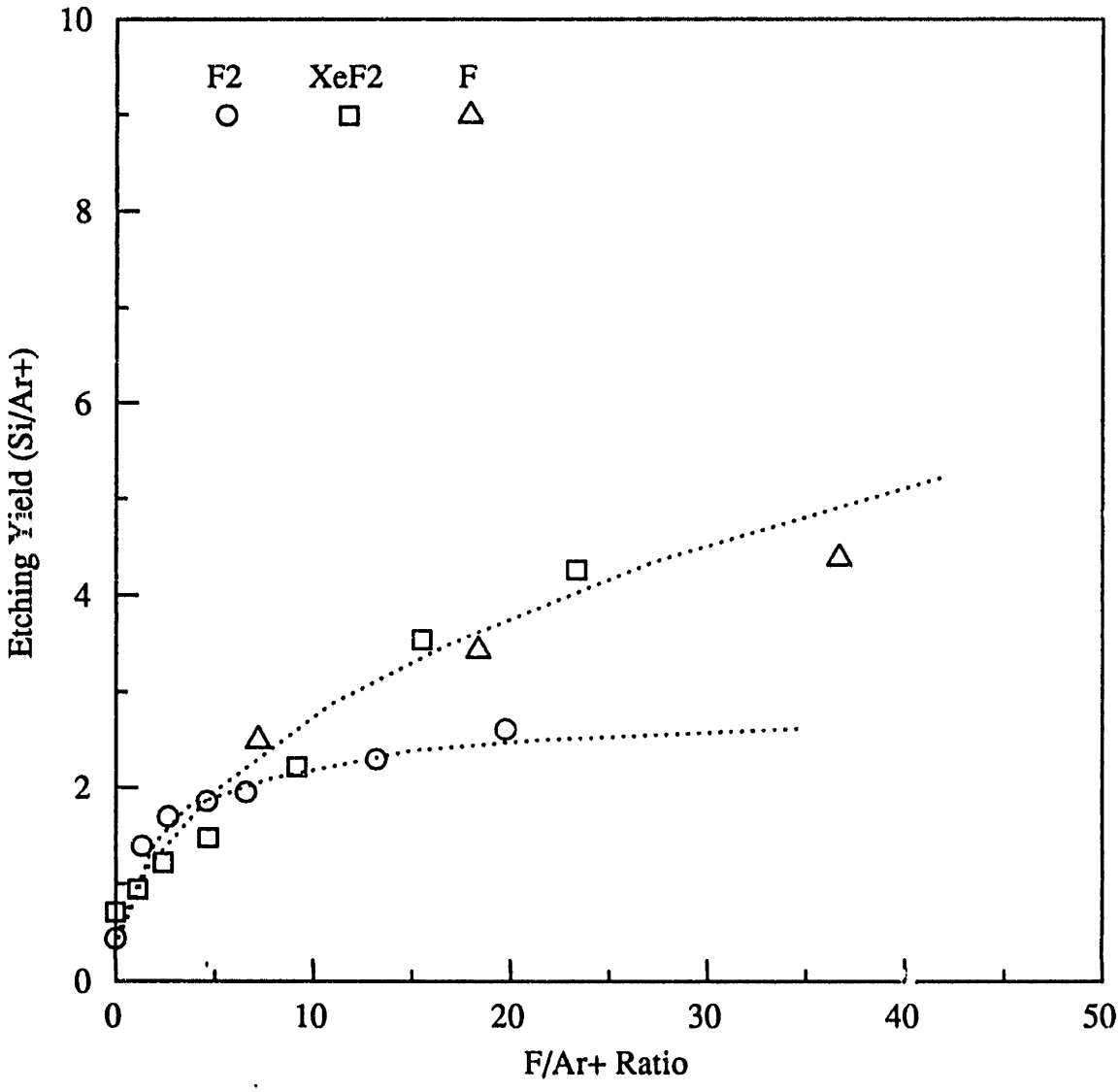

Figure 5-8. Comparison of 250 eV Ar+-enhanced etching by F, XeF2 and F2.

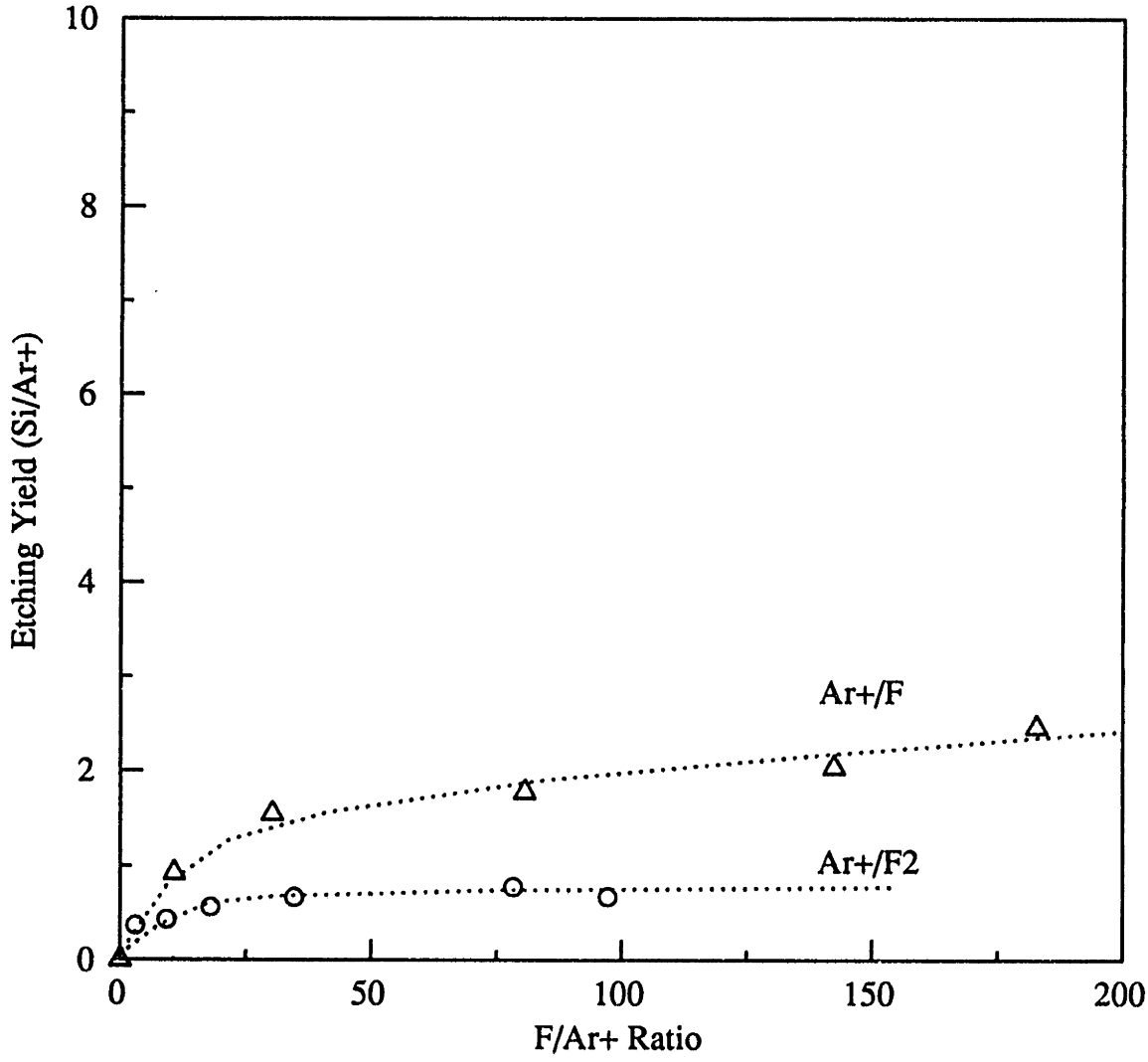

Figure 5-9. Comparison of Ar+/F versus Ar+/F2 etching of silicon at 20 eV.

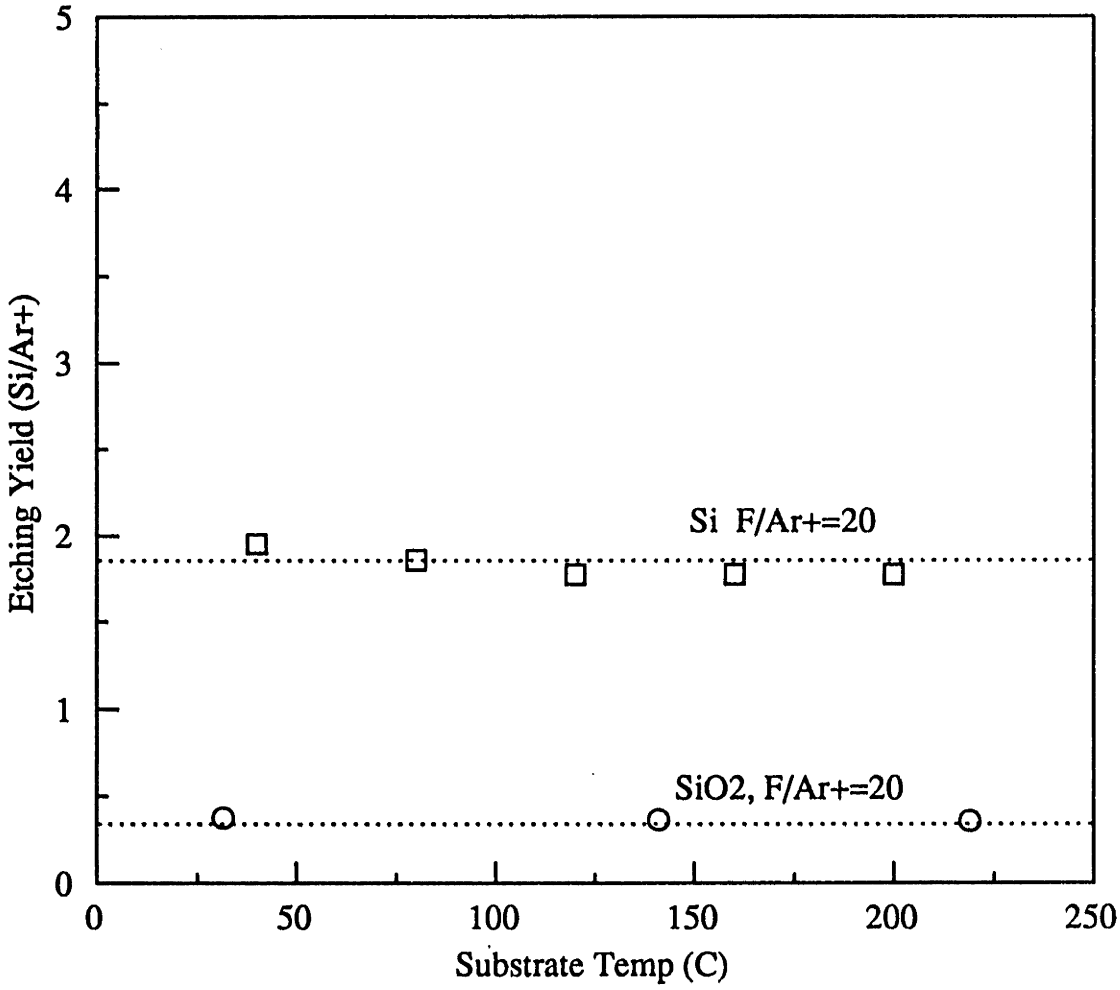

Figure 5-10. Effect of surface temperature, Ts, on Ar+/F etching of silicon and SiO2.

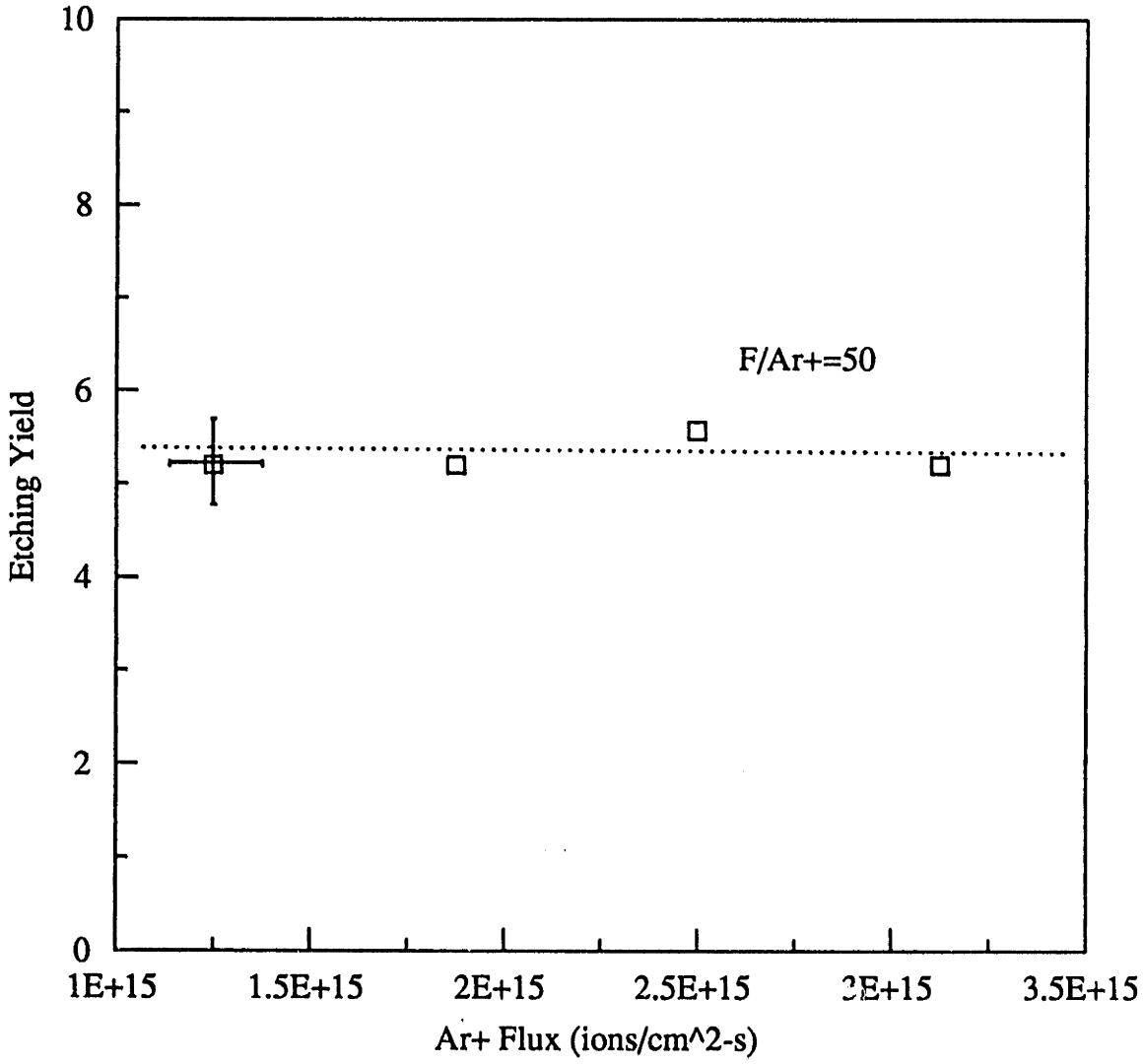

Figure 5-11. Dependence of silicon Ar+/F etching yield on absolute Ar+ ion flux at constant F/Ar+.

system parameter. Implications of these observations for mechanistic modeling of this system are discussed in Section 5.6.

Ar^+/F Etching of SiO_2

Experimental yield measurements in the Ar^+/F etching of SiO_2 are summarized in Figures 5-12 and 5-13, where the low ($F/Ar^+<200$) and high flux ratio regimes are explored, respectively. The measured yield curves are qualitatively similar to those found in the Ar^+/F etching of silicon, however, several contrasting points are worthy of note. In Figure 5-12 it is readily apparent that ion-flux-limited regime is attained at much low F/Ar^+ ratios for a given ion energy, in comparison to silicon etching. Apparently, the available "sites" for F sorption on the oxide surface are either much more easily saturated, or less readily available that in the case of ion-bombarded silicon. This observation is consistent with the hypothesis that F chemisorption occurs primarily on Si^* sites, whereas many of the surface sites on SiO_2 are O^* terminated. In addition, it is apparent that 100 eV increments in ion energy are much more significant in their relative effect on initial SiO_2 etching yields (SiO_2 per incoming Ar^+) than in the case of silicon etching. In fact, the initial slope of the yield curves was found to increase significantly with Ar^+ ion energy. As discussed in Section 5.6, the initial slope of the yield curves is related to the sticking probability of F on the ion-bombarded silicon or SiO_2 surface, suggesting that the SiO_2 surface becomes substantially "stickier" to fluorine with increasing bombardment energy. This is thought to be the result of both increased dangling Si^* bond production with increasing ion energy, and increasing Si-to-O surface elemental ratio due to the preferential sputtering of surface oxygen, resulting in the densification of Si^* surface sites. These contentions are discussed more in conjunction with the XPS data (Section 5.5).

The rapid onset of yield saturation is apparent in Figure 5-13, where higher flux ratios are

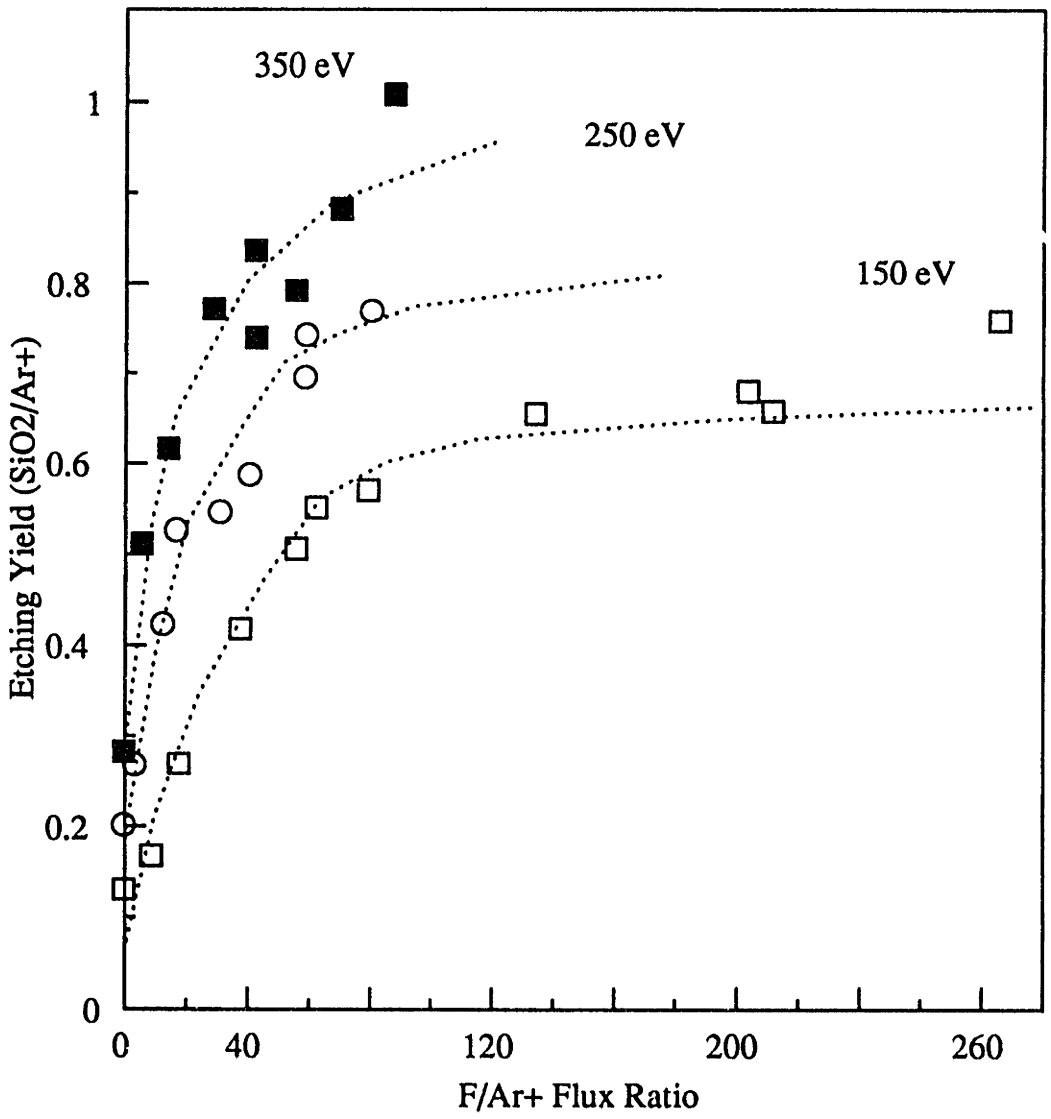

Figure 5-12. SiO2 etching yield (SiO2 removed per Ar+) versus F/Ar+ ratio in the mass-transfer-limited etching regime.

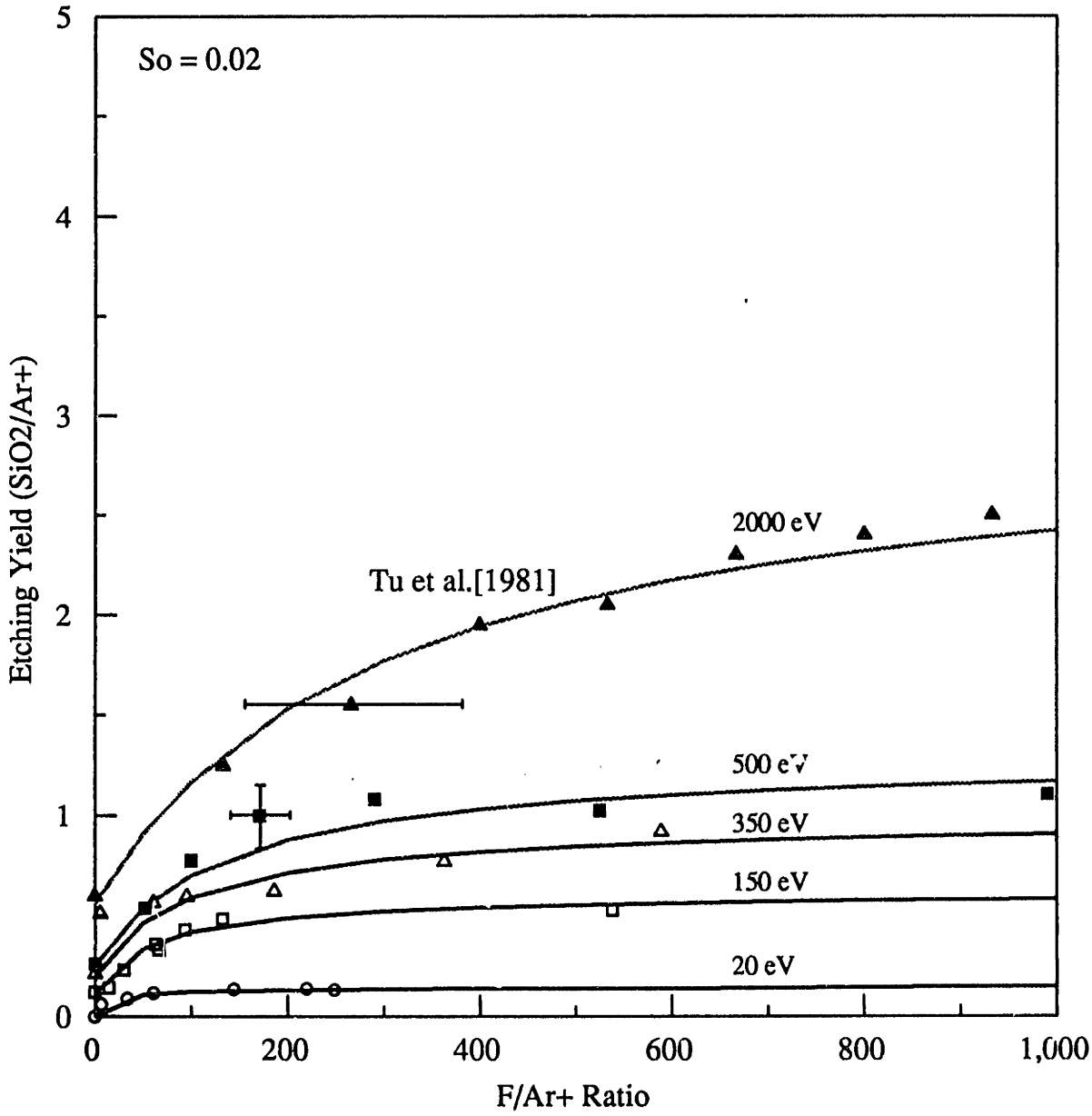

Figure 5-13. SiO2 etching yield versus F/Ar+ ratio showing the ion-flux-limited etching regime at large F/Ar+. Lines shown are fits of the surface kinetic model discussed in Section 5.6.

investigated, and comparison is made to available literature data at 2 keV [Tu et al., 1981]. At the ECR ion energy level (≈20 eV), the saturation in the Ar^+/F etching yield is almost immediate. It is also apparent from this data that the physical sputtering component of SiO_2 etching is much more important relative to the measured saturation etching yields. This results in a much lower average "chemical enhancement factor" (Figure 5-14) for oxide etching. These features are in agreement with the general industry observation that SiO_2 fluorocarbon plasma processes are much more "physical" or "ion-driven", e.g. SiO_2 etching rates correlate strongly with plasma power input. In general, the ion-enhanced reactivity of SiO_2 at saturation fluorine coverages is an order of magnitude lower than that observed in Ar^+/F etching of silicon. This same reactivity ratio is observed in thermal F etching, indicating that the effect of ion bombardment on the F-Si and F-SiO_2 chemistries is simply one of providing energy to surmount "thermal" activation barriers, as opposed to the creation of new mechanistic pathways.

A limited number of experiments were performed using XeF_2 to allow comparison of the XeF_2 and F ion-enhanced reactivity on SiO_2. Comparison of Ar^+/XeF_2 and Ar^+/F etching is shown in Figure 5-15 at 150 eV and 350 eV energy levels, where XeF_2 has been assumed to donate the stoichiometric 2 F atoms. This assumption does not appears to be valid on the SiO_2 substrate for low XeF_2 and F fluxes, where the XeF_2 appears to be more reactive initially. The yield curves seem to converge, however, at high neutral-to-ion flux ratios, suggesting that these are equivalent sources when the reactions are ion-flux-limited. Ar^+/F, Ar^+/XeF_2, and Ar^+/F_2 etching are compared in Figure 5-16, where it is once again apparent that the XeF_2 exhibits greater initial reactivity than either the atomic or the parent molecular gas. As expected, we found no effect of substrate temperature on SiO_2 etching in the range of 20° to 200°C (Figure 5-10) since the contribution of thermal etching mechanisms to the overall etching yield is 0.01% for the F atom fluxes employed. Flux dependencies in the Ar^+/F etching of SiO_2 were investigated in Figure 5-17, where etching

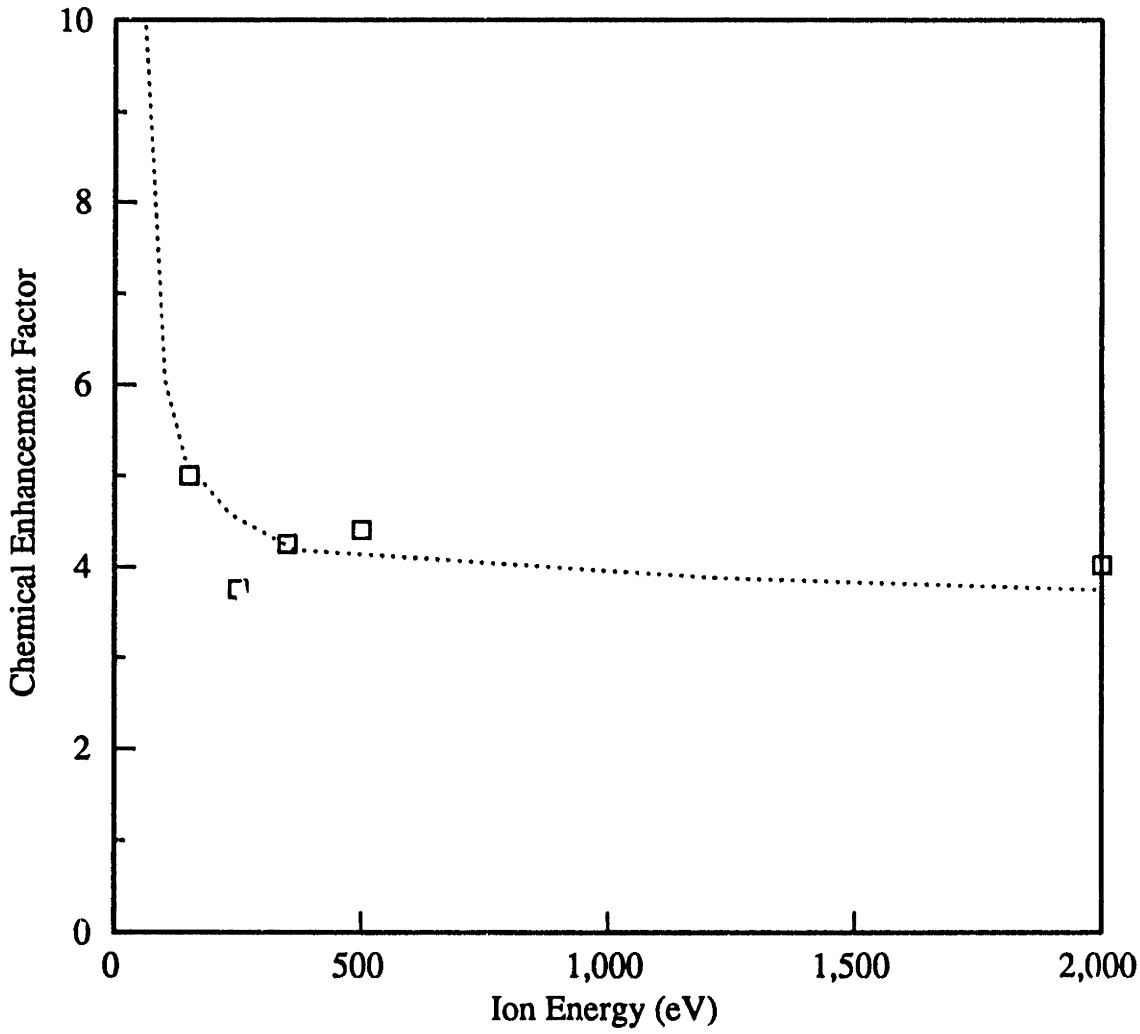

Figure 5-14. The "Chemical Enhancement Factor" for Ar+/F etching of SiO2 relative to Ar+ physical sputtering. Saturation Ar+/F etching yields were used in the ratio.

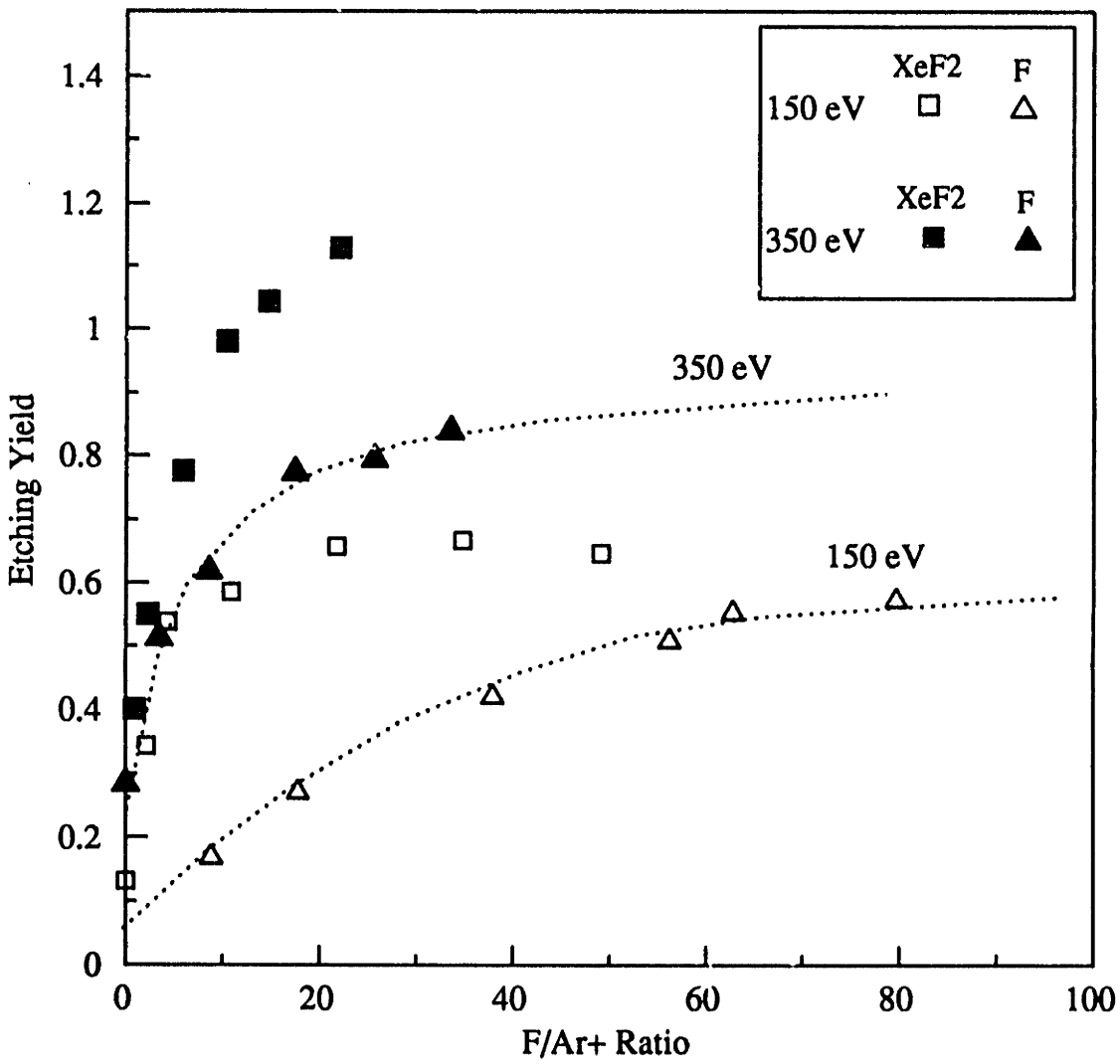

Figure 5-15. Ar+/XeF2 versus Ar+/F etching of SiO2 at 150 eV and 350 eV ion energy levels.

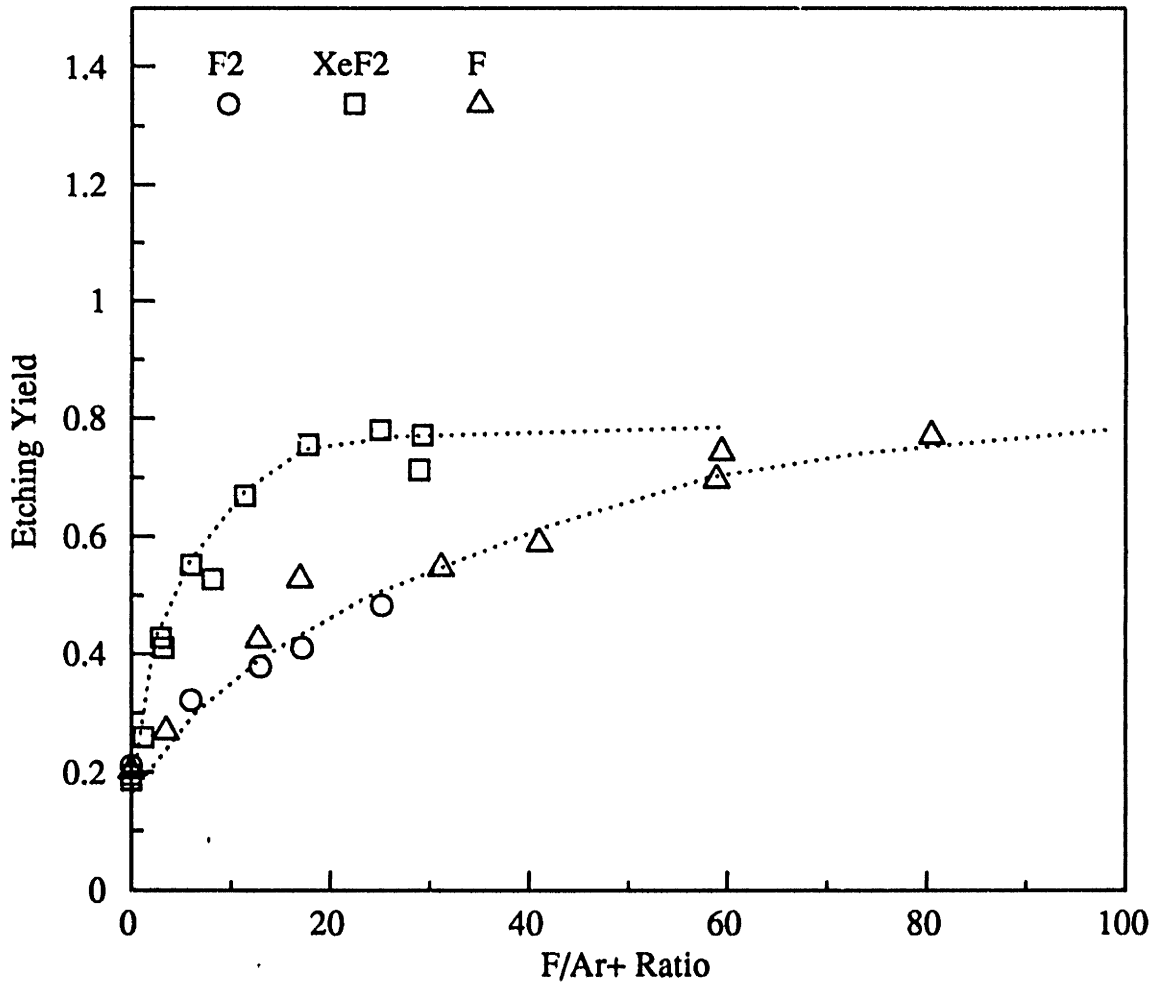

Figure 5-16. Comparison of 250 eV Ar+-enhanced etching of SiO2 by F, XeF2, and F2.

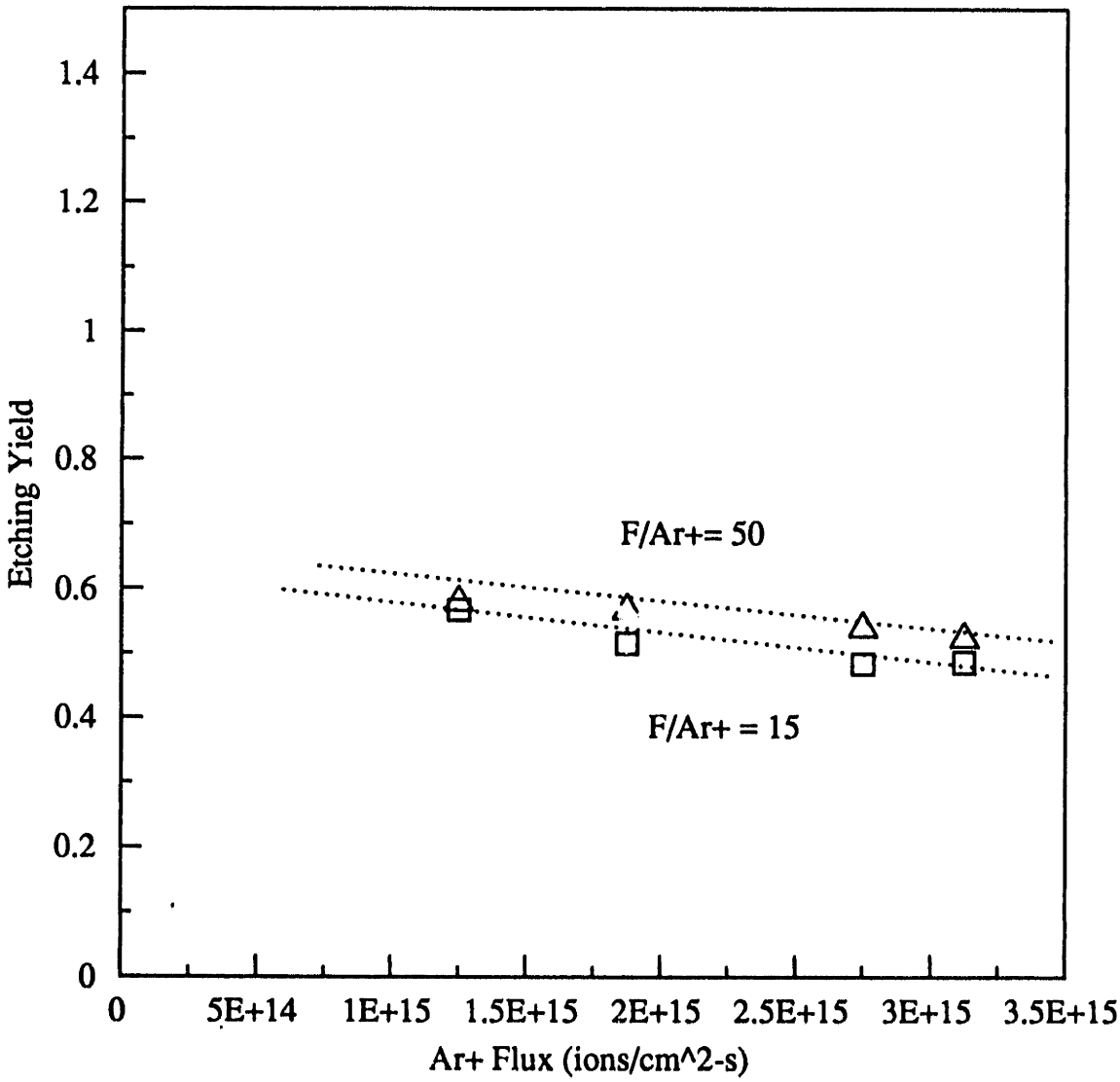

Figure 5-17. Dependence of SiO2 Ar+/F etching yield on absolute Ar+ ion flux at constant F/Ar+.

yields were measured as a function of Ar^+ flux at constant F/Ar^+. Within the accuracy of our data, SiO_2 etching yield is found to be a function only of the F/Ar^+ flux ratio in this regime, and not on the absolute Ar+ flux. Similar behavior was observed using XeF_2 as a fluorine source in both Si and SiO_2 etching.

5.4 Mass Spectrometric Studies of Product Distributions

Several sets of experiments were conducted to ascertain the nature of the etching products evolved from the silicon surface during these fluorocarbon beam simulation studies. A number of researchers have applied mass spectrometry to the study of product distributions in the spontaneous etching of silicon by atomic fluorine [Flamm et al. 1981, Vasile and Stevie, 1982, Winters and Plumb, 1991] or xenon difluoride [Vasile, 1983, Houle, 1986] and in the ion-enhanced etching of silicon by Ar^+ and XeF_2 or F [Winters and Plumb, 1991, Winters and Houle, 1983; Coburn and Winters, 1987]. The etching of silicon dioxide has been investigated in similar studies but in much less detail [Winters, 1983]. In general, these types of studies have been done in very clean UHV environments to eliminate the presence of coincidental background peaks in the product spectra and to eliminate effects of surface contaminants. Modulated beam mass spectrometry (MMS) has been universally employed as a method to discriminate line-of-sight products from those which experience wall collisions and possible recombination events, or cracking on the hot ionizer filaments. The major shortcoming of the studies to date has been the use of very low atom and ion fluxes, sometimes 2-3 orders of magnitude below those encountered in fluorocarbon plasma processes, requiring a dangerous extrapolation of the etching product information into the relevant regime. In addition, various authors have attempted the cross comparison of data taken at different ion energies, and varying neutral-ion flux ratio regimes, without recognition of the fact that product distributions are likely to change as a function of these

parameters. The goal of our mass spectrometric studies was to qualitatively demonstrate the shift in etching product distributions with F/Ar^+ ratio and ion energy, and to assimilate available quantitative data from the literature.

The details of the mass spectrometer and its differential pumping system are described in Chapter 2. The line-of-sight product stream to the ionizer is not modulated at present, however, a shudder is available for discrimination of line-of-sight products from chamber background. This technique is useful for product identification, but is non-quantitative because reaction products which interact with the mass spectrometer housing or which crack on the ionizer filaments can still be detected. In addition, the pumping speed of the various product species in the mass spectrometer housing may vary, creating ambiguity in the measurement of background levels. Accordingly, we have limited our analysis to the identification of product peaks, and the determination of trends in product distributions with changes in neutral-ion flux ratio and ion energy.

Product Distributions in Thermal Etching of Si and SiO_2 by Atomic Fluorine

It was not the intent of this thesis to study product distributions in the spontaneous etching of silicon by fluorine atoms since the product distributions and kinetics in this system have been studied in detail in the past. However, a limited amount of work was necessary for comparison of cracking patterns with and without ion bombardment. While most studies of the thermal etching system contend that SiF_4 is the major etching product, investigators have debated the importance of SiF_2 as a product, with estimates ranging from trace quantities up to 30% of the total product. Flamm and Donnelly [1981] initially implied that SiF_2 was a major silicon(100) etch product which subsequently recombined with gas phase F to produce the chemiluminescent species SiF_3^*. They based this supposition on the fact that the chemiluminescence signal and

silicon etching rate had identical activation energies. To reconcile these chemiluminescence experiments, the authors concluded that the activation energy of this process and the total etch rate could be identical only under two circumstances: (1) if the fraction of SiF_2 relative to all the etching products remained constant with temperature or (2) if the chemiluminescence and etching were associated with the same rate limiting process. Item (1) has been shown to be untrue over a wide temperature range through the recent work of Winters and Plumb [1991] which indicates that SiF_2 production is negligible at room temperature, but increases rapidly at surface temperatures above 300°C. It should be noted, however, that the investigation of Flamm and Donnelly [1981] extended only over a narrow temperature range (223-403K) where the SiF_2^+ peak growth is much less sensitive to temperature. Matsumi et al. [1986] saw a direct proportionality between SiF_2 LIF signals and etching rate in downstream CF_4 plasma etching of polysilicon, in support of item (2) above. Vanhaelemeersch et al. [1991] have also used LIF to show significant SiF_2 concentrations in the presence of Si<100> etching by F atoms, while SiF fragments were not observed. Rapid F-SiF_2 gas phase recombination rates were measured in this same study, and the authors suggested that large SiF_2 concentrations may not have been noted in some earlier studies due to rapid recombination with background fluorine. Vasile and Stevie [1982] concluded from an appearance potential study that while SiF_4 was the dominant reaction product, SiF_2 may comprise 10-30% of the total etching product stream. It must be noted that they did not consider possible contributions from higher fluorosilanes in this study. *Ab initio* calculations of Jenichen and Johansen [1988] resulted in a binding energy of only 13 kcal/mole for SiF_2 on silicon clusters, suggesting that it has a high probability of thermal desorption. Early studies of Coburn and Winters [1979] which employed XeF_2 as a fluorine source also supported SiF_4 as the predominant reaction product, with lesser amounts of SiF_x type product species hypothesized. Winters and Plumb [1991] recently contended that the presence of the SiF_2^+ peak in observed in room

temperature mass spectral studies of F-Si etching may be in large part due to the fragmentation of higher fluorosilanes such as Si_2F_6 and Si_3F_8, placing the quantitative interpretation of older data in question.

Based on all available information, it is reasonable to hypothesize that while SiF_4 is the major etch product, a certain probability exists for subsurface bond formation events to partition energy to and release unsaturated SiF_2 surface species. The branching ratio for this process may increase very slowly until surface temperatures reach 300 C, at which point the activation barrier for releasing surface SiF_2 species is apparently easily overcome through subsurface Si-F bond formation events, resulting in the rapid increase in the SiF_2/SiF_4 fraction. Based on these qualitative observations, it is reasonable to conclude that at room temperature, SiF_4 will result as the dominant etching product (>50%) with smaller amounts of SiF_2 being liberated as well as higher species such as Si_2F_6 and Si_3F_8. It is likely that the role of the higher fluorosilanes has been underestimated in the past due to the propensity of QMS type mass analyzers to discriminate against higher mass peaks as pointed out by Winters and Plumb [1991] and Houle [1986]. While it is straight forward to identify the mere existence of these various etching products, it is much more difficult to assess their relative abundances mass spectrometrically due to the overlap in the cracking patterns of the parent species, and the discrimination of quadrupoles to species mass and velocity. Nevertheless, several attempts have been made to compare cracking patterns of etch product streams to those of the parent gases SiF_4 and SiF_2. These studies have typically been done at either the standard 70 eV electron impact energy, or at 30 eV, which is near the appearance potential of SiF_2^+ or SiF^+ from the parent SiF_4 gas. Thus the 30 eV studies were thought to be a probe for the SiF_2 species. Winters and Plumb [1991] have recently shown the cracking of higher fluorosilanes may also contribute significantly to the SiF^+ and SiF_2^+ peaks at this energy, placing quantitative interpretation of mass spectral data in question.

Several studies have focused on the 70 eV cracking patterns of products in the F etching of single crystal silicon or polysilicon. The results of these types of studies are found to vary appreciably from system to system, such that it is difficult to obtain quantitative information on product distributions without continuous internal calibration of the individual mass spectrometer systems using the suspected product gases. A common technique has been to compare cracking patterns of etching products to that of SiF_4 gas, where differences in these two patterns may be assigned to "other" products. The cracking pattern of SiF_2 gas has also been utilized in this type of comparison, but the SiF and SiF_3 species have not been studied in isolation. Mass peaks which have been unambiguously identified to date in studies of fluorine-silicon etching products are indicated in Table 5-3, which list the entire spectrum of possible electron-impact fragments from mono to tri-fluorosilanes. The $Si_1F_x^+$ species have been universally observed as fragments of the etching product gases. In the modulated mass spectrometry studies, SiF_3^+ universally appears as the dominant fragment, while the fractions of SiF^+ and SiF_2^+ observed seem to vary widely. Houle [1986] recognized $Si_2F_5^+$ as a significant product fragment in this system and hypothesized that it originated from a Si_2F_6 product species. Winters and Plumb [1991] have recently suggested that Si_2F_6 can be a major etch product under certain circumstances, and have observed significant quantities of the $Si_2F_5^+$ fragment in the product spectra. They also noted that Coburn has observed $Si_3F_7^+$ and $Si_3F_8^+$, ostensibly a fragment of an Si_3F_8 etch product. The importance of these higher fluorosilanes has only recently come to light, so it is possible that other as yet unobserved fragments in this compilation may be identified. 70 eV cracking patterns of fluorine-silicon etch products measured in our studies are compared to the literature in Table 5-4. Cracking patterns measured for the parent SiF_4 gas are provided for reference in Figure 5-18. Given these cracking patterns, the real difficulty lies in assigning the electron impact fragments to their appropriate parent gas. This may be done in a qualitative sense through comparison of the product cracking

Table 5-3 Mass Peaks observed in the Si-F System (70 eV studies)

Fragment	AMU	Probable Parent(s)	Observation
SiF^+	47	SiF_2, SiF_4, Si_2F_6, Si_3F_8	yes
SiF_2^+	66	SiF_2, SiF_4, Si_2F_6, Si_3F_8	yes
SiF_3^+	85	SiF_4, Si_2F_6, Si_3F_8, (SiF_3)	yes
SiF_4^+	104	SiF_4	yes
Si_2F^+	75	Si_2F_6	no
$Si_2F_2^+$	94	Si_2F_6	no
$Si_2F_3^+$	113	Si_2F_6	no
$Si_2F_4^+$	132	Si_2F_6	Yes
$Si_2F_5^+$	151	Si_2F_6	Yes
$Si_2F_6^+$	170	Si_2F_6	no
Si_3F^+	103	Si_3F_8	no
$Si_3F_2^+$	122	Si_3F_8	no
$Si_3F_3^+$	141	Si_3F_8	no
$Si_3F_4^+$	160	Si_3F_8	no
$Si_3F_5^+$	179	Si_3F_8	no
$Si_3F_6^+$	198	Si_3F_8	no
$Si_3F_7^+$	217	Si_3F_8	Yes
$Si_3F_8^+$	236	Si_3F_8	Yes

patterns with those of the suspect product gases. Note first of all, in Table 5-4, that SiF_3^+ appears

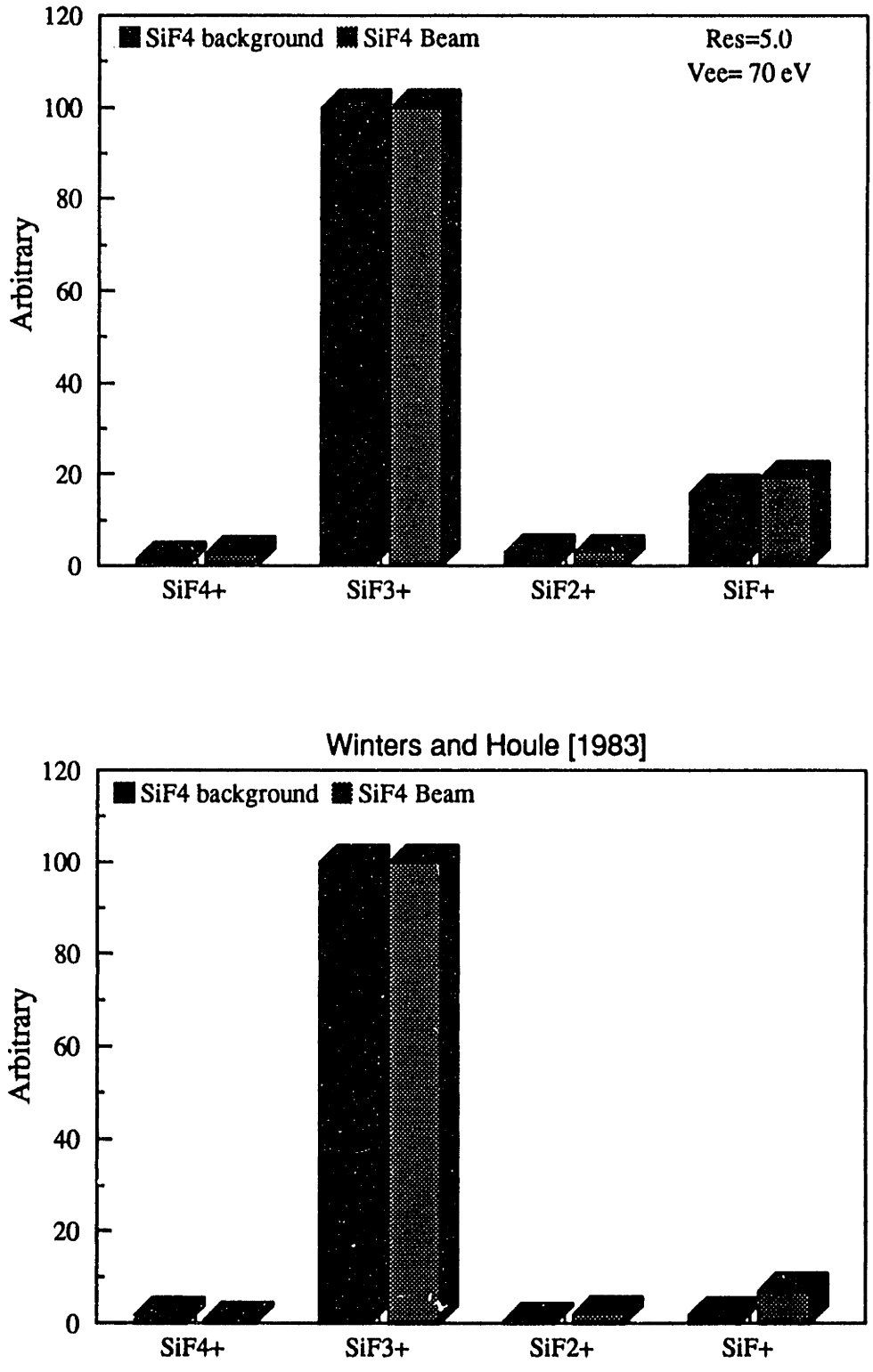

Figure 5-18. SiF_4 cracking patterns at 70 eV electron impact energy.

as the dominant fragment in each case. This finding has been interpreted

Table 5-4 Si-F System. 70 eV Product Cracking Patterns

SiF^+	SiF_2^+	SiF_3^+	SiF_4^+	$Si_2F_5^+$	Conditions
17	5	100	3	?	Vasile and Stevie [1982] polySi, 92°C, 10^{14} F, MMS
38	14	100	2.3	6.5	Winters and Plumb [1991] p-Si 111, 30°C, $2x10^{16}$ F, MMS
80	82	100	2.0	0.4	[Gray, 1992] p-Si 100, 30°C, 10^{17} F

as good evidence for SiF_4 being the dominant spontaneous etch product of atomic fluorine and silicon. However, when we look at 70 eV cracking patterns for SiF_4 in the literature (Figure 5-18), SiF^+ and SiF_2^+ fragments are found to be much less plentiful that in the product mass spectra (Figure 5-19). The amount of SiF^+ and SiF_2^+ found relative to SiF_3^+ varies widely in these studies as seen in Table 5-4, but is in each case substantially greater than that seen in the SiF_4 cracking pattern observed in the same system. This point is illustrated in Figure 5-19 where SiF_4 and etch product cracking patterns are compared in the studies of Winters and Plumb [1991] and in our system. The former study employed the modulated mass spectrometry technique to exclude all but first flight species from the product spectra. SiF^+, SiF_2^+ and $Si_2F_5^+$ are all observed in significantly greater quantities than found in the SiF_4 cracking pattern. This information leads us to conclude that products other than SiF_4 exist in appreciable quantities when silicon is etched by atomic fluorine, in agreement with other studies. Our study is different in nature in that we did not use modulated mass spectrometry. We do however, have the use of a shutter which allows us to distinguish line-of-sight product from the chamber background. We cannot, however,

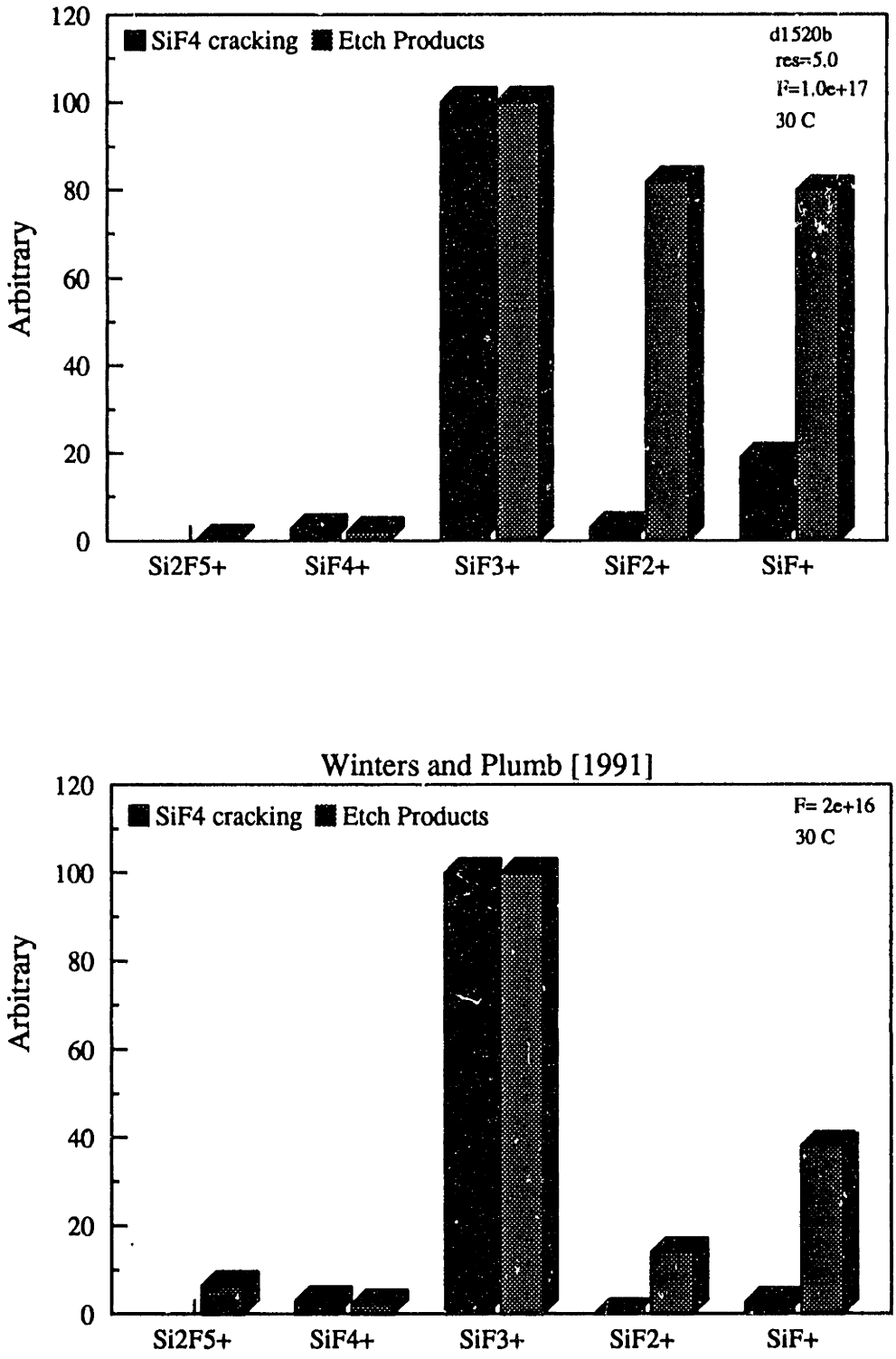

Figure 5-19. F-Si etching product cracking patterns at 70 eV electron impact energy.

exclude the detection of products which may desorb from the inner walls of the mass spectrometer housing, or products which pyrolyze on the ionizer filaments. In addition, we add small quantities of Xe to our F source which necessitates correction of the SiF_2^+(66) peak for the presence of Xe^{++}, and of the $Si_2F_5^+$(151) peak due to XeF^+. Nevertheless, the results of our studies are qualitatively similar to those of Winters and Plumb. The etching product cracking patterns shown for our study are the result of subtracting the measured background peak intensity (with the shutter closed) from the total peak intensity (shutter open) which we have referred to as the line-of-sight (LOS) signal intensity. It should be noted that in the total and background spectra, the SiF^+ peak is actually dominant in our system. We attribute this observation to the thermal cracking of SiF_4 on the ionizer filaments to produce fluorine and SiF_2, which may subsequently experience an electron impact event and appear as SiF^+ and SiF_2^+ in the SiF_4 spectra.

We have found the $Si_2F_5^+$ fragment to exist in appreciable quantities in our product spectrum. Although this peak appears in a region which is heavily populated with background peaks from our chamber, the $Si_2F_5^+$ fragment is clearly identified as originating from a line-of-sight etch product (Si_2F_6) by the degree to which it is modulated by the ionizer shutter. This is demonstrated in Figure 5-20 where the modulation in this mass peak with the shutter open and closed is shown. Winters and Plumb [1991] have recently published the 70 eV cracking patterns for the suspected products Si_2F_6 and Si_3F_8 showing the dominant fragments to be SiF^+ and SiF_2^+ in both cases. Due to the reduced sensitivity of the quadrupole instruments to higher mass fragments, these gases make large contributions at the SiF^+ and SiF_2^+ fragment positions even when the measured $Si_2F_5^+$ signal is relatively small. The magnitude of this effect is, however, to a large degree dependent on the individual QMS system employed. Winters and Plumb [1991] further show that the SiF^+ to SiF_2^+ ratios observed in their product spectra at room temperature etching are more characteristic of Si_2F_6 cracking pattern versus that of SiF_2, thus providing

a)

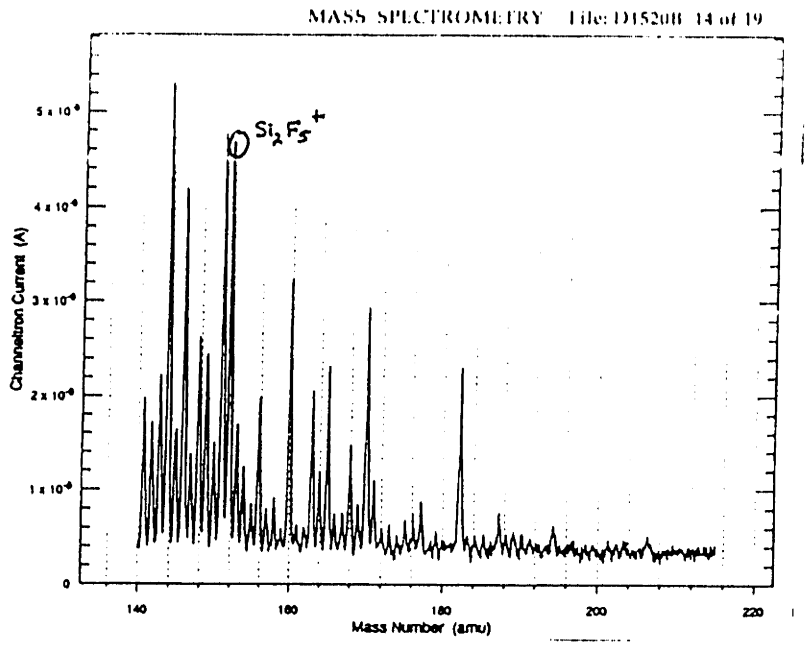

b)

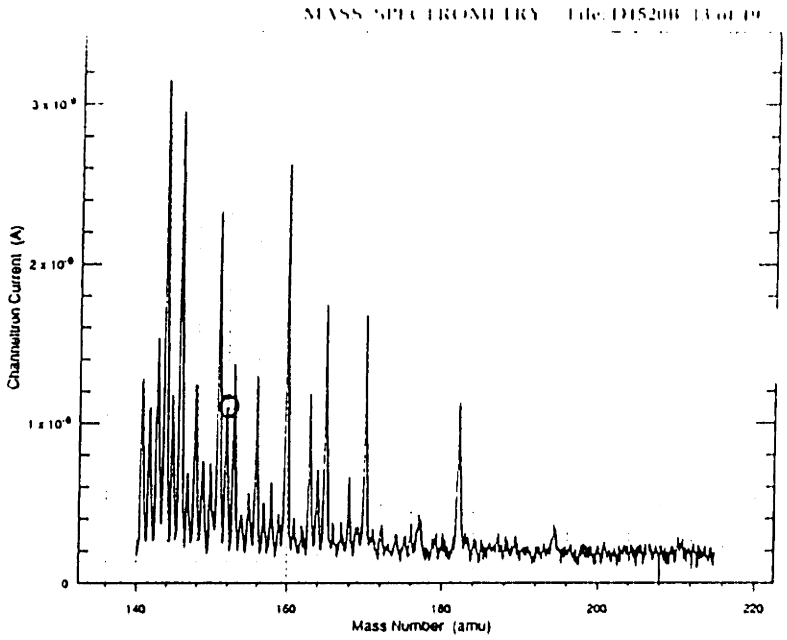

Figure 5-20. Identification of an Si2F6 product in F-Si etching via observation of the Si2F5+ peak with the line-of-sight shutter a) open and b) closed.

evidence that these peaks arise as a result of the higher fluorosilanes. Due to the large effect of SiF_4 (and Si_2F_6) pyrolysis in our unmodulated studies, we cannot confirm or refute the importance of SiF_2 at room temperature. But we must concur that Si_2F_6 is a significant etching product in this system in addition to SiF_4.

We performed additional studies on this system at 30 eV electron impact energy, which is near the appearance potential for the production of SiF^+ and SiF_2^+ from SiF_4 [Winters, 1983], but where Si_2F_6 and Si_3F_8 will also contribute to the SiF^+ and SiF_2^+ peaks. This technique may still be useful as probe for the behavior of products other that the dominant SiF_4 etch product. In Figure 5-21 we compare measured etching product cracking patterns to those of SiF_4 at 30 eV in studies by Winters and Houle [1983]. In contrast to the SiF_4 cracking patterns measured in the modulation studies where no SiF^+ is detected, our studies show an appreciable SiF^+ peak in the pattern. This observation is strong evidence for our theory that background SiF_4 is pyrolyzing to produce some SiF_2 which is subsequently detected in our mass spectra. Again in both studies, the etching product spectra show a great enhancement in the SiF^+ and SiF_2^+ peaks suggesting a significant secondary product other than SiF_4. If we accept the hypothesis of Winters and Plumb [1991] that SiF_2 production is negligible under room temperature conditions, the SiF^+ peak behavior in this system could also be associated with the Si_2F_6 product in our system. Since it is known that etching rate increases linearly with fluorine (XeF_2) flux in our experimental regime [Winters and Coburn, 1979], fragments associated with major etch products might be expected to grow linearly in intensity with F flux. This property has been exploited by Tu et al. [1981] where the SiF_3^+ peak has been calibrated and used as a probe of etch rate. We have found that while the total SiF^+ peak at 30 eV appears to grow linearly in the F atom flux, the response of the line-of-sight product may not be linear as shown in Figure 5-22. It is intriguing that any non-linearity in the peak ratios with F flux may result from a changing surface fluorination level and

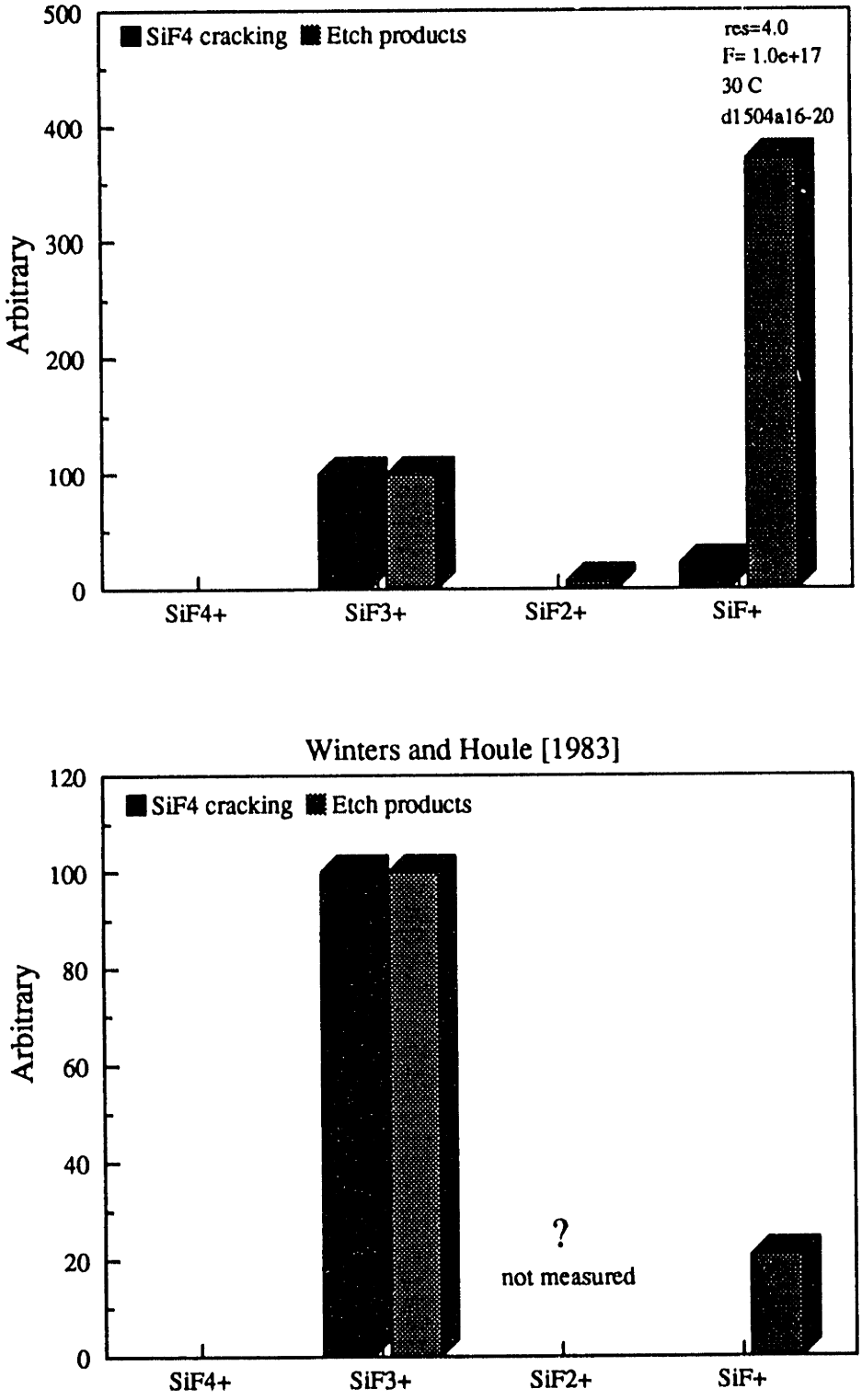

Figure 5-21. F-Si etching product cracking patterns at 30 eV electron impact energy.

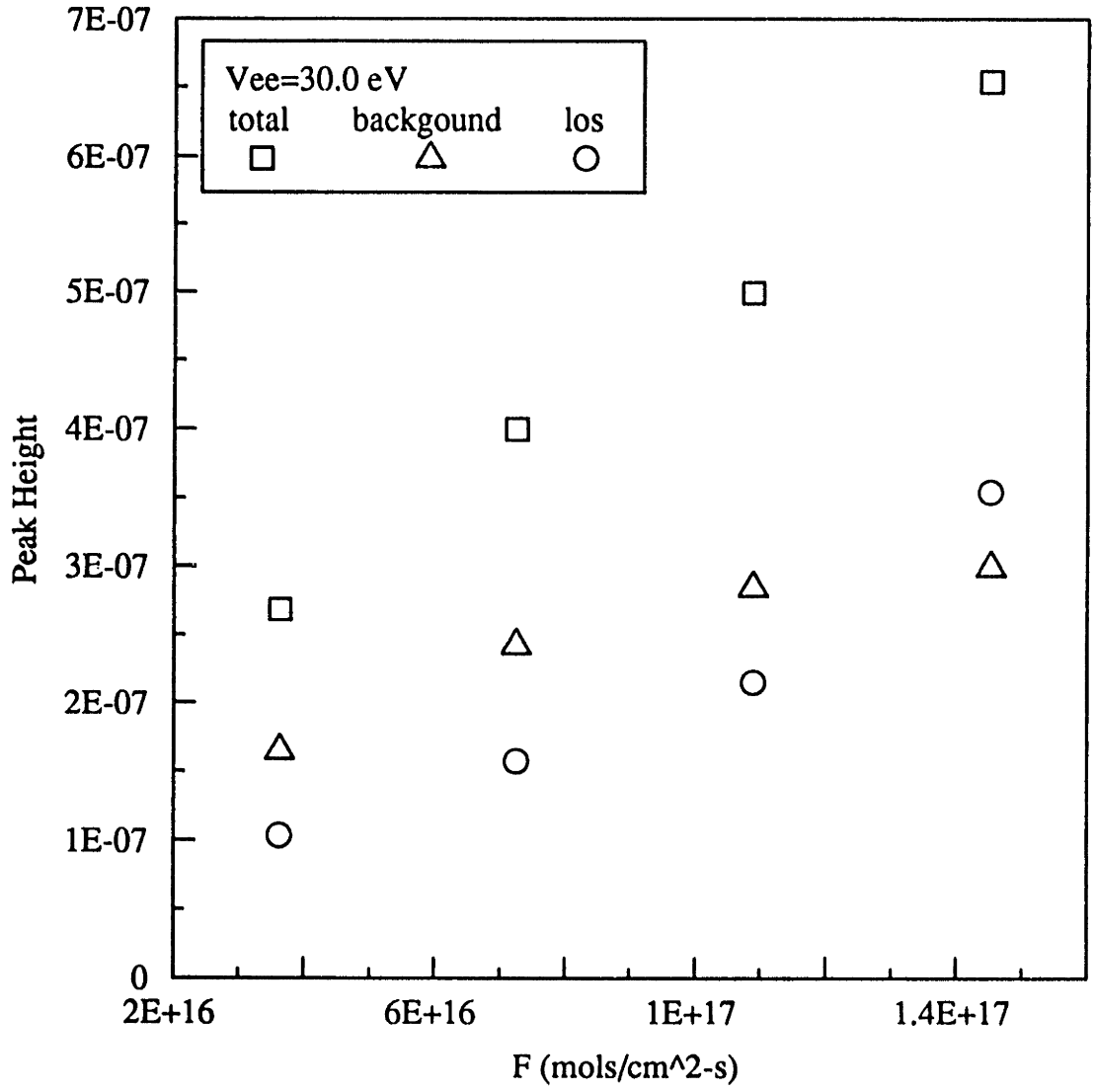

Figure 5-22. Increase in the SiF+ (AMU 47) peak versus F flux in room temperature F etching of silicon.

subsequent shift in the product distributions. To investigate this possibility, we observed the $Si_2F_5^+$ peak relative to SiF_3^+ at 70eV and as a function of F atom flux in Figure 5-23. It appears from these preliminary studies that the relative importance of the Si_2F_6 product may decrease as the surface fluorination level increases, which is intuitively plausible given that the more fluorine saturated product may be favored as more fluorine becomes available.

Much less information is available concerning the reaction product distribution in the thermal etching of SiO_2 by atomic fluorine. The reason for this is partly pragmatic, since the thermal etching rates of SiO_2 are too slow for this chemistry to have application in an industrial etching process. Mass spectral studies of this system are difficult even in the beam environment since F-SiO_2 reaction rates are an order of magnitude slower than the corresponding F-Si rates at a given temperature, resulting in very weak product signals. Such a study could be conducted given sufficiently low reactor base pressures, and the use of modulation and lock-in techniques to improve signal-to-noise. However, comprehensive study of this system was not possible with the signal-to-noise limitations in our current apparatus. Other types of studies have appeared in the literature which give important clues to the important products evolved in the F-SiO_2 etching reaction. Vanhaelemeersch et al. [1991] noted the complete absence of SiF_2 and SiF LIF signals while running a F_2/He microwave discharge in a quartz flow tube. Matzumi et al. [1986] also confirmed the absence of SiF_2 in LIF studies of SiO_2 etching in a CF_4 plasma downstream. We have, however, observed mass spectrometrically increases in chamber SiF_4 (SiF_3^+ peak) and O_2 while running an F_2/Ar discharge in quartz tubing. SiF_4 production from exposure of quartz chamber walls to atomic F has been observed by several other groups as well. These observations are in accord with the *ab initio* calculations of Jenichen and Johansen [1988], who found very large binding energies for SiF_x type fragments on oxide clusters. The lowest binding energy observed was 95 kcal/mole for SiF_3, indicating that the spontaneous release of SiF_x unsaturates

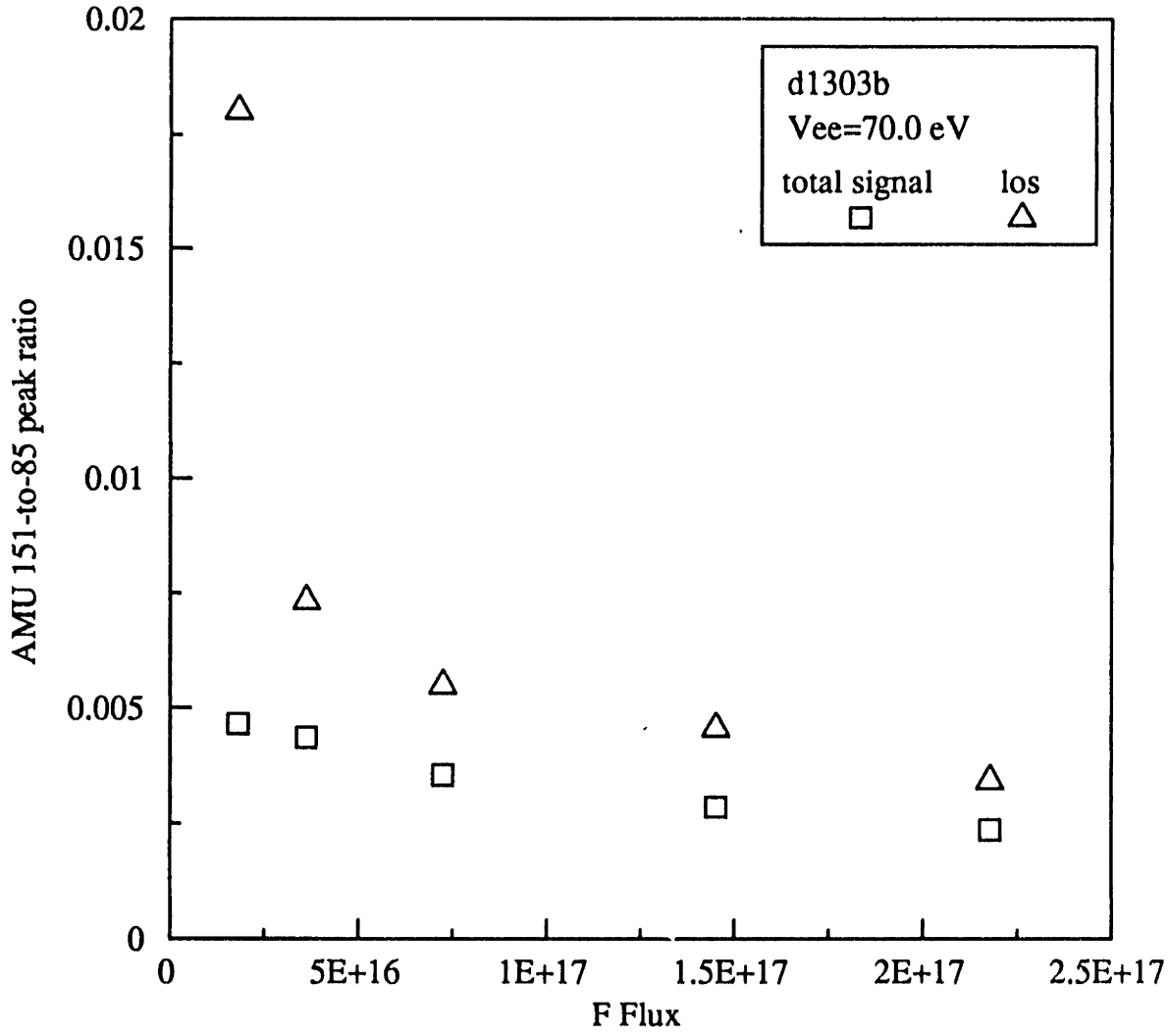

Figure 5-23. Behavior of the Si2F5+-to-SiF3+ peak ratio versus F flux in F etching of silicon.

in F etching of SiO_2 is very unlikely. Based on these observations, it is reasonable to hypothesize that SiF_4 is the major product of this reaction.

Product Distributions in the Ion-enhanced Etching of Si and SiO_2 by Atomic Fluorine

Given at least some qualitative understanding of the relative importance of the various etching products evolved in the thermal etching of silicon by fluorine atoms, we may now make comparisons to the case in which the fluorine chemistry is ion-assisted. Nearly all mass spectrometric studies of ion-enhanced fluorine chemistry have employed Ar^+ ions in the 1-3 keV energy range in addition to either XeF_2 or a discharge produced F atom source [Tu et al., 1981, Winters and Plumb, 1991, Haring et al., 1982 , Winters and Houle, 1983]. The F/Ar^+ ratios employed have varied widely making comparison across various studies difficult. Measured 70 eV and 30 eV cracking patterns of ion-enhanced fluorine silicon etch products are compared to studies in the literature in Tables 5-5 and 5-6. In general, these studies have all employed some type of modulation technique for line-of-sight product discrimination, except the data from our lab, in which background subtraction has been done through use of the shutter technique.

Table 5-5 Ar^+/F-Si System. 70 eV Product Cracking Patterns

SiF^+	SiF_2^+	SiF_3^+	SiF_4^+	$Si_2F_5^+$	Conditions
85	36	100	1.3	.11	Winters and Plumb [1991] $2x10^{16}$ F, F/Ar^+=330, 2 keV, MMS
275	250	100	63	26	[Gray, 1992] $2x10^{17}$ F, F/Ar^+=50, 250 eV

Table 5-6 Comparison of Ar^+/XeF_2-Si and SiO_2 Systems. 30eV Product Cracking Patterns

	SiF^+	SiF_2^+	SiF_3^+	SiF_4^+	Conditions
Si	120	140	100	0	Haring et al. [1982],3keV MMS
SiO_2	73	68	100	3	Oostra et al. [1986]
Si	22	23	100	2.5	Winters [1983]
SiO_2	9	14	100	0	2 keV, MMS
Si	55	43	100	?	Winters and Houle [1983] 2 keV, MMS

It is evident that results have varied widely in these studies. Haring et al. [1982] found the SiF^+ and SiF_2^+ peaks to be dominant in their system which they attributed to a large fraction of unsaturated SiF_x radicals relative to SiF_4 in the product stream. However, no observation of higher mass peaks was made in this study. In an early study, Tu et al.[1981] estimated that 75% of the silicon leaving the etching surface was in the form of SiF_4 (F/Ar+=100-1000, 500-2000 eV), while the rest was emitted as unsaturated radicals and sputtered silicon. Winters and Plumb [1991] recent work still shows the SiF_3^+ peak dominating the cracking pattern for the stream of ion-enhanced etch products, in contrast to the study of Haring et al. [1982]. One cannot ascribe too much significance to this discrepancy since the QMS is inherently a narrow band filter; its resolution may be tuned such that any number of peaks with similar intensity may dominate the spectra. It is thus more informative to examine data taken in a single system at identical instrument settings. Figure 5-24 compares measured cracking patterns for ion-enhanced etching products versus thermal products to the data of Winters and Plumb [1991]. The data of Winters and Plumb are in qualitative agreement with all other studies which show that the SiF^+ and SiF_2^+ peaks become relatively more important in the ion-enhanced system. We have found a similar trend in our system for the growth of the SiF^+ and SiF_2^+ peaks relative to the spontaneous etching

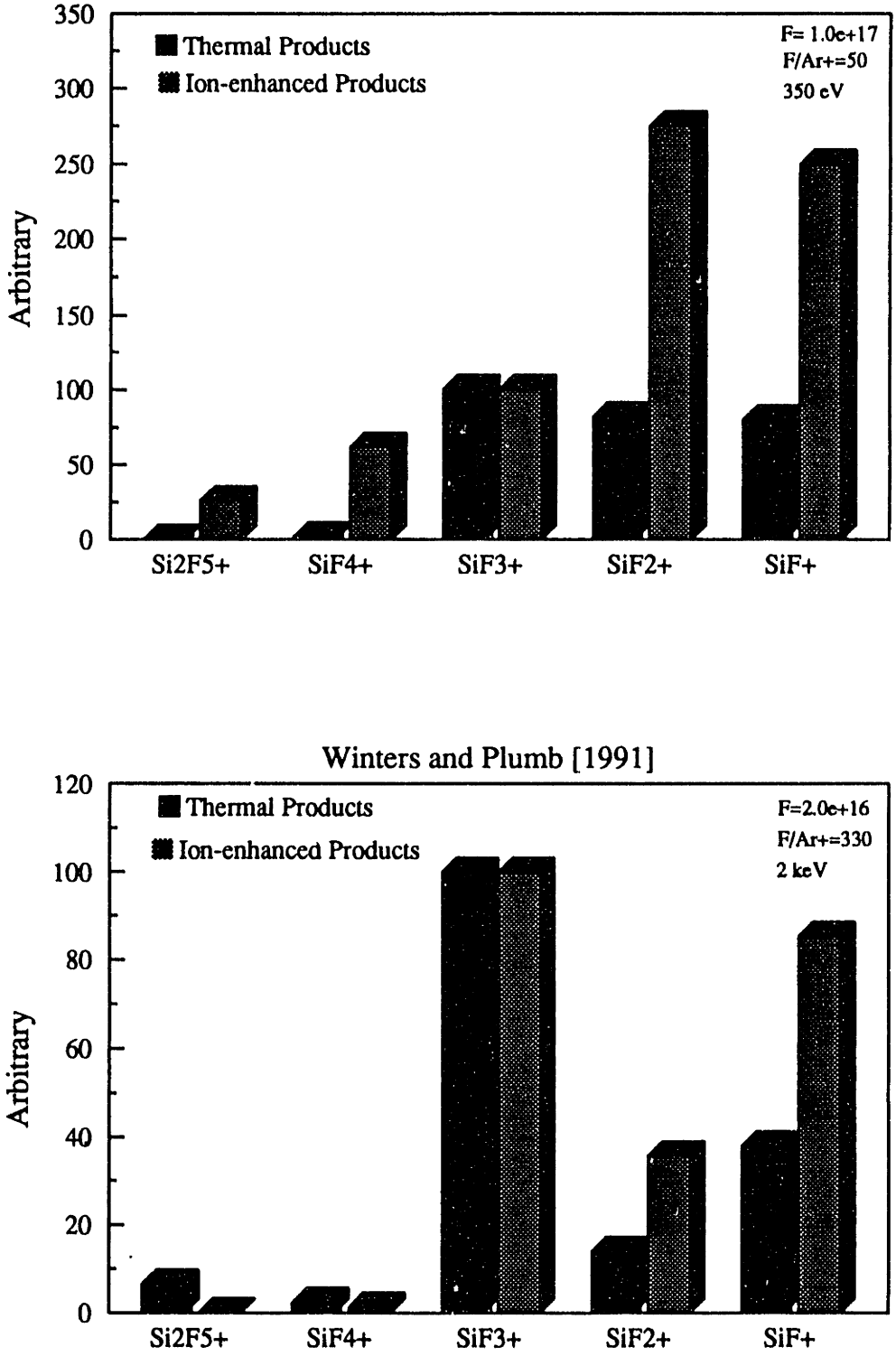

Figure 5-24. Comparison of Ar+/F-Si versus F-Si etching products at 70 eV electron impact energy.

case. The SiF^+/SiF_2^+ peak ratio again differs from that found by Winters, due to the overlap of the Xe^{++} peak and the detection of pyrolytic products. Winters and Plumb note that although the ion bombardment enhances the intensity of all product fragment peaks, the relative increase in the SiF^+ and SiF_2^+ peak may be ascribed to the chemical sputtering of SiF_2 and SiF_3, as well as an enhancement in the production of Si_2F_6.

It is interesting to note that our studies also showed a large percentage increase in the intensity of the $Si_2F_5^+$ peak as well as the SiF^+ and SiF_2^+. Mass scans in the region of the $Si_2F_5^+$ peak are provided in Figure 5-25 for comparison to Figure 5-20 to illustrate the marked effect of ion bombardment on the magnitude of this peak. Based on the cracking patterns for Si_2F_6 published by Winters and Plumb [1991], it would appear that cracking of an Si_2F_6 etching product is making a significant contribution to the increase in the SiF^+ and SiF_2^+ signals, but cannot account for the total enhancement over the case of spontaneous etching. The remainder of the enhancement is attributed without strong evidence to the presence to SiF_x radical species in the etching product stream. Similar comparisons of cracking patterns in case of thermal etching versus ion-enhanced etching have been made at the 30 eV electron impact energy in Figure 5-26. Once again the marked enhancement in the SiF_2^+ and SiF^+ fragment peaks are noted relative to the SiF_3^+ peak. Given the observation that the ion bombardment causes a marked shift in the etching product distribution in the silicon fluorine system, we felt it very likely that differing ion energies and neutral-to-ion flux ratios may also result in significant changes in the etching product mix. Increases in ion energy will change the lattice mixing depth and the fraction of cascade-induced products to thermalized etching products, while increasing the fluorine to ion flux will increase the availability of F reactant per unit energy input to the system. Winters and Plumb [1991] also note that such variables are likely to change the "surface condition" and result in shifts in favored products. To investigate the degree to which cracking patterns might change in the parameter

a)

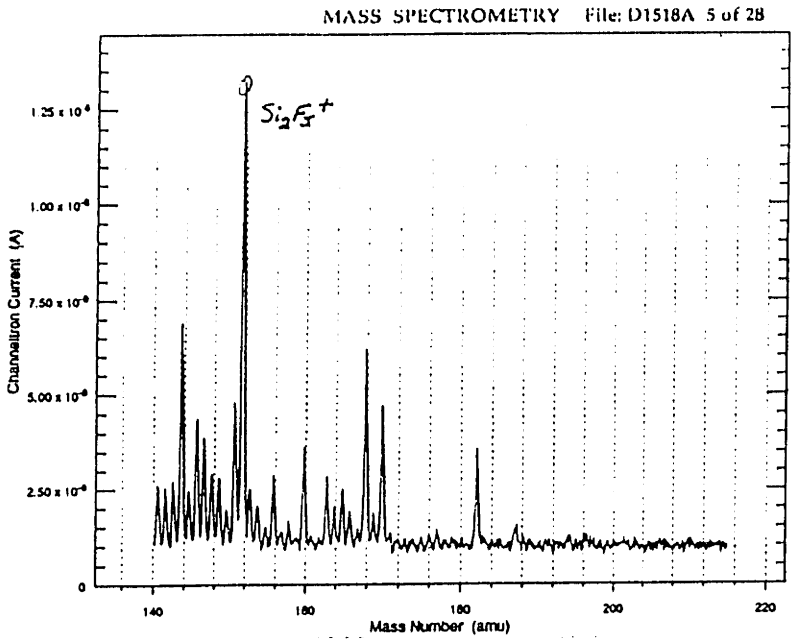

b)

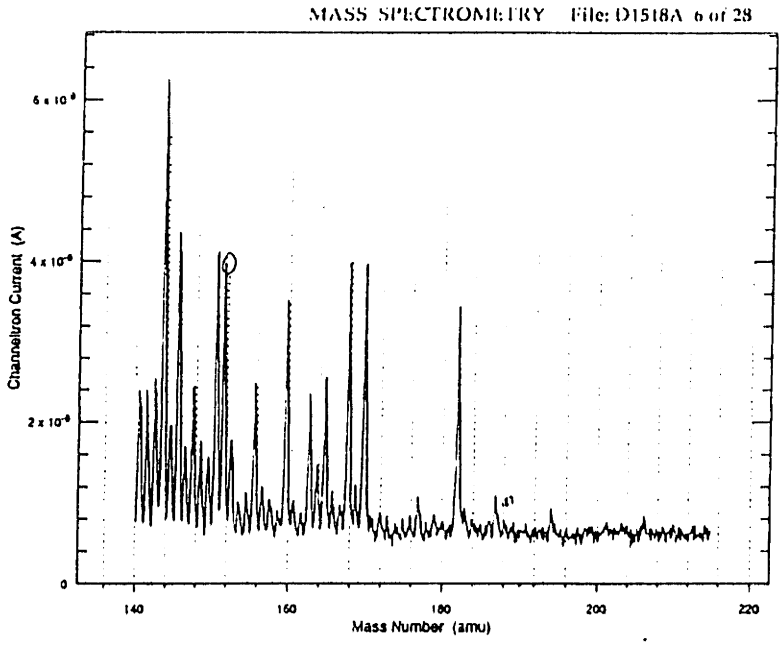

Figure 5-25. Enhancement in Si2F5+ fragment production in Ar+/F etching of silicon for a) open and b) closed shutter positions.

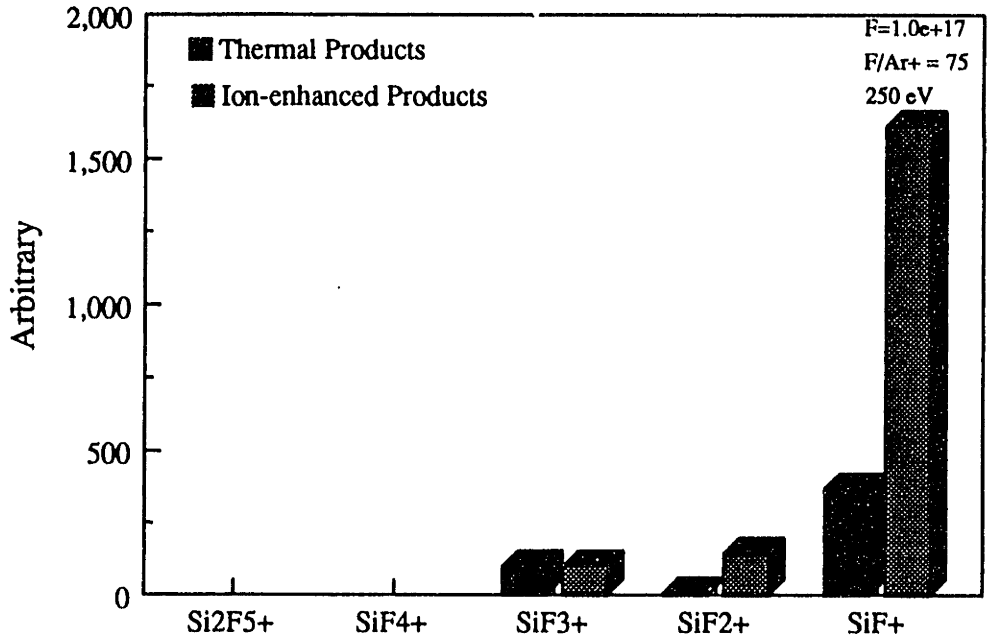

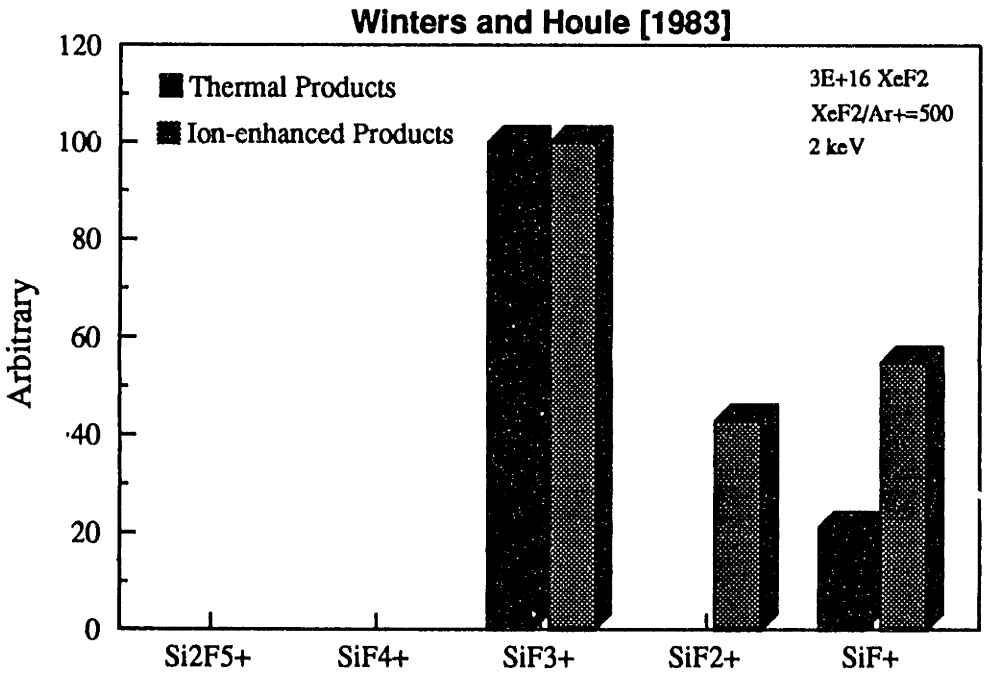

Figure 5-26. Comparison of Ar+/F-Si versus F-Si etching product cracking patterns at 30 eV electron impact energy.

space of our studies, we first looked at the effect of ion energy on 30 eV cracking patterns in the range of 150 eV to 450 eV. Over this small range of energy we noted small but measurable changes in the fraction of SiF^+ and SiF_2^+ to SiF_3^+ as shown in Figure 5-27. It is expected that SiF_2 and SiF_3 may both become more significant products as ion energy is increased, while the trend in Si_2F_6 is unknown. This trend toward increasing SiF^+/SiF_3^+ and SiF_2^+/SiF_3^+ with ion energy was also noted by Winters [1983] in studies using XeF_2 with 500eV and 2000 eV Ar+ ions. This trend in energy may also partly explain the discrepancy in the data of Haring et al. [1982] versus Winters [1983] shown in Table 5-6, since the data of Haring et al. was taken with 3keV bombarding ions versus 2 keV for Winter's study. The trend in the SiF^+/SiF_3^+ and SiF_2^+/SiF_3^+ peak ratios were also investigated as a function of F atom flux as shown in Figures 5-28. Somewhat surprisingly, these peak ratios were both found to increase with the increasing fluorination level of the surface instead of increasing the contribution of the fully saturated SiF_4 product, resulting in more SiF_3^+. We believe this trend is due to the pyrolysis of a large fraction of the SiF_4 produced, masking the trend we wish to see. In any case, these observations cannot be treated quantitatively due to the simplicity of our experiments. However, we do feel that these studies are conclusive in demonstrating changes in the product mix with ion energy and neutral-to-ion flux ratio in the region of interest to plasma etching. This observation suggests the need for a more rigorous and systematic study of these parameters on the etching product distributions, and warns us against comparison of these types of studies at differing ion energy and flux conditions.

It was necessary to attempt interpretation of the results discussed above in at least a semi-quantitative manner, to allow development of the surface kinetic models discussed in Section 5.6. We have chosen to consider only three reaction products in the Ar^+/F etching of silicon, to include sputtered Si, SiF_4 and SiF_2. In reality, SiF_2 appears to be the dominant member of the entire spectrum of SiF_x unsaturated products which arise due to ion-bombardment of the fluorinated

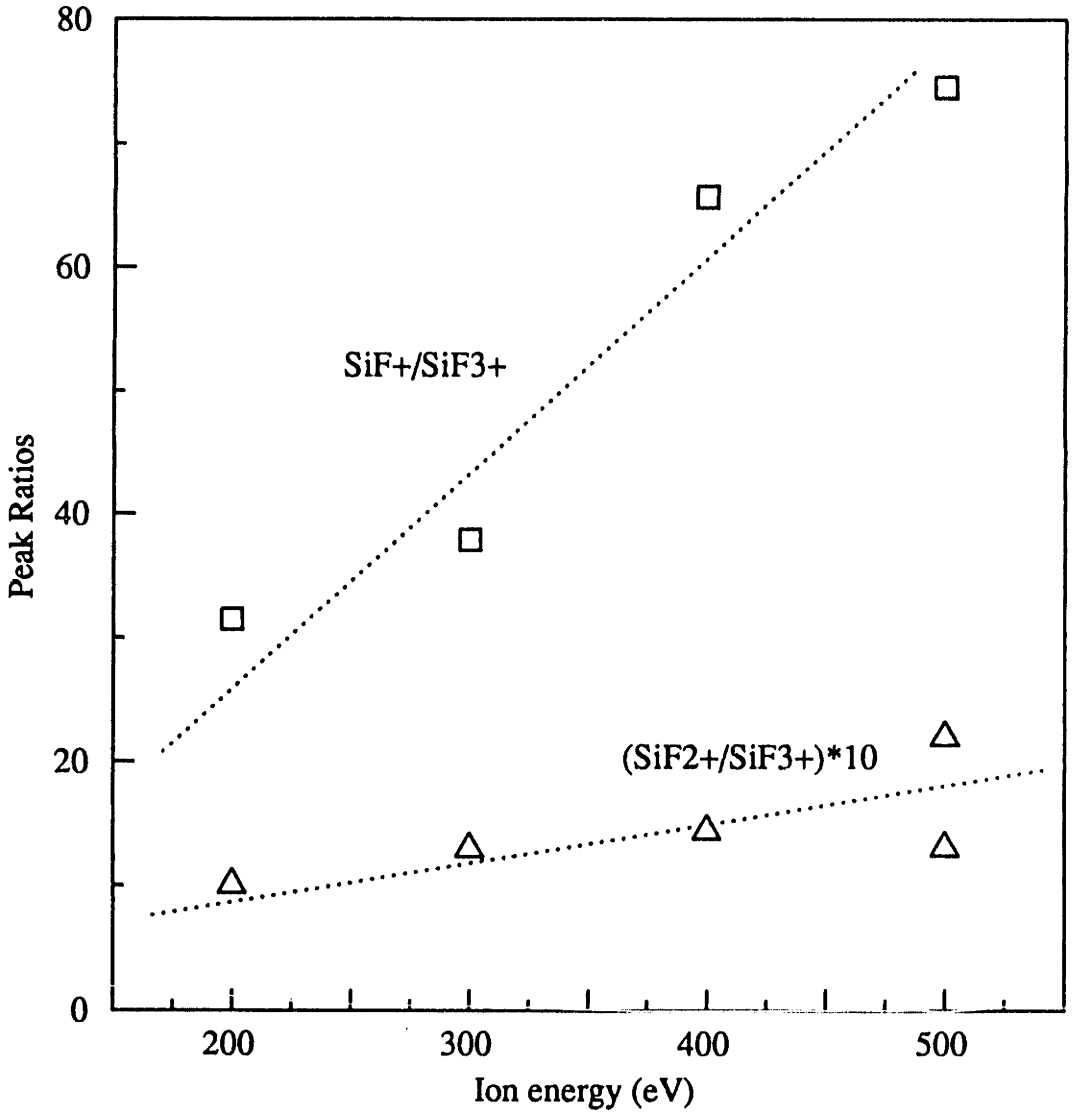

Figure 5-27. SiF+-to-SiF3+ and SiF2+-to-SiF3+ peak ratios versus ion energy in Ar+/F etching of silicon.

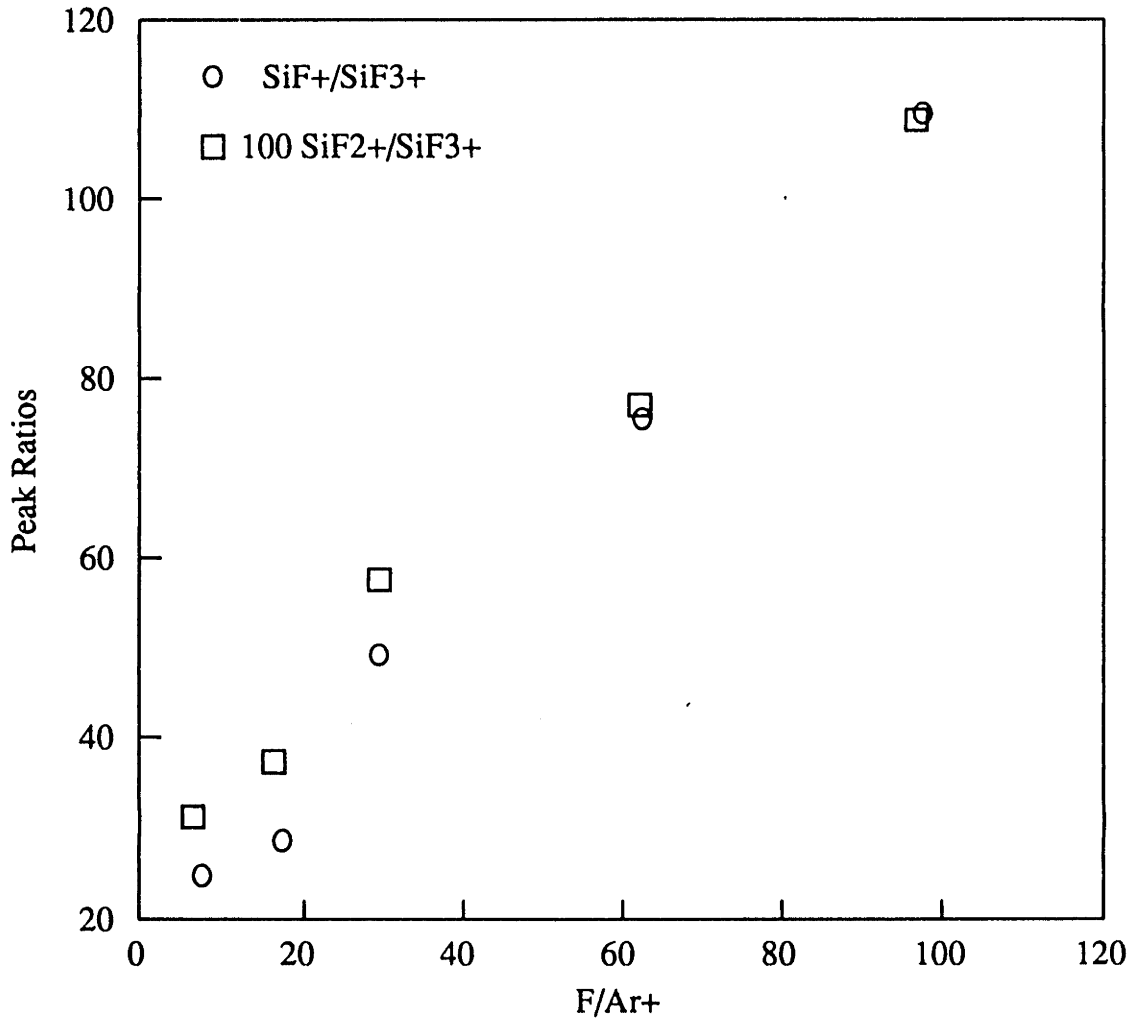

Figure 5-28. SiF+-to-SiF3+ and SiF2+-to-SiF3+ peak ratios versus F/Ar+ ratio in Ar+/F etching of silicon.

silicon surface. The feature we are most interested in quantifying is the behavior indicated in Figure 5-27, where the increase in bombardment energy increases the fraction of unsaturated SiF_x fragments liberated relative to SiF_4. We make the additional assumption that most of the SiF_2 which is liberated is the result of collision-cascades or "chemical sputtering" such that the yield production of SiF_2 scales with $(E_i)^{1/2}$ according to low energy sputtering yield model of Steinbrukel [1989]. Several of the mass spectrometric studies discussed above offered quantitative estimates of the fraction of SiF_x radicals produced relative to the fraction of SiF_4 (e.g. the branching ratio $b=\sum SiF_x/SiF_4$), which are plotted versus $(E_i)^{1/2}$ in Figure 5-29. The ratio $(SiF^+ + SiF_2+)/SiF_3^+$ measured in 30 eV mass spectrometric studies has been adopted as a semi-quantitative measurement of this branching parameter. The results of Tu [1981] show that 15-25% of silicon entering the gas phase is comprised of SiF_x radicals and Si_x sputtered species, placing the branching parameter in the range of 0.15 to 0.35. Similar results were seen at 500 eV and 2000 eV bombardment energies, with XeF_2/Ar^+ ratios in the range of 100-1000. Winters and Coburn [1985] later reported values of 0.4 for the fraction of total SiF_x^+ fragments observed relative to SiF_3^+, for saturation XeF_2 coverages ($XeF_2/Ar^+>100$) at 2 keV bombardment energy. They also demonstrated that decreasing the XeF_2/Ar^+ flux ration, increased this branching ratio and favored the production of unsaturated fragments. Winters and Houle [1983] claimed that 64-86% of the silicon product evolved in 2 keV bombardment of Si at $XeF_2/Ar^+\approx500$ is SiF_4, the remainder being SiF_x radicals, placing 'b' in the range 0.16-0.56. The study of Haring et al. [1982] reports more than twice the ratio of $\sum SiF_x^+/SiF_3^+$ (as compared to Winters et al.), where 3 keV bombardment energies were employed at XeF2/Ar+=250. These studies suggest a branching parameter in the range of 1.5-2.5, but the use of a 45° ion incidence angles probably increase the relative proportion of physically sputtered fragments by at least a factor of 2 [Mayer et al., 1981]. Making this correction, we obtain '**b**' values in the range of 0.75-1.25 which are more in accord with the

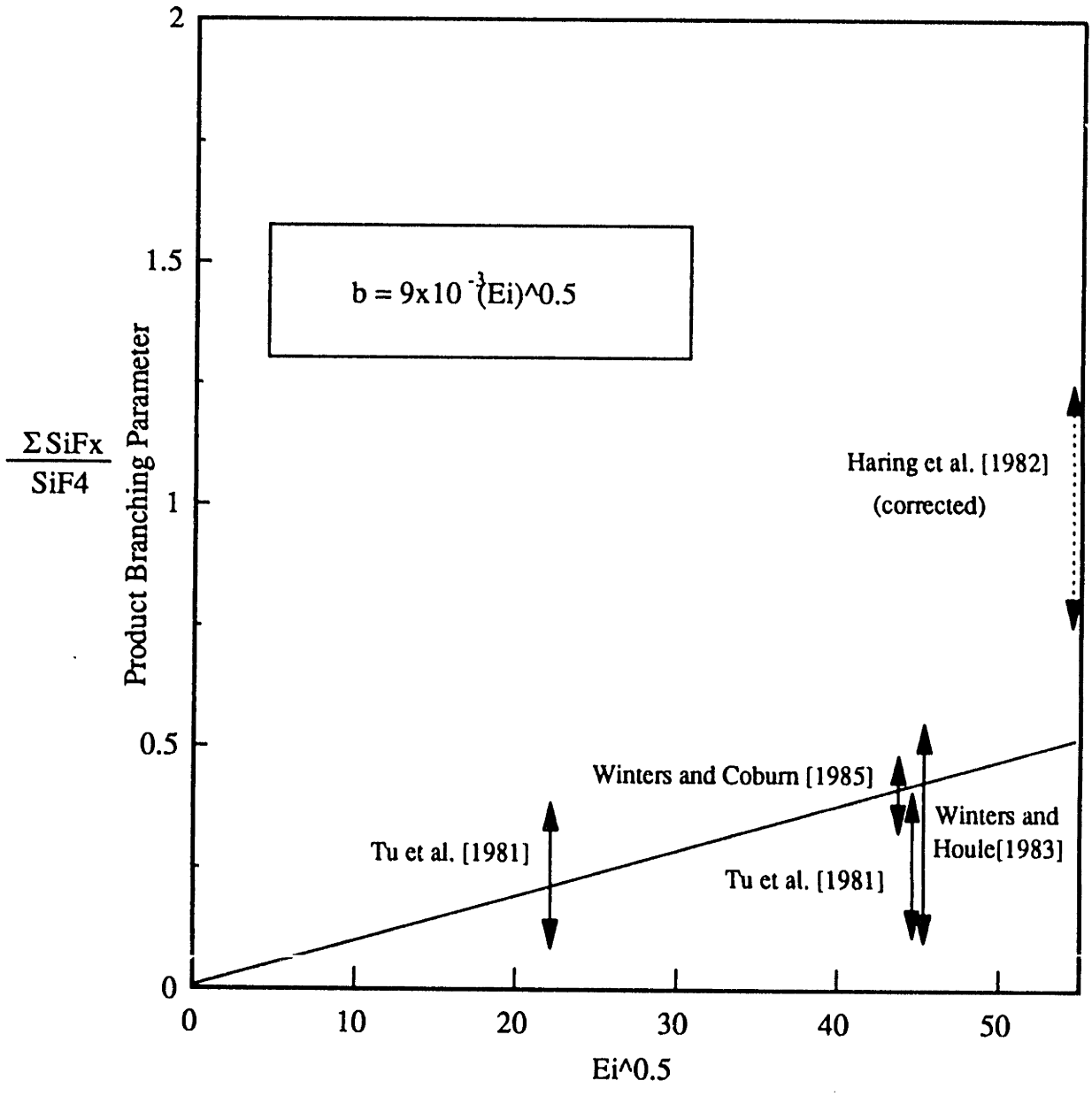

Figure 5-29. Hypothetical dependence of the product branching parameter b=ΣSiFx/SiF4 (x=1-3), versus root ion energy for Ar+/F etching of silicon. Semiquantitative results from various literature studies are shown.

other studies discussed. The uncertainties associated with these quantitative valves are quite large, but the general trend is clear, in that the relative fraction of SiF_x unsaturates to SiF_4 increases significantly with incoming ion energy. $F(XeF_2)/Ar^+$ flux ratios employed in these studies vary in the range of 100-1000, so there is some convolution of the data with fluorine surface coverage effects. The "best-fit" line shown in Figure 5-29 represents the model we have employed to describe the SiF_2/SiF_4 branching ratio as a function of ion bombardment energy (see equation 5-27).

The number of mass spectral studies of the $Ar^+/F\text{-}SiO_2$ etching product distribution have appeared in the literature is limited, once again due to the fact that signal-to-noise limitations make quantitative mass spectral studies of this system difficult. The data of Tu et al. [1981] gives the only true quantitative estimate of the fraction of Ar^+/XeF_2 SiO_2 etching products which are emitted as SiF_4 versus SiF_x fragments. Calibration of their mass spectrometer for SiF_4 allowed the researchers to estimate that 50% of the total Si which was liberated was evolved as SiF_4, using 2 keV ions over a range of XeF_2/Ar^+ ratio of approximately 100-1000. The remainder of the product spectrum was not resolved mass spectrometrically, but it was implied that most of the remaining oxide was sputtered as SiO_x fragments. Based on our etching models in which the physical sputtering component is solved self-consistently, we feel this assumption overestimated the percentage of "physical sputtering" at these conditions by at least a factor of 1.5. This places the branching ratio SiF_x/SiF_4 in the range of 0.2-0.4 for the experiments of Tu. (approximately 50% SiF_4, 30% SiO_x, 20% SiF_x). This analysis is consistent with more detailed mass spectrometric observations (30 eV) of this system reported by Winters [1983, 1988] in which SiF_4 was indicated as the dominant product, with smaller amounts of SiF_2 and SiF_1 indicated.

The studies of Winters [1983] and Oostra [1986] both indicate smaller fractions of SiF_x radicals relative to SiF_4 for Ar^+/XeF_2 etching of SiO_2 versus silicon etching at identical conditions

as summarized in Table 5-6. However, the 30 eV mass spectral studies of Oostra [1986] show much more significant quantities (a factor of 2-3x greater) than the studies of Winters, where 3kev Ar^+ ions and an F/Ar^+ ratio of 250 were employed. This difference may be attributed to the 1 keV increase in bombarding energy, and the 45° ion incidence angle employed in this work, which may enhance the proportion of physically sputtered fragments to SiF_4 by a factor of 2 or more as discussed previously. A gross quantitative interpretation could be made of Oostra's data if the relative ionization cross sections and ion extraction efficiencies of SiF_4, SiF_2, SiF and their ions were known. Vasile and Stevie [1982] have reported the relative total ionization 70 eV cross sections $Q_T(SiF_2)/Q_T(SiF_4)=0.75$ while the relative ion extraction efficiencies $\eta(SiF_2^+)/\eta(SiF_3^+)$ are related in an inverse square-root-mass manner, giving corrections of 1.13 and 1.34 for the extraction of SiF^+ and SiF_2^+ relative to SiF_3^+. These effects approximately cancel at 70 eV electron impact energy, giving a direct relationship between peak heights and the relative abundances of their SiF_x parent gases. Assuming (without support) that these corrections are also valid at a 30 eV electron impact energy, Oostra's data suggests a SiF_x/SiF_4 branching ratio in the range of 1.0 to 2.0. If we apply the possible factor of 2 correction for the ion incidence angle effect, these observations come into accord with those of Tu et al. [1981].

This information was used to construct the plot of the branching parameter $b=\sum SiF_x/SiF_4$ versus $(E_i)^{1/2}$ for the Ar^+/F etching of SiO_2 shown in Figure 5-30 (see also equation 5-28). Obviously, the error bounds on are branching parameter model are large due to a lack of quantitative data. No literature studies a lower ion bombardment energies more relevant to this thesis work are known to us, and have probably not been pursued due to signal-to-noise problems at low ion energies. This same limitation, and the non-quantitative nature of our mass spectrometric studies, precluded us from pursuing further mass spectrometric study of this system. Although mass scans during Ar^+/F etching of SiO_2 clearly showed growth of all SiF_x^+ peaks, LOS

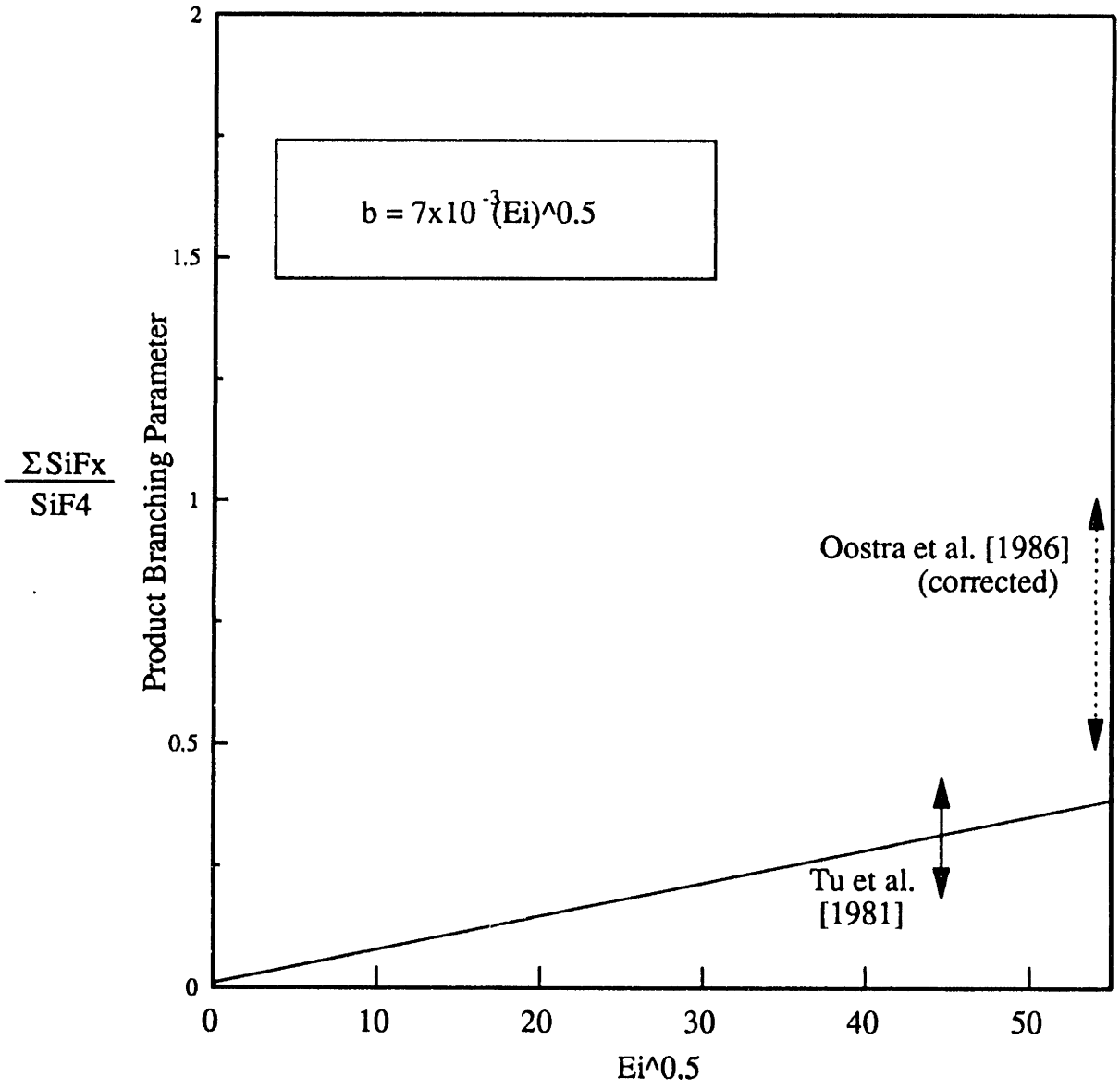

Figure 5-30. Hypothetical dependence of the product branching parameter b=ΣSiFx/SiF4 (x=1-3), versus root ion energy for Ar+/F etching of SiO2. Semiquantitative results from various literature studies are shown.

signals measured using our shutter technique are inconsistent due to large background gas levels.

5.5 XPS Studies of Ar^+/F Etched Surfaces

XPS studies of Si and SiO_2 surfaces simultaneously exposed to Ar^+ bombardment and fluxes of atomic F were performed as a function of the relative flux levels and the bombarding ion energy. A great number of XPS and Auger spectroscopic studies have been reported of fluorine [Chuang, 1980; McFeely et al., 1984; Ninomiya et al., 1984; Joyce, 1987; Brault et al., 1990] etched silicon and SiO_2. The goal of our XPS work was not to report new spectra, but to use XPS as a tool for validation of our surface kinetic models. Of primary interest was the extent to which the fluorination level of the etching surfaces represented the trends in overall etching yield. The XPS system used for these studies, as described in Chapter 2, has its electron energy analyzer at glancing incidence (~60°) with respect to the sample face normal. This feature effectively decreases the photoelectron escape depth, making the system "surface" sensitive to the top one or two monolayers. However, as discussed above, the ion-enhanced Ar^+/F etching chemistry occurs over the ion-mixing depth of 2-10 monolayers in the energy range we have explored. Therefore, spectroscopic analysis of the "surface proper" does not fully characterize the surface region (mixing-zone) over which reactions occur, especially at ion energies of several hundred eV. We have, nevertheless, used XPS to make rough quantitative estimates of the F-to-Si stoichiometric ratios during etching. Although it would be interesting to study the fluorine gradient as a function of substrate depth, the XPS system does not have depth profiling capabilities at present.

The experimental procedure used for XPS analysis of Ar^+/F etched samples was as follows. The Si or SiO_2 samples were exposed to F and Ar^+ at the desired flux and energy levels for several (~5) minutes such that several thousand angstroms of material were removed and a

steady-state surface "condition" was established. The samples were then withdrawn into the load-lock without interrupting the beam flows. Once sealed of from the multibeam chamber, the pressure in the load-lock and transfer tube dropped from the low 10^{-5} torr range to the mid 10^{-7} torr range in about 5-10 minutes. During this period the sample was exposed to a background flux of primarily molecular fluorine and argon from the beam chamber, where the oxygen and nitrogen partial pressure are on the order of 10^{-7} torr. Even at these medium vacuum partial pressures, surface impingement fluxes of oxygen are over $10^{13}/cm^{-2}\text{-}s^{-1}$, meaning that a 1L of oxygen strikes the sample face for every minute it spends in the transfer system. Depending on the relative flux conditions employed in the multibeam reactor, a substantial fraction of the etching surface may be left as $Si^{\bullet}$ dangling bonds in steady-state. Unfortunately, in the brief time the samples spend in the transfer system (5-15 minutes), these very reactive sites are oxygenated. This phenomenon, however, turned out to be a useful probe for the relative concentration of surface $Si^{\bullet}$ bonds versus $Si\text{-}F_x$ terminated surface sites. The rod transfer system was used to move the etched samples to the XPS load lock for insertion into the XPS system, where two persons were necessary to allow both manipulation of the sample insertion rod and XPS sample manipulator while viewing the sample. During a series of experiments where F/Ar^+ ratio or Ar^+ energy was incremental increased over a number of samples, time required to run XPS scans (~5 minutes each) became the rate limiting step. Typically three or four scans were completed on each sample; Si(2p), O(1s), F(1s), C(1s).

The behavior of the Si-2p XPS spectrum with increasing F/Ar^+ ratio is shown at a 150 eV Ar^+ bombardment energy in Figure 5-31. The Si-2p binding energy peak has been reported previously on clean silicon in the vicinity of 99 eV [Chuang, 1980]. In contrast, complete oxidation of the surface silicon to $Si\text{-}O_2$ is found to increased the Si-2p surface binding energy by about 4 eV [Feldman and Mayer, 1986]. The bottom most spectra shown in Figure 5-31 is

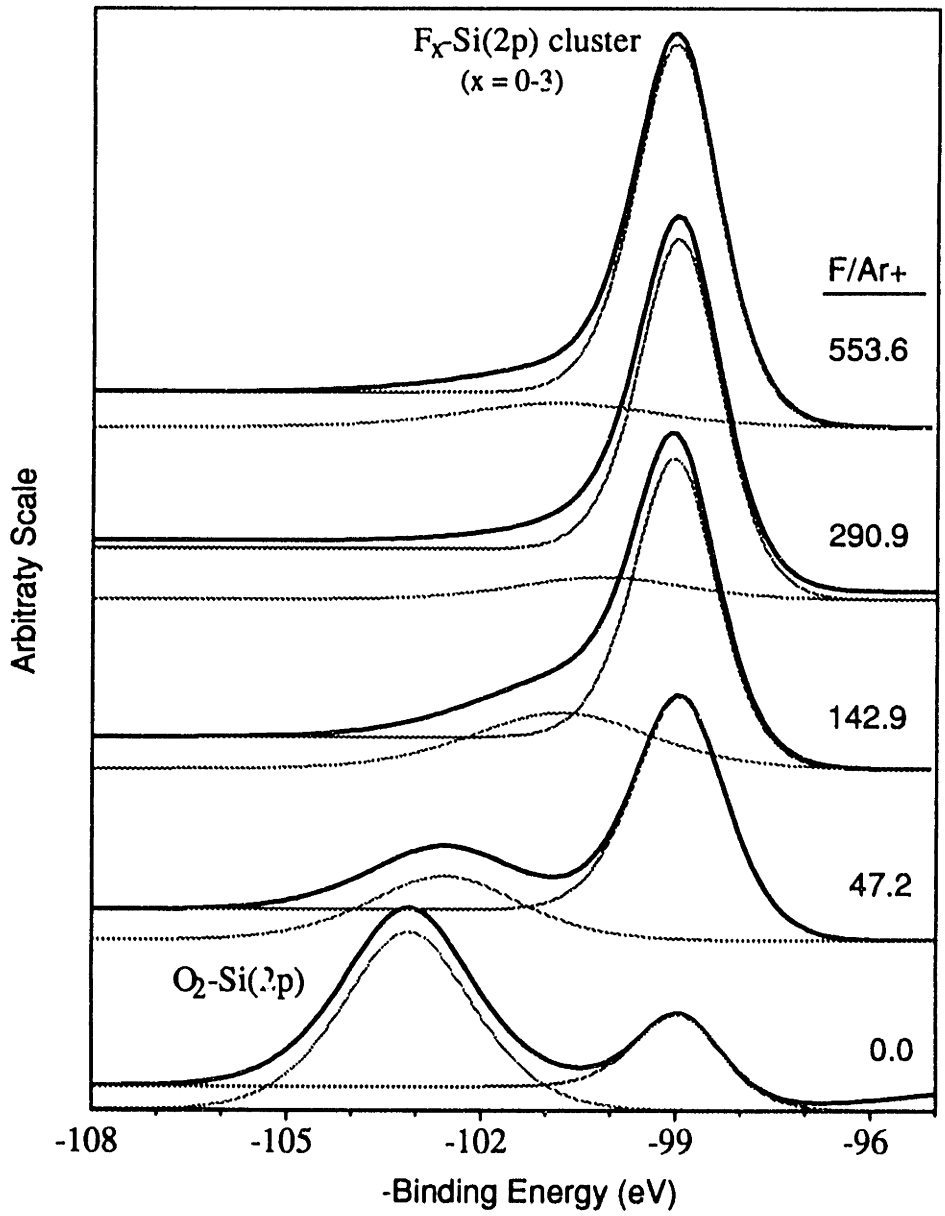

Figure 5-31. Behavior of the Si(2p) XPS peak versus F/Ar+ ratio in 150 eV Ar+/F etching of silicon.

for Ar^+ sputtered silicon with only slight residual fluorine present in the multibeam chamber. A large proportion of the ion-bombarded surface was found to be oxidized upon transfer to the XPS system, due to oxygen exposure of the "sticky" damaged surface in the transfer system. McFeely et al. [1984] performed synchrotron photoemission studies of fluorine exposed surfaces and reported approximately 1 eV chemical shift in Si-2p binding energy per bound fluorine, and was able to resolve the various SiF_x (x=1-3) surface populations. Due to the necessity of high throughput in the XPS system for our studies, electron energy resolution was limited to approximately 2 eV, such that the various SiF_x spectra could not be resolved but appeared as an SiF_x cluster with a high binding energy tail. The increase in the SiF_x cluster signal with increasing F/Ar^+ is evident in Figure 5-31, where the $Si-O_2$ bonded silicon signal is found to decrease proportionately. As the F/Ar^+ flux ratio increases, less Si^* dangling bonds are present on the etching surface in steady-state, such that less oxide is formed in the transfer tube. The $Si-F_x$ bonded silicon is very stable and the fluorine essentially "passivates" these sites so that no oxygen exchange is observed in transfer. At the highest F/Ar^+ ratios, no surface oxide is formed indicating that all available Si^* bonds are fluorinated in steady-state. Although a broad SiF_x feature is observed at high fluxes, the FWHM indicates that most of the surface is terminated in Si-F or $Si-F_2$ species, since the presence of large amounts of SiF_3 would be resolvable in our system.

The increase in the surface F-1s and $Si-F_x$ (2p) XPS peak intensities are plotted versus flux ratio in Figure 5-32 where the fluorine coverage seems to have a Langmuir type form. The corresponding decrease in the O-1s signal, and the $Si-O_2$ (2p) silicon are shown in Figure 5-33. A similar study was conducted at a 500 eV bombardment energy to investigate whether the fluorine surface saturation was a strong function of the ion energy. The F(1s) signal intensity as a function of F/Ar^+ at 150 eV and 500 eV are compared in Figure 5-34, where solid lines

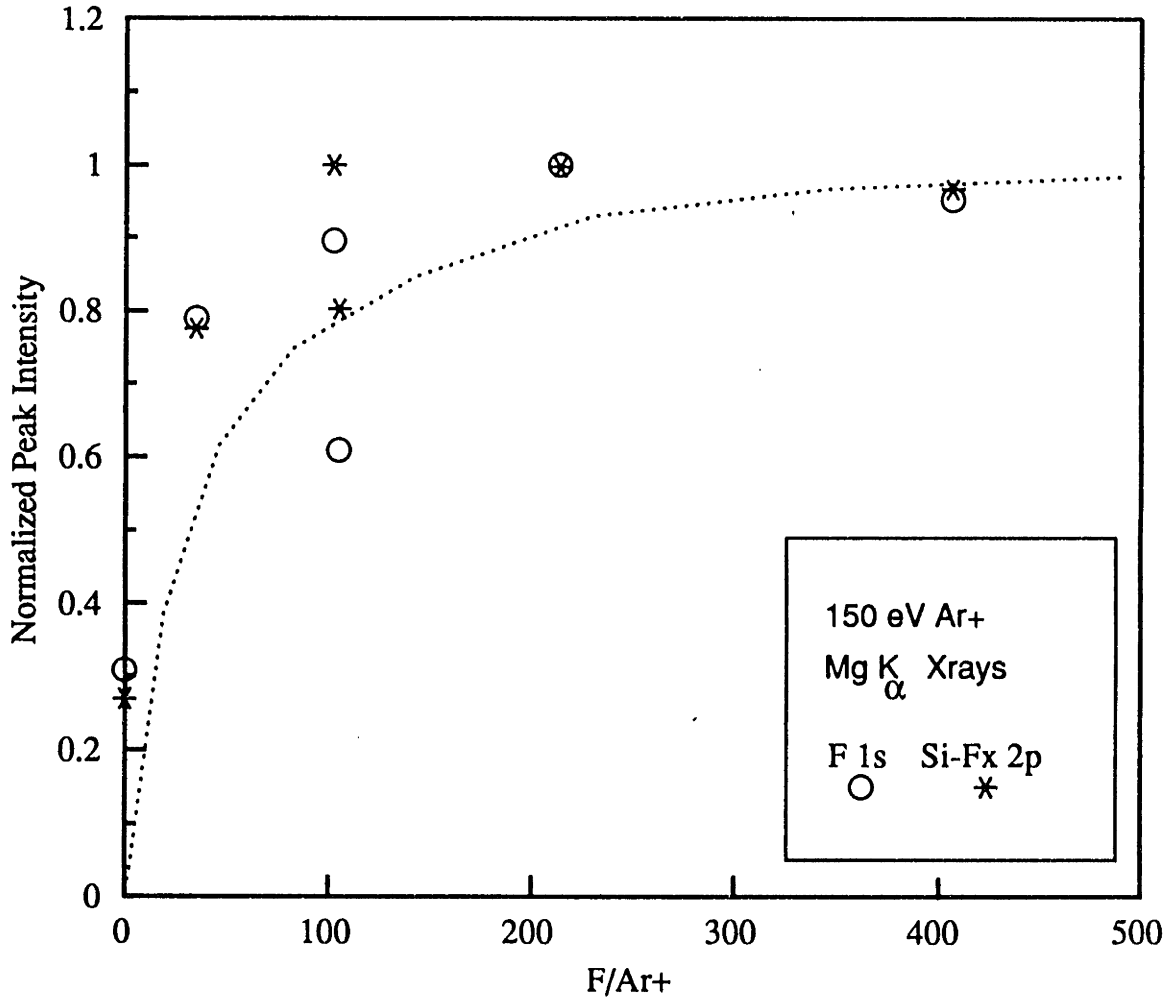

Figure 5-32. Behavior of the F(1s) XPS peak versus F/Ar+ ratio in the 150 eV Ar+/F etching of silicon. Peak areas are corrected and normalized by total Si(2p) intensity.

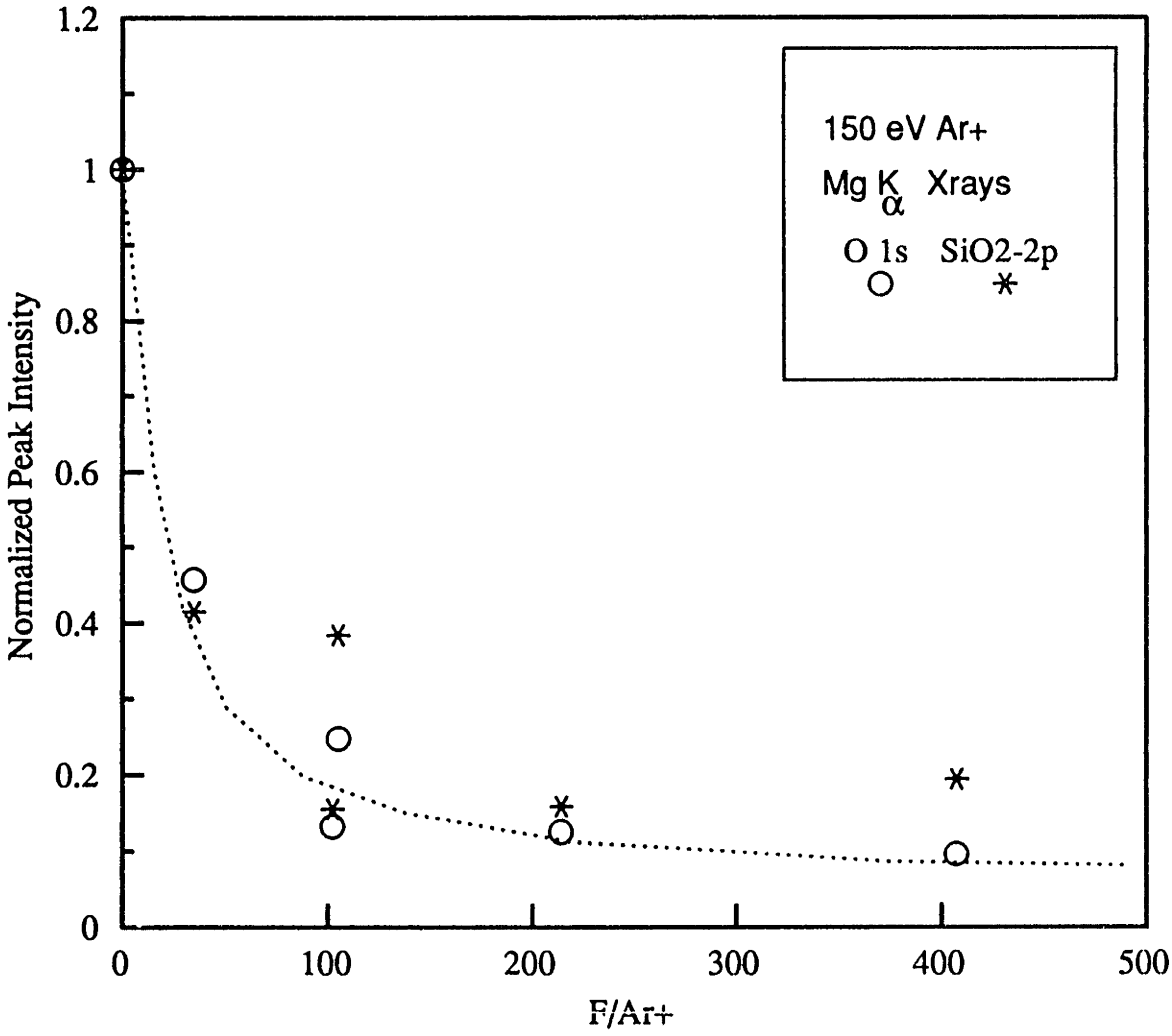

Figure 5-33. Behavior of the O(1s) XPS peak versus F/Ar+ ratio in the 150 eV Ar+/F etching of silicon. Peak areas are corrected and normalized by total Si(2p) intensity.

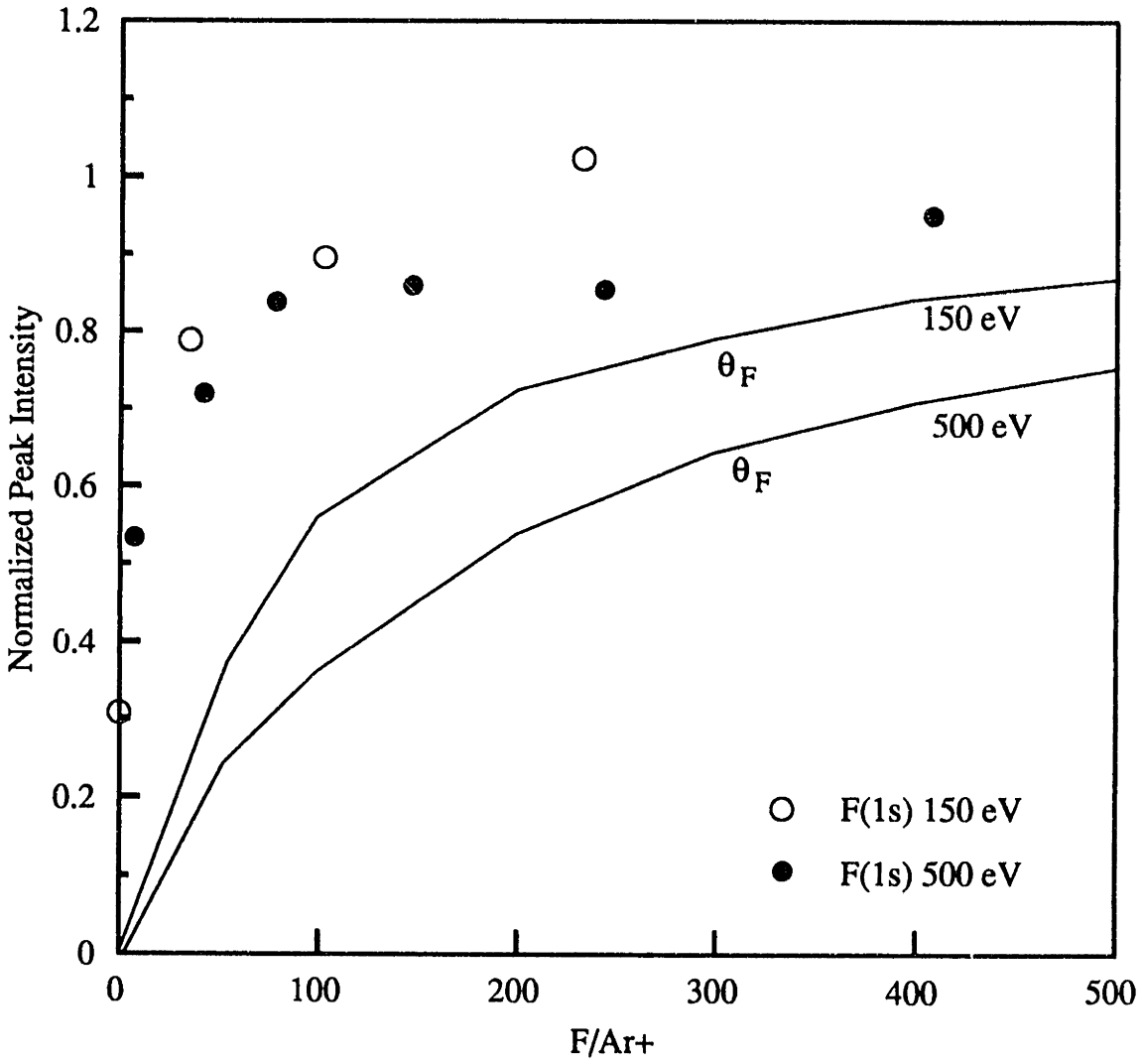

Figure 5-34. Comparison of the F(1s) peak growth versus F/Ar+ ratio at 150 eV and 500 eV ion bombardment energy. Solid lines represent model predictions for near-surface fluorination.

represent predictions of surface kinetic models. Within the error bars on these data, it is very difficult to conclude that increase of the bombarding ion energy results in lower steady-state surface fluorine coverage. The same conclusion may be drawn from Figure 5-35 where F-1s intensity at constant F/Ar^+ ratios of 150 and 850 is shown as a function of ion energy, and solid lines represent model predictions. It appears that the effect of increasing ion bombardment energy may be manifested more in the fluorine incorporation profile as a function of depth, rather than on the "surface proper" where the production of Si^* may not increase significantly in this energy range. Presence of residual fluorine in the system after etching may also wash out the expected surface coverage changes, and a true *in situ* measurement may be required to resolve these trends. The F-to-Si elemental ratio is shown at the 150 eV and 500 eV ion bombardment energy in Figure 5-36, where comparison is made to a silicon surface exposed to F only. These data have been corrected for the variation in photoelectric cross section and electron escape depth, and peaks intensities have been normalized by the total silicon (2p) signal. Figure 5-36 demonstrates nicely the change in the surface "condition" with increasing F/Ar^+. It is also evident that over the range investigated here, the assumption of an SiF_2 surface stoichiometry made in our surface kinetic model is supported by XPS data. Chuang [1980] noted the presence of "SiF_2-like" surface stoichiometry in the XeF_2 exposure of silicon. McFeely et al. [1984] found the SiF_1 state dominant in low exposure studies, but others have shown that very large F exposures result in an "SiF_3-like" surface. This general trend is expected and supported by our data. Very large F-to-Si ratios were found on the F-only exposed surfaces, which may be indicative of the presence of large amounts of unbound interstitial fluorine.

A similar set of studies was carried out in the Ar^+/F etching of SiO_2, where it was expected that surface fluorine coverage would saturate at lower F/Ar+ based on the comparison of SiO_2 versus Si etching yield data. Figure 5-37 shows the increase in the F-1s XPS signal

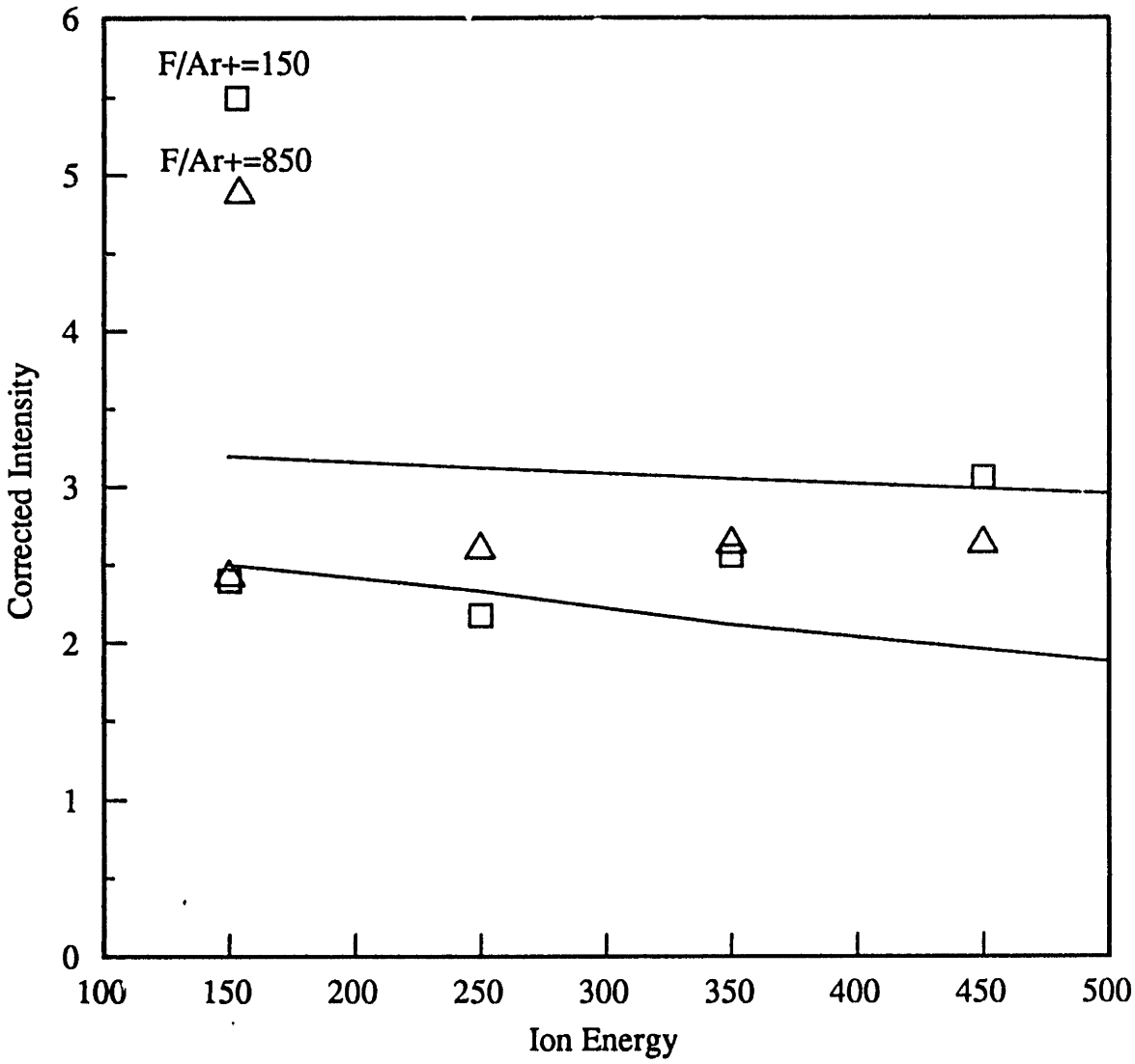

Figure 5-35. Behavior of the F(1s) peak versus ion energy at constant F/Ar+ for Ar+/F etching of silicon. Solid lines represent predictions of models.

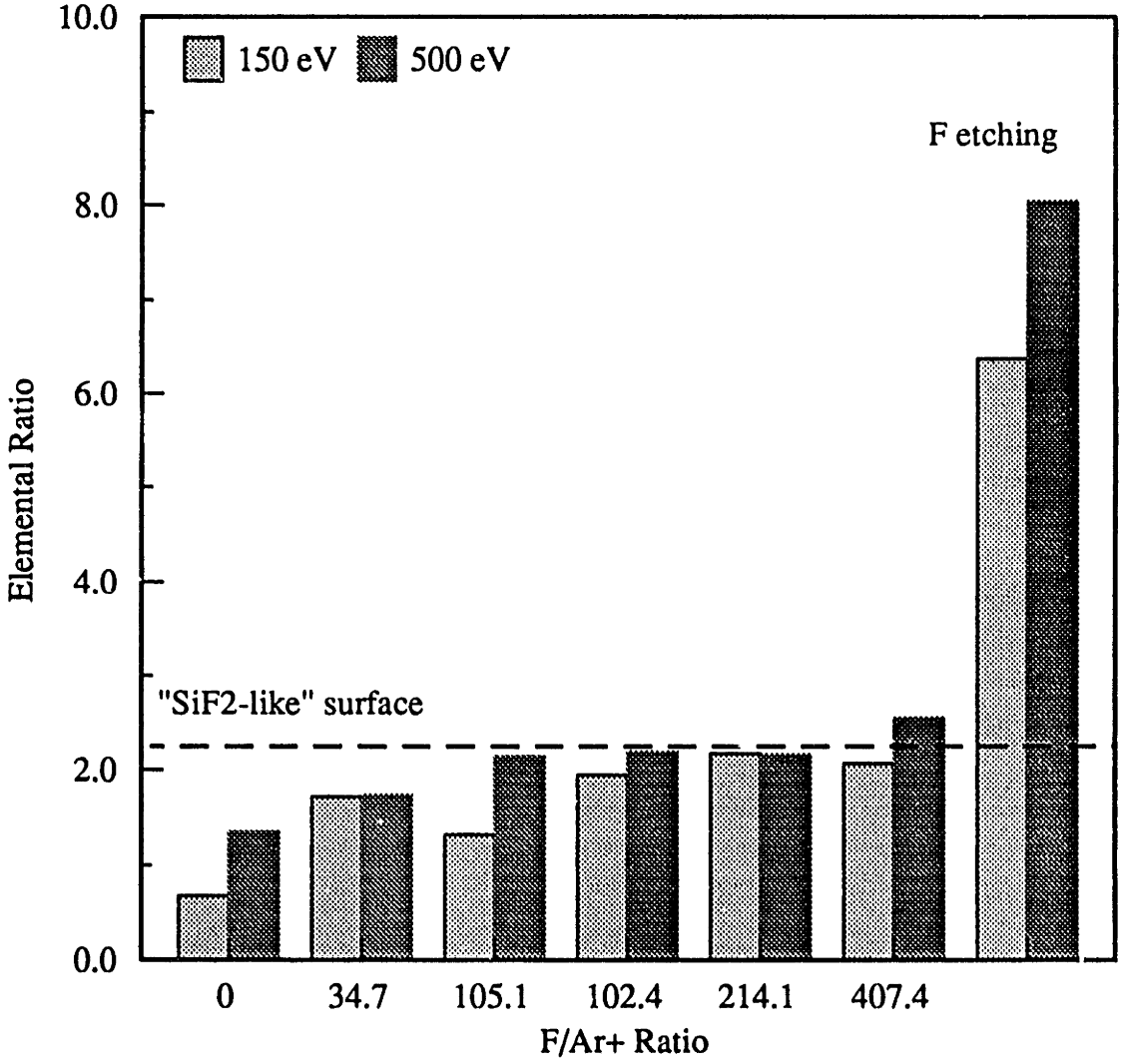

Figure 5-36. F(1s)-to-Si(2p) elemental ratios from corrected XPS data for Ar+/F etched silicon at 150 eV and 500 eV bombardment energies.

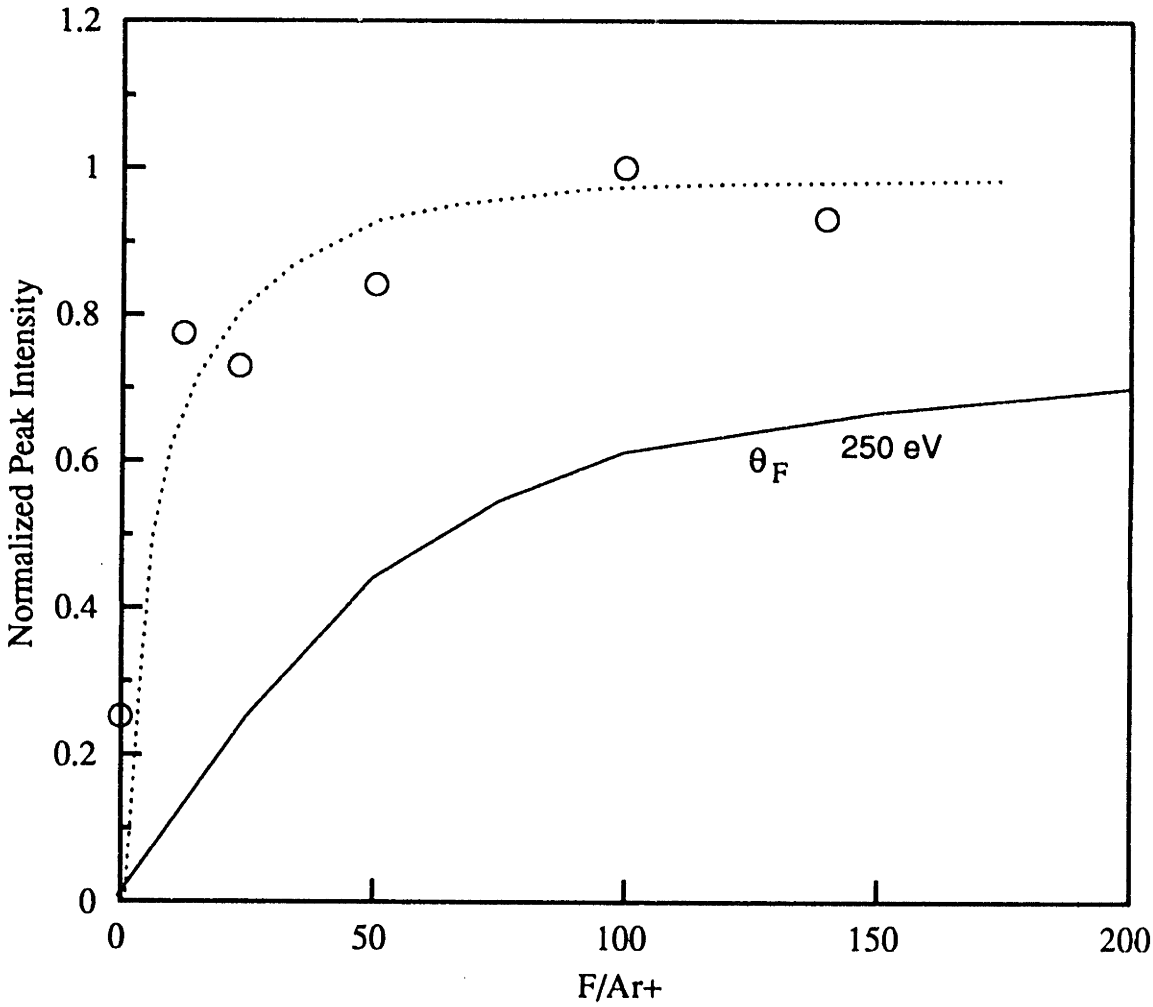

Figure 5-37. Behavior of the F(1s) XPS peak versus F/Ar+ ratio in the 250 eV etching of SiO2. Solid line represents model predictions.

versus F/Ar^+ at a 250 eV bombardment energy, where it is evident that the surface is fluorine saturated a very low F/Ar^+. It is assumed in our surface kinetic modeling that fluorine is exclusively Si-F bonded on the oxide surface. The presence of this bond appears as a low energy tail in the Si-O_2 (2p) feature as shown in Figure 5-38. A tail toward the low binding energy side of the O-1s feature was also observed which may indicate some O-F bonding. These trends were also noted by Joyce [1987] in an XPS system with much better energy resolution. The F-to-Si elemental ratio on the SiO_2 etched surfaces is investigated in Figure 5-39, where the trend of increasing F-to-Si with F/Ar^+ is observed, similar to the case of silicon etching. However, the SiO_2 surface stoichiometry might suggest a more "SiF_3-like" surface, except that we have not accounted for the presence of oxygen-bound fluorine in this analysis. We know of no studies where the relative population of SiF_x and O-F_x states on the oxide surface has been resolved to allow comparison. Finally, the effect of ion bombardment energy in Ar^+/F etching of SiO_2 at constant F/Ar^+ is investigated in Figure 5-40. A slight trend toward increasing surface fluorine with increasing energy is noted, and may be a result of the net increase in the ratio of surface Si^* to oxygen sites with the selective sputtering of oxygen. The effect of bombardment energy on O (1s) supports this contention. The dominant effect may therefore be the increased "stickiness" of the SiO_2 surface with increasing bombardment energy as noted in the etching yield studies, resulting in the surface F increase.

5.6 "Site" Models of Ion-Enhanced Etching

As discussed in Chapter 1, comprehensive models of the ion-enhanced surface kinetics described above would require complete knowledge of product distributions, species concentrations and spacial gradients in the "near-surface" region, and radical sticking coefficients in the presence of energetic ion bombardment. All of these issues have been discussed above to some degree,

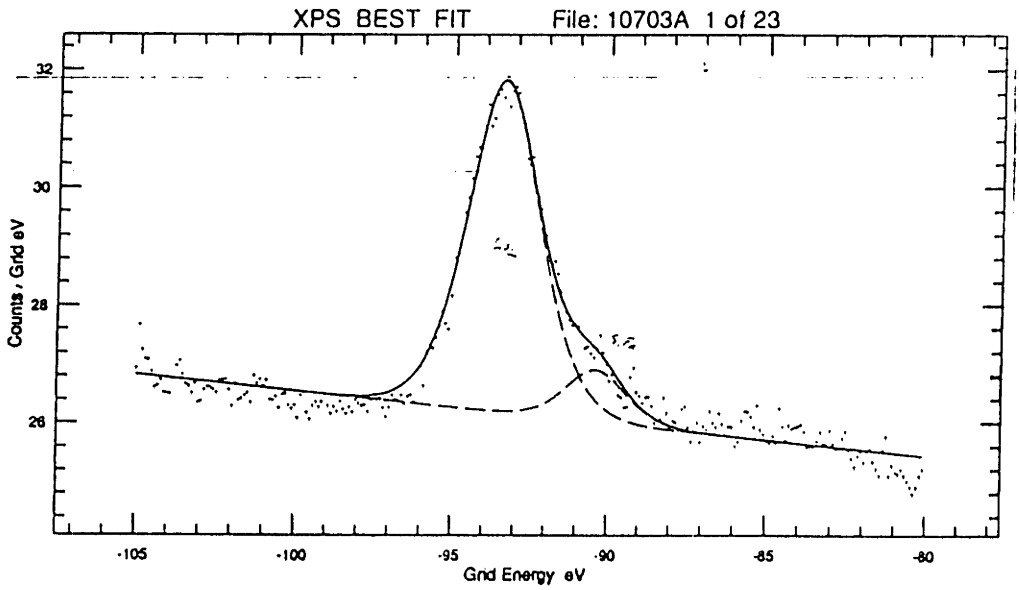

Figure 5-38. Si(2p) XPS spectra for Ar+/F etched SiO2 showing low binding energy tail due to Si-Fx bonding.

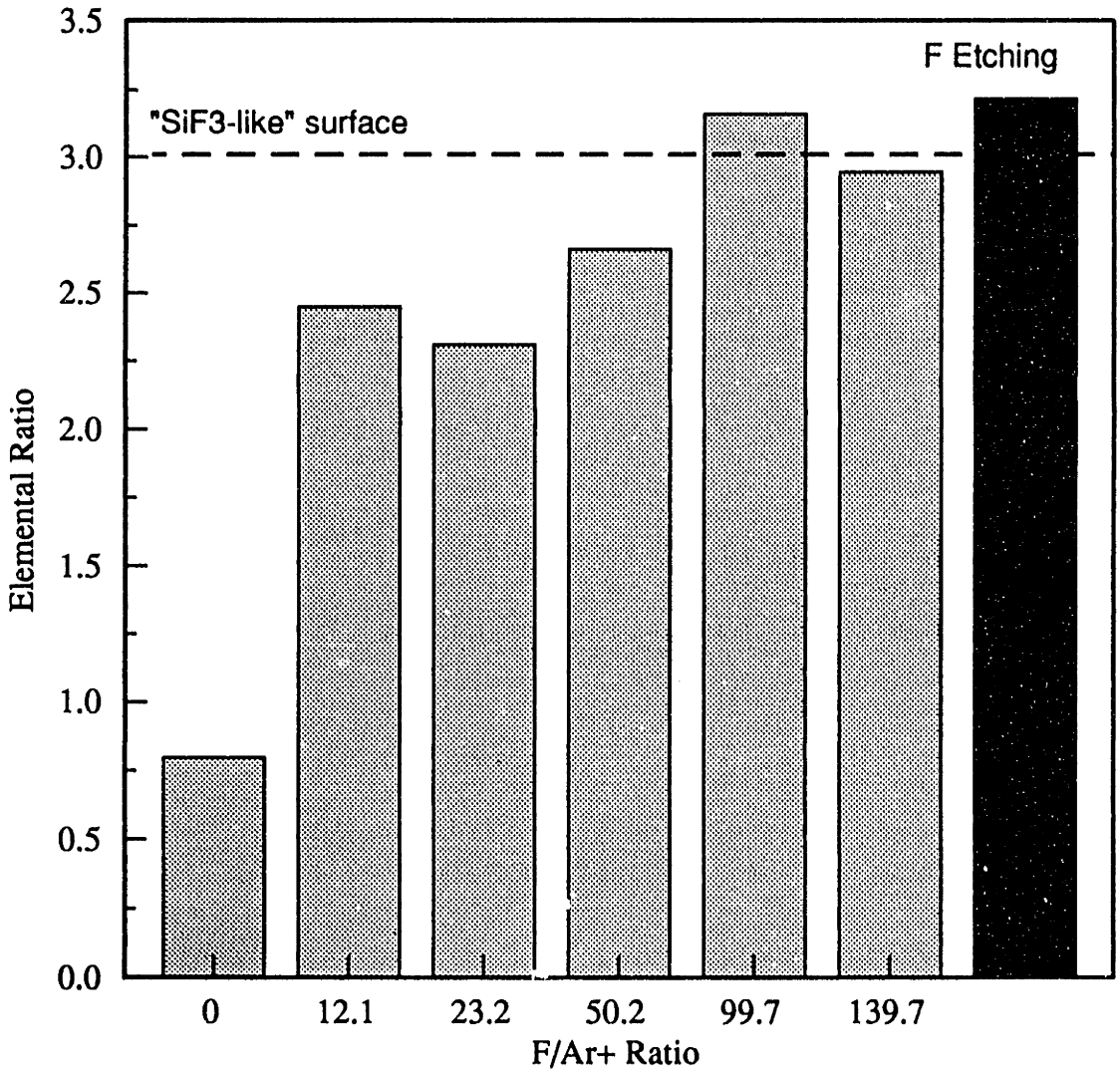

Figure 5-39. F(1s)-to-Si(2p) elemental ratios from corrected XPS data for Ar+/F etched SiO2 at 250 eV ion bombardment energy.

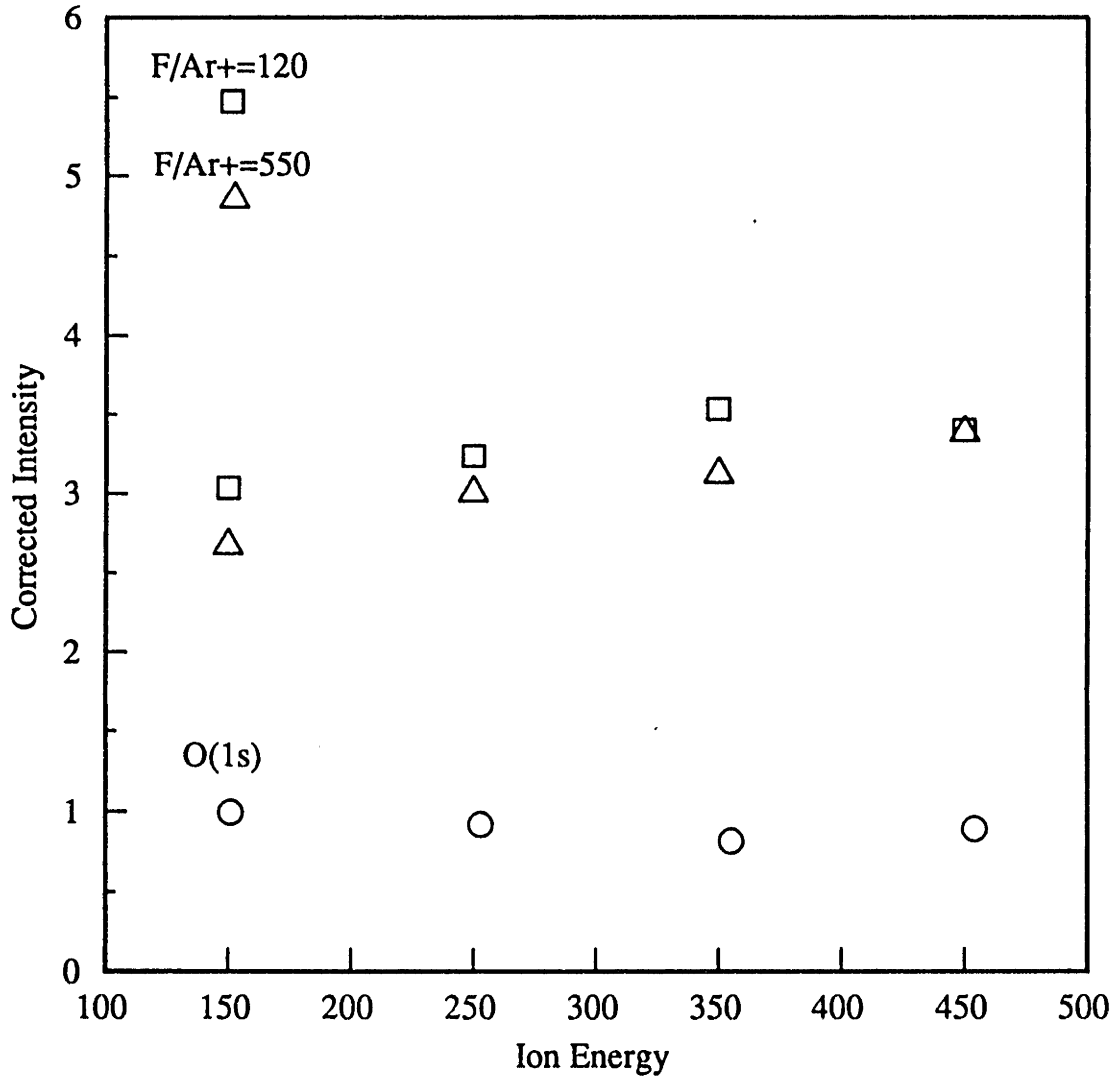

Figure 5-40. Behavior of the F(1s) peak versus ion energy at constant F/Ar+ for Ar+/F etching of SiO2. O(1s) peak behavior is also shown.

however, the exact mechanistic details by which silicon and its oxide are converted to volatile fluorides are still not well understood. In order to quantify our data for use in simulation of etching profile evolution, we have constructed simplified mechanistic models which decouple radical adsorption/recombination effects from the ion-driven reaction and mixing steps, in a manner analogous to the well known Langmuir-Hinshelwood mechanism. We have represented the complex process of "ion-enhanced etching" with simplified global reaction models with which we can capture the correct functional dependencies, but do not treat the elementary surface reaction steps. Conceptually, we have applied the "well-mixed" or CSTR assumption to the near surface region as shown in Figure 5-41, where reactant and product concentrations are replaced by average concentrations in the ion "mixing zone". The concept of the ion mixing depth, l, in Section 5.1 allows conversion of surface species concentrations into volumetric concentrations to complete the CSTR reactor analogy.

The basic requirements of an effective etching profile simulator necessitate knowledge of the total etching rate on any differential surface segment as a function of arriving species fluxes, energies, chemical types, and as a function of surface properties such as temperature, composition, and structure (e.g. bond strengths). In the simplified case of Ar^+/F etching of Si and SiO_2, we have reduced the parameter space of the problem to:

$$ER_{tot} = f(N, I^+, E_i, E_{th}, T_s) \qquad (5\text{-}13)$$

N = F atom flux ($0\text{-}10^{19} cm^{-2}s^{-1}$)

I^+ =Ar ion flux ($0\text{-}10^{16} cm^{-2}s^{-1}$)

E_i =Ion energy (20-500 eV)

E_{th}=Surface process energy threshold

T_s =Surface temperature (25-300 C)

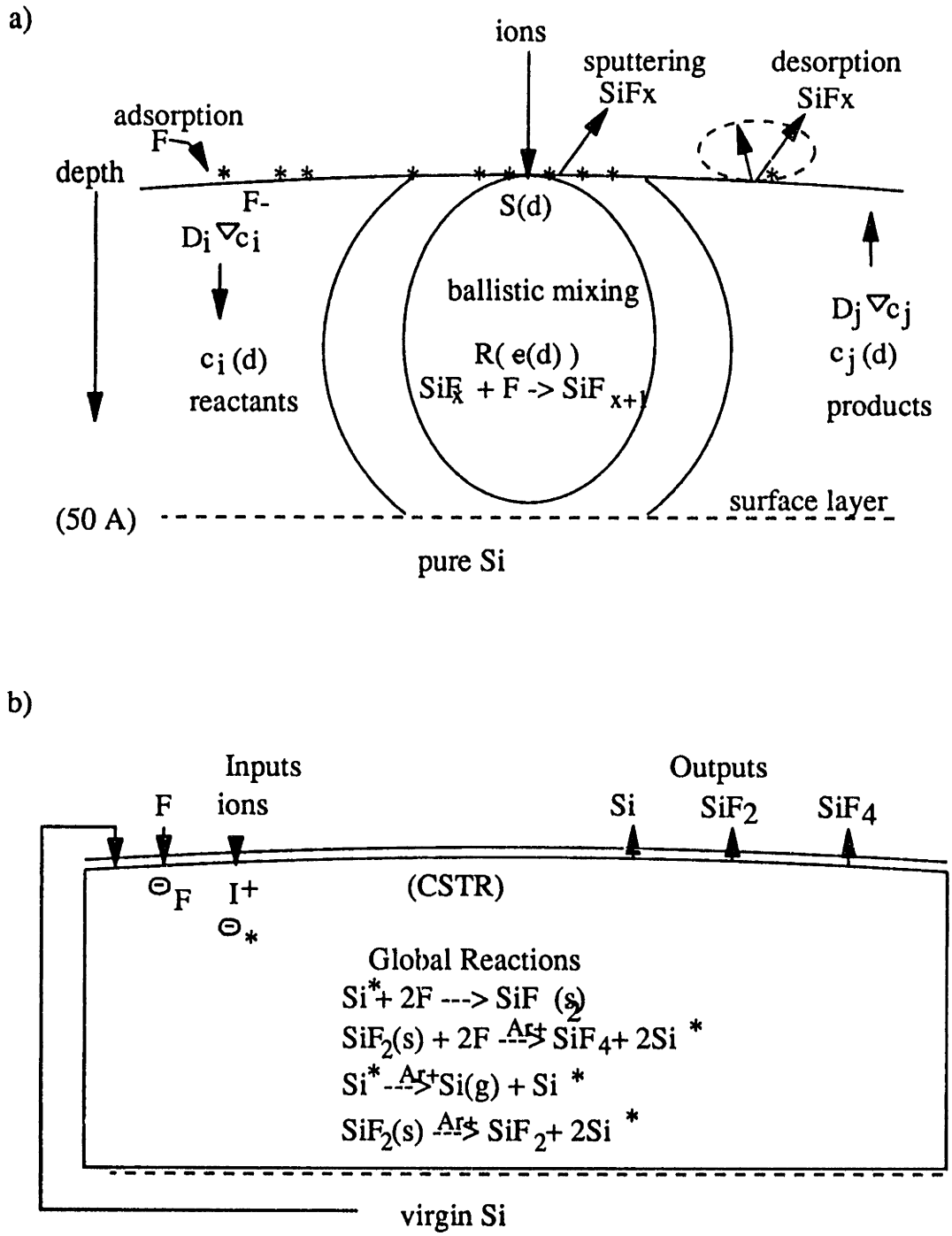

Figure 5-41. Conceptual comparison of a) a mechanistic Ar+/F surface kinetic model and b) the CSTR-"site" model.

In these studies ion were normally incident on the substrates, so the effect of ion incidence angle on yield is not considered. In general, the observed etching rates are well represented as a combination of three components, including 1) physical sputtering, ER_p, 2) ion-enhanced chemical reaction, ER_i, 3) and spontaneous thermal etching by ER_s. i.e.

$$ER_{tot} = ER_p + ER_i + ER_s. \qquad (5\text{-}14)$$

This sum is not directly linear, but must be solved self-consistently based on conservation of free surface "sites" versus the fluorinated surface fraction. From here on in we take the term "surface" to represent the entire near-surface volume as suggested by our CSTR approximation. The mechanistic framework of our Ar^+/F-Si surface kinetic models is shown in Figure 5-42, where three pathways exist for the volatilization of silicon and SiO_2 as suggested by equation (5-14) above. In the discussion to follow, we reduce these mechanistic models of Ar^+/F etching to simpler "semi-empirical" models based on reasonable assumptions, allowing us to reduce the number of fitted parameters. Much less is understood concerning the mechanistic pathways in Ar^+/F-SiO_2 etching, especially concerning the F-Si versus F-O surface chemical interactions. For the sake of simplicity, we neglect the O-F chemistry in O_2-Si etching entirely. We first consider the problem of F physisorption on the SiF_x and O_2-SiF_x surfaces, and the subsequent chemisorption of F(p) to active Si^* sites

F Atom Physisorption and Recombination

A treatment of recombination behavior in Ar^+/XeF_2 etching models has been largely neglected in the past, without justification. This aspect of the surface model is important if one considers the feedback between surface reactions products, including potential recombination

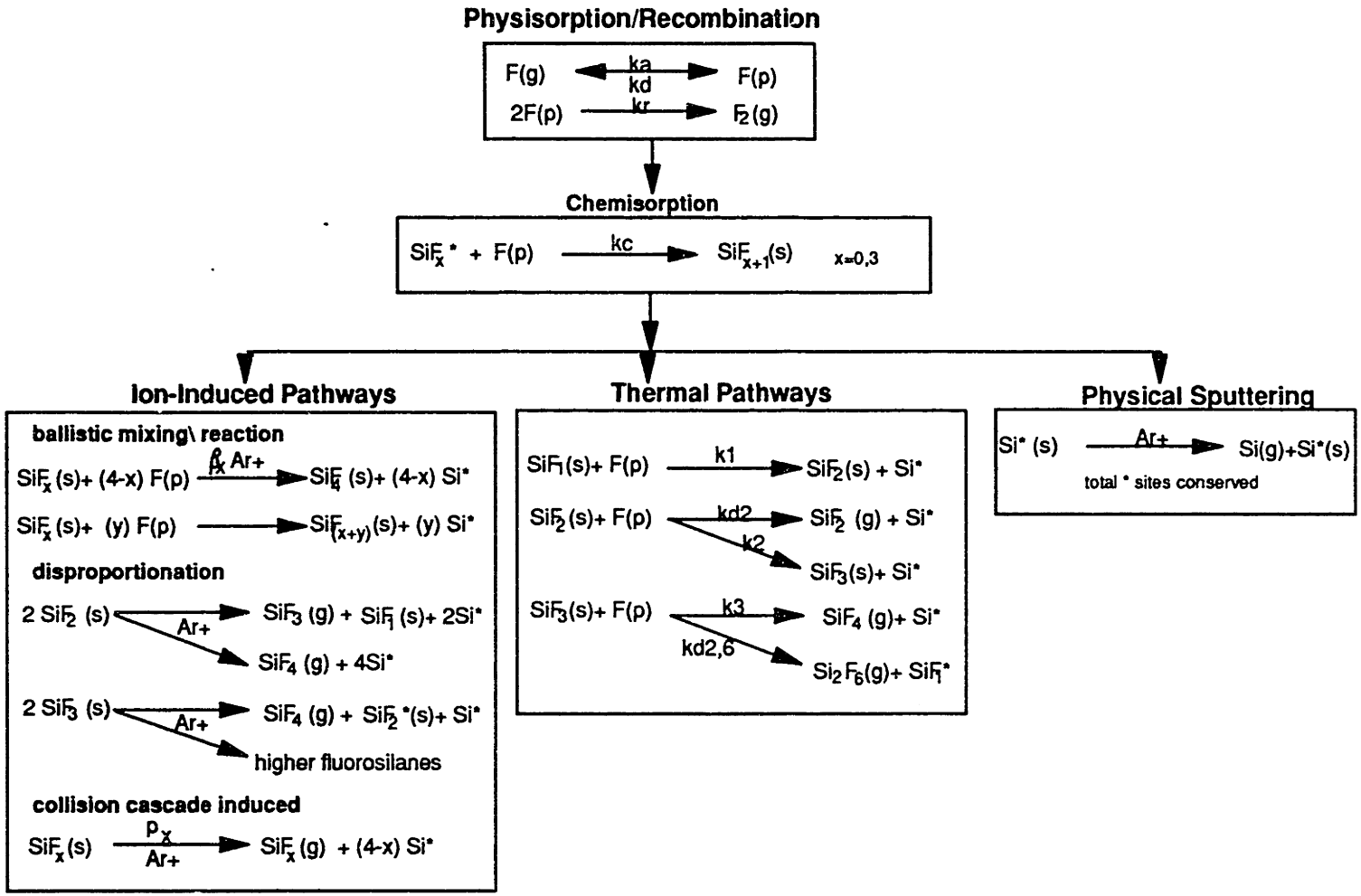

Figure 5-42. Mechanistic model of Ar+/F etching of silicon showing hypothetical reaction pathways to volitile products.

products, and the gas-phase chemistry in a self-consistent etching model. In addition, the fitted surface kinetic parameters lose physical significance when important loss processes are not considered as separate reactions. F atom-metal chemistry is unusual, as pointed out by Nordine and Lagrange [1976], in that the metal-F chemisorption bond is very strong (~150 kcal/mole for Si-F), while the F_2 dissociation energy is small (~38 kcal/mole). As a result, the recombination of surface fluorine from surface chemisorption sites is generally thermodynamically unfavorable, and atomic fluorine tends to quickly fluorinate metal surface chemisorption sites, passivating it toward further rapid uptake of fluorine. Thermal reaction of atomic fluorine with such a passivated surface is generally slow and, as is shown below, physisorption coverages are too low at typical gas pressures to make recombination a likely event. As a result, total loss coefficients for atomic fluorine on many fluorine-passivated metal surfaces, and particularly on SiO_2, are extremely low in the pure fluorine system. F surface loss coefficients in the fluorocarbon plasma environment, however, are notably larger (~0.01) due to large physisorption coverages of CF_x type radicals which readily recombine with unbound fluorine (see Chapter 7).

Data of Nordine and Lagrange [1976] and Flamm et al. [1981] allow derivation of an approximate F_2 recombination rate constant for atomic fluorine on quartz, based on a measured total loss coefficient of 1.5×10^{-4} for atomic F on room temperature quartz at approximately 15 Pa F. (The loss coefficient on pyrex at steady-state was found to be identical to that of quartz within the experimental accuracy). The data of Flamm et al. [1981] predict a thermal reaction rate coefficient of about 5×10^{-5} under these conditions, leaving the F recombination loss coefficient, γ_r, on fluorinated quartz at 10^{-4} (15 Pa F, 300 K). Using this data, the recombination rate constant, k_r, may be estimated from the definition

$$\gamma_r = 10^{-4} - \frac{2k_r n_m^2 \theta_f^2}{Q_f}, \qquad (5\text{-}15)$$

where n_m represents monolayer physisorption density, θ_f is the fractional surface coverage, and Q_f is the F atom flux at 15 Pa. A classical Langmuir physisorption model, using an adsorption energy of 5 kcal/mole and an oscillator period of 10^{-12} s, reveals extremely low fractional physisorption surface coverage (~ 10^{-5}), even at this moderate F pressure, due to the short surface residence time. Using this value places the recombination rate constant, k_r, at 7×10^{-9} cm^2/mole-s at 300 K. This analysis indicates that recombination processes in the Ar^+/F etching of silicon are negligible compared to atom desorption rates at low to moderate F pressures. Surface recombination should not become the dominant F atom loss process until the F atom pressures exceed 1 torr. Recombination rates for F on fluorinated silicon surfaces (SiF_x) have not been reported to our knowledge. However, the data of Nordine would suggest an upper limit of 10^{-3} for the F total loss coefficient on the thick SiF_3-like overlayer which forms at large F atom exposures. Accordingly, F atom physisorption coverages would not exceed 0.01 (surface fraction) until F atom fluxes (Q_F) exceed 10^{21}/cm^2-s or about 10 mtorr equivalent pressure.

Given these observations, we neglect F atom surface recombination effects in our Ar^+/F etching models and assume that physisorbed F(p) atoms either find a reactive Si^* site resulting in chemisorption, or hop back off the surface as F(g). Accordingly, we can make an estimate of the F(p) via a Langmuir type model

$$F(p)/\Gamma_m = b'Q_F/(1+b'Q_F) \qquad (5\text{-}16)$$

where Γ_m is monolayer F(p) coverage and b' is the Langmuir parameter [Adamson, 1985]. As

we discussed above, the F(p) surface coverages in our flux regime are very low such that we can apply the low pressure limit approximation,

$$F(p) \approx \Gamma_m b' Q_F. \qquad (5\text{-}17)$$

F(p) Atom Chemisorption

Because the reaction probability of the F atoms with an atomically clean metal surface is effectively unity, an F(p) atom physisorbed in the vicinity (within 1 atomic radius) of an Si^* dangling bond is assumed to react to form an Si-F bond instantaneously. However, the hopping of physisorbed F(p) from passivated SiF_x areas to active Si^* sites is not probable due to the small physisorption energy and subsequent short surface residence time ($\sim 10^{-12}$ sec). This hopping mechanism would also lead to a strong temperature dependence of etching yield which is not observed experimentally. In theory, a chemisorption rate constant for F(p) on clean Si^* sites could be calculated based on initial rate studies of F atom sorption on Si and SiO_2 if we had a method for quantifying the Si^* "sites" via

$$-d[Si^*]/dt = k_c\,[F(p)]\,[Si^*] = [s_F\,Q_F]_{t=0} \qquad (5\text{-}18)$$

where s_F is the apparent F atom sticking coefficient. Loudiana and Schmidt [1984] provide initial rate data for the sorption of atomic F on a clean, sputtered SiO_2 surface, where they calculate an initial F sticking coefficient of 0.14 for F fluxes of $7 \times 10^{15}/cm^2$-s (Q_F). Given our simple Langmuir model for physisorption, F(p) concentrations of 10^7 cm^2 are expected at this flux. If we make the gross assumption that $10^{13}/cm^2$ active Si^* sites (1% of the clean SiO_2 surface) exist, k_c is on the order of 10^{-5} cm^2/s. The density of active sites on clean, ion-bombarded silicon is expected to be much higher, but given an initial F sticking coefficient of unity, a similar k_c value might be

expected. Detailed mechanistic studies of thermal F etching of silicon suggest that F^- ion states may exist in these systems [Houle 1983, 1984] with appreciable lifetimes which are not represented in our analysis. It is clear from the Ar^+/F silicon and SiO_2 etching yield data that at low F/Ar^+ ratios, the process of F atom chemisorption or "sticking" becomes rate limiting. For lack of better information, we lump the F(p) surface coverage and chemisorption rate parameters together into an apparent F atom sticking coefficient on clean Si* sites, s_o, based on the total F atom flux, Q_F,

$$-d[Si^*]/dt = k_c\ [\Gamma_m\ b'\ Q_F\ ]\ [Si^*] = s_o\ Q_F. \qquad (5\text{-}19)$$

Ion-induced desorption of F from both chemisorption and physisorption sites is neglected. Calculations below indicate that F(p) physisorption coverages are extremely low at the flux levels used here, making an ion-induced desorption event from the physisorption state very unlikely. Moreover, fluorine is bound to Si very tightly (~150 kcal/mole) in its chemisorption state, making an ion-induced cleavage of this bond more unlikely than the release of an SiF_x unsaturate species which have binding energies on the order of 90 Kcal/mole [Jenichen and Johansen, 1988]. Therefore, in the approximation of our simple model, ion bombardment has no effect on the F atom sorption kinetics other than the creation of active Si^* sites, allowing the strong chemisorption of physisorbed F(p).

Reaction Pathways to SiF_x Products

We now consider three mechanisms by which the SiF_x and O_2-SiF_x surfaces may be volatilized or "etched". To begin with, Flamm et al. [1981] hypothesized a sequential thermal fluorination mechanism for the production of volatile products such as SiF_4, SiF_2 via F atom attack

of silicon as shown in Figure 5-42. However, as discussed in Section 5.2, it is the barrier to F atom diffusion through the top SiF_x-layer which is the rate-limiting step in this reaction network. Mechanistic details concerning the F atom etching of SiO_2 have not been proposed to our knowledge. We have taken the Arrhenius parameters suggested by Flamm et al. [1981] in calculation of thermal (ER_s) rates of silicon and SiO_2 etching, suggesting that even in the presence of ion bombardment, a small probability exists for an F atom to "hop" over the diffusional energy barrier and react with a near surface SiF_x species without the aid of an ion impact event.

$$ER_{s,\,Si} = 3.59\times10^{-15}\, Q_F \exp(-0.108/k_bT) \qquad (5\text{-}20)$$

$$ER_{s,\,SiO2} = 7.37\times10^{-16}\, Q_F \exp(-0.163/k_bT) \qquad (5\text{-}21)$$

The functional form used in calculation of the physical sputtering yields is given in equation (5-7), where the required parameters for bare silicon and SiO_2 sputtering are provided in Table 5-1. Any of the SiF_x species, where we limit our consideration to x=0-3, may be released as the result of a collision cascade, as demonstrated in the time-of-flight mass spectral studies of Haring et al. [1982] and Houle [1987]. SiF_4 is assumed to desorb instantaneously via thermal mechanisms upon its production. The "physical sputtering" component of our model is the zeroth order reaction of the family of collision-cascade-induced processes, which may take place only on bare "sites" i.e. regions where Si^* species are bound only to other Si or O, but not to F. Since we are considering the steady-state only, not net production or loss of Si^* active sites is allowed in the regions which are physically sputtered, thus

$$Si^*(s) \text{ --}P_o,\ Ar^+\text{--> } Si(g) + Si^*(s) \qquad (5\text{-}22)$$

$$O_2\text{-}Si^*(s) \text{ --}P_o,\ Ar^+\text{--> } Si(g) + 2O(g) + O_2\text{-}Si^*(s), \qquad (5\text{-}23)$$

where by definition $p_o = Y_p$. It has been shown by Coburn [in Chapman, 1980] that up to 10% of SiO_2 sputtered in the energy range of interest may be liberated as SiO(g), and others have observed O_2 as an SiO_2 sputtering product, such that equation (5-23) describes only the dominant oxide sputtering pathway.

Application of the pure thermal F etching model of Flamm et al. [1981] and the pure physical sputtering model of Steinbrukel [1989] allows us to capture the correct limiting behaviors in our Ar^+/F etching model. In the intermediate regimes, application of these forms is a conceptual division, in which we are essentially making the definition

$$ER_i \equiv ER_{tot} - ER_s - ER_p. \qquad (5\text{-}24)$$

Although the work of Coburn and Winters [1985] as well as others have eliminated many of the potential mechanisms by which ions enhance F-Si and F-SiO_2 chemistry, several important pathways warrant consideration. To begin with, the time-of-flight mass spectral studies of Haring et al. [1982] and Houle [1987] suggest that a large proportion of the Ar^+/F etching products may be evolved as the result of collision cascades, especially under conditions of low F coverage and high bombardment energy. These collision cascade induced processes are considered in the form

$$SiF_x(s) \text{ --}P_x,\ Ar^+\text{--> } SiF_x(g) + (4\text{-}x)\ Si^* \qquad (5\text{-}25)$$

$$O_2\text{-}SiF_x(s) \text{ --}P_x,\ Ar^+\text{--> } SiF_x(g) + O_2(g) + 2^* \qquad (5\text{-}26)$$

where p_i describes the probability or "yield" for releasing a surface SiF_i species via collision cascade and etc.... The net number of Si^* active sites produces in these collision cascade-induced etching events is somewhat arbitrary since the bonding environment of a given SiF_x surface

species will vary. For the case of silicon etching we might consider the production of a maximum of (4-x) new Si^* dangling bonds, given that any unfluorinated site is bonded to another silicon at sufficiently high fluorine coverage. In the case of SiO_2 etching, although four Si-O bonds must be ruptured on average to release a silicon, Si^* and O^* are not equivalent "sites" for fluorine sorption. For lack of better information, we make the arbitrary assumption of the net production of two new Si* sites per cascade-induced etching event. Two other general families of ion-induced etching reactions may be considered. The first are termed "disproportionation" reactions as suggested in the simple mechanism of Winters [1985], and basically involved the interconversion of SiF_x species upon ion bombardment to produce a certain yield of SiF_{x+1} more volatile products, while reducing a stoichiometric equivalent of products to SiF_{x-1}. The most interesting feature of these reactions is that they suggest a higher order dependence with respect to SiF_2 or SiF_3 coverage, since the occurrence of highly fluorinated nearest neighbors would increase the rate of this pathway. Since we have no mechanistic evidence to confirm or refute the importance of "disporportionation", we consider instead a more general class of reactions which we refer to as the "ballistic mixing" pathways as shown in Figure 5-42. This reaction pathway allows the incorporation of surface fluorine e.g. F(p) into the SiF_x or O_2-SiF_x layer via knock-on implantation and/or F(p) diffusion enhanced via ion collision thermal spikes or lattice damage. Reaction of the interstitial F(i) then proceeds as a results of the ballistic mixing action of the ions, resulting in Si-F subsurface bond formation. Such a mechanism incorporates both the observations of Mizutani et al. [1985] and Winters [1988]. The net conversion of SiF_x species to the final SiF_4(g) volatile product via this pathway is described by a yield per incoming ion, β_x.

Consideration of the full blow mechanistic description of these systems is beyond the scope of this thesis, and could not be verified due to lack of *in situ* studies of SiF_x species concentrations as a function of energy and flux regimes. We do however have some knowledge

of the product distributions in this system, and the surface "condition" in this regime as discussed above. Based on studies of the ratio of unsaturated fragments to SiF_4, $\sum SiF_x/SiF_4$ from mass spectral studies, we know that although SiF_4 is the major Ar^+/F silicon and SiO_2 etching product, fragment production increases as a function of ion bombardment energy. In addition, based on our XPS data , it is not unreasonable to assume that the silicon surface is stoichiometrically "SiF_2-like" over a wide range of F/Ar^+ ratios. We therefore made the gross simplification that $SiF_2(s)$ is the only prevalent SiF_x unsaturate in the "mixing zone CSTR" in both the case of silicon and SiO_2 etching. Production of an $SiF_2(g)$ gas phase product via a collision-cascade mechanism is allowed in both cases. The branching ratios, $b=\sum SiF_2/SiF_4$ for the collision-cascade product versus the thermal SiF_4 product are defined by the semi-quantitative observations of Figures 5-29 and 5-30,

$$b_{Si} = 9x10^{-3} (E_i)^{1/2} \qquad (5\text{-}27)$$

$$b_{SiO2} = 7x10^{-3} (E_i)^{1/2} \qquad (5\text{-}28)$$

Finally, the correct functional dependencies of the ion-enhanced etching yields ($Y_i=ER_i/I^+$) on F atom-to-ion flux ratios are found to be well represented when the ion-enhanced reaction rates are assumed to be first order in ion flux and fluorine near-surface site occupation, in the form:

$$Y_i = \beta_2(I^+)^1(\theta_F)^1 \qquad (5\text{-}29)$$

The result of these assumptions and simplifications are the semi-empirical models for the Ar^+/F etching of silicon and SiO_2 shown in Tables 5-7 and 5-8. Although it is certain that the

Table 5-7. Ar^+/F-Si Phenomenological Surface Kinetic Model

$$F(g) \text{ <--}k_a,k_{a-1}\text{--> } F(p)$$

$$2\ F(p) + Si^* \text{ --}k_c\text{--> } Si\text{-}F_2(s)$$

$$2\ F(p) + Si\text{-}F_2(s) \text{ --}\beta_2,Ar^+\text{--> } SiF_4(g) + 2\ Si^*$$

$$Si\text{-}F_2(s) \text{ --}p_2,Ar^+\text{--> } SiF_2(g) + 2\ Si^*$$

$$Si^* \text{ --}p_o,Ar^+\text{--> } Si(g) + Si^*$$

$$2\ F(p) + Si\text{-}F_2(s) \text{ --}k_{T,Si}\text{--> } SiF_4(g)$$

Table 5-8. Ar^+/F-SiO_2 Phenomenological Surface Kinetic Model

$$F(g) \text{ <--}k_a,k_{a-1}\text{--> } F(p)$$

$$2\ F(p) + O_2\text{-}Si^* \text{ --}k_c\text{--> } O_2\text{-}Si\text{-}F_2(s)$$

$$2\ F(p) + O_2\text{-}Si\text{-}F_2(s) \text{ --}\beta_2,Ar^+\text{--> } SiF_4(g) + O_2(g) + 2\ O_2\text{-}Si^*$$

$$O_2\text{-}Si\text{-}F_2(s) \text{ --}p_2,Ar^+\text{--> } SiF_2(g) + O_2(g) + 2\ O_2\text{-}Si^*$$

$$O_2\text{-}Si^* \text{ --}p_o,Ar^+\text{--> } Si(g) + 2\ O(g) + O_2\text{-}Si^*$$

$$2\ F(p) + O_2\text{-}Si\text{-}F_2(s) \text{ --}k_{T,ox}\text{--> } SiF_4(g) + O_2(g)$$

stoichiometric production of Si^* sites per volatile product formed is not the same for silicon and SiO_2, we make this gross approximation such that the difference in the Si and SiO_2 chemistries are reflected entirely in the fitted model parameters. Since we are only considering one type of near-surface species, that being SiF_2, we can do a "site balance" on the fraction of fluorinated, θ_F, versus unfluorinated, θ^*, surface sites resulting in,

$$\theta_F = \frac{s_o R}{s_o R + 2\beta_2(1+b)} \tag{5-30}$$

where **R** is the neutral-to-ion flux ratio, Q_F/Ar^+. Equation (5-14) may then be expanded through appropriate substitutions to derive the etching yield per ion coming ion, as a function of the unknown parameters s_o and β_2,

$$R_{tot} = k_o Q_F \exp(\frac{-E_a}{k_b T}) + p_o(1 - \theta_F)I^+ + \beta_2(1+b)\theta_F I^+ \tag{5-31}$$

These forms may be rewritten in the following form which allows determination of the unknown parameters from a linear regression of the etching yield data,

$$C = Y_{tot} - Y_s - p_o = \frac{[\beta_2(1+b) - p_o]s_o R}{s_o R + 2\beta_2(1+b)} \tag{5-32}$$

$$1/C = \frac{2\beta_2(1+b)}{[\beta_2(1+b) - p_o]s_o}(1/R) + \frac{1}{[\beta_2(1+b) - p_o]} \tag{5-33}$$

where β_2 is regressed from the intercept of a plot of 1/C versus 1/R, and s_o is derived from the slope. Parameters regressed from available yield data are presented in Tables 5-9 and 5-10. We found that to a good approximation, the available etching yield data could be well represented by allowing β_2 to vary, while setting s_o=0.2 and 0.02 for the cases of silicon and SiO_2 etching respectively. "Best fit" values of β_2 using this constant initial sticking coefficient approximation are also provided in Tables 5-9 and 5-10. Fits of this model to the etching yield data are presented in Figures 5-5 and 5-13. Only data with R>15 was used because the 1/R regression

form statistically overweights data taken in the low flux ration regime, where the relative error in flux measurements is largest. The fact that these yield expressions are a function only of the F/Ar^+ flux ratio (R), and not on the absolute fluxes of these species is consistent with the behaviors shown in Figures 5-11 and 5-17.

Table 5-9. Ar^+/F-Si Model Parameters

E_i	b	s_o	β_2
20	0.040	0.216 (0.2)	2.46 (2.5)*
150	0.110	0.203 (0.2)	6.95 (7.0)
250	0.142	0.308 (0.2)	7.71 (8.5)
350	0.168	0.231 (0.2)	9.58 (11.0)
500	0.201	0.126 (0.2)	15.20 (14.0)
1000	0.284	0.177 (0.2)	21.19 (21.0)

* β_2 values in parentheses were adjusted to fit based on the constant sticking coefficient of 0.2

Table 5-10. Ar^+/F-SiO_2 Model Parameters

E_i	b	s_o	β_2
20	0.031	0.013 (0.02)	0.143 (0.13)
150	0.086	0.017 (0.02)	0.587 (0.55)
250	0.111	0.022 (0.02)	0.536 (0.6)
350	0.131	0.033 (0.02)	0.740 (0.85)
500	0.157	0.045 (0.02)	0.892 (1.10)
2000	0.313	0.013 (0.02)	2.845 (2.25)

Interpretation of Model Results

Consideration of the total silicon and SiO_2 etching yields as the sum of ion-enhanced etching, spontaneous F atom etching, and physical sputtering allows an illustrative graphical decomposition of the etching yield data. Figure 5-43 demonstrates the relative importance of these three mechanisms in the case of Ar^+/F etching of SiO_2 at 150 eV, versus the 20 eV Ar^+/F etching of polysilicon. The oxide etching mechanism is almost entirely "enhanced", while at low ion energies and high F/Ar+ ratio, there is a significant contribution of thermal F etching in the removal of silicon. This observation is consistent with the fact that significant undercut is seen in SF_6 ECR etching of polysilicon Tachi et al. [1991]. Taking the high and low flux ratio limits of the yield equation (5-31), reveals that the parameter β_2 is related to the saturation etching yield, while the initial apparent sticking coefficient, s_o, is directly proportional to the initial slope of the yield curve. In the simplest interpretation, β_2 is the number of SiF_4 molecules removed from fluorine saturated surface regions per incoming ion and is a strong function of ion energy. β_2 may also be expected to vary within a factor of two or so over ion incidence angles of 0-60°, and with incoming ion mass. Extension of this concept to reactive ion systems is not straight-forward and is beyond the present scope of our modeling effort. The effect of incident ion energy on the etching yield parameter, β_2, must be quantified in order to assess the etching yield of a given plasma ion striking a fluorinated surface. Given that we have employed a "ballistic mixing" mechanism leading to the production of the primary SiF_4 product, one might expect β_2 to scale in the same manner as the ion-sputtering process, which is also ballistically driven. Plots of β_2 versus $(E_i)^{1/2}$ are shown in Figures 5-44 and 5-45 for the case of silicon and SiO_2 etching respectively. In the case of silicon etching, β_2 is found to scale well with root ion energy from 1 keV down to a threshold value near 4 eV. It is significant that the Ar^+/F etching threshold values predicted are on the order of Si-F bond energies, versus physical sputtering thresholds

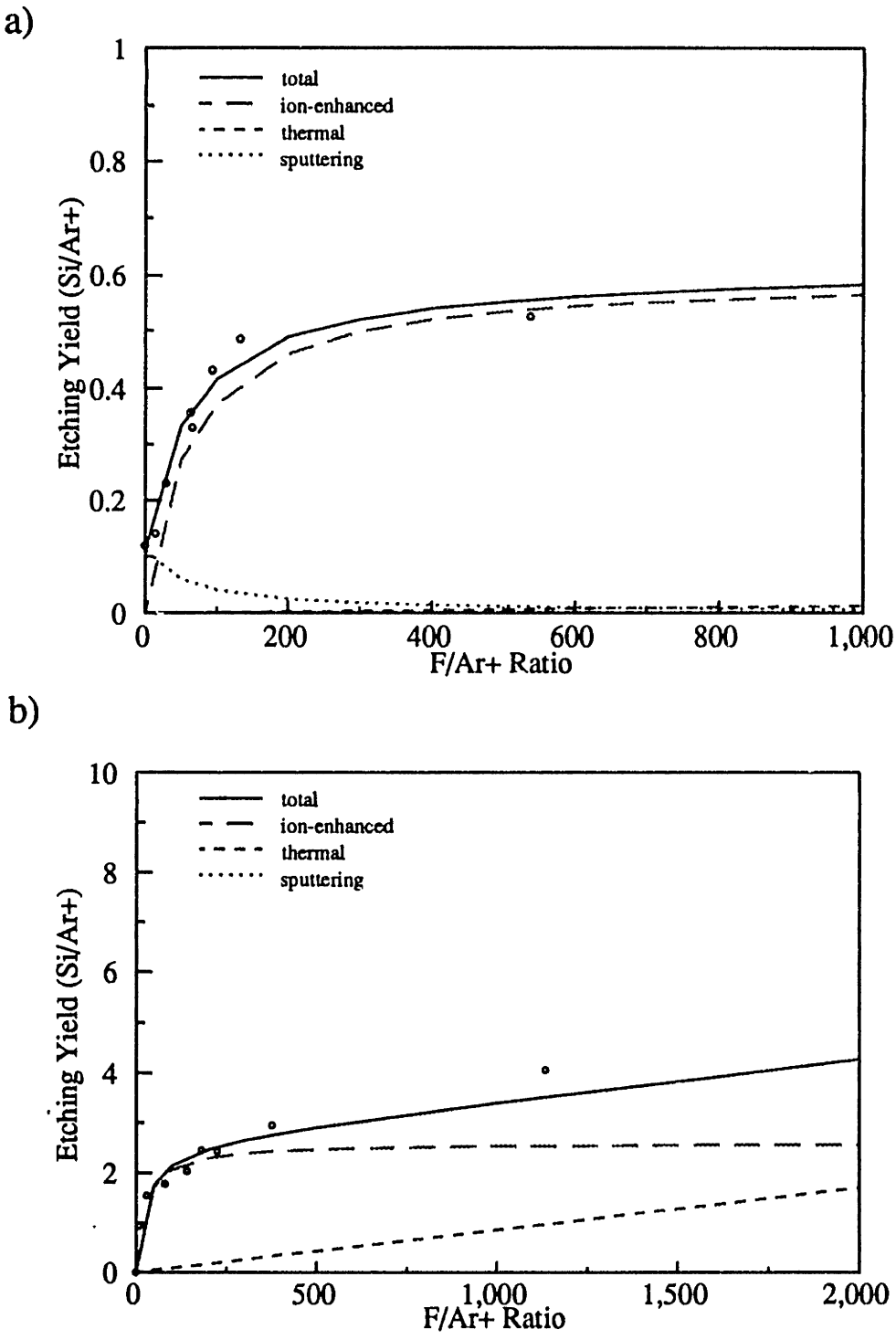

Figure 5-43. Graphical decomposition of Ar+/F etching yield data for the a) 150 eV etching of SiO2, and b) the 20 eV etching of silicon showing the relative contributions of physical sputtering, thermal etching, and ion-enhanced etching to the total measured yields.

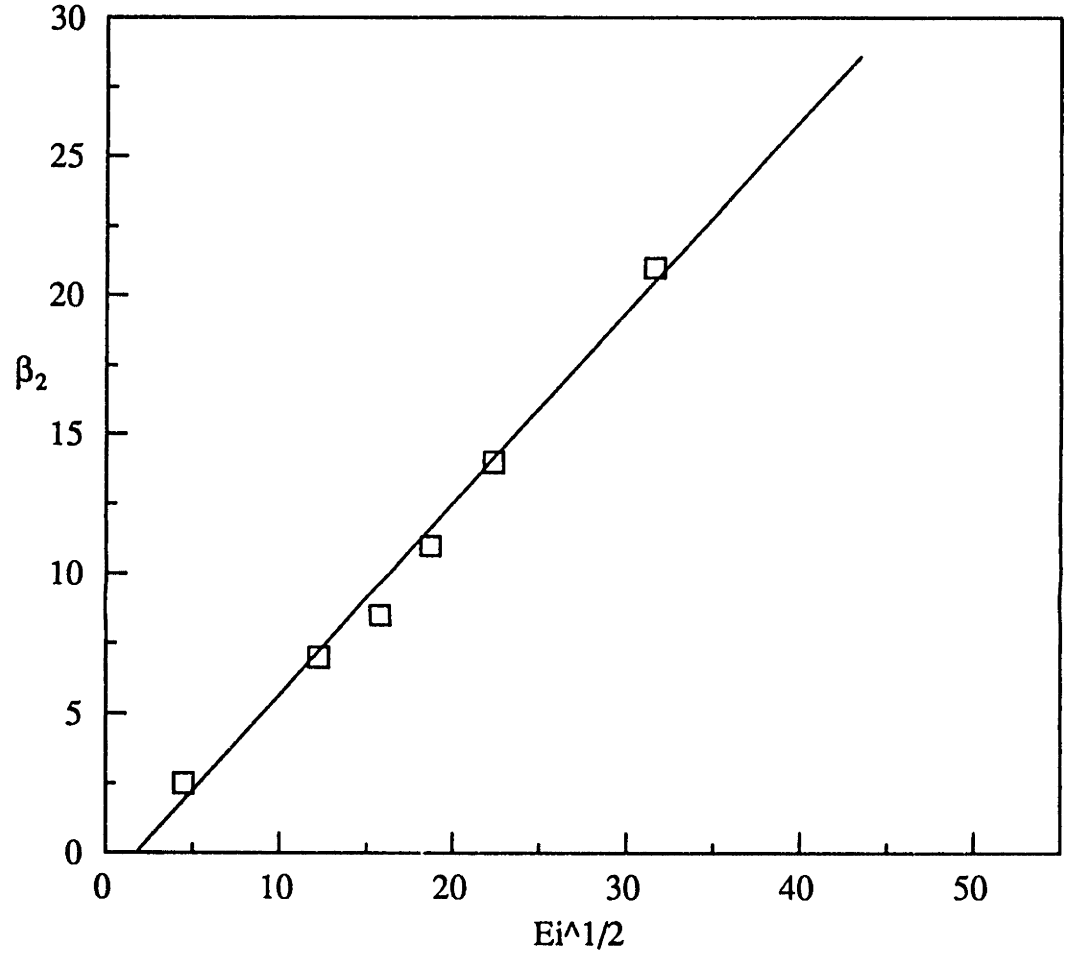

Figure 5-44. Behavior of the fitted$\beta_2$parameter versus root ion energy for the Ar+/F etching of silicon.

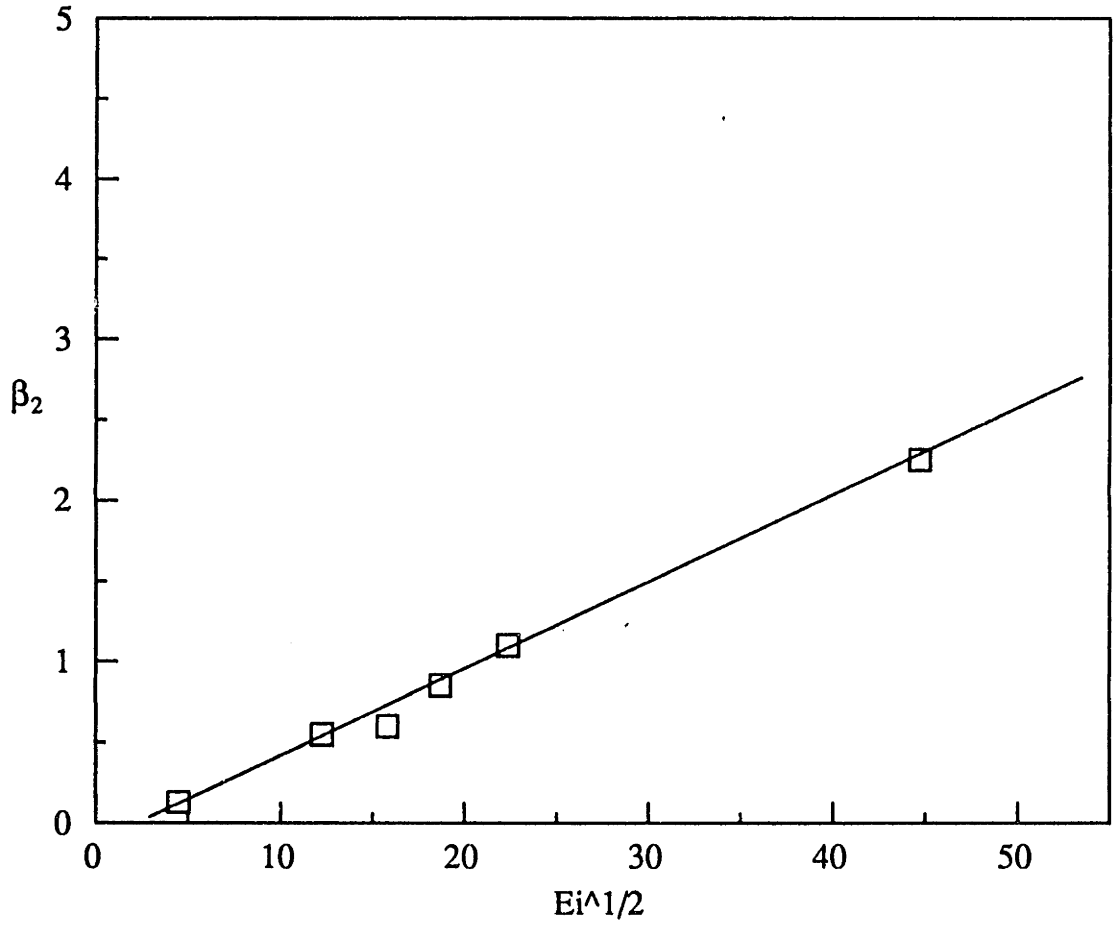

Figure 5-45. Behavior of the fittedβ_2 parameter versus root ion energy for the Ar+/F etching of SiO2.

which are on the order of Si lattice displacement energies (~13 eV). The $E_i^{1/2}$ scaling is also observed in the case of SiO_2 etching over the range of 20 eV to 2000 eV. Best fit lines to this data give the following energy dependencies,

$$\beta_{2,Si} = 0.687\ (Ei^{1/2} - 4^{1/2}) \qquad (5\text{-}34)$$

$$\beta_{2,SiO2} = 0.053\ (Ei^{1/2} - 4^{1/2}) \qquad (5\text{-}35)$$

The initial sticking probabilities calculated for this data are three orders of magnitude higher than those found absence of ion bombardment. We propose that this effect is due to the presence of "dangling bonds", or free adsorption sites, which are constantly renewed on the ion-bombarded surface. In the case of silicon etching, the apparent sticking coefficient does not change significantly over the ion energy range investigated, and a value of 0.2 was found to fit the entire set of data. It was shown in Figure 5-12, that in the case of SiO_2 etching, F adsorbs more readily as the energy of the ions bombarding the SiO_2 surface increases and the surface becomes "stickier". This effect leads to an energy dependence of the regressed sticking coefficient s_o as discussed by Butterbaugh et al. [1991] in a similar type of model, where low F/Ar^+ data was used in the regression. This effect is not obvious in the high F/Ar^+ ratio studies due to problems of F contamination when high F fluxes are employed.

While the initial sticking coefficient, s_o, for F on clean Si^* sites is constant to a good approximation, the apparent sticking coefficient for F on the $Si\text{-}F_x$ surface falls off with surface fluorination in this model,

$$s_F = s_o\ (1-\theta_F) \qquad (5\text{-}36)$$

The behavior of the sticking coefficient, s_F, with increasing F/Ar^+ for 150 eV silicon etching is shown in Figure 5-46 where the surface coverage behavior is also shown. This behavior is in qualitative agreement with the observations Winters and Coburn [1985]. Implications of this type

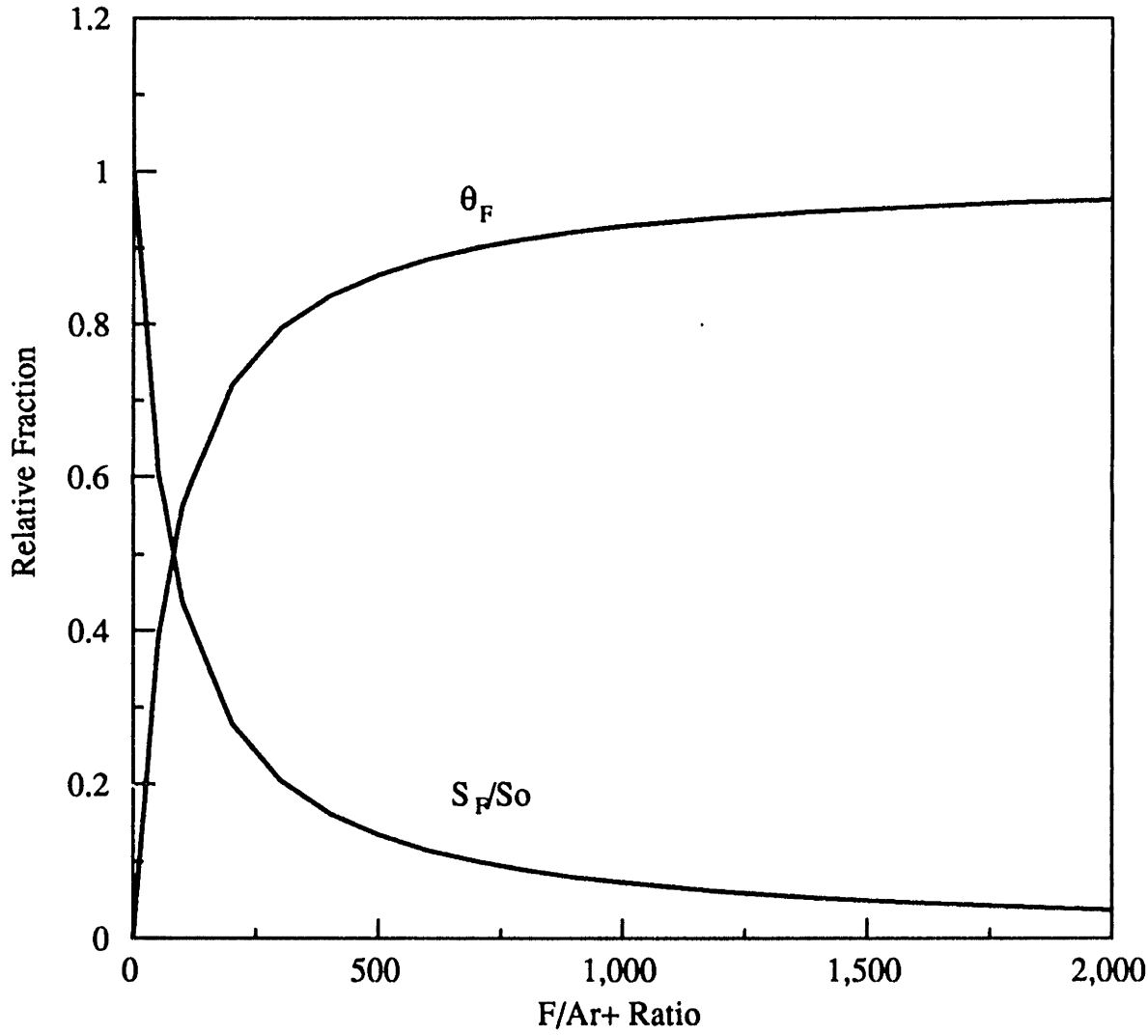

Figure 5-46. Predicted behavior of the near-surface fluorination, θ_F , and the relative F atom sticking coefficient, S_F /So, versus F/Ar+ ratio for the 150 eV Ar+/F etching of silicon.

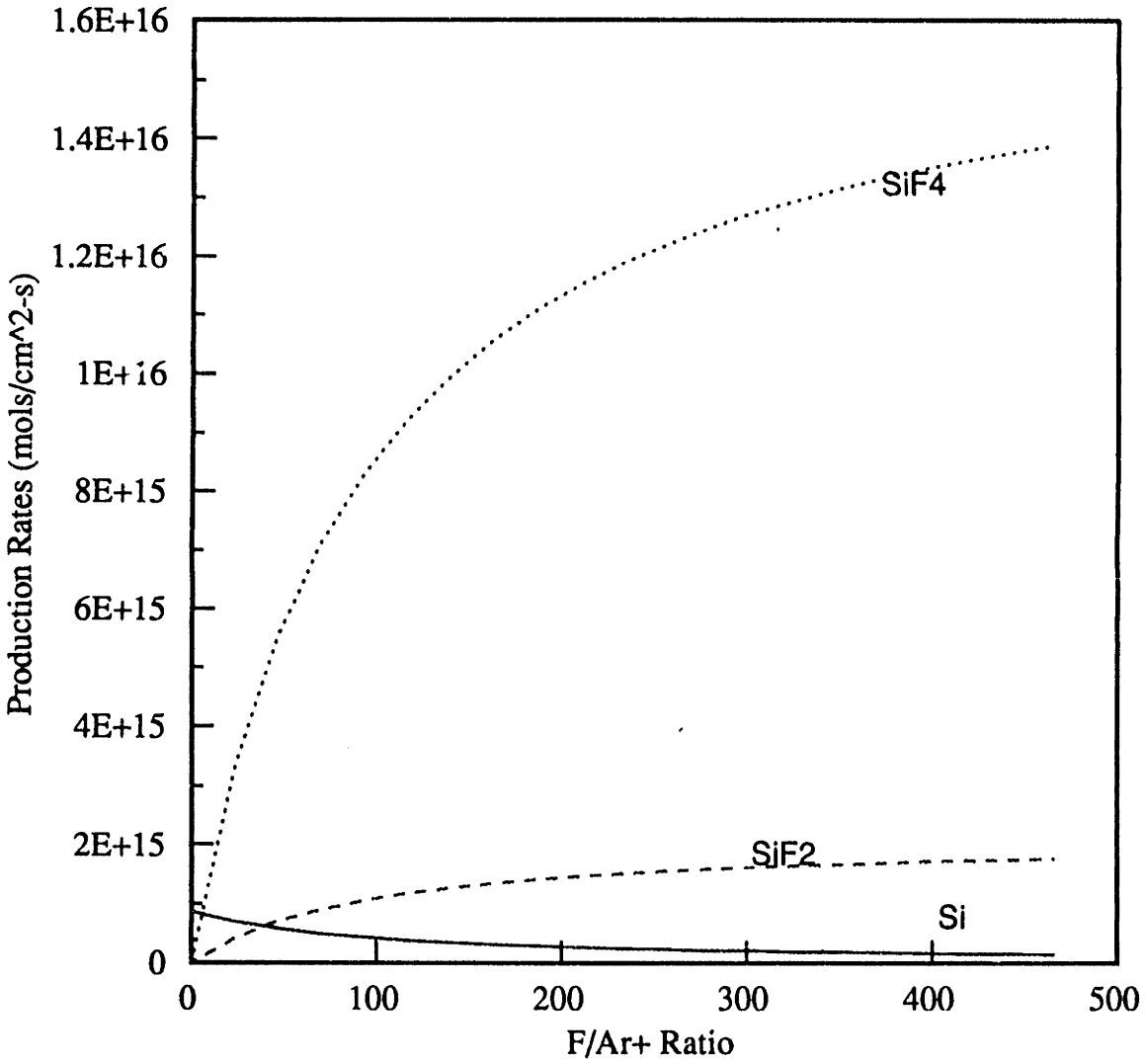

Figure 5-47. Predicted product distribution behavior in the Ar+/F etching of silicon as a function of F/Ar+ ratio at 200 eV

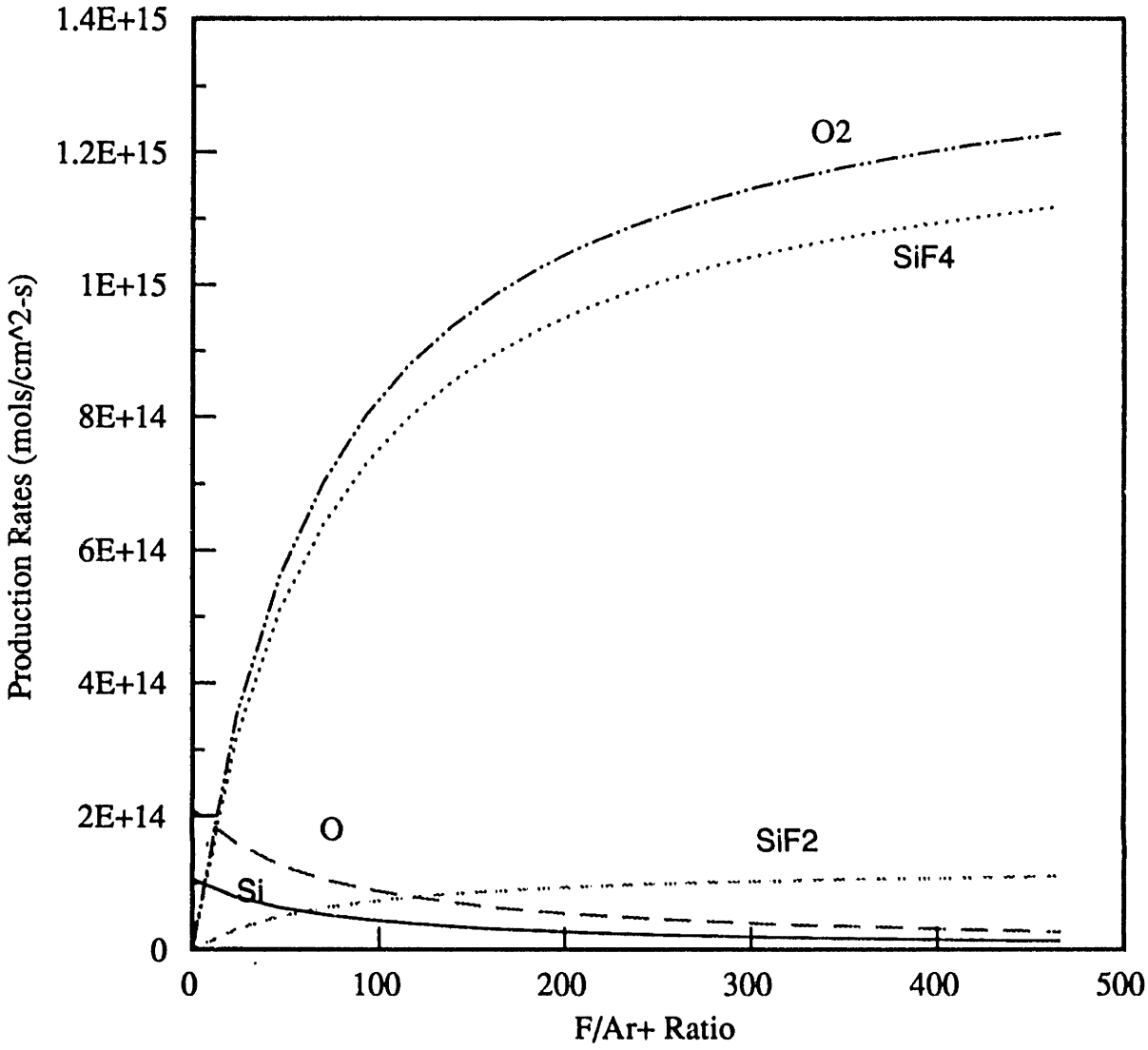

Figure 5-48. Predicted product distribution behavior in the Ar+/F etching of SiO2 as a function of F/Ar+ ratio at 200 eV.

of surface kinetic model for product distribution behavior in Ar+/F etching of silicon and SiO_2 are shown in Figures 5-47 and 5-48 as function of F/Ar+ ratio and ion energy respectively. These behaviors are discussed in detail in Chapter 8.

5.7 Summary

Silicon and SiO_2 etching yields were measured as a function of F/Ar^+ flux ratio, bombarding ion energy, and surface temperature. The steady-state etching kinetics were found to exhibit both mass-transfer-limited and reaction-rate (ion-flux) limited etching regimes in the flux range of interest. Mass spectral studies of ion-enhanced etching in these systems indicate that although SiF_4 is the major reaction product of Ar^+/F silicon and SiO_2 etching, substantial amounts of SiF_x unstaturates are produced in regimes of low fluorine coverage, or high ion bombardment energy. XPS studies of Ar^+/F etched surfaces showed that fluorination of near-surface "sites" increase in a Langmuir fashion with increasing F/Ar^+, consistent with model predictions. The F-to-Si surface stoichiometry was shown to increase with increasing F/Ar^+ for both substrates, indicating the change in surface "condition" which can alter the relative product distribution.

Simple site-occupation models of Ar^+/F etching were developed which incorporated the correct limiting behaviors of F atom thermal etching, and low energy Ar^+ physical sputtering. The conceptual basis of our ion-enhancement mechanism involves both an enhanced adsorption of fluorine on silicon dangling bonds (free valences) generated by ion bombardment, and subsequent "ion-mixing" of the surface chemisorbed fluorine with the lattice, which in a global sense leads to production of the volatile SiF_4 product. This mechanism is consistent with the observations of Joyce [1987], in which fluorine uptake by SiO_2 was enhanced after ion bombardment of the surface, and with the experiments of Winters [1988], which show that ion-mixing must be present for reaction of the fluorinated oxide to proceed to completion.

Chapter 6

CF_2 Radical Interactions with Si and SiO_2

In the set of experiments discussed in this chapter, we have studied the interaction of CF_2 radicals with Si and SiO_2 surfaces, alone and in combination with energetic Ar^+ ion bombardment. It has been widely contended in the literature that CF_2, and other fluorocarbon radicals prevalent in the plasma environment, are primary etchants for SiO_2 [Heinecke, 1975; Flamm and Donnelly, 1981], while they lead to the formation of thick passivating polymers on Si surfaces. As discussed in Chapter 1, several researchers have studied the spontaneous interaction of fluorocarbon radicals with silicon and silicon dioxide surfaces. However, to our knowledge, no one has actually measured the extent to which CF_2 may enhance SiO_2 etching rates in the presence of ion bombardment, nor the extent to which CF_2 may suppress the ion sputtering of silicon via the formation of passivating films. The goal of this work was to clarify these issues by conducting a series of two beam (Ar^+ and CF_2) etching yield studies. Etching yields on both material surfaces were measured interferometrically, where the relative species fluxes, ion energy levels, and substrate temperatures were all studied in their effect on the measured yields. Product distributions in these systems were studied mass spectrometrically, and fluorocarbon surface contaminations resulting from CF_2 exposure were studied via XPS. The interaction of CF_2 radicals with the Ar^+/F kinetics reported in the previous chapter is discussed in Chapter 7.

6.1 Spontaneous Interaction of CF_2 with Si and SiO_2

As was discussed in Section 1.3, several researchers have considered the spontaneous interaction of CF_3 and CF_2 radical sources with silicon and SiO_2 surfaces. The general conclusion of these studies is that although initial chemisorption, and limited dissociative chemisorption of

these species on clean Si<100>, Si<111>, is observed, neither spontaneous etching nor growth of thick fluorocarbon overlayers occurs on either silicon or SiO_2. The most relevant work in this area has been conducted by the Steinfeld group at MIT [Joyce, 1987; Joyce et al., 1988; Langan et al, 1989]. Joyce et al. [1988] showed while CF_3 initially undergoes limited chemisorption on thermal SiO_2 and dissociative chemisorption on Si<100>, no steady-state spontaneous etching of either substrate is observed. Joyce et al. contend, and we agree, that previous reports of steady-state etching by carbonaceous radicals [Selamoglu, 1986; Brannon, 1986] have been confounded by the simultaneous irradiation of the sample surfaces or other experimental artifacts. Joyce et al. also concluded that at high CF_3 doses, the initial formation of Si-F and Si-C bonds inhibits further dissociation of adsorbed CF_3 radicals, disallowing the formation of thick polymeric fluorocarbon films. Very little if any dissociative chemisorption of the CF_3 radical on SiO_2 was observed, ostensibly due to the lack of surface "dangling bonds". Joyce et al. made the important observation that ion bombardment of either film increased the rate of radical chemisorption through the production of dangling bonds i.e lattice damage, but that non-dissociatively absorbed CF_3 species are easily "resputtered" and removed from the surfaces.

Much less work had been reported concerning the spontaneous interaction of CF_2 radicals with Si and SiO_2 surfaces at the start of this thesis work. Langan et al. [1989] generated a CF_2 source through the UV photolysis of C_2F_4, and again observed no steady-state etching of Si<100> or SiO_2 surfaces. XPS studies of exposed silicon surfaces showed initial dissociative chemisorption on clean silicon, which became inhibited at high surface coverages, disabling further fluorine transfer from the sorbed dicarbene radicals to the silicon lattice. This situation directly parallels observations discussed above concerning CF_3 radicals. Although the CF_2 radicals were found to chemisorb on clean SiO_2, little or no fluorine transfer to the SiO_2 lattice was reported. In addition, ion bombardment of the SiO_2 sample did not markedly enhance the uptake

of CF_2 radicals, as was the case with CF_3. Langan et al. suggested that although spontaneous interactions of CF_2 radicals with Si and SiO_2 in the plasma environment could not explain the observed selectivity behavior, ion-bombardment mechanisms could be important. We report the effect of the simultaneous presence of CF_2 radicals and Ar^+ ion bombardment on etching selectivity in Section 6.2.

The pyrolytic production technique for CF_2 radicals employed in this thesis has allowed us to study the spontaneous interaction of these radicals with Si and SiO_2 surfaces at much higher fluxes than those achieved in the Steinfeld group. Our observations concerning these systems are, nevertheless, in very good agreement with observations reported by Langan et al. [1989]. We studied the effect of high fluence CF_2 exposures on Ar^+ bombarded Si and SiO_2 surfaces over a temperature range of 25°C to 300°C. The films were Ar^+ sputtered preceding CF_2 exposure both to clean ambient surface contaminations and remove native oxide from the polysilicon films, and also to present a "damaged", amorphized surface region as would be present in the plasma etching environment. No measurable spontaneous etch rate of either polysilicon or silicon dioxide films was observed over the temperature range investigated, using in situ laser interferometry during CF_2 beam exposure in the flux range of 10^{15} to $10^{16}/cm^2$-s. Although very slow etching rates (<10 Å/min) would not be observable via the interferometry technique over a reasonable experiment time (<1 hour), neither would such slow spontaneous reaction rates be relevant in a typical 1-5 minute plasma etching process. We did, however, observe the very slow growth of a surface film in the interferometry signal, during the exposure of Ar^+ sputtered polysilicon to large fluxes of CF_2 as shown in Figure 6-1a. The initial interference cycle shown in this figure corresponds to the Ar^+ sputter cleaning of the polysilicon film, after which the Ar^+ ion flux was turned off, and the CF_2 radical beam was turned on. The slow increase in laser reflected intensity seen upon CF_2 exposure can be distinguished from etching due to the change in "direction" of the interferometry

a) polysilicon

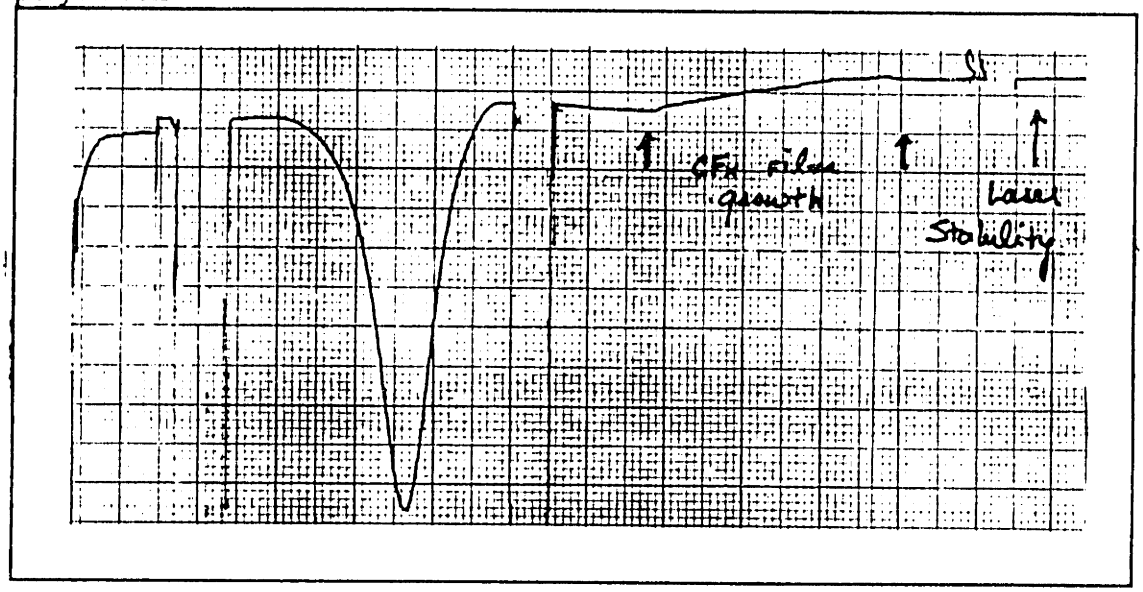

b) silicon dioxide

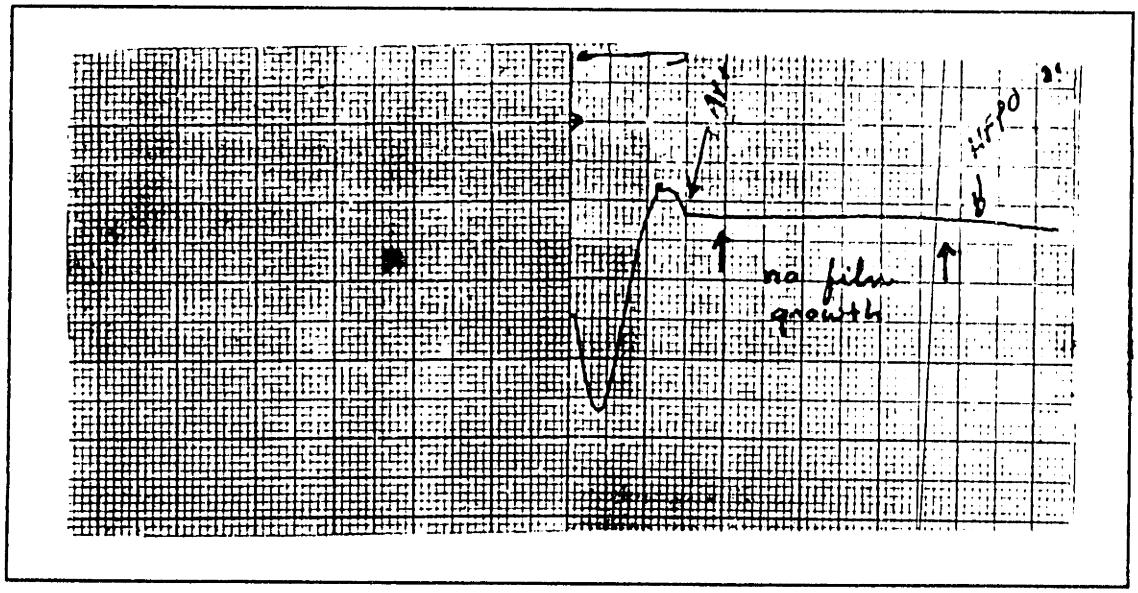

Figure 6-1. Laser interferometry signals during exposure of Ar+ sputtered a) polysilicon, and b) SiO2 films to a CF2 flux of $5.6 \times 10^{15} cm^{-2} s^{-1}$ major chart divisions are 4 minutes. Initial cycle shown is during Ar+ sputter cleaning.

trace. Although the measured deposition rate is slow, in the range of 1-10 Å/min, this signal is much greater than the measured fluctuation in laser intensity, and is not observed during room temperature HFPO exposure. We therefore attribute it to the slow growth of a fluorocarbon overlayer on polysilicon due to CF_2 exposure. We did not observe any evidence for the growth of a surface film when ion bombarded SiO_2 samples were exposed to similar fluxes of CF_2 as shown in Figure 6-1b.

Although it was concluded that exposure of the bombarded polysilicon to CF_2 resulted in a slow growing fluorocarbon surface film, the slow rate of growth was somewhat surprising, and is essentially insignificant during the 1-5 minute time duration of the typical fluorocarbon plasma process. A CF_2 beam flux of about $5x10^{15}/cm^2$-s, and a film growth rate on the order of 1-10 Å/min, would suggest a CF_2 "self-sticking" coefficient on the order of 10^{-4} to 10^{-3}. We conjectured that although the CF_2 apparently strongly chemisorbs to clean ion-bombarded silicon, its "self-sticking" coefficient was several orders of magnitude lower i.e. CF_2 has a low sticking coefficient on "teflon-like" surfaces. An experiment was performed in which CF_2 radicals were reflected from a CF_2-saturated silicon sample surface to the quartz crystal microbalance assembly (QCM) as shown in Figure 6-2. As expected, the calculated ("apparent") CF_2 sticking coefficient based on the QCM deposition rate, showed a sharp drop with total CF_2 exposure. At a calculated dose of 1L (e.g. 1 monolayer), the apparent sticking coefficient had fallen to 10^{-4}, in good agreement with the interferometry data discussed above. It should be noted that a sputter deposited silicon surface was present on the QCM at the start of this experiment. In addition, we have shown that the cracking patterns of the CF_2 beam appear identical whether reflected from the silicon sample face, or impinging directly upon the mass spectrometer ionizer, such that CF_2 recombination on the Si reflector was not problematic.

XPS studies of CF_2 exposed Si<100> and steam grown thermal SiO_2 were performed.

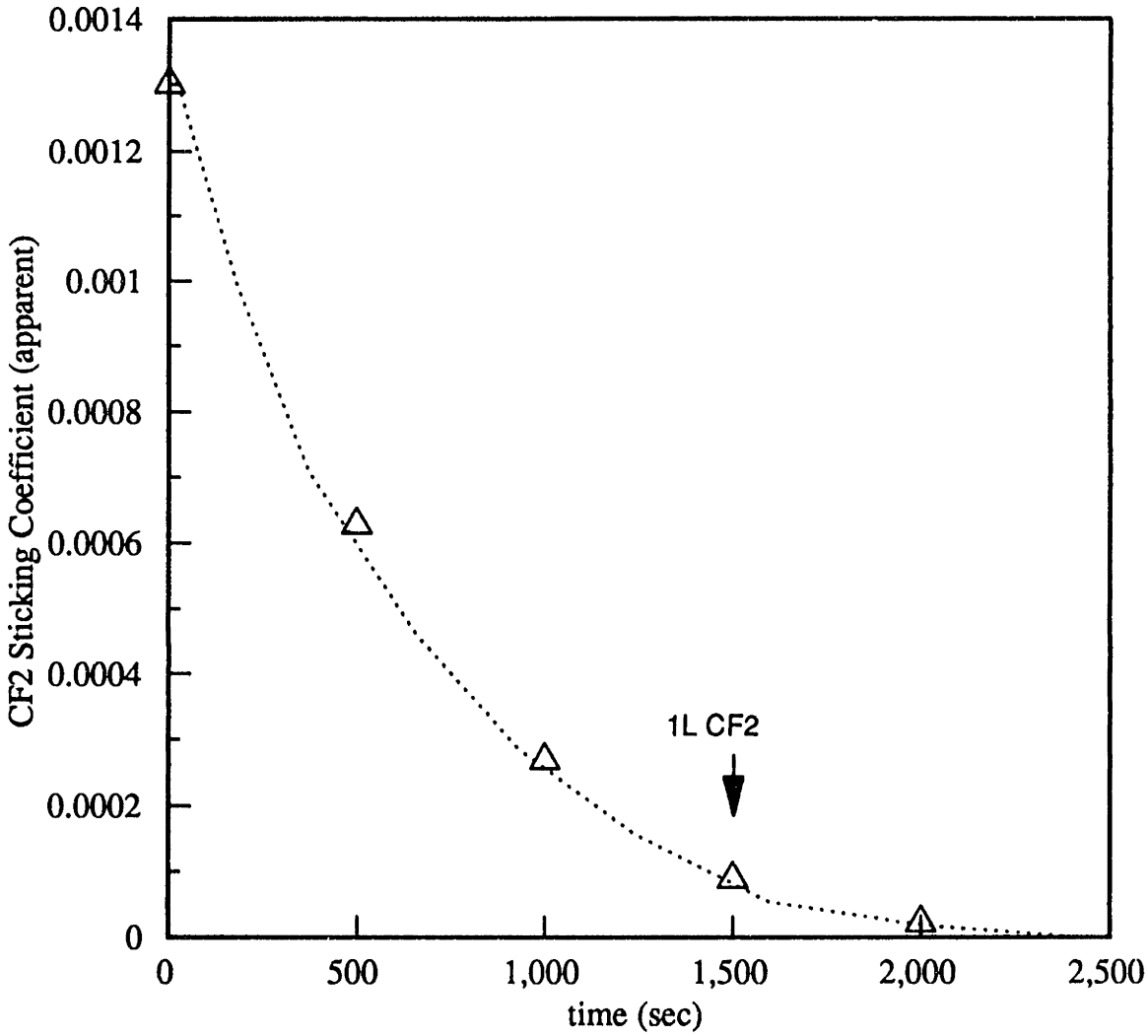

Figure 6-2. Variation of apparent CF2 sticking coefficient on the non-bombarded QCM surface with total CF2 exposure.

Again the surfaces were Ar^+(500 eV) sputter cleaned prior to CF_2 exposure at an approximate flux of $10^{16}/cm^2$-s for 5 minutes. The calculated C(1s)-to-Si(2p) and F(1s)-to-Si(2p) elemental ratios are shown in Figure 6-3, where appropriate corrections for photoelectric cross section and electron escape depth have been made. These data indicate that multi-layer film growth, although slow, is possible on silicon where a C-to-Si ratio of 3 was calculated. In contrast, similar exposure resulted in at most monolayer CF_2 coverage on SiO_2, where a C-to-Si ratio of 1 was calculated. The data also suggest qualitatively that the probability for dissociative chemisorption of CF_2 on Si is much larger than that on SiO_2. An F-to-Si ratio of 3 is measured for the SiO_2 sample, giving a F-to-C ratio in the range of 2-3 and suggesting that CF_2 sorbs to the surface stoichiometrically, with very little F transfer to the oxide. In contrast, an F-to-C ratio of 0.7 is measured for the silicon surface, suggesting that some dissociation of surface CF_2 takes place, where the F may bind to free silicon bonds and result initially in the production of some volatile products, or diffuse into the lattice.

Much more information can be gleaned by observing the XPS spectra directly for the Si(2p), C(1s), and F(1s) peaks as provided in Figures 6-4 to 6-6 where comparison to background peak heights measured on Ar^+ sputtered silicon is provided for reference. First, comparing the Si(2p) peaks for "clean" Ar^+ bombarded silicon versus bombarded silicon exposed to large fluences of CF_2 (>1000L; Figure 6-4) shows two major peaks in each case, but markedly different peak position. The nominally "clean" Ar^+ bombarded silicon shows a Si-Si_x peak, nominally at 99.4 eV [Chuang, 1980]), and a large O_2-Si peak at ~4 eV larger binding energy [Feldman and Mayer, 1986] due to oxidation of the "sticky" damaged silicon surface in the vacuum transfer to the XPS facility. It should be noted that the individual Si-F_x (x=0 to 3) peaks cannot be resolved in the 2 eV resolution of the XPS analyzer as discussed in Chapter 5, such that the lower binding energy peak is a convolution of both types when surface fluorine is present. In contrast, the CF_2

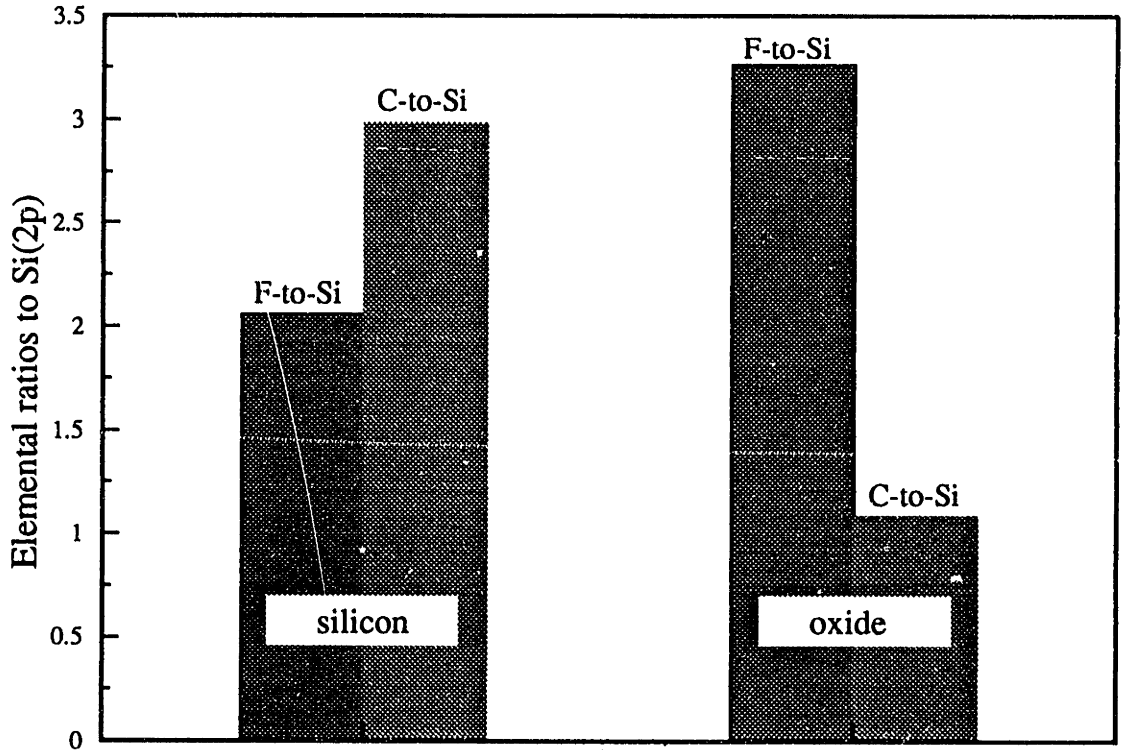

	silicon	silicon dioxide
F-to-Si	2.05	3.26
C-to-Si	2.98	1.08

Figure 6-3. Calculated C-to-Si and F-to-Si elemental ratios from XPS studies of CF2 exposed Si and SiO2 surfaces

a)

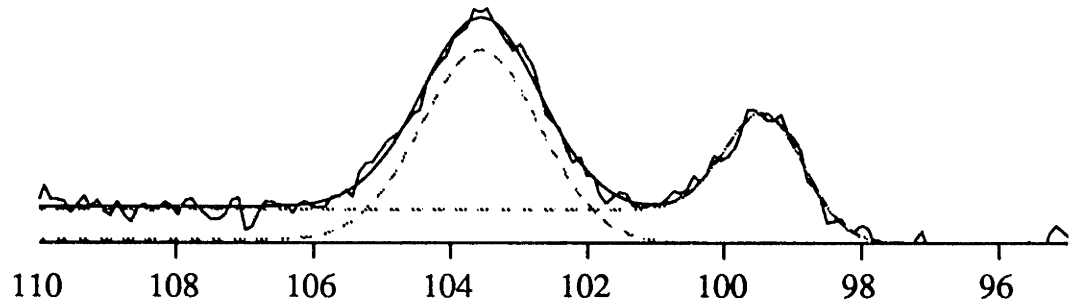

b)

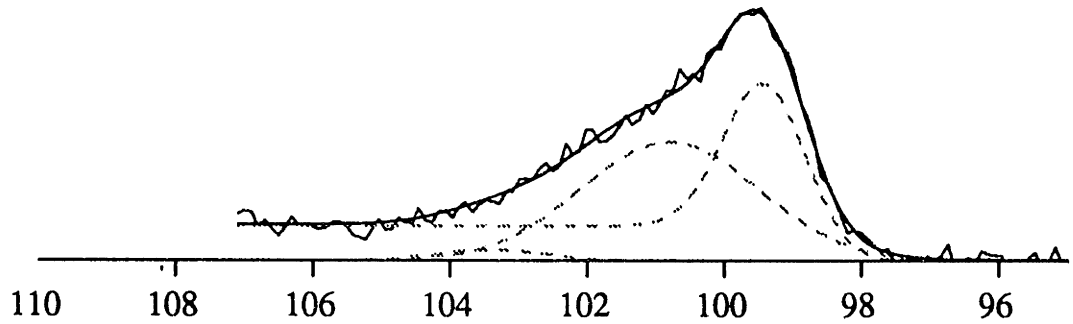

Figure 6-4. Comparison of Si(2p) XPS spectra of a) "clean" Ar+ sputtered silicon with b) silicon exposed to a CF_2 flux of 3.0×10^{16} for 5 minutes (>1000 L).

a)

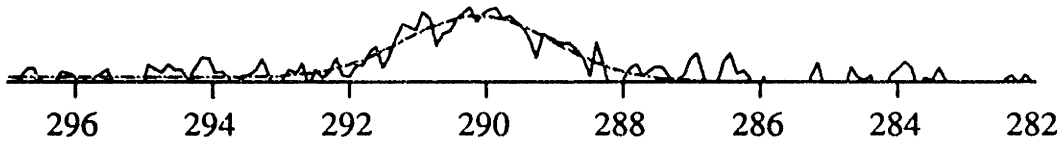

BINDING ENERGY (eV)

b)

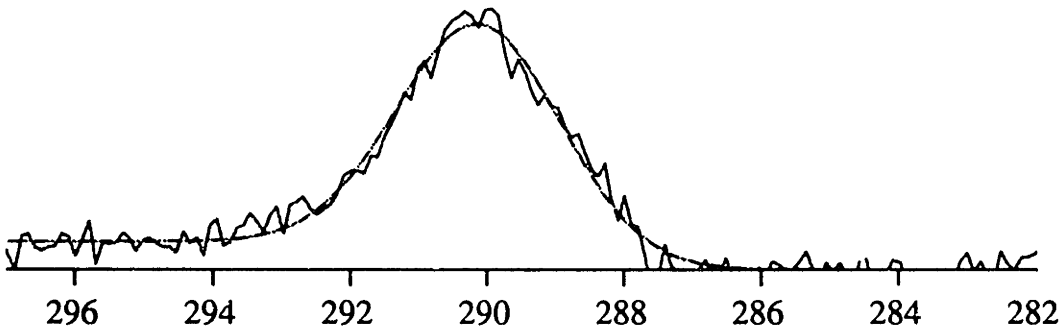

BINDING ENERGY (eV)

Figure 6-5. Comparison of C(1s) XPS spectra of a) "clean" Ar+ sputtered silicon with b) silicon exposed to a CF_2 flux of 3.0×10^{16} for 5 minutes (>1000 L).

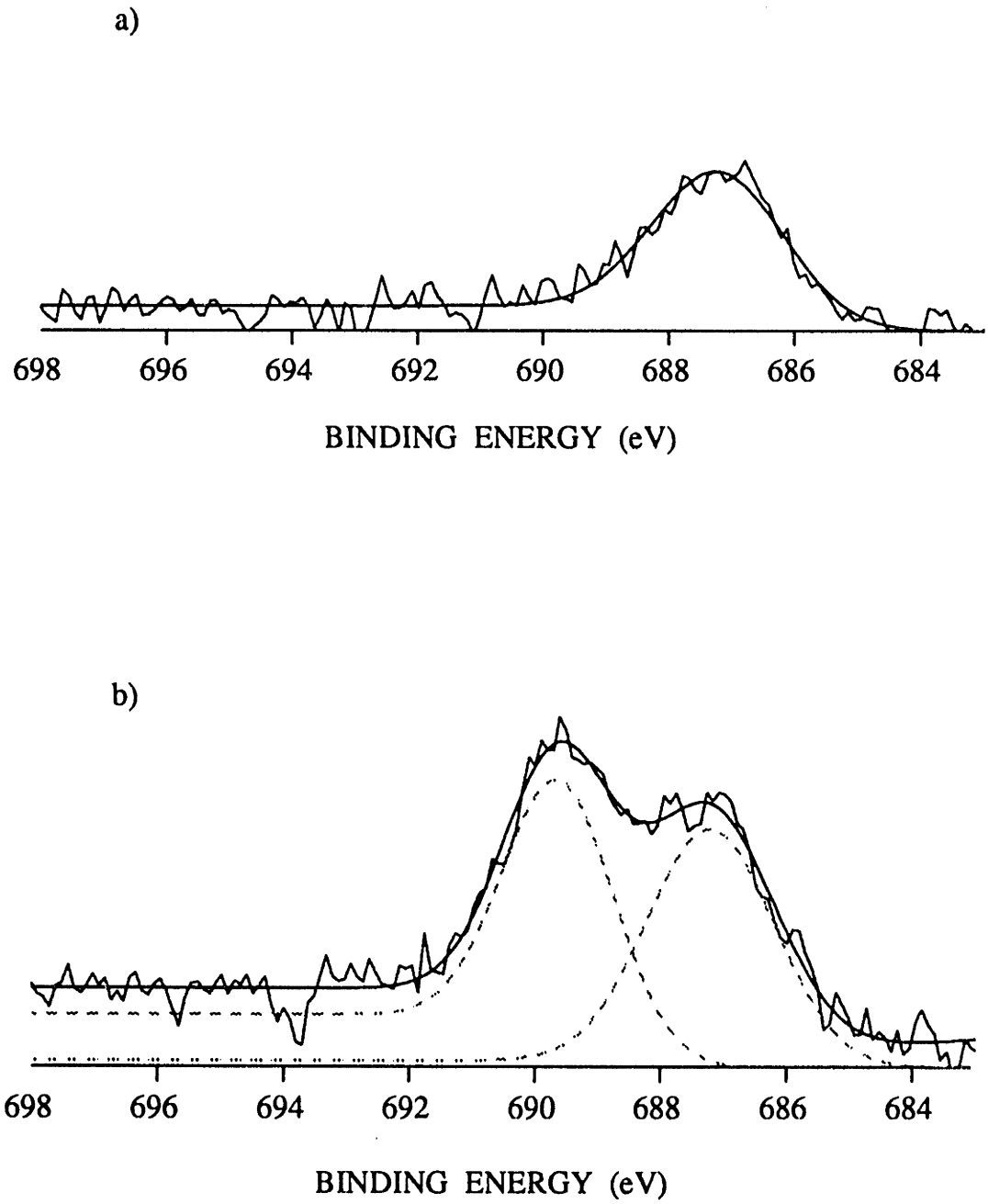

Figure 6-€. Comparison of F(1s) XPS spectra of a) "clean" Ar+ sputtered silicon with b) silicon exposed to a CF_2 flux of 3.0×10^{16} for 5 minutes (>1000 L).

exposed sample (Figure 6-4b) shows little or no Si-O_2 peak since the Si sample has been passivated to oxygen uptake by the formation of a fluorocarbon overlayer. Instead, a peak appears shifted approximately 2eV (nominally at 101.3 eV) from the primary Si-Si_x (Si-F_x) peak, ostensibly due to the production of silicon carbide (Si-CF_x) bonds with the chemisorbed CF_2 species. The presence of this silicon-carbide peak has been well documented in XPS studies of fluorocarbon plasma etched silicon [Thomas et al, 1987; Yun et al., 1990; Oehrlein, 1986]. Some of the broadening in the primary Si peak may be due to the formation of Si-F_x bonds as discussed in Chapter 5. Only one type of C(1s) peak is observed in Figure 6-5 for the CF_2 exposed silicon, which matches the 283 eV peak position of adventitious carbon contamination (e.g. Si-C and C-C), suggesting the majority of the carbon on the surface may be involved in a single bond state. This observation is in contrast to those of Langan et al.[1989] who observed two distinct carbon peaks at much lower CF_2 fluences, attributed to F_2-C(1s) and Si-C(1s), demonstrating the transfer of F from some of the sorbed CF_2 to free silicon sites. Oehrlein et al. [1989] have resolved the various C-F_x species on CF_4/H_2 etched silicon surfaces, showing an approximate 2.5 eV shift to the C(1s) XPS peak for each additional bound fluorine. It is possible than we did not scan to high enough binding energy to observe a secondary C(1s) feature. Figure 6-6, however, shows the growth of two separate F(1s) peaks after F exposure. The peak nominally at 687 eV is due to F_x-Si bonded fluorine [Oehrlein et al., 1989], and is substantially larger than background levels, suggesting some spontaneous F transfer from the sorbed CF_2 to the silicon lattice is taking place. The second peak shifted to ~2 eV higher binding energy is due to carbon bonded fluorine (F_2-C) as discussed by Langan et al [1989], suggesting that both dissociated and undissociated CF_2 species exist on the exposed silicon surface.

A similar set of data is presented for the spontaneous interaction of CF_2 with the Ar^+ bombarded SiO_2 surfaces in Figures 6-7 to 6-9. Single Si(2p) peaks are observed in Figure 6-7

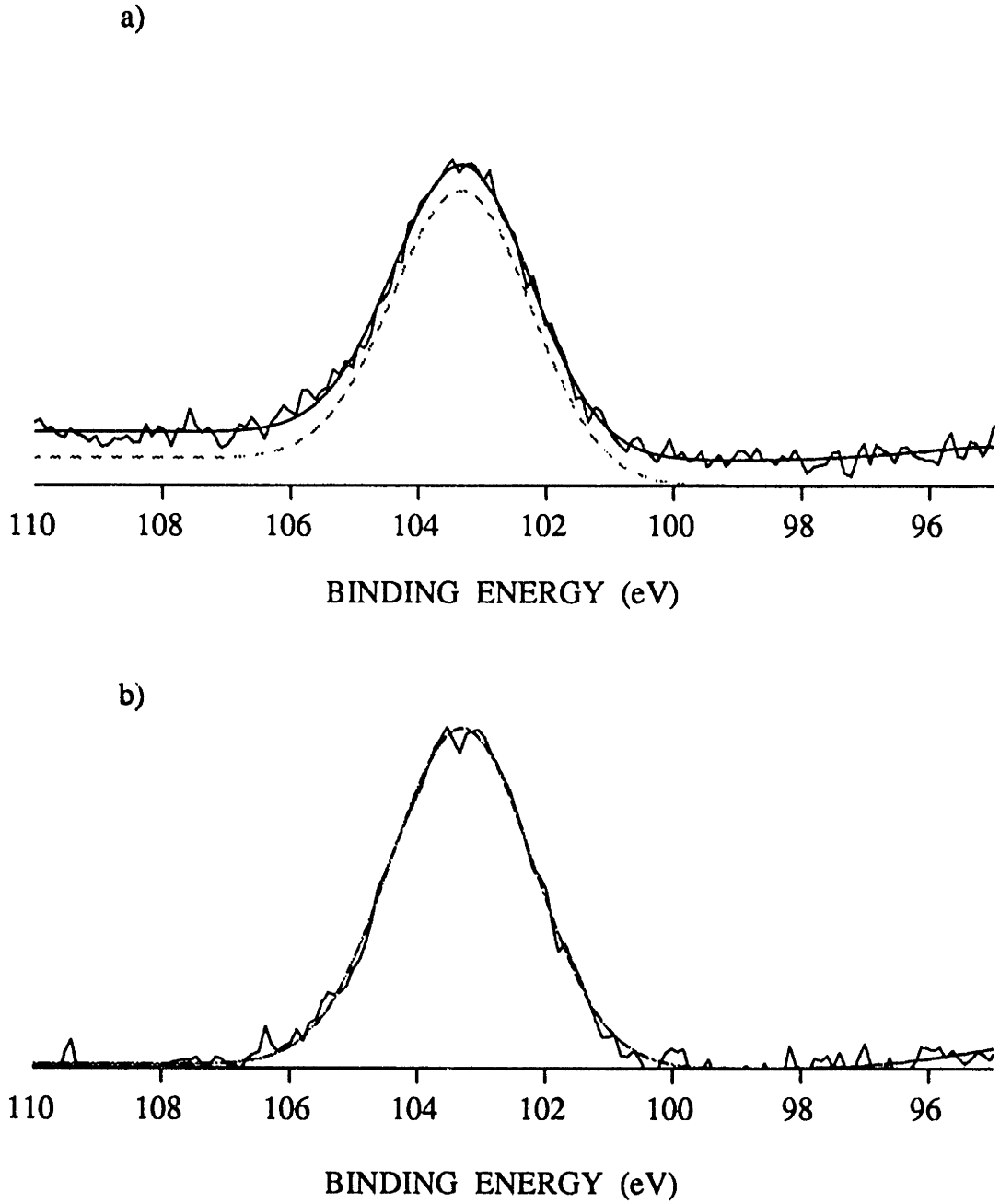

Figure 6-7. Comparison of Si(2p) XPS spectra of a) "clean" Ar+ sputtered SiO_2 with b) SiO_2 exposed to a CF_2 flux of 3.0×10^{16} for 5 minutes (>1000 L).

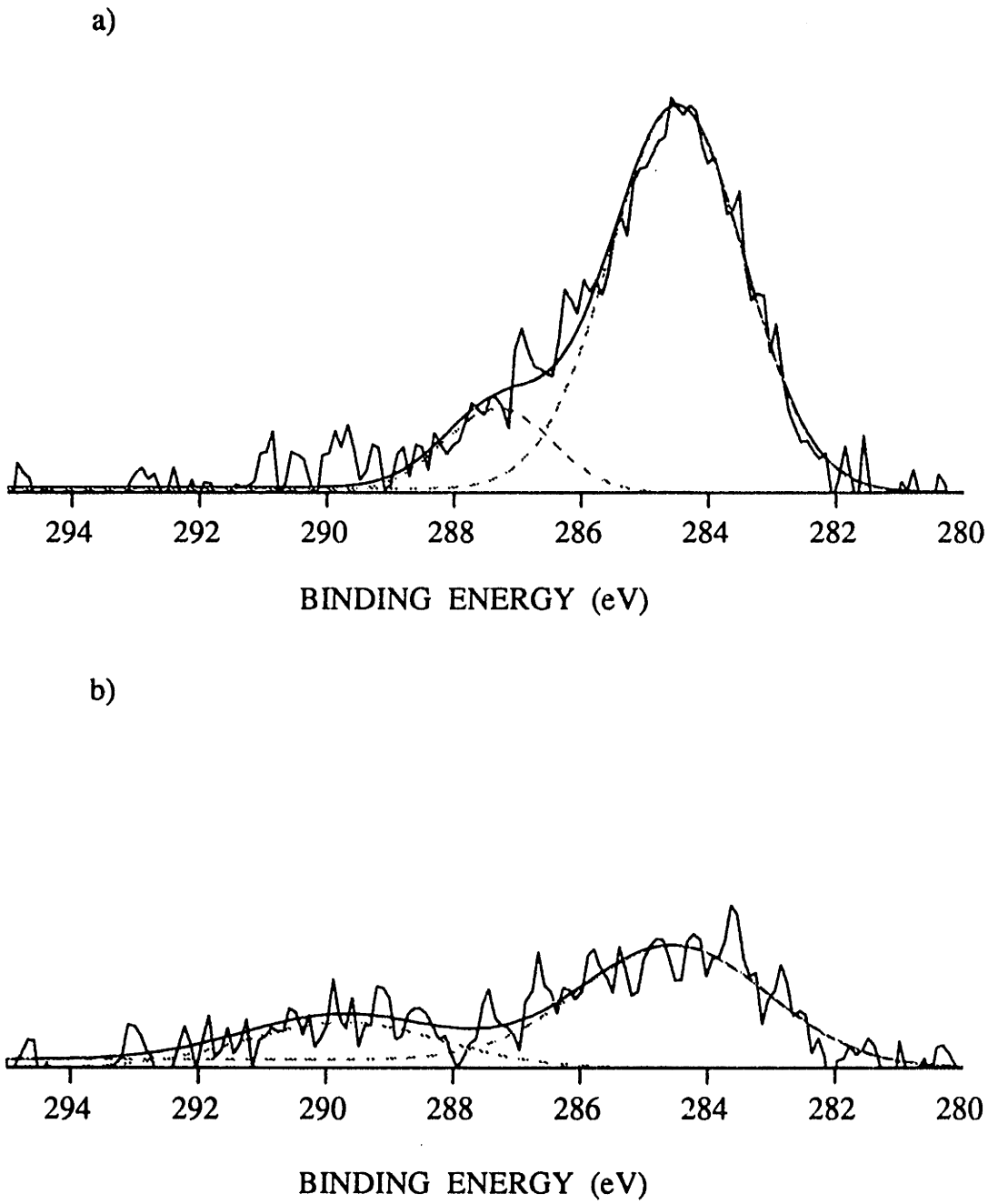

Figure 6-8. Comparison of C(1s) XPS spectra of a) "clean" Ar+ sputtered SiO_2 with b) SiO_2 exposed to a CF_2 flux of $3.0x10^{16}$ for 5 minutes (>1000 L).

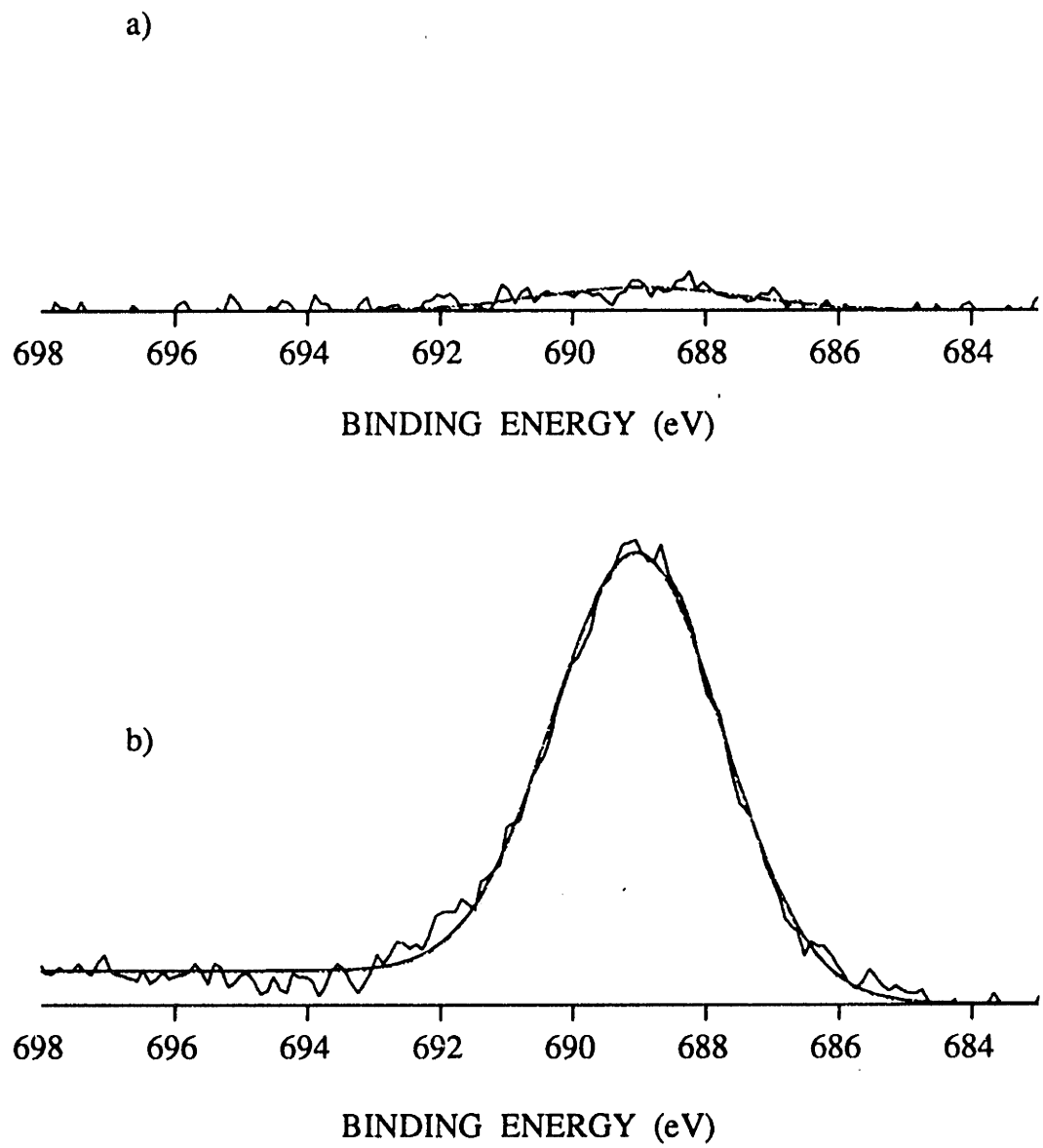

Figure 6-9. Comparison of F(1s) XPS spectra of a) "clean" Ar+ sputtered SiO_2 with b) SiO_2 exposed to a CF_2 flux of $3.0x10^{16}$ for 5 minutes (>1000 L).

suggesting only Si-O_2 bonded silicon is present with or without CF_2 exposure. Presence of a substantial fraction of carbon bonded silicon would have resulted in a resolvable low binding energy feature in the Si(2p) spectra. This observation supports the contention made in Chapter 7 that CF_2 resides on oxygen sites on SiO_2, and not on silicon sites. A preference to oxygen surface sites is suggested also by the *ab initio* thermochemical calculations of Jenichen and Johansen [1988], and by the observation of COF_2 by-production in the fluorocarbon plasma etching of SiO_2 [Butterbaugh, 1990]. The C-1s peak behavior (Figure 6-8), however, clearly indicates that two different types of surface carbon are present on CF_2 exposed SiO_2. The peak at higher binding energy (nominally 291.3 eV) has been attributed to doubly fluorinated carbon [Langan,1988], while the second peak is attributed to non-fluorinated surface carbon and is largely comprised of background carbon. Within our resolution limits, it is impossible to resolve the chemical bonding state of the background carbon (e.g. whether is it oxygen or silicon bound), however, the absence of a Si-C feature in the Si(2p) spectra would suggest it is largely oxygen bound. These findings are in agreement with the observations of Langan et al. [1989] discussed above, and suggest that very little dissociate adsorption of CF_2 on SiO_2 takes place. Figure 6-9 further supports this hypothesis since only one type of F-1s peak is observed on the oxide sample, thought to be carbon bonded (F-C-F(1s)) fluorine, whereas both silicon bonded and carbon bonded F-1s signals were hypothesized in the case of CF_2-silicon interaction.

Finally, mass spectra of silicon and SiO_2 samples exposed to CF_2 were studied in an effort to detect the appearance of fluorinated etching products such as SiF_4 and SiF_2. Small AMU 85(SiF_3^+, COF_3^+) and AMU 66(SiF_2^+, COF_2^+) mass peaks were found during the exposure of a Si sample to CF_2 without the simultaneous presence of ions. However, both of these peaks were present in high resolutions scans of the CF_2 beam, and of the chamber background. Increases in the height of SiF_x^+ fragment peaks with the insertion of the silicon sample were not significant

in comparison to the large background levels of COF_x^+-type fragments. SiF_3^+ and SiF_2^+ peaks measured in SiO_2 exposure to CF_2 were also not significantly above background levels. These observations are consistent with the inability of CF_2 to etch silicon or silicon dioxide in the steady-state.

6.2 Yield Studies of Ar^+/CF_2 Etching of Si and SiO_2

Interactions with Polysilicon

Although carbonaceous surface films have been identified as the predominant mechanism for SiO_2-to-Si etching selectivity in CF_4/H_2 plasmas, as discussed in Chapter 1, the relative importance of direct sticking of gas-phase fluorocarbon free radicals versus carbon ion implantation or redeposition of sputtered fragments was unclear at the start of this thesis. The initial sets of studies presented here examine the degree to which silicon etching by Ar^+ can be suppressed through the sticking of gas-phase CF_2 radicals and subsequent formation of fluorocarbon surface films. Although the studies of spontaneous CF_2 interactions with silicon and SiO_2 discussed above indicate that neither etching nor substantial surface polymer growth takes place, the addition of simultaneous Ar^+ bombardment had the potential of enabling either of these processes. It was expected that the reaction between SiO_2 and chemisorbed CF_2 could be enabled through the "ion-mixing" of CF_2 into the oxide lattice, where hundred eV ions ensure the breakage of multiple surface bonds, surmounting the activation barrier to CF_2 dissociation on SiO_2. Similarly, it was possible that the CF_2 "self-sticking" coefficient might be increased due to ion-induced production of active "sites", enabling the propagation of thick fluorocarbon polymer films. Net growth of surface films are possible in this scenario only if the rate of CF_2 sorption is larger than the rate of fluorocarbon removal by ion sputtering.

Figure 6-10 shows the measured suppression in silicon etching yields (Si per incoming

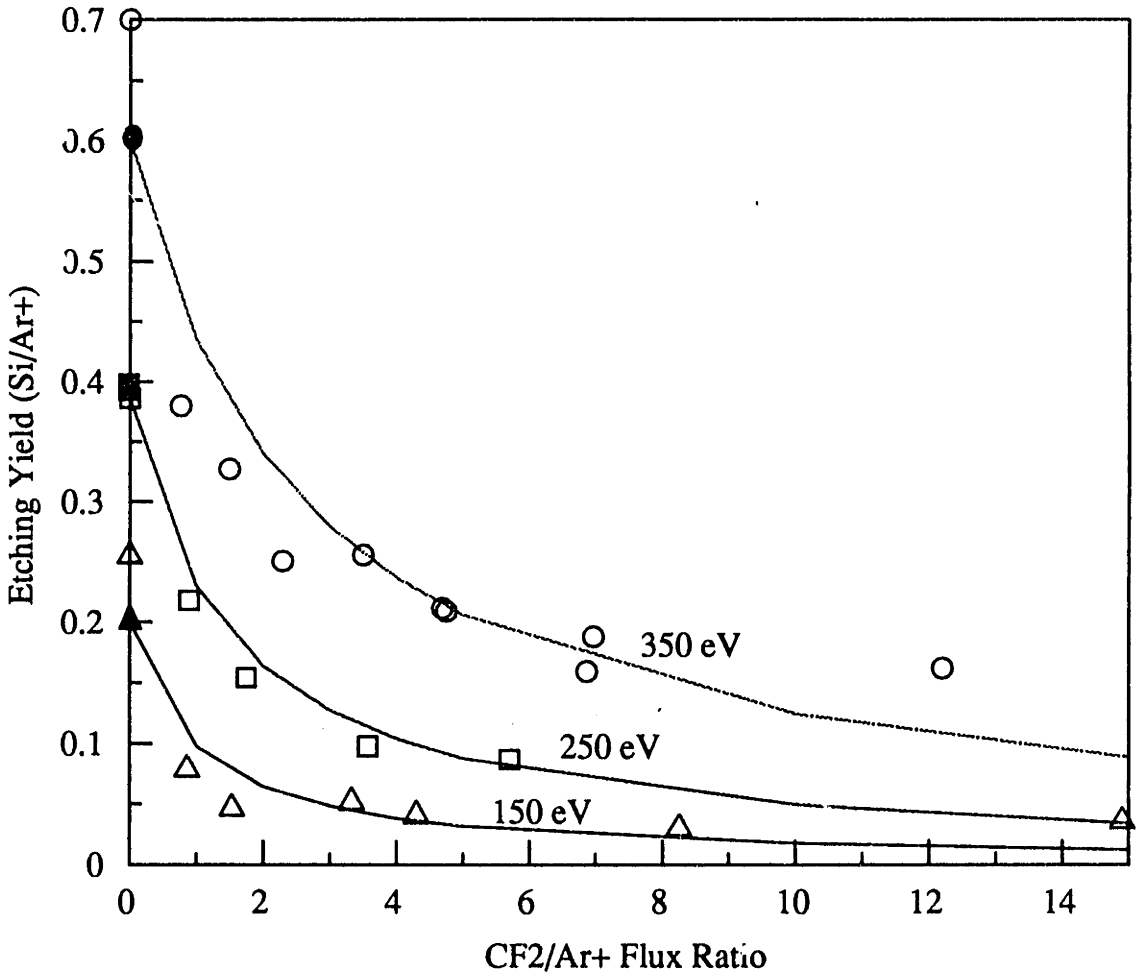

Figure 6-10. Measured silicon etching yield versus CF2/Ar+ flux ratio. Solid lines represent model results.

Ar^+) with increasing CF_2/Ar^+ flux ratio at ion energy levels of 150, 250 and 350 eV. Baseline sputtering rates measured in a clean reactor system were in good agreement with literature values, but were found to drift upwards once the ion gun was contaminated with fluorocarbon residues (filled versus unfilled symbols). Etching yields at all energies intially fell off very sharply with increasing CF_2/Ar^+, due to the high sticking probability of fluorocarbon radicals on clean, "damaged" silicon which is rich in surface dangling bonds. The suppression effect, however, saturated at non-zero etching rates at all energy levels investigated, indicating the presence of a thin steady-state $Si_xC_yF_z$ surface film, the thickness and composition of which is ion energy dependent. Although the Ar^+/CF_2 exposed polysilicon surfaces looked visually "smeared" as if a substantial surface film was present, a CF_2-saturated surface returned to the baseline Ar^+ sputtering rate within one interferometry cycle after the CF_2 flow was stopped. Given ion fluxes on the order of $10^{15}/cm^2$-s and sputtering yields of surface carbon species on the order of 0.01 to 0.1 indicated that the fluorocarbon layers formed were at most several monolayers thick. The growth of the passivating fluorocarbon films is self-limiting due to both the decreased sticking probability of CF_2 on teflon-like surfaces, and the competition between polymeric chain propagation and physical sputtering of fluorocarbon fragments. Joyce [1987] found that ion bombardment of CF_3 radicals chemisorbed on Si and SiO_2 surfaces resulted largely in the removal of these species, rather than their dissociation and incorporation into the fluorocarbon surface film. The inability of large CF_2 fluxes to completely stop the silicon etching process, as is observed in CF_4/H_2 plasma etching at large hydrogen levels [Coburn, 1981], suggests that the carbonaceous content of the plasma ions is more important in determining selectivity behavior. We cannot, however, rule out the possibility that CF radicals have a higher sticking probability on "teflon-like" surfaces, allowing them to contribute significantly to the propagation of thick passivating films.

We studied the dependence of this suppression effect on the silicon substrate temperature and the absolute flux of bombarding ions at constant CF_2/Ar^+ flux ratios. No significant change in silicon etching yield was seen over a 3x increase in ion flux (250 eV Ar^+) at a variety of CF_2/Ar^+ flux ratios as shown in Figure 6-11, validating the use of this ratio as a dimensionless system parameter. Modeling results indicate that a direct dependence of etching rate on absolute ion flux is expected in the instance where the main removal mechanism for surface CF_x fragments is thermal reaction/desorption [Butterbaugh, 1990], instead of an ion-induced reaction or sputtering process. The etching rate suppression effect was found to be dependent on substrate temperature at low CF_2/Ar^+ ratios, as shown in Figure 6-12, where the etching rate was found to rise sharply and exceed baseline physical sputtering levels at a sufficiently large substrate temperatures. This effect may be interpreted in terms of a two step mechanism which involves: 1) reduced CF_2 physisorption coverage on the "teflon-like" surface layer, leading to a reduction in the CF_2 chemisorption coverage and exposure of the underlying Si-CF_x "bridging" layer to incoming ions; 2) thermal enhancement in the rate of dissociative chemisorption of CF_x fragments i.e fluorine transfer to available silicon sites. This interpretation predicts the CF_2 flux dependence of the "break-point" temperature, and brackets the CF_x-surface physisorption energy at 15-20 Kcal/mole, consistent with the data in Figure 6-12. The effect is not seen at large CF_2 fluxes shown in Figure 6-12 because the incoming radical flux is large enough to maintain CF_2 surface-saturation even at high temperatures. A fluorine transfer reaction leading to the spontaneous production of Si-F_x surface bonding has also been hypothesized by Langan et al. [1988] when the total dicarbene radical coverage is relatively low. The temperature dependence of our data may reveal the activation barrier to this fluorine transfer process, which allows subsequent ion-enhanced reaction of the fluorinated surface sites.

Mass spectrometric and XPS studies (section 6.4) were performed to ascertain whether F

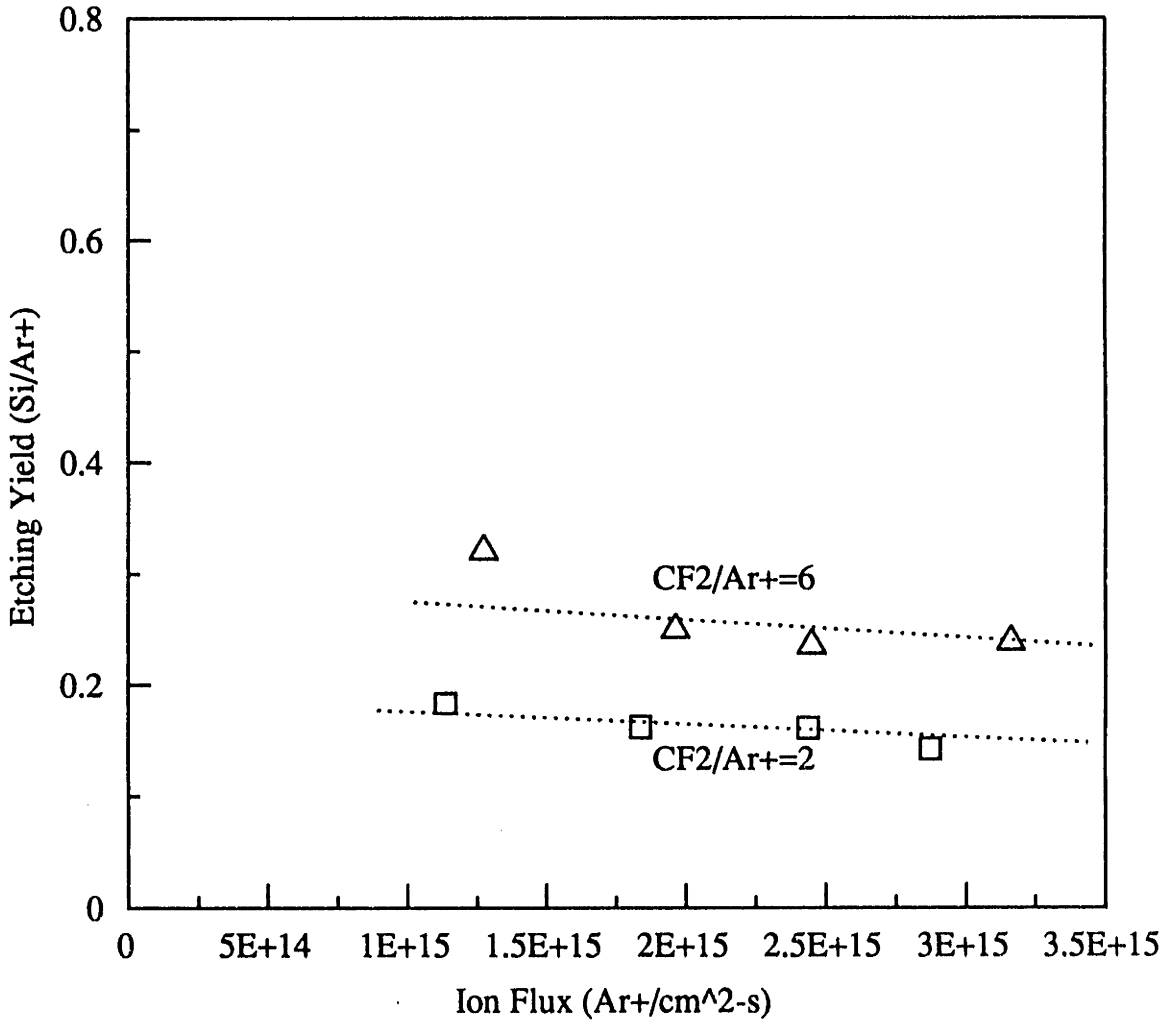

Figure 6-11. Measured silicon etching yield versus absolute Ar+ flux. at constant CF2/Ar+.

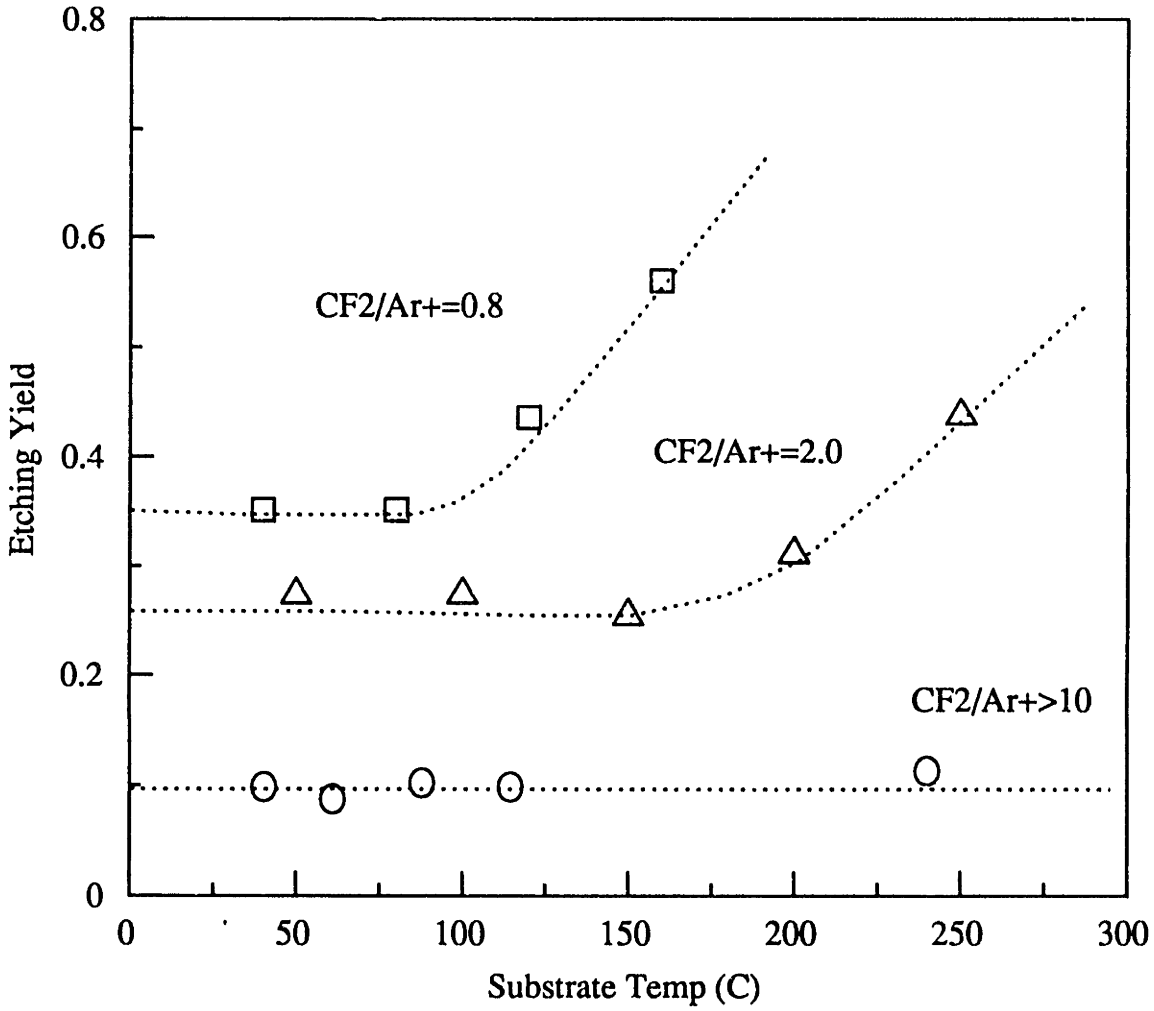

Figure 6-12. Effect of substrate temperature on CF2/Ar+ silicon etching yields.

transfer from chemisorbed CF_2 to the silicon lattice was enhanced due to simultaneous ion bombardment. As discussed above, interpretation of SiF_x mass spectral patterns is difficult in the presence of the CF_2 beam due to the overlap of COF_x type species with the silicon product peaks. However, a qualitative comparison can be made as in Figure 6-13, where the AMU 85 (SiF_3^+, COF_2^+) peaks are compared at the same CF_2 flux, with and without Ar+ ion flux. The AMU 81 peak ($C_2F_3^+$) is a direct signature of the CF_2 beam background, and can be used for relative comparison to AMU 85. The presence of energetic ion bombardment (350 eV Ar^+) results in a factor of 2-3 enhancement in AMU 85-to-AMU 81 peak ratio, suggesting the production of significant quantities of SiF_4 via bombardment of CF_2 chemisorbed on silicon. The proportion of SiF_x products relative to sputtered products cannot be ascertained due to the large chamber background and overlap of cracking patterns. However, it can be concluded that ion bombardment and "mixing" facilitate some transfer of fluorine to silicon sites, enabling the production of volatile products. Defluorination of the surface carbon is supported by XPS data as well. The role of the remaining carbon is to "poison" silicon surface sites to the uptake of fluorine, requiring physical sputtering for "etching" of these sites.

Interactions with Silicon Dioxide

Interactions of CF_2 radicals with SiO_2 surfaces were studied in collaboration with the thesis work of Jeffery Butterbaugh [1990], where some of the results below have been previously reported. The ion-enhanced etching of SiO_2 by Ar^+/CF_2 is shown in Figure 6-14 in which the etching yield, the number of SiO_2 molecules leaving the surface per incident Ar^+ ion, is plotted against the CF_2-to-Ar^+ flux ratio for ion energies of 150, 250, and 350 eV. As in the case of polysilicon etching, after the system was exposed to HFPO, the apparent baseline physical sputtering rates were higher than in a well-cleaned system due to residual fluorocarbon

a)

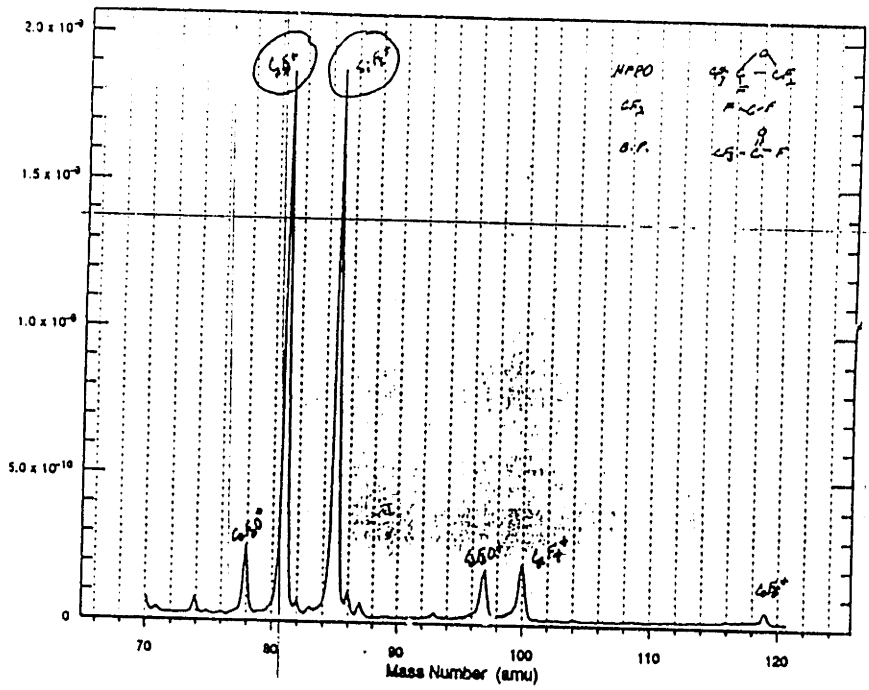

b)

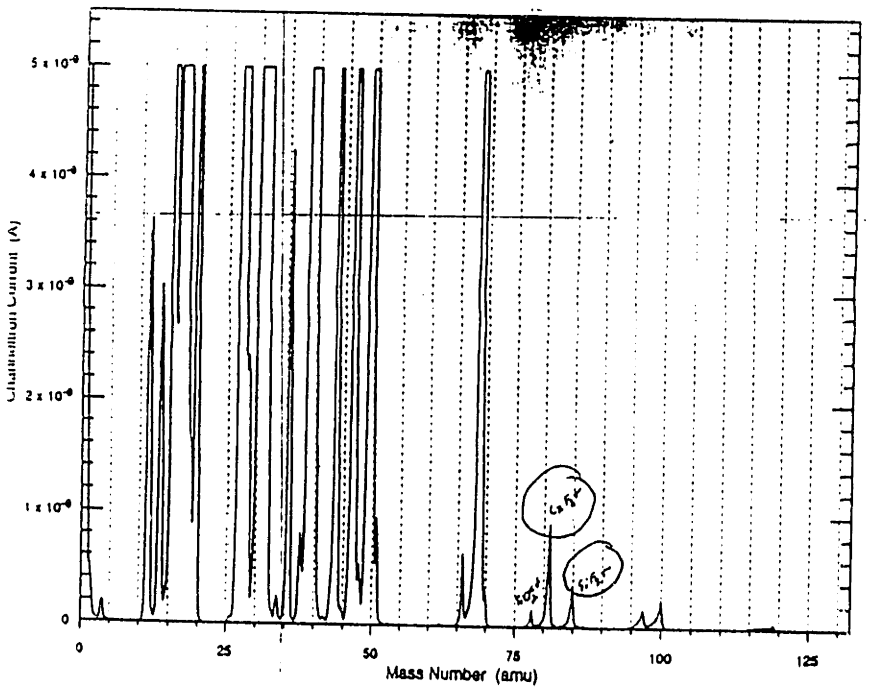

Figure 6-13. Mass spectral comparison of AMU 85 (SiF3+) to fluorocarbon background AMU 81 (C2F3+) in a) Ar+/CF2 etching of silicon versus b) CF2 exposure only.

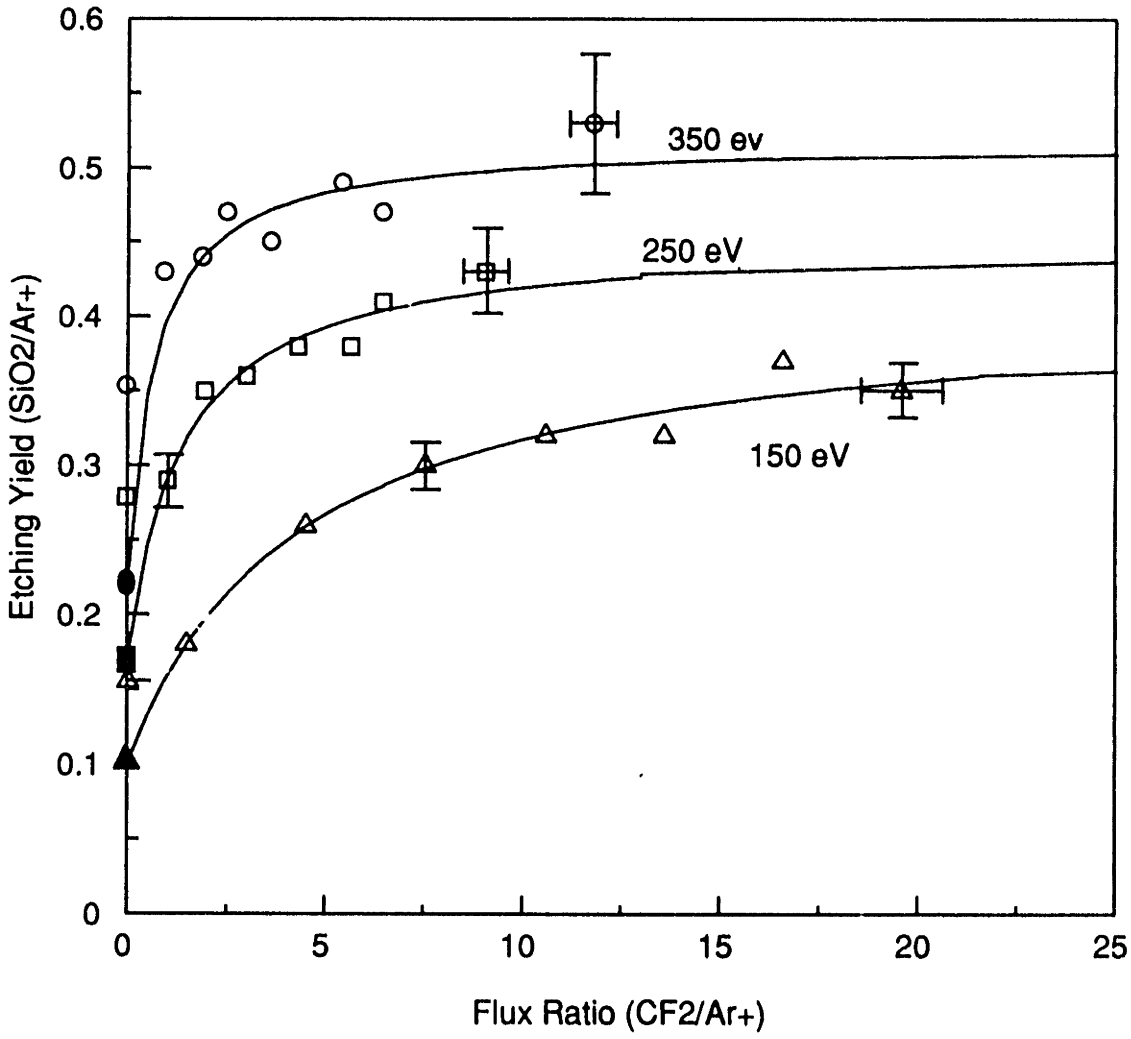

Figure 6-14. Measured SiO2 etching yield versus CF2/Ar+ ratio. Solid lines represent model results.

contamination in the ion gun. We saw no visual indications of fluorocarbon film deposition on the surface by the CF_2 and furthermore, the SiO_2 etching rate immediately returned to its baseline level without an induction period after the CF_2 flux was terminated. Results presented in Figure 6-14 indicated that the Ar^+ etching yield is enhanced by a factor of 2-3 over the baseline sputtering rate, at saturation fluxes of CF_2 to the surface. The initial rate of increase of the SiO_2 etching yield with CF_2/Ar^+ ratio is very large, due to the high sticking coefficient of CF_2 on clean, Ar^+ bombarded SiO_2. This effect is contrary to the findings of Langan et al. [1989] who did not see enhanced CF_2 chemisorption on SiO_2 after a 0.1 L 500 eV Ar^+ ion dose. The yields tend toward an asymptotic value as the ratio of CF_2 to Ar^+ increases, i.e. increasing amounts of CF_2 have less of an effect on the yield, and the yield saturation point occurs at lower flux ratios for higher energy ions. This last feature is counter-intuitive in that one would expect higher energy ions to be more efficient at removing products from the surface, causing saturation to occur at higher flux ratios. However, it is likely that the CF_2 sticking probability increases with ion energy due to two effects. First, more lattice damage is expected from higher energy ions, offering more adsorption sites (dangling bonds) and increasing the sticking probability of the CF_2 radical. Secondly, it is well known that ion bombardment of SiO_2 results in deoxygenation of the surface region due to preferential sputtering of the lighter component, effectively causing the density of available silicon surface sites to increase. These effects were discussed in Chapter 5 in conjunction with the Ar^+/F etching of SiO_2.

No measurable effect of surface temperature was noted in the Ar^+/CF_2 etching of SiO_2 over the temperature range of 25°-300°C. This is not unexpected since no thermal etching of SiO_2 by CF_2 is observed, and the CF_2 chemisorption bonds on SiO_2 are much stronger than the kT energy at these temperatures [Jenichen and Johansen, 1988]. As in the case of silicon etching, it was found that the etching yield is dependent only on the neutral-to-ion flux ratio and not on

the absolute neutral or ion flux level, as shown in Figure 6-15. It was found that any dependence of the yield on the absolute flux level is within the experimental uncertainty of this data over a 10x change in absolute flux, validating the use of this ratio as a dimensionless system parameter. The CF_2 radical interaction with SiO_2 versus silicon surfaces (Figure 6-16) illustrates the importance of fluorocarbon radicals in determining SiO_2-to-Si etching selectivity in the simultaneous presence of energetic ion bombardment. CF_2 enhances the Ar^+ etching yield of SiO_2 while suppressing that of Si, due to the formation of fluorocarbon surface films. Therefore, the selectivity of SiO_2-to-Si etching increases with increasing CF_2 flux. This selectivity effect is quantified in Figure 6-16 for an Ar^+ ion energy level of 250 eV and substrate temperature of 80°C, where SiO_2:Si selectivities of 10 (based on film etching rates) are obtained in saturation. Although these data would indicate that CF_2 radicals are a primary selectivity mechanism in the fluorocarbon plasma environment, as discussed in Chapter 7, this ratio is reversed in the presence of large atomic fluorine fluxes. We expect that the formation of passivating fluorocarbon films on silicon is very much enhanced through the presence of carbonaceous, rather than inert ions.

Mass spectrometric studies of product distributions from Ar^+/CF_2 etching of SiO_2 were inconclusive due to the presence of overlapping peaks with the cracking patterns of the CF_2 beam products, and the chamber background. Expected products include sputtered Si, SiO, and O, and ion-enhanced products such as SiF_4, SiF_2, COF_2, CO, CO_2, and O_2. However, Si^+ (AMU 28), O^+(AMU 16), O_2^+ (AMU 44), and SiO^+ and CO_2^+ (both AMU 44) are obscured by the chamber background N_2, O_2, and CO_2. Potential SiF_x^+ product peaks overlap with COF_x^+ peaks from reaction products or the CF_2 beam background.

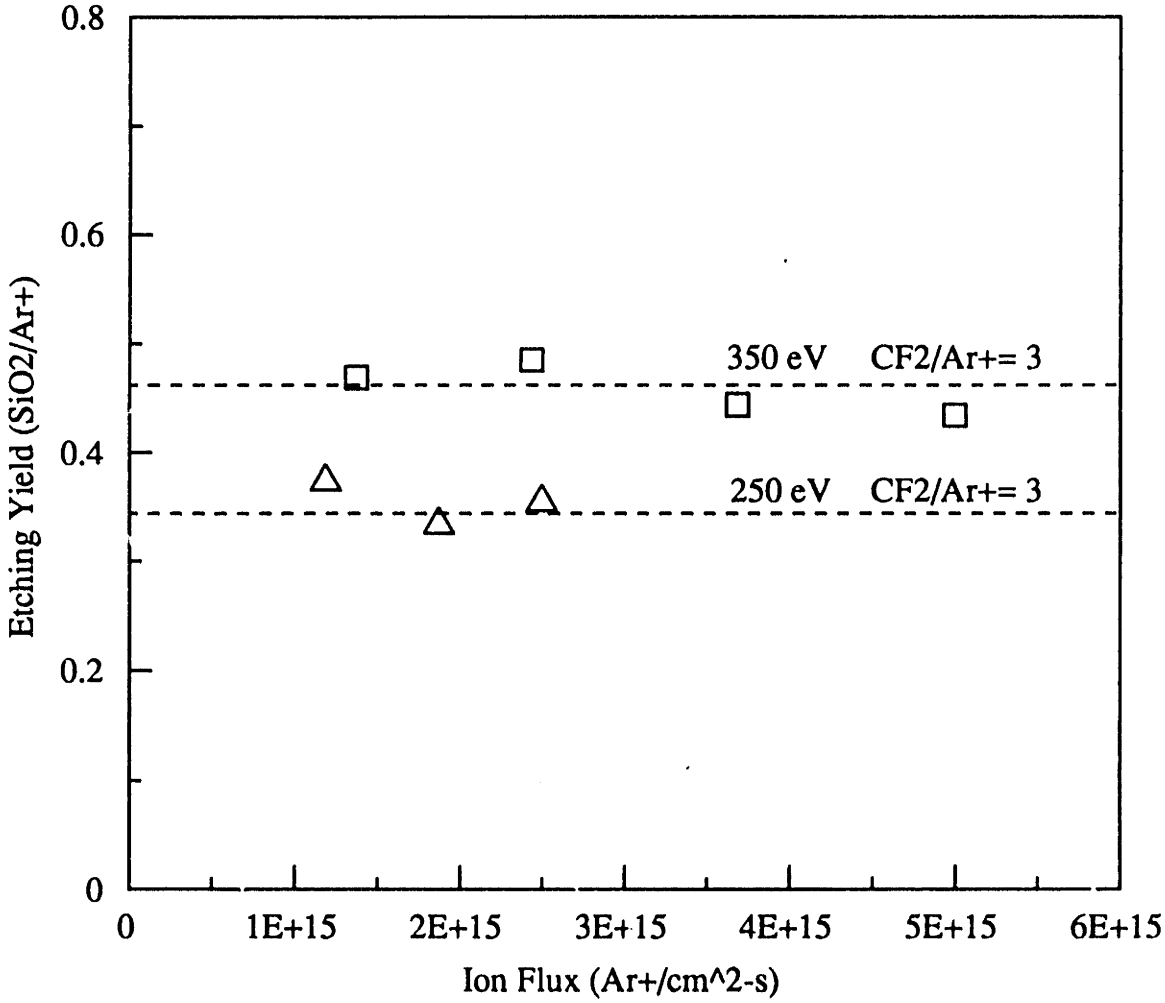

Figure 6-15. Measured SiO2 etching yield versus absolute Ar+ flux, at constant CF2/Ar+.

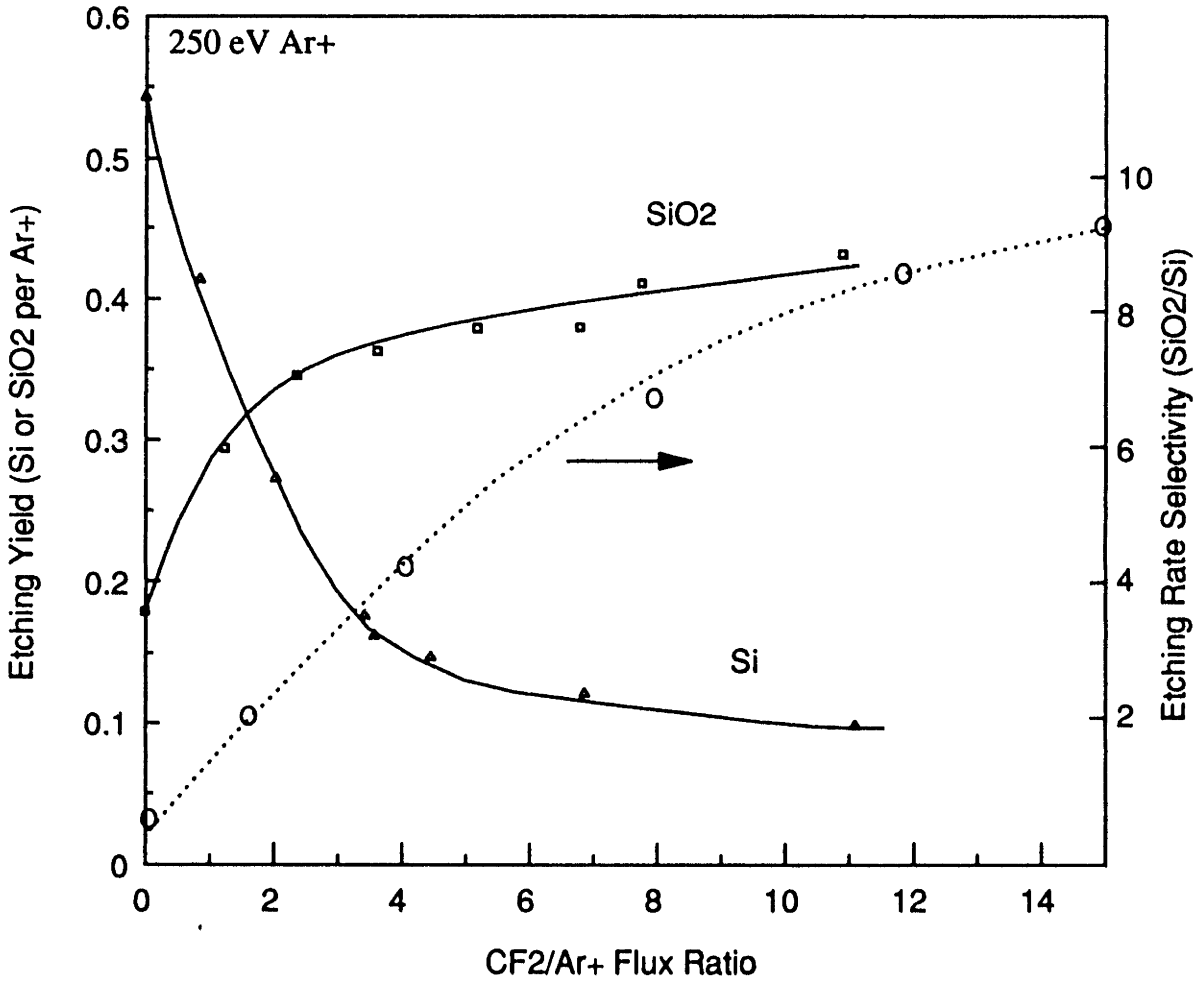

Figure 6-16. Effect of CF2/Ar+ ratio on SiO2-to-Si etching rate selectivity.

6.3 XPS Studies of Fluorocarbon Films

Interactions with Silicon

XPS studies of Si and SiO_2 surfaces simultaneously exposed to fluxes of CF_2 and Ar^+ bombardment were performed as a function of the relative flux levels and bombarding ion energy. Contrasting results were expected in comparison of the two material systems since CF_2 acts as an ion enhanced etchant for SiO_2, while it forms a fluorocarbon overlayer on silicon. As in the XPS studies discussed previously, all Si and SiO_2 samples were Ar+ sputter cleaned prior to CF_2 exposure. Considering the silicon system first, consistent with the hypothesis that the Si sputtering rate suppression mechanism involves formation of surface Si-CF_x species, we observed the increase in the surface carbon C(1s) (~283 eV) peak with increasing CF_2/Ar^+ flux ratio, at a 150 eV bombardment energy as shown in Figure 6-17. The surface binding energy of Si bonded carbon (Si-C) is reported at ~283 eV [Oehrlein et al., 1989], close to where we observe our major C(1s) peak. As discussed above, Langan et al. [1988] observed a second C(1s) peak at approximately 7 eV higher binding energy which he assigned to undissociated, sorbed CF_2 species. Joyce [1987] observed similar dual C(1s) features upon Si<100> exposure to CF_3 radicals, but noted the disappearance of the higher binding energy peak upon ion bombardment. He attributed this behavior to the preferential sputtering of undissociated sorbed CF_3 radicals. Given the relatively large ion fluences used in our experiments simultaneous with the CF_2 fluxes, it is not surprising that the main carbon feature we observe is due to silicon carbide, suggesting the dissociation and mixing of most of the chemisorbed CF_2 species. The increase in this C(1s) feature with flux ratio (Figure 6-17) mirrors the sputtering rate suppression shown in Figure 6-10.

The behavior of the Si(2p) spectrum with increasing CF_2/Ar^+ ratio at a 150 eV Ar^+ bombardment energy is shown in Figure 6-18. The bottom-most and top-most plots correspond to Ar^+ sputtering only, and CF_2 exposure only, respectively. As discussed previously, Ar^+

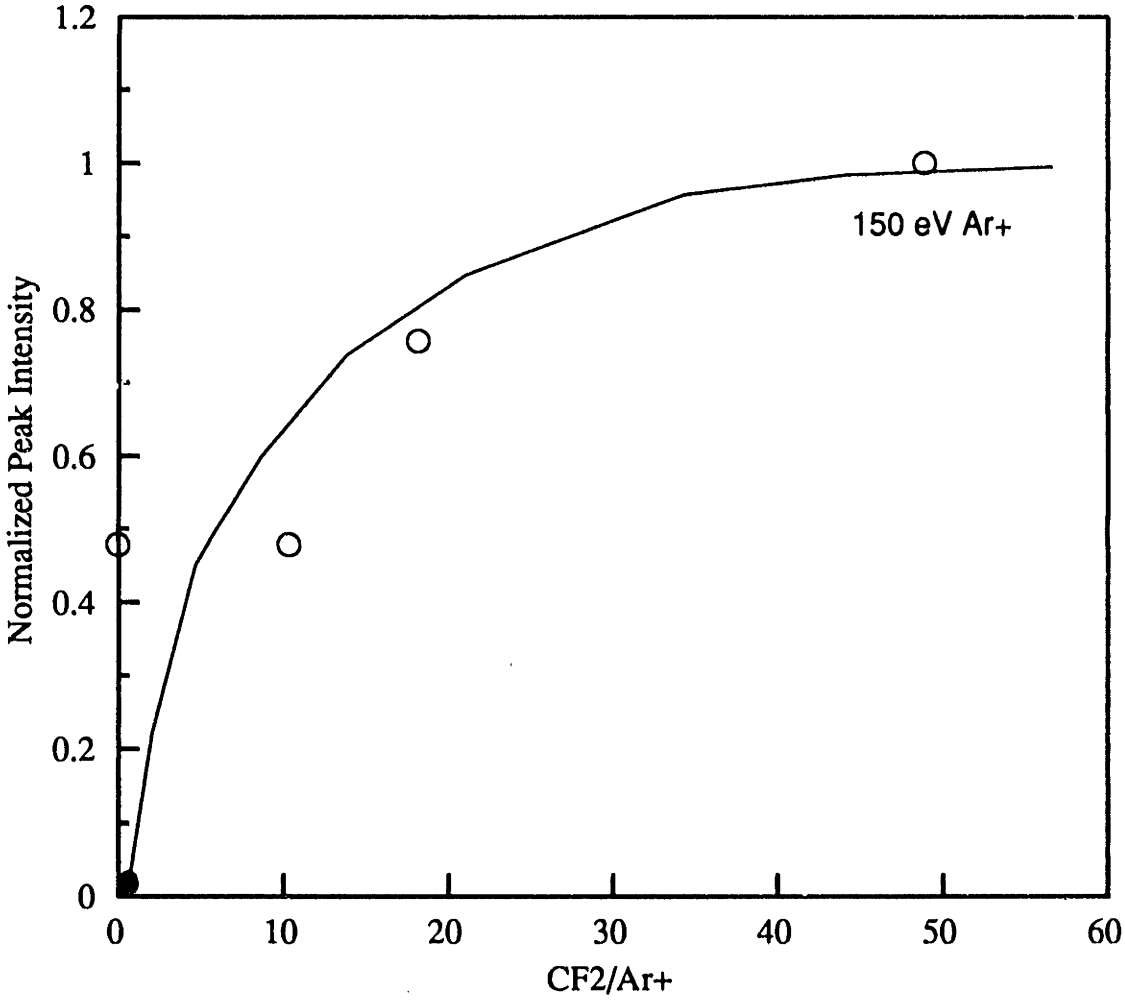

Figure 6-17. C-1s peak intensity of silicon exposed to increasing CF2/Ar+ flux ratio. C-1s peak area is corrected and normalized by total Si-2p.

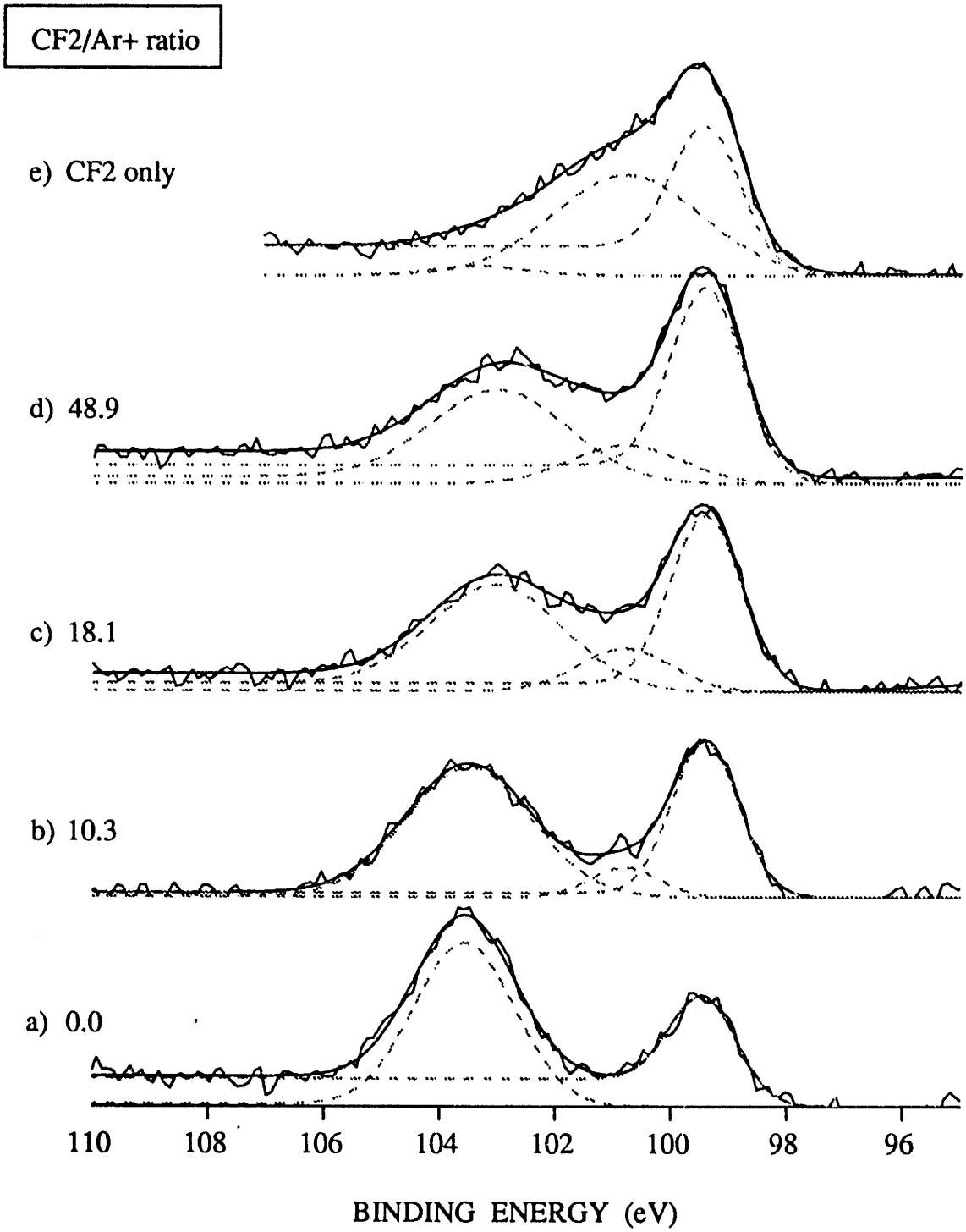

Figure 6-18. Comparison of Si(2p) spectra of silicon exposed to increasing CF_2/Ar^+ flux ratio.

sputtered silicon shows a dual peak Si-2p spectrum after transfer from the multibeam to the XPS system due to oxidation of Si^* dangling bonds, resulting in the higher (+4eV shifted) binding energy feature. The series in Figure 6-18 shows the gradual disappearance of the SiO_2 feature with increasing CF_2/Ar^+ flux ratio, due to the decrease in Si^* dangling bonds as the relative CF_2 flux increases. CF_2 exposure with no simultaneous ion bombardment results in complete coverage of surface dangling bonds, giving no available surface sites for oxidation in sample transfer. Also noted in this series is the growth of an intermediate feature which is associated with the convolution of both Si-C (101.3 eV) and Si-F_x bond formation, as discussed previously. The net result as CF_2/Ar^+ increases is the production of a continuum region between the Si and SiO_2 features which cannot be deconvoluted due to the energy resolution limitations. Also interesting to observe is the C(1s)-to-Si(2p) surface elemental ratio as the CF_2/Ar^+ ratio increases (Figure 6-19). The surface carbon incorporation increases from a stoichiometric ratio of 1:2 (C-to-Si), to about 3:1 as was previously shown in the case of no ion bombardment. The important feature of note here is that in the presence of Ar^+ ion bombardment, in "yield saturation" the C-to-Si ratio does not significantly exceed the value of unity, indicating that only strongly silicon-bonded carbon adheres to the surface in steady-state. This observation is consistent with those of Langan et al. [1989] and Joyce et al [1988] who saw the preferential sputtering of sorbed by undissociated surface CF_x radicals, and with our observation of a single C(1s) feature.

We also observed the F(1s) peak behavior in this system, as is shown as a function of CF_2/Ar^+ ratio in Figure 6-20, where the case of physical sputtering and spontaneous CF_2 interaction are shown for reference. F_x-C bonded photoelectrons are reported to be ~2 eV higher in binding energy [Oehrlein et al., 1989] than F_x-Si bound fluorine. It is evident that only one type of surface fluorine, that being silicon-bonded fluorine, is prevalent upon simultaneous CF_2 and Ar^+ bombardment. This is in contrast to the case of spontaneous CF_2 exposure of Ar^+

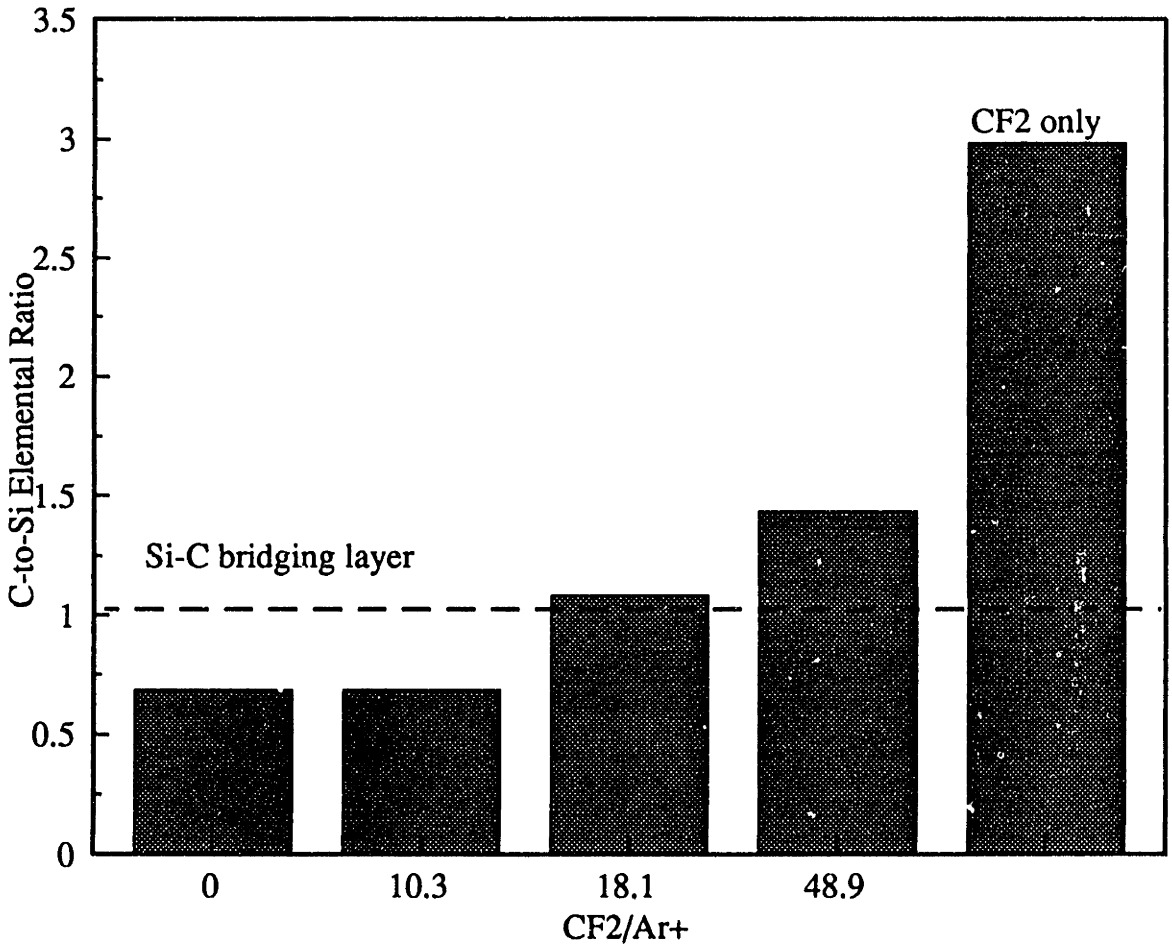

Figure 6-19. Calculated C-to-Si elemental ratios from XPS studies of Ar+/CF2 exposed silicon.

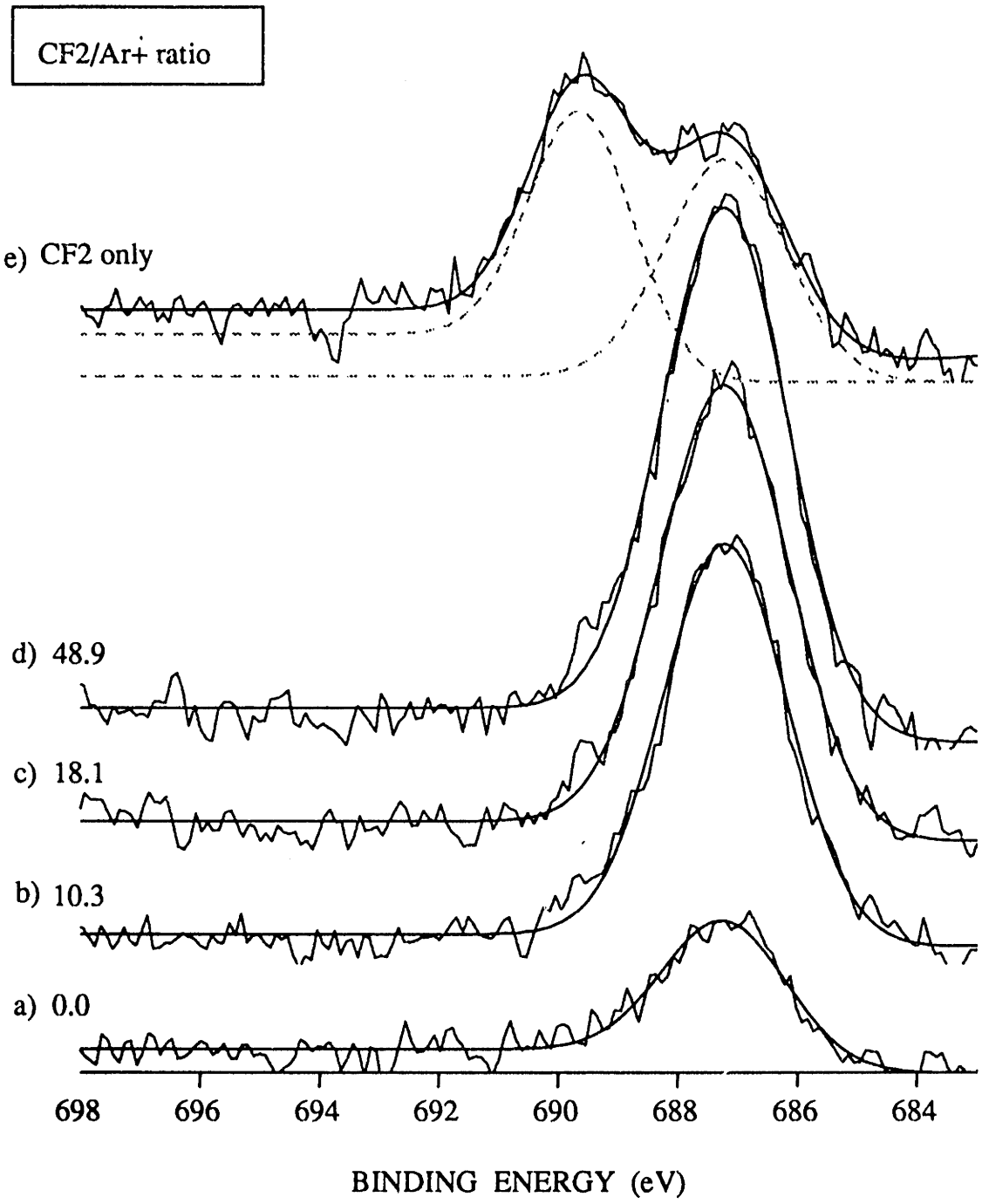

Figure 6-20. Comparison of F(1s) spectra of silicon exposed to increasing CF_2/Ar^+ flux ratio, 150 eV Ar+.

bombarded fluorine where the carbon bounded fluorine feature is observed as well, suggesting the multi-layer sorption of CF_2 species. Multi-layer adsorption was also supported by the C-to-Si ratio of 3 observed in the case of spontaneous CF_2 interaction. The surface F(1s)-to-Si(2p) ratio is shown in Figure 6-21, where the general trend observed is increasing surface fluorine to silicon with increasing CF_2/Ar^+. The most significant feature is the fact that in yield saturation, a F-to-Si ratio of 2 is observed, which in comparison to the observed C-to-Si ration of 1, suggests that the only fluorine donated to the surface comes from the CF_2 "bridging layer" [Oehrlein et al., 1989]. Neither multilayer CF_2 adsorption nor further F transfer from sorbed CF_2 radicals takes place after this layer is established; instead they desorb or are resputtered.

Trends in these various XPS peaks with increasing Ar^+ ion energy at a constant CF_2/Ar^+ of about 25 were observed. Figure 6-22 shows the behavior of the Si(2p) spectrum with increasing ion energy. As discussed in Chapter 5, increasing the ion energy increases the penetration depth and effective "mixing zone" of the ions, enabling more CF_x incorporation into the surface region. The result is the increased production of Si-F_x and Si-C bonds, as seen in the virtual broadening of the secondary Si-C/Si-F_x feature. The breadth of this high binding energy feature developed during 500 eV Ar^+/CF_2 etching versus CF_2 exposure alone would suggest that substantial fluorination of the surface silicon has resulted, in addition to silicon-carbide formation. Figure 6-23 shows the behavior of the C-to-Si and F-to-Si elemental ratios as the bombarding ion energy is increased. While the F surface concentrations remain fairly constant, retention of surface carbon is increased with increasing ion energy due to the production of silicon-carbides in the ion "mixing" process. The surface layer is effectively stoichiometrically "defluorinated" since the silicon-fluoride species are easily removed. At a 500 eV ion energy level, the C-to-F ratio is 1:1. This defluorination or "graphitization" phenomenon due to high energy bombardment of the fluorocarbon overlayer has been shown in the etching of other fluorinated polymers

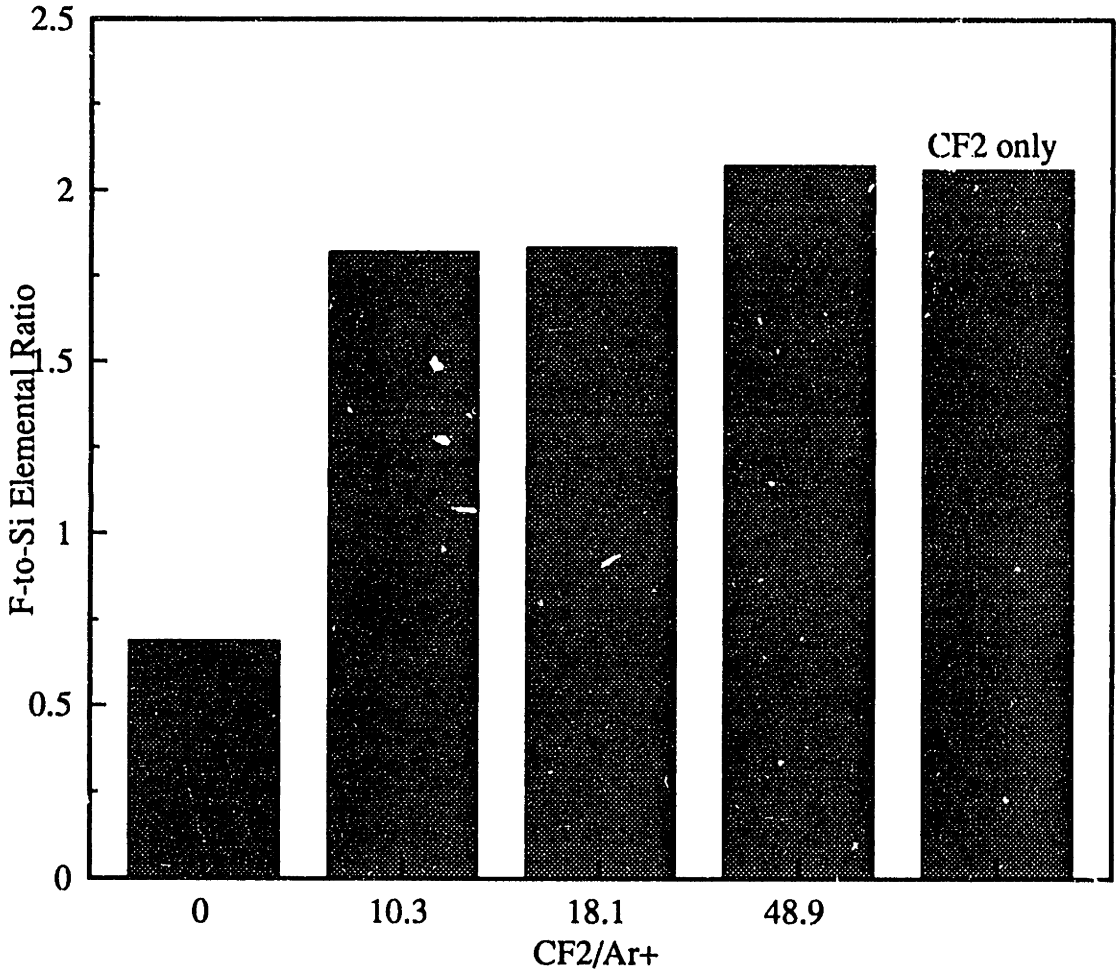

Figure 6-21. Calculated F-to-Si elemental ratios from XPS studies of Ar+/CF2 exposed silicon.

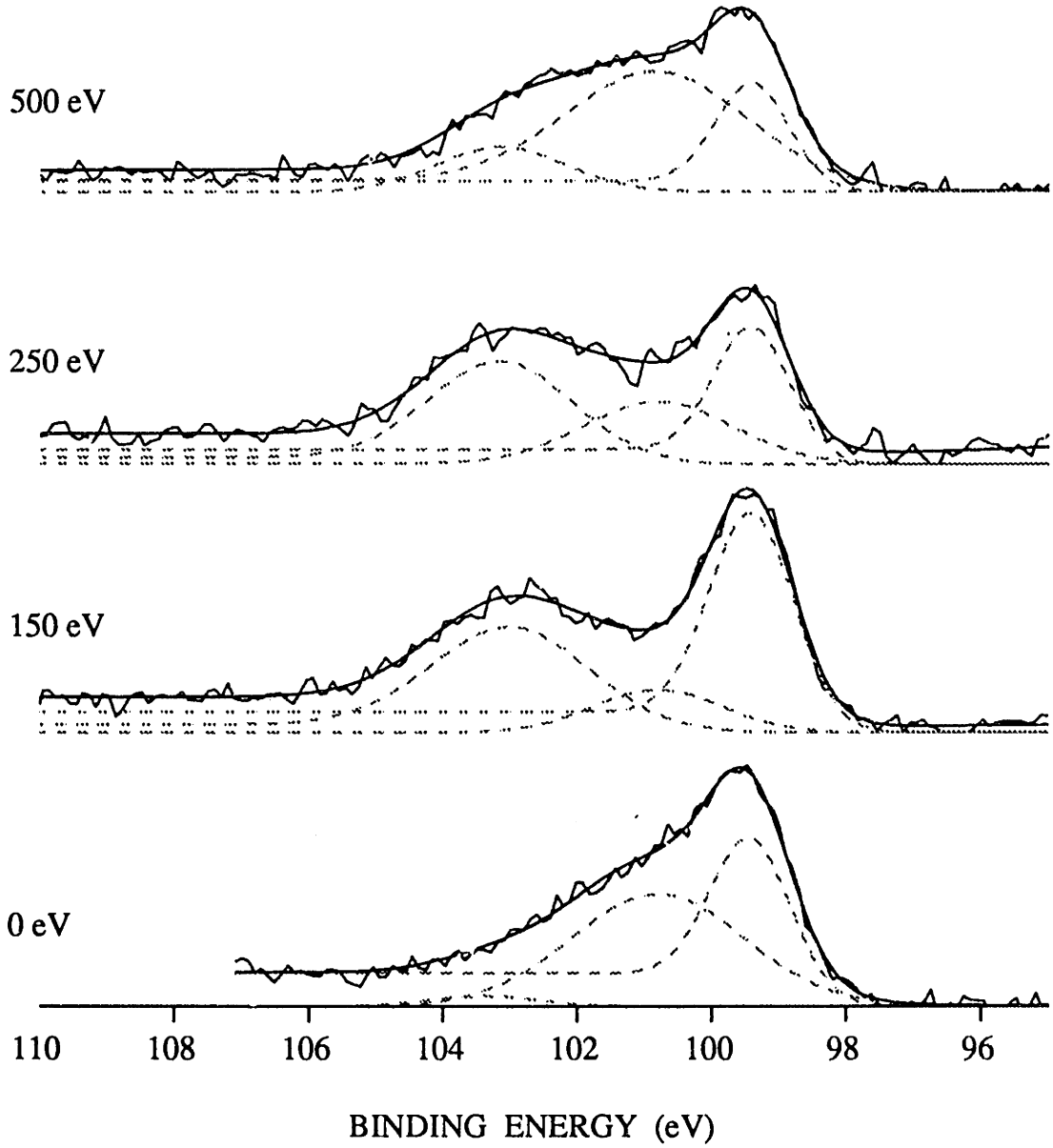

Figure 6-22. Comparison of Si(2p) spectra of silicon with increasing Ar+ energy at constant CF_2/Ar^+ =48.9.

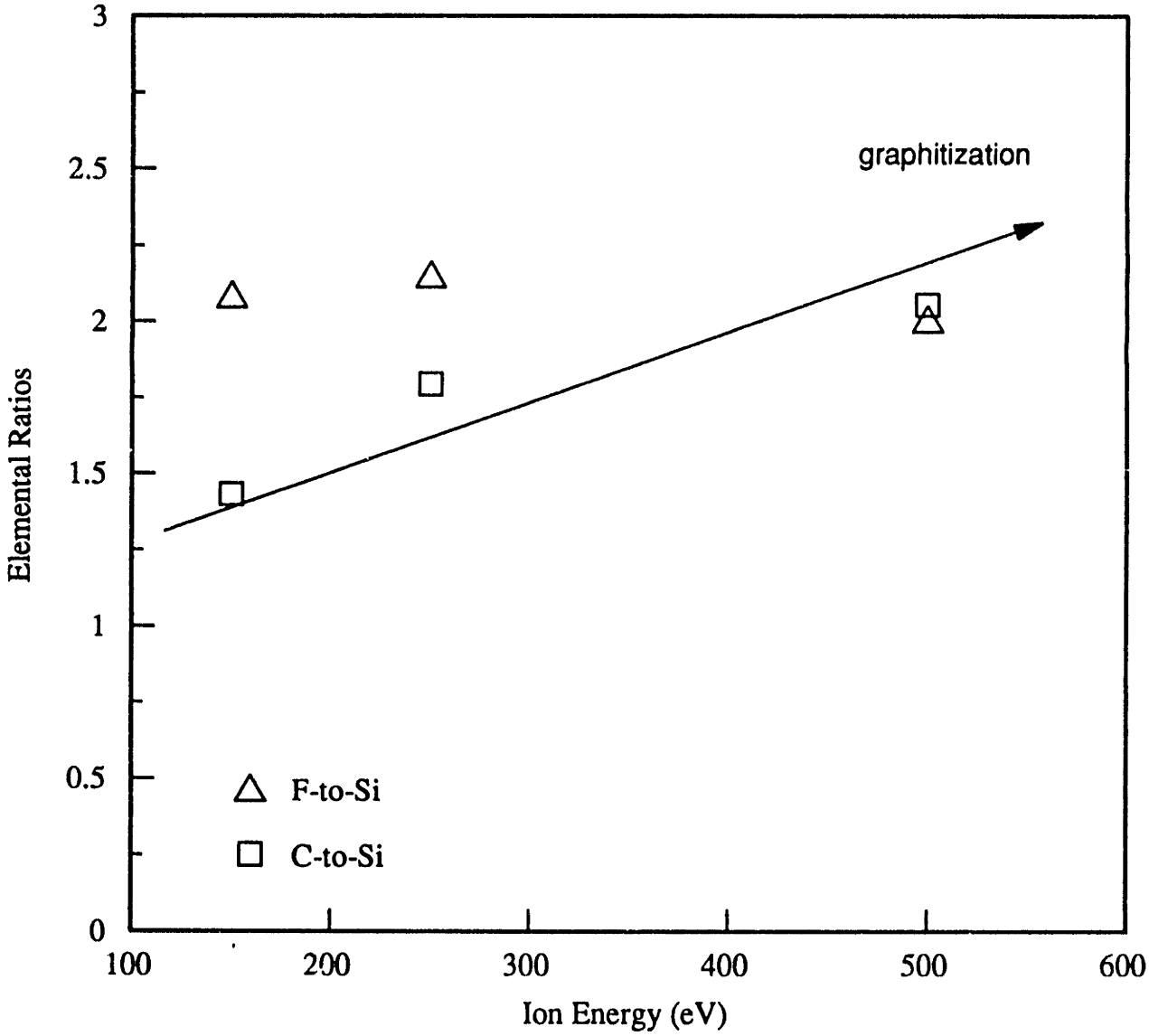

Figure 6-23. Calculated C-to-Si and F-to-Si elemental ratios from XPS studies of Ar /CF exposed silicon with increasing Ar energy, at constant CF /Ar = 48.9.

[Teppermeister, 1992]. The effect of a simultaneous F flux on this surface carbon residue is discussed in Chapter 7.

Interactions with Silicon Dioxide

A similar set of XPS experiments was performed on SiO_2, but with sharply contrasting results. The behavior of the C(1s) peak with increasing CF_2/Ar^+ ratio at constant ion energy of 150 eV is shown in Figure 6-24. Amazingly, the surface carbon was found to decrease with increasing relative CF_2 flux i.e as etching yields of SiO_2 increase, more residual carbon is carried off the surface in the form of CO_x and COF_x products. From our observations above concerning the spontaneous interaction of CF_2 radicals with SiO_2 surfaces, we concluded that the CF_2 was apparently residing on surface oxygen sites, with very little fluorine transfer (dissociative chemisorption) to the surface. This hypothesis was based on the finding of a C(1s) peak characteristic of C-F_2 bonding, but no evidence of multiple Si or F bonding states, consistent with the conclusions of Langan et al. [1989]. Figure 6-25 shows the series of C(1s) spectra with increasing CF_2/Ar^+ ratio, it can be seen that initially only the "adventitious" or graphitic background carbon peak is observed on the SiO_2 surface under simultaneous CF_2/Ar^+ bombardment. As this ratio is increased, however, the fluorine-bonded carbon feature develops at higher binding energies, indicating the presence of undissociated CF_2 on the surface. Evidently, the barrier to ion bombardment-induced dissociation of CF_2 on SiO_2 is larger than on the Si surface, since no evidence for undissociated sorbed CF_2 is found on Si. This observation is consistent with the much larger bond energy of Si-O relative to Si-Si, which makes ion-induced "mixing" on the oxide surface less efficient [Oostra et al., 1986]. As in the case of spontaneous interaction of CF_2 with SiO_2, only single F(1s) and Si(2p) peaks are seen in the CF_2/Ar^+ bombardment of SiO_2. Behavior of the C(1s)-to-Si(2p) elemental ratio is examined in Figure 6-26.

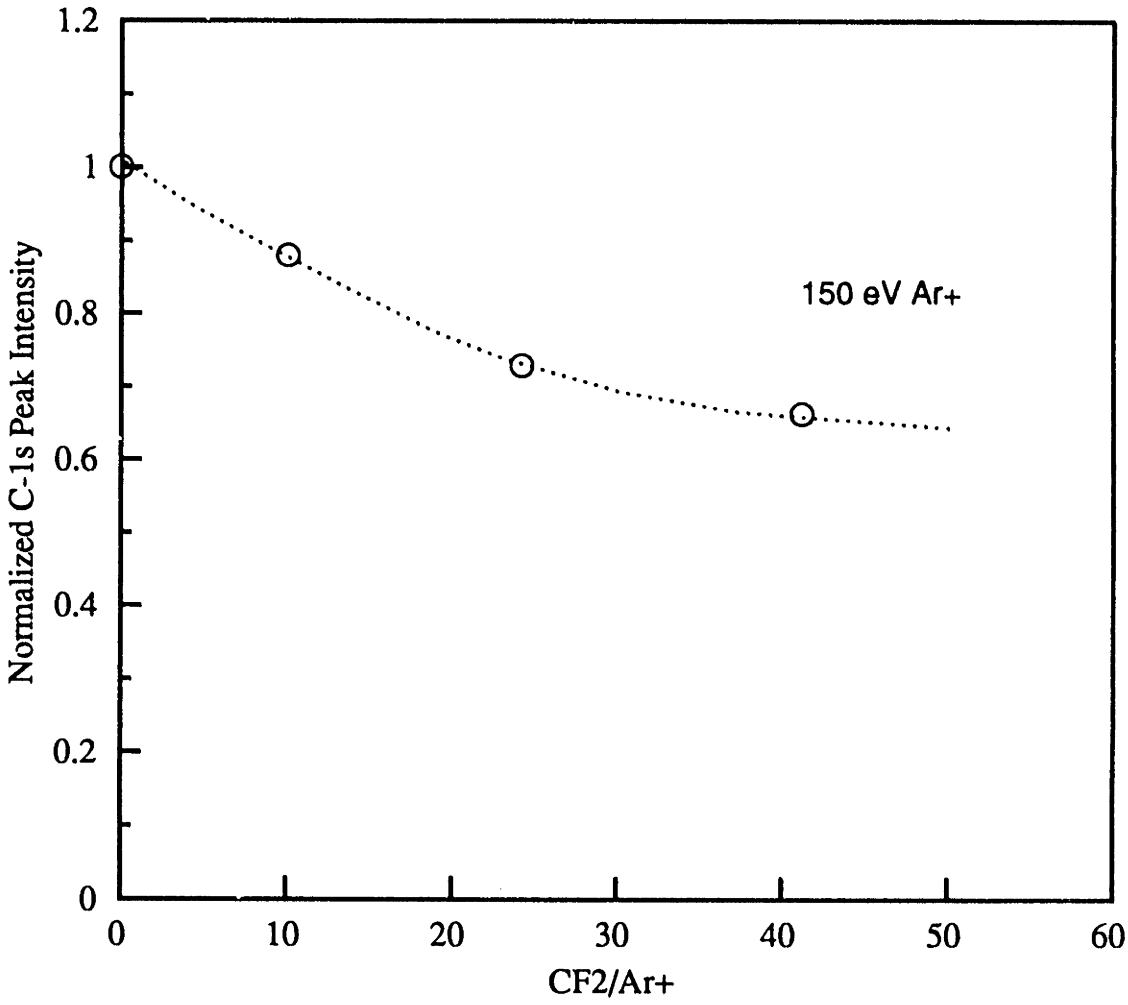

Figure 6-24. C-1s peak intensity of SiO exposed to increasing CF2/Ar+.

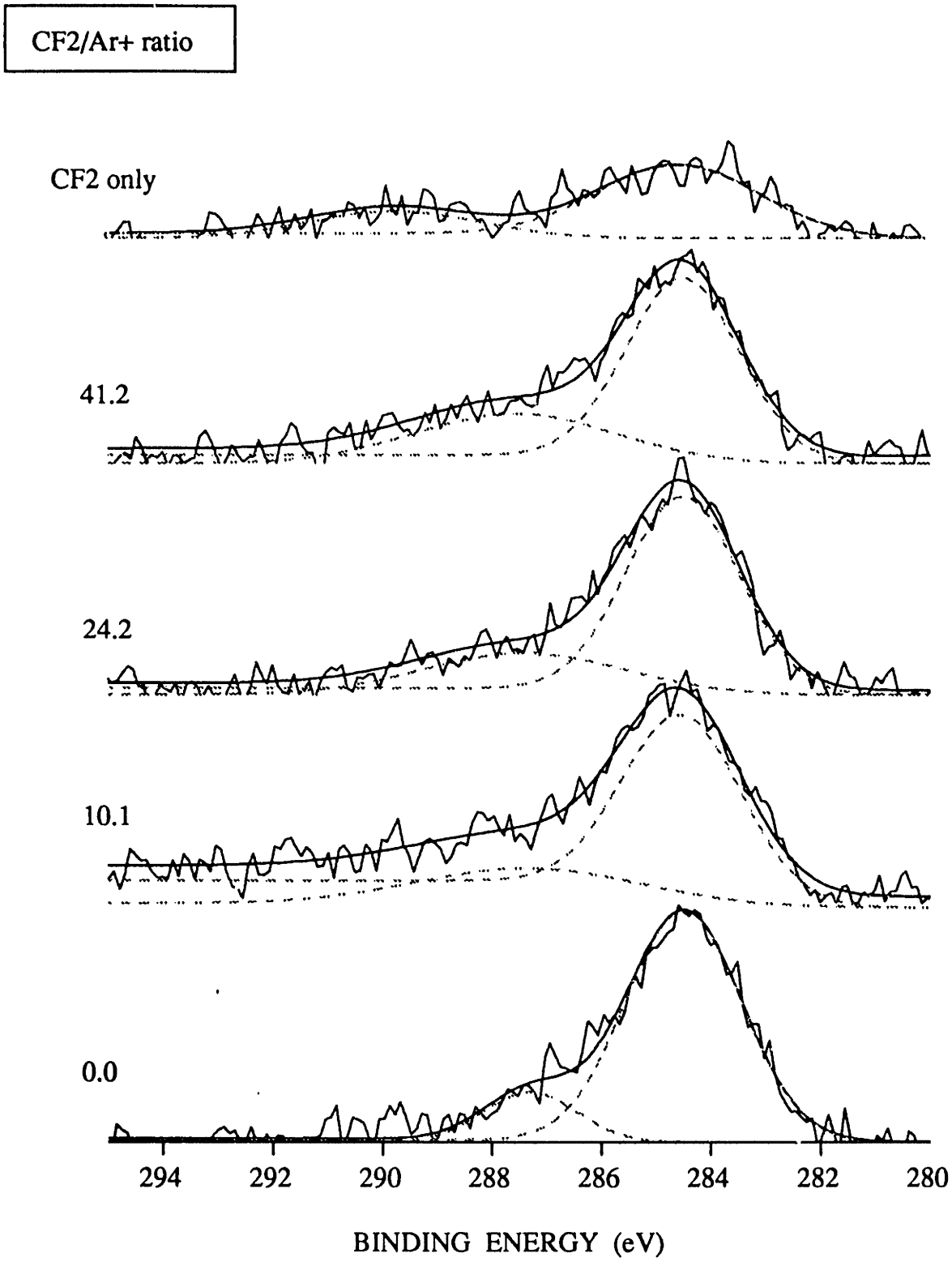

Figure 6-25. Comparison of C(1s) spectra of SiO_2 exposed to increasing CF_2/Ar^+ flux ratio, 150 eV Ar+.

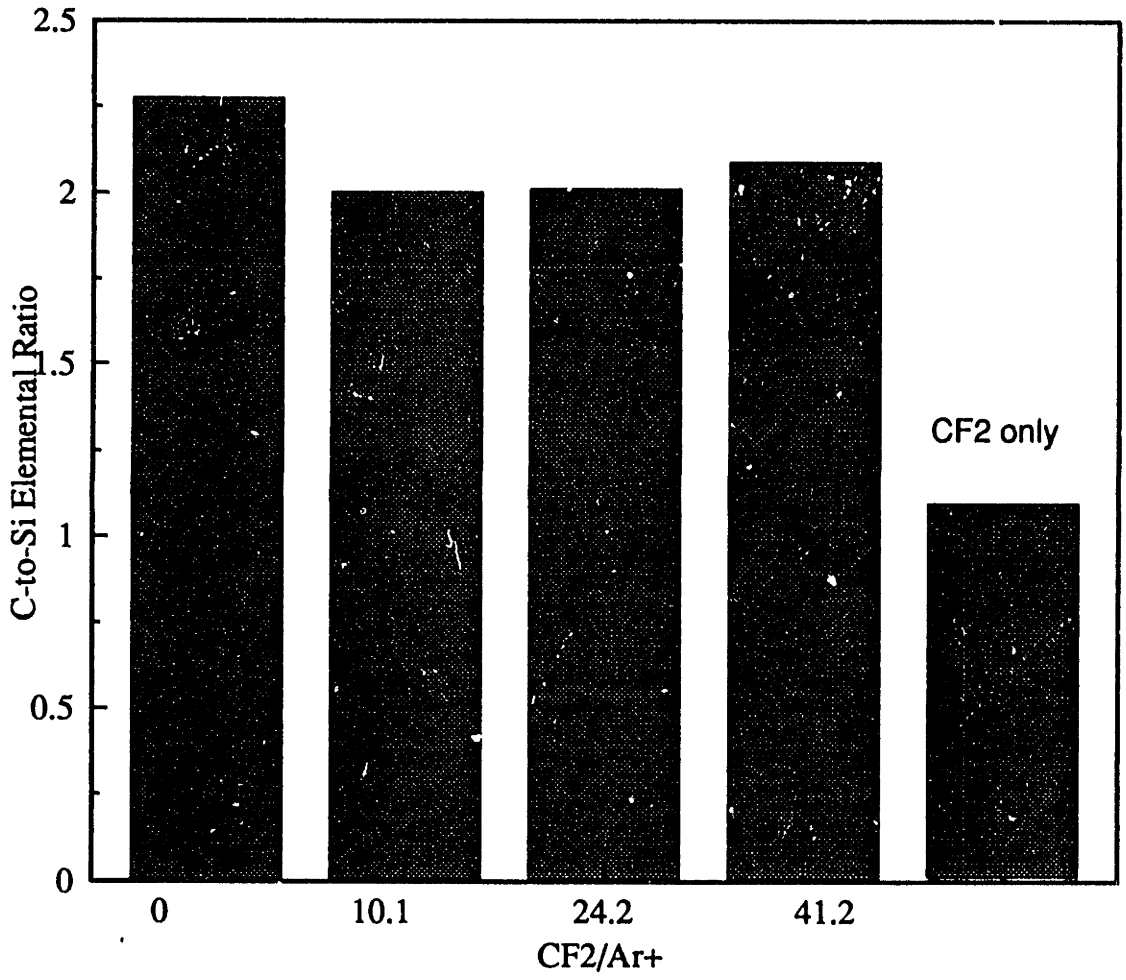

Figure 6-26. Calculated C-to-Si elemental ratios from XPS studies of Ar+/CF2 exposed SiO2.

In comparison to the case of spontaneous CF_2 interaction, it is clear that simultaneous ion bombardment enhances the uptake of CF_2 radicals. The F(1s)-to-Si(2p) ratio is examined in Figure 6-27, where the general trend of increasing surface fluorine with CF_2/Ar^+ ratio is observed. From comparison of 6-26 and 6-27 we see that the effective C-to-F ratio in the presence of ion bombardment is 2:1, suggesting that fluorine is readily liberated from the surface in the form of SiF_x products. The fact that this ratio is reversed in the case of CF_2 only interacting with SiO_2 demonstrates the role of ion bombardment in inducing dissociation of the otherwise inert CF_2.

The role of increasing ion energy in the Ar^+/CF_2 etching of SiO_2 was also investigated. Figure 6-28 shows the behavior of the C(1s) peak with increasing ion energy, at constant CF_2/Ar^+. It appears from these data that the relative amount of undissociated CF_2 (higher binding energy peak) is decreasing as the ion energy is increasing. This would indicate that the major effect of the increasing ion bombardment energy is the increase in adsorption sites, allowing dissociative chemisorption of CF_2. Figure 6-29 shows the behavior of the C-to-Si and F-to-Si elemental ratios with ion energy. As energy is increased in this case, the surface concentration of both species increase with the F-to-C ratio remaining constant at about 2:1, in contrast to the silicon surface where defluorination of the surface film is observed. This observation is consistent with the hypothesis that the main effect of increasing ion energy is to increase the density of CF_2 sorption sites, while relative reaction probabilities of the F versus carbon remain approximately constant in this energy regime. The role of an atomic fluorine flux concurrent with the CF_2/Ar^+ etching in this system is discussed in Chapter 7.

6.4 "Site" Models of CF_2 Radical Interactions

The application of simple surface kinetic models based on the concept of reactive "sites" to ion-enhanced etching was discussed in detail in Chapter 5. Ion-enhancement in the

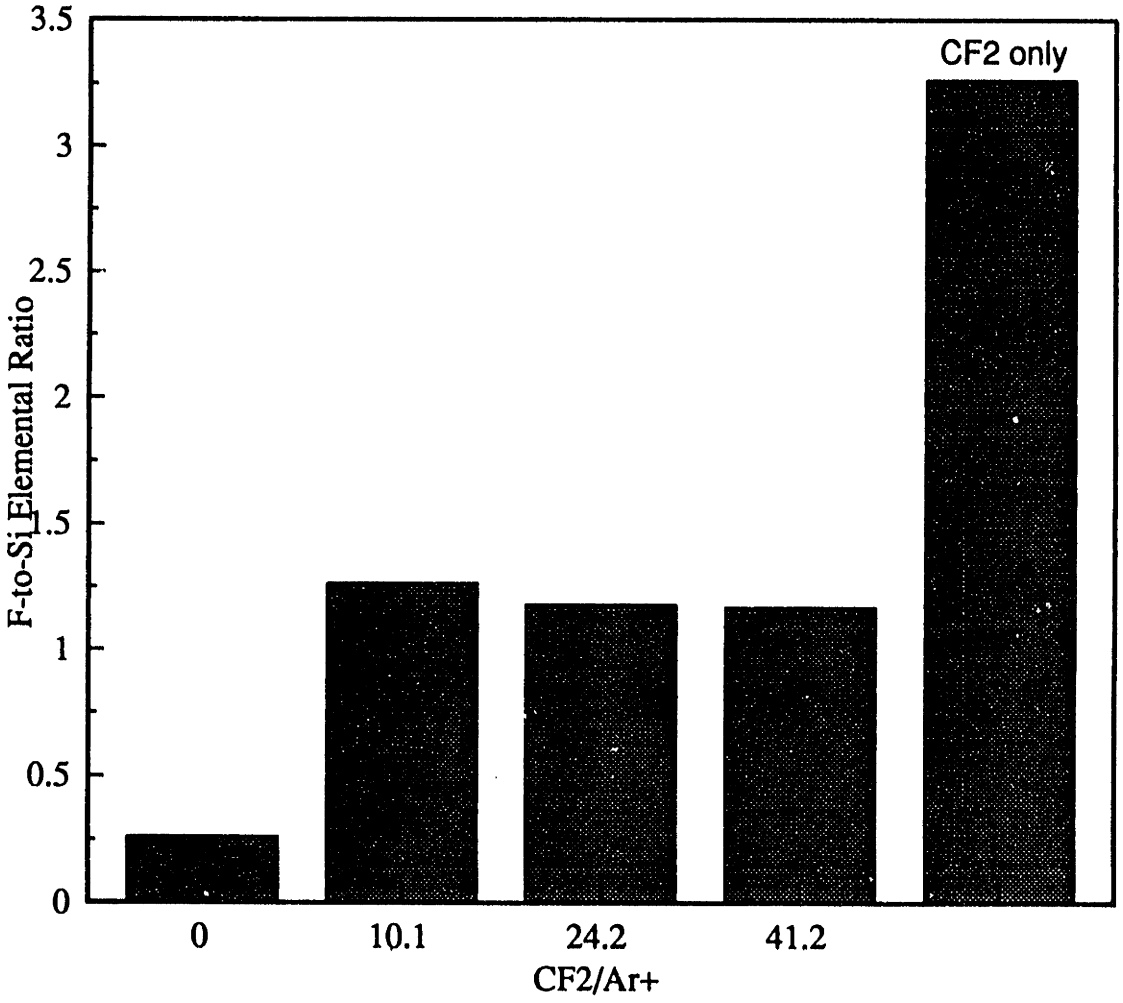

Figure 6-27. Calculated F-to-Si elemental ratios from XPS studies of Ar+/CF2 exposed SiO2.

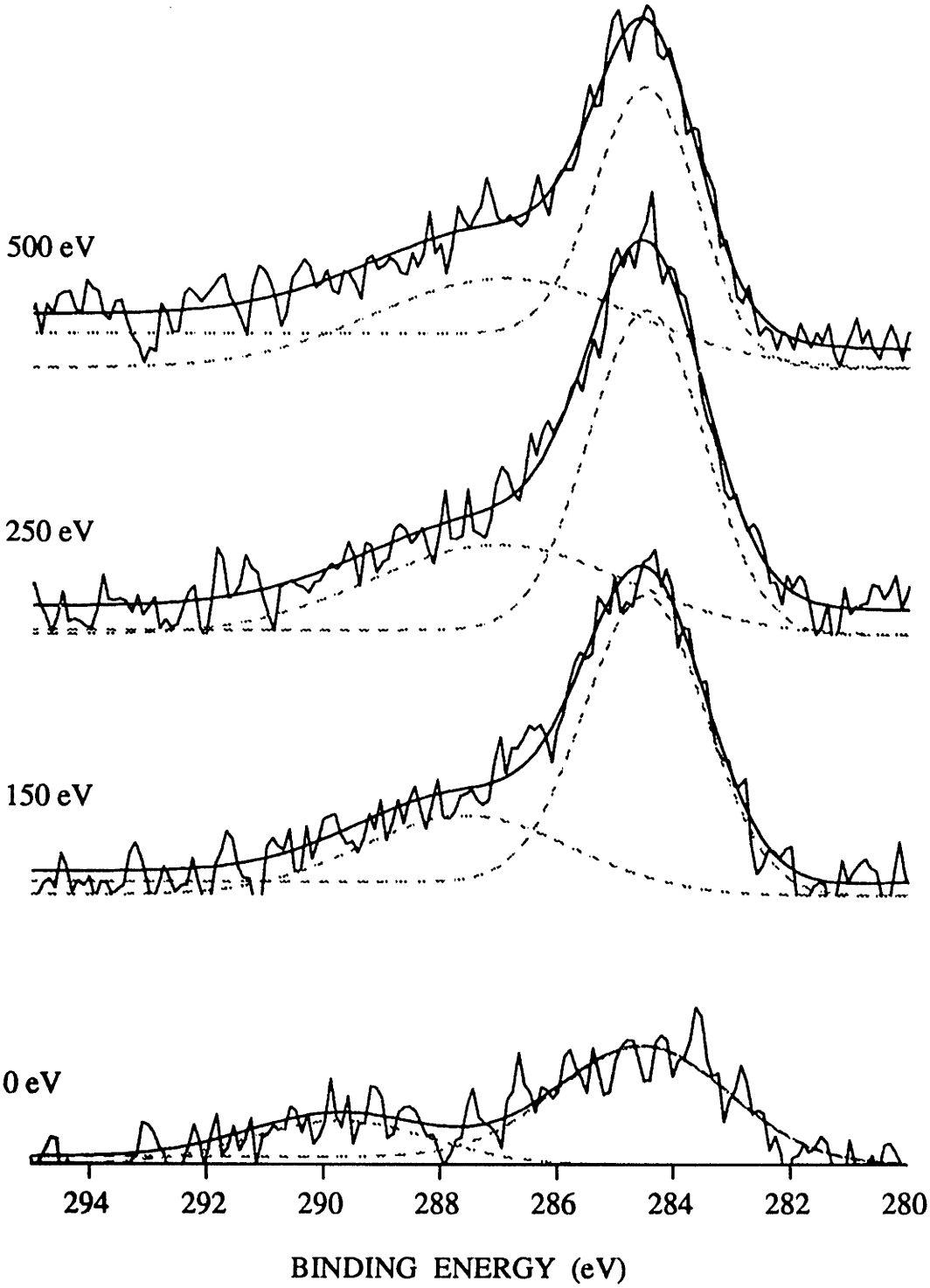

Figure 6-28. Comparison of C(1s) spectra of SiO_2 with increasing Ar+ energy, at constant CF_2^+/Ar^+ =41.2

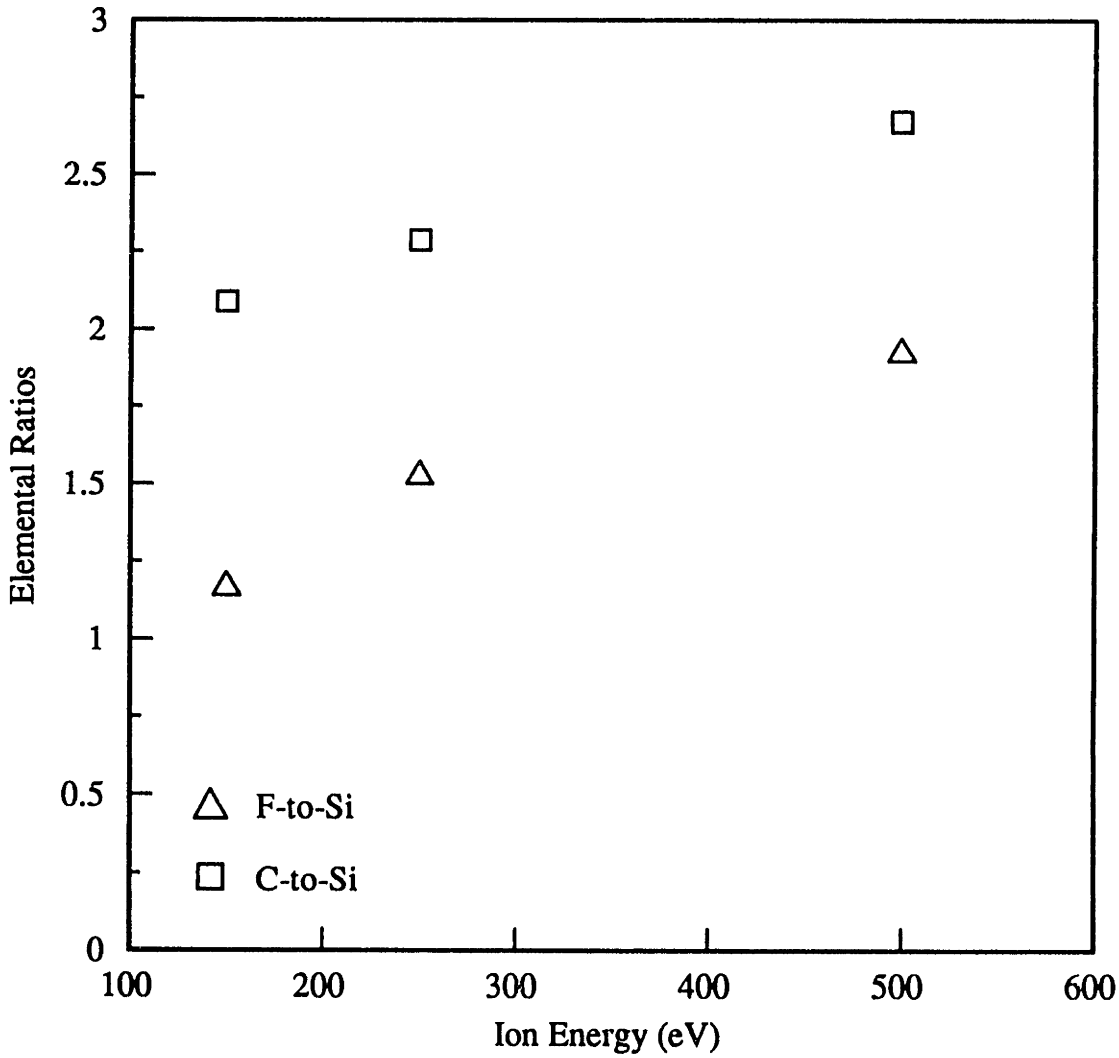

Figure 6-29. Calculated C-to-Si and F-to-Si elemental ratios from XPS studies of Ar+/CF2 exposed SiO2 with increasing Ar+ energy, at constant CF2/Ar+ = 41.2

Ar^+/CF_2 etching of SiO_2 was modeled using similar concepts, but with some important differences in the chemical nature of the radical sorption "sites". As mentioned above, there is evidence that the CF_2 bonds preferentially to O^* sites at the SiO_2 surface by a C-O bond, which makes necessary the transfer of fluorine from carbon to silicon in the mixing process. Based on mass spectral studies of fluorocarbon plasma etching of SiO_2 [Butterbaugh, 1990], it is clear that CO and COF_2 are evolved as products of the etching reaction in addition to O_2, while the importance of oxy-fluoride species is not clear. SiF_4 has been identified as the dominant plasma etching reaction product, but unsaturated SiF_x species may be more important in the Ar^+/CF_2 etching of SiO_2 due to the limited availability of fluorine. Due to the limitations discussed above in characterizing major reaction products in this system, we have assumed that SiF_4 and CO are the major reaction products of the ion-enhanced reaction pathway, allowing us to close an overall material balance. Subsequent modification of this type of model to include multiple reaction pathways will change the quantitative values of the regressed parameters, but not the qualitative features of the model.

The overall reaction network applied to the Ar^+/CF_2 etching of SiO_2 is as follows,

$$CF_2(g) \text{ <----> } CF_2(p)$$

$$CF_2(p) + O^* \text{ ----> } CF_2(s)$$

$$O_2\text{-}Si(s) + 2CF_2(s) \text{ -- } \beta_c, I^+ \text{ --> } SiF_4(g) + 2CO(g) + 2O^*$$

$$O_2^*\text{-}Si \text{ -- } p_o, I^+ \text{ --> } Si(g) + 2O(g) + O_2^*\text{-}Si$$

where most of the assumptions discussed in Chapter 5 have been applied. No evidence for CF_2 radical self-recombination has been found in the presence of ion bombardment, and XPS results show that non-dissociatively sorbed radicals are rapidly resputtered, suggesting that this recombination is negligible. Also based on XPS observations, this model contends that oxygen

dangling bonds are the major sorption "sites" for CF_2 on SiO_2. Physical sputtering of the SiO_2 surface occurs in parallel with the ion-enhanced "mixing" mechanism, but results in no net increase in surface sites in steady-state. No spontaneous etching of SiO_2 by CF_2 is observed, allowing us to write the total SiO_2 etching rate as,

$$R_{tot} = (Y_i + Y_p)\, I^+ = p_o(1-\theta_c)I^+ + \beta\theta_c I^+ \qquad (6\text{-}1)$$

resulting in a two-parameter model for the total etching yield of SiO_2 per incoming Ar^+ ion used,

$$Y_{tot} = p_o + (\beta_c - p_o)\frac{s_c R_c}{s_c R_c + 2\beta_c} \qquad (6\text{-}2)$$

In this case, R_c is the ratio of CF_2 flux to Ar^+ flux. The lines in Fig 6-14 are the model results at each energy level and the fitted parameter values are listed in Table 6-1, as previously reported in the thesis work of Butterbaugh [1990].

Table 6-1. Ar^+/CF_2 SiO_2 Etching Model Parameters

	s_c	β
Ion Energy		
150 eV	0.19	0.41
250 eV	0.66	0.45
350 eV	1.50	0.52

The values for the apparent sticking probability of CF_2 in Table 6-1 are significantly higher than the total loss coefficient of 0.04 on a non-bombarded surface reported by Booth et al. [1989], or the value of 0.02 reported by Kiss [1991]. Both researchers made their measurements

via in situ LIF in a parallel plate CF_4 plasma reactor. These measured values are total observed surface loss coefficients for CF_2 on reactor surfaces and include recombination effects as well as loss due to radical "sticking". Based on the fact that CF_2 was not observed to grow thick polymeric layers on either silicon or its oxide, we feel that it is very unlikely that substantial CF_2 is lost in steady-state due to "sticking" on non-bombarded reactor surfaces. Rather, results presented in Chapter 7 suggest that surface recombination of CF_2 with F is the dominant loss process. In addition, XPS data discussed above show definitive increase in CF_2 radical sorption with ion bombardment, so it is not surprising that the sticking coefficients regressed from our model are substantially higher than loss coefficients on passive surfaces. It is evident that the value of s_c for the 350 eV data is unphysical and indicates over-simplification of the model and lack of complete knowledge of product distributions, which affect the value of s_c extracted from the fitted data. Butterbaugh et al. [1991] note that if SiF_2 and CO_2 are assumed to be the etching products instead of SiF_4 and CO, then the values for s_c would be one half of the values in Table 6-1. Furthermore, it may be that CF_2 chemisorbs with high probability to Si^* sites as well as to O^*, in which case each SiF_4 product liberated results in the production of 4 new "sites" instead of two, since 4 bonds must be broken for every silicon removed. This likelihood of multiple sorption sites also reduces the calculated sticking coefficient by a factor of 2. The dependence of the apparent sticking probability on ion energy for CF_2 is much stronger than that observed for atomic fluorine. As was the case with F, it appears that CF_2 adsorbs more readily as the energy of the ions bombarding the SiO_2 surface increases. Again, we propose that this trend is due to the creation of more adsorption sites by the higher energy ions, which may be dangling bonds at surface oxygen sites. The exact nature of these "sites", or how their production correlates with ion energy is difficult to quantify.

The values of β_c for the Ar^+/CF_2 system are only weakly dependent on the ion energy,

much less so than in the case of Ar^+/F etching. Due to the size of the CF_2 radical as compared to F, it has a much lower mobility in the "mixing zone" created by the bombarding ions, reducing the apparent reactivity of the fluorine it carries. Consequently, the increase in the "mixing zone" thickness with ion energy cannot be sampled by the surface CF_2 radicals, and the main effect of increasing ion energy is to increase surface sorption through dangling bond production. In fact, the physical sputtering yield, p_o, (Ar^+ only) shows a stronger dependence on ion energy than does the parameter β_c. Therefore, as the ion energy increases, the etching process becomes less chemical and more physical. This is consistent with observations made by Mayer et al. [1981] in the ion-enhanced etching of SiO_2 by CF_x^+ ions. Mayer et al. found that the angular dependence of the sputtering yield was peaked at normal incidence for ion energies less than 400 eV, but became peaked at an increasing angle off normal for energies greater than 400 eV, which could be an indication of the increased importance of physical sputtering.

A simple model was also developed to explain the silicon sputtering rate suppression due to the formation of a fluorocarbon overlayer, as given by the lines in Figure 6-10. The model basically assumes that CF_2 radicals which stick to available silicon surface sites form strong silicon-carbon bonds, effectively burying the Si species. The only etching mechanism considered is physical sputtering, where the probability of sputtering a "buried" silicon species is considered negligible. Neglecting the production of volatile products via fluorine transfer from the film to the underlying virgin silicon, we considered the following "site poisoning" model where physical sputtering is the only material removal mechanism,

$$CF_2(g) \text{ <----> } CF_2(p)$$

$$CF_2(p) + Si^* \text{ ----> } CF_2(s)$$

$$Si\text{-}(CF_2)_j + CF_2(p) \text{ --}k_{aj}\text{--> } Si\text{-}(CF_2)_{j+1}$$

$$Si\text{-}(CF_2)_{j+1} \text{ --}\beta_{cj+1},I^+ \text{ --> } Si\text{-}(CF_2)_j + CF_2(g)$$

$$Si^* \text{ --}p_o,I^+ \text{ --> } Si(g) + Si^*$$

Obviously this mechanism is oversimplified because we have qualitative mass spectral evidence, at least, that some SiF_x species are formed. Also sputtering of $Si\text{-}CF_x$ is not considered as silicon removal mechanism; only removal of single CF_2 species to decrease the fluorocarbon layer thickness, or the sputtering of bare Si^* sites is allowed. Since we saw no evidence for multilayer polymerization in the Ar^+/CF_2 etching of silicon, we considered only the j=1 process. Total silicon sputter etch rate may then be written,

$$R_{tot} = p_o\, I^+ (1-\theta_c) \qquad (6\text{-}3)$$

or in terms of total etching yield,

$$Y_t = \frac{p_o \beta_c}{\beta_c + s_c R_c} \qquad (6\text{-}4)$$

where the silicon sputter yield p_o is known. Unfortunately, the regression form of this model does not give s_c and β_c independently, but only their ratio. We have therefore assumed a reasonable sticking coefficient of 0.15 for CF_2 on Si^*, resulting in the regressed β_c values shown in Table 6-2.

Table 6-2 Ar^+/CF_2 Silicon Etching Model Parameters

	s_c	β
Ion Energy		
150 eV	0.15	0.14
250 eV	0.15	0.22
350 eV	0.15	0.39

Although oversimplified, the model gives reasonable CF_2 fragment sputtering yields, which increase with incoming Ar^+ energy, capturing the dynamic equilibrium between site "poisoning" and CF_x resputtering. Qualitatively, the increasing ion energy is reducing the thickness and/or coverage of the fluorocarbon overlayer as contended earlier. Additional complexities in this model such as multilayer growth, F transfer and diffusion, and SiF_x product formation were considered, but cannot be supported by available data.

6.5 Summary

The nature of the spontaneous and ion-enhanced interactions of CF_2 radicals with Si and SiO_2 surfaces has been studied. It was found that CF_2 enhances the Ar^+ etching yield of SiO_2 in the presence of Ar^+ ion bombardment, while it suppresses the etching yield of polysilicon through the formation of a thin fluorocarbon overlayer. XPS studies of CF_2 exposed silicon and SiO_2 surfaces showed limited chemisorption and formation of multi-layers on ion-bombarded silicon, whereas little dissociation is observed on the SiO_2 surface. Ion bombardment was found to enhance radical sorption, as well as F-Si and C-Si bonding in both cases due to the ballistic "mixing" action of the ions. A simple model involving adsorption and ion-induced surface reaction was developed which captures the trends in the data and indicates that the sticking probability of CF_2 on SiO_2 increases with the energy of ion bombardment. Suppression of silicon sputtering can be modeled as a simple site "poisoning" effect where non-volatile Si-CF_x species are formed, reducing the net sputter rate of silicon.

Chapter 7

Plasma-Surface Interactions in Fluorocarbon Etching

In the studies presented in this chapter, we have considered the competitive interaction of the carbonaceous species present in the fluorocarbon etching environment with the ion-enhanced F-Si and F-SiO_2 chemistries discussed in Chapter 5. With the addition of competing carbon chemistries, these studies are a much more realistic model for the dominant plasma-surface interactions in fluorocarbon plasmas. Steady-state etching kinetics in $Ar^+/F/CF_2$ etching of silicon and SiO_2 were measured in three-beam studies to assess the competitive interaction between the F etchant, and the carbonaceous radicals. XPS spectra of $Ar^+/F/CF_2$ etched surfaces were compared to the case of Ar^+/CF_2 etching alone in order to compare the relative incorporation of surface carbon and fluorine. Evidence for effective surface carbon removal by the large F atom flux is presented. A CF_4 discharge was used in the CECR source to allow comparison of low energy CF_x^+/F and Ar^+/F etching.

7.1 Influence of CF_2 radicals on Ar^+/F etching

The results of full three-beam studies of F-CF_2 interactions in $Ar^+/F/CF_2$ etching of silicon under 250 eV ion bombardment are plotted in Figure 7-1. Data used to construct this plot were taken along the Ar^+/F and Ar^+/CF_2 axes, and along constant F/Ar^+ isolines at approximate flux ratios of 15, 50 and 70. One might expect a large poisoning effect of the silicon-fluorine chemistry by CF_2 based on the complete suppression of silicon etching observed in CF_4/H_2 plasmas at large H_2 mole fractions [Coburn and Winters, 1979]. Instead, we measured at most a 20-30% suppression in silicon etching yields with large simultaneous F and CF_2 fluxes, and 250 eV Ar^+ ions. We initially hypothesized that the silicon etching suppression might become much

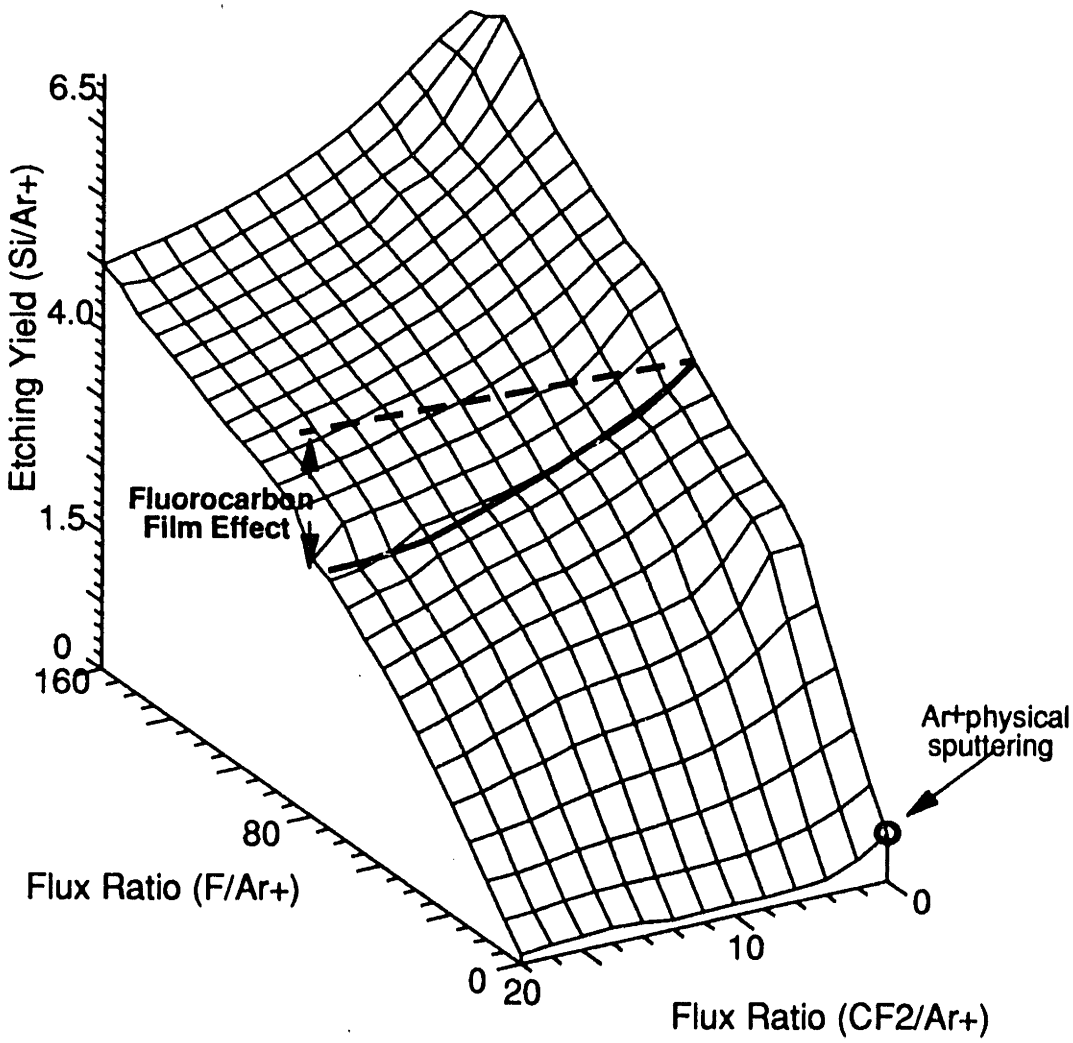

Figure 7-1. Three beam studies of Ar+/F/CF2 interactions on silicon at 250 eV ion bombardment energy.

more efficient at lower ion energies more representative of mean ion energies in CF_4 plasma processes (e.g. 50 eV) where the sputter removal of CF_x surface species is reduced. However, similar studies at a 20 eV Ar^+ energy shown in Figure 7-2 showed no measurable suppression of the Ar^+/F silicon etching, indicating that the mixing action of the high energy ions is necessary to promote carbon incorporation and Si-C bond formation in the silicon near-surface. The importance of the mixing action of the high energy ions is further illustrated in Figure 7-3 where the Ar^+/F etching rate suppression by CF_2 is examined at 20 eV, 250 eV, 500 eV. It would appear that surface carbon which is not "ion-mixed" into the lattice or dissociatively chemisorbed at the surface can be rapidly removed by: i) preferential sputtering of undissociated sorbed CF_2 as discussed in Chapter 6, and/or ii) rapid surface recombination of CF_2 with F atoms as discussed below. As a result of these removal mechanisms, thick fluorocarbon overlayer growth as has been reported in studies of Oehrlein et al. [1989], is prevented in $Ar^+/F/CF_2$ etching, suggesting that the CF_x^+ ions play a critical role in this film growth. The slight etching rate suppression shown in Figure 6-1 can be quantified in terms of a competitive adsorption model [Butterbaugh et al., 1991], where the effect of CF_2 is to poison a limited number of Si^* sites to F sorption.

Results of $Ar^+/F/CF_2$ etching of SiO_2 in Figure 7-4 show complete dominance of the Ar^+/F etching kinetics, suggesting that the F and CF_2 radicals were sorbing on different sites [Butterbaugh et al., 1991], or that the F was passivating the majority of sites to CF_2 sorption. The work of McFeely et al. [1988] suggests, in agreement with our work, that adsorbed CF_x species may preferentially bond to oxygen at the surface which would keep it from interfering with F adsorption on Si adsorption sites. The XPS data presented in Chapter 6 is in agreement with this hypothesis where no evidence of Si-C bonding was observed in Ar^+/CF_2 etched SiO_2 surfaces. In addition, the *ab initio* calculations of Jenichen and Johansen [1988] show that the $Si-OCF_2$ bond dissociation energy on SiO_x clusters is very weak, suggesting that COF_2 may be the

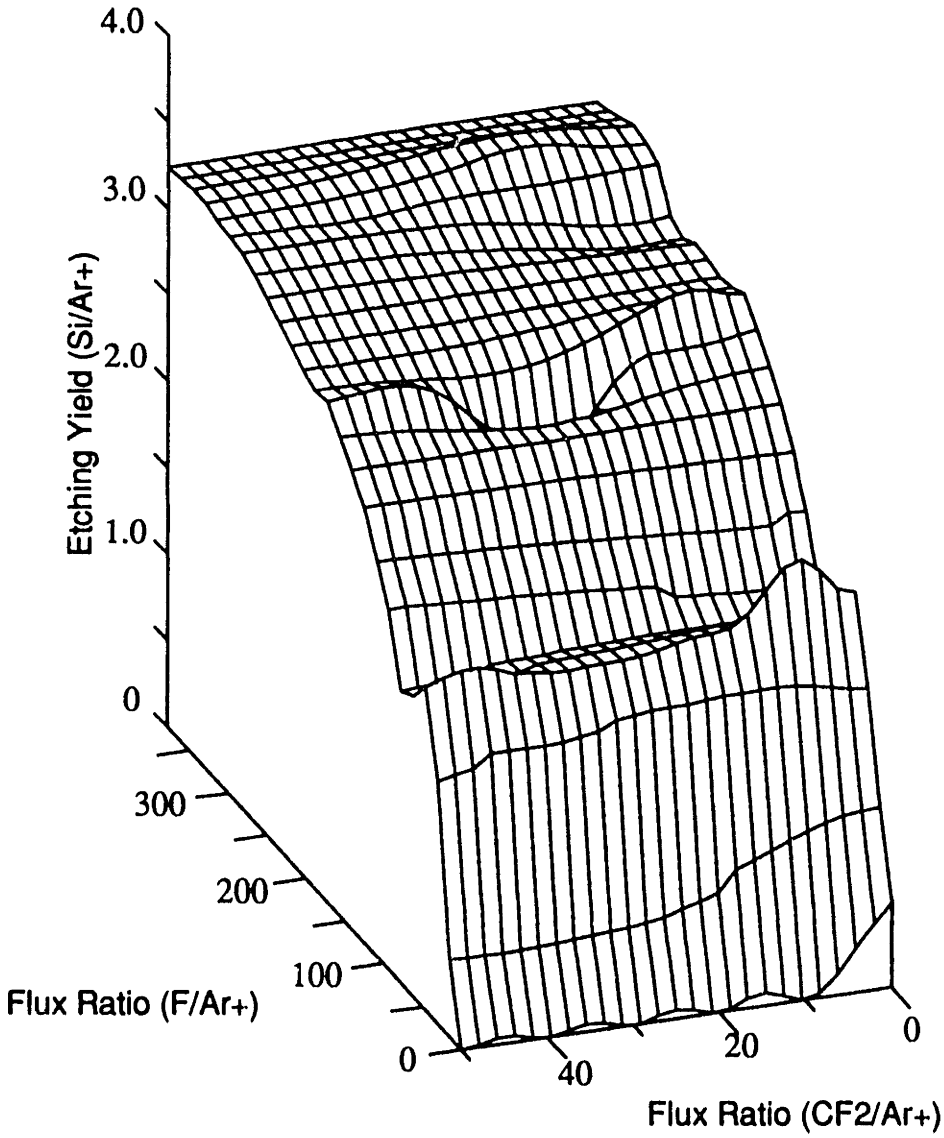

Figure 7-2. Three beam studies fo Ar+/F/CF2 interactions on silicon at 20 eV ion bombardment energy.

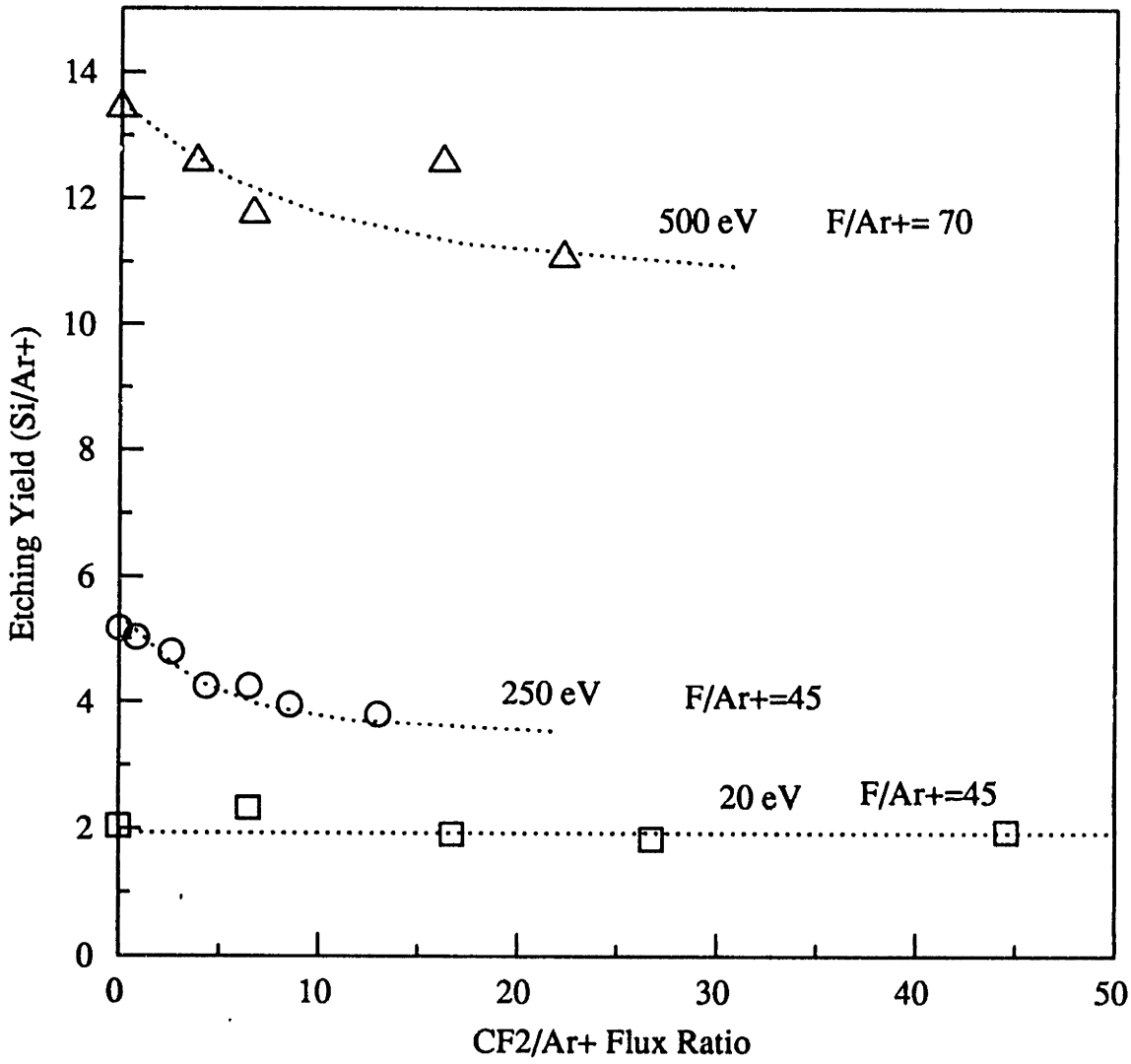

Figure 7-3. Effect of ion bombardment energy on Ar+/F silicon etching rate suppression by CF2.

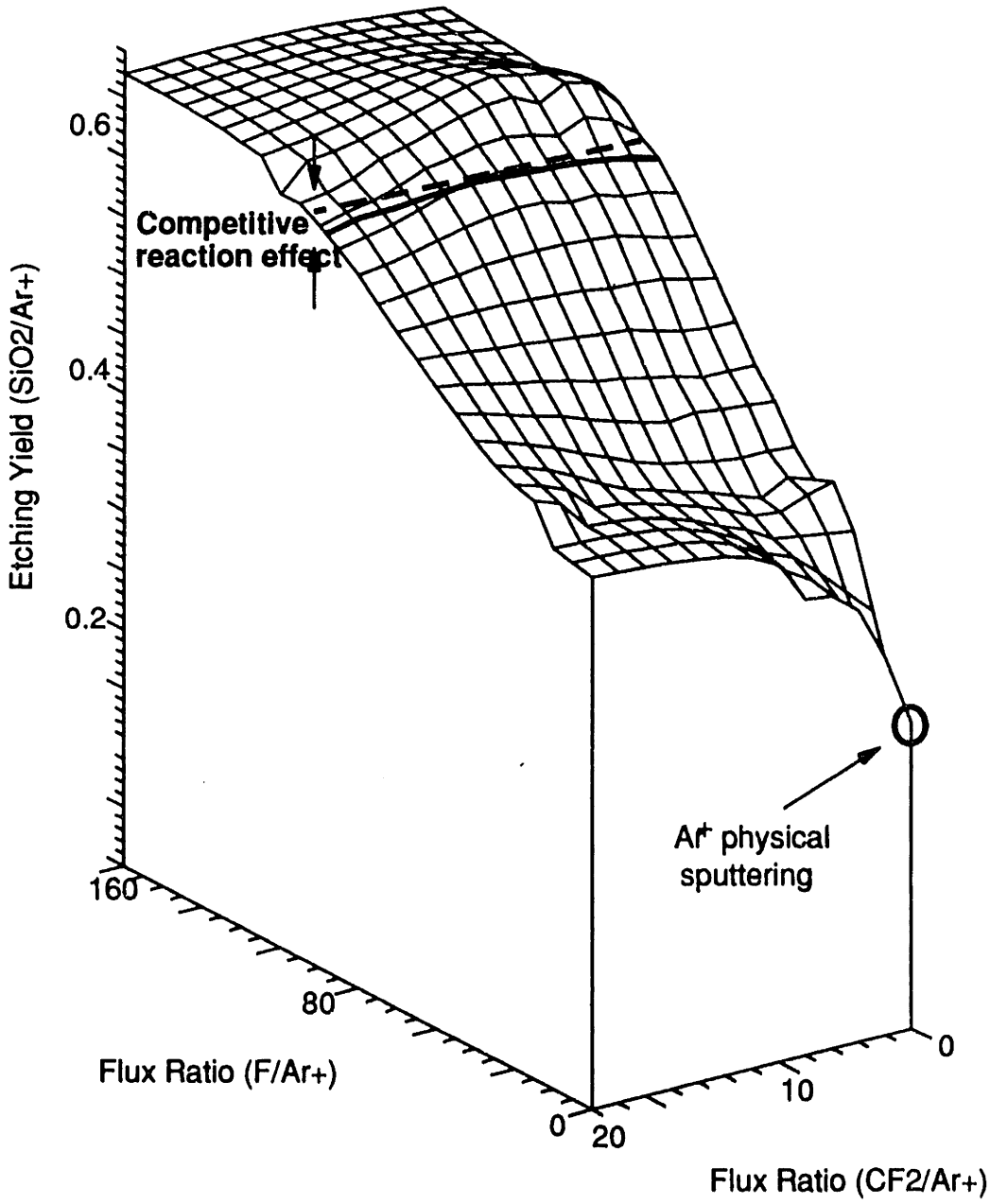

Figure 7-4. Three beam studies of Ar+/F/CF2 interactions on SiO2 at 250 eV ion bombardment energy.

thermodynamically favored product of CF_2 sorption. In any case, it is clear that while CF_2 is in its own right an ion-enhanced etchant for SiO_2, it is not the primary oxide etchant in CF_4 plasma etching of SiO_2 as has been contended in the literature. These results are consistent with the observations in plasma processes, that SiO_2 etching in F containing discharges is relatively unaffected by increases in fluorocarbon radicals [Coburn and Kay, 1979]. These results also indicate that CF_2 is not a limiting reagent to the etching of SiO_2, i.e. is not necessary for the removal of oxygen, consistent with the experimental work of Donnelly et al. [1984] in which SiO_2 films were etched in both CF_4/O_2 and NF_3/Ar plasmas. Donnelly et al. found that the SiO_2 etching rate correlated with the F concentration and was insensitive to source gas (CF_4 or NF_3). The reactivity of CF_x species to the surface oxygen probably modify the distribution of O-containing etch products, while the ion-enhanced F-SiO_2 chemistry limits the overall etching rates. It is also worthy of note that the etching rate enhancement seen by Tu et al. [1981] and Mayer et al. [1981] for CF_x^+/XeF_2 versus Ar^+/XeF_2 etching of SiO_2 at large ion energies (>300 eV), is not seen when the CF_x species is introduced as a radical instead of an energetic ion. This observation again points to the importance of high energy carbonaceous ion mixing in determining the selectivity behavior in fluorocarbon plasmas.

7.2 F-CF_2 Surface Recombination Kinetics

We have shown above that F chemistry dominates these ion enhanced systems when both CF_2 and F radical fluxes impinge upon the Si and SiO_2 substrates. In addition, as shown in Chapter 8, a flux of CF_2 to the Ar^+/F etching systems does not significantly change the redeposition rates from those observed for the Ar^+/F etching of Si and SiO_2 alone. Since there is no ion bombardment to the QCM surface during these studies, it would appear that sputtering is not a necessary removal mechanism for CF_2. We therefore hypothesized that F was passivating

the surface toward adsorption of CF_2, or was preventing CF_2 deposition via recombination. To investigate these hypothesis we began etching a silicon sample with Ar^+/F, and subsequently turned off the Ar+ beam to load the QCM surface with fluorine. We then turned off the F flux and scattered CF_2 from the sample face, which under all other circumstances resulted in CF_2 deposition on the QCM. However, dosing the F-rich QCM surface with CF_2 resulted in the net removal of material from the QCM, which we believe is due to the recombination reaction:

$$\mathbf{2F(p) + CF_2(p) \text{ --kr--> } CF_4(g).} \qquad \mathbf{(7\text{-}1)}$$

The rate curve, shown in Figure 7-5a, shows an initial rapid rate of mass removal from the QCM, which then slows down as surface F is depleted. Continued CF_2 exposure resulted in eventual deposition as shown in Figure 7-5b. This surface recombination reaction has been suggested as the major loss process for F and CF_x type radicals in several fluorocarbon plasma models [Kiss, 1991; Butterbaugh, 1990; Dalvie and Jensen, 1990; Thoman et al. 1986], however, the exact chemical pathway has not been clear. Each of these modeling efforts has required a CF_2 total surface loss coefficient on the order of 0.01-0.1 to explain overall CF_2 losses in plasma reactor models. The initial rate data presented in Figure 7-5a gives a mass loss rate of order 10^{13}/ mols/cm^2-s, which if we propose is due to F(p) removal via reaction (1), gives an apparent total loss coefficient of 0.01 for estimated 1 L/s CF_2 exposure. Dalvie and Jensen [1990] discussed the importance of F and O atom losses at reactor walls in CF_4/O_2 plasma etching, and suggested atomic recombination processes to form F_2 and O_2 as the operative mechanisms. Our results would indicate that CF_x-F type recombinations at the wall play a significant role in the surface loss processes for these radicals. It is possible that modification of the QCM method described herein may provide a method for measurement of fast surface recombination rates in plasma

a) t = 0

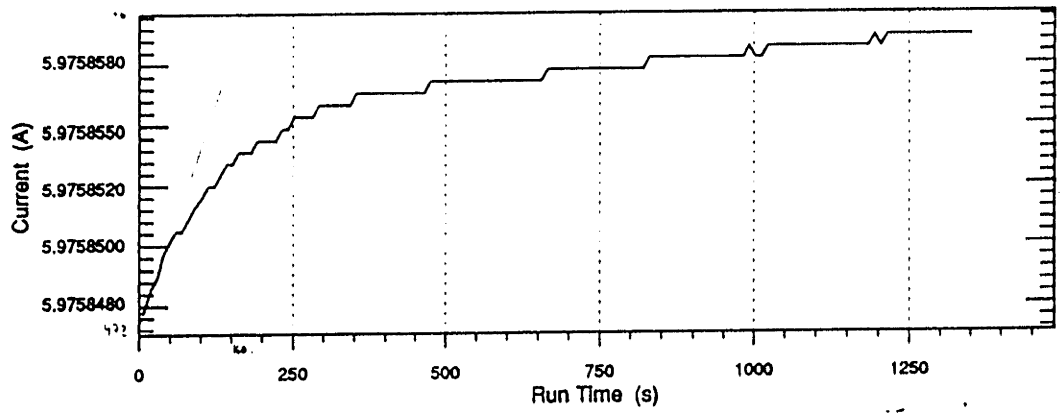

b) t= 30 minutes

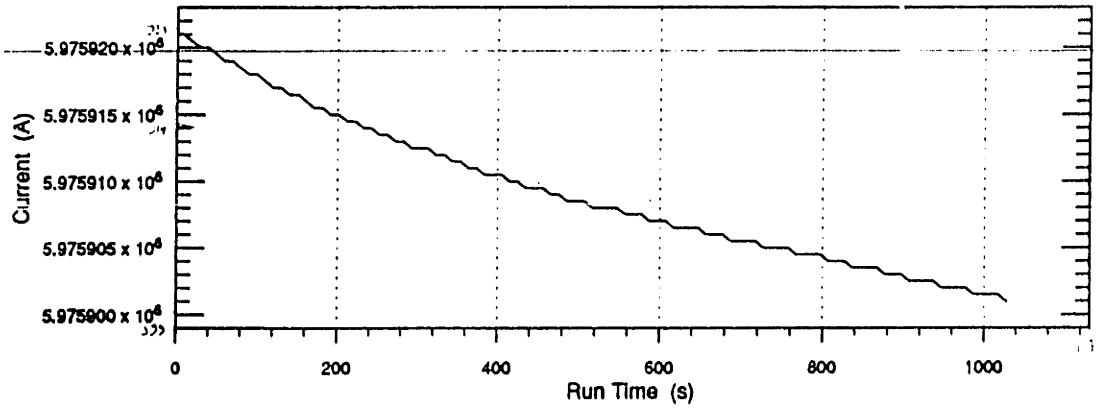

Figure 7-5. QCM studies showing the a) initial rate removal of F from the QCM surface via F-CF2 recombination and b) the eventual net deposition of CF2.

systems.

7.3 XPS studies of $Ar^+/F/CF_2$ etched surfaces

XPS studies were performed to ascertain the effect of F in competition with CF_2 on the Ar^+ bombarded silicon and SiO_2 surfaces. Comparison of Si(2p) spectra for 150 eV Ar^+/CF_2 versus $Ar^+/CF_2/F$ etching of silicon is provided in Figure 7-6. As discussed in Chapter 6, the Ar^+/CF_2 etching of silicon (Figure 7-6a) results in Si-F and Si-C bonding due to the dissociative chemisorption of CF_2, as well as the production of vacant Si^* dangling bonds which are subsequently oxidized in the sample transfer. The addition of F atoms (Figure 7-6b) at the same Ar^+/CF_2 flux levels almost completely eliminates the higher binding energy features, indicating that all available Si^* sites are F terminated in Si-F bonds, preventing the subsequent formation of $Si-O_2$ in transfer. The high binding energy tail which remains is probably due to a limited amount of surface Si-C since this feature was not observed on Ar^+/F etched silicon surfaces. With the limited quantitative resolution of the XPS analysis, no significant change in the total surface fluorine or carbon observed due to the addition of the F atoms could be concluded.

Comparison of Si(2p), C(1s), and F(1s) spectra for 150 eV Ar^+/CF_2 versus $Ar^+/CF_2/F$ etching of SiO_2 are provided in Figure 7-7. As discussed in Chapter 6, the C(1s) spectra for Ar^+/CF_2 etched SiO_2 (Figure 7-7b) shows a high energy feature which we attributed to surface C-F_2 groups versus Si-C bonded carbon. The addition of F results in a reduction in the total C(1s) signal intensity (Figure 7-7e) and the relative proportion of the carbon which is fluorine bound. Correspondingly, the total F(1s) peak intensity (Figures 7-7c,d) increases markedly, and a high binding energy feature develops which is most likely due to C-F_x bound fluorine [Joyce, 1987] versus silicon bound fluorine. The single F(1s) peak observed in Figure 7-7c is most likely from the C-F_x bound fluorine since limited dissociative adsorption is observed. However, the relative

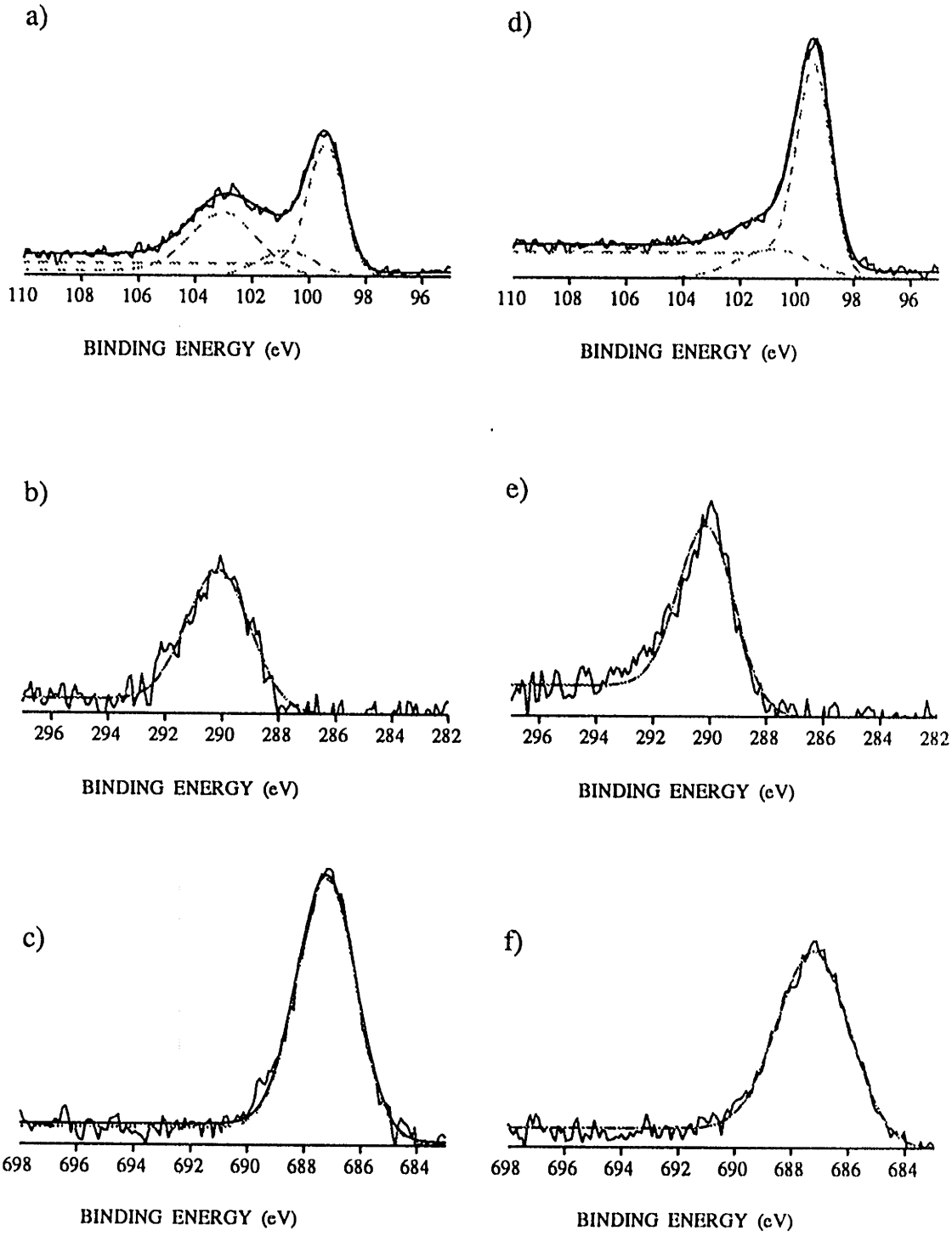

Figure 7-6. Comparison of Ar+/CF2 etched silicon a) Si(2p) b) C(1s) and c) F(1s) XPS spectra to Ar+/F/CF2 etched silicon surfaces d)-f) at 150 eV where CF2/Ar+=50 and F/Ar+=400.

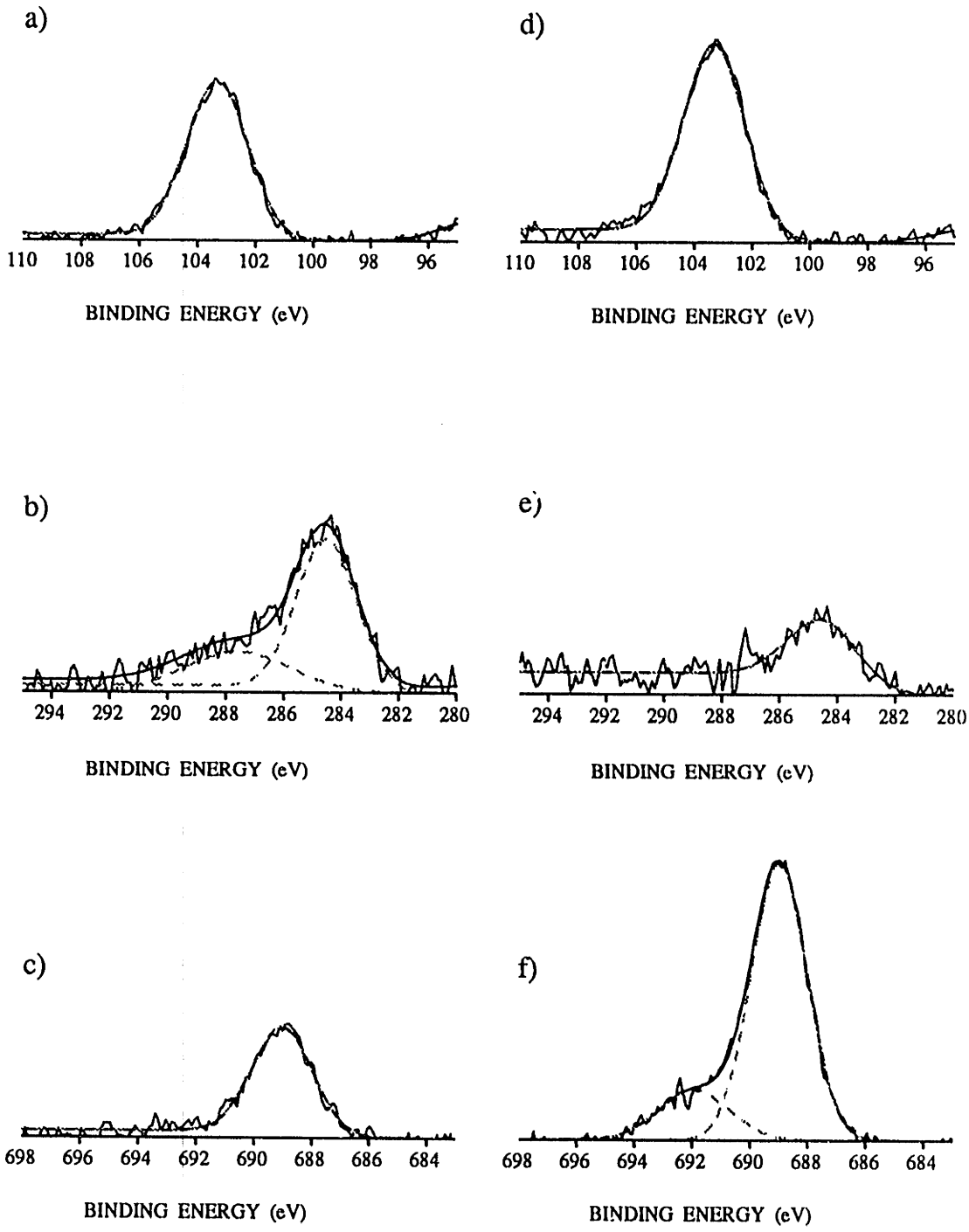

Figure 7-7. Comparison of Ar+/CF2 etched SiO2 a) Si(2p) b) C(1s) and c) F(1s) XPS spectra to Ar+/F/CF2 etched SiO2 surfaces d)-f) at 150 eV where CF2/Ar+=50 and F/Ar+=400.

fraction of O-F bonding is unknown and convolutes this measurement.

7.4 CF_x^+/F etching of Si and SiO_2

The results presented above and throughout this thesis work lead one to the conclusion that high energy carbonaceous ions in CF_4/H_2 and $C_xH_yF_z$ plasma etching processes are essential for obtaining SiO_2-to-Si selectivity observed in these plasmas. Mayer and Barker [1982a], Coburn et al.[1977], and Harper et al.[1981] have shown that the replacement of inert Ar^+ ions with fluorocarbon ions enhances SiO_2-to-Si selectivity as the CF_x^+ ion energy is increased. All of these studies were performed using a Kaufman-type CF_4 discharge from which a mixture of CF_x^+ ions is extracted, and the entire spectrum of CF_x and F radicals may effuse. Mayer and Barker [1982b] performed mass spectral studies in an attempt to quantify the ionic and radical components of his CF_4 plasma beam. Although CF_3^+ was shown to be the dominant ion extracted over a wide range of operating conditions, the plasma beam composition varied widely with discharge parameters, making quantitative interpretation of this type of data difficult. Tachi et al. [1991] was, however, able to achieve mass separation of the various CF_x^+ ionic components using magnetic sector techniques. His work demonstrates nicely the dependence of silicon etching/ deposition rates on the C-to-F ratio of the ion, and the relative bombardment energy, where CF_2^+ and CF_3^+ were found to result only in etching of silicon over the energy range of 0.1-3 keV.

The role of CF_x^+ ions in achieving SiO_2-to-Si selectivity at energies above 200 eV is evident from the studies cited above. However, the work of Mayer and Barker [1982a] extended only to 200 eV, and extrapolation of his data trends suggests that SiO_2-to-Si selectivity falls off drastically at near-threshold energies (<50 eV). The data of Harper et al. [1981] in the 50 eV to 200 eV energy regimes suggests that CF_x^+ and Ar^+ sputtering rates of silicon are very similar, while CF_x^+ ions enhance SiO_2 etching rates by 5-10x versus Ar^+ sputtering in this regime. We

have employed a CF_4 discharge in our CECR source to produce a CF_x^+ low energy (nominal 20 eV) ion flux in order to further study the role of carbonaceous ions at near threshold energies. In agreement with the work of Harper et al., CF_x^+ ion beam etching yields of silicon shown in Figure 7-8 were found to be on the order of 0.1, while SiO_2 CF_x^+ etching yields were found to be slightly higher on average. The data presented in Figure 7-8 was taken at constant CECR discharge source pressure, while varying the magnetic field strength to modify the ion flux. Over the ion current range of 10^{15} to 10^{16} ions/cm^2-s, it would seem that the CF_x^+ plasma beam composition is relatively constant since no drastic changes in the etch rates are seen.

Given that the CF_x^+ beam composition seemed fairly stable with extracted ion current, we then used this ion source in combination with a F radical beam in order to compare CF_x^+/F etching and Ar^+/F etching of silicon and SiO_2. The results of these experiments are shown in Figures 7-9 and 7-10, respectively. It is important to note that the CECR CF_4 discharge is itself a source of F atoms such that the CF_x^+/F etching data does not regress to zero etching yield as $F/I^+ \rightarrow 0$ as the Ar^+/F etching data presented in Chapter 5 does. 20 eV CF_x^+/F etching of silicon revealed etching yields approximately an order of magnitude lower than the Ar^+/F etching of silicon. The 20 eV CF_x^+/F etching of SiO_2 gave initial etching yields about a factor of 2 larger than the Ar^+/F etching of SiO_2. However, the SiO_2 etching studies were not well behaved at large F atom fluxes where the apparent etching yields were found to scatter over an order of magnitude. We believe that the SiO_2 films were charging and that a secondary source of neutralizing electrons used in conjunction with the CECR source will be necessary to further pursue these studies. As shown in Figure 7-11, the CF_x^+/F (versus Ar^+/F) etching results in SiO_2-to-Si selectivity of about 2-to-1 at 20 eV, compared to a selectivity of about 1-to-10 observed for Ar^+/F etching. It is evident that the mixing action of high energy carbonaceous ions is necessary to achieve large SiO_2-to-Si selectivities as reported by Mayer et al. [1981].

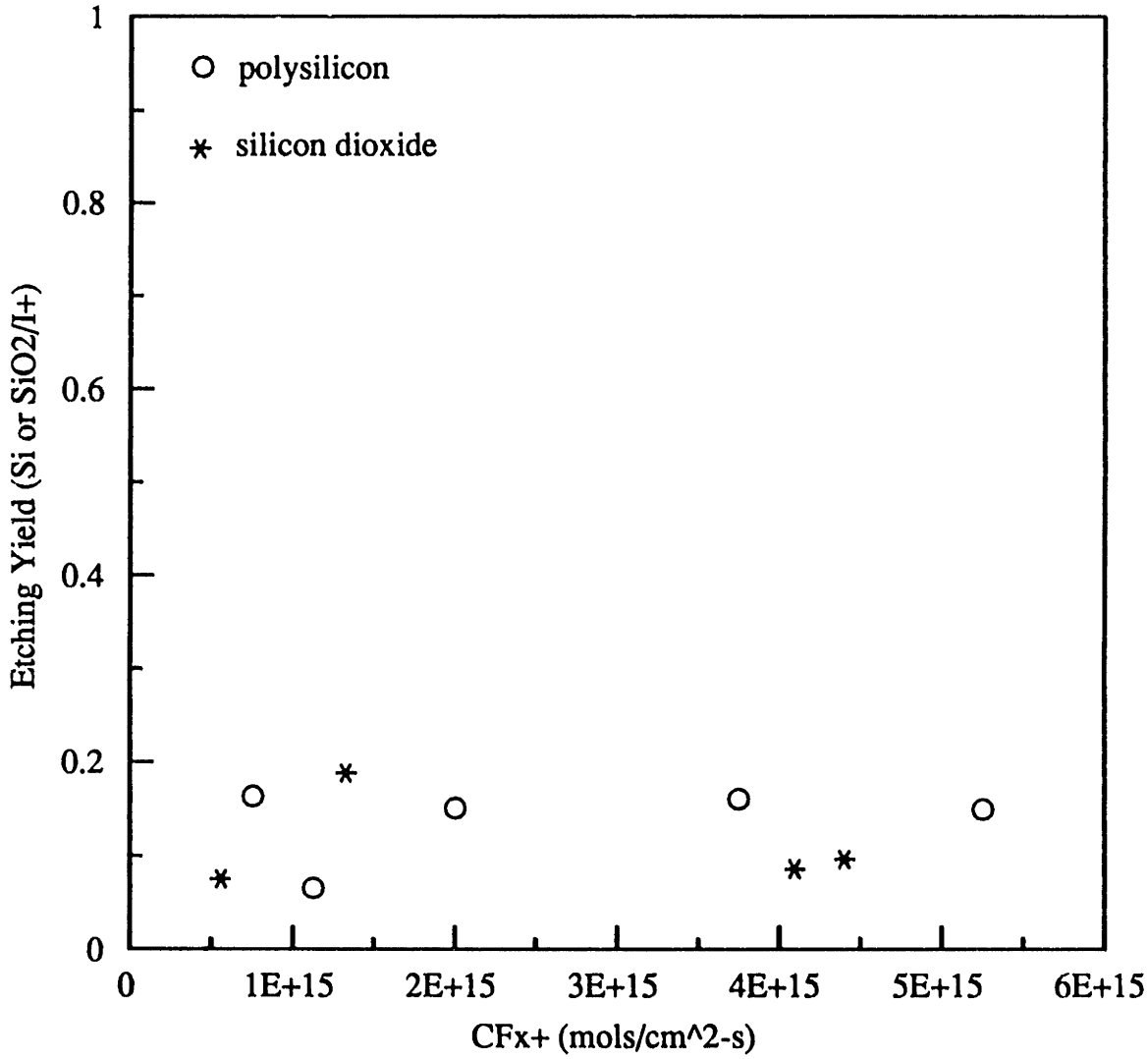

Figure 7-8. CFx+ etching of silicon and SiO2 using a CF4 CECR plasma beam.

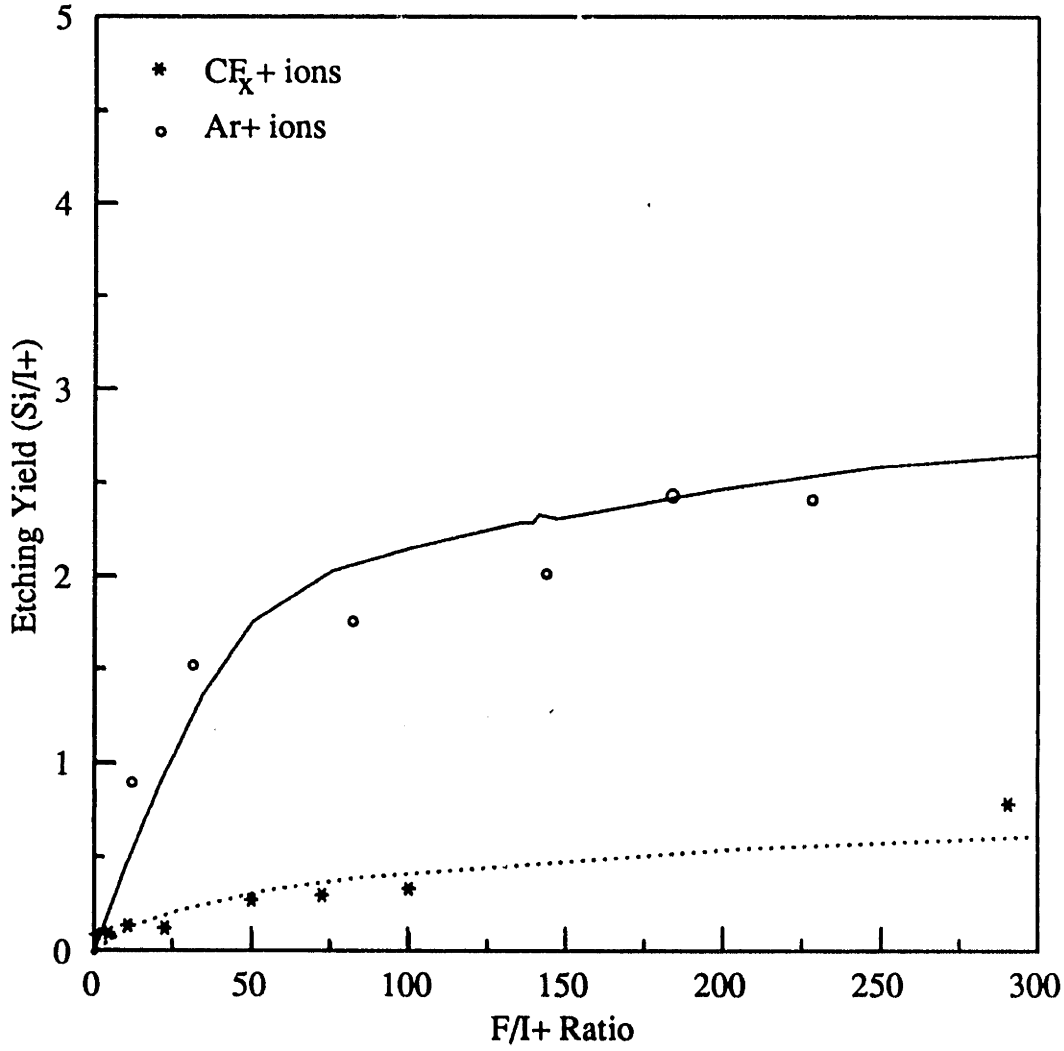

Figure 7-9. CF_x+/F versus Ar+/F etching of silicon at 20 eV (nominal).

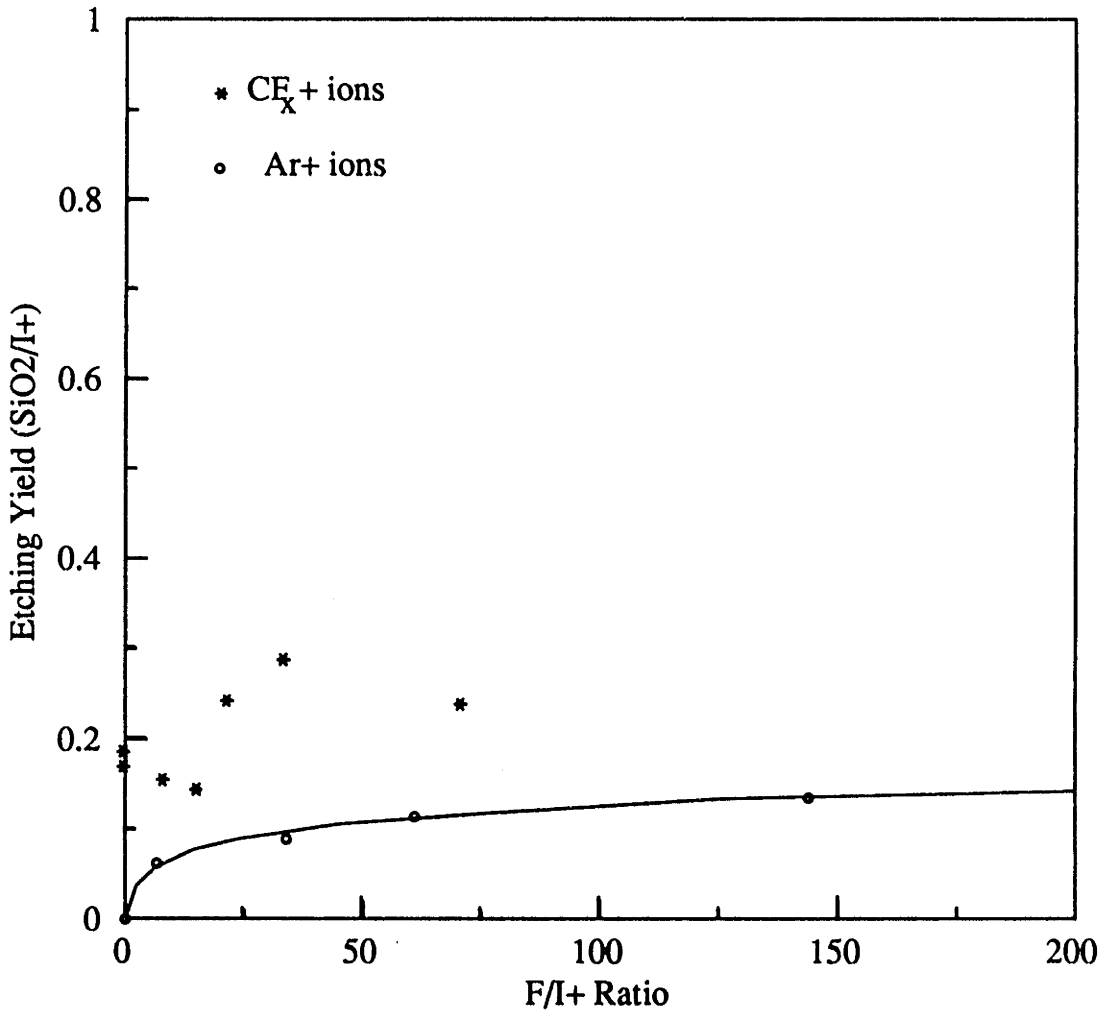

Figure 7-10. CF_x+/F versus Ar+/F etching of SiO2 at 20 eV.

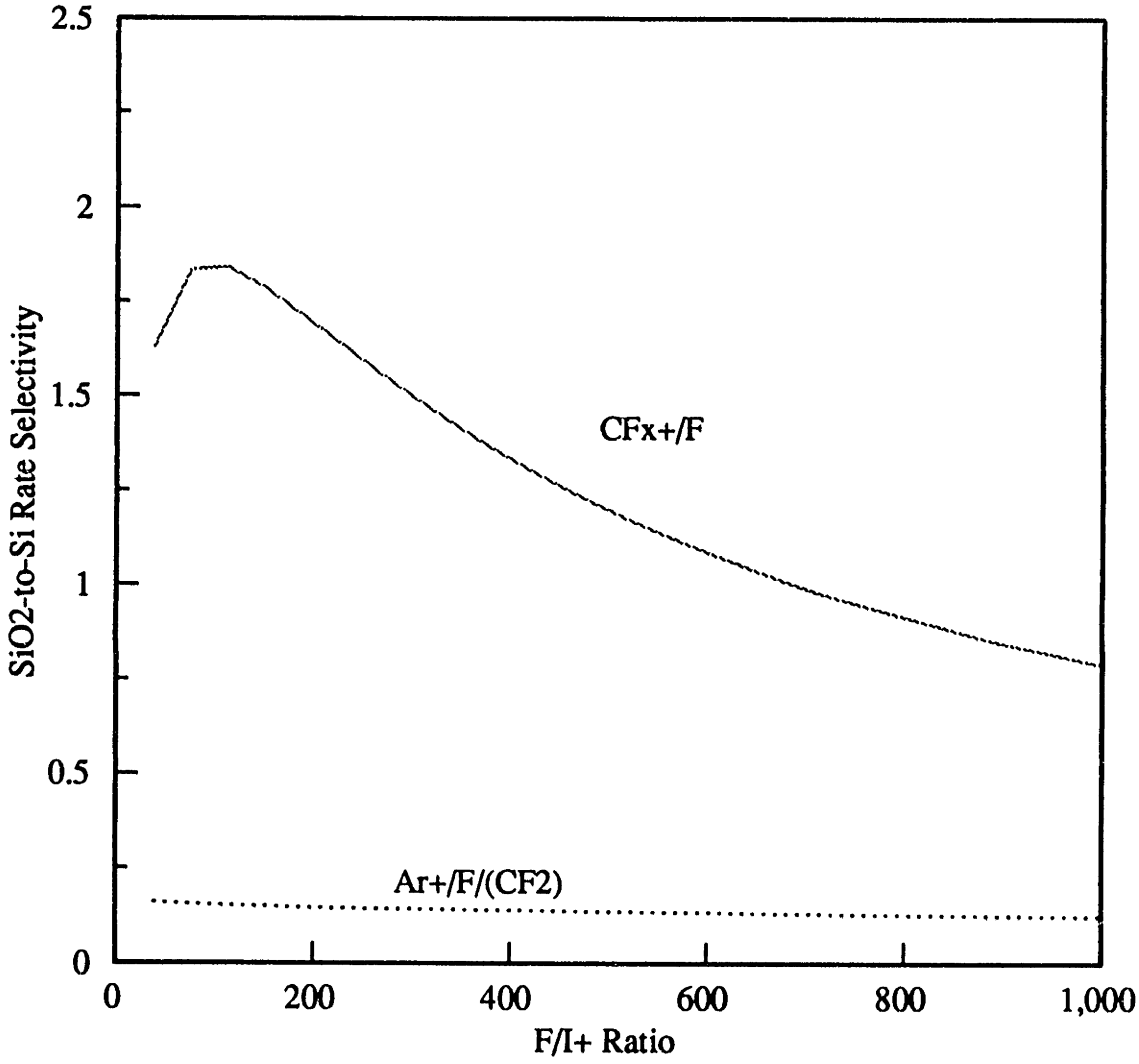

Figure 7-11. Comparison of SiO2-to-Si etching rate selectivity in 20 eV Ar+/F/(CF2) etching and CFx+/F etching.

7.5 Summary

The competitive interaction of CF_2 radicals with ion-enhanced F-Si and F-SiO_2 etching kinetics was measured. CF_2 was found to suppress Ar^+/F etching of silicon at most by 20%-30% at high relative CF_2 fluxes and ion energies above 250 eV. No suppression of Ar^+/F silicon etching by CF_2 was observed at 20 eV ion bombardment energy. Ar^+/F kinetics were found to completely dominate the etching of SiO_2 in the presence of CF_2, where no effect of the carbon chemistry on etching yield was observed. CF_2 was found to rapidly recombine with F on a fluorine saturated microbalance in redeposition experiments, in agreement with fluorocarbon plasma processes models in the literature. CF_x^+/F etching at 20 eV was compared to Ar^+/F etching using a CF_4 discharge in the CECR source. 20 eV CF_x^+ ions were found to increase SiO_2-to-Si selectivity by an order of magnitude, but much higher ion energies are necessary to achieve the high selectivities noted in CF_4/H_2 oxide plasma etching processes.

Chapter 8

Redeposition Processes in Fluorocarbon Plasmas

In this series of studies, we present experimental measurements of redeposition kinetics in fluorocarbon plasma etching processes. In these studies, a quartz crystal microbalance(QCM) was placed in close proximity to Si or SiO_2 samples being etched by the combined flux of energetic ions and free radicals (see Figure 2-9). This technique allows us to make measurements of the redeposition flux of materials which may deposit on a feature sidewall which itself does not experience directed ion bombardment, but is in line-of-site view of the trench bottom which is rapidly etching. The quartz crystal surfaces were rapidly coated with etching products in these studies, so the redeposition rates measured involve the "self-sticking" probability of the product stream on a composite surface, just as in the case of sidewall deposition as shown schematically in Figure 8-1.

In order to quantify the redeposition process for implementation in profile simulations, several pieces of information are necessary. The most important of these include the distribution of products evolved in the etching process, the relative sticking probability of these various products, and the emission characteristics e.g. directionality of the products. Our experiments provide quantitative measurements of total product redeposition rates in the ion-enhanced fluorine etching of silicon and SiO_2 at room temperature, and in the directional characteristics of this emission. Lightly doped single crystal silicon <100> substrates (p/boron 5-20 ohm-cm) were used in the silicon redeposition studies while commercially available quartz plate was used for studies of redeposition during SiO_2 etching. Comparison studies using undoped steam grown SiO_2 films were performed to verify that no differences existed in the redeposition of product species coming from the quartz samples. Redeposition rates of products during the etching of silicon and silicon

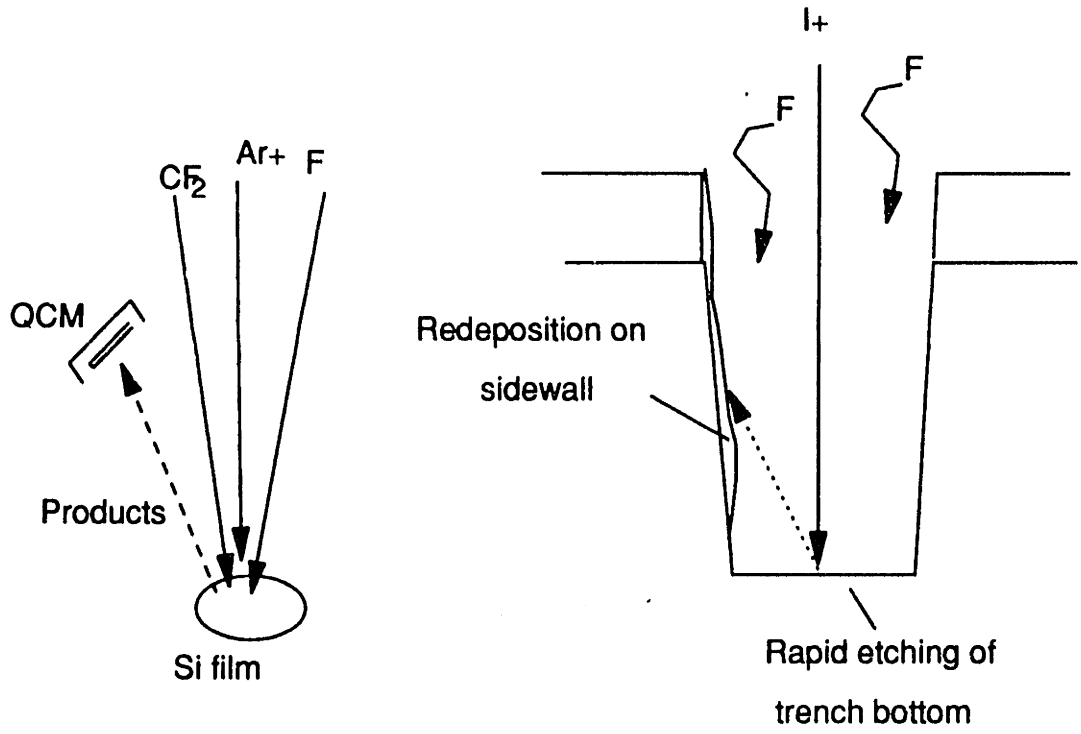

Figure 8-1. Schematic representation of the redeposition experiments showing the analogy to trench sidewall deposition in plasma etching.

dioxide by Ar^+, F, CF_2, and combinations thereof were measured as a function of species fluxes, ion energy, and detector angle. It is important to note that the quartz crystal surface was at times during these experiments exposed to large fluxes of species other than etching products, including the chamber background flux, and the flux of neutrals and ions which are scattered from the sample face without reacting. These fluxes resulted in "baseline" deposition or etching rates for some sets of experiments, requiring careful interpretation of the data. Several conclusions may be drawn concerning the relative sticking probability of various etching products based on measurement and models of product distributions in these systems.

8.1 Redeposition in Ar^+ Sputtering of Si and SiO_2

The redeposition of physically sputtered material from Si and SiO_2 was studied to allow comparison to redeposition rates during ion-enhanced F and/or CF_2 etching of these materials. The purely physical removal mechanism during inert Ar^+ ion bombardment evolves primarily pure silicon metal atoms and ions in the case of Si, in addition to O atoms, O_2, and SiO_x clusters in the case of SiO_2 sputtering. Since the free metals and radicals have a sticking coefficient on the order of unity, redeposition rates observed at a given ion energy were maximized during pure Ar^+ sputtering.

Total product redeposition rates measured during the Ar^+ sputtering of Si and SiO_2 are shown in Figure 8-2 as a function of Ar^+ ion flux at 500eV. The sputtering of steam grown SiO_2 films and quartz plate were compared and showed no observable difference in redeposition characteristics. The physical sputtering yield of polysilicon is observed to be linear in Ar^+ flux and $\sqrt{E_i}$ in the low energy physical sputtering model of Steibrukel [1989] given in Equation (5-7), where model parameters were presented in Table 5-1. If we wish to study the angular emission characteristics of the sputtered material we must rewrite the Si sputter yield in a differential form

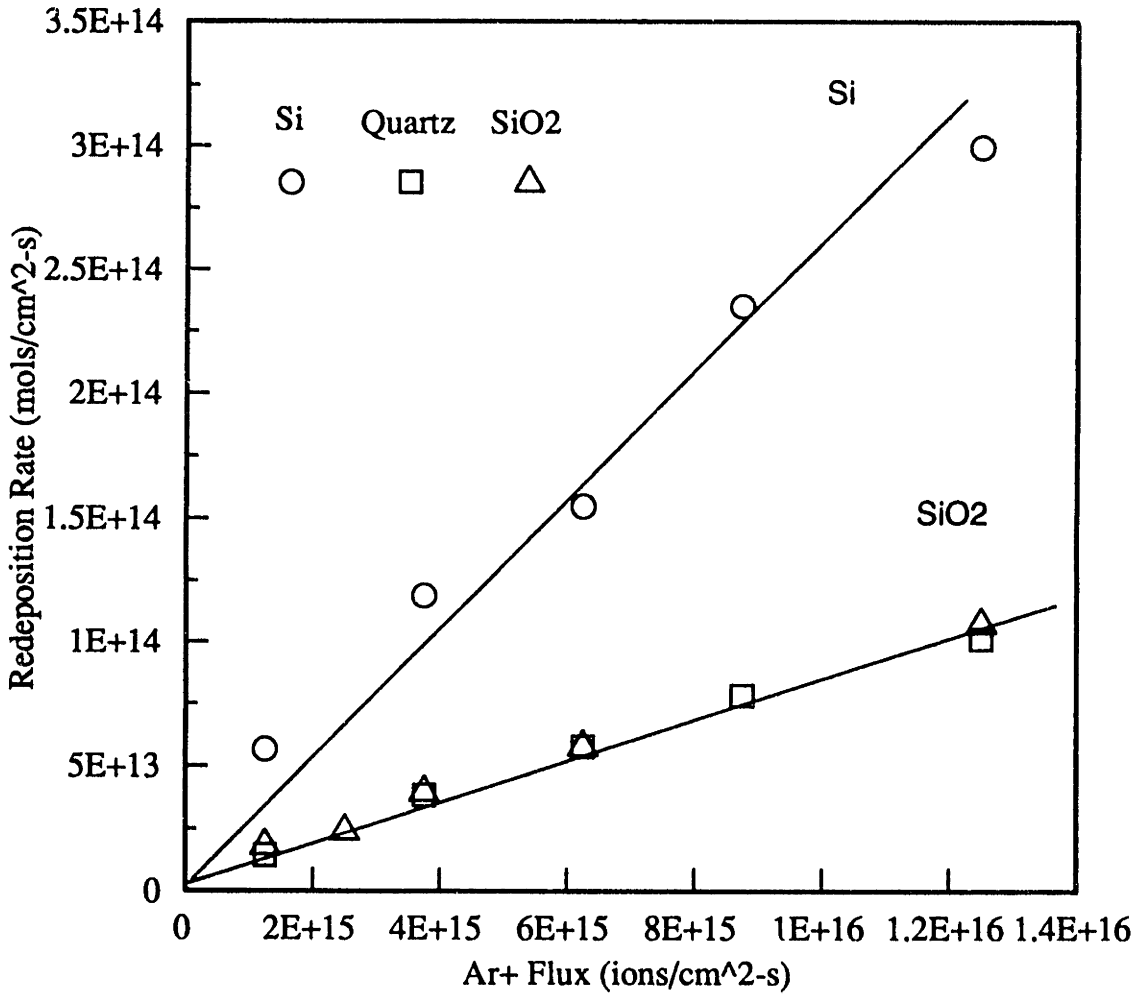

Figure 8-2. Redeposition rates measured during the sputtering of silicon and SiO2 as a function of Ar+ ion flux at 500 eV.

as a function of the product emission angle θ. Given the angular emission function J(θ) [=]sr-1 for the sputtered silicon, the flux of sputtered silicon to the solid angle dω is,

$$d^2R_{Si} = S\,J(\theta)\,dA_s\,d\omega \qquad S = \frac{totalSi}{cm^2\text{-}s} \tag{8-1}$$

Given our quartz crystal detector of known area, and assuming a constant ion flux over the die area, we may approximate the sputtered Si flux to the QCM at any angle through the appropriate integrations,

$$\Delta R_{Si} = Y_{Si}\,I^+ \int J(\theta)\,d\omega \tag{8-2}$$

In general we must perform the integration over the angular emission function J(θ) which satisfies the criterion,

$$\iint J(\theta)\,\sin(\theta)\,d\theta\,d\phi = 1.0 \tag{8-3}$$

However, if the detector is small we may make the approximation,

$$\delta R_{Si} \approx A\,(E_i^{0.5}-E_{th}^{0.5})\,I^+\,J(\theta)\,\gamma_{Si}\,\frac{A_{det}}{d^2} \tag{8-4}$$

Assuming a constant sticking coefficient for the sputtered Si product, γ_{si}, results in a linear relationship between the ion flux and total redeposition rate at a given ion energy in the form,

$$r_{d,Si} = \delta R_{Si}\ \gamma_{Si} = A_{Si}(E_i^{0.5} - E_{th,Si}^{0.5})\ I^+\ J_{Si}(\theta)\ \gamma_{Si}\ \frac{A_{det}}{d^2} \qquad (8\text{-}5)$$

Error in these approximations is acceptable compared to that caused by fluctuations in the ion current, and limitations in the QCM sensitivity. The Ar^+ ion energy dependence of Si redeposition is shown in Figure 8-3 to be a linear function of the square root of ion energy (E_i), at constant Ar^+ flux as predicted by equation (8-5). This again suggests a constant sticking coefficient for the metal atoms as expected. Given the calibration constant, C= 12 ng/Hz, for the quartz crystal employed, equation (8-5) may be used to back calculate the apparent sticking coefficient for the sputtered Si shown in Figures 8-4 and 8-5, where the net deposition rate is determined by:

$$r_{d,net} = F\ C\ \frac{N_a}{M} = r_{d,i} - r_{etching} \qquad (8\text{-}6)$$

The Si sticking probability was found to be near unity and was expected to be insensitive to surface condition of the quartz microbalance. To test this hypothesis the crystal was exposed to approximately 1L CF_2 coverage (see Figure 8-4), after which the Si sputtering was resumed and revealed the same sticking coefficient within experimental error. The slight decrease in the apparent sticking coefficient with ion flux may be due to etching of the microbalance surface by high energy reflected and sputtered particles and/or inaccuracies in our sputtering model.

Extension of the Steinbrukel [1989] model to the physical sputtering of composite materials such as SiO_2 is not rigorous, but was shown in Chapter 5 to result in a good empirical approximation to SiO_2 sputtering data when the parameters in Table 5-1 are employed. Equation (8-5) must be modified to include the emission of multiple products,

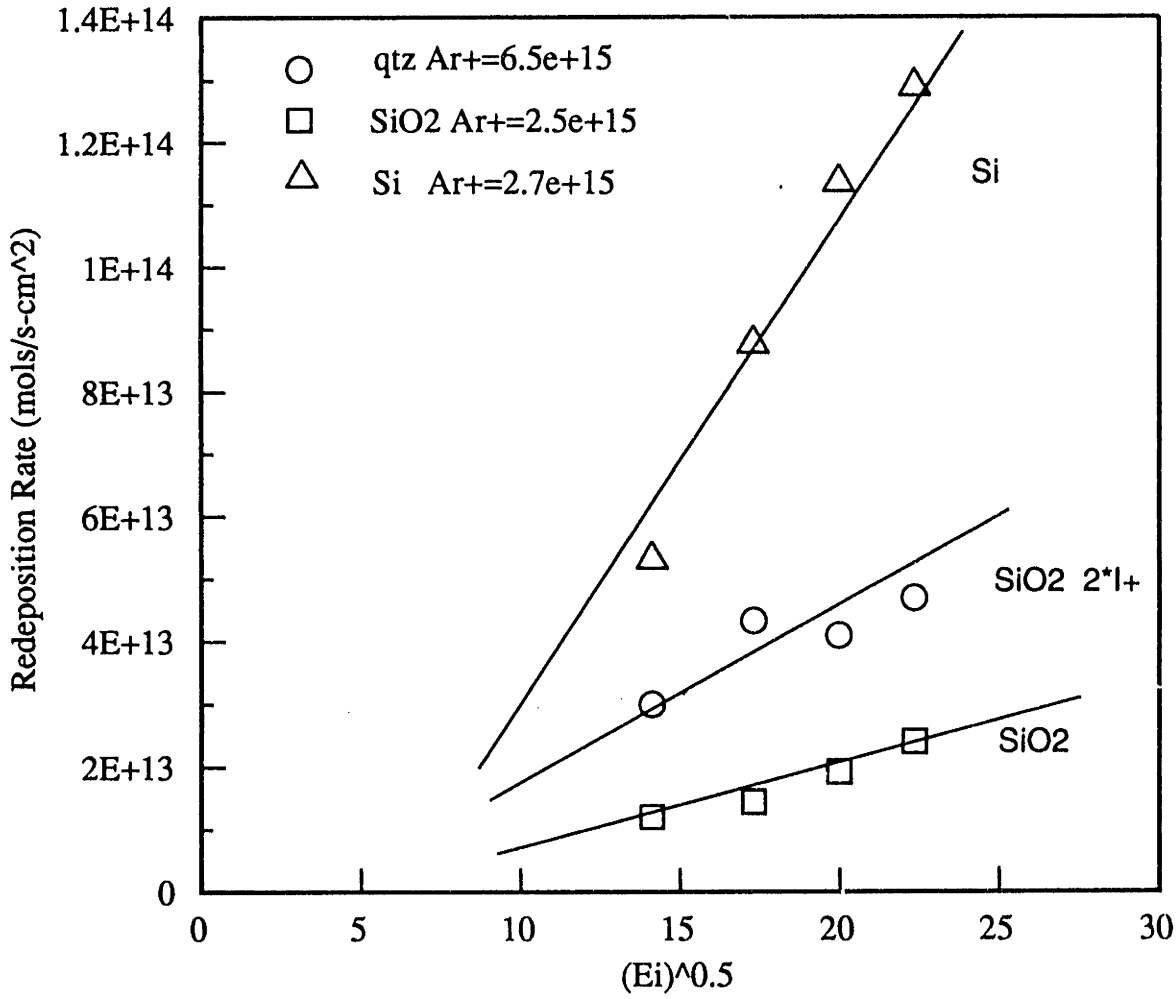

Figure 8-3. Redeposition rates measured during the sputtering of silicon and SiO2 as a function of (Ei)^0.5.

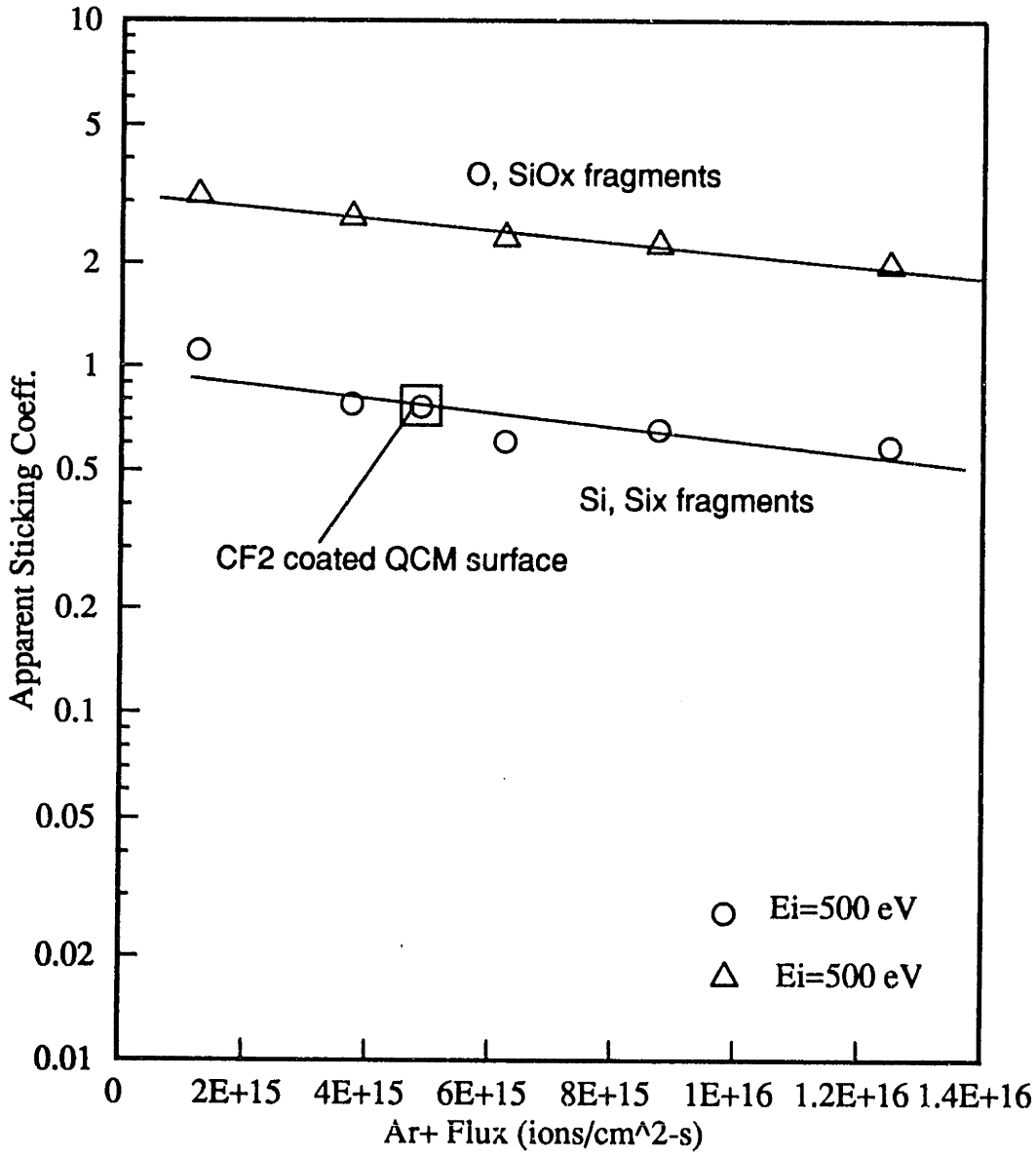

Figure 8-4. Apparent sticking coefficient for sputtered silicon and SiO2 redepositing on the QCM surface as calculated from equation (5-7) as a function of ion flux.

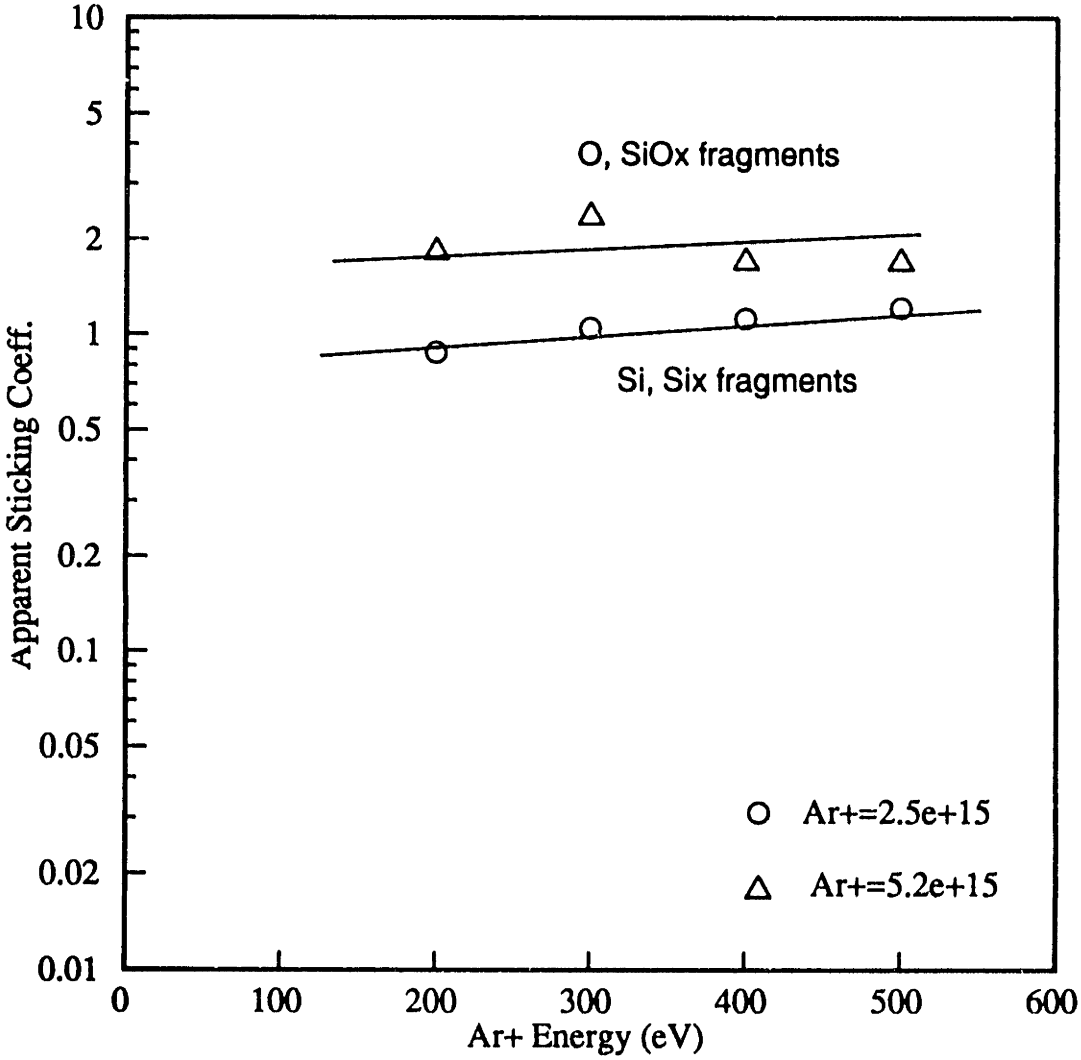

Figure 8-5. Apparent sticking coefficient for sputtered silicon and SiO2 redepositing on the QCM surface as calculated from equation (5-7) as a function of ion energy.

$$r_d = \sum_{i=1}^{n} r_{d,i} = \sum_{i=1}^{n} A_i \, (E_i^{0.5} - E_{th,i}^{0.5}) \, I^+ \, J_i(\theta) \, \gamma_i \, \frac{A_{det}}{d^2} \qquad (8\text{-}7)$$

Assuming constant product distributions and sticking coefficients for the SiO_2-sputtering product stream, we may again expect a linear relationship between the total product redeposition rate and the Ar^+ ion flux shown in Figure 8-2 for 500eV. A linear proportionality in $\sqrt{E_i}$ is suggested in Figure 8-3, where two different ion flux levels have been employed. Back-calculation of the product sticking coefficients in the SiO_2 sputtering provides some interesting insight. If only the Si metal in the oxide film were assumed to redeposit e.g. molecular oxygen being the other sputtering by product, an apparent sticking coefficient for Si in the range of 3 to 6 is calculated. This is not in good agreement with the Si redeposition data. If we instead take a unity sticking coefficient for silicon, and assume the remainder of the SiO_2 sputtering by-product is atomic O, we calculate O sticking coefficient in the range of 1-3 (Figures 8-4,5). The sputtering of O_2 or SiO_x clusters is also possible, and expected to be on the order of 10% of the total product stream for our conditions as suggested by the data of Coburn [in Chapman, 1980]. The anomalously high apparent O sticking coefficient is most likely due to the gettering of background oxygen in the film depositing on the QCM, increasing the observed net deposition rate.

The angular characteristic of Si and SiO_2 physical sputtering were also investigated, and are shown in Figures 8-6 and 8-7. Measurement of the Si redeposition rate as a function of detector angle was measured by rotating the QCM assembly in a 180° plane around the sample face, revealing the data in Figure 8-6 which includes polar angles of 27° to 90°; other angles are excluded due to the finite size of the QCM assembly. The data was found to be symmetric on both sides of the sample face and suggests that the angular distribution of the sputtered product stream is over-cosine e.g. more peaked than a cosine distribution as represented by the solid line

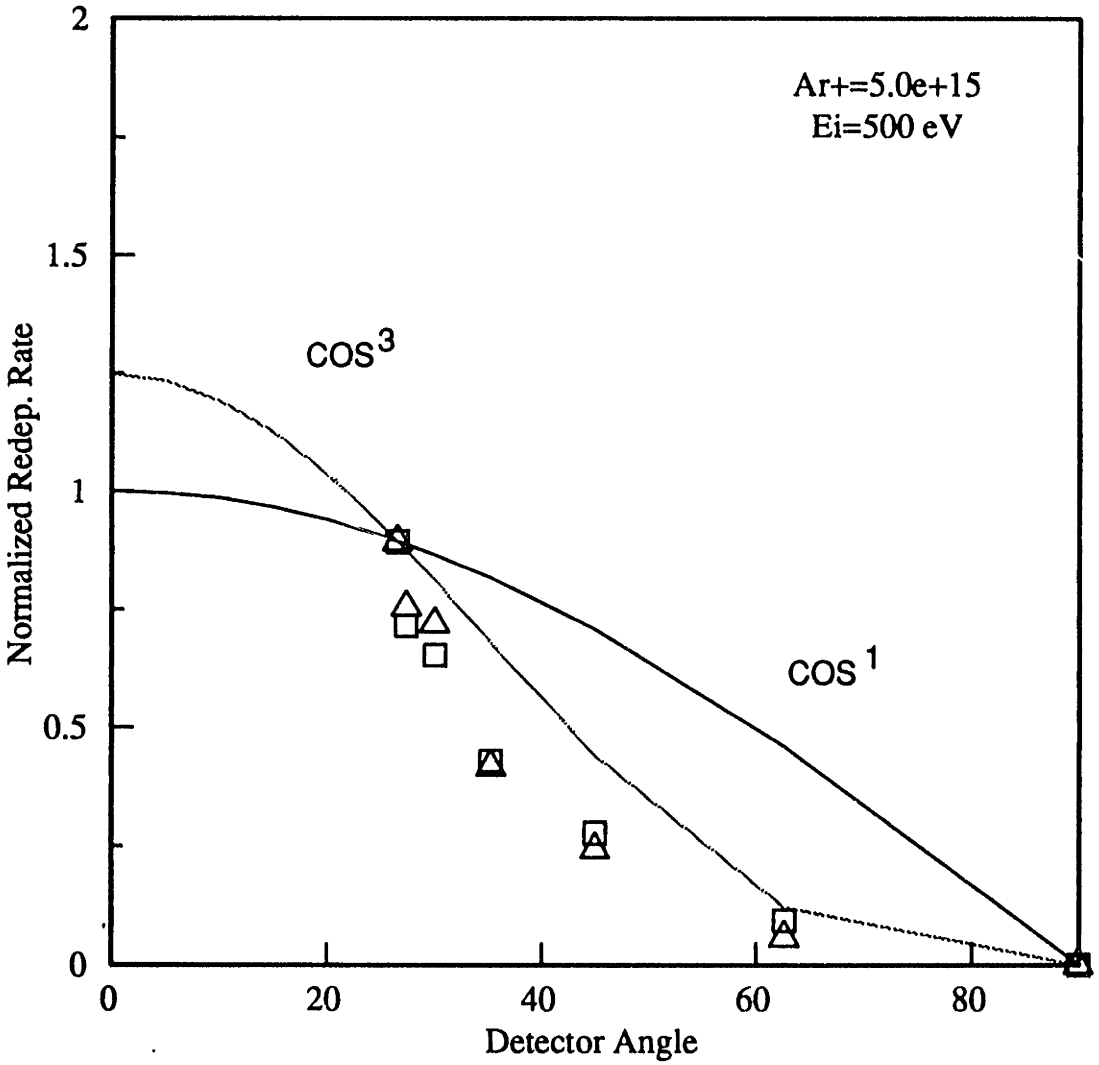

Figure 8-6. Angular characteristics of sputtered silicon redeposition.

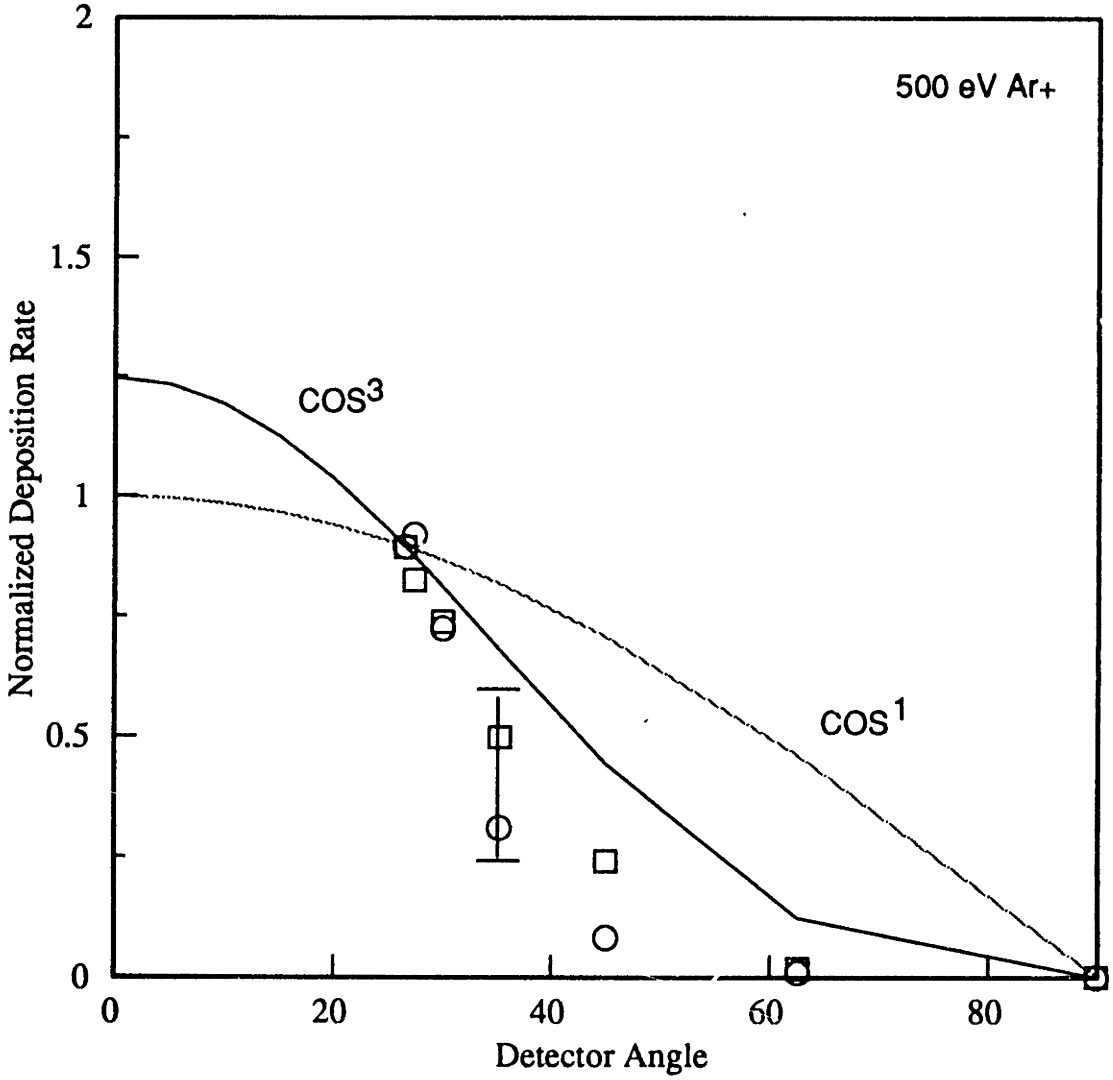

Figure 8-7. Angular characteristics of sputtered SiO2 redeposition.

in Figure 8-7. Error bars in the angular data are significant due to fluctuations in ion current and limitations in positioning precision, but the qualitative trends are reproducible. Previous studies of angular emission characteristics in homogenous film sputtering show increasing directionality with ion-to-target mass ratio, and increasing ion energy [Wucher and Reuter, 1988]. Low energy sputtering <100 eV of some metals such as Al by light ions is known to give undercosine, and possibly lobed distributions [Chapman, 1980], however as ion mass and energy are increased overcosine emission usually results [Behrisch, 1991]. The limited sensitivity of the QCM technique, and the ion current fluctuations made measurement of angular emission characteristics at lower energies irreproducible.

A similar over-cosine distribution is suggested in the angular distribution of SiO_2 etching products as shown in Figure 8-7. Over cosine, bi-modal, and lobed angular distributions have been observed in the sputtering of composite materials in various energy and mass regimes [Behrisch, 1991], but a theoretical understanding of the relative behaviors has not been developed. Wucher and Reuter [1988] demonstrate that in the sputtering of metal alloys, the lighter component may have an over-cosine emission characteristic at low energies, while the heavier component tends to come off in a side lobe. At 2 keV bombardment energies, both species were emitted in a overcosine manner, and were reasonably fit by a $\cos^3(\theta)$ functionality. Due to the relatively large Ar/Si and Ar/O mass ratios, the observation of slightly overcosine angular distributions in the 500 eV sputtering of Si and SiO_2 is not unreasonable, however, the large error bars and missing angular data allow only qualitative interpretation of this data. In addition, correction of the data for the effect of finite detector area would tend to decrease the apparent directionality of the redeposition i.e making the measured distributions appear more cosine.

8.2 Redeposition in Ar^+/F Etching

Product redeposition characteristics are significantly changed with the introduction of an etchant species such as atomic F. Exposure of the Si and SiO_2 samples to simultaneous fluxes of F and Ar^+ results in fluorination of an increasing fraction of the near surface silicon as the F/Ar^+ ratio is increased, and the ion-enhanced production of volatile species such as SiF_4. The net result is a near order of magnitude reduction in redeposition rates below those observed for pure Ar+ sputtering, as shown in Figures 8-8 and 8-9. There is, however, a significant fraction of unsaturated species such as Si, SiF, SiF_2, and SiF_3 released as the result of collision cascades which overcome their surface binding energy [Winters, 1983] as discussed in Chapter 5. Tu et al. [1981] have estimated this fraction in the range of 15-35% for the 500 eV Ar^+ etching of silicon at XeF_2/Ar^+ ratios on the order of 500-1000. Much higher fractions of free radicals have been suggested in semi-quantitative studies of Ar^+/F etching at 2-3 keV energies [Haring et al., 1982, Winters and Coburn, 1985] and at lower F/Ar^+ ratios where fragment production is maximized. A somewhat smaller percentage of SiFx species is qualitatively observed in SiO_2 etching [Tu et al., 1981]. Empirical models for the branching parameter $\mathbf{b} = \sum SiF_x/SiF_4$ in Ar^+/F etching of silicon and SiO_2 which make use of all available quantitative studies in the literature were presented in Figures 5-29 and 5-30, respectively, as discussed in Chapter 5.

Since SiF_x radical species typically have a much lower volatility than the molecular species, they will subsequently stick on sidewall surfaces with high probability. The sticking coefficients of these radical species in the plasma environment are not precisely known, but are on the order of 0.01 to 0.1, whereas the sticking probability of the molecular species (SiF_4) is on the order of 10^{-5} [Winters, 1978]. In addition to these "sticky" free radical species, unfluorinated free Si and O/ SiO_x fragments in the case of SiO_2 etching are still removed from these surfaces in significant fractions under certain conditions. In general, exposing the surfaces to lower F/Ar^+

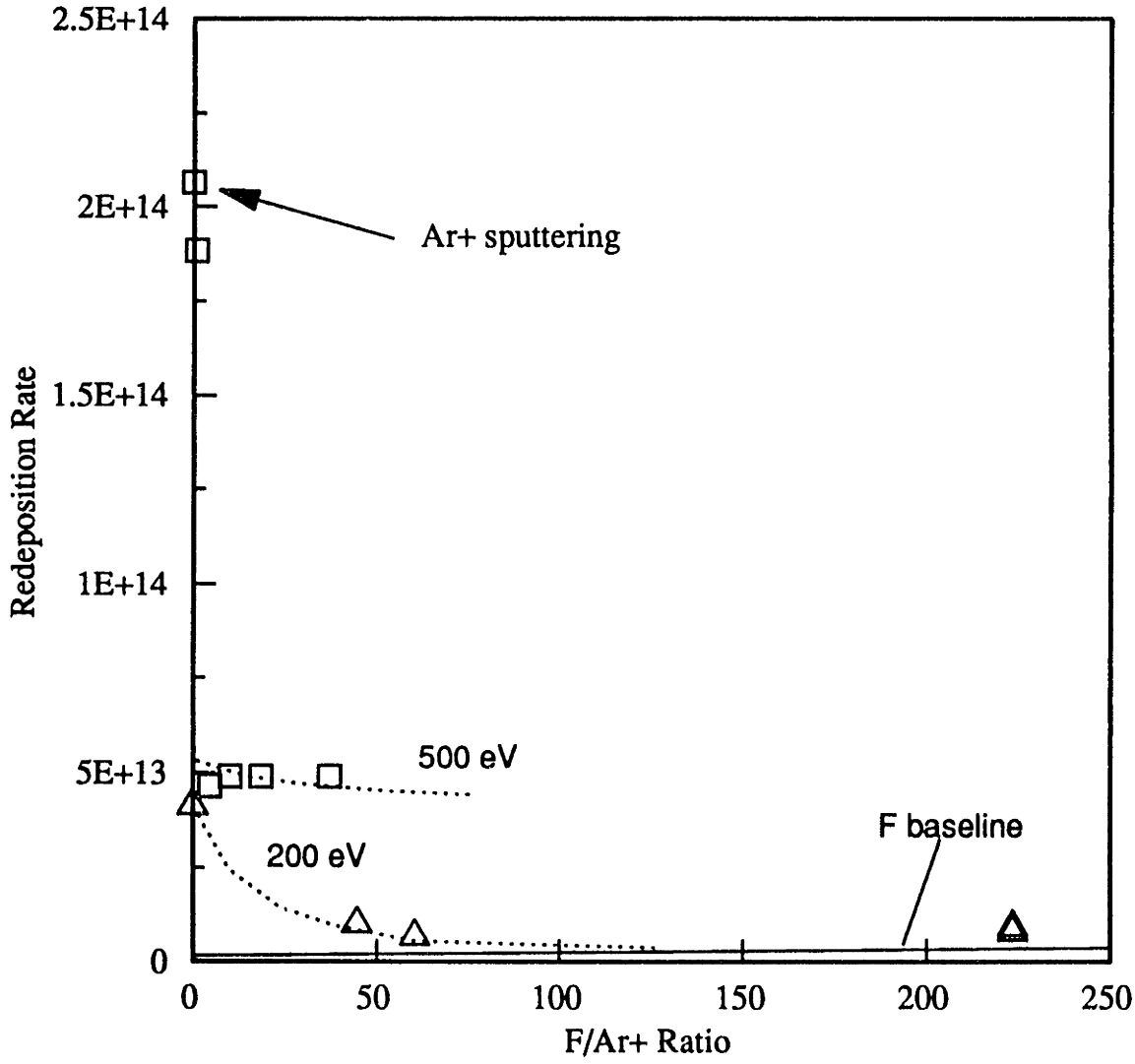

Figure 8-8. Redeposition rates measured during Ar+/F etching of silicon as a function of F/Ar+ flux ratio.

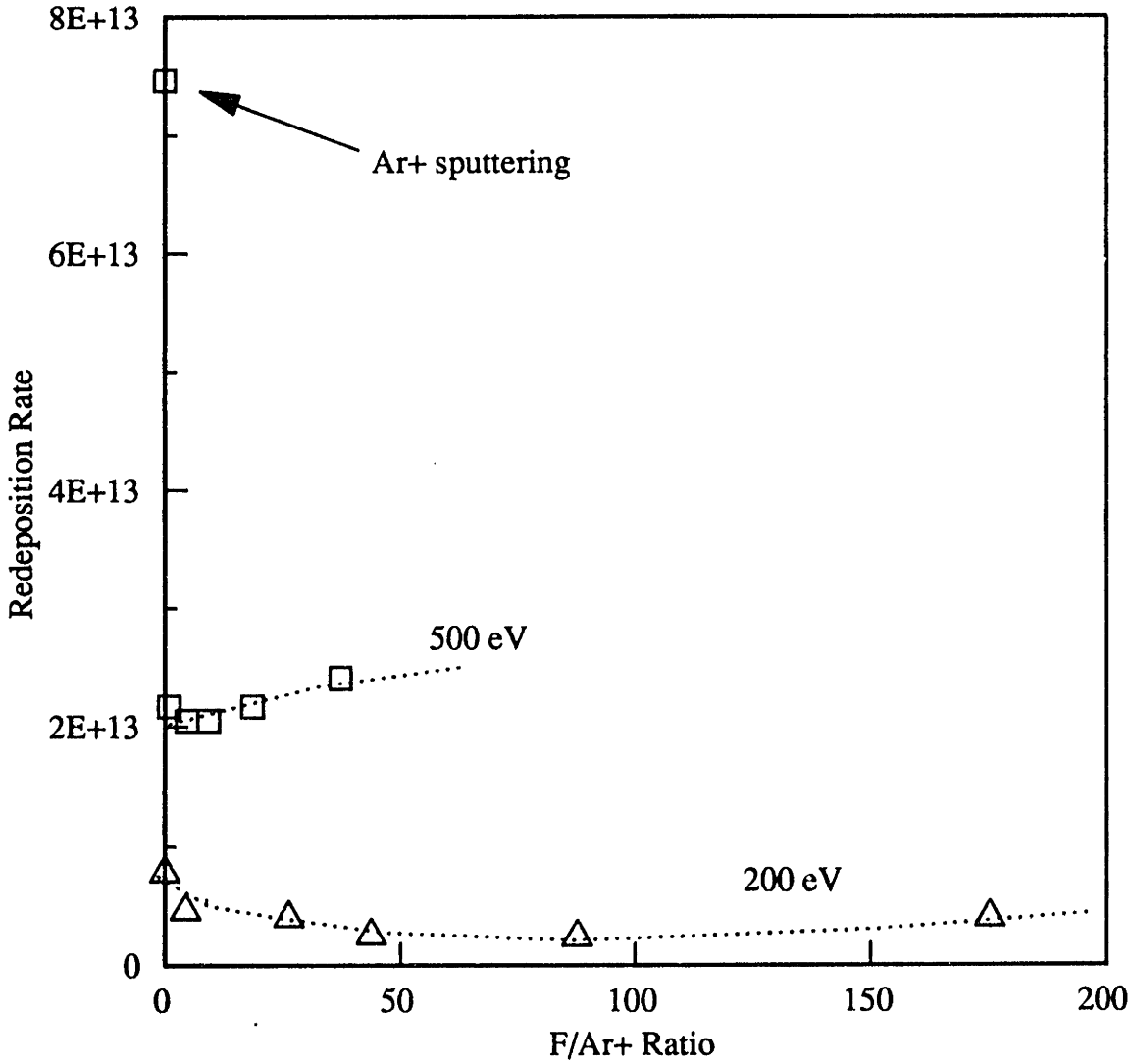

Figure 8-9. Redeposition rates measured during Ar+/F etching of SiO2 as a functicn of F/Ar+ ratio.

flux ratios, or increasing the ion bombardment energy at a given F/Ar^+, decreases the fractional fluorination of available near-surface "sites", and results in the production of a "stickier" product stream i.e. containing a higher percentage of free Si, SiF_x, and O and SiO_x in the case of SiO_2 etching. The predicted effects of increasing flux ratio at on production rates of these various species at 200 eV versus 500 eV are compared in Figures 8-10 and 8-11 for Ar^+/F etching of Si and SiO_2, respectively.

Given model prediction of evolution rates for the various products of Si and SiO_2 etching, we may estimate redeposition rates using the appropriate form of equation (8-7) given that approximate values for sticking species sticking coefficients are known. In the case of Ar^+/F etching of Si, free sputtered Si and SiF_2 are the only "sticky" products in our model system, since the sticking coefficient of SiF_4 is orders of magnitude lower. Our first inclination was to assign the fraction of free silicon evolved a sticking coefficient of 1.0, based on the silicon sputtering data. However, this procedure overestimates redeposition rates in the presence of background atomic fluorine by nearly an order of magnitude, and suggests that fluorine sorbed on the QCM surface "passivates" the surface toward sticking of Si and other radicals. This effect results in the initial precipitous drop in measured redeposition rates shown in Figures 8-8 and 8-9 with the addition of small amounts of F to the system, an effect which is not observed for surface coverage of fluorocarbon radicals such as CF_2 (see section 8.3). In the case of free Si deposition, it is likely that the F "passivation" effect arises from the high probability of re-etching where the Si encounters large concentration of surface F. This is in contrast to the more standard passivation mechanism which involves the blocking of adsorption "sites". This type of radical sidewall passivation has been suggested in chlorocarbon based etching systems where recombination reactions with Cl adsorbed on trench sidewalls precludes the deposition of polymers and increases etching anisotropy [Mogab and Levinstein, 1980].

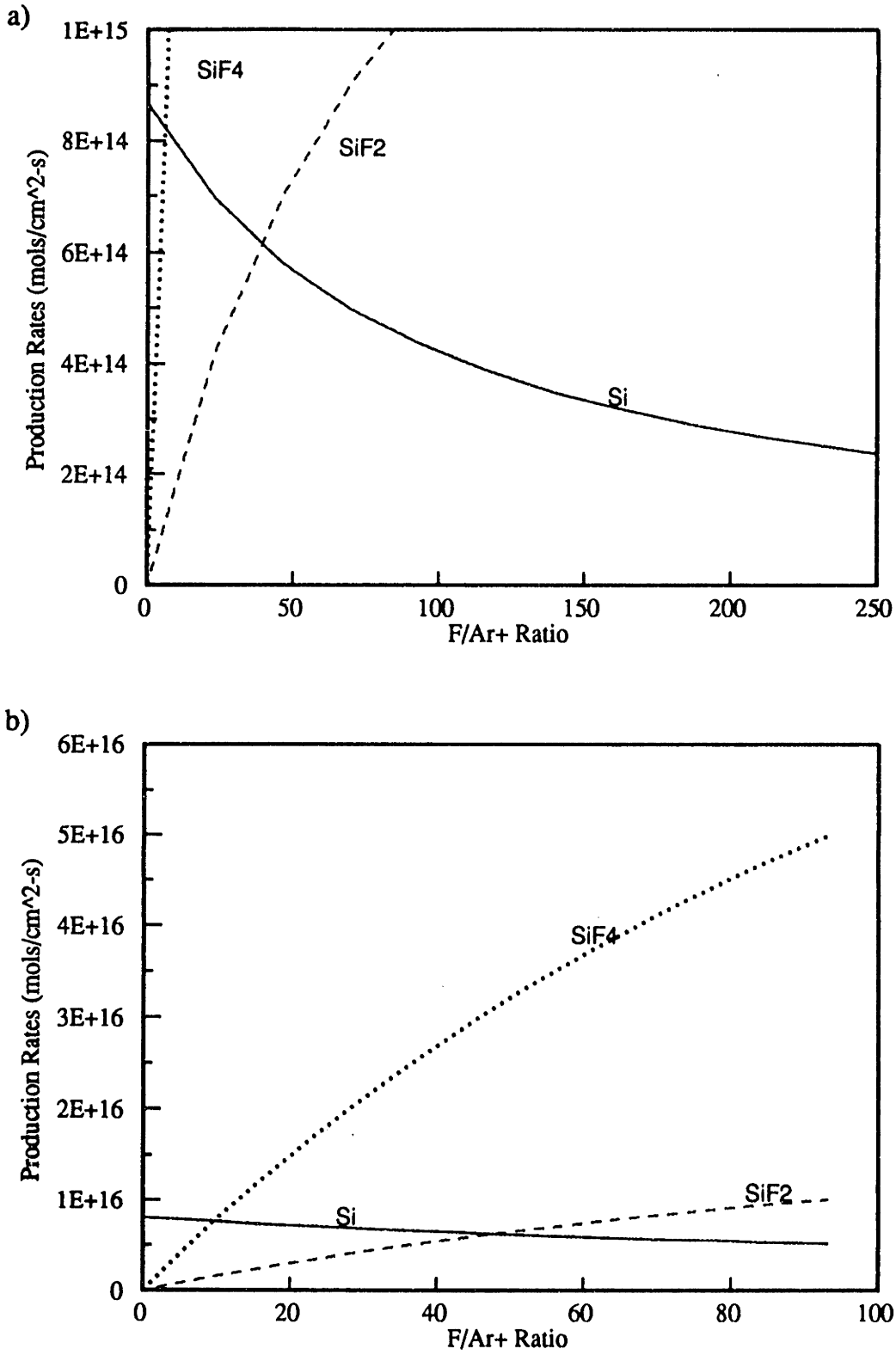

Figure 8-10. Predicted production rates for Ar+/F etching of silicon as a function of F/Ar+ ratio at a) 200 eV and b) 500 eV ion energy.

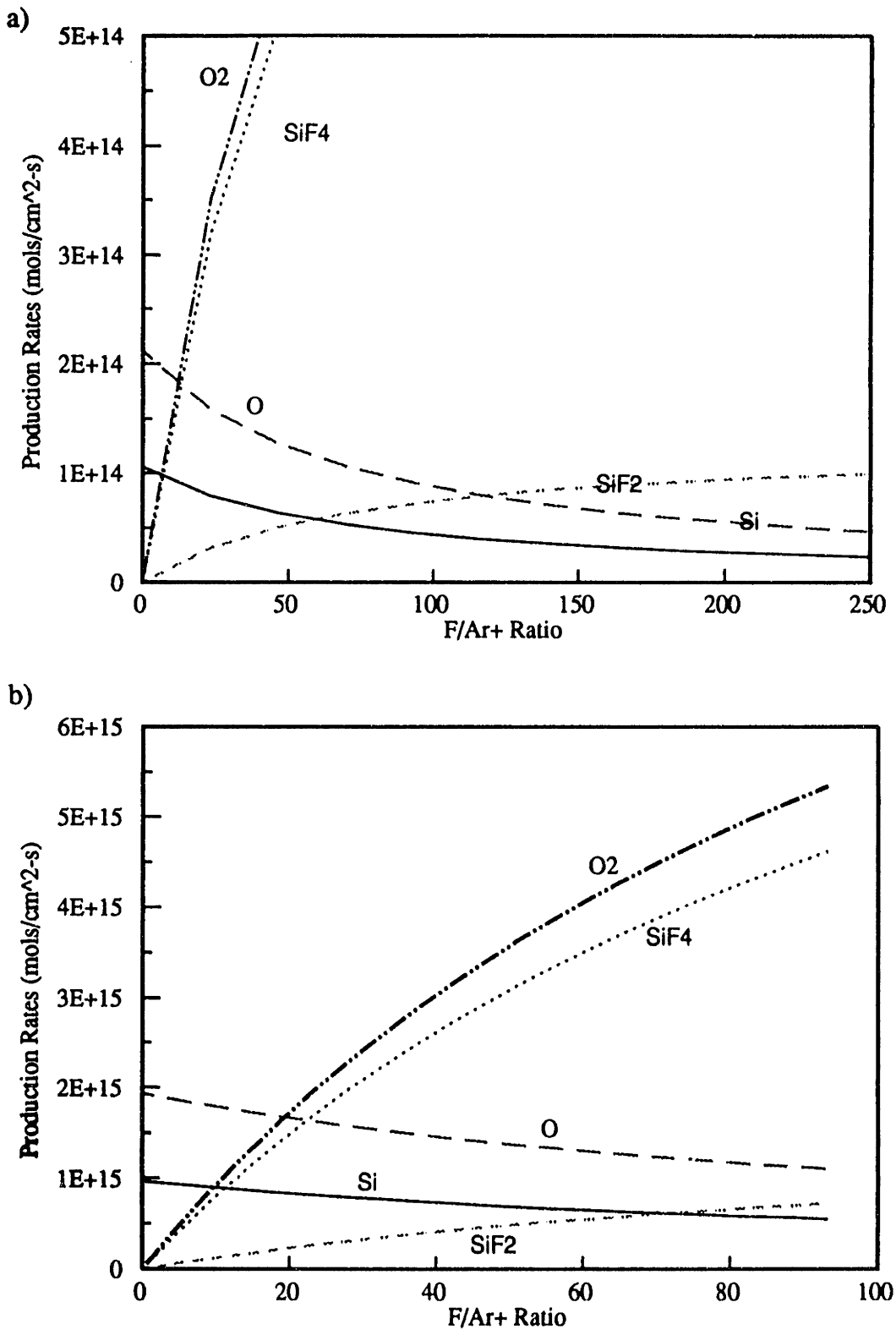

Figure 8-11. Predicted production rates for Ar+/F etching of SiO2 as a function of F/Ar+ ratio at a) 200 eV and b) 500 eV ion energy.

At both energy levels investigated for the Ar^+/F etching of Si, the data suggests approximately an order of magnitude reduction in the Si sticking coefficient (γ_{si}=0.1-0.2) in the presence of a fluorine background; the apparent Si sticking coefficient which best fits the 500 eV data in Figure 16 is slightly lower because higher Ar^+ fluxes were employed (see the effect of increasing Ar^+ flux in Figure 8-4). Given this observation, we can then estimate the SiF_2 (SiF_x) radical sticking coefficient on the order of 0.01 as required to maintain the relatively flat trend in redeposition rates observed in Figures 8-12 and 8-13. Although this is a reasonable sticking coefficient for SiF_x-like products, conclusive measurement of sticking coefficients would require simultaneous measurement of product emission rates and redeposition rates at a given detector angle.

The effect of baseline F adsorption and/or etching on the net QCM signals was also considered. It was found that in the case of Si etching, stopping the flux of Ar^+ ions resulted in the etching of the deposit on the QCM by F scattered from the sample face and in the chamber background. However, there may have been a brief sorption period which was not observed in the several seconds taken to set up the experiment. In studies of redeposition rate as a function of polar angle, θ, it was found that F sorption at 90° polar angles resulted in a baseline deposition signal of approximately 10% of the total signal at $F=5x10^{16}$. An effective sticking coefficient for F based on this data and the F flux to the QCM is then on the order of about 10^{-4}. At the higher F fluxes and low energies where F sorption could be most problematic, etching or nonlinearity in the QCM signal was not observed, indicating that the F sorption rate was not dominating. Similar background F sorption rates were noted in the Ar^+/F etching of SiO_2. However, when the Ar^+ flux was stopped in the SiO_2 etching experiments, a brief period of F sorption followed by etching of the QCM deposit was observed.

The oxide etching system has the additional complication of a large fraction of atomic

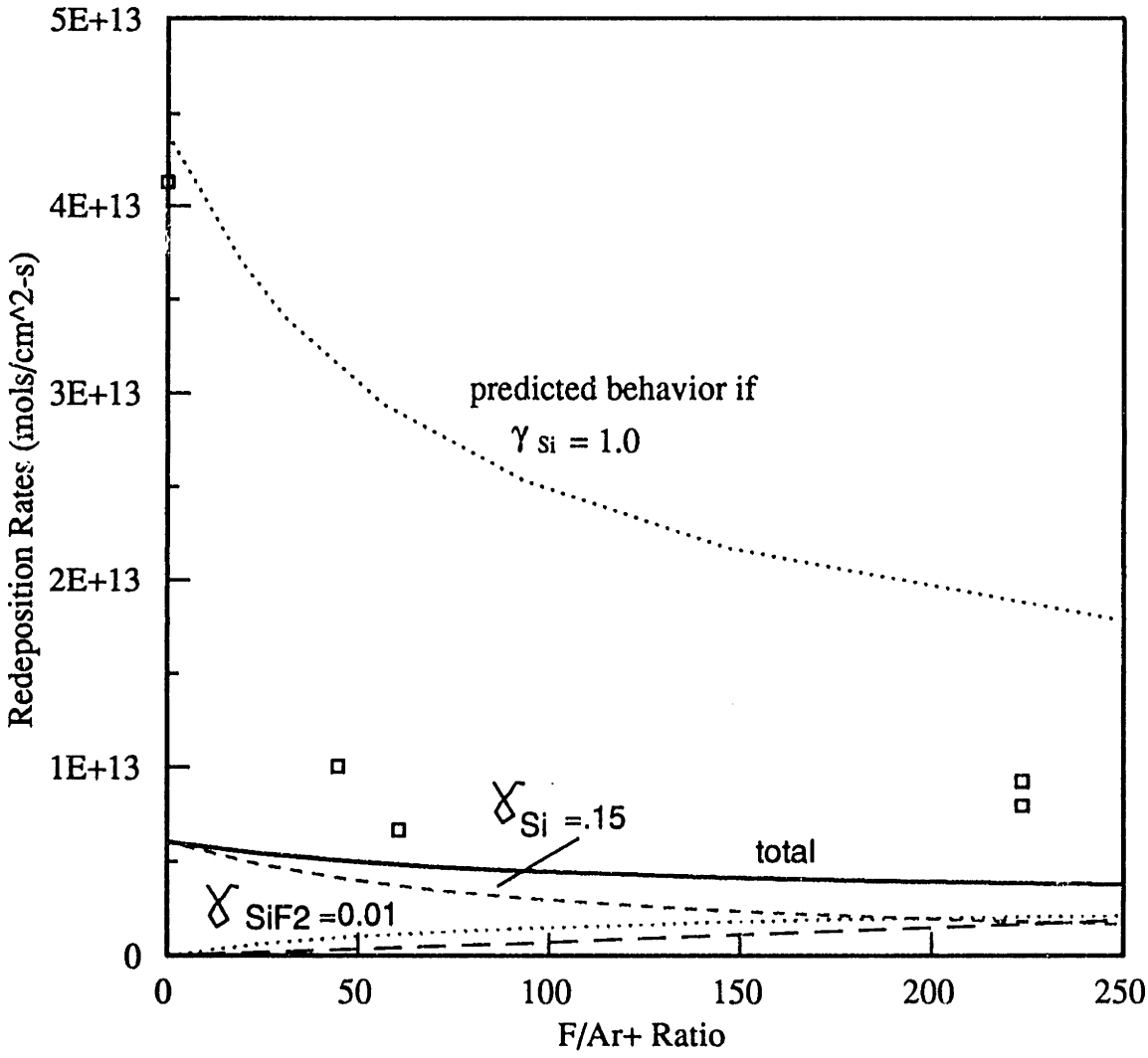

Figure 8-12. Predicted trends in product redeposition for 200 eV Ar+/F etching of silicon given γ_{Si}= 0.15 and γ_{SiF_x}= 0.01.

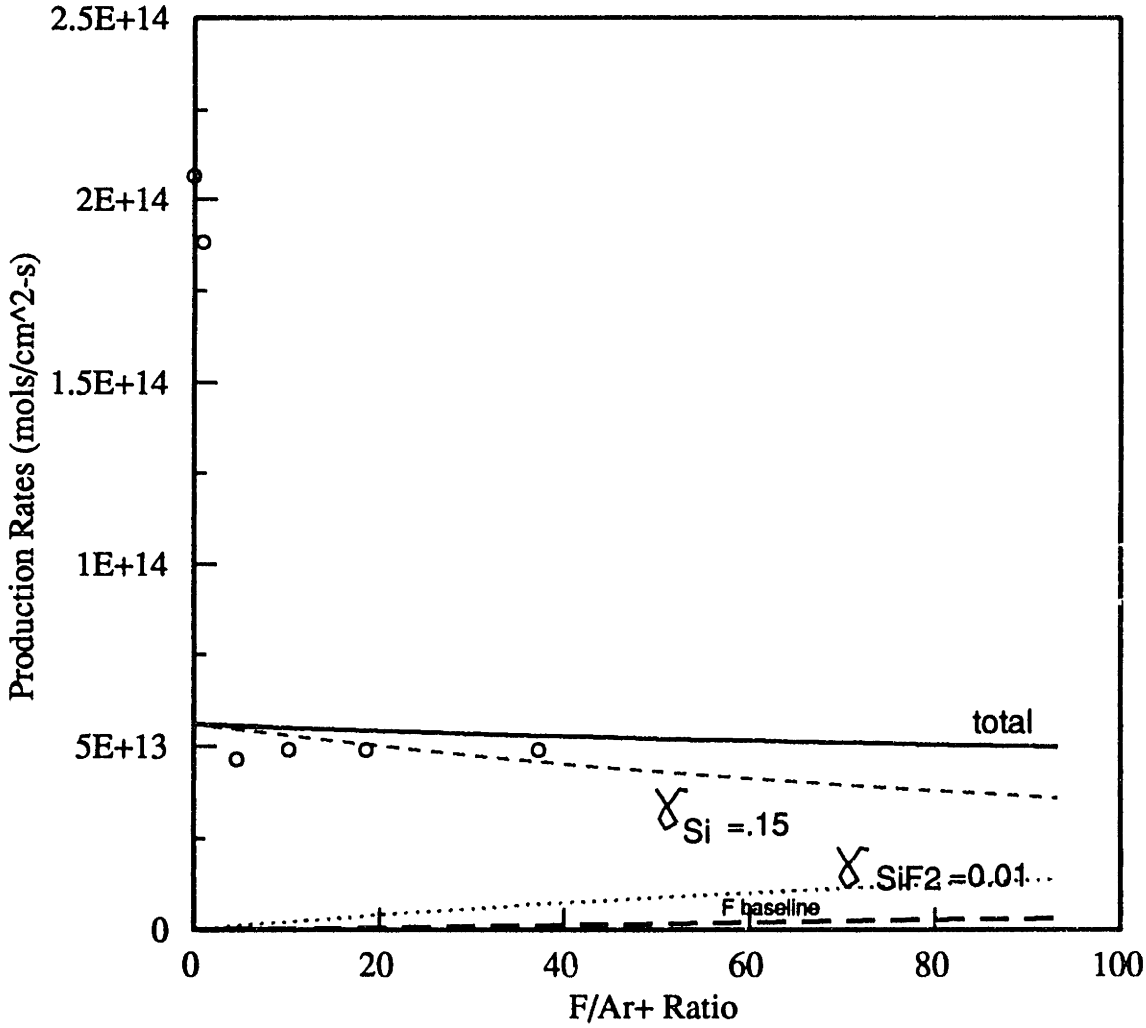

Figure 8-13. Predicted trends in product redeposition for 500 eV Ar+/F etching of silicon given $\gamma_{Si} = 0.15$ and $\gamma_{SiF_x} = 0.01$.

oxygen being liberated and subsequently sticking on the QCM. If we assume that the sticking probability of Si and the relatively small fraction of SiF_2 produced are not changed by the oxygen addition, an apparent O sticking coefficient of about 0.5 is required to fit the data in Figures 8-14 and 8-15. The reduction in O sticking coefficient is also thought to reflect the F passivation, and/or F-O recombination kinetics on the QCM surface. From modeling results presented above, it becomes clear that the bulk of the redeposition measured in the Ar^+/F etching of Si and SiO_2 is a result of the small fraction of Si and O/SiO_x which are physically sputtered from the respective surfaces.

The effects of ion bombardment energy on redeposition rates at constant F/Ar+ are illustrated in Figures 8-16 and 8-17 for Si and SiO_2 etching respectively. It was demonstrated in Figure 8-3 that redeposition of fragments for Ar^+ sputtering of Si and SiO_2 showed a linear increase as $\sqrt{E_i}$. Since we have recognized that the redepositing products in these systems are those which originate from physical removal mechanisms (i.e collision cascade-induced), one might expect the fragment redeposition in the Ar^+/F systems to show a similar energy dependence. However, due to the non-linear decrease in F site occupation with increasing ion energy predicted by our model, the distribution of "sticky" products evolved in these systems respond in a non-linear fashion to increases in $\sqrt{E_i}$, as shown in the model results of Figures 8-18 and 8-19 at F/Ar^+ ratios of 50 versus 500. This non-linearity can be seen in the data presented in Figures 8-16 and 8-17. Comparisons of our model predictions to this data in Figures 8-20 and 8-21, where the sticking coefficients discussed above were employed. Although the qualitative trends and nonlinearity are described by our model, we underpredict the rapid increase in redeposition rates with energy in both the Si and SiO_2 etching studies. In addition, we fail to capture an important feature in the data presented in Figures 8-16 and 8-17, which is the relative ordering of the redeposition rates at flux ratios (F/Ar^+) of 50 and 500 eV i.e. redeposition rates at F/Ar^+=500 are

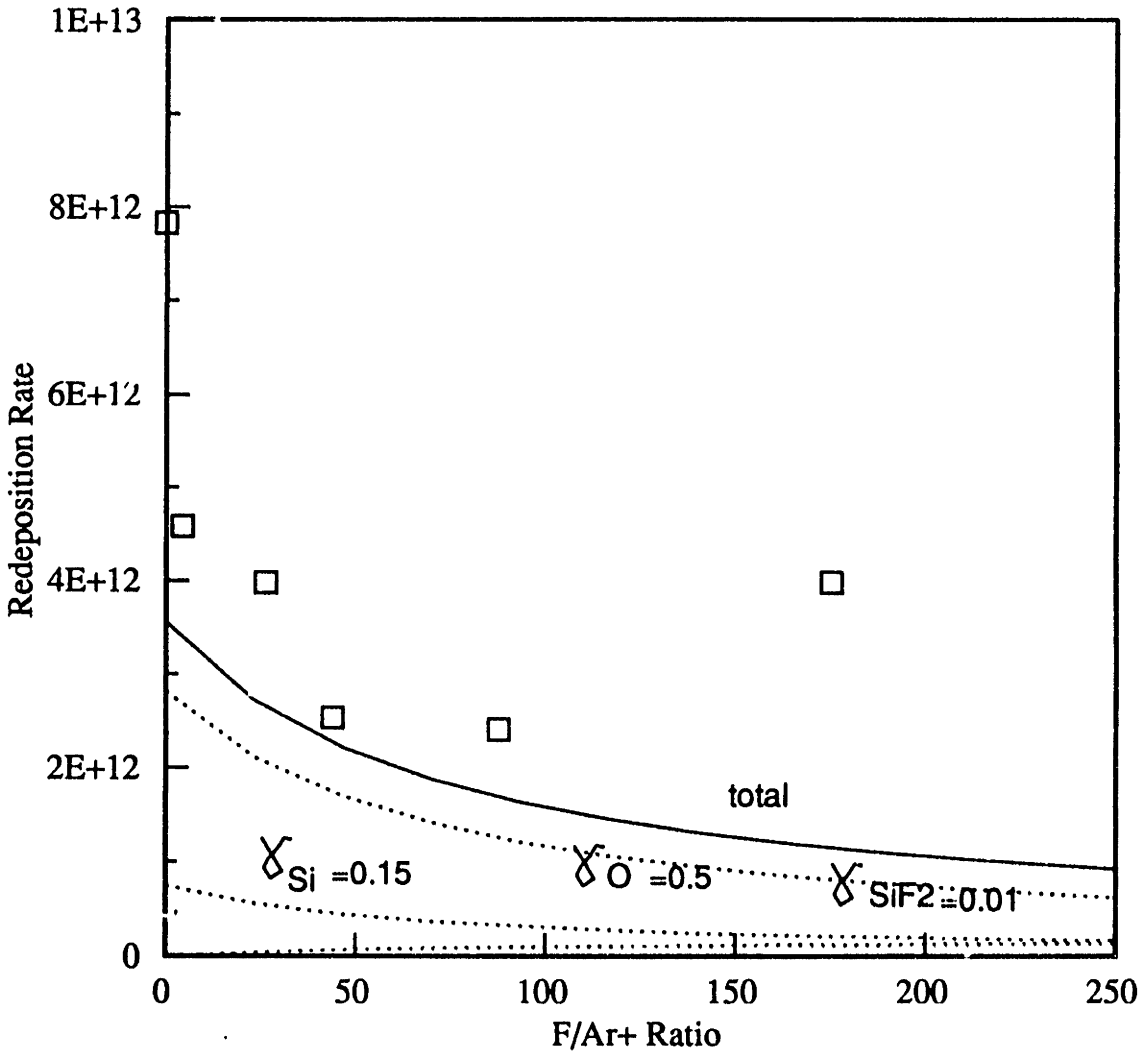

Figure 8-14. Predicted trends in product redeposition for 200 eV Ar+/F etching of SiO2.

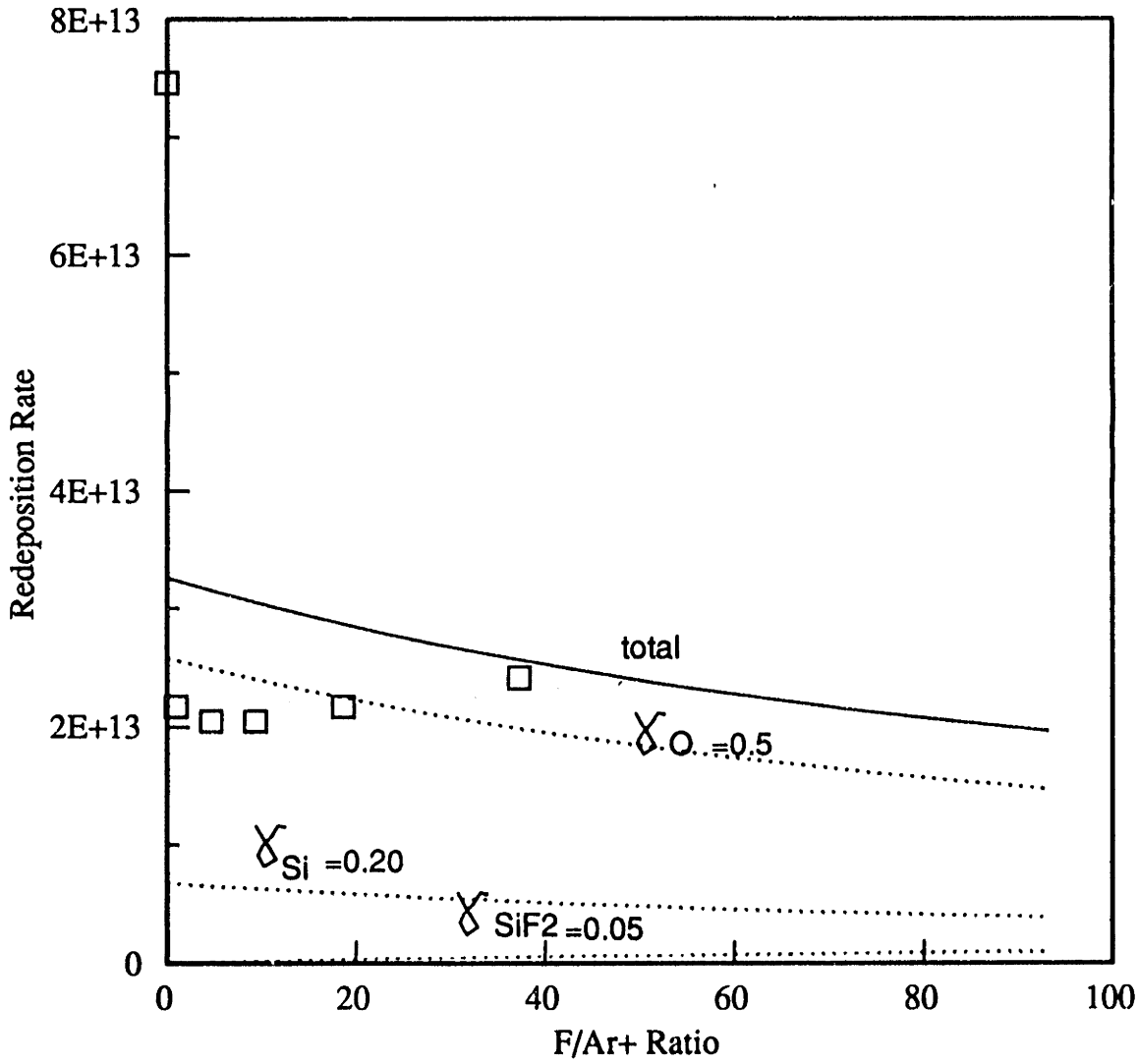

Figure 8-15. Predicted trends in product redeposition for 500 eV Ar+/F etching of SiO2.

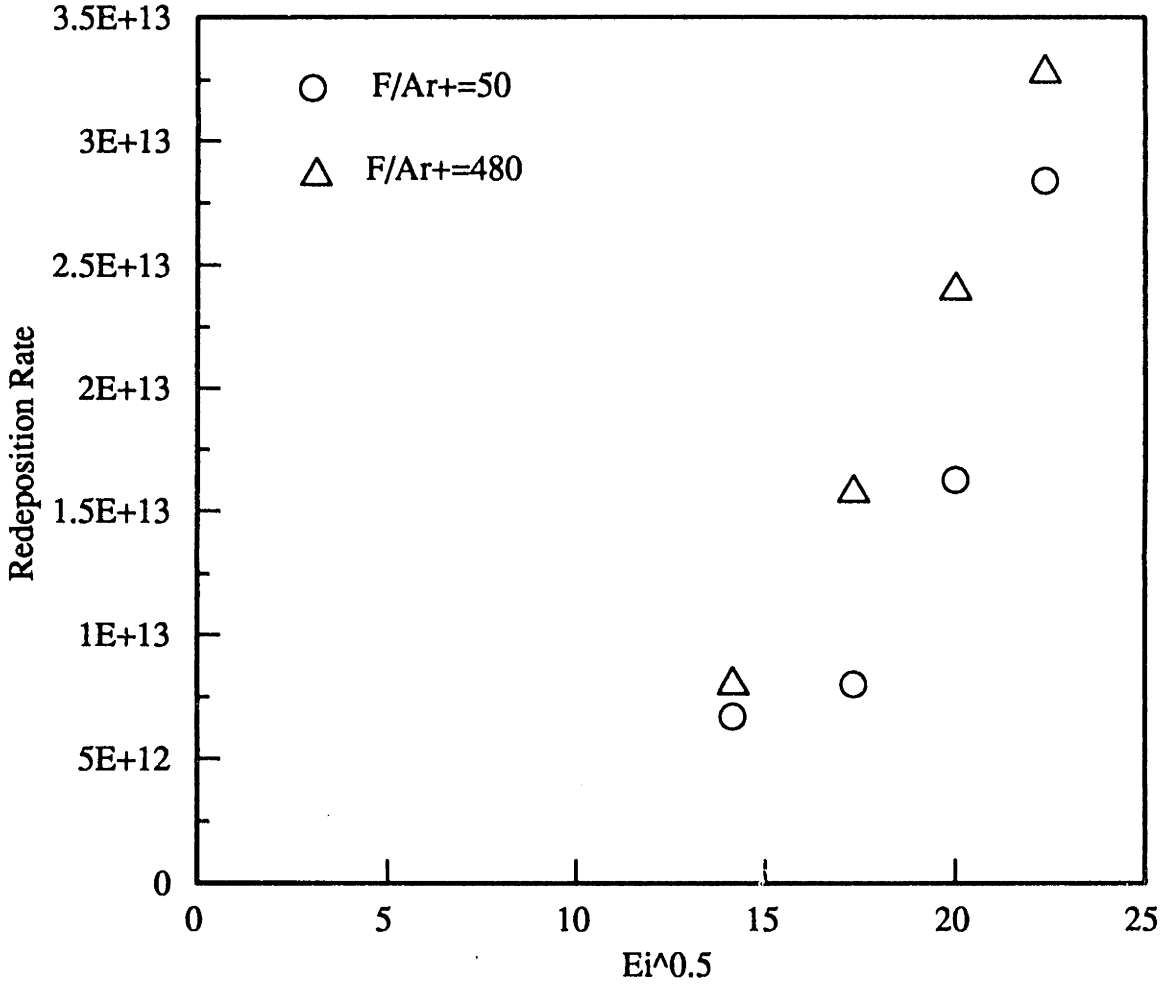

Figure 8-16. Redeposition rates measured during Ar+/F etching of silicon as a function of (Ei)^0.5.

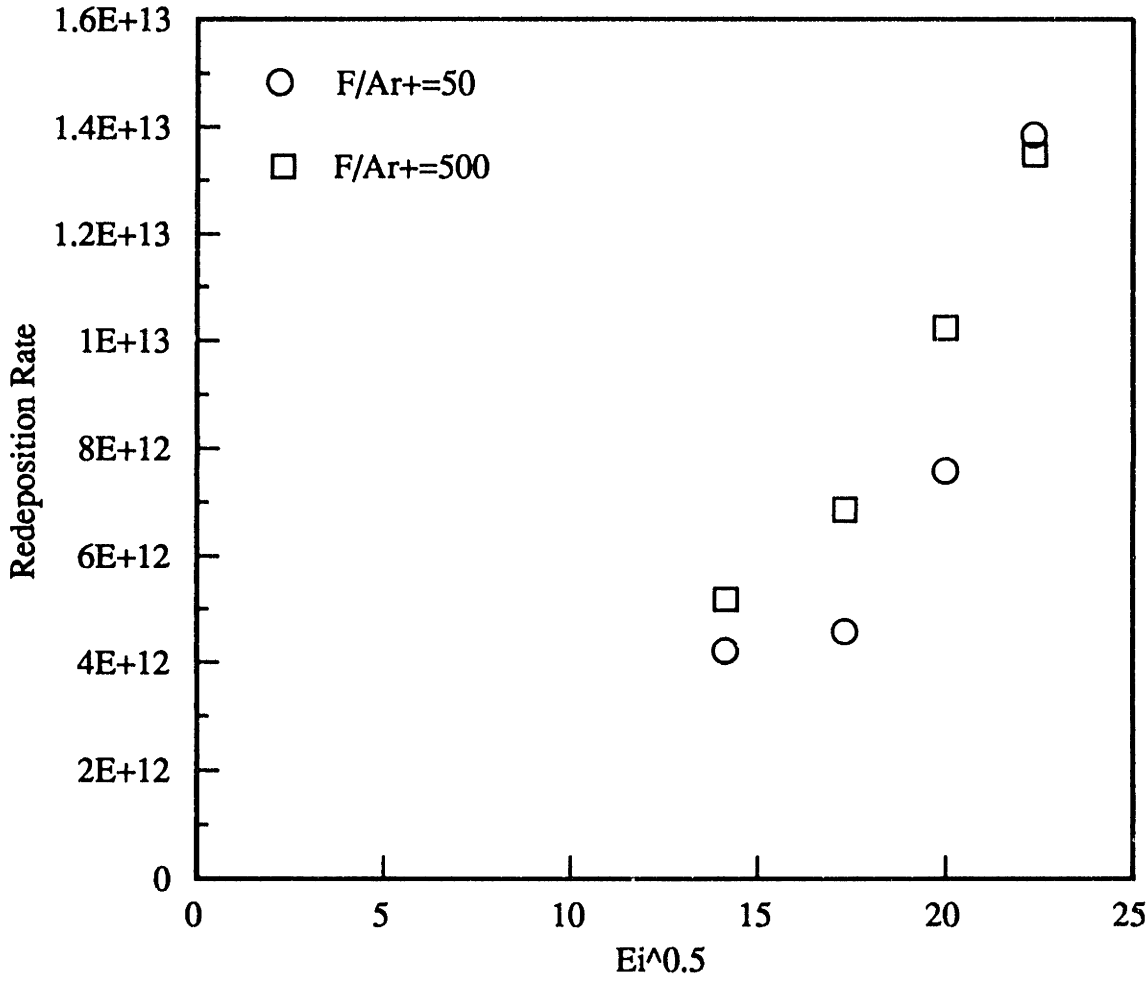

Figure 8-17. Redeposition rates measured during Ar+/F etching of SiO2 as a function of (Ei)^0.5.

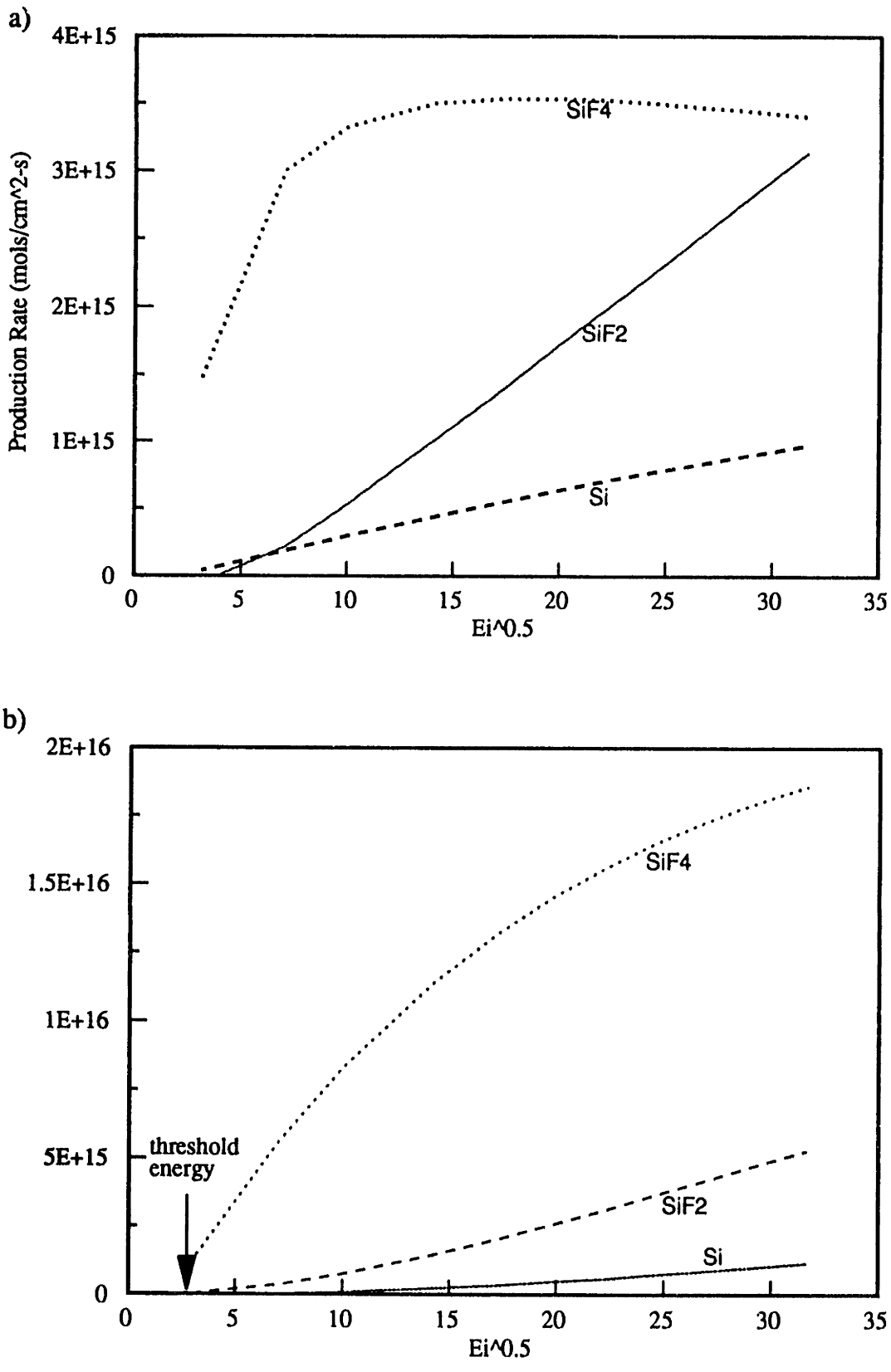

Figure 8-18. Predicted production rates for Ar+/F etching of silicon as a function of (Ei)^0.5 at F/Ar+ ratios of a) 50 and b) 500.

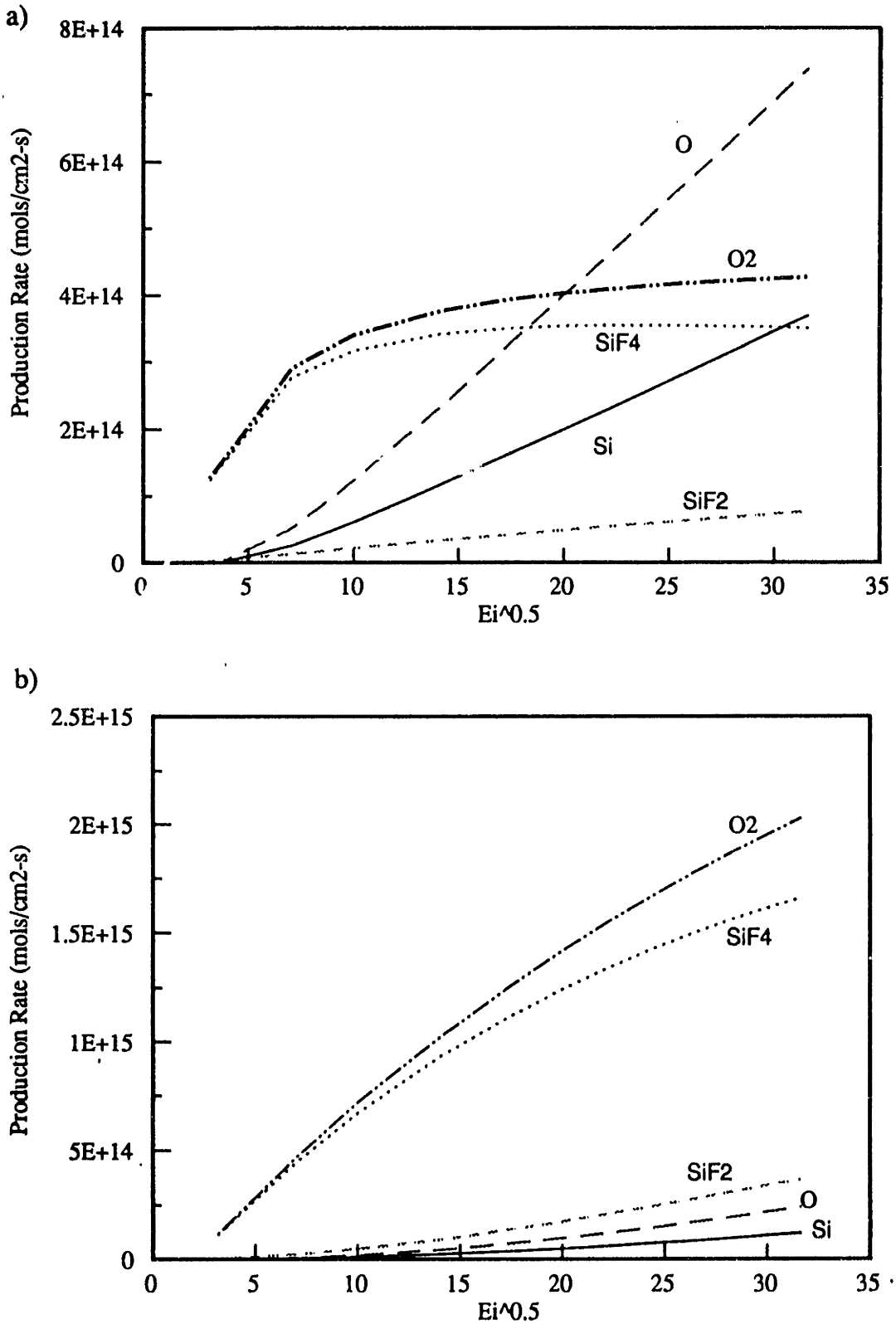

Figure 8-19. Predicted prodcution rates for Ar+/F etching of SiO2 as a function of (Ei)^0.5 at F/Ar+ ratios of a) 50 and b) 500.

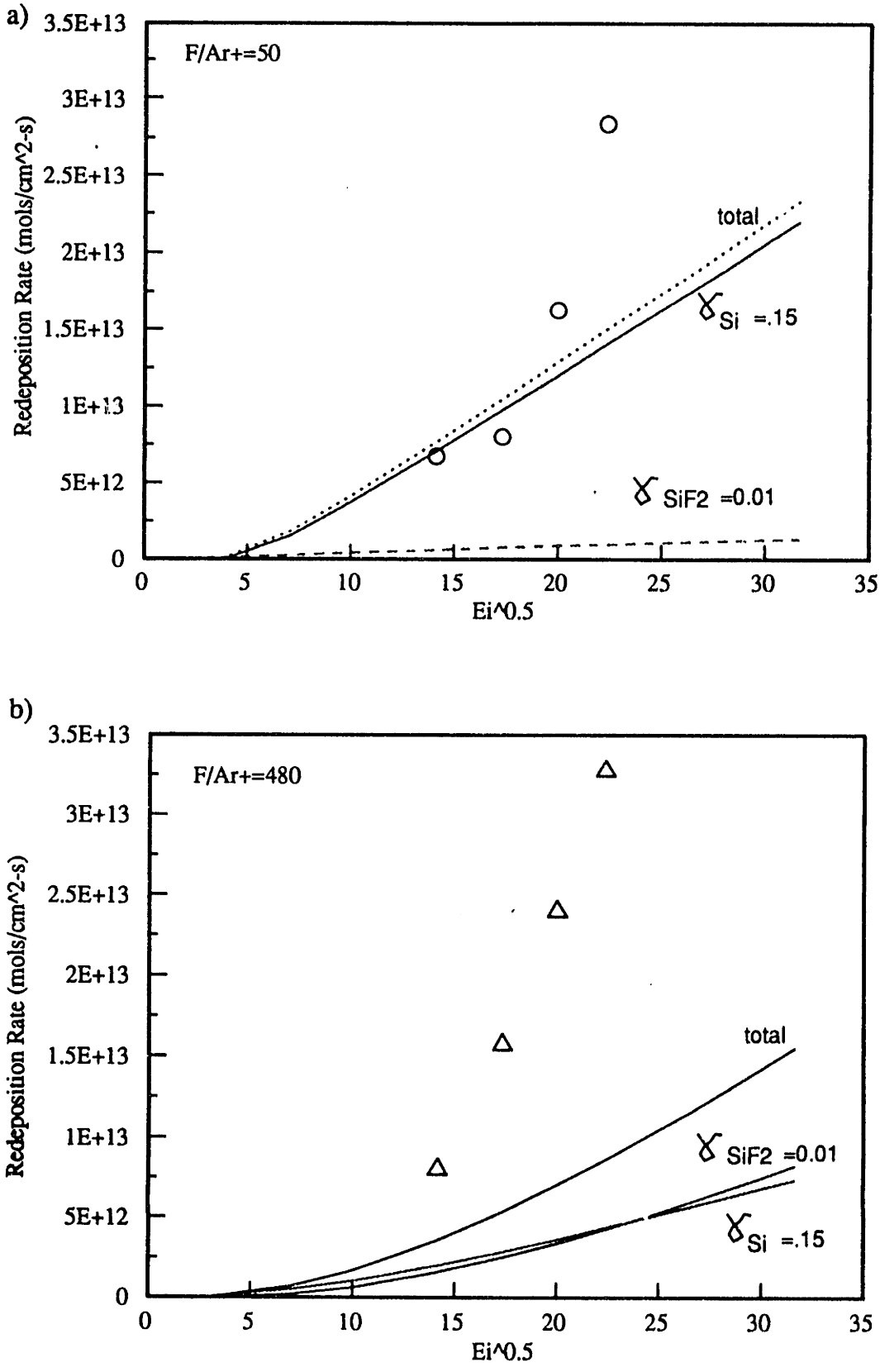

Figure 8-20. Predicted trends in product redeposition versus (Ei)^0.5 for Ar+/F etching of silicon at F/Ar+ ratios of a) 50 and b) 500.

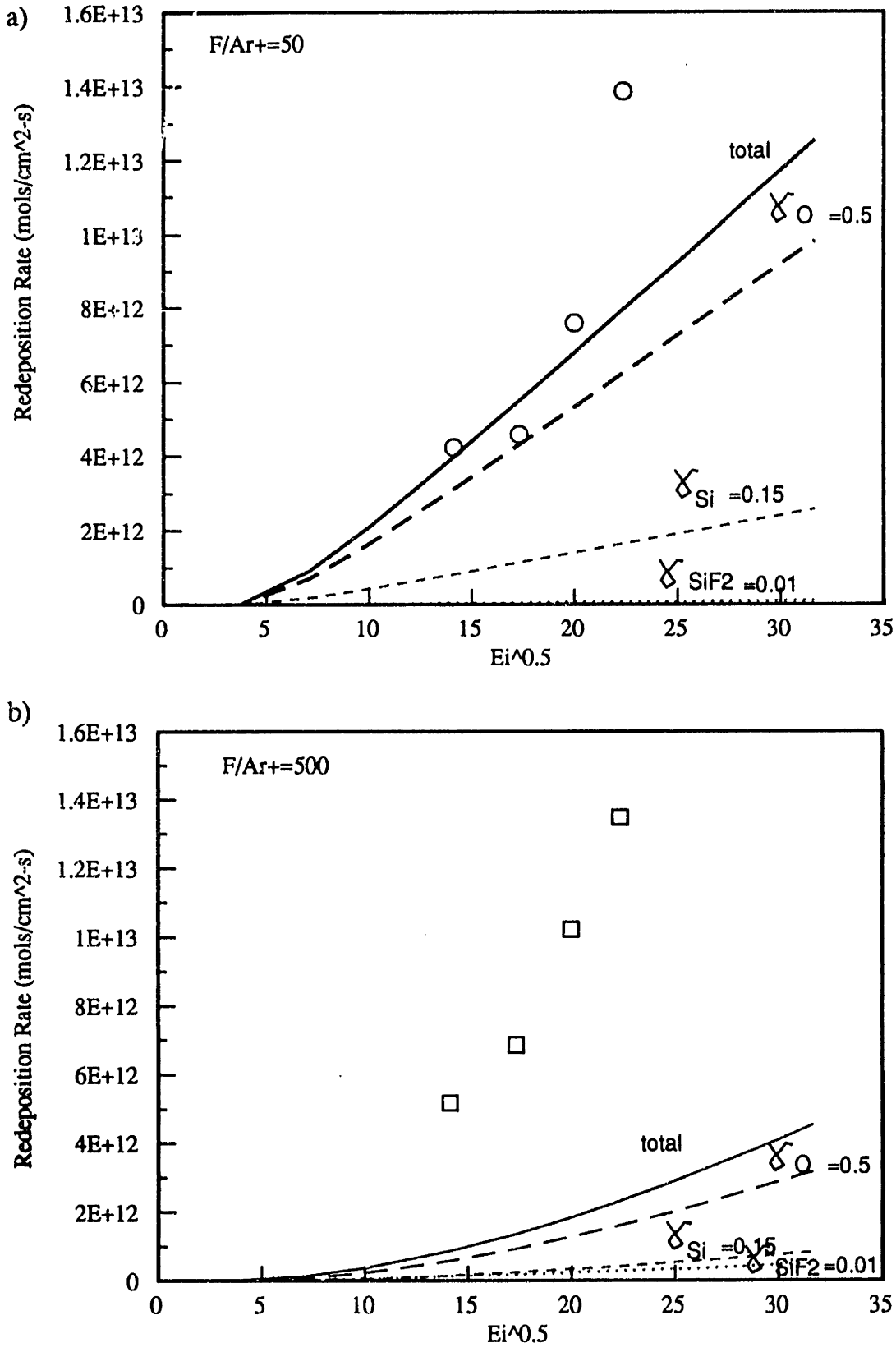

Figure 8-21. Predicted trends in product redeposition versus (Ei)^0.5 for Ar+/F etching of SiO2 at F/Ar+ ratios of a) 50 and b) 500.

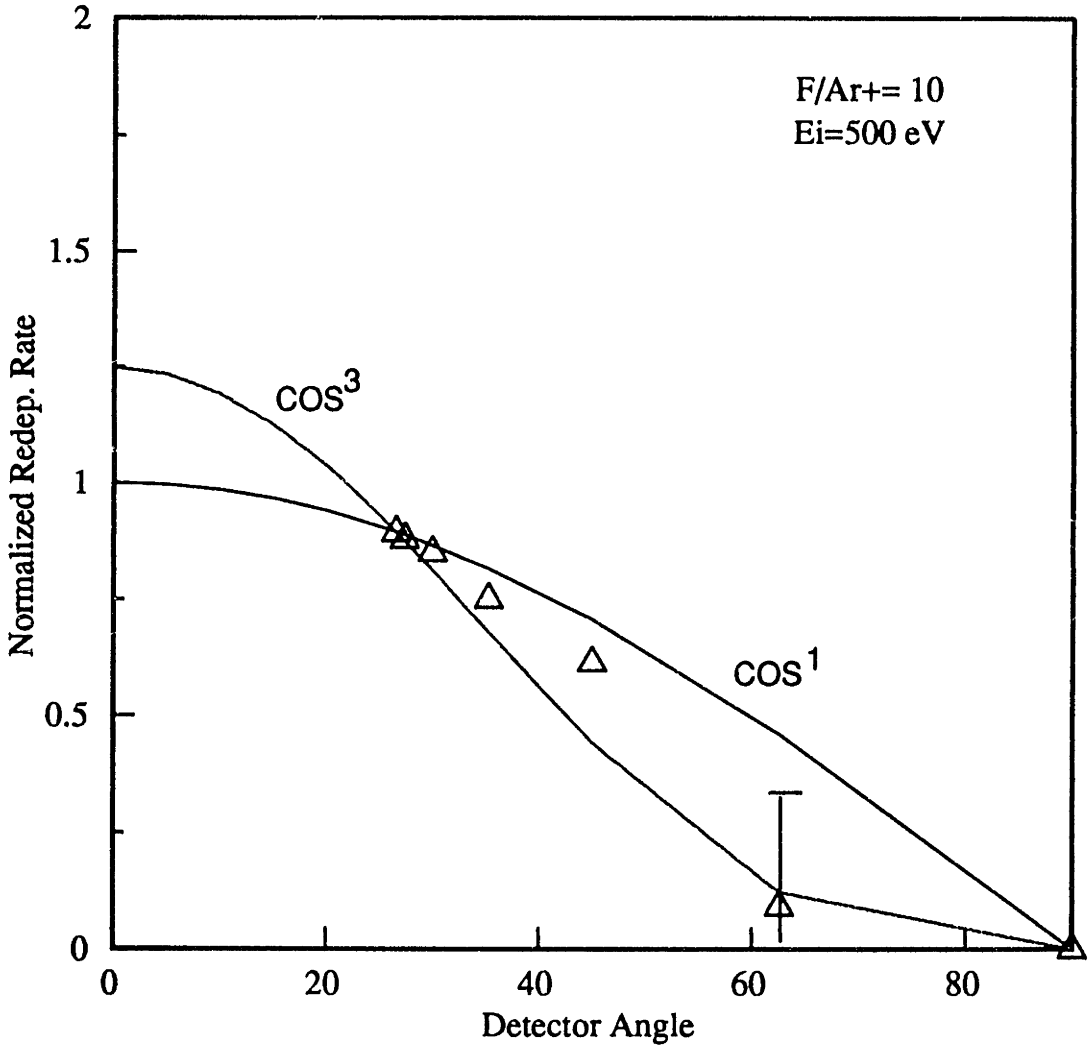

Figure 8-22. Angular characteristics for redeposition in Ar+/F etching of silicon.

slightly but repeatably higher. Both of these shortcomings of the model suggest that we are underpredicting the fraction of "sticky" SiF_x radicals produced in these systems as energy increases. A more comprehensive quantitative study of product distributions in these ion enhanced etching systems over a wide parameter space of flux ratios and incident ion energies is needed to improve our understanding.

Finally the angular deposition characteristics in the 500 eV Ar^+/F etching of Si was studied at a flux ratio of approximately 10, the results of which are presented in Figure 8-22. Signal-to-noise levels in the Ar^+/F of SiO_2 at large polar angles were too poor to allow repeatable measurements in this system. The data shown in Figure 8-22 suggests an angular distribution for the redepositing species which is more "cosine-like" than in the case of pure physical sputtering (Figure 8-6). This trend would be expected as a greater fraction of the depositing species are emitted from the etching surface via reactive versus physical mechanisms.

8.3 Influence of CF_2 Radicals on Redeposition Rates

The effect of CF_2 radicals on the redeposition kinetics in these systems was investigated first with Ar^+ alone, and then in combination with the Ar^+/F etching system. The effect of increasing CF_2/Ar^+ ratios on redeposition rates in Si and SiO_2 etching is presented in Figures 8-23 and 8-24 respectively. In the case of Si sputtering, CF_2 radicals have been shown in Chapter 6 to suppress Si sputtering rates up to 70% via the formation of a fluorocarbon overlayer which inhibits the collision-cascade induced removal of silicon from the under layers. The net result is a suppression of the amount of Si free metal available for deposition on the QCM surface. It was also shown that the fluorocarbon overlayer which is formed on the silicon by a CF_2 radical flux or under simultaneous fluxes of CF_2 and Ar^+ is self-limiting, in that once monolayer coverage is obtained, the CF_2 "self-sticking" coefficient falls by several orders of magnitude and precludes the

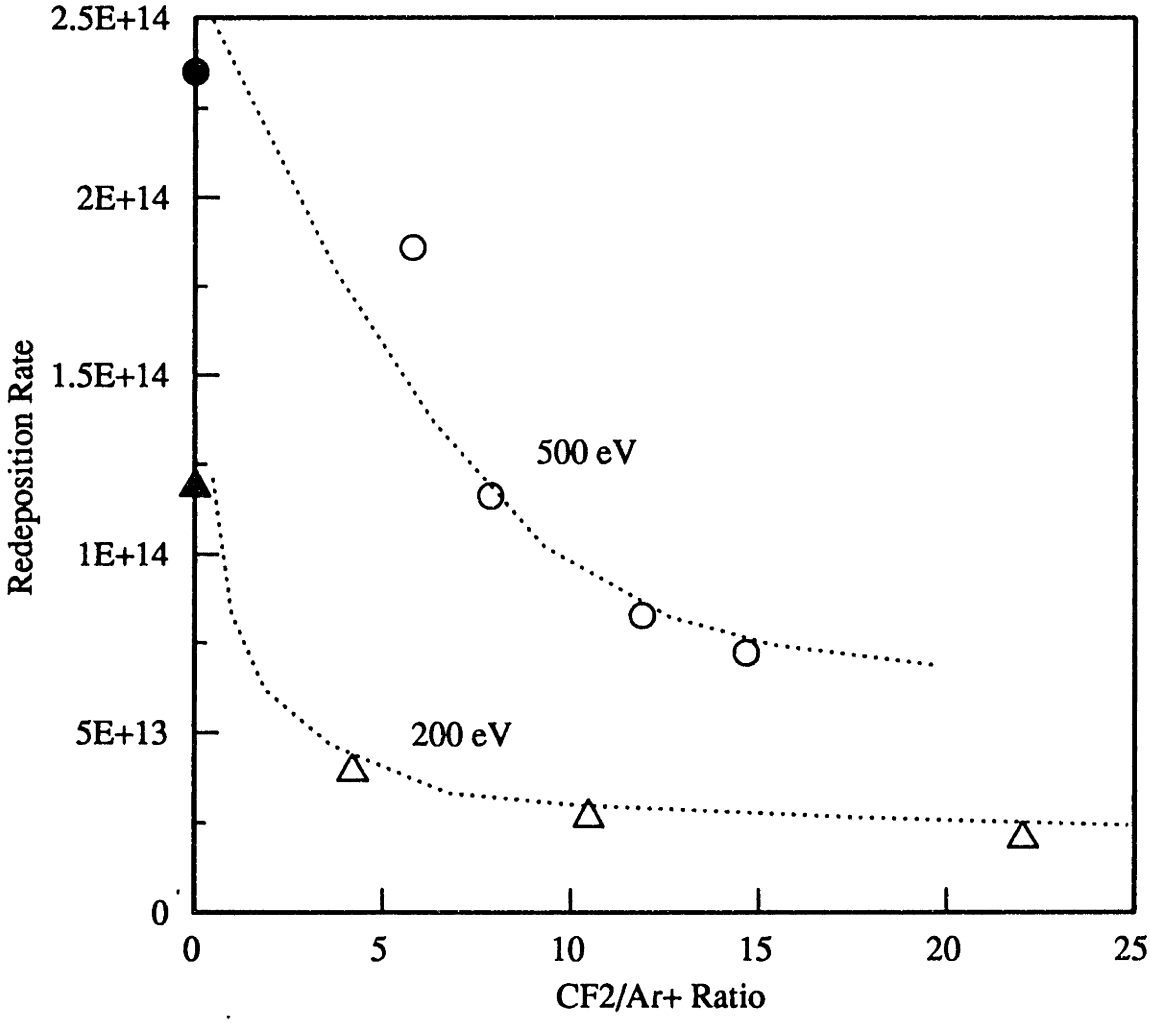

Figure 8-23. Redeposition rates measured during Ar+/CF2 etching of silicon as a function of CF2/Ar+ ratio.

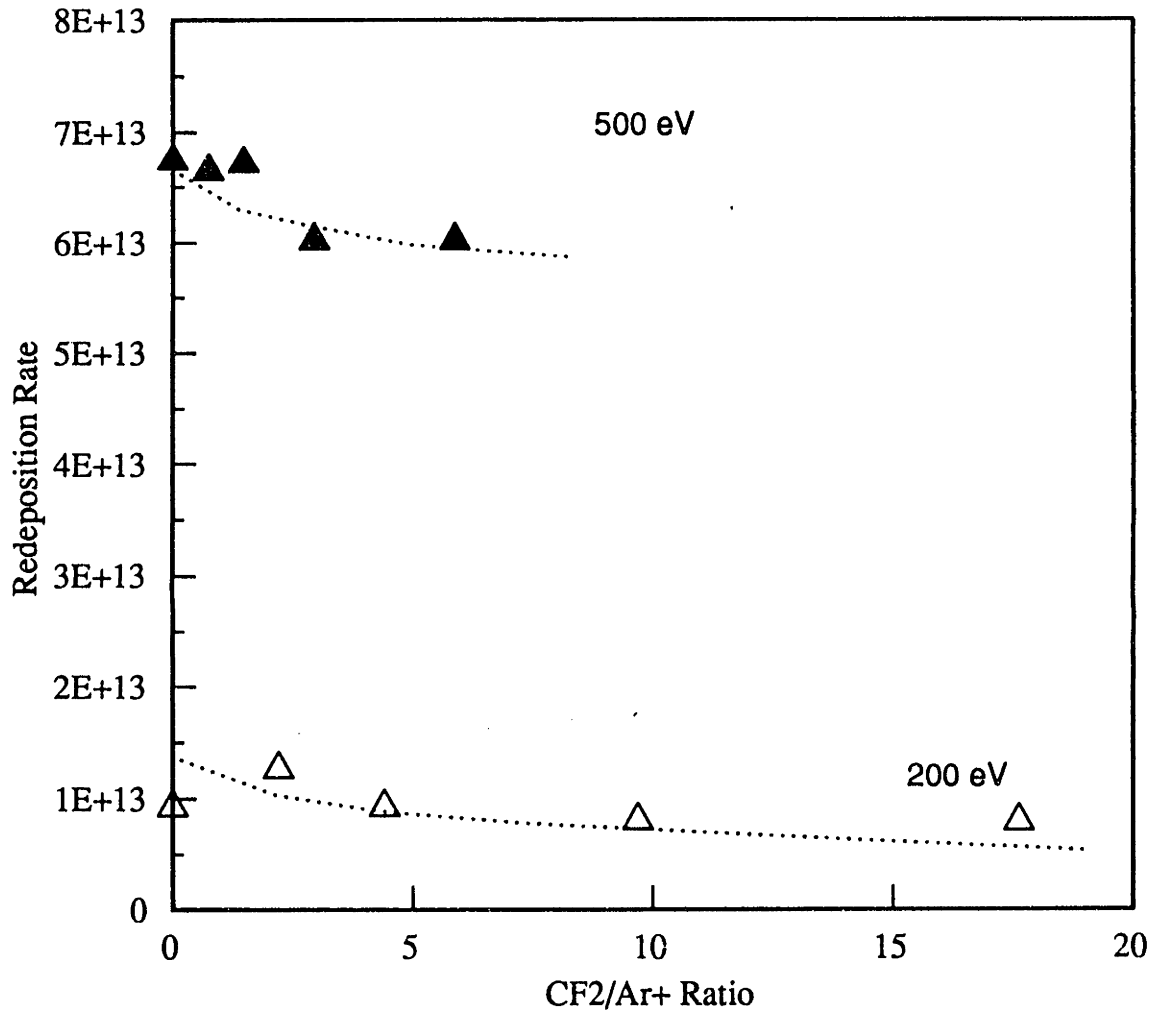

Figure 8-24. Redeposition rates measured during Ar+/CF2 etching of SiO2 versus CF2/Ar+ ratio.

formation of thick fluorocarbon films. This same saturation effect is seen on the sputtered Si surface and results in the behavior shown in Figure 8-23. Increasing bombarding ion energy in the CF_2-monolayer saturation regime increases the amount of subsurface Si which can be sputtered, thus increasing the net redeposition rate. Since the CF_2 layer on the sputtering silicon reaches a steady-state thickness, the total amount of CF_2 species impinging upon the sample face, and CF_x species being emitted from the sample face (primarily scattered CF_2) are approximately equivalent. We can therefore calculate the total flux of CF_x species intercepted by the microbalance, and bracket the subsequent sticking coefficient. Assuming that γ_{si} is 1.0, the total fraction of the Ar^+/CF_2-Si redeposition signal which is attributed to free silicon and to CF_x fragments is shown in Figure 8-25. The apparent sticking coefficient for the CF_x fragments on the QCM as a function of CF_2/Ar^+ is shown in Figure 8-26. This trend again demonstrates that as the percentage of CF_x fragments in the QCM deposit is increased (relative to the amount of Si), the apparent CF_x sticking coefficient on the QCM decreases.

Redeposition rates measured during Ar^+/CF_2 etching of SiO_2 were only slightly suppressed with increasing CF_2/Ar^+ flux (Figure 8-24), relative to redeposition rates for Ar^+ sputtered SiO_2. A more drastic suppression might be expected based on the finding that CF_2 can enhance the Ar^+ etching rates of SiO_2 by a factor of 2-3 over the physical sputtering rates, ostensibly via the formation of volatile compounds such as SiF_4, CO_2, and COF_2 [Butterbaugh et al., 1991]. However, it is possible that a large fraction of the ion-enhanced products in this system are in the form of unsaturated SiF_x radicals, since the transfer of F to Si sites from the CF_2 is not 100% efficient. In addition, model calculations indicate that the percentage of physically sputtered products in this system remains fairly high at saturation CF_2/Ar^+ levels, as discussed in Chapter 6, and the deposition rates of scattered CF_2 on the QCM surface masks the expected suppression effect as indicated in Figure 8-27. This hypothesis leads to the sticking coefficient

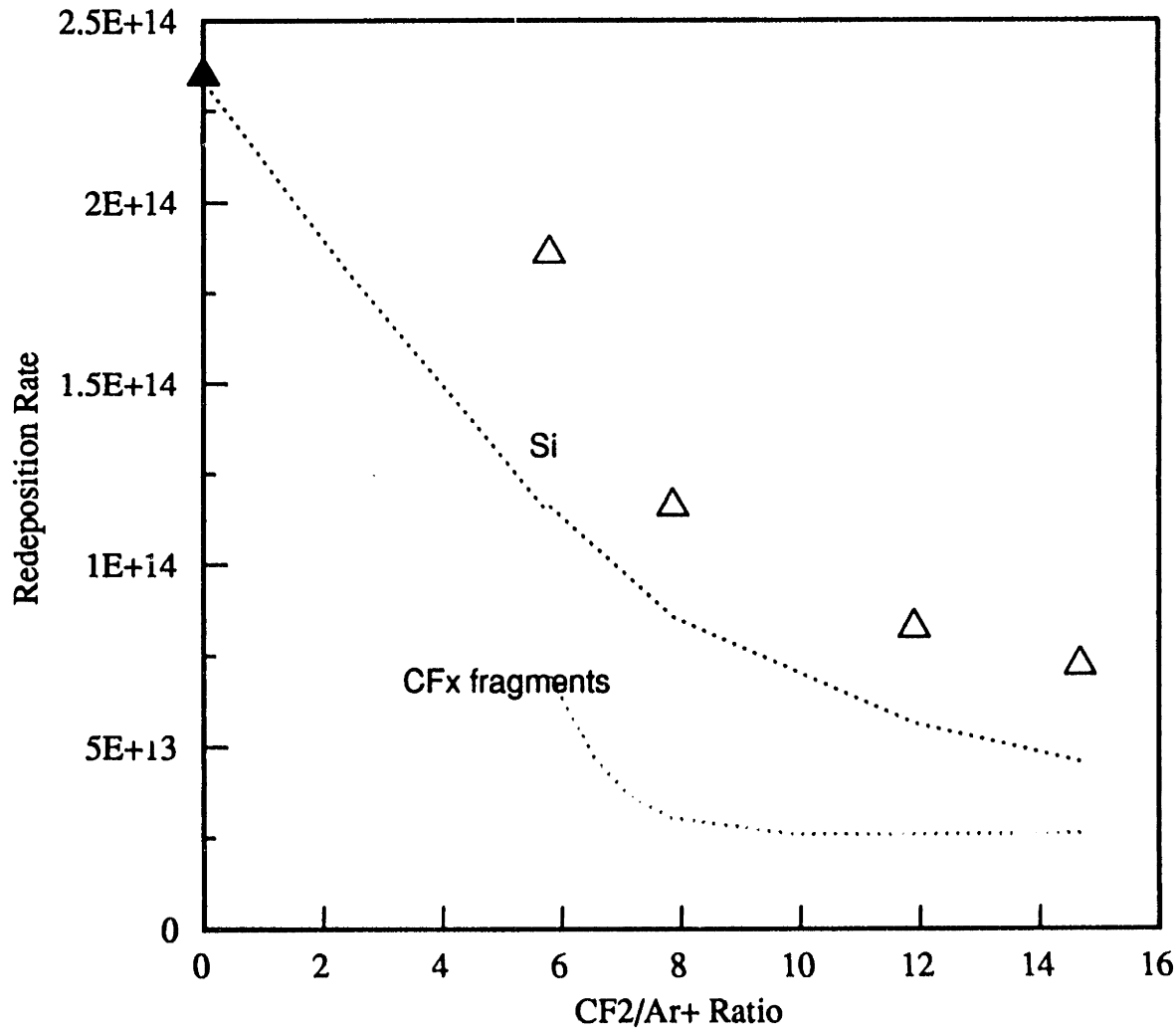

Figure 8-25. Relative contributions of silicon and CFx fragment redeposition in the Ar+/CF2 etching of silicon at 500 eV.

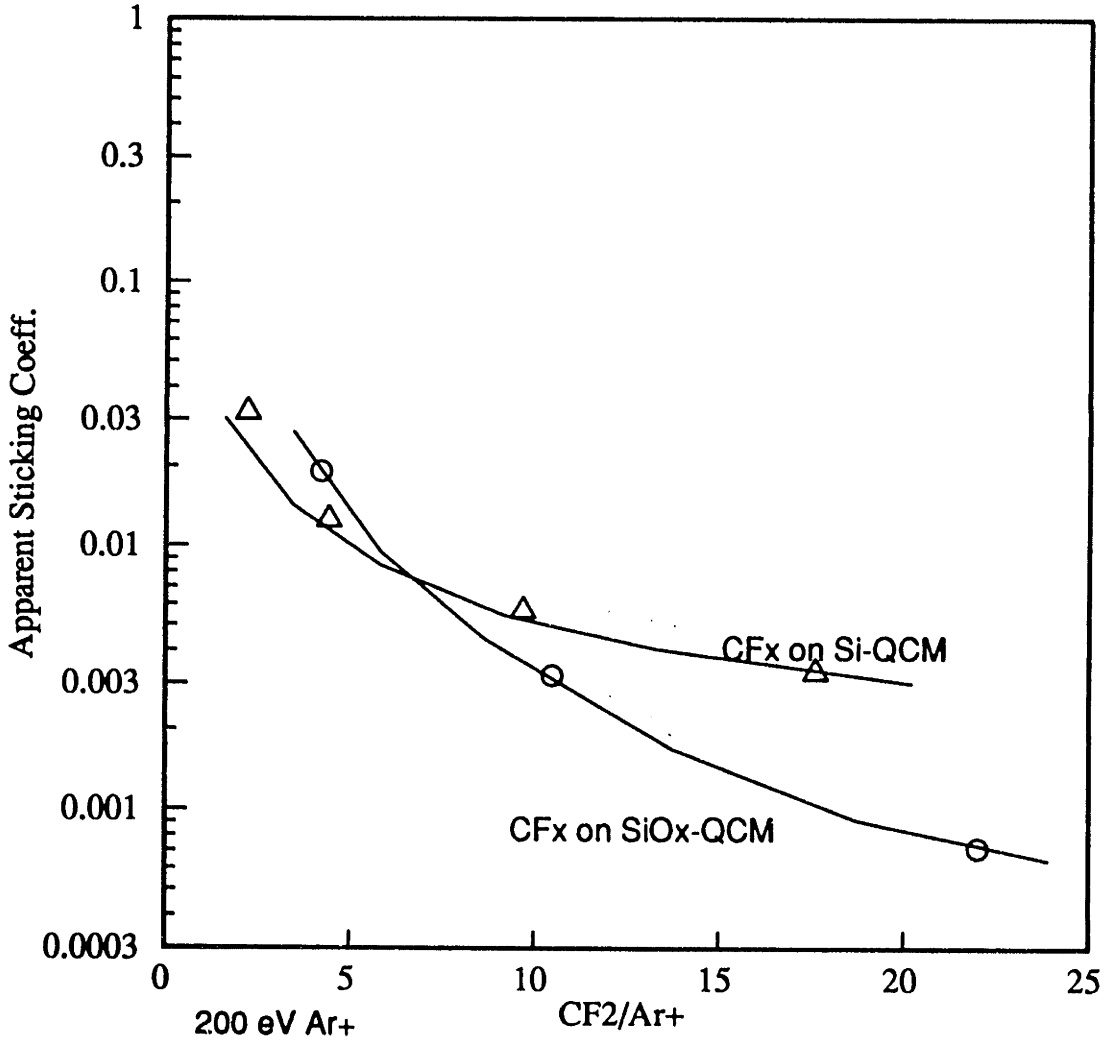

Figure 8-26. Apparent sticking coefficient for CFx fragments in Ar+/CF2 etching of silicon and SiO2.

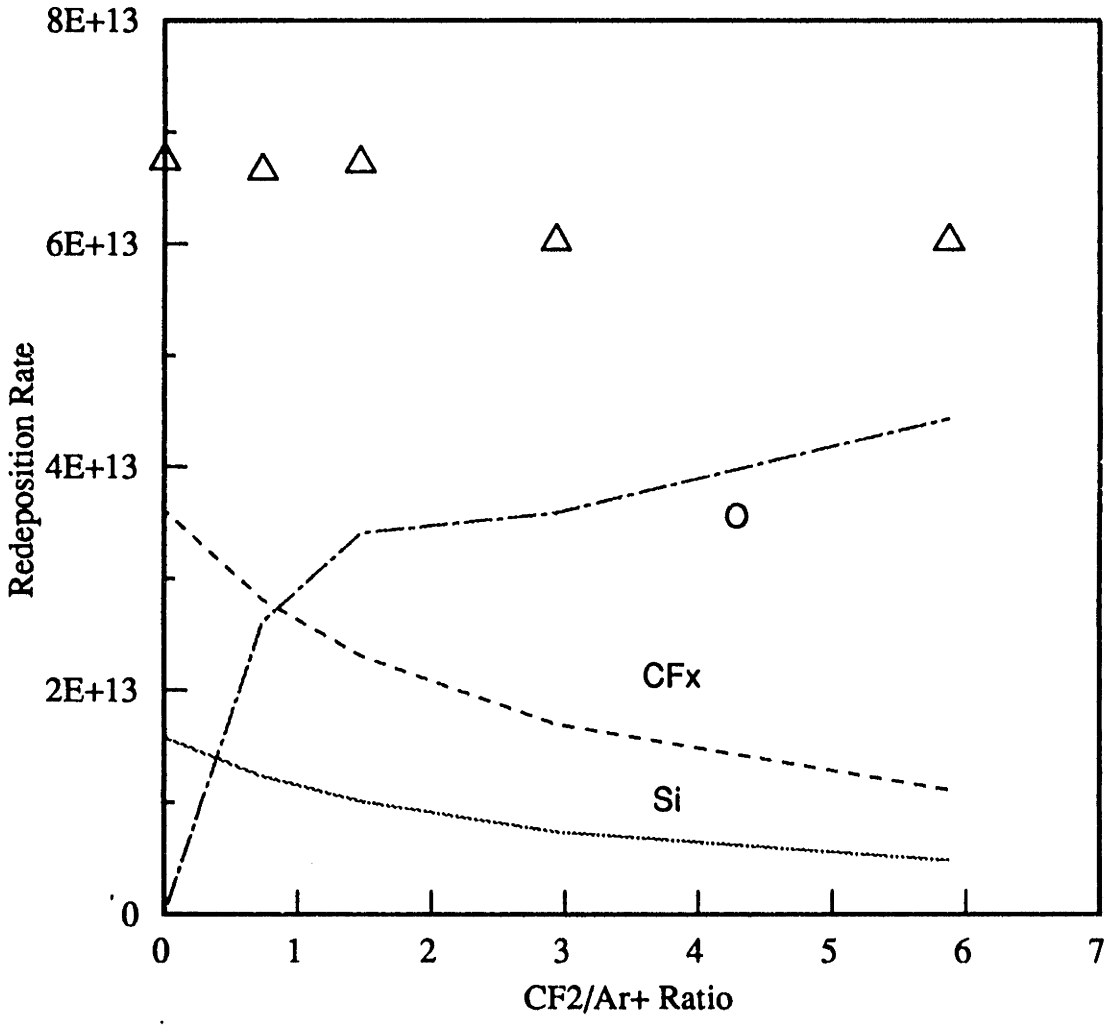

Figure 8-27. Relative contributions of Si, O, and CFx fragment redeposition in the Ar+/CF2 etching of SiO2 at 500 eV.

behavior shown in Figure 8-26 which suggests similar initial sticking coefficients on the order of 0.1 for CF_2 on the QCM during Si and SiO_2 etching. γ_{CF2} falls off more rapidly in the silicon system, which is consistent with the observation that CF_2 may act as an oxide etchant, preventing the formation of fluorocarbon overlayers which suppress further sticking. Finally, it is interesting to note in Figures 8-23 and 8-24, that the presence of CF_2 radical fluxes to the QCM surface does not passivate the surface toward the sticking of Si or O radicals, as in the case of F. This finding supports our hypothesis that the mechanism of F surface passivation involves recombination and/or re-etching of Si, O, SiO_x fragments which would otherwise redeposit.

Changes in the redeposition rates with incident ion energy are shown in Figures 8-28 and 8-29 for Ar^+/CF_2 etching of Si and SiO_2 respectively. In both cases, increases in CF_2/Ar^+ level shift the energy curves to lower redeposition rates; recall that the opposite trend was observed for the Ar^+/F etching of Si and SiO_2. This observation may be understood in the following manner. Increasing F/Ar^+ ratios results in a drastic increase in the total product yield, which overwhelms the decrease in the fraction of "sticky" species in the product stream, resulting in a net increase in redeposition rate with F/Ar^+. Increasing CF_2/Ar^+ ratios only modestly increases SiO_2 etching yields, and reduces the "stickiness" of the product stream by approximately the same magnitude, resulting in a small but perceptible reduction in redeposition flux with CF_2/Ar^+ ratio. Increasing CF_2/Ar^+ levels in Si sputtering experiments as a function of ion energy initially results in a reduction of redeposition rates, after which the effect saturates and the curves are no longer expected to shift. Figure 8-30 demonstrates the increase in apparent sticking coefficient for CF_x fragments as a function of ion energy for Ar^+/CF_2 etching of Si and SiO_2. The increase in apparent sticking coefficient with bombardment energy is expected as the relative fraction of sputtered Si redepositing on the QCM surface is increased, providing new "sites" for CF_x sorption.

Angular deposition characteristics in the Ar^+/CF_2 etching studies are shown in Figures 8-31

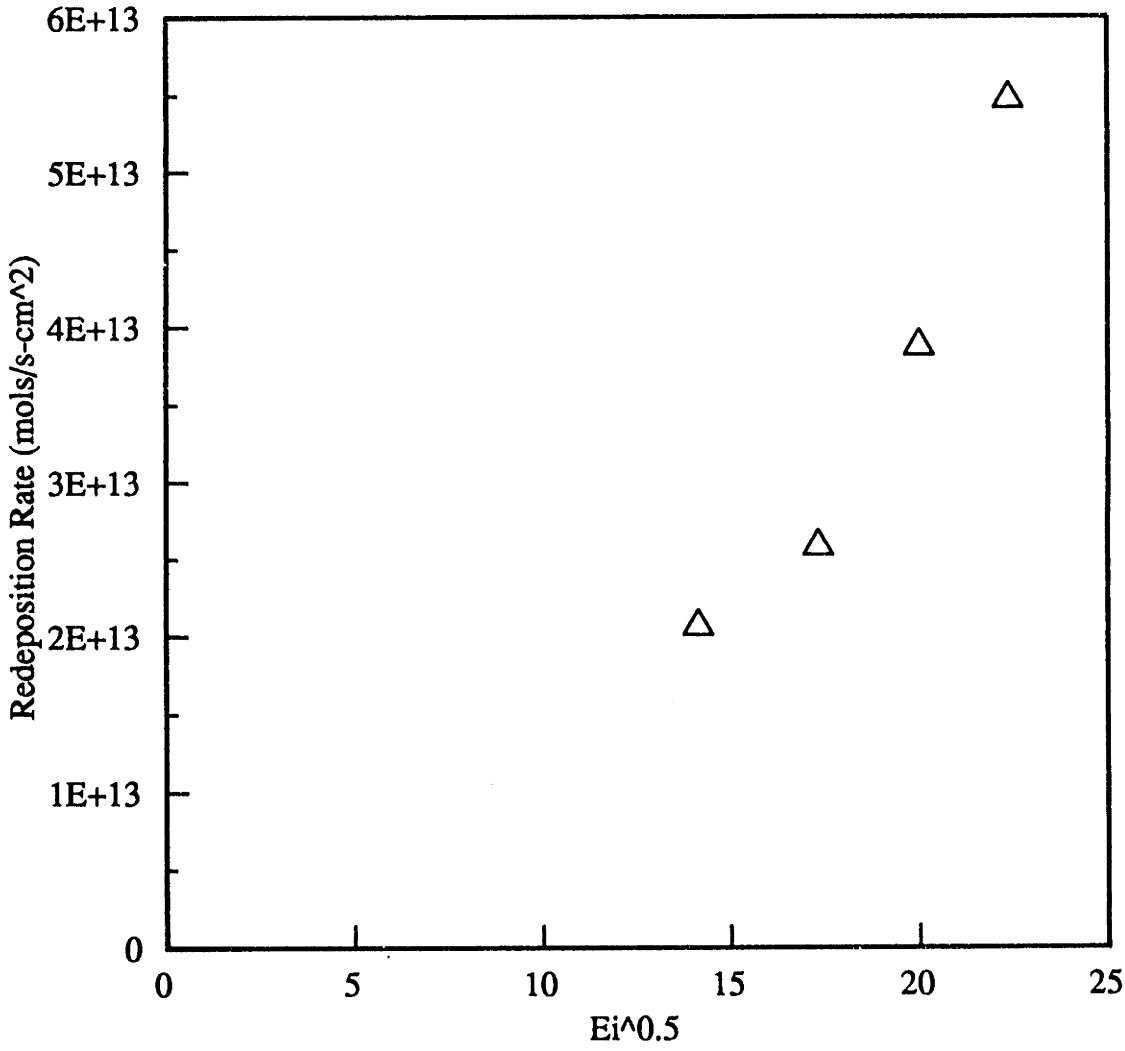

Figure 8-28. Measured redeposition rates in Ar+/CF2 etching of silicon versus (Ei)^0.5.

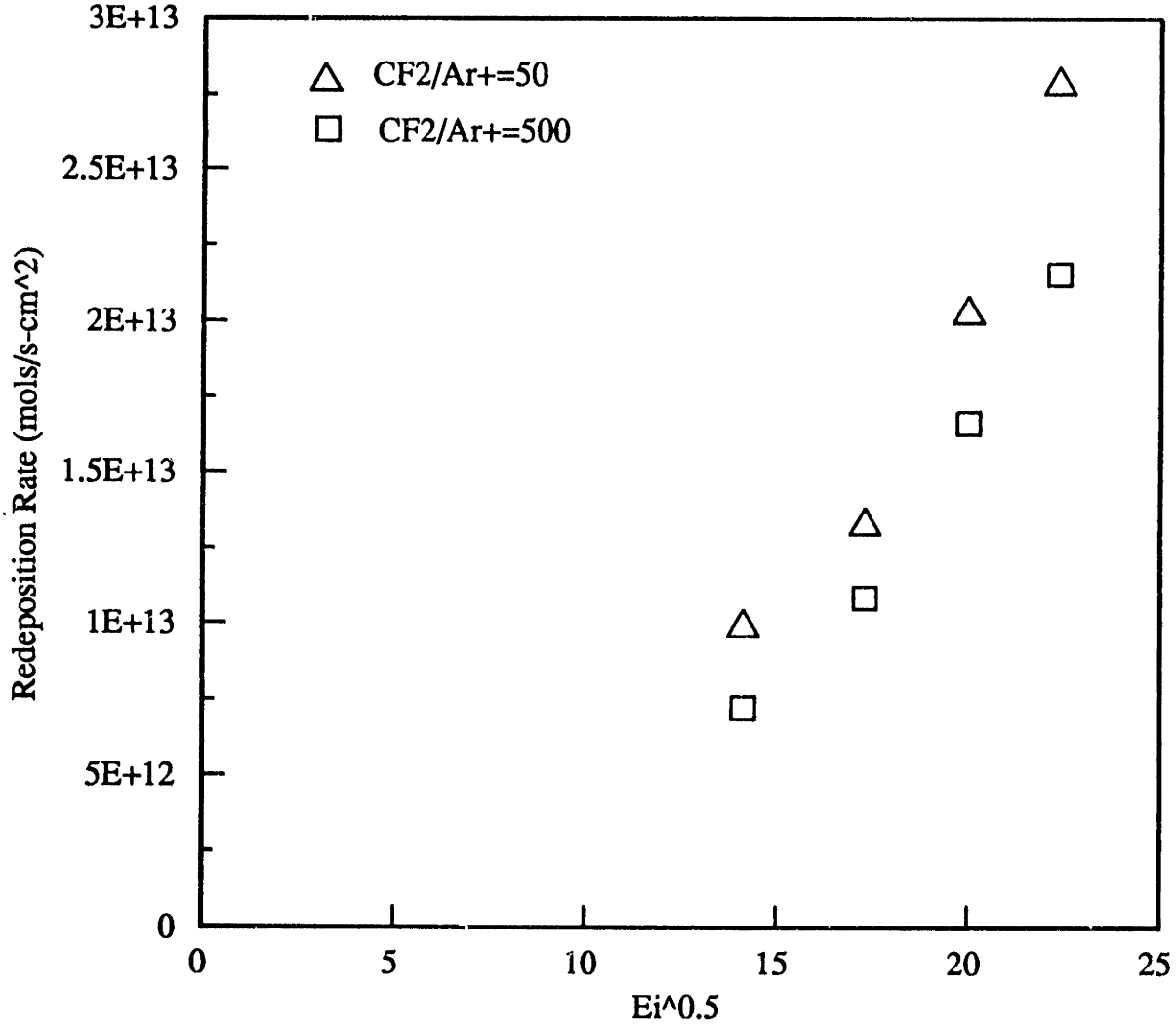

Figure 8-29. Measured redeposition rates in Ar+/CF2 etching of SiO2 versus (Ei)^0.5.

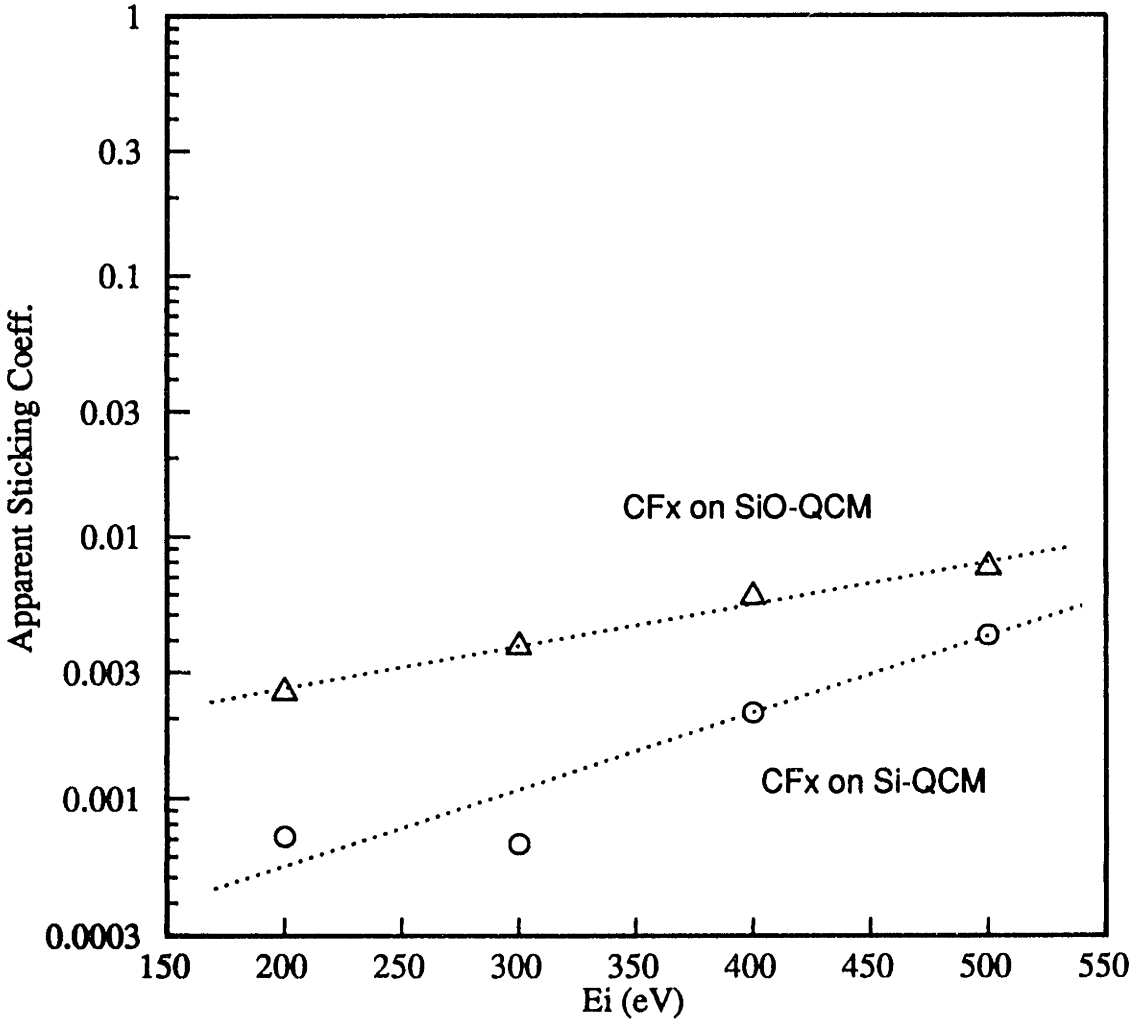

Figure 8-30. Apparent sticking coefficient for CFx fragments in Ar+/CF2 etching of silicon and SiO2 versus ion energy.

and 8-32. The available data would again indicate a shift toward more "cosine-like" behavior in contrast to the physical sputtering data. This trend could partly be explained by the large percentage of CF_2 radicals sticking on the QCM surface, which would be scattered from the QCM in a cosine manner. This emission characteristic may be superimposed on a more directional characteristic for the sputtered fragments reaching the QCM.

8.4 Summary

The effects of relative ionic and radical fluxes, representative of the fluorocarbon plasma environment, on redeposition rate kinetics have been quantified. The addition of a primary etchant such as F, was shown to drastically reduce redeposition rates over the pure Ar^+ sputtering of Si and SiO_2 as expected intuitively. The mechanism for this reduction appears to be two-fold, and involves reduction in the proportion of physically removed surface material (e.g. free Si and O), as well as the F passivation and/or re-etching of free Si and O which would otherwise deposit on a sidewall surface. Although the addition of surface fluorine greatly decreases the percentage of sputtered Si and O/SiO_x fragments, surface kinetic models suggest that the redeposition behavior in the Ar^+/F-Si and Ar^+/F-SiO_2 systems is dominated by this small percentage of sputtered material at low to moderate F/Ar^+ ratios, with SiF_x radical sticking becoming important at high F/Ar^+ levels.

Redeposition rates at a given F/Ar^+ ratio increase sharply with incident ion energy due to the increase in the sputter component of etching, and the subsequent release of less saturated or "stickier" species in the product stream. Although the percentage of "sticky" products in the product stream decreases with increasing F/Ar^+, the total etch yield also increases dramatically, resulting in fairly constant redeposition rates. Although CF_2 radicals suppress redeposition rates in Ar^+/CF_2-Si and Ar^+/CF_2-SiO_2 etching relative to physical sputtering, addition of CF_2 does not

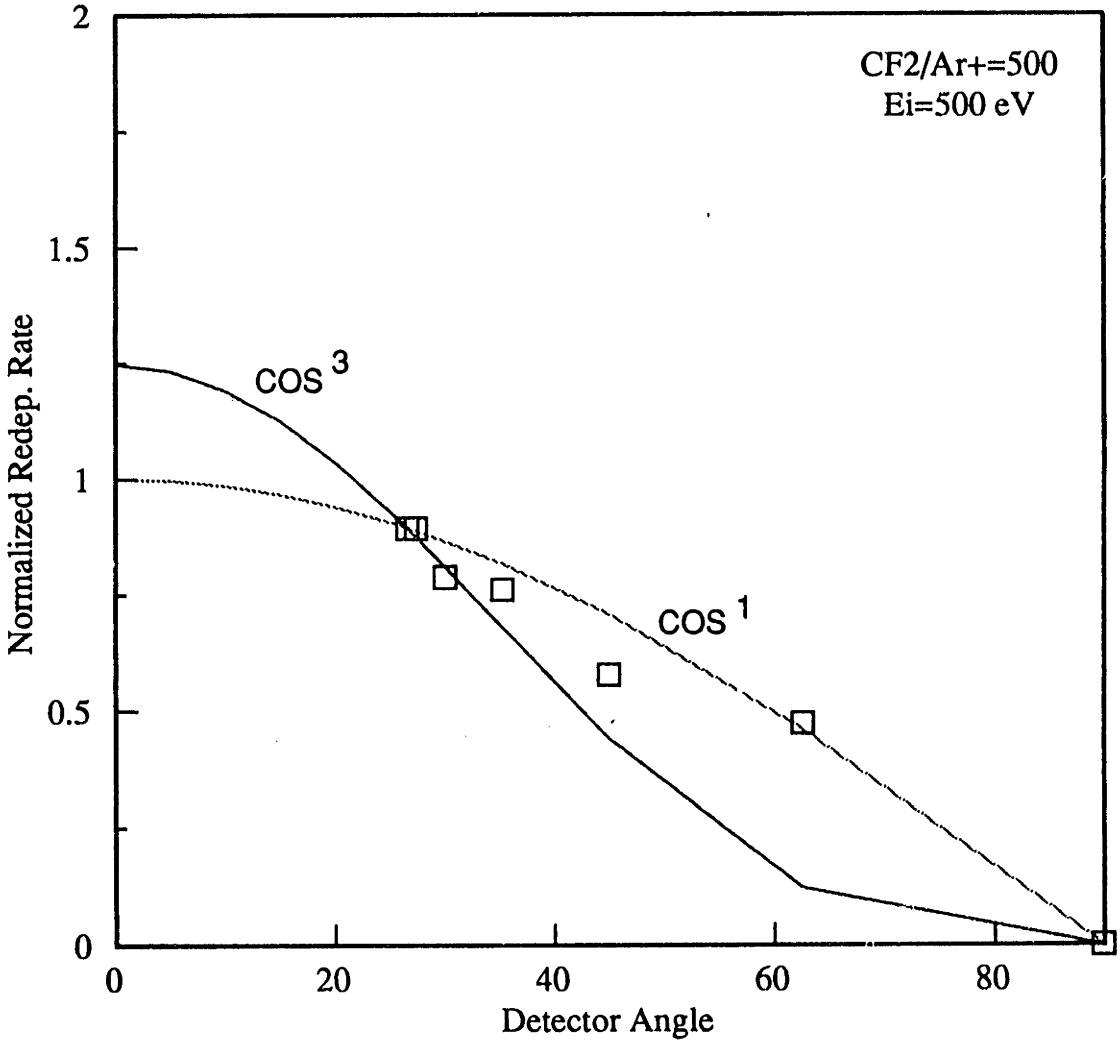

Figure 8-31. Angular characteristics for redeposition in Ar+/CF2 etching of silicon at 500 eV.

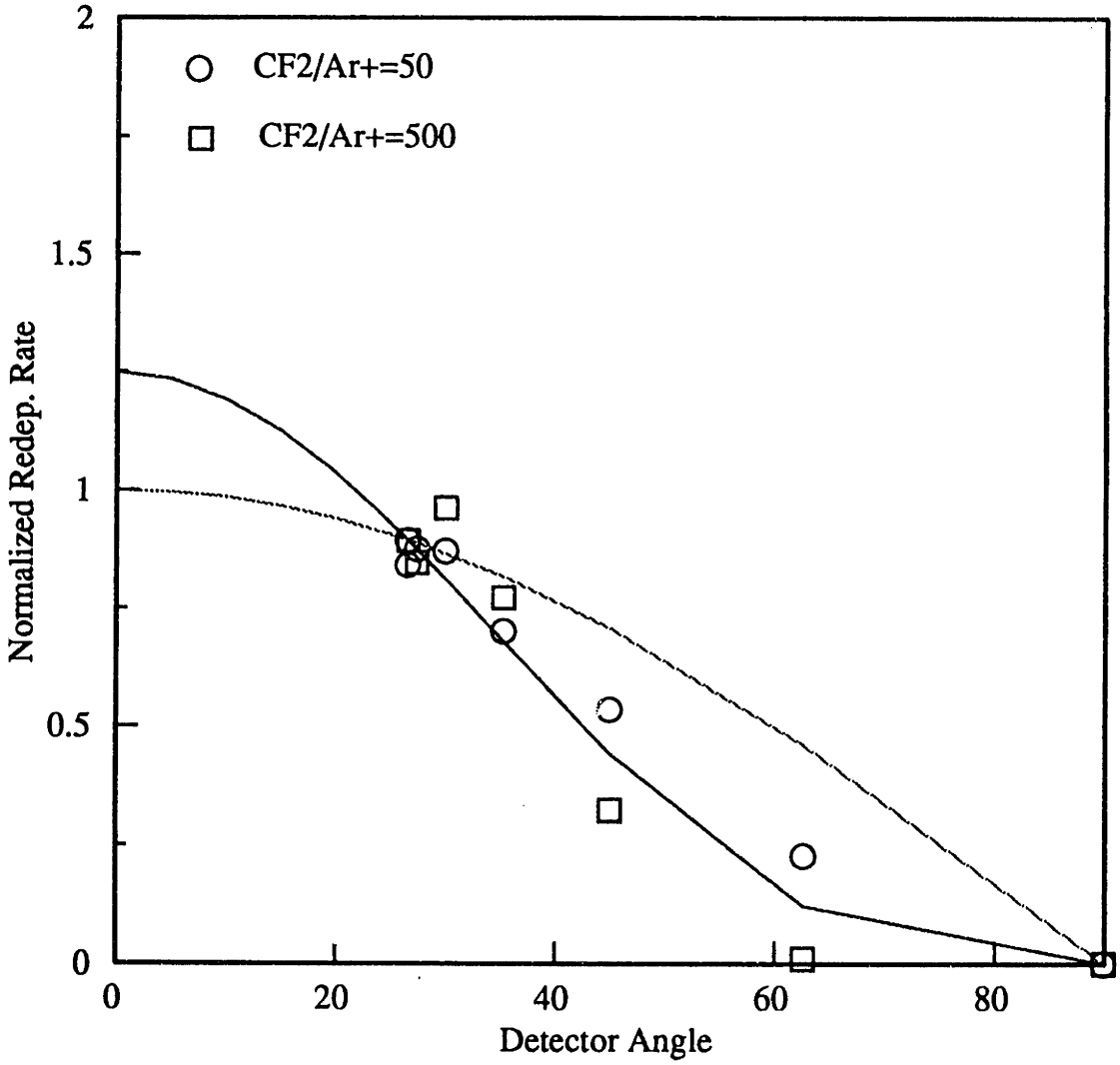

Figure 8-32. Angular characteristics for redeposition in Ar+/CF2 etching of SiO2 at 500 eV.

measurably effect redeposition rates in the Ar^+/F etching systems. CF_2 deposition on non-bombarded surfaces during Ar^+/F etching is suppressed due to a rapid surface recombination reaction between sorbed F and CF_2, ostensibly producing CF_4. Comparison of surface kinetic models to our redeposition data suggests that while we may be underpredicting production of "sticky" unsaturated radicals somewhat, the overall deposition rates of these types of species are relatively low. Redeposition of unsaturated silicon-halide radicals is expected to occur much more rapidly in Cl and Br etching systems, especially at cryogenic temperatures.

References

Adamson, A.W., Physical Chemistry of Surfaces , John Wiley and Sons, New York, 1982.

Ai, B., S.B. Thesis, MIT Dept. of Chemical Engineering, 1989.

Alfred, D. et al., "Film Redeposition on Vertical Surfaces During Reactive Ion Etching", J.Vac.Sci.Technol., 7(3), p.505, 1989.

Allen, K.D., H.H.Sawin and A. Yokozeki, "The Plasma Etching of Polysilicon with CF_3Cl/Argon Discharges III. Modeling of Etching Rate and Directionality", J.Electrochem.Soc., 133(11), p.2331, 1986.

Arnold, J. and H.H.Sawin, "Charging of Pattern Features During Plasma Etching", J.Appl.Phys., 70(10), p.5314, 1991.

Asmussen, J., "Electron Cyclotron Resonance Microwave Discharges for Etching and Thin-Film Deposition", J.Vac.Sci.Technol.A, 7(3), p.883, 1989.

Barker, R.A., T.M. Mayer and W.C. Pearson. "Surface Studies of and a Mass Balance Model for Ar^+ ion-assisted Cl_2 Etching of Si", J.Vac.Sci.Technol.B, 1(1), p.37, 1983.

Behrisch, R. ed., Sputtering by Particle Bombardment I, Springer-Verlag, Berlin, 1981.

Behrisch, R. and Wittmaack, K. eds., Sputtering by Particle Bombardment III, Springer-Verlag, Berlin, 1991.

Booth, J.P. et al., "Spatially and Temporaly Resolved Laser-Induced Fluorescence Measurements of CF_2 and CF Radicals in a CF_4 RF Plasma", J.Appl.Phys., 66(11), p.5251, 1989.

Brannon, J.H., "Glass Etching Initiated by Excimer Laser Photolysis of CF_2Br_2", J.Phys.Chem., 90(9), p.1784, 1986.

Brault, P., et al., "Chemical Physics of Fluorine Plasma-Etched Silicon Surfaces: Study of Surface Contaminations", J.Appl.Phys., 68(4), p.1702, 1990.

Buchmann, L.M., et al., "Analysis of a CF_4/O_2 Plasma Using Emission, Laser Induced Fluorescence, Mass and Langmuir Spectroscopy", J.Appl.Phys., 67(8), p3635, 1990.

Butterbaugh, J., "Characterization and Modeling of Silicon Dioxide Etching in Tetrafluoromethane RF Glow Discharges", Ph.D. Thesis, MIT Dept. of Chemical Engineering, 1990.

Butterbaugh, J., D.C. Gray and H.H. Sawin, "Plasma-Surface Interactions in Fluorocarbon Etching of Silicon Dioxide", J.Vac.Sci.Technol., B 9(3), p.1461, 1991.

Campbell, Charles T. and Steven M. Valone, "Design Considerations for Simple Gas Dosers in Surface Science Applications", J.Vac.Sci.Technol.A, 3(2), p.408, 1985.

Chapman, B., Glow Discharge Processes, John Wiley and Sons, NY, 1980.

Chin, D., S. Dhong, and G.J. Long, "Structural Effects on a Submicron Trench Process", J.Electrochem.Soc., 132(7), p.1705, 1985.

Chuang, T.J., "Electron Spectroscopy Study of Silicon Surfaces Exposed to XeF_2 and the Chemisorption of SiF_4 on Silicon", J.Appl.Phys., 51(5), p.2614, 1980.

Clyne, M.A. and A. Hodgson, "Kinetics and Detection of $F(^2P)$ Atoms in a Discharge Flow System", Chem.Phys.79, p.351, 1983.

Clyne, M.A. et al., "Reaction Kinetics of Ground State Fluorine, $F(^2P)$, Atoms. I.", Can.J.Chem., 51, p.3596, 1973.

Coburn J.W. and H.F. Winters, personal communication, 1990.

Coburn, J.W. and H. Winters, "Conductance Considerations in the Reactive Ion Etching of High Aspect Ratio Features", Appl.Phys.Lett., 55(26), p.2730, 1989.

Coburn, J.W., and H.F. Winters, "The Role of Energetic Ion Bombardment in Silicon-Fluorine Chemistry", Nucl.Instr.Meth., B27, p.243, 1987.

Coburn, J.W. and H.F. Winters, "Plasma-Assisted Etching: Ion-Assisted Surface Chemistry" Appl.Surf.Sci., 22/23, p.63, 1985.

Coburn, J.W., "Plasma Etching and Reactive Ion Etching", Oficina Brasileira de Microelectronica IV, p.41, 1981

Coburn, J.W. and E. Kay, "Some Chemical Aspects of Fluorocarbon Plasma Etching of Silicon and its Compounds", IBM J.Res.Devel., 23(1), p.33, 1979.

Coburn, J.W. and H.F. Winters,"Ion- and Electron-Assisted Gas-Surface Chemistry-An Important Effect in Plasma Etching", J.Appl.Phys., 50(5), p.3189, 1979.

Coburn, J.W. and H.F. Winters, "Plasma Etching- A Discussion of Mechanisms", J.Vac.Sci.Technol., 16(2), p.391, 1979.

Coburn, J.W., H.F. Winters and T.Chuang, "Ion-Surface Interactions in Plasma Etching", J.Appl.Phys., 48(8), p.3532, 1977.

Dalton, T. et al, "Microtrench Formation During Plasma Etching", J.Electrochem.Soc., submitted May 1992.

Dalvie, M., and K.F. Jensen, "The Importance of Free Radical Recombination Reactions in CF_4/O_2 Plasma Etching of Silicon", J.Vac.Sci.Technol.A, 8(3), p.1648, 1990.

Donnelly, V.M., et al., "Anisotropic Etching of SiO_2 in Low-Frequency CF_4/O_2 and NF_3/Ar Plasmas", J.Appl.Phys., 55(1), p.242, 1984.

Dulgnan et al. "Multiphoton Ionization of the CF_3 Radical", J.Phys.Chem., 86, p.4156, 1982.

Engstrom, J.R., M. Nelson, and T. Engel, "The Adsorption and Reaction of Fluorine on the Si(100) Surface", Surf.Sci., 215, p.437, 1989.

Feldman, L.C. and J.W. Mayer, Fundamentals of Surface and Thin Film Analysis, North-Holland, NY, p.224, 1986.

Flamm, D.L. and V.M. Donnelly, "The Design of Plasma Etchants", Plasma.Chem.Plasma.Proc., 1(4), p.317, 1981.

Flamm, D.L., V.M. Donnelly, and J.A. Mucha, "The Reaction of Fluorine Atoms with Silicon", J. Appl. Phys., 52(5), p.3633, 1981.

Flamm, D.L., C.J. Mogab, and E.R. Sklaver, "The Reaction of Fluorine Atoms with SiO_2", J. Appl.Phys., 50(10), p.6211, 1979.

Gerlach-Meyer, U., "Ion-Enhanced Gas-Surface Reactions: A Kinetic Model for the Etching Mechanism", Surf.Sci., 103, p.524, 1981.

Gibson, G., Ph.D. Thesis, MIT Dept. of Physics, 1993.

Giordmaine, J.A. and T.C. Wang, "Molecular Beam Formation in Long Parallel Tubes", J.Appl.Phys., 31(3), p.463, 1960.

Gloersen, P.G., Solid State Technol.,"Masking for Ion Beam Etching", p.68., April 1976.

Gloersen, P.G., "Ion Beam Etching", J.Vac.Sci.Technol., 12(1), p.28., 1975.

Gottscho, R.A., C.W. Jurgensen, and D.J. Vitkavage, "Microscopic Uniformity in Plasma Etching", submitted to J.Vac.Sci.Technol., 1992.

Gray, D.C. and J.Butterbaugh, unpublished data, 1989.

Gray, D.C., unpublished data, 1990.

Haring et al.,"Mass and Energy Distribution of Particles Sputter Etched from Si in a XeF_2 Environment", Appl.Phys.Lett., 41(2), p.174, 1982.

Harper, J.M.E., et al., "Low Energy Ion Beam Etching", J.Electrochem.Soc., 128(5), p.1077, 1981.

Heath, B.A., "Selective Reactive Ion Beam Etching of SiO_2 over Polycrystalline Si", J. Electrochem.Soc., 129(2), p.396, 1982.

Heinecke, R., "Plasma Reactor Design for the Selective Etching of SiO_2 on Si", Solid State Electronics 18, p.1146, 1975.

Houle, F.A., "On the Relative Importance of Physical and Chemical Sputtering during Ion-Enhanced Etching of Silicon by XeF_2", Appl.Phys.Lett., 50(25), p.1838, 1987.

Houle, F.A., "A Reinvestigation of the Etch Products of Silicon and XeF_2: Doping and Pressure Effects", J.Appl.Phys., 60(9), p.3018, 1986.

Houle, F.A., "Photoeffects on the Fluorination of Silicon. II. Kinetics of the Initial Response to Light", J.Chem.Phys., 80(10), p.4851, 1984.

Houle, F.A., "Photoeffects on the Fluorination of Silicon.I. Influence of Doping on Steady-State Phenomenon", J.Chem.Phys., 79(9), p.4237, 1983.

Hutchinson, I.H., Principles of Plasma Diagnostics, Cambridge University Press, Cambridge England, 1987.

Jackson, S.C., and T. Dalton, " A Profile Evolution Model with Redeposition", Proc. SPIE, 1185, p.225, 1989.

Jaso, M.A. and G.S. Oehrlein, "Transient Fluorocarbon Film Thickness Effects Near the Silicon Dioxide/Silicon Interface in Selective Silicon Dioxide Reactive Ion Etching", J.Vac.Sci. Technol.A, 6(3), 1397 (1988).

Jenichen A., and H. Johansen, "Chemisorption of the SiO_2 and Silicon Surfaces and the Influence of Infared Laser Excitation", Surface Sci., 203, p.143, 1988.

Jones, R.H., D.R. Olander and V.R. Kruger, "Molecular Beam Sources Fabricated from Multichannel Arrays.I. Angular Distributions and Peaking Factors", J.Appl.Phys., 40(11), p.4641, 1969.

Jones, R.H., V.R. Kruger and D.R. Olander, "Characterization of Multichannel Sources and Design of Molecular Beam Systems for Their Utilization", USAEC Rept. UCRL-17859, 1968.

Joyce, S., J.G. Langan, and J.I. Steinfeld, "Chemisorption of Fluorocarbon Free Radicals on Silicon and SiO_2", J.Chem.Phys., 88(3), p.2027, 1988.

Joyce, S., "Reactive Processes on Silicon and Silicon Dioxide Surfaces", Ph.D. Thesis, MIT Dept. of Chemistry, 1987.

Kaufman, H.R., Fundamentals of Ion-Source Operation, Commonwealth Scientific Corp, Alexandria VA, 1984.

Kaufman, H.R., J.J. Coumo and J. Harper, "Technology and Applications of Broad-Beam Ion Sources used in Sputtering. Part I. Ion Source Technology", J.Vac.Sci.Technol., 21(3), p.725, 1982.

Kaufman, H.R., J.M.Harper and J.J. Cuomo, "Developments in Broad-Beam, Ion-Source Technology and Applications", J.Vac.Sci.Technol., 21(3), p.764, 1982.

Kiss, L.D.B., "Study of Plasma Chemical Kinetics by Modulated Power Relaxation", Ph.D. Thesis, MIT Dept. of Chemical Eng., 1991.

Knickelbein, M.A., D. Webb and E. Grant, "New Devices fo the Production of Intense Pulsed Jets of CF_2: Laser Spectroscopic Characterization", MRS Symp.Proc., v38, p.23, 1985.

Kojima, M. et al., "Model for Dry Etching of Silicon", J.Appl.Phys., 70(6), p.2901, 1991.

Langan, J.G., J.A. Shorter, X. Xin, S.A. Joyce, and J.I. Steinfeld, "Reactions on Laser-Generated CF_2 on Silicon and Silicon Oxide Surfaces", Surface Sci., 207, p.344, 1989.

Lehmann, H. W., L.Krausbauer, and R.Widmer, "Redeposition-A Serious Problem in RF Sputter Etching of Structures with Micrometer Dimensions", J.Vac.Sci.Technol., 14(1), p281, 1977.

Lii T., and J. Jorne, "Redeposition during Deep Trench Etching", J. Electrochem. Soc., 137(9), p.2837, 1990.

Lossing, F.P., "Mass Spectrometry of Free Radicals" in Mass Spectrometry, C.A. McDowell, ed., p 442, McGraw-Hill, 1963.

Loudiana, M.A., A. Schmid, J.T. Dickinson, and E.J. Ashley, "The Chemical Sputtering of Silica by Ar^+ Ions and XeF_2", Surface Sci., 141, p.409, 1984.

Lui, J., G. Huppert, and H.H. Sawin, "Ion Bombardment in RF Plasmas", J.Appl.Phys., 68(8), p.3916, 1990.

Maissel, L.I. and R. Glang eds., Handbook of Thin Film Technology , McGraw-Hill, New York, 1970.

Manenschijn, A. et al. "Cl_2 reactive ion etching mechanisms studied by in situ determination of ion energy and ion flux", J.Appl.Phys., 69(12), p.7996, 1991.

Matsumi, Y., et al., "Laser-Induced Fluorescence Study of Silicon Etching Process: Detection of SiF_2 and CF_2 Radicals", J.Appl.Phys., 60, p.4102, 1986.

Matsunami, N. et al.,"A Semiempirical Formula for the Energy Dependence of the Sputtering Yield", Rad.Effects.Lett., 57, p.15, 1980.

Mayer, T.M., and R.A. Barker, "Simulation of Plasma-Assisted Etching Processes by Ion-Beam Techniques", J.Vac.Sci.Technol., 21(3), p.757, 1982a.

Mayer, T.M., and R.A. Barker, "Reactive Ion Beam Etching with CF_4: Characterization of a Kaufman Ion Source and Details of SiO_2 Etching", J.Electrochem.Soc., 129(3), p.585, 1982b.

Mayer, T.M., R.A. Barker, and L.J. Whitman, "Investigation of Plasma Etching Mechanisms using Beams of Reactive Gas Ions", J.Vac.Sci.Technol., 18(2), p.349, 1981.

McFeely, F.R. et al., "Synchrotron Photoemission Investigation of the Initial Stages of Fluorine Attack on Si Surfaces: Relative Abundance of Fluorosilyl Species", Phys.Rev.B, 30(2), p.764, 1984.

Mcfeely, F.R., J.A. Yarmoff, A. Taleb-Ibrahimi, and D.B. Beach, " The Interaction of CF_3 Radicals and CF_3 Radical Precursors with SiO_2 Surfaces", Surface Sci. 206, p.371, 1988.

McNevin, S.C. and G.E.Becker, "Investigation of Kinetic Mechanism for the Ion-Assisted Etching of Si in Cl_2", J.Vac.Sci.Technol.B, 3(2), p.485, 1985.

McVittie, J.P. et al., "SPEEDIE: A Profile Simulator for Etching and Deposition", Proc. SPIE, 1392, p.126, 1990.

Mitzutani, T., et al., "Surface Modification in Plasma-Assisted Etching of Silicon", Nucl.Inst.Meth., B7/8, p.825, 1985.

Mogab, C.J., and H.J. Levinstein, "Anisotropic Plasma Etching of Polysilicon", J.Vac.Sci.Technol., 17(3), p.721, 1980.

Murphy, Daniel M., "Wall Collisions, Angular Flux, and Pumping Requirements in Molecular Flow Through Tubes and Microchannel Arrays", J.Vac.Sci.Technol.A, 7(5), p. 3075, 1989.

Ninomiya, K. et al., "Reaction of Atomic Fluorine with Silicon", J.Appl.Phys., 58(3), p.1177, 1985.

Ninomiya, K., et al., "An Experimental System for Surface Reaction Studies of Microwave Plasma Etching", J.Vac.Sci.Technol.B, 2(4), p.645, 1984.

Nordine P.C. and J.D. Lagrange, "Heterogeneous Fluorine Atom Recombination/Reaction on Several Materials of Construction", AIAA J. 14(5), p.644, 1976.

Nordine P.C. and D.E. Rosner, "Chemiluminescent Tritration of F with Cl_2 and Microwave Production of Atomic Fluorine", Faraday.Trans. 5/1197, p.1526, 1976.

Oehrlein, G. et al. "Surface Modifications of Electronic Materials Induced by Plasma Etching", J. Electrochem. Soc., 136(7), p.2050, 1989.

Oehrlein, G.S., "Reactive Ion Etching", Phys.Today, p. 26, October 1986.

O'hanlon, John F., A User's Guide to Vacuum Technology, Wiley-Interscience, New York, 1980.

Olander, D.R. and V. Kruger, "Molecular Beam Sources Fabricated from Multichannel Arrays.III. The Exit Density Problem", J.Appl.Phys., 41(7), p.2769, 1970.

Oshima, M.,"A Study of Dry Etching-Related Contaminations on Si and SiO_2", Surface Sci., 86, p. 858, 1979.

Oostra, D.J., A. Haring and A.E. De Vries,"Sputtering of SiO_2 in a XeF_2 and in a Cl_2 Atmosphere", J.Vac.Sci.Technol.B, 4(6), p.1278, 1986.

Pelka, J., W.W. Hoppe, and D. Mewes, "The Influence of Ion Scattering on Dry Etch Profiles", J.Vac.Sci.Technol.B, 7(6), p.1483, 1989.

Pelletier, J. and M.J. Cooke, "Microwave Plasma Etching of Si and SiO_2 in Halogen Mixtures: Interpretation of Etching Mechanisms", J.Vac.Sci.Technol.B, 7(1), p.59, 1989.

Pulker, H.K. et al., "Progress in Monitoring Thin Film Thickness with Quartz Crystal Resonators", Thin Solid Films, 32, p27, 1976.

Robertson, R.M., D. Golden and M. Rossi, "Reaction Probability for the Spontaneous Etching of Silicon by CF_3 Free Radicals", J.Vac.Sci.Technol.B, 6(6), p.1632, 1988.

Ryan, K.R. and Plumb, I.C., "Gas-Phase Reactions of CF_3 and CF_2 with Hydrogen Atoms: Their Significance in Plasma Processing", Plasma Chem. Plasma Proc., 4(3), p.141, 1984.

Sawin, H.H., D.C. Gray, and T.Dalton, "Pattern Independent Dry Etching Processes", Massachussets SCOE review, 1990.

Selamoglu, N., M.J. Rossi, and D.M. Golden, "Reaction of CF_3 Radicals on Fused Silica Between 320 and 530 K", J.Chem.Phys., 84(4), p.2400, 1986.

Shaqfeh, E.S.G., and C. Jurgensen, "Simulation of Reactive Ion Etching Pattern Transfer", J.Appl.Phys., 66(10), p.4664, 1989.

Sigmund, P., "Theory of Sputtering.I. Sputtering Yield of Amorphous and Ploycrystalline Targets", Phys. Rev., 184(2), p.383, 1969.

Solberg, W.A. and I.L.Spain, "The Role of Sputter Redeposition in the Growth of Cones and Filaments on Carbon Surfaces during Ion Bombardment", J.Vac.Sci.Technol.A, 8(6), p3907, 1990.

Steinbruchel, C., "Universal Energy Dependence of Physical and Ion-Enhanced Chemical Etch Yields at Low Ion Energy", Appl.Phys.Lett., 55(19), p.1960, 1989.

Stevie, F.A., and M.J. Vasile, "Electron Impact Ionization Cross Sections of F_2 and Cl_2", J.Chem.Phys., 74(9), p.5106, 1981.

Suzuki, Keizo, S. Hiraoka and S. Nishimatsu, "Anisotropic Etching of Polycrystalline Silicon with a Hot Cl_2 Molecular Beam", J.Appl.Phys., 64(7), p.3697, 1988.

Tachi, S. et al., "Low Temperature Dry Etching", J.Vac.Sci.Technol.A, 9(3), p.796, 1991.

Tepermeister, I., "Study of Plasma-Polymer Surface Interactions in Fluorine and Oxygen Discharges", Ph.D. Thesis, MIT Dept. of Chemical Eng., 1992.

Thoman, J.W. et al., "Laser-Induced Fluorescence Measurement and Analytical Model for the Reaction Probability of CF_2 on Si", J.Appl.Phys., 60(8), p.2775, 1986.

Thomas, J.H.,X. Chun Mu and S.J. Fonash, "An X-Ray Photoelectron Spectroscopy Study of CF_4/H_2 Reactive Ion Etching Residue on Silicon", J.Electrochem.Soc., 134(12), p.3122, 1987.

Tu, Y., T.J. Chuang, and H.F. Winters, " Chemical Sputtering of Fluorinated Silicon", Pys.Rev.B, 23(2), p.823, 1981

Vanhaelemeersch, S., et al., "SiF_2 as a Primary Desorption Product of Si Etching by F Atoms: Interpretation of Laser-Induced Fluorescence Spectra; Rate Constant of the Gas Phase SiF_2+F Reaction", J.Appl.Phys., 70(7), p.3892, 1991.

Vasile, M.J., "The Reaction Probability of XeF_2 with Silicon", J.Appl.Phys., 54(11), p.6697, 1983.

Vasile, M.J. and F.A. Stevie, "Reaction of Atomic Fluorine with Silicon: The Gas Phase Products", J.Appl.Phys., 53(5), p.3799, 1982.

Wajid, A., "Improving the Accuracy of a Quartz Crystal Microbalance with Automatic Determination of Acoustic Impedance Ratio", Rev.Sci.Instrum., 62(8), p.2026, 1991.

Winkler, A. and J.T. Yates, "Capillary Array Dosing and Angular Distribution Measurements: A General Formalism", J.Vac.Sci.Technol.A, 6(5), p.2929, 1988.

Wilson, W.D., L.G. Haggmark, and J.P. Beirsack, "Calculations of Nuclear Stopping, Ranges, and Straggling in the Low-Energy Region", Phys. Rev. 15, p.2458, 1977.

Winters, H.F. and I.C. Plumb, "Etching Reactions for Silicon with F Atoms: Product Distributions and Ion Enhancement Mechanisms", J.Vac.Sci.Technol.B, 9(2), p.197, 1991.

Winters, H.F., "Ion-Induced Etching of SiO_2: The Influence of Mixing and Lattice Damage", J Appl.Phys., 64(5), p.2805, 1988.

Winters, H.F. and J.W. Coburn, "Plasma-Assisted Etching Mechanisms: The Implications of Reaction Probability and Halogen Coverage", J.Vac.Sci.Technol.B, 3(5), p.1376, 1985.

Winters, H.F., J.W. Coburn, and T.J. Chuang, "Surface Processes in Plasma-Assisted Etching Environments", J.Vac.Sci.Technol.B, 1(2), p.469, 1983.

Winters, H.F. and F.A. Houle, "Gaseous Products from the Reaction of XeF_2 with Silicon", J.Appl.Phys., 54(3), p.1218, 1983.

Winters, H.F., "Etch Products from the Reaction of XeF_2 with SiO_2, Si_3N_4, SiC, and Si in the Presence of Ion Bombardment", J.Vac.Sci.Technol.B, 1(4), p.927, 1983.

Winters, H.F. and J.W. Coburn, "The Etching of Silicon by XeF_2 vapor", Appl.Phys.Lett., 34(1), p.70, 1979

Winters, H.F.,"The Role of Chemisorption in Plasma Etching", J.Appl.Phys., 49(10), p.5165, 1978.

Winters, H.F. in Radiation Effects on Solid Surfaces, Kaminsky, M. ed., Amer.Chem.Soc., Washington DC, 1976.

Wolf, S. and R.N. Tauber, Silicon Processing for the VLSI Era, Lattice Press, Sunset Beach CA, 1986.

Wucher, A. and W. Reuter, "Angular Distribution of Particles Sputtered from Metals and Alloys", J.Vac.Sci.Technol.A, 6(4), p.2316, 1988.

Yun, et al., "Characterization of Silicon Surface Contamination in Near-Surface Damage Caused by C_2F_6/CHF_3 Reactive Ion Etching", J.Electrochem.Soc., 137(8), p.2634, 1990.

Zalm, P.C., "Some Useful Yield Estimates for Ion Beam Sputtering and Ion Plating at Low Bombarding Energies", J.Vac.Sci.Technol.B, 2(2), p.151, 1984.

Zau, G. et al. "Threshold Levels and Effects of Feed Gas Impurities on Plasma Etching Processes", J.Electrochem.Soc., 137(11), p.3526, 1990.

Zau, G., Ph.D. Thesis, MIT Dept. of Chem. Eng., 1993.

Appendix A: Mechanical Drawings

This appendix contains the mechanical drawings describing the multi-beam apparatus discussed in Chapter 2 of this thesis. The drawing set has been broken down into ten broad categories, in which the individual drawings are ordered as follows:

1. Main Chamber Assemblies

CHAMBER ORIGINALS	PROFILE VIEWS
CHAMBER ORIGINALS	SCATTERING PLANE
COMP1	CHAMBER PROFILE
COMP2	SAMPLE MOUNTING ASSEMBLY
SURFTAB1	MULTI-BEAM/XPS SYSTEM TOP VIEW

2. Top Flange Components

3BEAM01	FLANGE ROTATION BASE
3BEAM02	ROTATABLE MASS SPEC FEEDTHROUGH
3BEAM03	ROTATABLE MASS SPEC FEEDTHROUGH (SIDE)
3BEAM18	FLAG ROD RETAININER
3BEAM20	DIFFERENTIAL PUMPING PORT
3BEAM45	TOP FLANGE CLIPS
3BEAM52	TOP FLANGE ROTATION HANDLE
3BEAM55	DIFF PUMPED MASS SPEC FEEDTHROUGH
3BEAM56	MASS SPEC FEEDTHROUGH-TOP
3BEAM57	MASS SPEC FEEDTHRU-BOTTOM
3BEAM58	MASS SPEC FEEDTHROUGH-C.S. B-B'
3BEAM59	MASS SPEC FEEDTHROUGH-C.S. C-C'
3BEAM60	MASS SPEC CAP

3. Side Flange Components

3BEAM00	FLANGE ADAPTER
3BEAM10	SIDE FLANGE PORT ASSIGNMENTS

4. Transfer System Components

3BEAM26	3/8" TFE SLIDE SEAL
3BEAM27	3/8" RETAINING RINGS
3BEAM29	5/8" TFE SLIDE SEAL
3BEAM30	5/8" RETAINING RINGS
3BEAM32	UP-TO-AIR FLANGE
3BEAM33	WELDED BELLOWS ADAPTER
3BEAM34	3/8" WOBBLE ROD
3BEAM35	3/8" SLIDE SEAL ASSEMBLY
3BEAM36	5/8" SLIDE SEAL ASSEMBLY
3BEAM36B	5/8" SLIDE SEAL ASSEMBLY DETAIL
3BEAM37	5/8" SLIDE ROD
3BEAM37B	3-BEAM SAMPLE PUSHROD
3BEAM37C	3-BEAM SAMPLE PUSHROD RETAINER
3BEAM40	3/8" DOUBLE GLAND RING
3BEAM41	5/8" DOUBLE GLAND RING
3BEAM42	PUSHROD ADAPTER
3BEAM43	5/8" ROD RETAINER
3BEAM44	3/8" ROD RETAINER
3BEAM46	3/8" SLIDE ROD
3BEAM49	VACUUM TRANSFER TUBE
COMP9	WOBBLE STICK ASSEMBLY

5. Sample Mounting System Components

3BEAM04	PLATEN MOUNTING RODS
3BEAM05	SAMPLE HOLDER ALIGNMENT PINS
3BEAM06	MOTOR MOUNT PLATEN
3BEAM07	SAMPLE MOUNTING PLATE
3BEAM08	MOTOR PLATEN MOUNTING PLATE
3BEAM38	SAMPLE MOUNT DRILL JIG
3BEAM39	SAMPLE MOUNT TAP JIG
3BEAM47	SAMPLE MOUNT
3BEAM48	SAMPLE MOUNTING PIN
3BEAM75	SAMPLE ELECTRICAL SOCKET
3BEAM76	SAMPLE ELCTRICAL PLUG
3BEAM77	ELECTRICAL CONNECTOR RETAINER
3BEAM78	SAMPLE EXTENSION PEDESTAL

6. Diagnostic Probe Components

3BEAM13	IMPACT TUBE COUPLER
3BEAM14A	IMPACT TUBE CAP
COMP6	IMPACT TUBE ASSEMBLY
3BEAM14B	PROBE ALIGNMENT JIG
3BEAM15A	FARADAY CUP COUPLING ROD
3BEAM15B	FARADAY CUP SUPPORT ROD
3BEAM16A	FARADAY CUP SLIDING BASE
3BEAM16B	FARADAY CUP FACE SEAT
3BEAM17	FARADAY CUP ASSEMBLY

7. Beam Flange Components

3BEAM19	4.62" FORMED BELLOWS ADAPTER
3BEAM22	DISCHARGE DOSER FLANGE
3BEAM23	PYROLYSIS DOSER FLANGE
3BEAM50	KAUFMAN GUN RADIATION SHIELD
3BEAM51	KAUFMAN GUN SHIELD CAP
3BEAM61	ECR ADAPTER ASSEMBLY A-A'
3BEAM62	ECR ADAPTER ASSEMBLY B-B'
3BEAM64	ECR ADAPTER ASSEMBLY-END ON
3BEAM65	ECR EXTENSION NIPPLE
3BEAM66	KAUFMAN GUN EXTENSION RODS
3BEAM67	KAUFMAN GUN EXTENSION MOUNT
3BEAM68	CT100 GATE VALVES-SPECIAL
3BEAM69	ECR ADAPTER-SHORT

8. QCM System Componenents

3BEAM24	QCMB HOLDER
3BEAM25	QCMB MOUNTING ROD
3BEAM72	QCM MOUNTING PIN
3BEAM73	QCM MOUNTING BRACKET
3BEAM74	QCM RETAINER

9. Beam Chopping System Components

CHAMBER ORIGINALS	BEAM CHOPPING LOGISTICS
COMP5	CHOPPER MOTOR ASSEMBLY
3BEAM09	CHOPPER MOTOR MOUNTS
3BEAM11	50% DUTY CHOPPER BLADE

3BEAM12	CHOPPER BLADE COLLAR
3BEAM79	CHOPPER MOTOR COOLING SLEAVE
3BEAM80	MOTOR DEPOSITION SHIELD

10. Optical Components

3BEAM21	BREWSTER WINDOW FLANGES

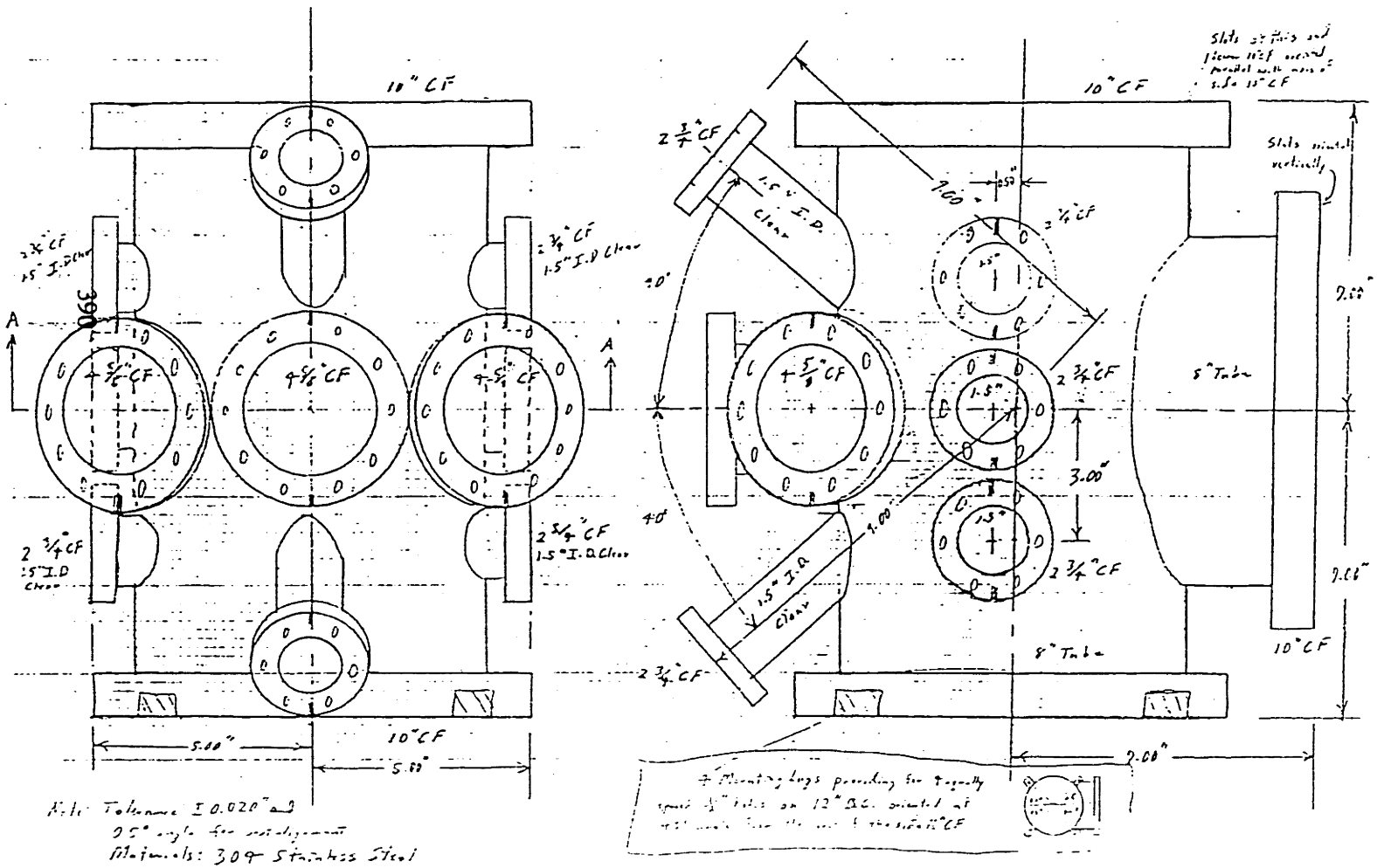

All Tolerance ± 0.020" and 0.5° angle for misalignment
Materials: 304 Stainless Steel

MIT CHEMICAL ENGINEERING

GENERAL INFORMATION

SCALE:	SHEET 1 OF 1
DIMENSIONS ARE IN INCHES	REVISION NO 1.0

DESIGNED BY: DAVID C. GRAY
DRAFTED BY: DAVID C. GRAY

PRIMARY ASSEMBLY: 3-BEAM REACTOR
SECONDARY ASSEMBLY:

DRAWING TYPE: STANDARD MACHINE

MTL:

ITEM IDENTIFICATION

NAME: CHAMBER ORIGINALS
CODE:

FILE:

DESCRIPTION:

TOLERANCE SPECIFICATIONS

X	+/- .05	XX	+/- .02
XXX	+/- .005	XXXX	+/- .0005
X/XX	+/- 1/64	ANGULAR	+/- 1°

FLATNESS .010 TOTAL
PERPENDICULARITY: .005 PER INCH
PARALLELISM .005 TOTAL

I.D.'S TO BE WITHIN .002 T.I.R.

1) FINISHING MARKS CONFORM TO AMERICAN STANDARD CONVENTIONS.
2) BREAK ALL SHARP EDGES .005 - .015
3) REMOVE ALL BURRS. LEAVE NO HEAVY MILL FILE, TOOL OR CHATTER MARKS.

LEGAL NOTES:

CONTRACTOR INFORMATION:

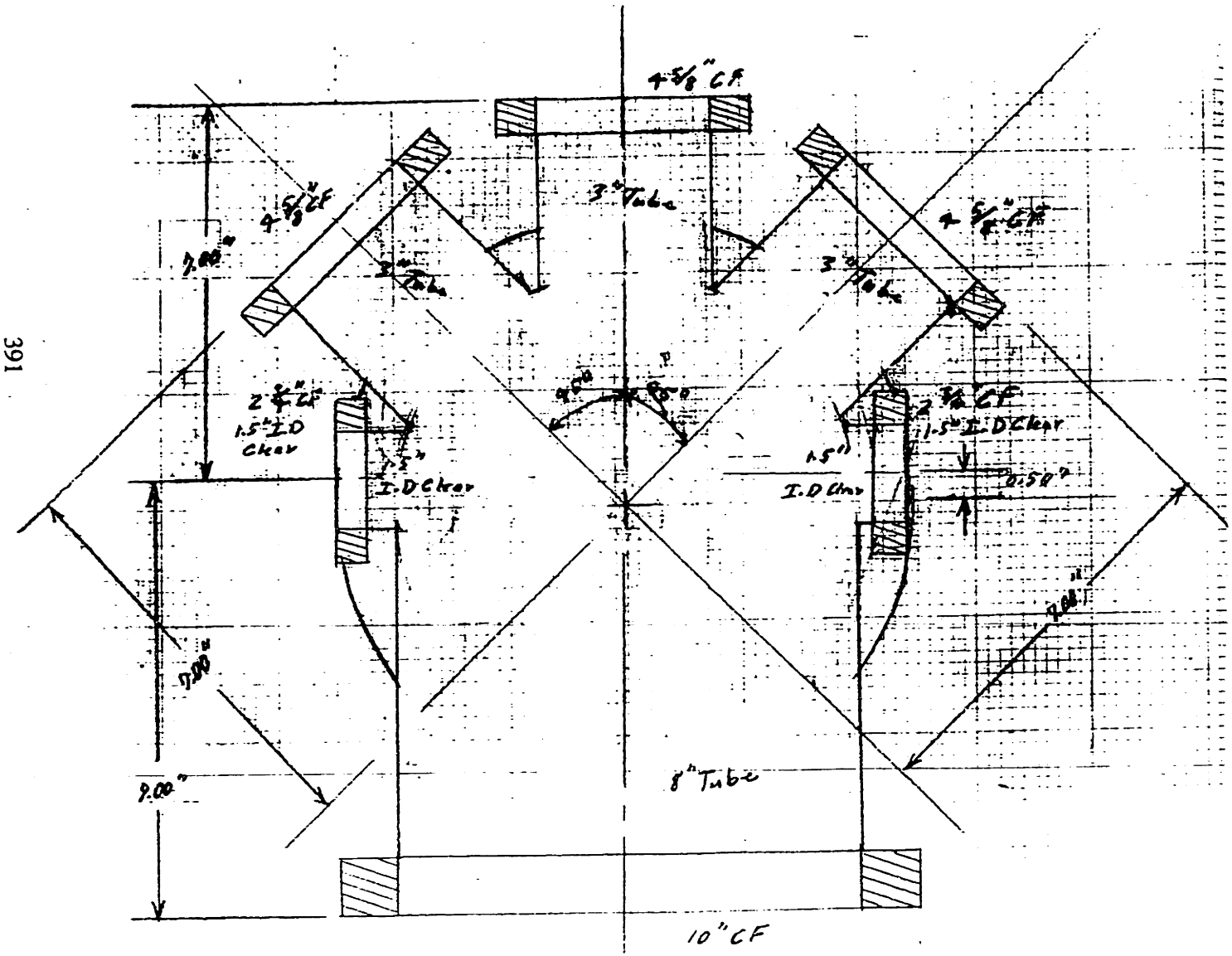

MIT CHEMICAL ENGINEERING

GENERAL INFORMATION

SCALE:

SHEET 1 OF 1

DIMENSIONS ARE IN INCHES

REVISION NO: 18

DESIGNED BY: DAVID C. GRAY
DRAFTED BY: DAVID C. GRAY

PRIMARY ASSEMBLY: 3-BEAM REACTOR
SECONDARY ASSEMBLY:

DRAWING TYPE: STANDARD MACHINE

MTL:

ITEM IDENTIFICATION

NAME: CHAMBER ORIGINALS
CODE:

FILE:

DESCRIPTION:

TOLERANCE SPECIFICATIONS

X	+/- .05	XX	+/- .02
XXX	+/- .005	XXXX	+/- .0005
X/XX	+/- 1/64	ANGULAR	+/- 1°

FLATNESS: .010 TOTAL
PERPENDICULARITY: .001 PER INCH
PARALLELISM: .005 TOTAL

I.D.'S TO BE WITHIN .002 T.I.R.

1) FINISHING MARKS CONFORM TO AMERICAN STANDARD CONVENTIONS.
2) BREAK ALL SHARP EDGES .005 - .015
3) REMOVE ALL BURRS. LEAVE NO HEAVY MILL FILE, TOOL, OR CHATTER MARKS.

LEGAL NOTES:

CONTRACTOR INFORMATION:

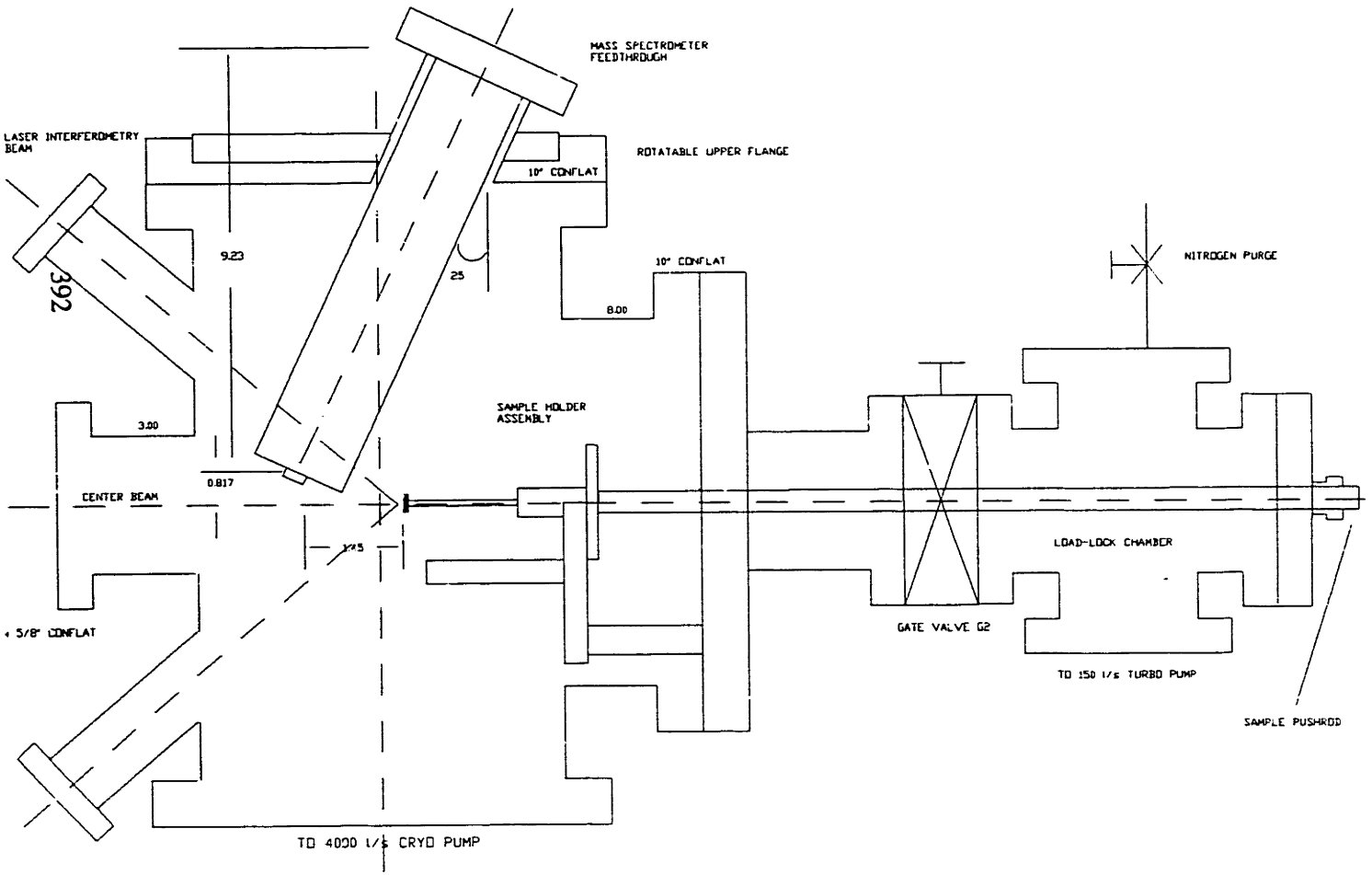

MIT CHEMICAL ENGINEERING

GENERAL INFORMATION

SCALE:

SHEET 1 OF 1

DIMENSIONS ARE IN INCHES

REVISION NO: 10

DESIGNED BY: DAVID C GRAY
DRAFTED BY: DAVID C. GRAY

PRIMARY ASSEMBLY: 3-BEAM REACTOR
SECONDARY ASSEMBLY:

DRAWING TYPE: STANDARD MACHINE

MTL:

ITEM IDENTIFICATION

NAME: CHAMBER PROFILE
CODE: COMPLDWG

FILE: 3-BEAM

DESCRIPTION:

TOLERANCE SPECIFICATIONS

X	+/- .05	XX	+/- .02
.XXX	+/- .005	XXXX	+/- .0005
X/XX	+/- 1/64	ANGULAR	+/- 1°

FLATNESS: .010 TOTAL
PERPENDICULARITY: .001 PER INCH
PARALLELISM: .005 TOTAL

I.D.'S TO BE WITHIN .002 TLR

1) FINISHING MARKS CONFORM TO AMERICAN STANDARD CONVENTIONS.
2) BREAK ALL SHARP EDGES .005 - .015
3) REMOVE ALL BURRS LEAVE NO HEAVY MILL FILL TOOL OR CHATTER MARKS

LEGAL NOTES:

CONTRACTOR INFORMATION:

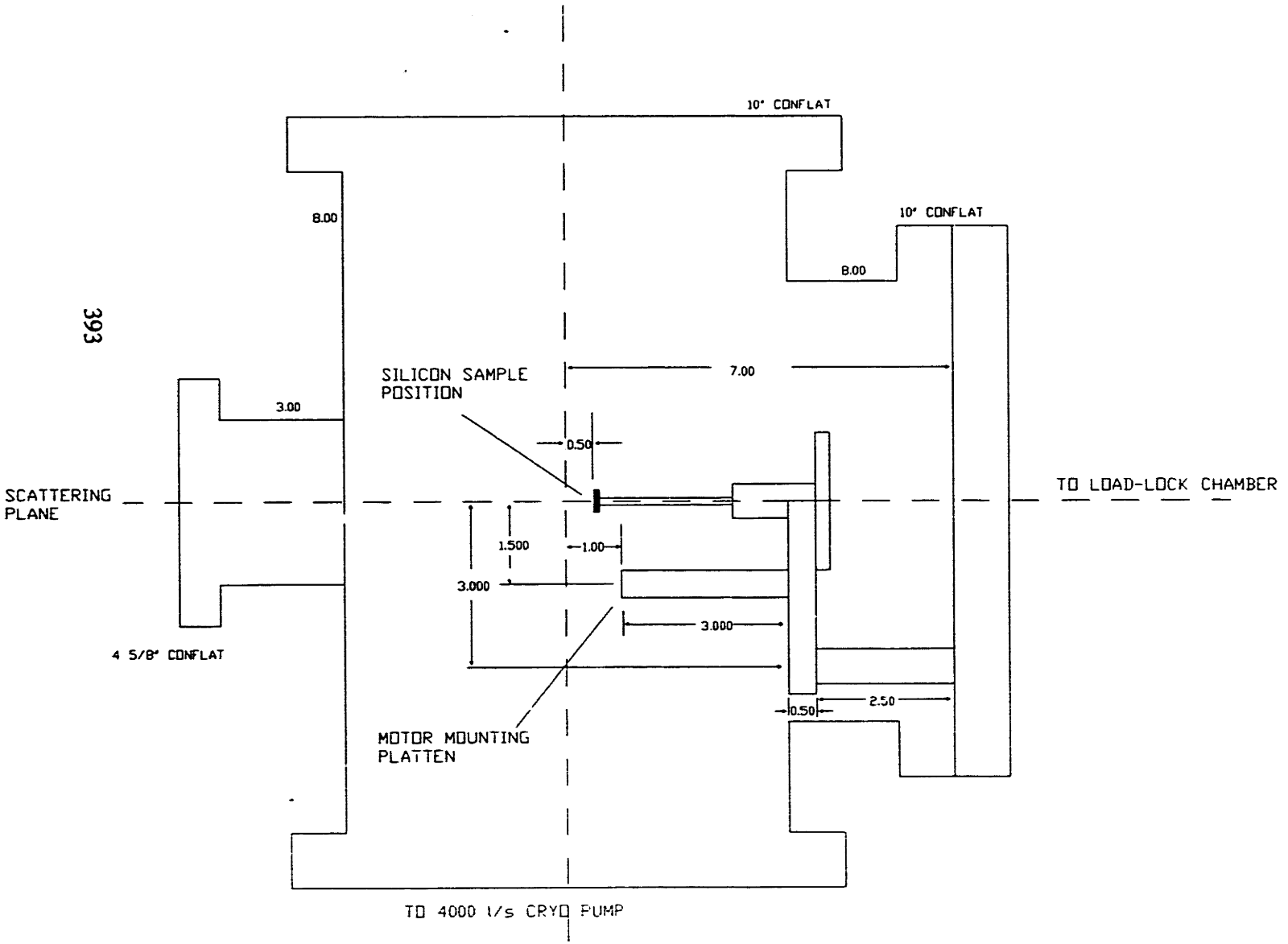

MIT CHEMICAL ENGINEERING

GENERAL INFORMATION

SCALE 1:1 | SHEET 1 OF 1

DIMENSIONS ARE IN INCHES | REVISION NO: 10

DESIGNED BY: HERBERT H. SAVIN, Ph.D.
DRAFTED BY: DAVID C. GRAY

PRIMARY ASSEMBLY: 3-BEAM REACTOR
SECONDARY ASSEMBLY: SAMPLE MOUNTING ASSEMBLY

DRAWING TYPE: STANDARD MACHINE

MTL:

ITEM IDENTIFICATION

NAME: SAMPLE MOUNTING ASSEMBLY
CODE: COMPZ.DWG

FILE: 3-BEAM

DESCRIPTION:

TOLERANCE SPECIFICATIONS

.X	+/- .05	.XX	+/- .02
.XXX	+/- .005	.XXXX	+/- .0005
X/XX	+/- 1/64	ANGULAR	+/- 1°

FLATNESS: .010 TOTAL
PERPENDICULARITY: .001 PER INCH
PARALLELISM: .005 TOTAL

I.D.'S TO BE WITHIN .002 T.I.R.

1) FINISHING MARKS CONFORM TO AMERICAN STANDARD CONVENTIONS.
2) BREAK ALL SHARP EDGES .005 - .015
3) REMOVE ALL BURRS LEAVE NO HEAVY ROLL FREE TOOL OR CHATTER MARKS.

LEGAL NOTES:

CONTRACTOR INFORMATION:

CROSS-SECTION A-A'

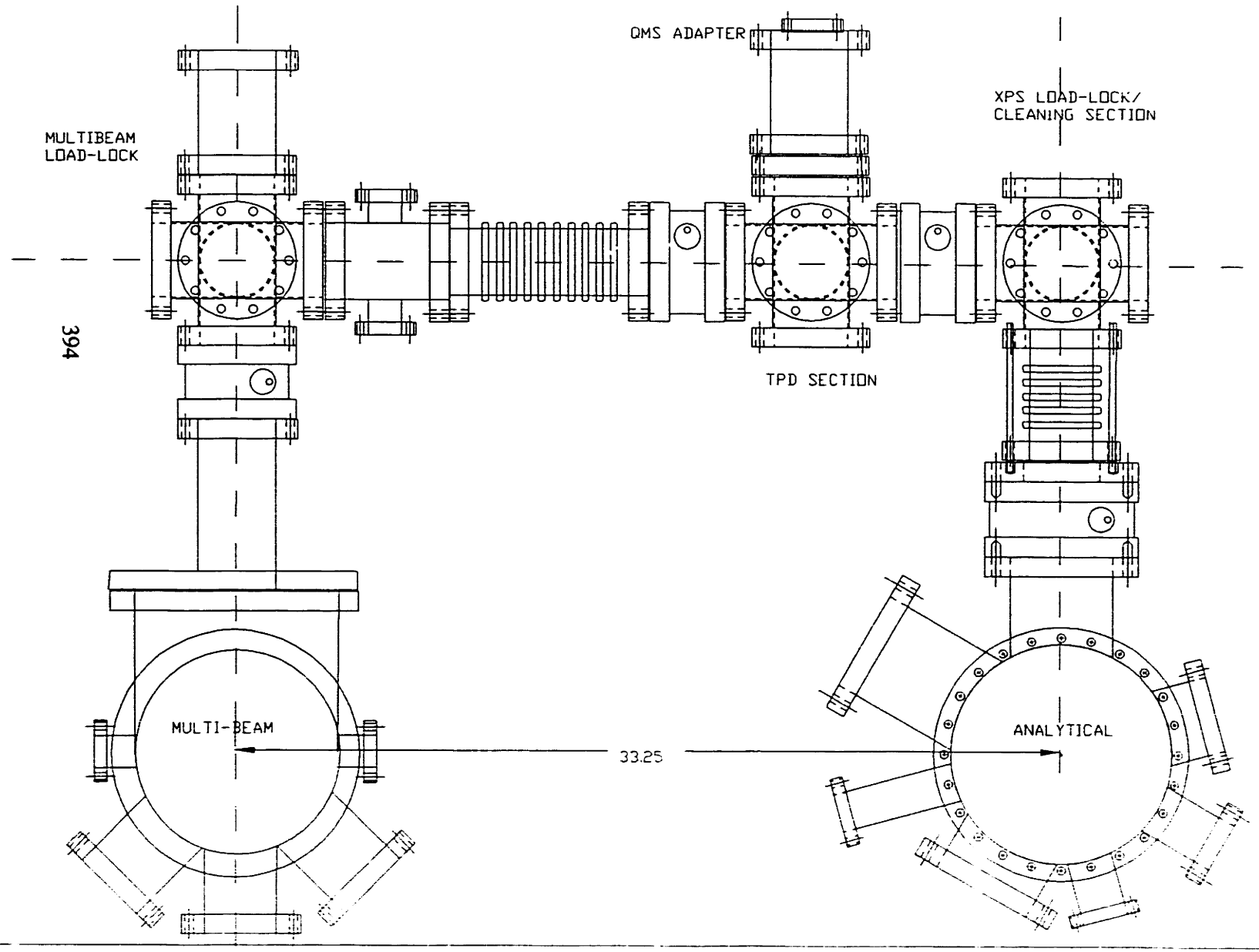

MIT CHEMICAL ENGINEERING

GENERAL INFORMATION

SCALE: 1" = 4" | SHEET 1 OF 1

DIMENSIONS ARE IN INCHES | REVISION NO 16

DESIGNED BY: DAVID C. GRAY
DRAFTED BY: DAVID C. GRAY

PRIMARY ASSEMBLY: SURFACE ANALYTICAL TABLE
SECONDARY ASSEMBLY:

DRAWING TYPE: STANDARD MACHINE

MTL:

ITEM IDENTIFICATION

NAME:
CODE:

FILE: SURFTAB1.DWG

DESCRIPTION:

CROSS SECTION OF SURFACE TABLE
WITH UV/HIGH PRESSURE CLEANING
MODULE AND TPD CHAMBER INSTALLED

TOLERANCE SPECIFICATIONS

X	+/- .5"	XX	+/- .02
XXX	+/- .005	XXXX	+/- .0005
X/XX	+/- 1/64	ANGULAR	+/- 1°

FLATNESS: .010 TOTAL
PERPENDICULARITY: .001 PER INCH
PARALLELISM .005 TOTAL

I.D.'S TO BE WITHIN .002 TLR

1) FINISHING MARKS CONFORM TO AMERICAN STANDARD CONVENTIONS
2) BREAK ALL SHARP EDGES .005 - .015
3) REMOVE ALL BURRS LEAVE NO HEAVY MILL FILE TOOL OR CHATTER MARKS

LEGAL NOTES:

CONTRACTOR INFORMATION

MIT DEPT. OF CHEMICAL ENGINEERING

PART: FLANGE ROTATION BASE

CODE: 3B.01 FILE NO: 3-BEAM

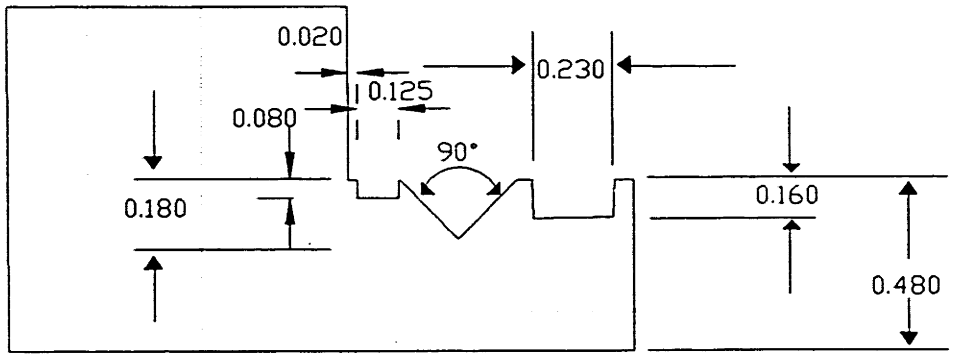

GROOVE DETAIL

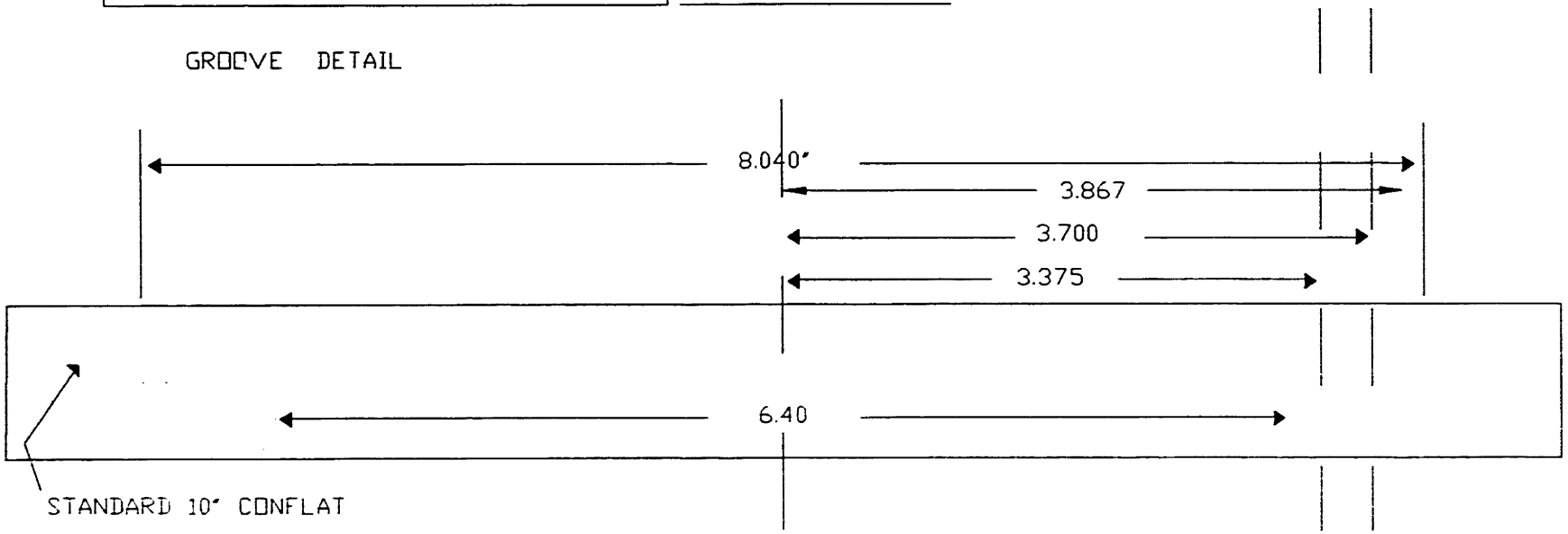

DESIGNER: D. GRAY H. SAWIN

CONTRACTOR: NOR CAL

COMMENTS: BEARING GROOVES TO FIT .250 DIAMETER BEARINGS WITH .020 GAP
INNER O-RING IS 3/16" OD VITON
OUTER O-RING IS 1/8" OD VITON

REVISION 4/25/89

DWG SCALE: MAIN 1"= 1" | DETAIL 2"= 1"

QUANTITY: 1

TOLERANCES: X.X = +/-.050
.XXX = +/-.010
.XXXX = +/-.002

MATERIAL: STAINLESS
10" CONFLAT

1 OF 1

MIT DEPT. OF CHEMICAL ENGINEERING

PART: ROTATABLE MASS SPEC FEEDTHROUGH

CODE: 3B.02 FILE NO: 3-BEAM

BOTTOM VIEW

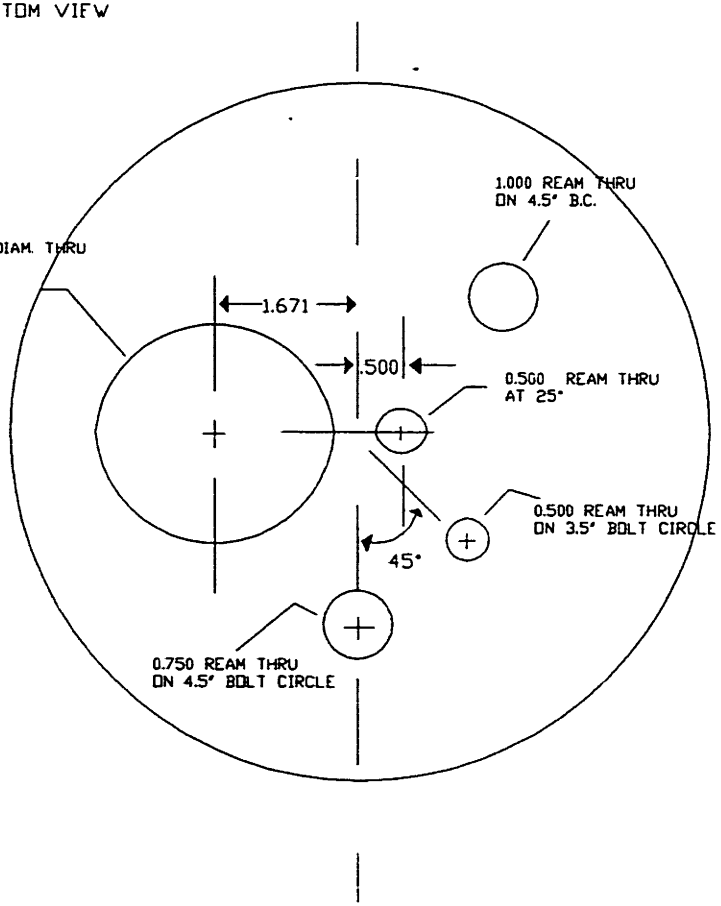

TOP VIEW

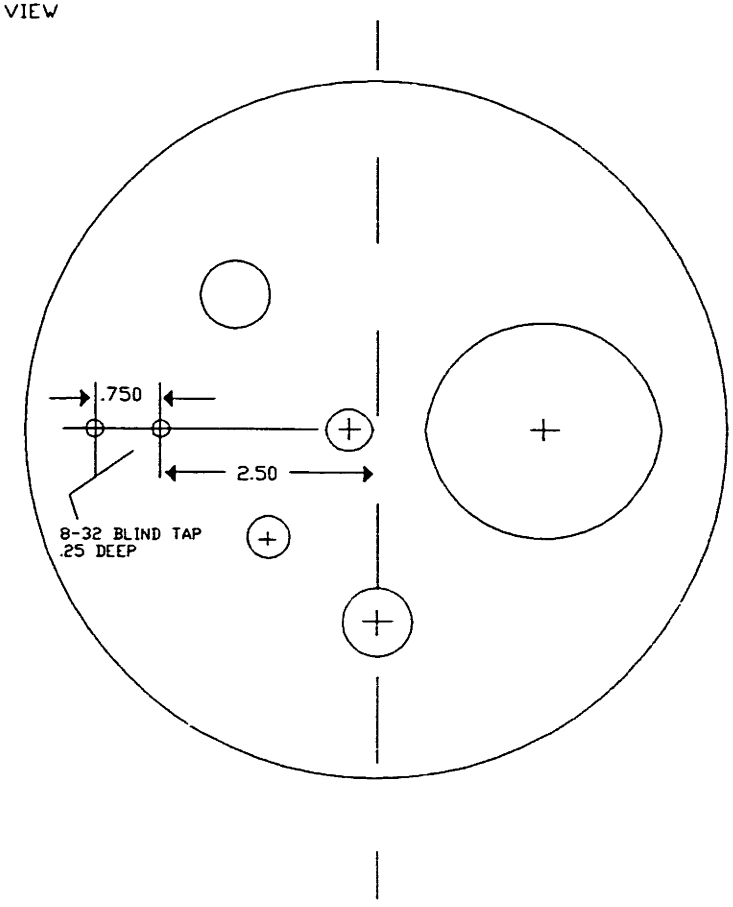

DESIGNER: D. GRAY H. SAWIN
CONTRACTOR: NOR-CAL

COMMENTS: .500 HOLES ARE FOR 1/4" CAJON FITTINGS
.750 HOLE FOR MINI CONFLAT FEEDTHRU
ALL FITTINGS SHOULD PRESS FIT FOR WELDING

REVISION 9/1/91

DWG SCALE: 1" = 2"
QUANTITY: 1

MATERIAL: STAINLESS

1 OF 2

TOLERANCES
X.X = ±.050
X.XX = ±.010
X.XXX = ±.002

MIT DEPT. OF CHEMICAL ENGINEERING

PART: ROTATABLE MASS SPEC FEEDTHROUGH

CODE: 3B.03 FILE NO: 3-BEAM

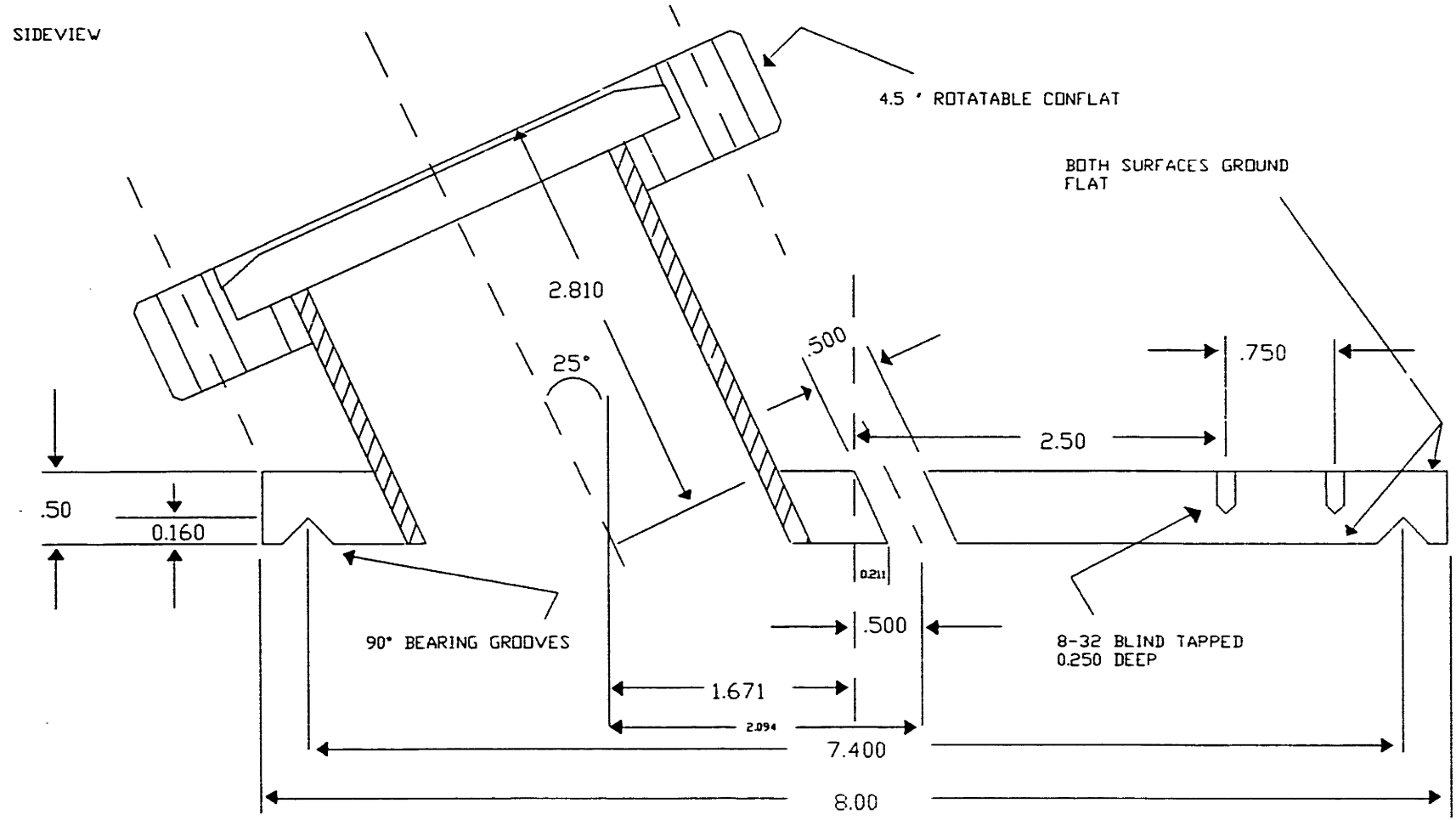

DESIGNER: D. GRAY H. SAWIN

CONTRACTOR: NOR-CAL

COMMENTS: 0.500" CAJON FITTING AND CONFLAT NIPPLE SHOULD PRESS FIT INTO FLANGE TOP

REVISION 4/25/89

DWG SCALE: 1" = 1"

QUANTITY: 1

MATERIAL: STAINLESS

1 OF 2

TOLERANCES:

X.X = ±.050

X.XX = ±.010

X.XXX = ±.002

MIT DEPT. OF CHEMICAL ENGINEERING

PART: FLAG ROD RETAINING RING

CODE: 3B.18 FILE NO: 3-BEAM

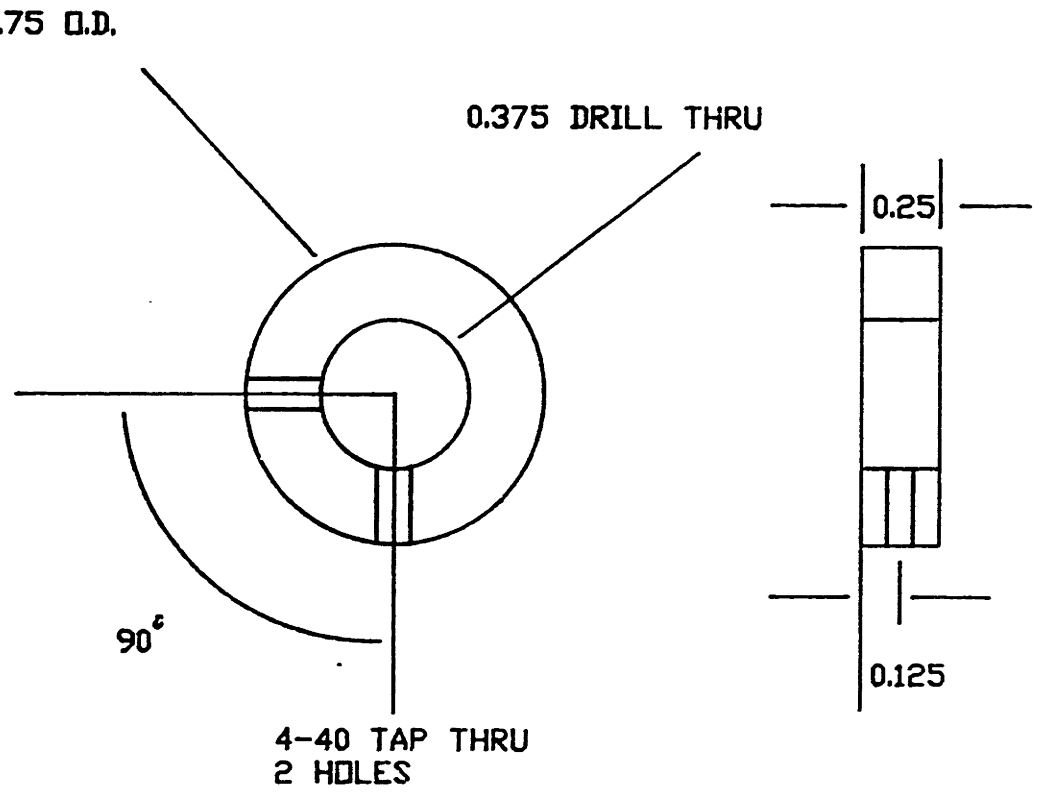

DESIGNER: H. SAWIN D. GRAY
CONTRACTOR: REACTOR SHOP

COMMENTS:

DWG SCALE: 2" = 1"
QUANTITY: 1

MATERIAL: 6061 AL

1 OF 1

TOLERANCES:
X.X = +/- 050
X.XX = +/- 010
X.XXX = +/- 002

MIT DEPT. OF CHEMICAL ENGINEERING

PART: FLANGE ROTATION BASE
DIFFERENTIAL PUMPING PORT

CODE: 3B.20 FILE NO: 3-BEAM

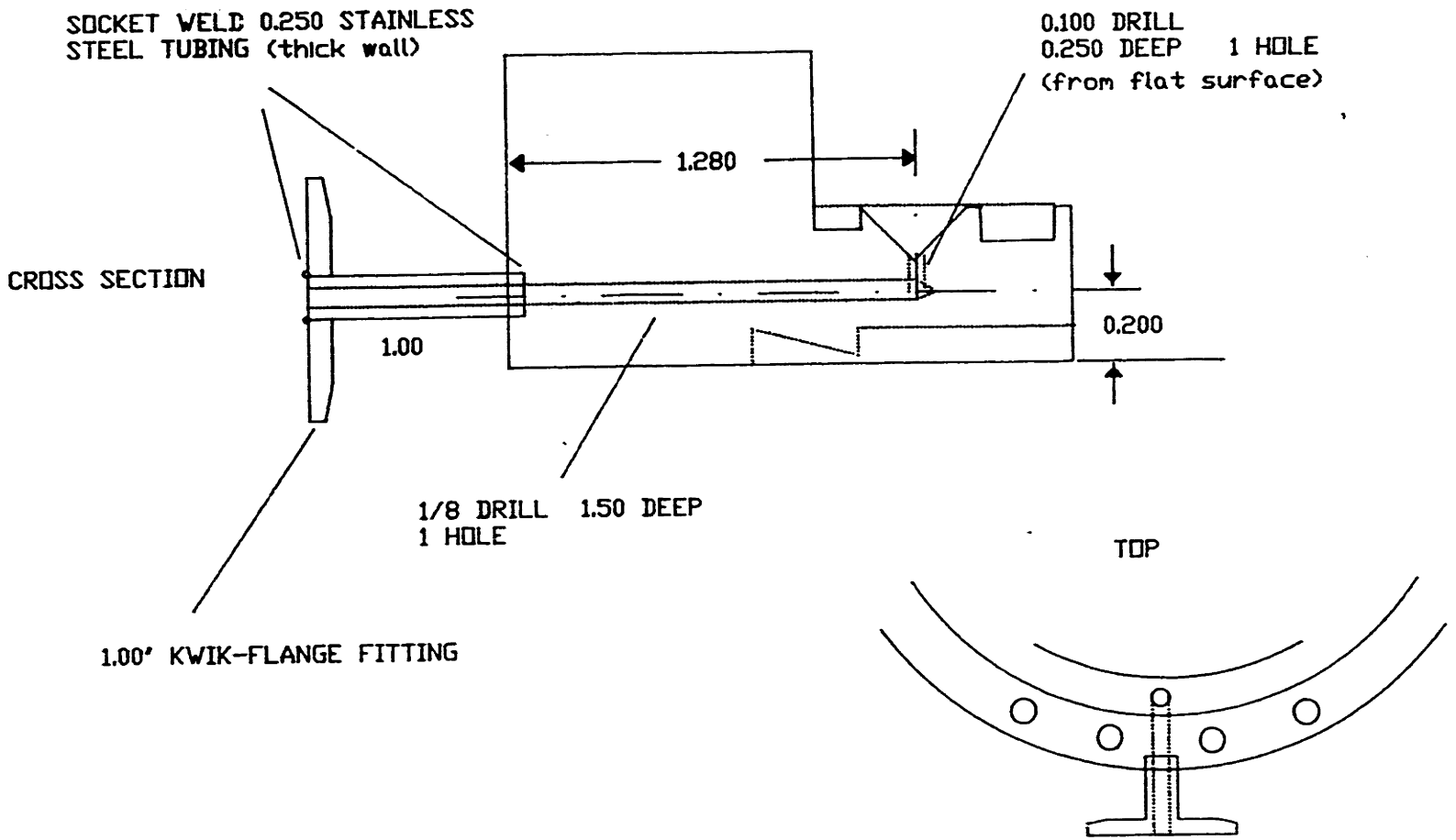

DESIGNER: H. SAWIN / D. GRAY
CONTRACTOR:

COMMENTS:

DWG SCALE: MAIN 1"= 1" | DETAIL 2"= 1" 1 OF 1
QUANTITY: 1

TOLERANCES: XX = +/-.030
XXX = +/-.010
XXXX= +/-.002

MATERIAL: 0.25 S.S. TUBING
1.0" KWIK-FLANGE BLANK

MIT DEPT. OF CHEMICAL ENGINEERING
CAMBRIDGE, MASSACHUSETTS 02139
Bldg. 66-219, (617) 253-6587

PART: TOP FLANGE CLIPS

CODE: 3B.45 REVISION: 1/22/90

400

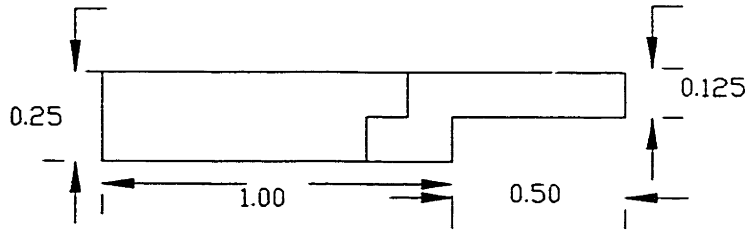

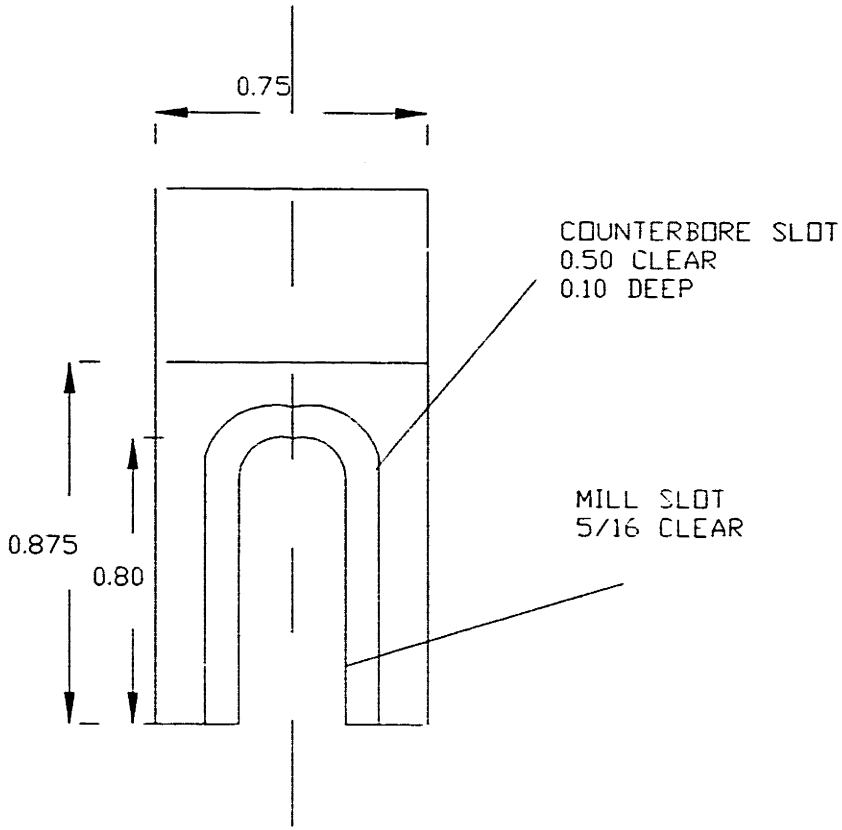

DESIGNER: D.C. GRAY
CONTRACTOR: CHEM ENG SHOP

COMMENTS:

DWG SCALE: 2" = 1"
QUANTITY: 2 REQUIRED

MATERIAL: 316 STAINLESS STEEL
0.25 PLATE STOCK

1 OF 1

TOLERANCES:
X.X = +/-.050
X.XX = +/-.010
X.XXX = +/-.002

MIT DEPT. OF CHEMICAL ENGINEERING
CAMBRIDGE, MASSACHUSETTS 02139
Bldg. 66-221 METL LAB (617) 253-6587

PART: TOP FLANGE ROTATION HANDLE

CODE: 3B.52 REVISION: 1/90

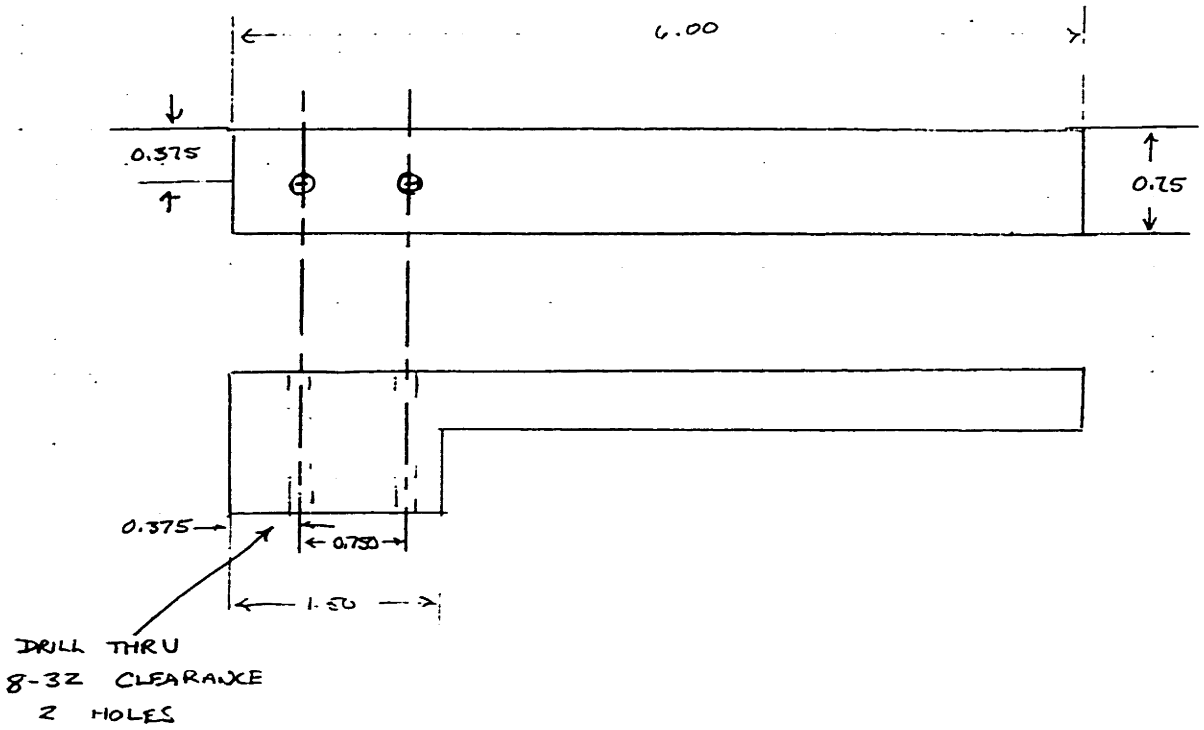

DESIGNER: D.C. GRAY
CONTRACTOR:

COMMENTS:

DWG SCALE:
QUANTITY: 1 REQUIRED

MATERIAL 6061 Al

MIT DEPT. OF CHEMICAL ENGINEERING

PART: ROTATABLE MASS SPEC FEEDTHROUGH
WITH DIFFERENTIAL PUMPING

CODE: 3B.55 FILE NO: 3-BEAM

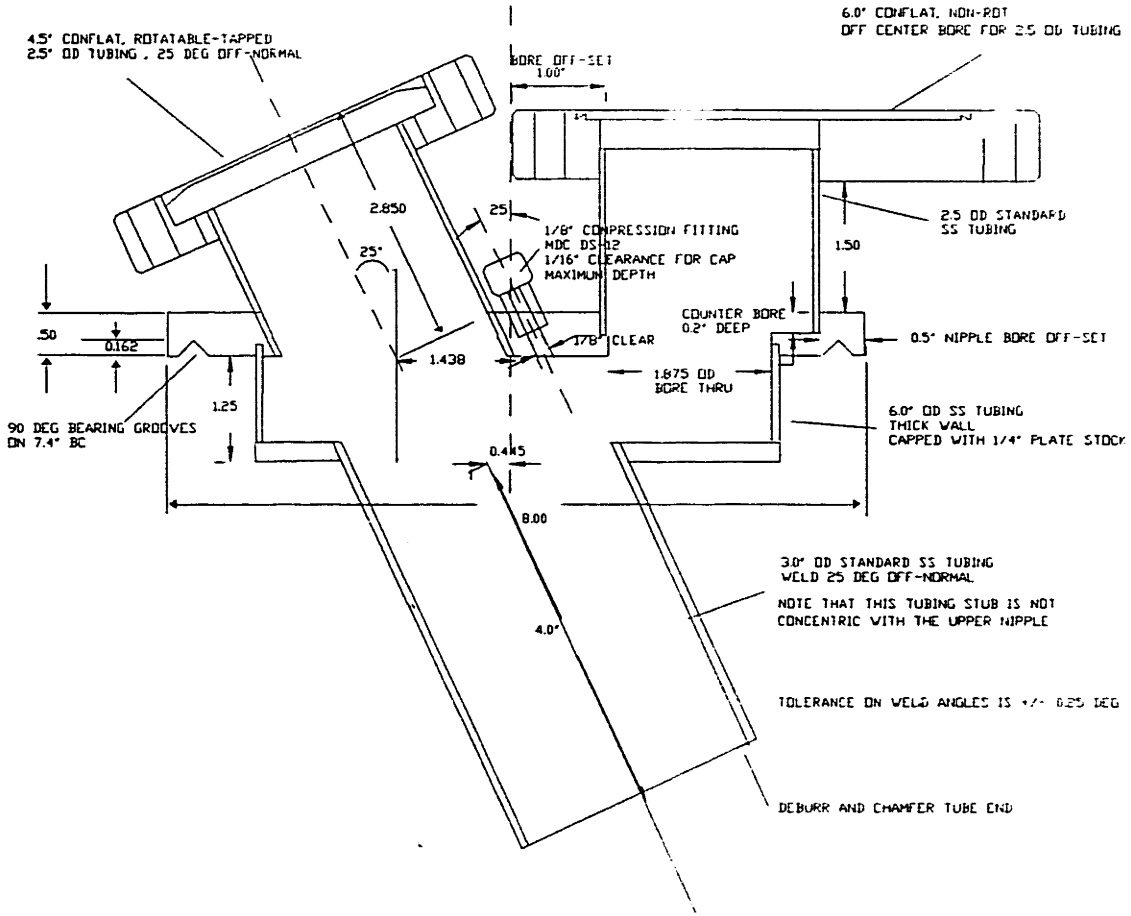

DESIGNER: D.C. GRAY
CONTRACTOR: SHARON VACUUM. BROCKTON MA

COMMENTS:

REVISION: 11/6/90 FINAL

DWG SCALE: SCALE
QUANTITY: 1

MATERIAL: STAINLESS

1 OF 6

TOLERANCES:
X.X = ±.05
X.XX = ±.01
X.XXX = ±.00

MIT DEPT. OF CHEMICAL ENGINEERING

PART: ROTATABLE MASS SPEC FEEDTHROUGH WITH DP, TOP VIEW

CODE: 3B.56 FILE NO: 3-BEAM

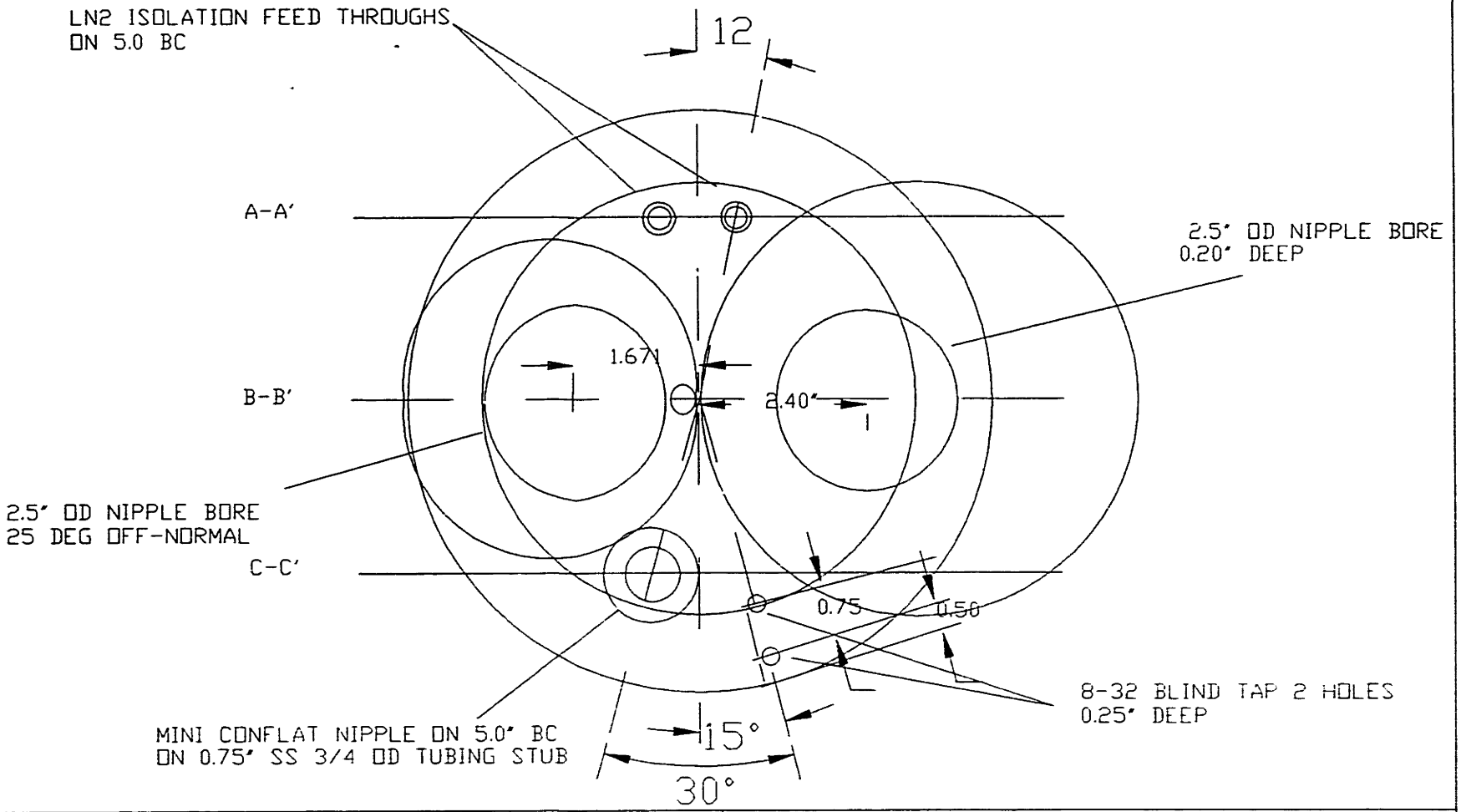

DESIGNER: D.C. GRAY

CONTRACTOR: SHARON VACUUM

COMMENTS:

REVISION 11/6/90 FINAL

DWG SCALE: 1" = 2"

QUANTITY: 1

MATERIAL: STAINLESS

2 OF 6

TOLERANCES:

X.X = ±.050

X.XX = ±.010

X.XXX = ±.002

MIT DEPT. OF CHEMICAL ENGINEERING

PART: ROTATABLE MASS SPEC FEEDTHROUGH WITH DP, BOTTOM VIEW

CODE: 3B.57 FILE NO: 3-BEAM

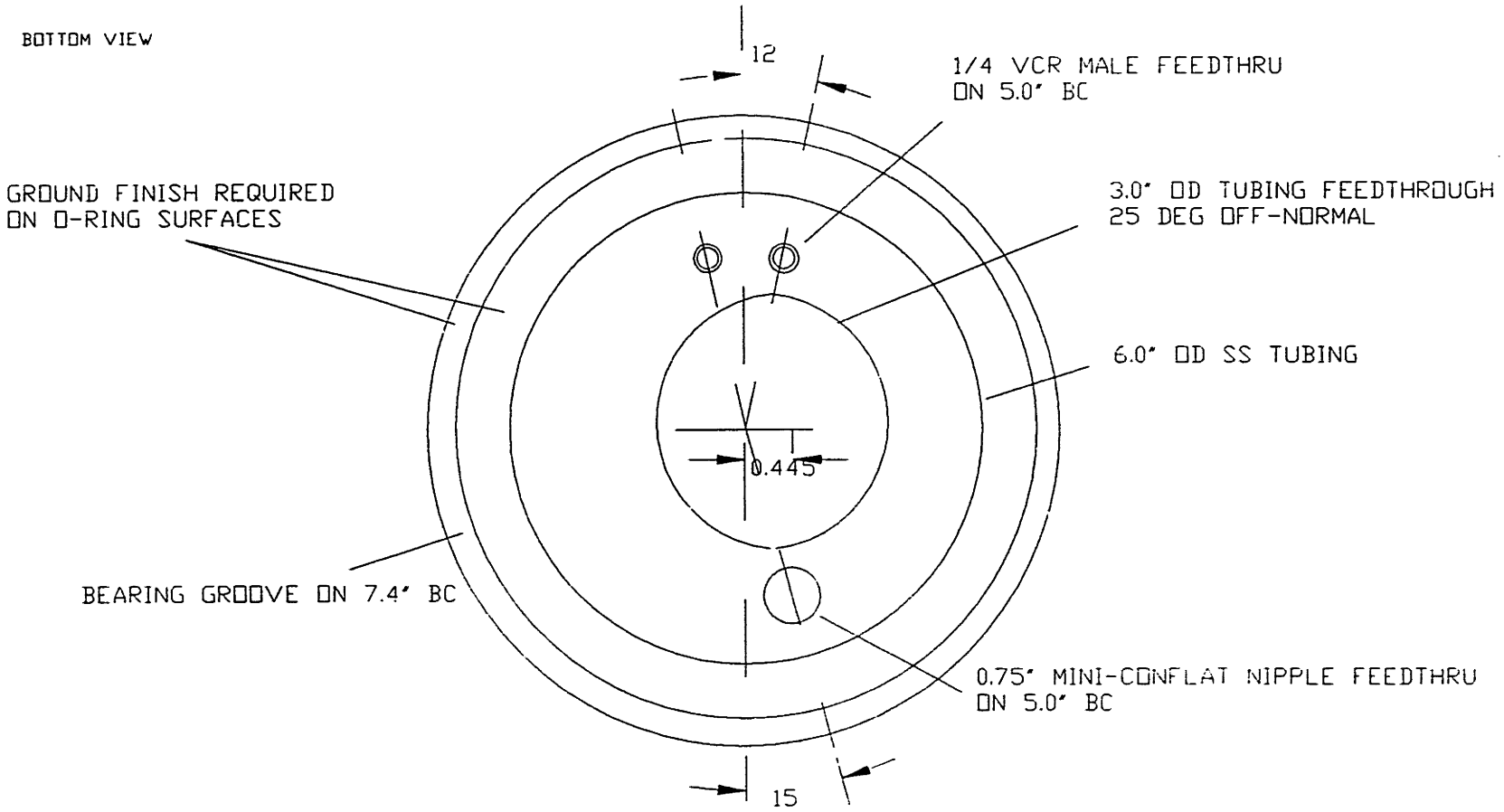

DESIGNER: D.C. GRAY
CONTRACTOR: SHARON VACUUM

COMMENTS:

REVISION 11/6/90 FINAL

DWG SCALE: 1" = 2"
QUANTITY: 1

MATERIAL: STAINLESS

3 OF 6

TOLERANCES:
X.X = ±.050
X.XX = ±.010
X.XXX = ±.002

MIT DEPT. OF CHEMICAL ENGINEERING

PART: ROTATABLE MASS SPEC FEEDTHROUGH
WITH DP, LN2 FEED DETAIL
CODE: 3B.58 FILE NO: 3-BEAM

CROSS SECTION B-B'

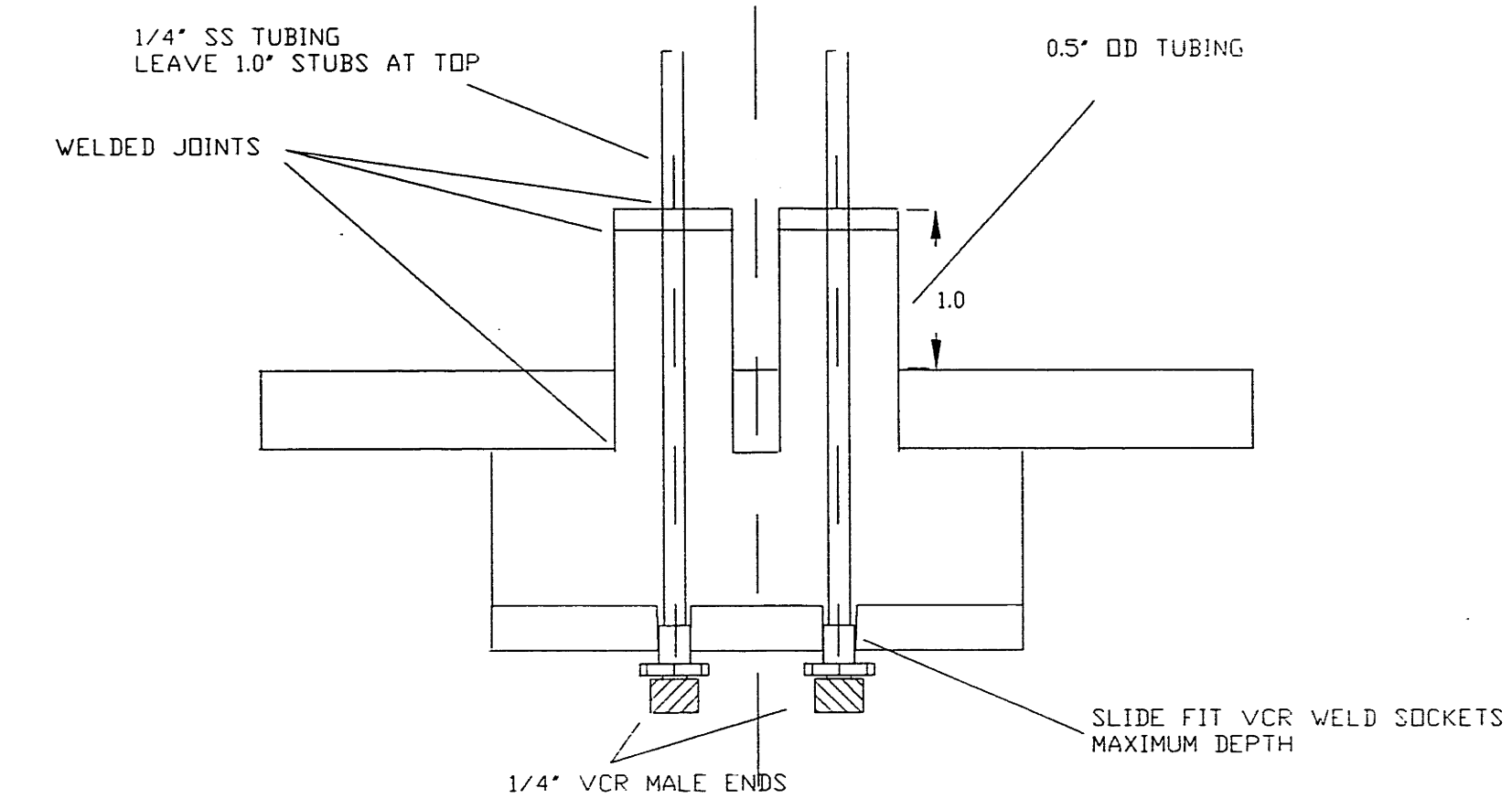

DESIGNER: D.C. GRAY
CONTRACTOR: SHARON VACUUM

COMMENTS:

REVISION 11/6/90 FINAL

DWG SCALE: 1" = 1"
QUANTITY: 1

MATERIAL: STAINLESS

4 OF 6

TOLERANCES:
X.X = ±.050
X.XX = ±.010
X.XXX = ±.002

MIT DEPT. OF CHEMICAL ENGINEERING

PART: ROTATABLE MASS SPEC FEEDTHROUGH
WITH DP, MINI FEED DETAIL
CODE: 3B.59 FILE NO: 3-BEAM

CROSS SECTION C-C'

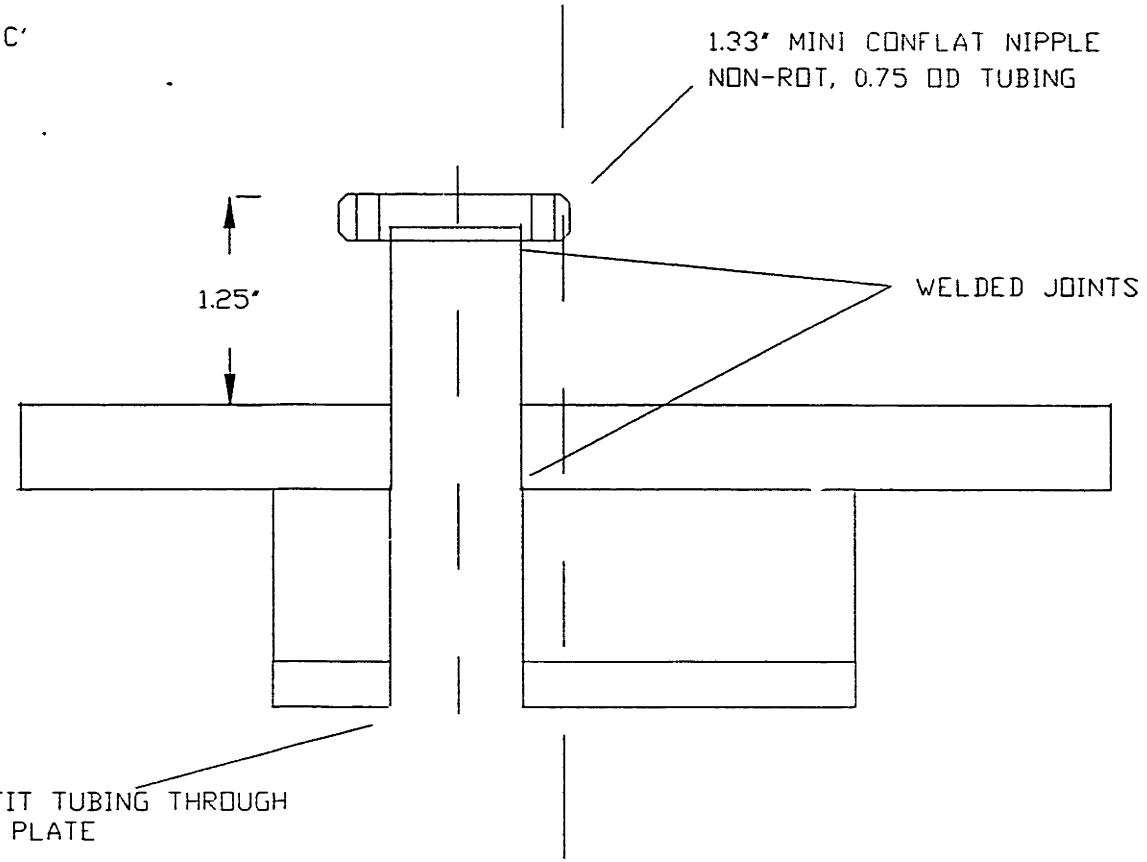

DESIGNER: D.C. GRAY
CONTRACTOR:

COMMENTS:

REVISION 11/6/90 FINAL

DWG SCALE: 1" = 1"
QUANTITY: 1

MATERIAL: STAINLESS

5 OF 6

TOLERANCES:
X.X = ±.050
X.XX = ±.010
X.XXX = ±.002

MIT DEPT. OF CHEMICAL ENGINEERING
CAMBRIDGE, MASSACHUSETTS 02139
Bldg. 66-221 METL LAB (617) 253-6587

PART: MASS SPEC CAP

CODE: 3B.60 REVISION: 6/20/91

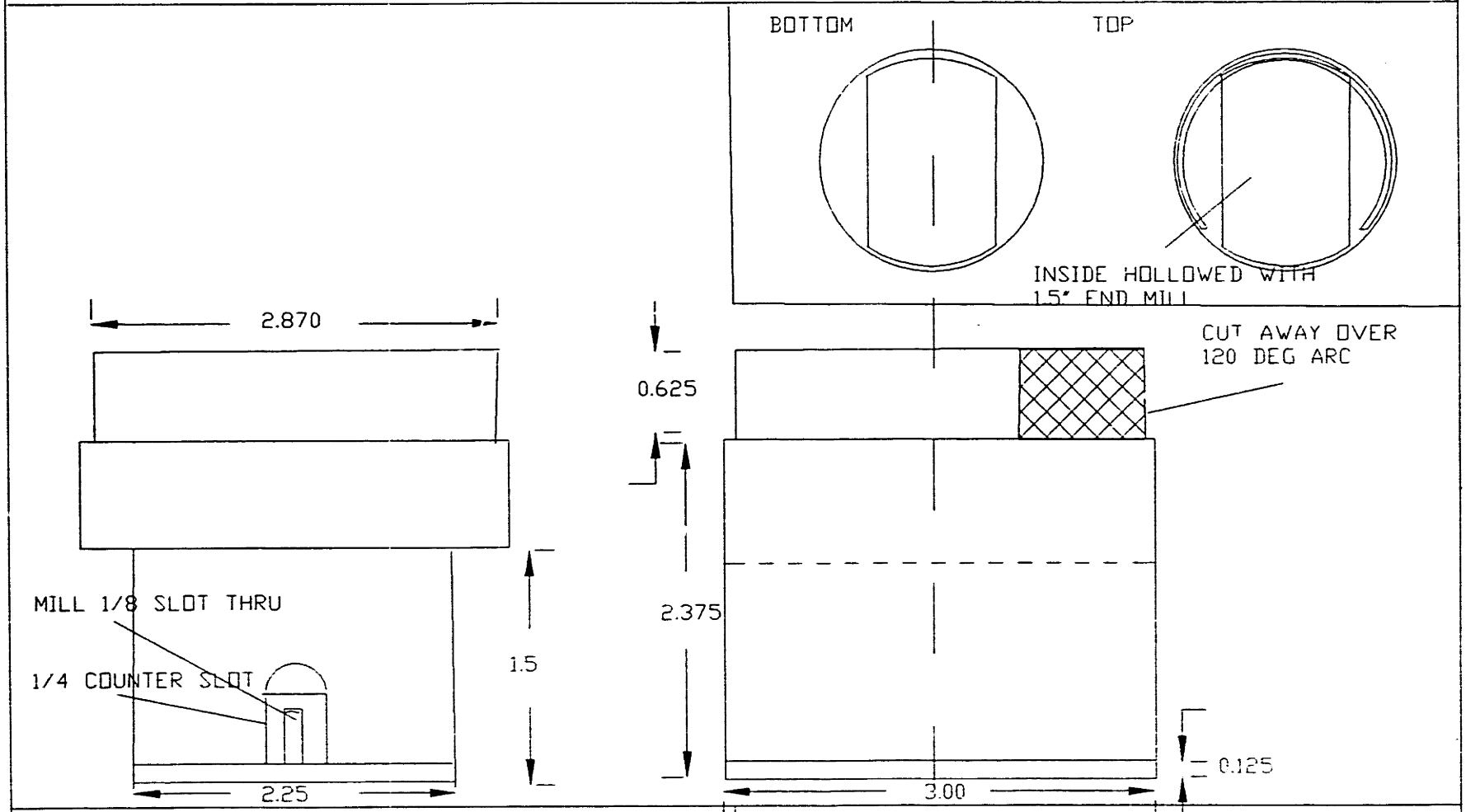

DESIGNER: D.C. GRAY
CONTRACTOR:

COMMENTS:

DWG SCALE: 1" = 1" DETAIL 2" = 1"
QUANTITY: 1 REQUIRED

MATERIAL: 6061 AL

1 OF 1

TOLERANCES:
X.X = +/- 050
X.XX = +/- 010
X.XXX = +/- 002

MIT DEPT. OF CHEMICAL ENGINEERING

PART: MASS SPEC FLANGE ADAPTER

CODE: 3B.00 FILE NO: 3-BEAM

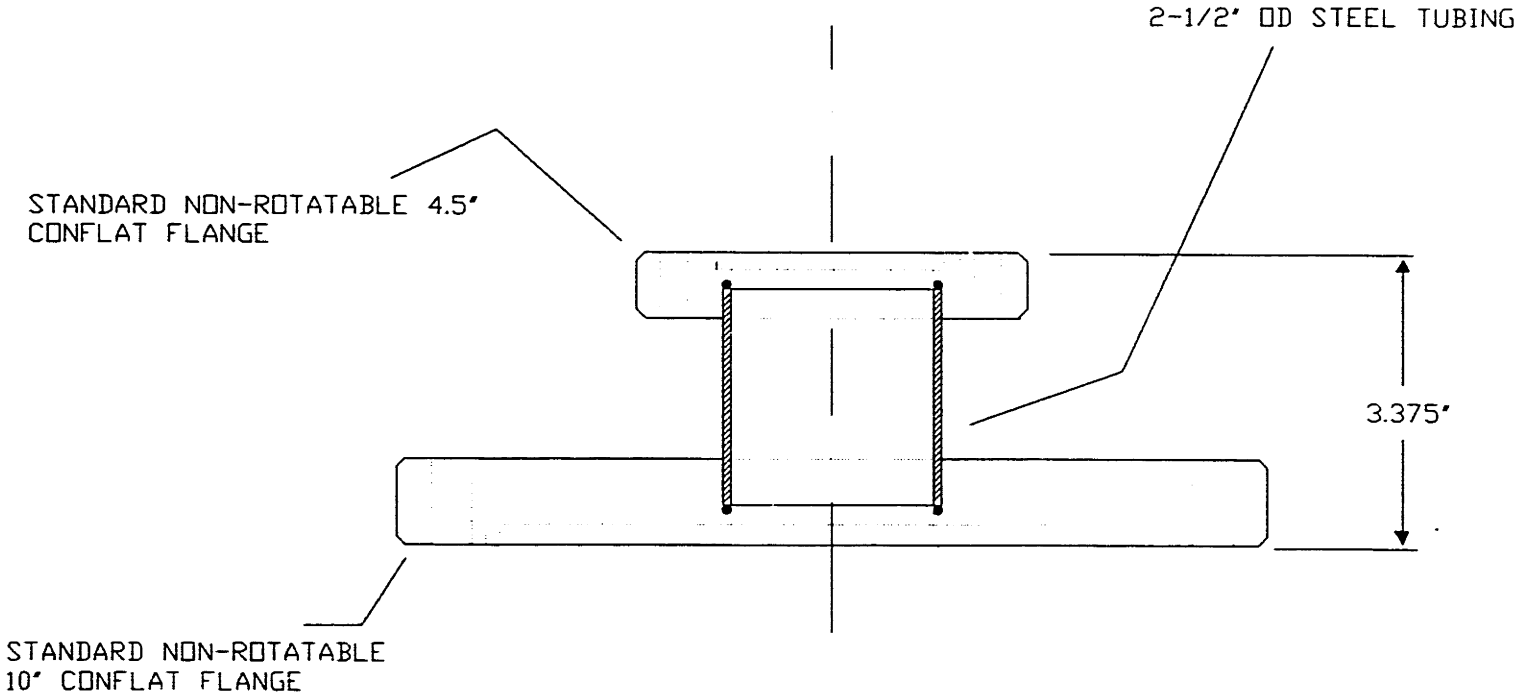

DESIGNER: D. GRAY H. SAWIN
CONTRACTOR: NOR-CAL

COMMENTS:

REVISION 4/25/89

DWG SCALE: 1" = 2"
QUANTITY: 1

MATERIAL: STAINLESS

1 OF 1

TOLERANCES:
X.X = ±.050
X.XX = ±.010
X.XXX = ±.002

MIT DEPT. OF CHEMICAL ENGINEERING

PART: FLANGE MODIFICATIONS

CODE: 3B.10 FILE NO: 3-BEAM

BOTTOM VIEW (VACUUM SIDE)

PORT ASSIGNMENTS:

1. FARADAY CUP ELECTRICAL 10 PIN
2. FARADAY CUP ASSEMBLY
3. SAMPLE MOUNT ELECTRICAL (IC PIN)
4. MISC. ELECTRICAL
5. IMPACT TUBE ASSEMBLY
6. MOTORS/ PHOTODIODES 10 PIN ELECTRICAL

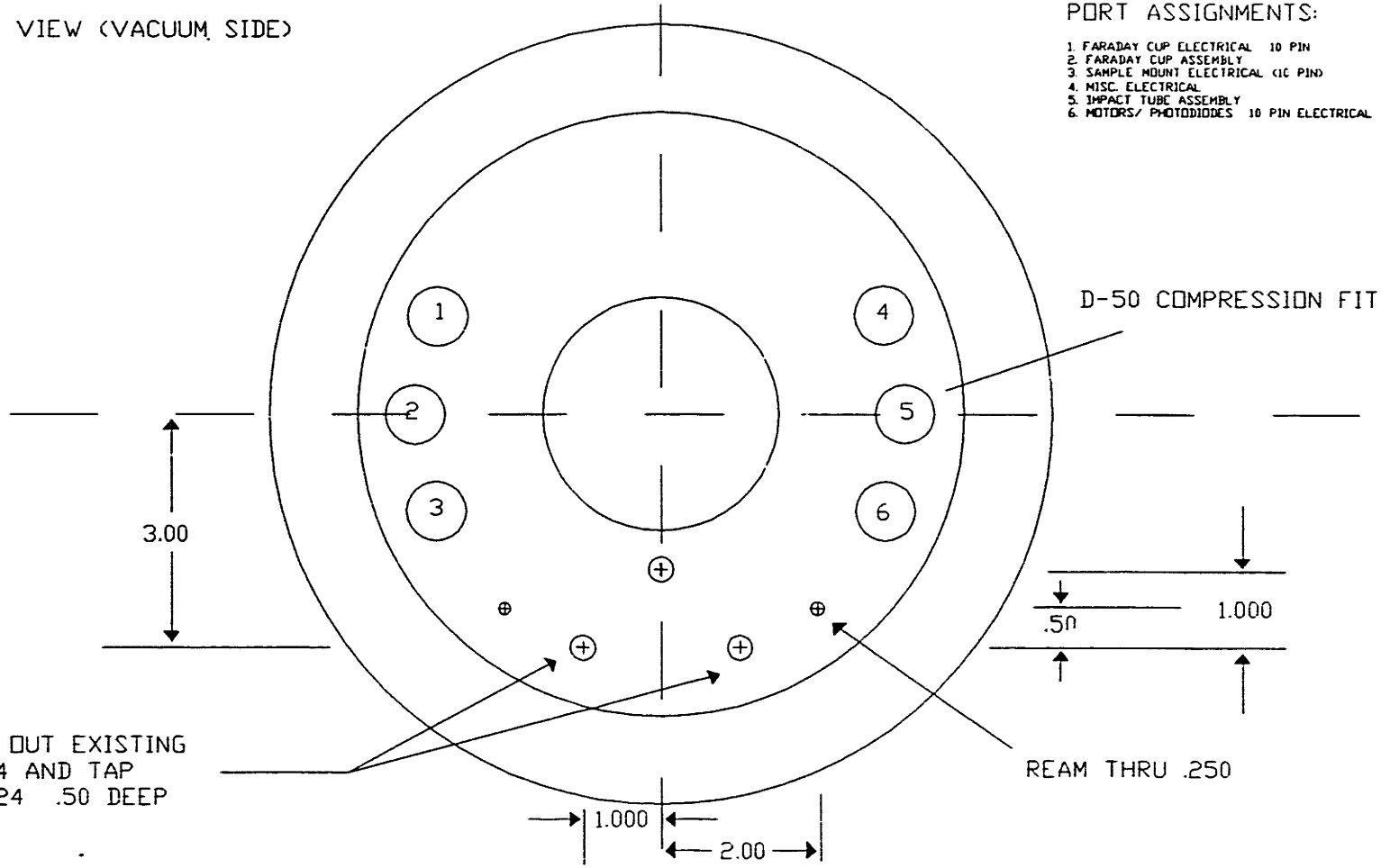

DESIGNER: D. GRAY H.SAWIN

CONTRACTOR: LNS MACHINE SHOP

COMMENTS: .250 STEEL TUBING SHOULD PRESS FIT IN REAMED HOLES FOR WELDING

REVISION 4/25/89

DWG SCALE: 1" = 2"

QUANTITY: 1

MATERIAL: EXISTING 10" CONFLAT

1 OF 1

TOLERANCES:

X.X = ±.050
X.XX = ±.010
X.XXX = ±.001

MIT DEPT. OF CHEMICAL ENGINEERING
CAMBRIDGE, MASSACHUSETTS 02139
Bldg. 66-219, (617) 253-6587

PART: 3/8 TFE SLIDE SEAL
SS-8-UT-A-12 ULTRATORR MODIFICATIONS
CODE: 3B.26 REVISION: 1/22/90

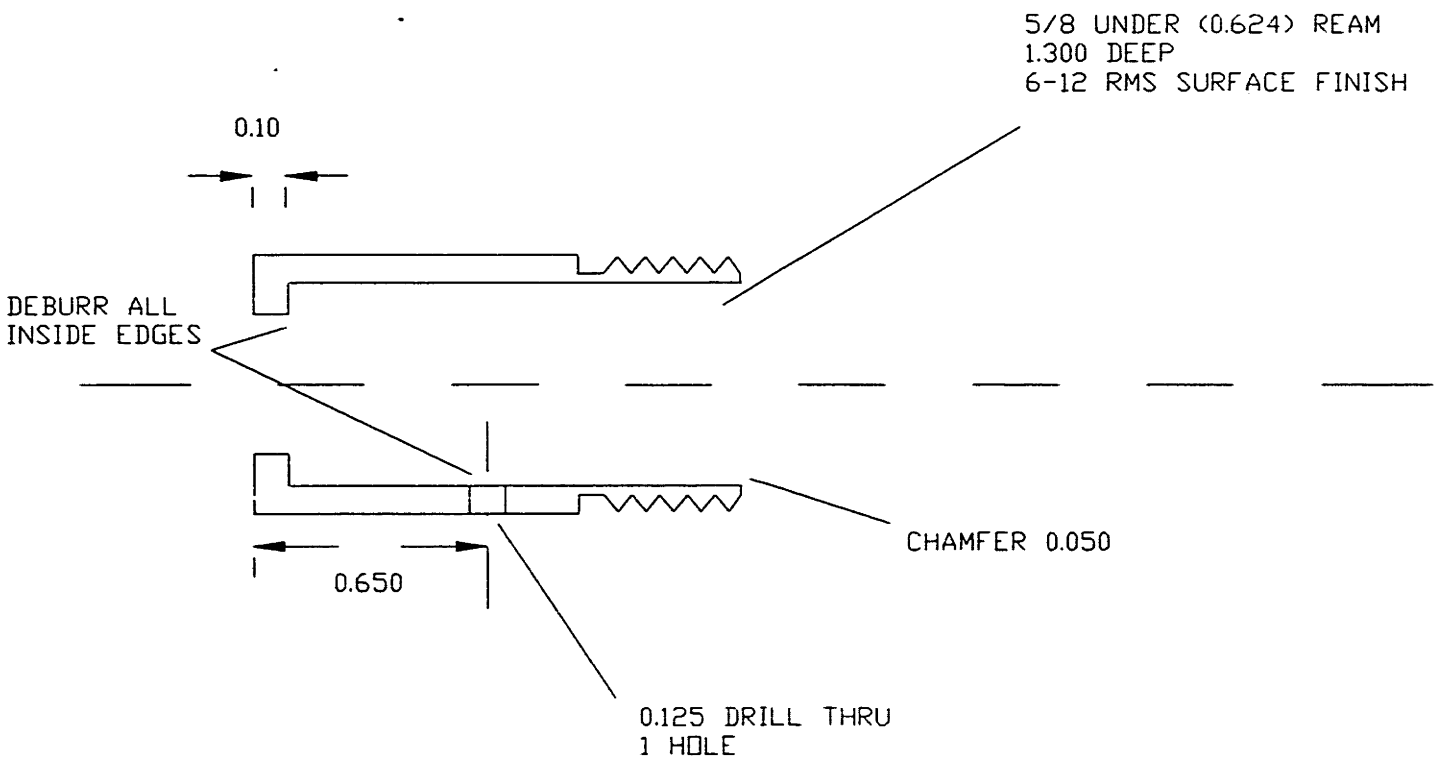

NOTE: HOLD ALL TOLERANCES
SURFACE FINISH IS CRITICAL

DESIGNER: D.C. GRAY
CONTRACTOR: NOR-CAL

COMMENTS: INSIDE SURFACE MUST BE FREE OF BURRS TO FORM VACUUM SEAL

DWG SCALE: 2" = 1"
QUANTITY: 1 REQUIRED

MATERIAL: ULTRA-TORR
SS-8-UT-A-12

1 OF 1

TOLERANCES:
X.X = +/-.050
X.XX = +/-.010
X.XXX = +/-.002

MIT DEPT. OF CHEMICAL ENGINEERING
CAMBRIDGE, MASSACHUSETTS 02139
Bldg. 66-219, (617) 253-6587

PART: 3/8" TFE SLIDE SEAL RETAINER RINGS
CODE: 3B.27 REVISION: 1/22/90

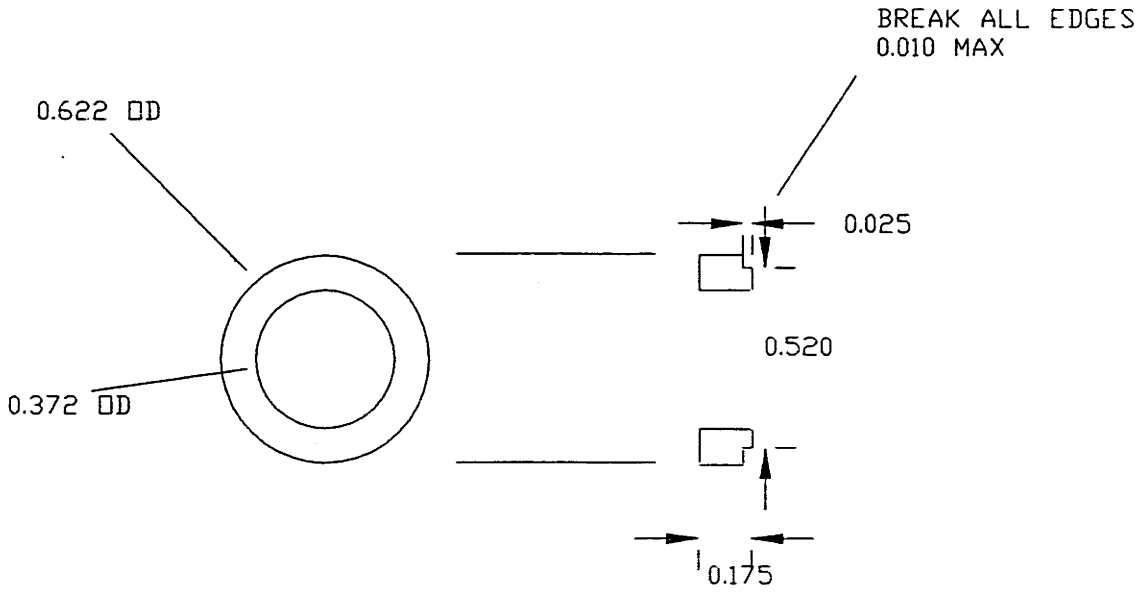

DESIGNER: D.C. GRAY
CONTRACTOR: NOR-CAL

COMMENTS: EDGES MUST BE DEBURRED AND FINISHED

DWG SCALE: 2" = 1"
QUANTITY: 2 REQUIRED

MATERIAL: 6061 ALUMINUM ROD STOCK

1 OF 1

TOLERANCES:
X.X = +/-.050
X.XX = +/-.010
X.XXX = +/-.002

MIT DEPT. OF CHEMICAL ENGINEERING
CAMBRIDGE, MASSACHUSETTS 02139
Blg. 66-219, (617) 253-6587

PART: 5/8" TFE SLIDE SEAL
SS-12-UT-A-16 MODIFICATIONS
CODE: 3B.29 REVISION: 1/22/90

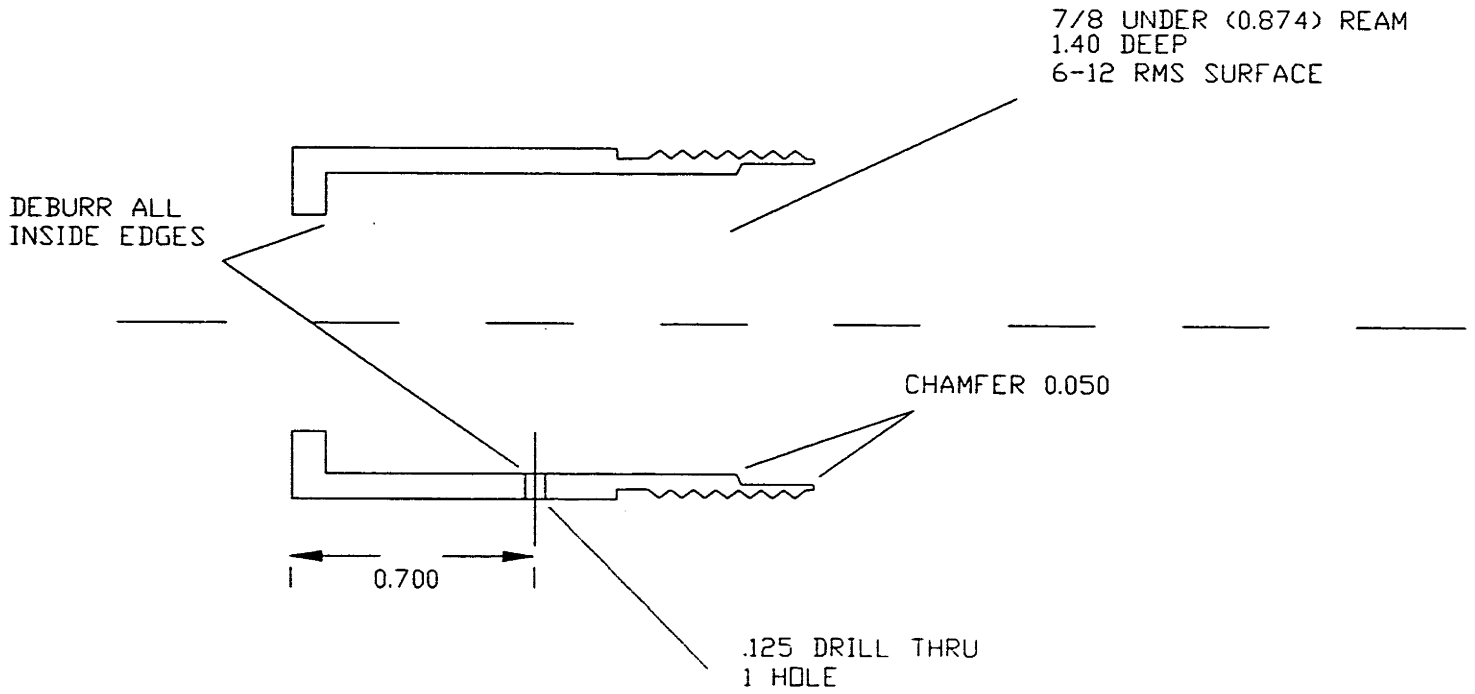

DESIGNER: D.C. GRAY
CONTRACTOR: NOR-CAL

COMMENTS: INSIDE SURFACE MUST BE FREE OF BURRS TO FORM VACUUM SEAL

DWG SCALE: 2" = 1"
QUANTITY: 1 REQUIRED

MATERIAL: SS-12-UT-A-16
ULTRA-TORR FITTING

1 OF 1

TOLERANCES:
X.X = +/- .050
X.XX = +/- .015
X.XXX = +/- .002

MIT DEPT. OF CHEMICAL ENGINEERING
CAMBRIDGE, MASSACHUSETTS 02139
Blg. 66-219, (617) 253-6587

PART: 5/8" TFE SLIDE SEAL RETAINER RINGS
CODE: 3B.30 REVISION: 12/5/89

BREAK ALL EDGES
0.010 MAX

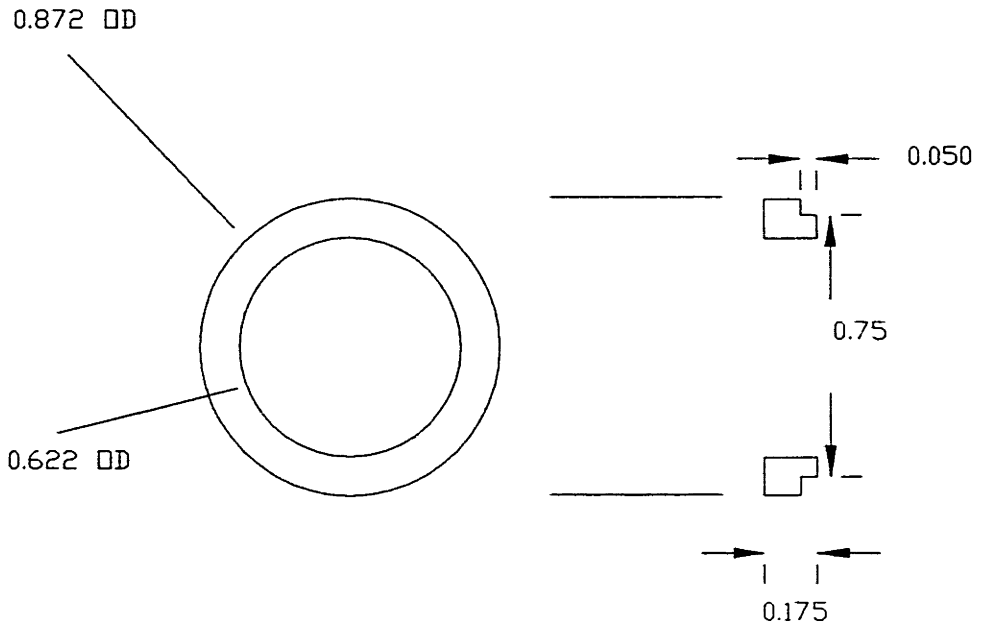

DESIGNER: D.C. GRAY
CONTRACTOR: NOR-CAL

COMMENTS:

DWG SCALE: 2" = 1"
QUANTITY: 2 REQUIRED

MATERIAL: 6061 ALUMINUM ROD STOCK

1 OF 1

TOLERANCES:
X.X = +/- 050
X.XX = +/- 010
X.XXX = +/- 002

MIT DEPT. OF CHEMICAL ENGINEERING
CAMBRIDGE, MASSACHUSETTS 02139
Bldg. 66-219, (617) 253-6587

PART: UP-TO-AIR FLANGE

CODE: 3B.32 REVISION: 5/10/89

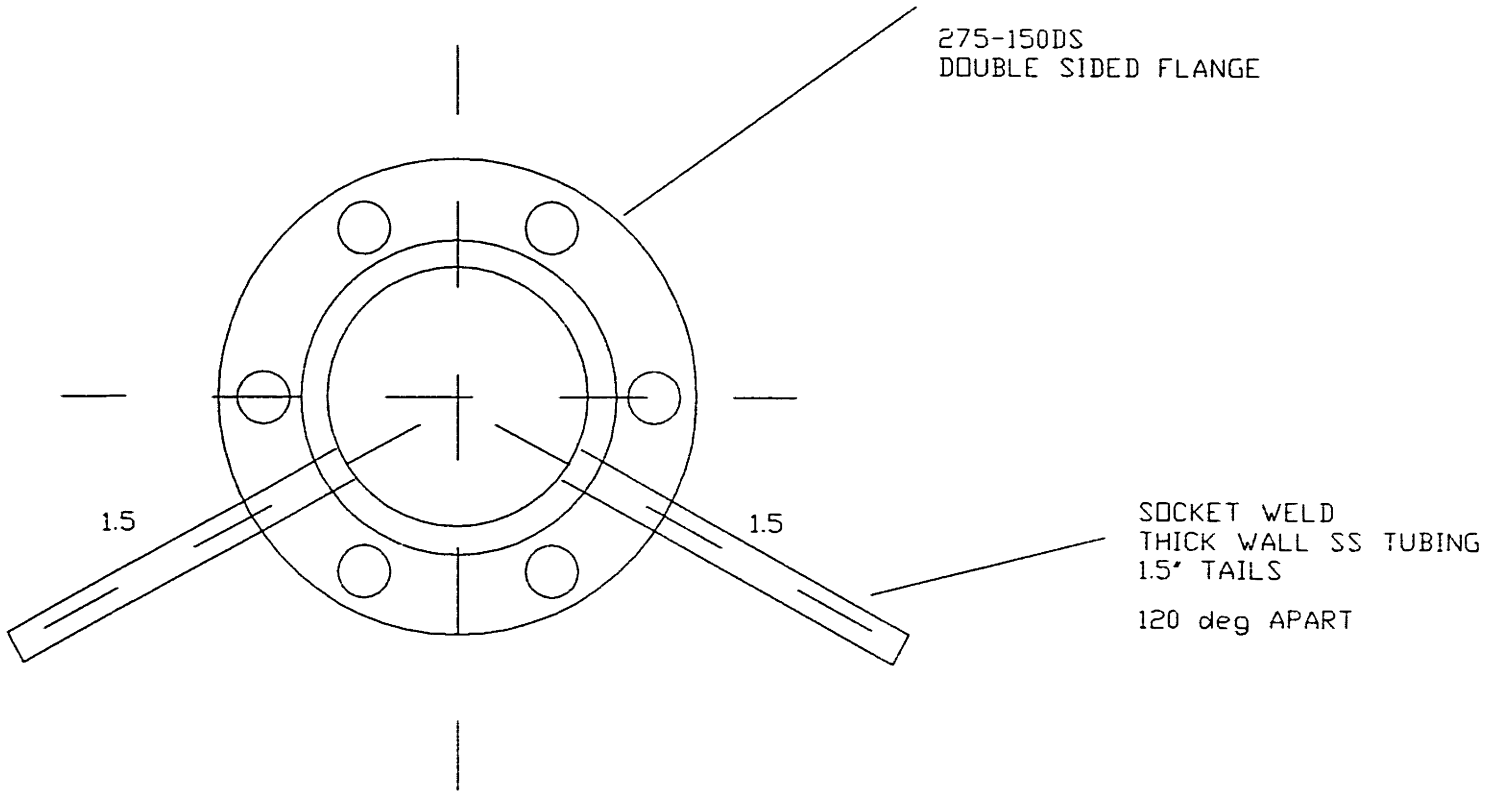

DESIGNER: D.C. GRAY
CONTRACTOR: NOR-CAL

COMMENTS:

DWG SCALE: 1" = 1"
QUANTITY: 1 REQUIRED

MATERIAL: 2.75 CONFLAT DOUBLE SIDED

1 OF 1

TOLERANCES:
XX = +/- .050
XXX = +/- .010
XXXX = +/- .002

MIT DEPT. OF CHEMICAL ENGINEERING
CAMBRIDGE, MASSACHUSETTS 02139
Bldg. 66-219, (617) 253-6587

PART: WELDED BELLOWS ADAPTER

CODE: 3B.33 REVISION: 5/16/89

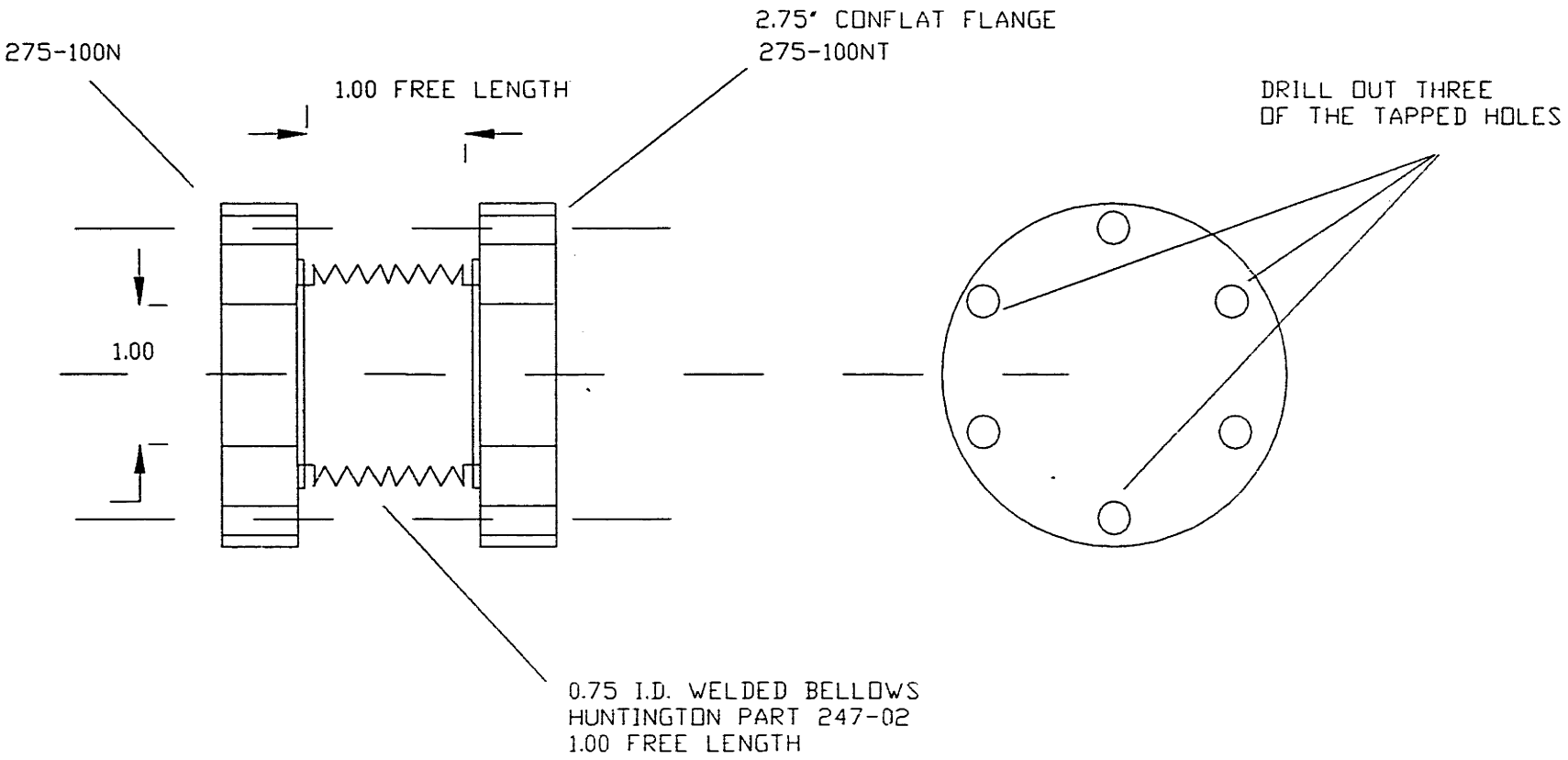

DESIGNER: D.C. GRAY
CONTRACTOR: NOR-CAL

COMMENTS:

DWG SCALE: 1" = 1"
QUANTITY: 1 REQUIRED

MATERIAL: STOCK ITEMS

1 OF 1

TOLERANCES:
X.X = +/-.050
X.XX = +/-.010
X.XXX = +/-.002

MIT DEPT. OF CHEMICAL ENGINEERING
CAMBRIDGE, MASSACHUSETTS 02139
Bldg. 66-219, (617) 253-6587

PART: 3/8" WOBBLE ROD

CODE: 3B.34 REVISION: 1/22/90

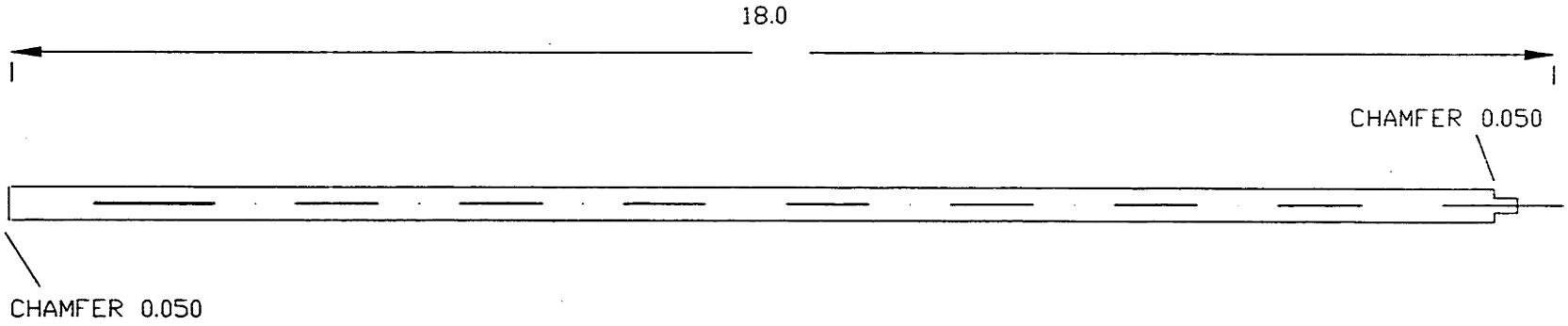

END DETAIL

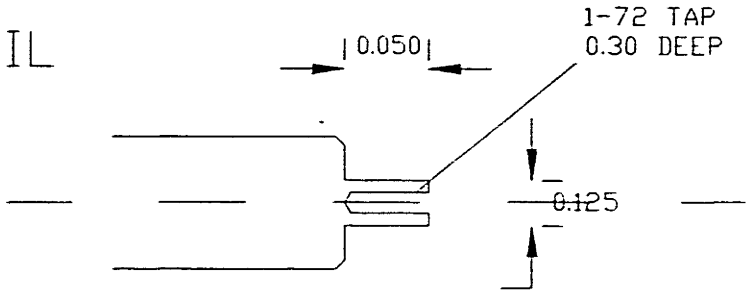

DESIGNER: D.C. GRAY
CONTRACTOR: NOR-CAL
BOSTON CENTERLESS INC
COMMENTS:

DWG SCALE: 1"=2" DETAIL 2" = 1"
QUANTITY: 1 REQUIRED

MATERIAL: 0.370 ACCUROD STOCK
PRECISION GROUND SS

1 OF 1

TOLERANCES:
X.X = +/-.050
X.XX = +/-.010
X.XXX = +/-.002

MIT DEPT. OF CHEMICAL ENGINEERING
CAMBRIDGE, MASSACHUSETTS 02139
Bldg. 66-219, (617) 253-6587

PART: 3/8 SLIDE SEAL ASSEMBLY

CODE: 3B.35 REVISION: 12/5/89

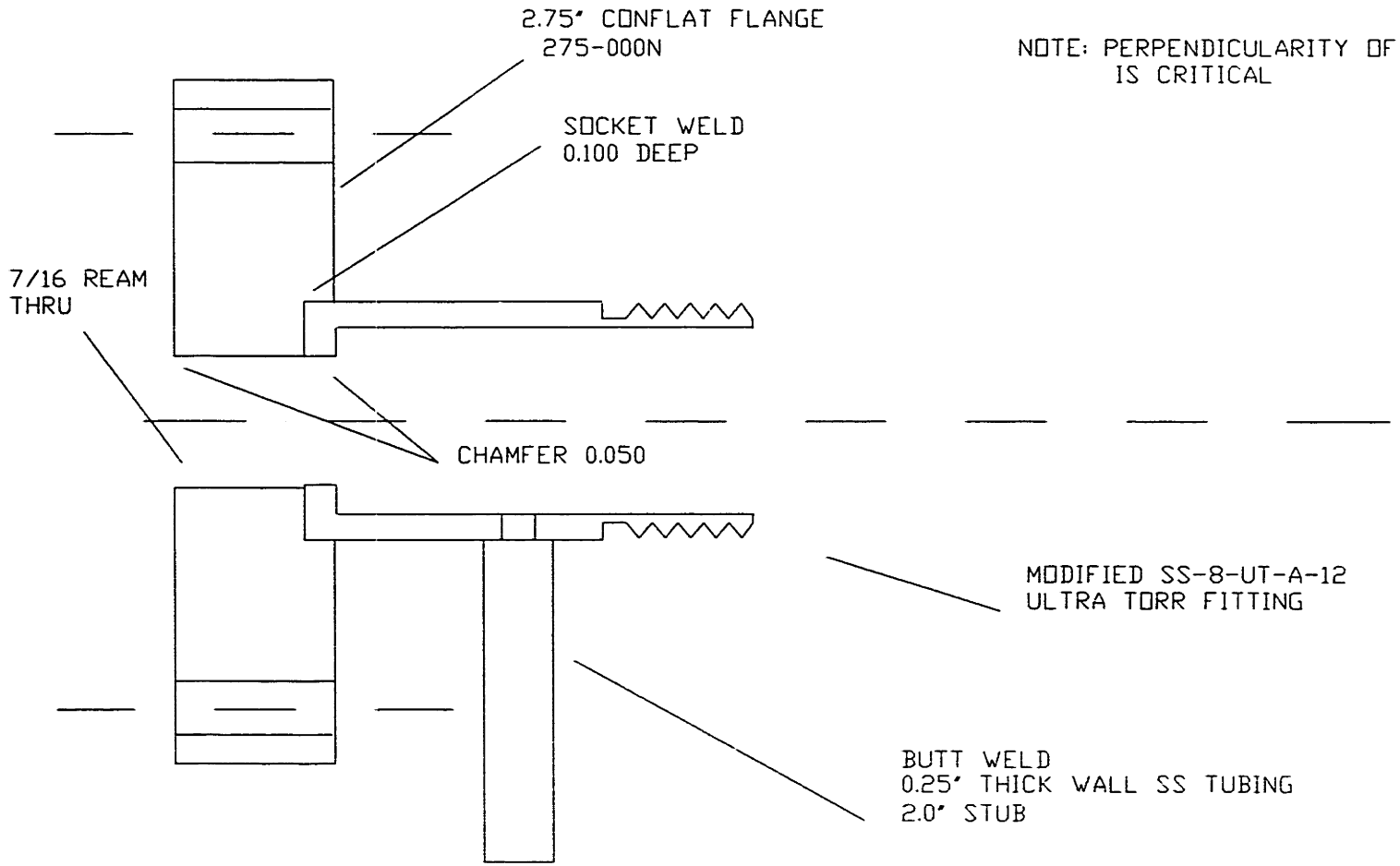

NOTE: PERPENDICULARITY OF WELD IS CRITICAL

DESIGNER: D.C. GRAY
CONTRACTOR: NOR-CAL

COMMENTS:

DWG SCALE: 2" = 1"
QUANTITY: 1 REQUIRED

MATERIAL: ULTRA-TORR
SS-8-UT-A-12

1 OF 1

TOLERANCES:
XX = +/-.050
X.XX = +/-.010
X.XXX = +/-.002

MIT DEPT. OF CHEMICAL ENGINEERING
CAMBRIDGE, MASSACHUSETTS 02139
Bldg. 66-219, (617) 253-6587

PART: 5/8" SLIDE SEAL ASSEMBLY

CODE: 3B.36 REVISION: 12/5/89

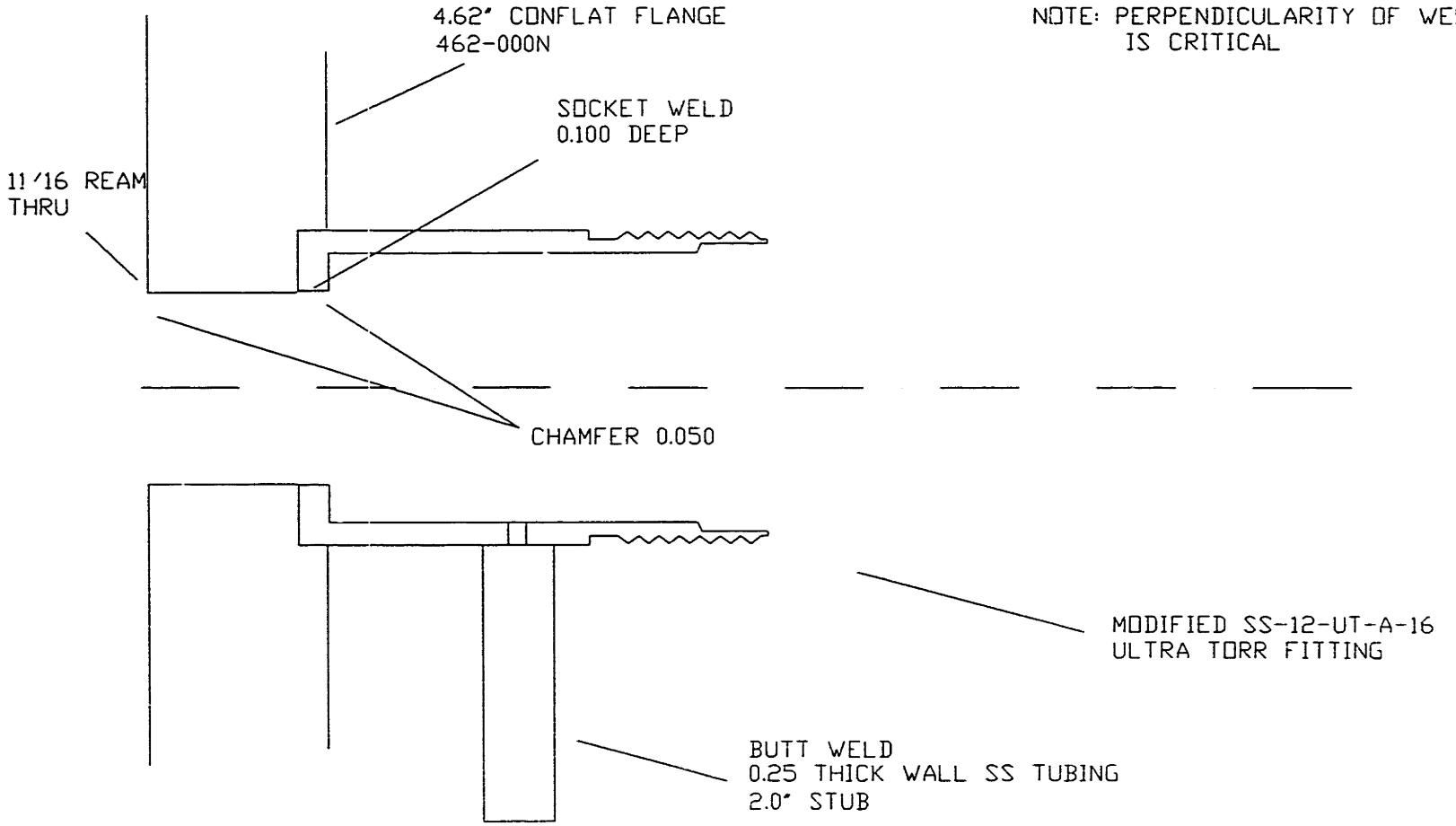

NOTE: PERPENDICULARITY OF WELD IS CRITICAL

DESIGNER: D.C. GRAY
CONTRACTOR: NOR-CAL

COMMENTS:

DWG SCALE: 2" = 1"
QUANTITY: 1 REQUIRED

MATERIAL: SS-12-UT-A-16
ULTRA-TORR FITTING

1 OF 1

TOLERANCES:
X.X = +/-.050
X.XX = +/-.010
X.XXX = +/-.002

MIT DEPT. OF CHEMICAL ENGINEERING
CAMBRIDGE, MASSACHUSETTS 02139
Bldg. 66-219, (617) 253-6587

PART: 5/8" SLIDE SEAL ASSEMBLY

CODE: 3B.36B REVISION: 12/5/89

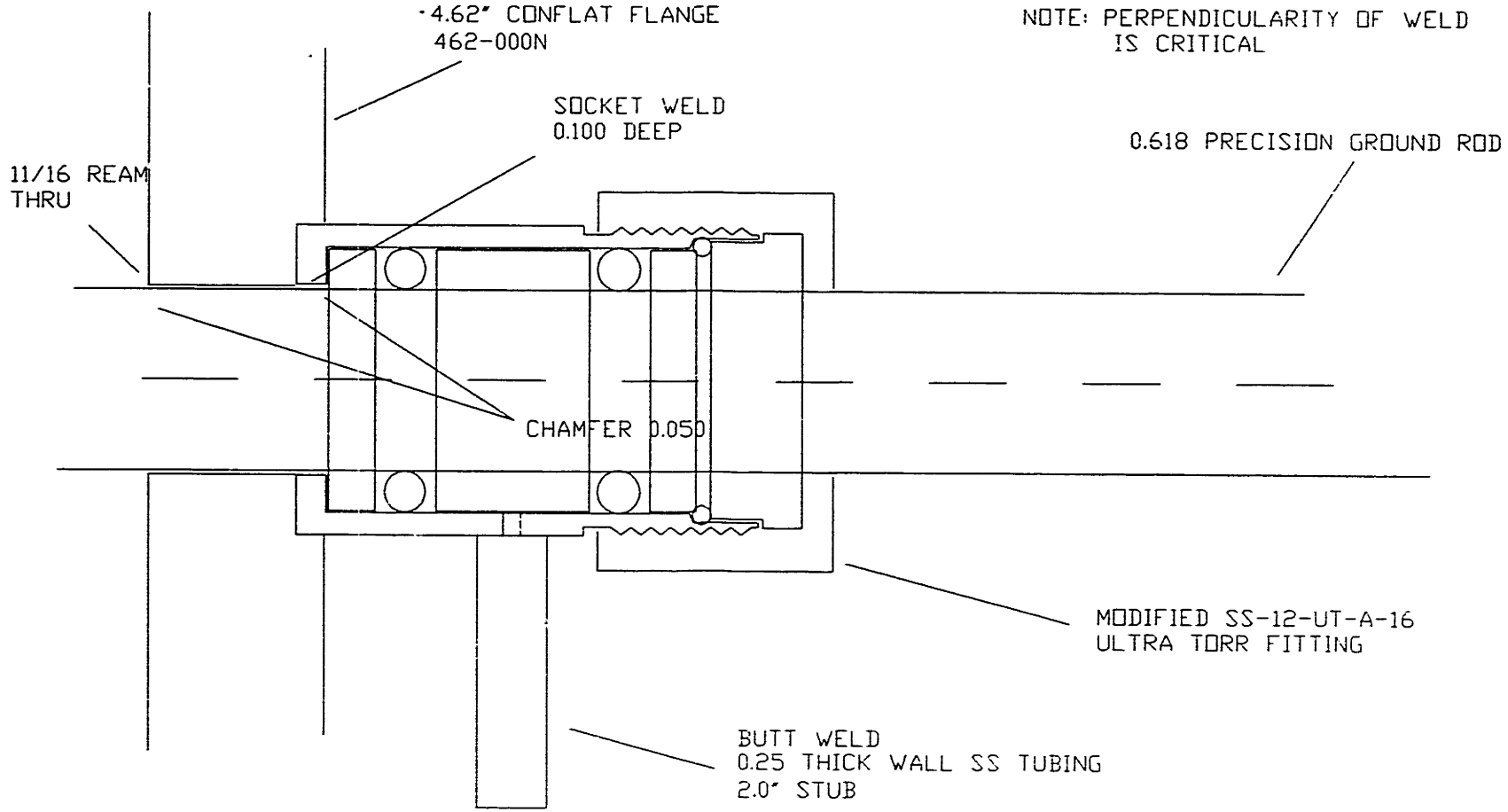

DESIGNER: D.C. GRAY
CONTRACTOR: NOR-CAL

COMMENTS:

DWG SCALE: 2" = 1"
QUANTITY: 1 REQUIRED

MATERIAL: SS-12-UT-A-16
ULTRA-TORR FITTING

1 OF 1

TOLERANCES:
XX = +/-.050
XXX = +/-.010
XXXX = +/-.002

MIT DEPT. OF CHEMICAL ENGINEERING CAMBRIDGE, MASSACHUSETTS 02139 Bldg. 66-219, (617) 253-6587	PART: 5/8" SLIDE ROD CODE: 3B.37 REVISION: 1/22/90

420

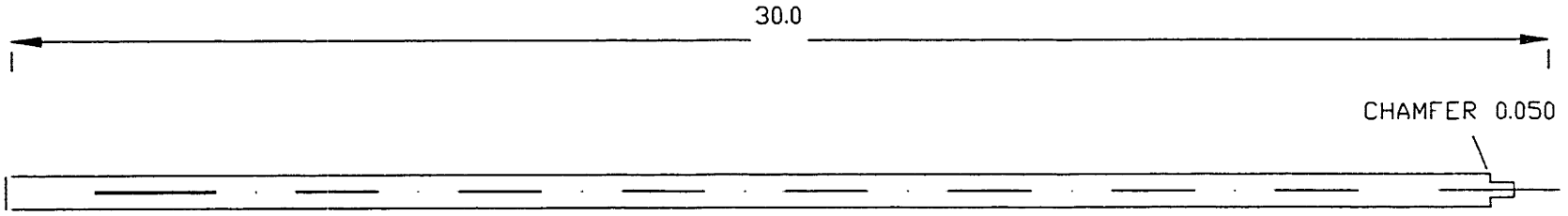

END DETAIL

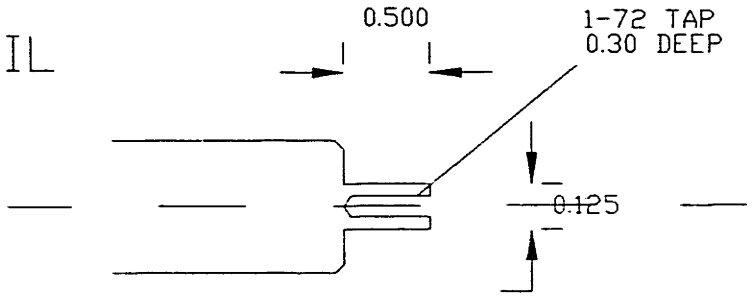

DESIGNER: D.C. GRAY CONTRACTOR: NOR-CAL BOSTON CENTERLESS INC COMMENTS:	DWG SCALE: 1"=2" DETAIL 2" = 1" QUANTITY: 1 REQUIRED MATERIAL: 0.618 ACCUROD STOCK PRECISON GROUND SS	1 OF 1 TOLERANCES: X.X = +/-.050 X.XX = +/-.010 X.XXX = +/-.002

MIT DEPT. OF CHEMICAL ENGINEERING
CAMBRIDGE, MASSACHUSETTS 02139
Bldg. 66-221 METL LAB (617) 253-6587

PART: 3-BEAM SAMPLE PUSHROD

CODE: 3B.37B REVISION: 1/92

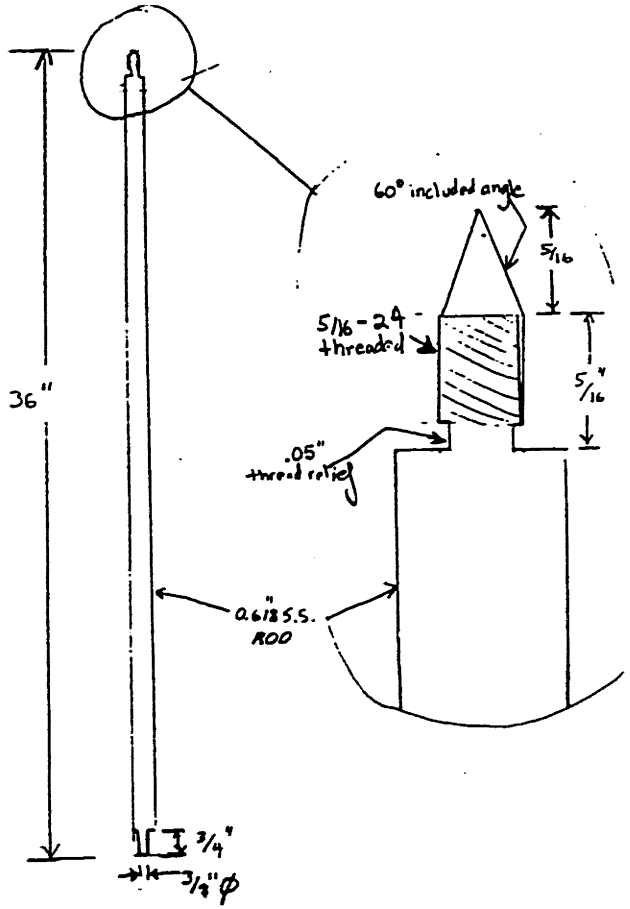

DESIGNER: D.C. GRAY
CONTRACTOR: BOSTON CENTERLESS

COMMENTS:

DWG SCALE
QUANTITY
MATERIAL

MIT DEPT. OF CHEMICAL ENGINEERING CAMBRIDGE, MASSACHUSETTS 02139 Bldg. 66-221 METL LAB (617) 253-6587	PART: PUSHROD RETAINING COLLAR CODE: 3B.37C REVISION: 1/90

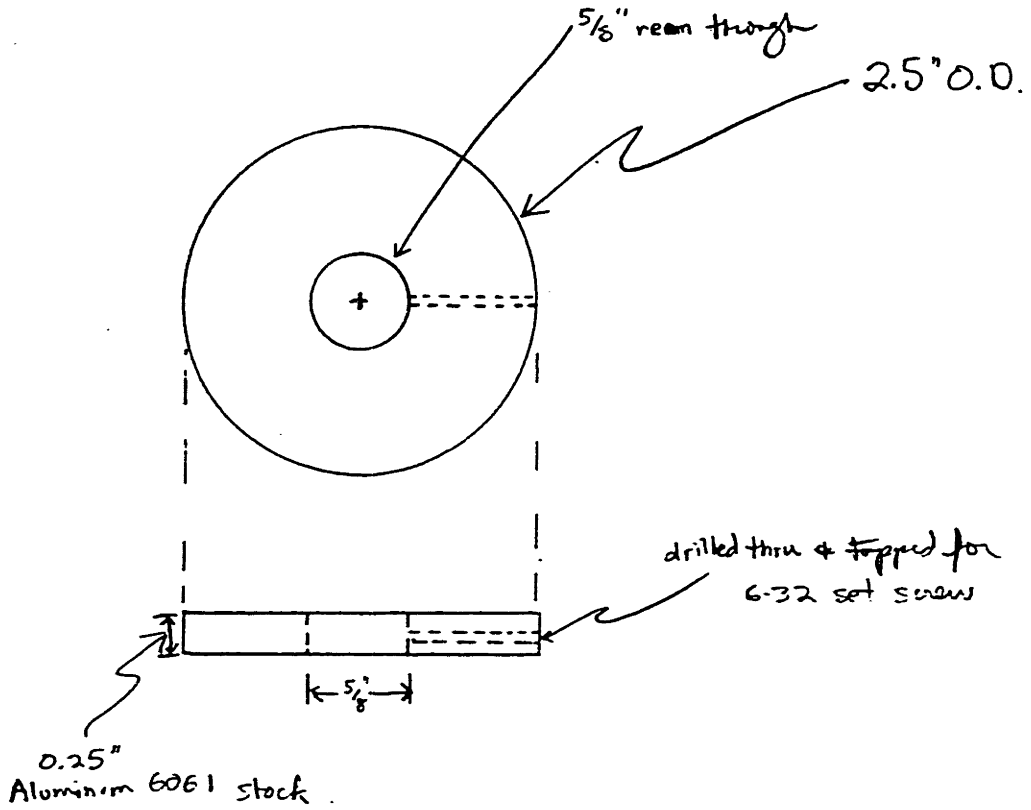

DESIGNER: D.C. GRAY CONTRACTOR: COMMENTS	DWG SCALE: QUANTITY: MATERIAL 6061 Al

MIT DEPT. OF CHEMICAL ENGINEERING
CAMBRIDGE, MASSACHUSETTS 02139
Bldg. 66-219, (617) 253-6587

PART: 3/8" TFE SLIDE SEAL
DOUBLE SEAL GLAND RING
CODE: 3B.40 REVISION: 1/22/90

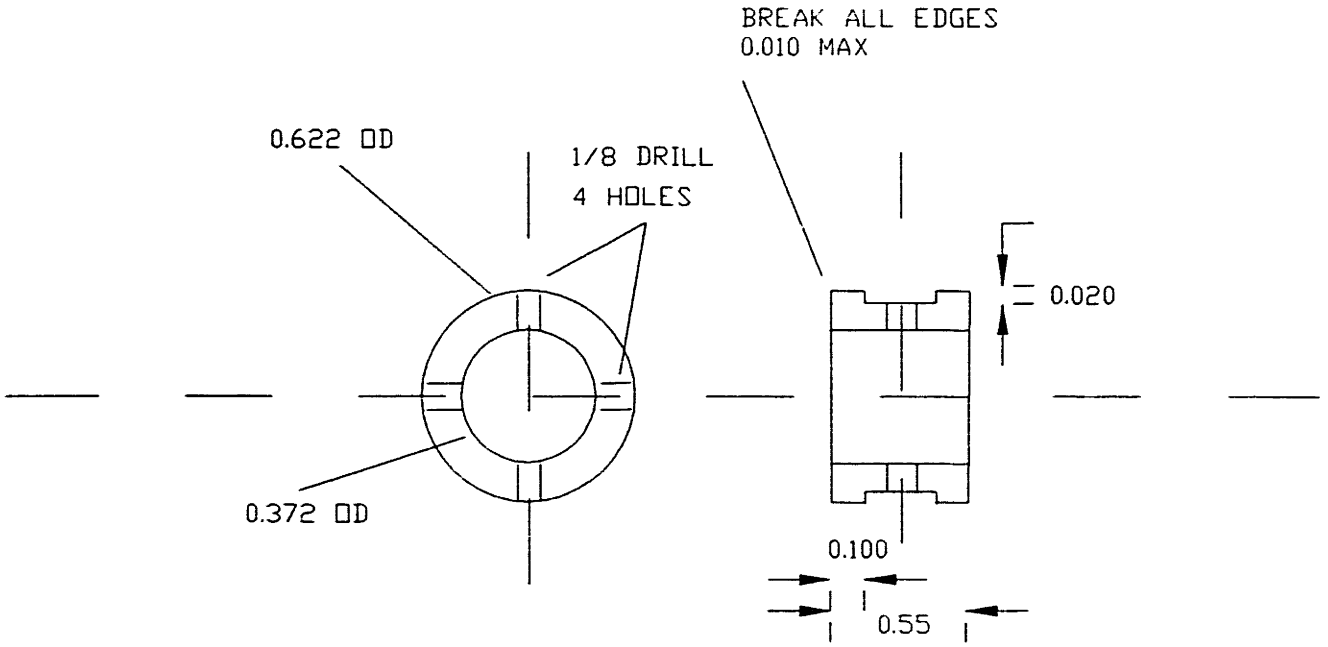

DESIGNER: D.C. GRAY
CONTRACTOR: NOR-CAL

COMMENTS: EDGES MUST BE DEBURRED AND FINISHED

DWG SCALE: 2" = 1"
QUANTITY: 1 REQUIRED

MATERIAL 6061 ALUMINUM ROD STOCK

1 OF 1

TOLERANCES:
X.X = +/- 050
X.XX = +/- 010
X.XXX = +/- 002

MIT DEPT. OF CHEMICAL ENGINEERING
CAMBRIDGE, MASSACHUSETTS 02139
Bldg. 66-219, (617) 253-6587

PART: 5/8" TFE SLIDE SEAL
DOUBLE SEAL GALND RING

CODE: 3B.41 REVISION: 1/22/90

BREAK ALL EDGES
0.010 MAX

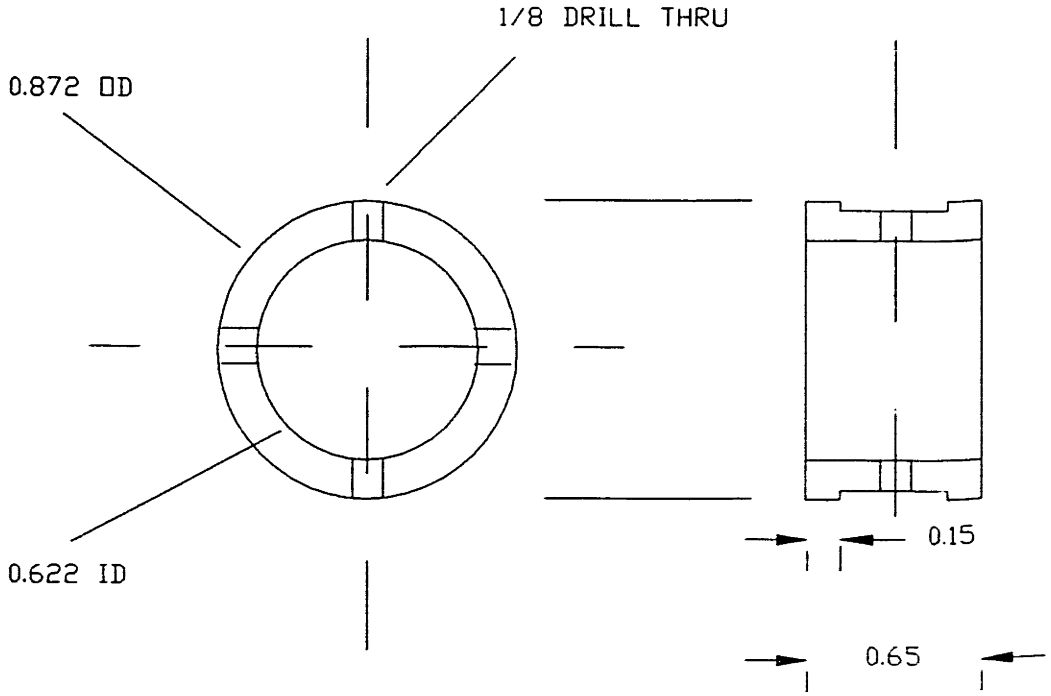

DESIGNER: D.C. GRAY
CONTRACTOR: NOR-CAL

COMMENTS: EDGES MUST BE DEBURRED AND FINISHED

DWG SCALE: 2" = 1"
QUANTITY: 1 REQUIRED

MATERIAL: 6061 ALUMINUM ROD STOCK

1 OF 1

TOLERANCES:
X.X = +/-.050
X.XX = +/-.010
X.XXX = +/-.002

MIT DEPT. OF CHEMICAL ENGINEERING
CAMBRIDGE, MASSACHUSETTS 02139
Bldg. 66-219, (617) 253-6587

PART: PUSHROD ADAPTER

CODE: 3B.42 REVISION: 1/16/90

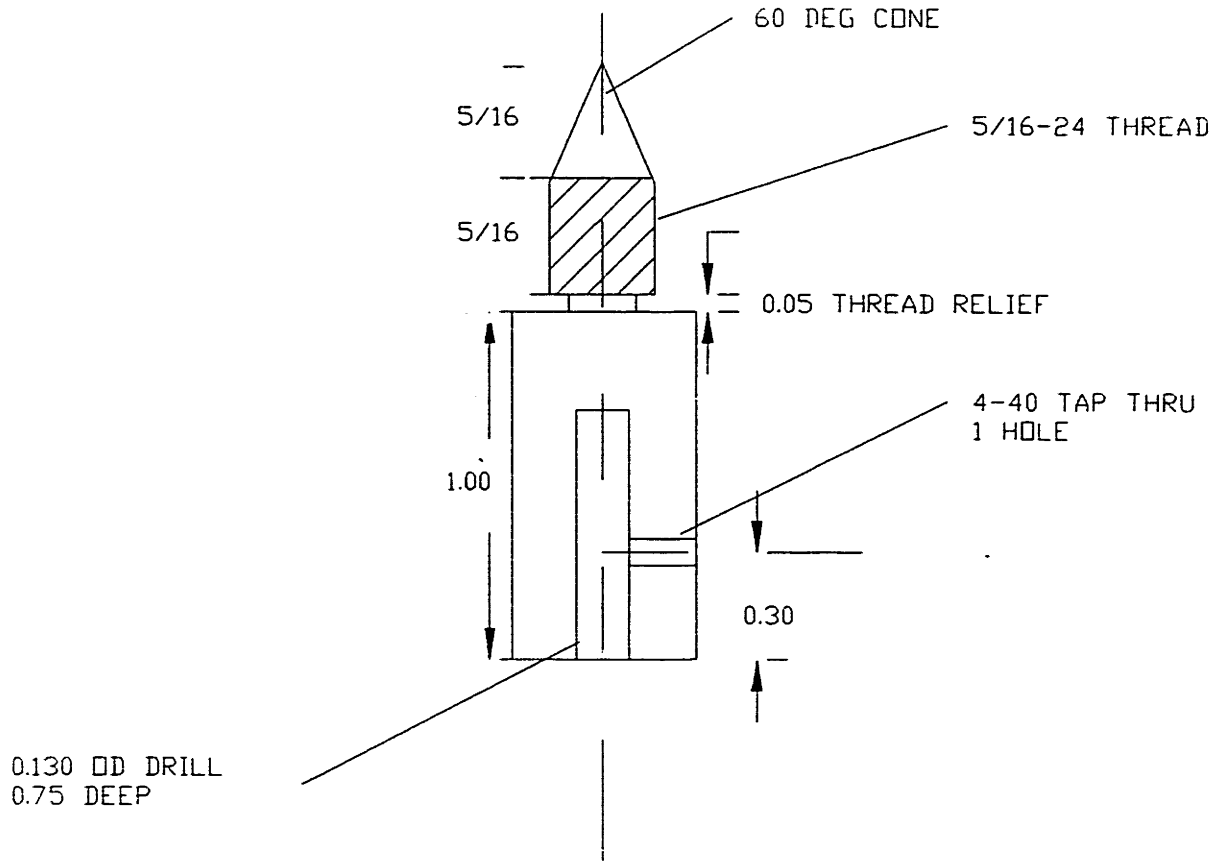

DESIGNER: D.C. GRAY
CONTRACTOR: CHEM ENG SHOP

COMMENTS:

DWG SCALE: 1" = 1"
QUANTITY: 1 REQUIRED

MATERIAL: 5/8 DD ROD STOCK
STAINLESS STEEL

1 OF 1

TOLERANCES:
X.X = +/-.050
X.XX = +/-.010
X.XXX = +/-.002

MIT DEPT. OF CHEMICAL ENGINEERING
CAMBRIDGE, MASSACHUSETTS 02139
Bldg. 66-219, (617) 253-6587

PART: 5/8 ROD RETAINER

CODE: 3B.43 REVISION: 1/22/90

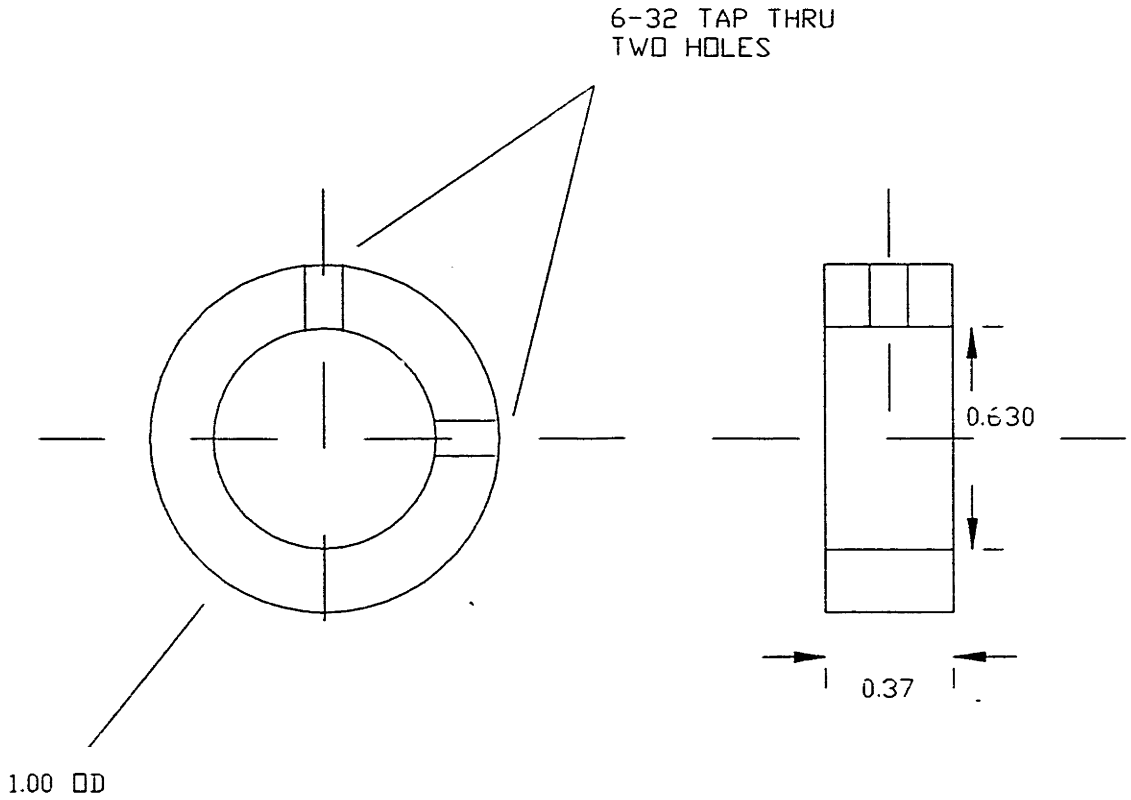

DESIGNER: D.C. GRAY
CONTRACTOR: CHEM ENG SHOP

COMMENTS: ALL SURFACES MUST BE SMOOTH AND FINISHED FOR UHV COMPATABILITY

DWG SCALE: 2" = 1"
QUANTITY: 2 REQUIRED

MATERIAL: ALUMINUM 6061

1 OF 1

TOLERANCES:
X.X = +/-.050
X.XX = +/-.010
X.XXX = +/-.002

MIT DEPT. OF CHEMICAL ENGINEERING
CAMBRIDGE, MASSACHUSETTS 02139
Blg. 66-219, (617) 253-6587

PART: 3/8 ROD RETAINER

CODE: 3B.44 REVISION: 1/22/90

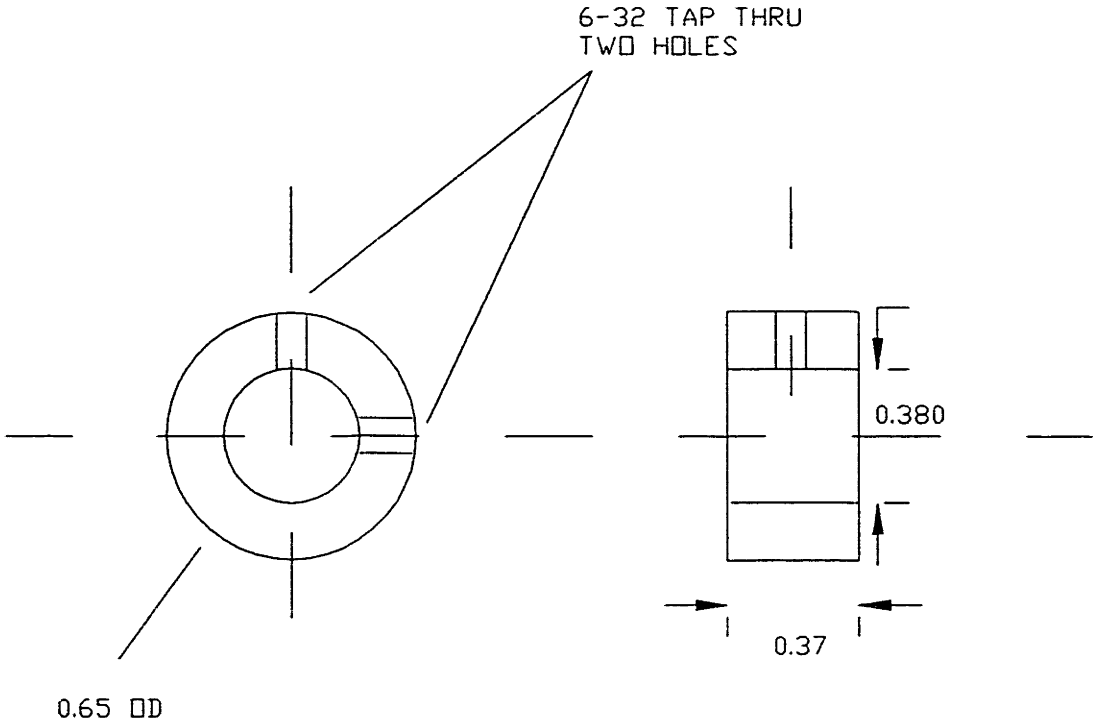

DESIGNER: D.C. GRAY
CONTRACTOR: CHEM ENG SHOP

COMMENTS: ALL SURFACES MUST BE SMOOTH AND FINISHED FOR UHV COMPATABILITY

DWG SCALE: 2" = 1"
QUANTITY: 2 REQUIRED

MATERIAL: ALUMINUM 6061

1 OF 1

TOLERANCES:
X.X = +/-.050
X.XX = +/-.010
X.XXX = +/-.002

MIT DEPT. OF CHEMICAL ENGINEERING
CAMBRIDGE, MASSACHUSETTS 02139
Blg. 66-219, (617) 253-6587

PART: 3/8 SLIDE ROD

CODE: 3B.46 REVISION: 1/22/90

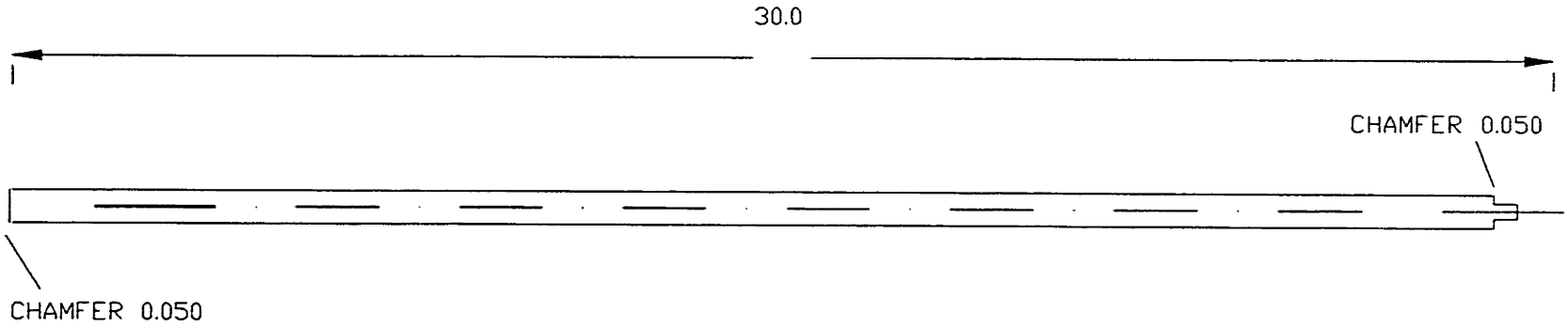

END DETAIL

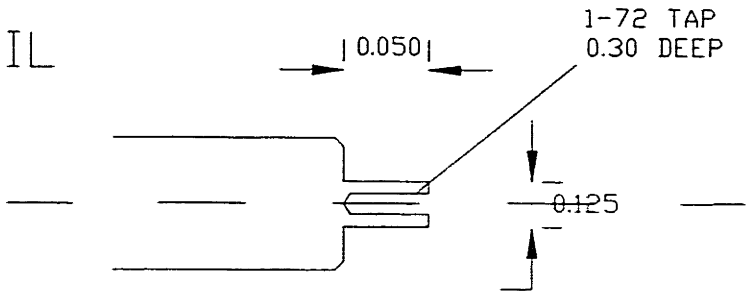

DESIGNER: D.C. GRAY
CONTRACTOR: NOR-CAL
BOSTON CENTERLESS INC
COMMENTS:

DWG SCALE: 1"=2" DETAIL 2" = 1"
QUANTITY: 1 REQUIRED

MATERIAL: 0.370 ACCUROD STOCK
PRECISION GROUND SS

1 OF 1

TOLERANCES:
X.X = +/-.050
X.XX = +/-.010
X.XXX = +/-.002

MIT DEPT. OF CHEMICAL ENGINEERING
CAMBRIDGE, MASSACHUSETTS 02139
Bldg. 66-221 METL LAB (617) 253-6587

PART: VACUUM TRANSFER TUBE

CODE: 3B.49 REVISION: 3/90

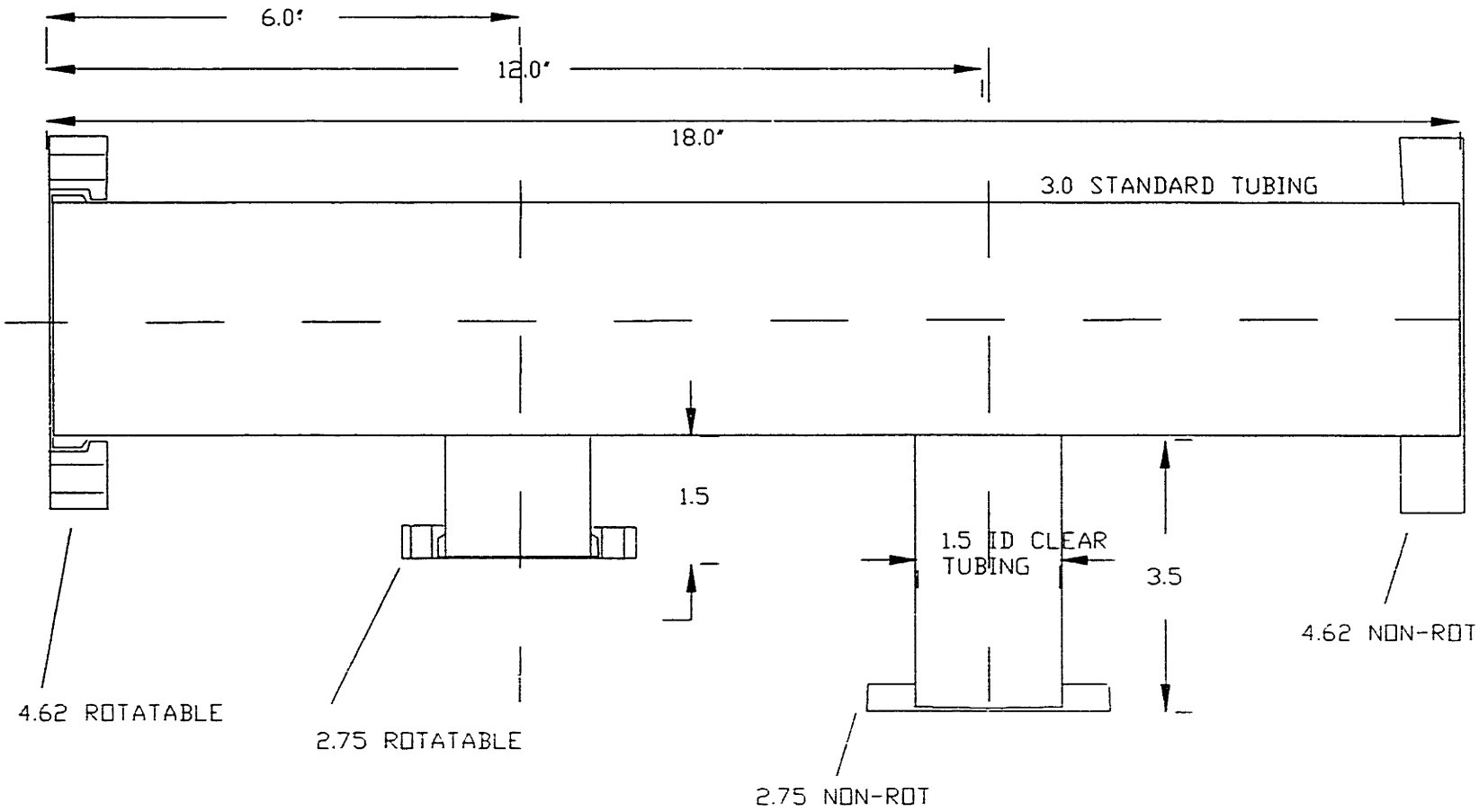

DESIGNER: D.C. GRAY
CONTRACTOR:

COMMENTS:

DWG SCALE: 2" = 1"
QUANTITY: 1 REQUIRED

MATERIAL:

1 OF 1

TOLERANCES:
X.X = +/-.050
X.XX = +/-.010
X.XXX = +/-.002

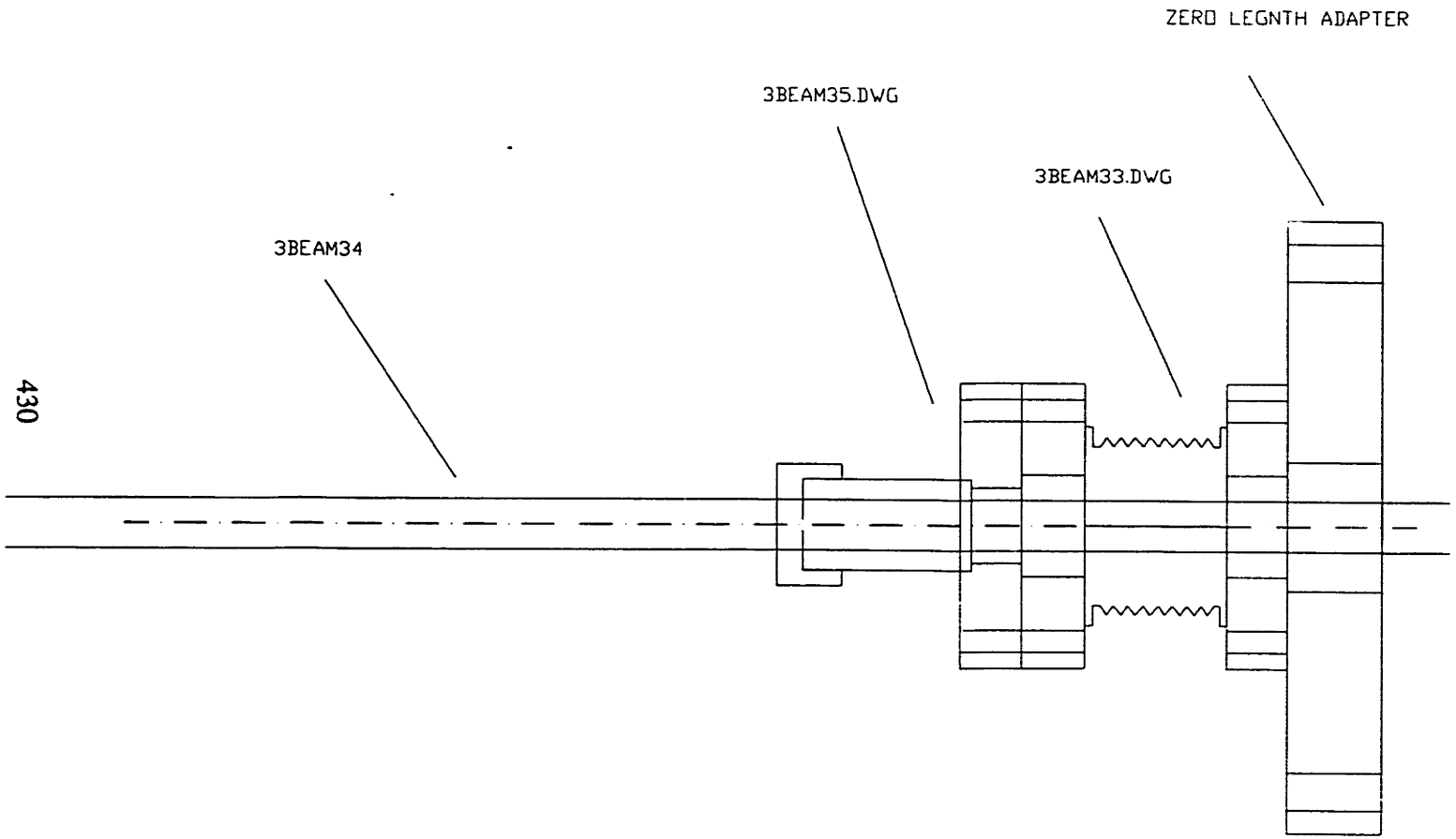

MIT CHEMICAL ENGINEERING

GENERAL INFORMATION

SCALE 1 : 1	SHEET 1 OF 1
DIMENSIONS ARE IN INCHES	REVISION NO: 10

DESIGNED BY: DAVID C. GRAY
DRAFTED BY: DAVID C. GRAY

PRIMARY ASSEMBLY: 3-BEAM REACTOR
SECONDARY ASSEMBLY:

DRAWING TYPE: STANDARD MACHINE

MTL:

ITEM IDENTIFICATION

NAME: WOBBLE STICK ASSEMBLY
CODE: COMP9.DVG

FILE: 3-BEAM

DESCRIPTION:

TOLERANCE SPECIFICATIONS

X	+/- .05	.XX	+/- .02
.XXX	+/- .005	.XXXX	+/- .0005
X/XX	+/- 1/64	ANGULAR:	+/- 1°

FLATNESS: .010 TOTAL
PERPENDICULARITY: .001 PER INCH
PARALLELISM: .005 TOTAL

I.D.'S TO BE WITHIN .002 TLR

1) FINISHING MARKS CONFORM TO AMERICAN STANDARD CONVENTIONS.
2) BREAK ALL SHARP EDGES .005 - .015
3) REMOVE ALL BURRS LEAVE NO HEAVY MILL FILE TOOL OR CHATTER MARKS.

LEGAL NOTES:

CONTRACTOR INFORMATION:

MIT DEPT. OF CHEMICAL ENGINEERING	PART: PLATEN MOUNTING RODS CODE: 3B.04 FILE NO: 3-BEAM

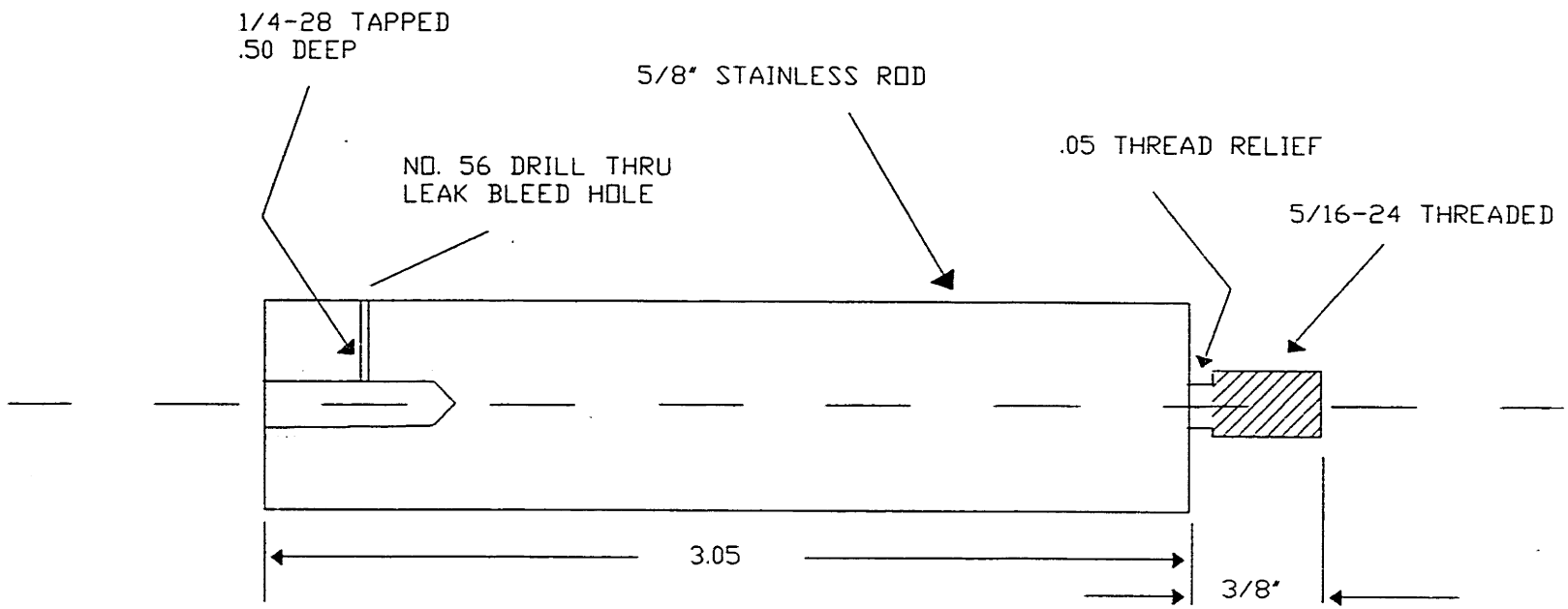

DESIGNER: D. GRAY H. SAWIN CONTRACTOR: LNS MACHINE SHOP COMMENTS: REVISION 4/25/89	DWG SCALE: 2" = 1" QUANTITY: 3 MATERIAL: GROUND STAINLESS ROD 5/8" OD

1 OF 1

TOLERANCES:

X.X = ±.050
X.X.X = ±.010
X.XXX = ±.002

MIT DEPT. OF CHEMICAL ENGINEERING

PART: SAMPLE HOLDER ALIGNMENT PINS

CODE: 3B.5 FILE NO: 3-BEAM

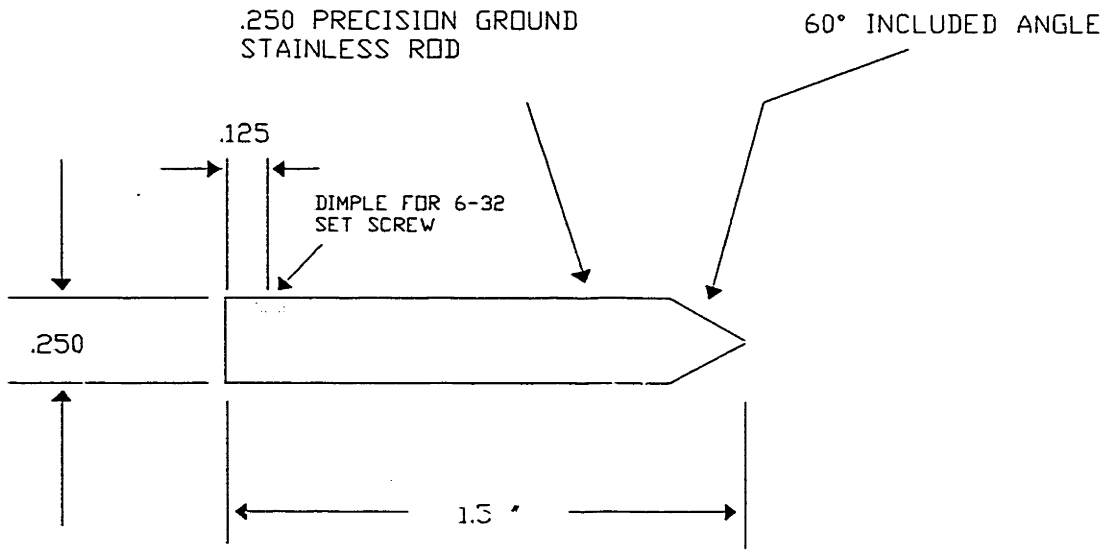

DESIGNER: D. GRAY H. SAWIN
CONTRACTOR: LNS MACHINE SHOP

COMMENTS:

REVISION 4/25/89

DWG SCALE: 2" = 1"
QUANTITY: 2

MATERIAL: .250 PRECISION GOUND S.S. ROD

1 OF 1

TOLERANCES:
XX = ±.050
X.XX = ±.010
X.XXX = ±.001

MIT DEPT. OF CHEMICAL ENGINEERING

PART: MOTOR MOUNT PLATEN

CODE: 3B.6 FILE NO: 3-BEAM

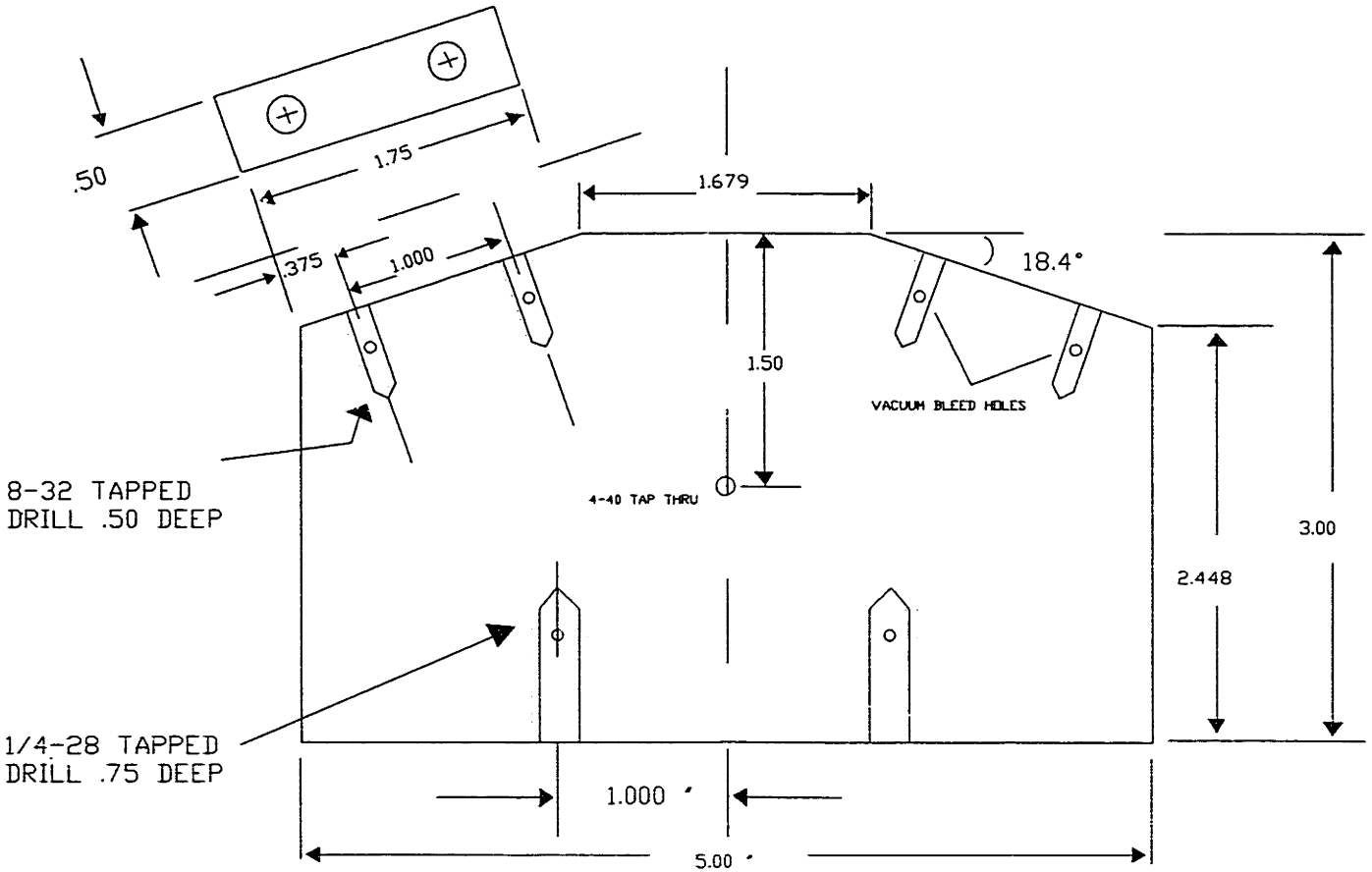

DESIGNER: D. GRAY H. SAWIN
CONTRACTOR: LNS MACHINE SHOP

COMMENTS:

REVISION 4/25/89

DWG SCALE: 1" = 1"
QUANTITY: 1

MATERIAL: 1/2 " ALUMINUM PLATE 6061

1 OF 1

TOLERANCES:
X.X = ±.050
X.XX = ±.010
X.XXX = ±.002

MIT DEPT. OF CHEMICAL ENGINEERING

PART: SAMPLE MOUNTING PLATE

CODE: 3B.7 FILE NO: 3-BEAM

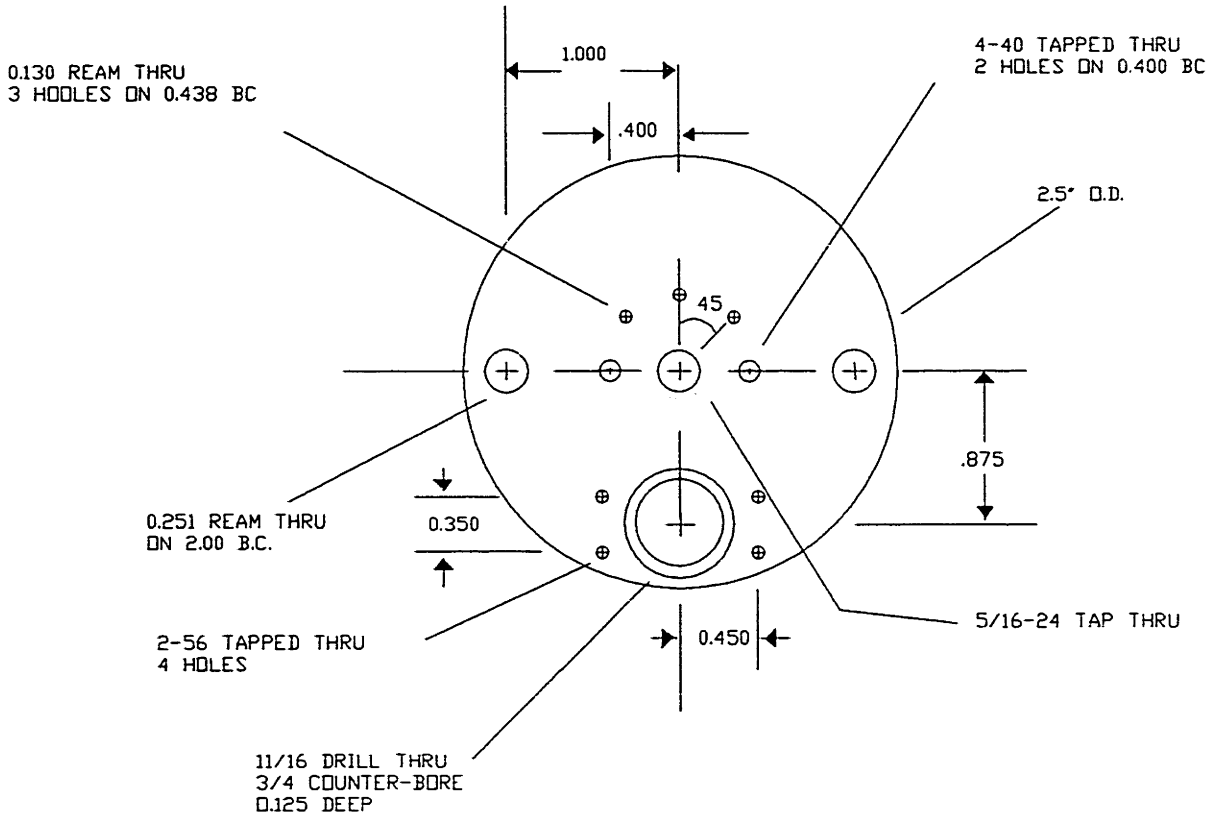

DESIGNER: D. GRAY H. SAWIN

CONTRACTOR: LNS MACHINE SHOP

COMMENTS:

REVISION 4/25/89

DWG SCALE: 1" = 1"

QUANTITY: 2

MATERIAL: 0.25" ALUMINUM 6061

1 OF 1

TOLERANCES:

X.X = ±.050
X.XX = ±.010
X.XXX = ±.002

MIT DEPT. OF CHEMICAL ENGINEERING

PART: MOTOR PLATEN MOUNTING PLATE

CODE: 3B.8 FILE NO: 3-BEAM .

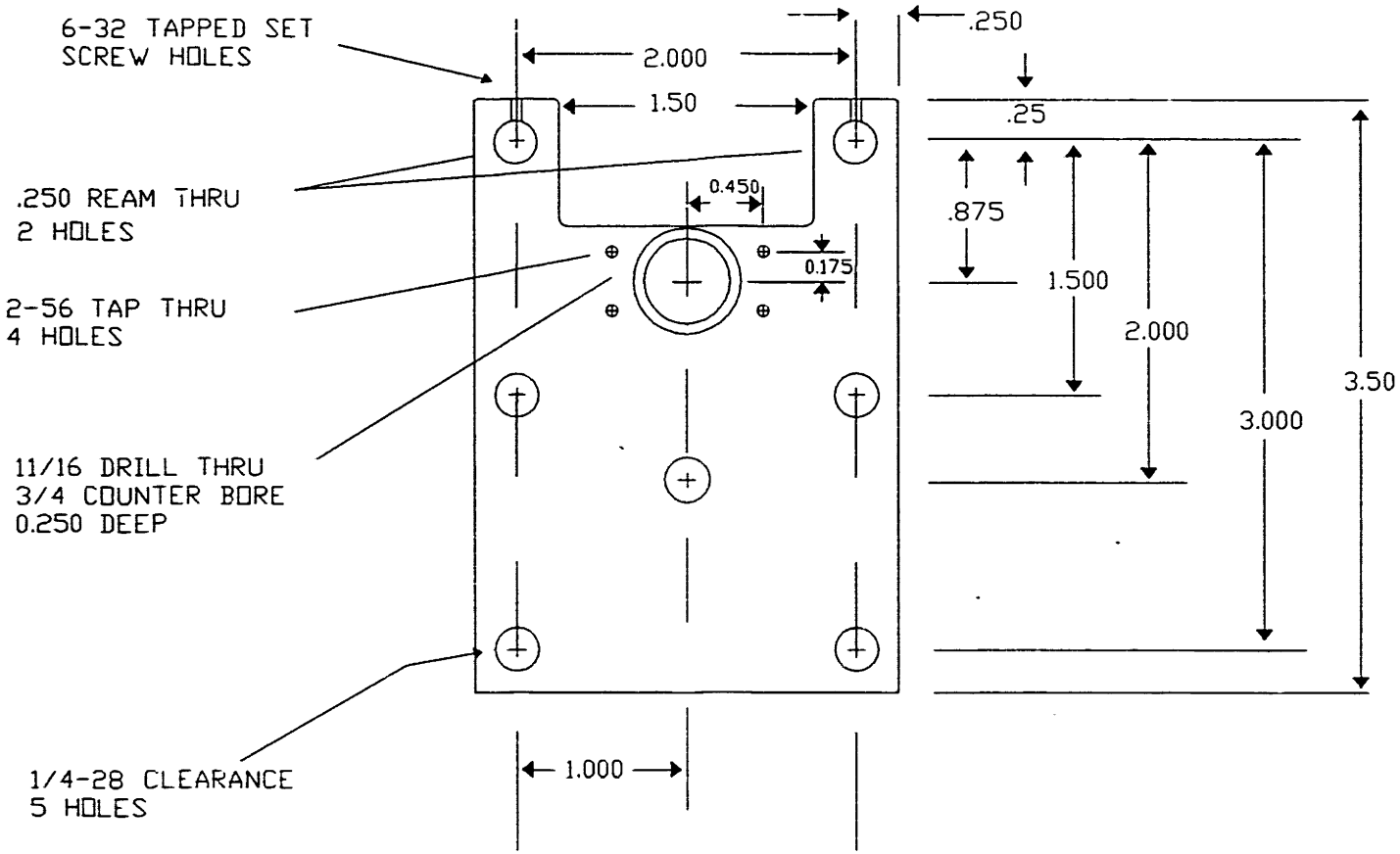

DESIGNER: D. GRAY H. SAWIN

CONTRACTOR: LNS MACHINE SHOP

COMMENTS: 0.250 PRECISION GROUND PINS SHOULD PRESS FIT INTO REAMED HOLES

REVISION 4/25/89

DWG SCALE: 1" = 1"

QUANTITY: 1

MATERIAL: .50 " ALUMINUM PLATE 6061

1 OF 1

TOLERANCES:

X.X = ±.050

X.XX = ±.010

X.XXX = ±.001

MIT DEPT. OF CHEMICAL ENGINEERING
CAMBRIDGE, MASSACHUSETTS 02139
Bldg. 66-219, (617) 253-6587

PART: SAMPLE MOUNT DRILL JIG

CODE: 3B.38 REVISION: 6/10/89

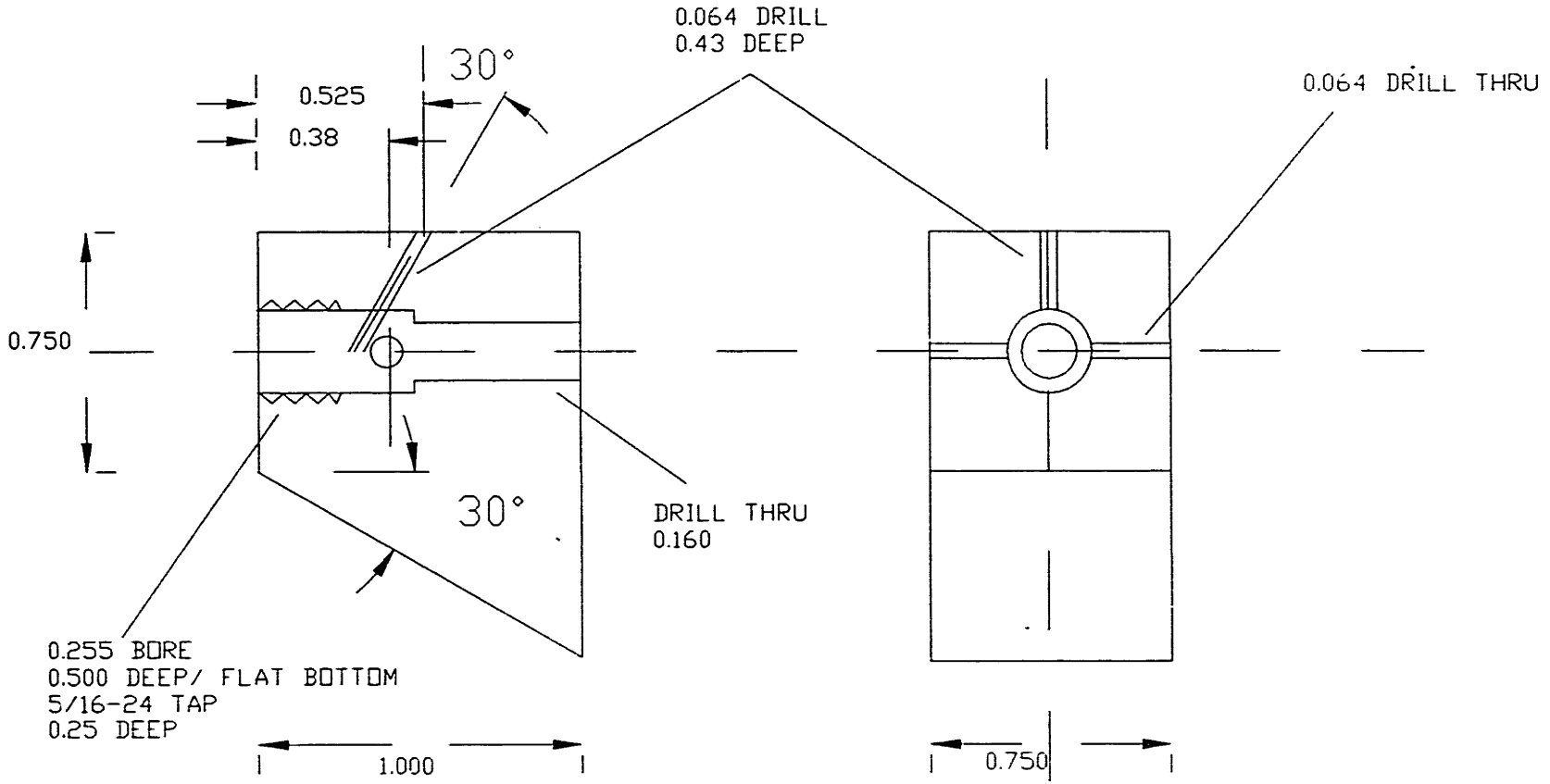

DESIGNER: D.C. GRAY
CONTRACTOR: LNS

COMMENTS:

DWG SCALE: 2" = 1"
QUANTITY: 1 REQUIRED

MATERIAL: STAINLESS STEEL

1 OF 1

TOLERANCES:
X.X = +/-.050
X.XX = +/-.010
X.XXX = +/-.002

MIT DEPT. OF CHEMICAL ENGINEERING
CAMBRIDGE, MASSACHUSETTS 02139
Bldg. 66-219, (617) 253-6587

PART: SAMPLE MOUNT TAP JIG

CODE: 3B.39 REVISION: 6/10/89

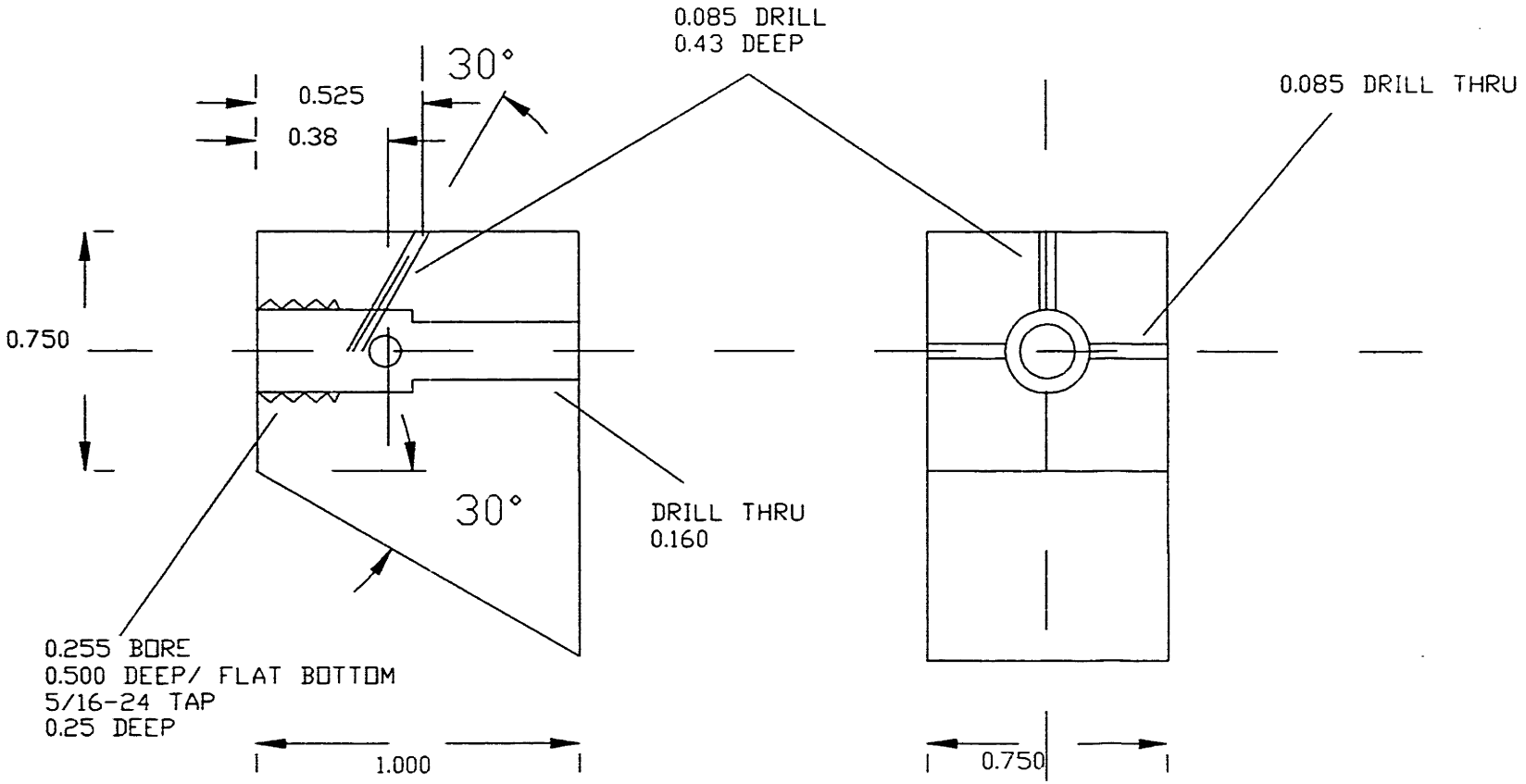

DESIGNER: D.C. GRAY
CONTRACTOR: LNS

COMMENTS:

DWG SCALE: 2" = 1"
QUANTITY: 1 REQUIRED

MATERIAL: STAINLESS STEEL

1 OF 1

TOLERANCES:
X.X = +/-.050
X.XX = +/-.010
X.XXX = +/-.002

MIT DEPT. OF CHEMICAL ENGINEERING
CAMBRIDGE, MASSACHUSETTS 02139
Bldg. 66-221 METL LAB (617) 253-6587

PART: SAMPLE MOUNT

CODE: 3B.47 REVISION: 9/89

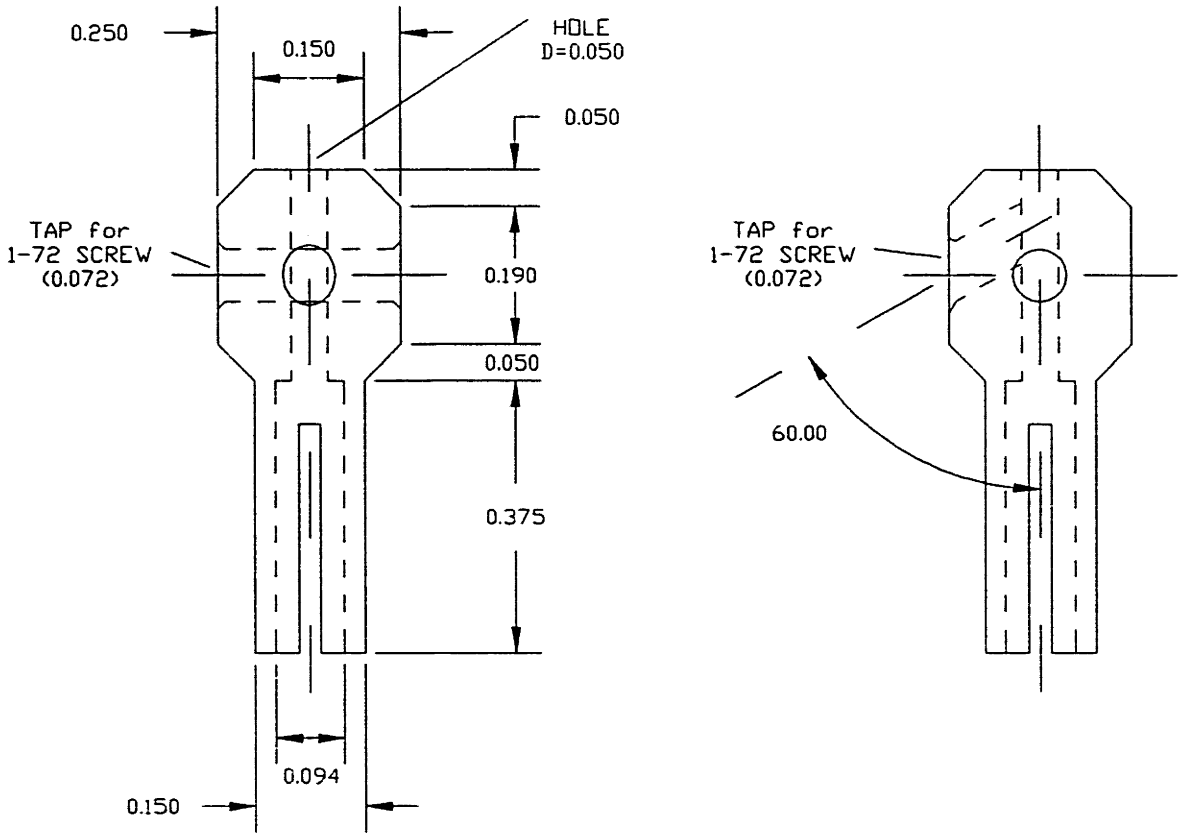

DESIGNER: D.C. GRAY
CONTRACTOR:

COMMENTS:

DWG SCALE:
QUANTITY:

MATERIAL: Be-Cu WIRE CONNECTORS
ISI STOCK PART

1 OF 1

TOLERANCES:
X.X = +/-.050
X.XX = +/-.010
X.XXX = +/-.003

MIT DEPT. OF CHEMICAL ENGINEERING
CAMBRIDGE, MASSACHUSETTS 02139
Bldg. 66-221 METL LAB (617) 253-6587

PART: SMAPLE MOUNTING PIN

CODE: 3B.48 REVISION: 9/89

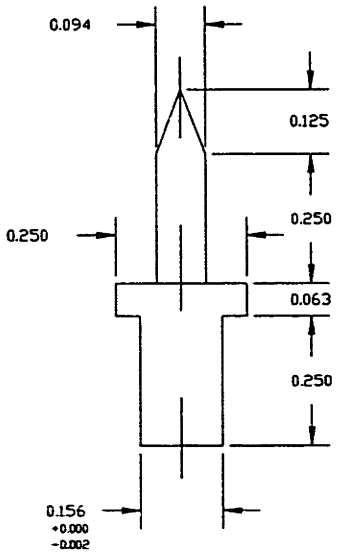

SIDE VIEW

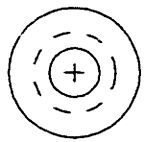

TOP VIEW

DESIGNER: D.C. GRAY
CONTRACTOR: LNS MACHINE SHOP

COMMENTS:

DWG SCALE:
QUANTITY:

MATERIAL: 316 SS

1 OF 1

TOLERANCES:
X.X = +/-.050
X.XX = +/-.010
X.XXX = +/-.002

MIT DEPT. OF CHEMICAL ENGINEERING
CAMBRIDGE, MASSACHUSETTS 02139
Bldg. 66-221 METL LAB (617) 253-6587

PART: SAMPLE ELECTRICAL SOCKET

CODE: 3B.75 REVISION: 1/88

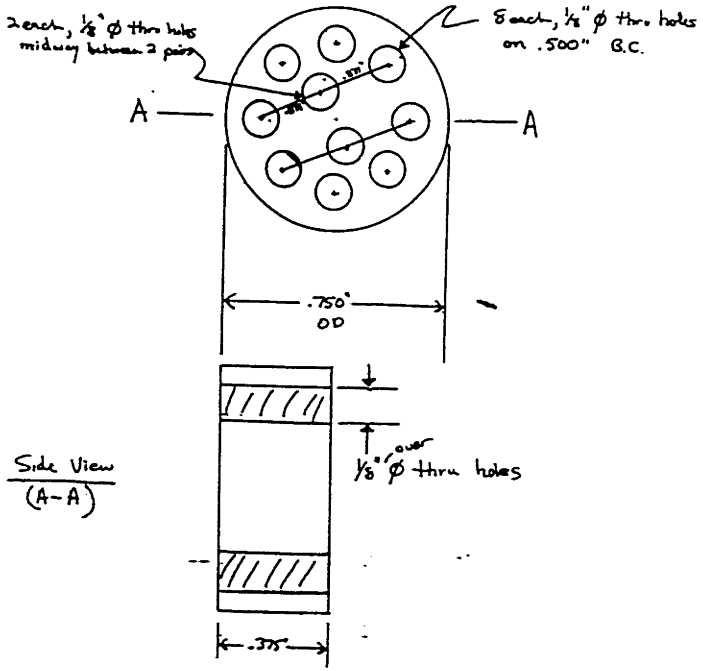

Special Note: holes Must align with plug

DESIGNER: BJ STANBURY
CONTRACTOR:

COMMENTS:

DWG SCALE:
QUANTITY: 1 REQUIRED
MATERIAL: MACOR CERAMIC

MIT DEPT. OF CHEMICAL ENGINEERING CAMBRIDGE, MASSACHUSETTS 02139 Bldg. 66-221 METL LAB (617) 253-6587	PART: SAMPLE ELECTRICAL PLUG CODE: 3B.76 REVISION: 1/89

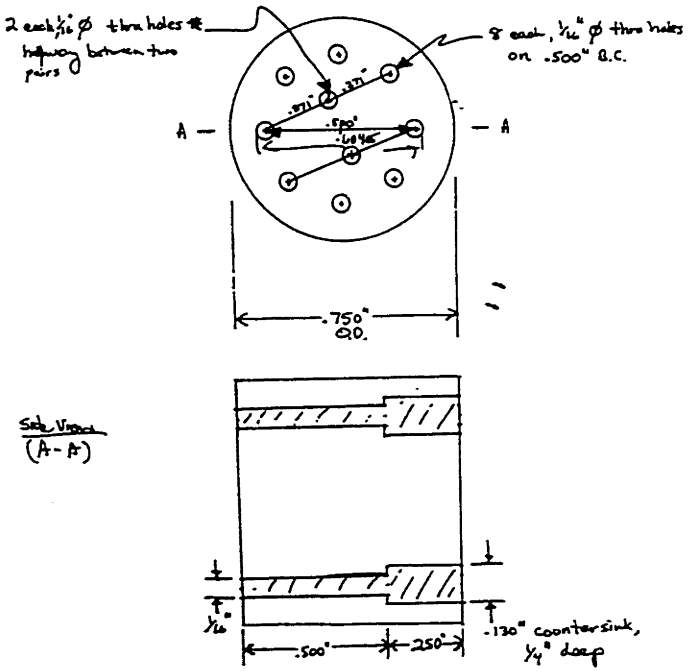

Special Note: holes must align w/ socket

DESIGNER: BJ STANBURY CONTRACTOR: COMMENTS:	DWG SCALE: QUANTITY: 1 REQUIRED MATERIAL: MACHINABLE FOAM	TOLERANCE:

MIT DEPT. OF CHEMICAL ENGINEERING CAMBRIDGE, MASSACHUSETTS 02139 Bldg. 66-221 METL LAB (617) 253-6587	PART: ELECTRICAL CONNECTOR RETAINERS CODE: 3B.77 REVISION: 1/89

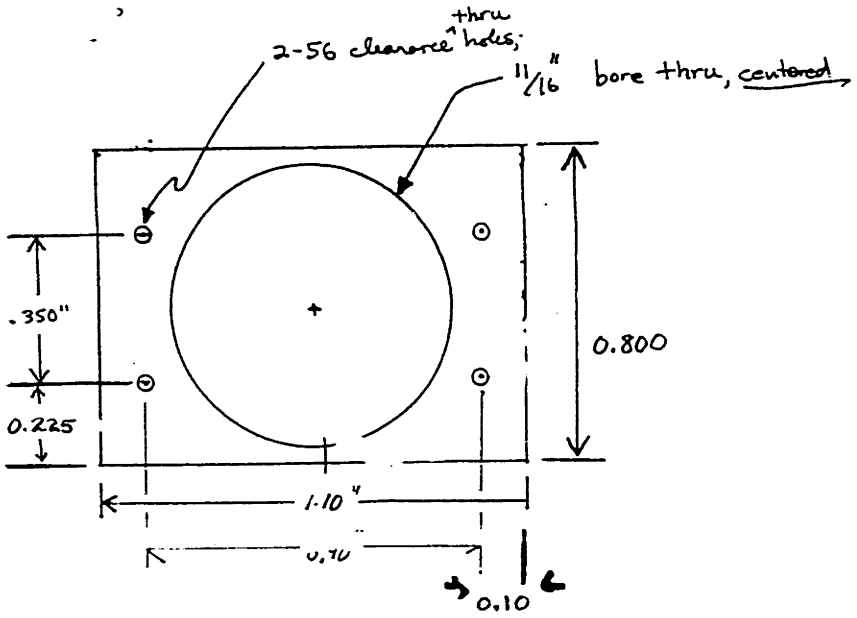

DESIGNER: BJ STANBURY CONTRACTOR: COMMENTS:	DWG SCALE: QUANTITY: 2 REQUIRED MATERIAL: 0.25 6061 AL PLATE	1 OF 1 TOLERANCES: XX = +/-.050 XXX = +/-.010 XXXX = +/-.002

MIT DEPT. OF CHEMICAL ENGINEERING

CAMBRIDGE, MASSACHUSETTS 02139
Bldg. 66-221 METL LAB (617) 253-6587

PART: SAMPLE EXTENSION PEDESTAL

CODE: 3B.78 REVISION: 1/89

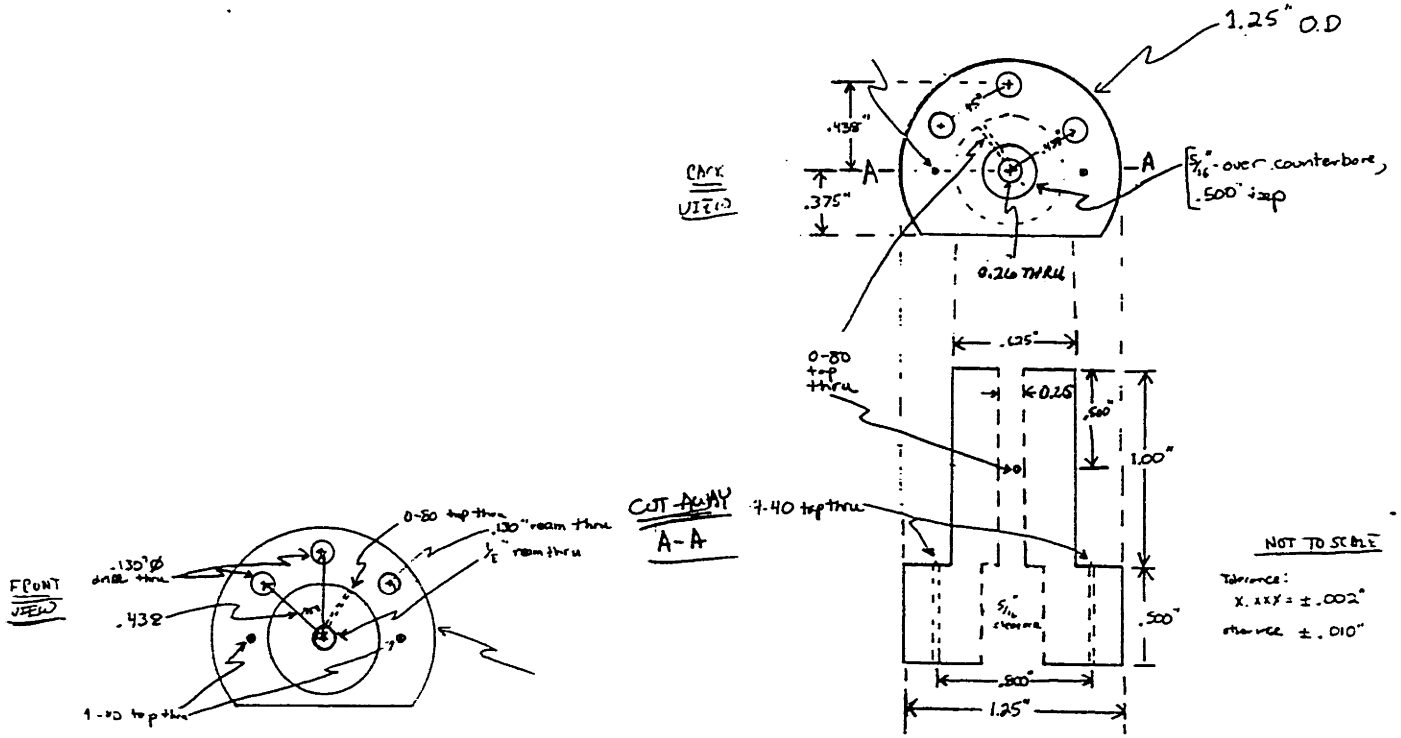

DESIGNER: BJ STANBURY
CONTRACTOR:

COMMENTS:

DWG SCALE:
QUANTITY: 1 REQUIRED

MATERIAL: 6061 AL

1 OF 1

TOLERANCES:
X.X = +/-.050
X.XX = +/-.010
X.XXX = +/-.002

MIT DEPT. OF CHEMICAL ENGINEERING

PART: IMPACT TUBE COUPLER

CODE: 3B.13 FILE NO: 3-BEAM

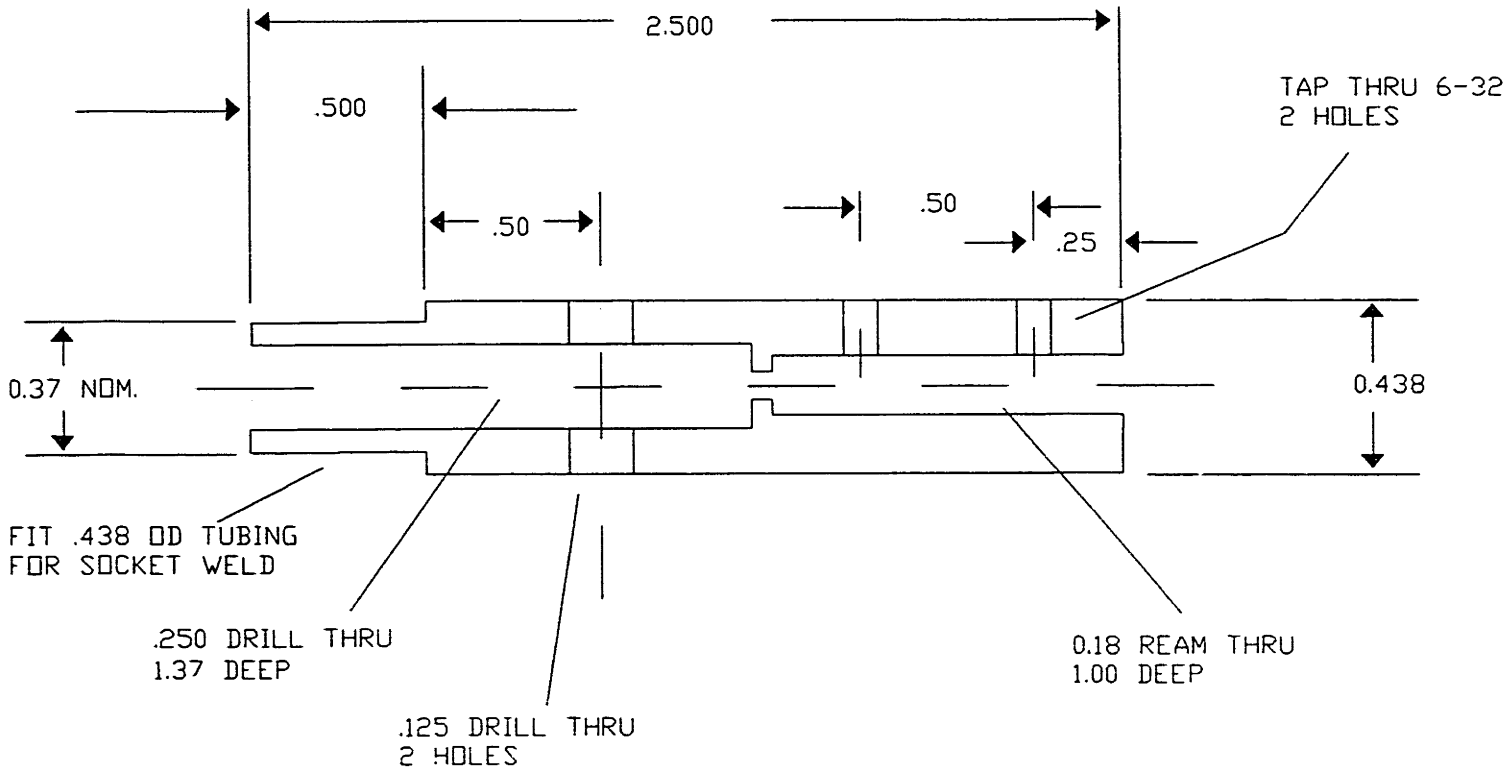

DESIGNER: D.GRAY H.SAWIN
CONTRACTOR: LNS MACHINE SHOP

COMMENTS: .500 STAINLESS STEEL TUBING SHOULD FIT TIGHTLY OVER SMALLER O.D.

REVISION 4/25/89

DWG SCALE: 2" = 1"
QUANTITY: 1

1 OF 1

MATERIAL: .50 O.D. STAINLESS STEEL ROD 316

TOLERANCES:
X.X = +/-.050
X.XX = +/-.010
X.XXX = +/-.002

MIT DEPT. OF CHEMICAL ENGINEERING	PART: IMPACT TUBE END CAP CODE: 3B.14 FILE NO: 3-BEAM

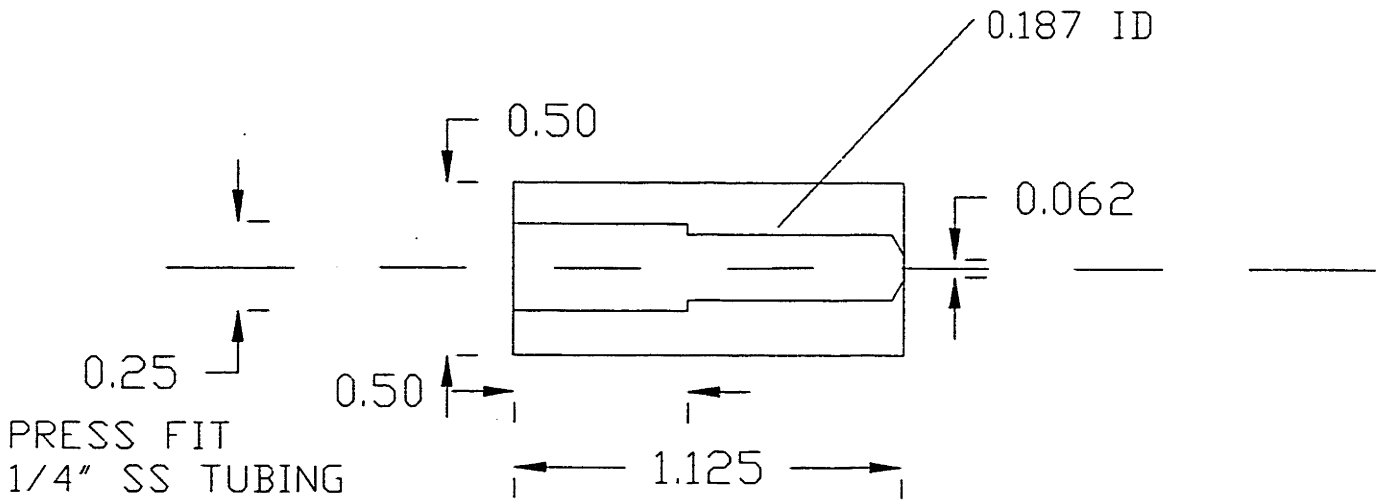

DESIGNER: D. GRAY CONTRACTOR: CHEM.ENG. MACHINE SHOP COMMENTS: END CAP SHOULD PRESS FIT ON TO 0.25" IMPACT TUBING REVISION 4/25/89	DWG SCALE: 2" = 1" QUANTITY: 1 MATERIAL: 6061 ALUMINUM 1 OF 1 TOLERANCES: X.X = +/-.050 X.XX = +/-.010 X.XXX = +/-.002

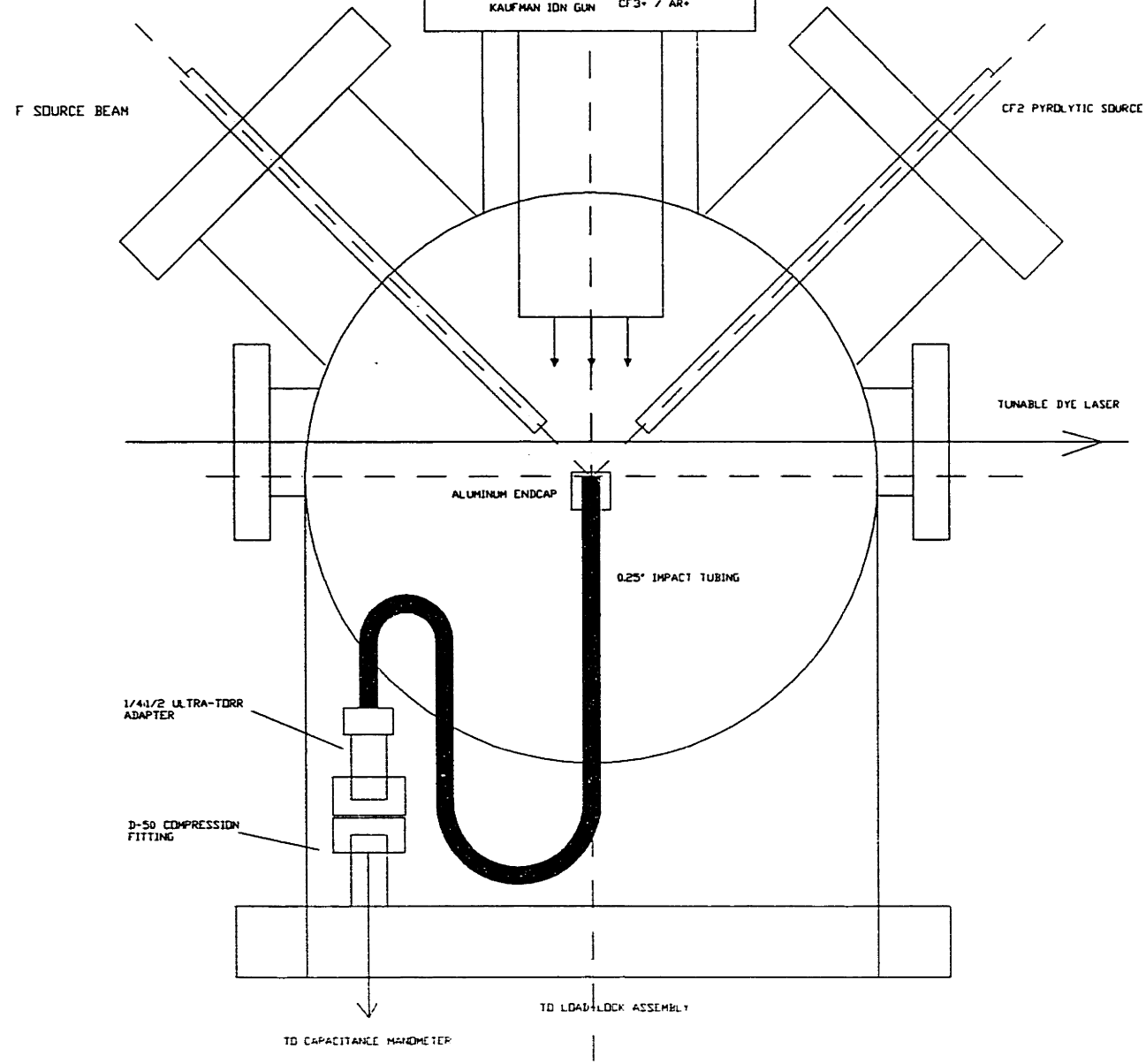

MIT CHEMICAL ENGINEERING

GENERAL INFORMATION

SCALE:	SHEET 1 OF 1
DIMENSIONS ARE IN INCHES	REVISION NO 1.0

DESIGNED BY: DAVID C. GRAY
DRAFTED BY: DAVID C. GRAY

PRIMARY ASSEMBLY: 3-BEAM REACTOR
SECONDARY ASSEMBLY:

DRAWING TYPE: STANDARD MACHINE

MTL:

ITEM IDENTIFICATION

NAME: IMPACT TUBE ASSEMBLY
CODE: COMP6.DWG

FILE:

DESCRIPTION:

TOLERANCE SPECIFICATIONS

X +/- .05	XX +/- .02
XXX +/- .005	XXXX +/- .0005
X/XX +/- 1/64	ANGULAR +/- 1°

FLATNESS: .010 TOTAL
PERPENDICULARITY: .001 PER INCH
PARALLELISM: .005 TOTAL

I.D.'S TO BE WITHIN .002 TLR

1) FINISHING MARKS CONFORM TO AMERICAN STANDARD CONVENTIONS
2) BREAK ALL SHARP EDGES .005 - .015
3) REMOVE ALL BURRS, LEAVE NO HEAVY MILL FILE, TOOL, OR CHATTER MARKS

LEGAL NOTES

CONTRACTOR INFORMATION:

MIT DEPT. OF CHEMICAL ENGINEERING CAMBRIDGE, MASSACHUSETTS 02139 Bldg. 66-221 METL LAB (617) 253-6587	PART: PROBE ALIGNMENT JIGS CODE: 3B.14B REVISION: 1/90

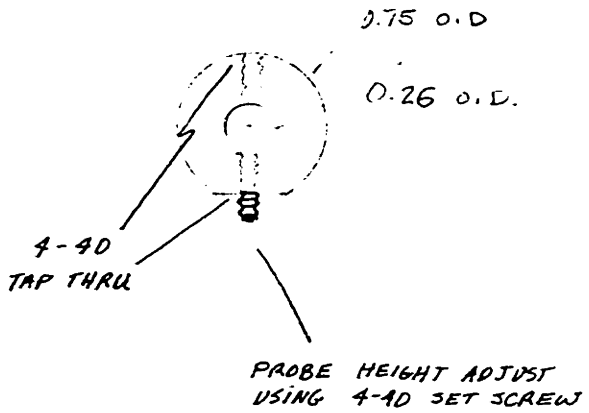

DESIGNER: D.C. GRAY CONTRACTOR:	DWG SCALE: QUANTITY:

MIT DEPT. OF CHEMICAL ENGINEERING

PART: FARADAY CUP SUPPORT RODS

CODE: 3B.15A FILE NO: 3-BEAM

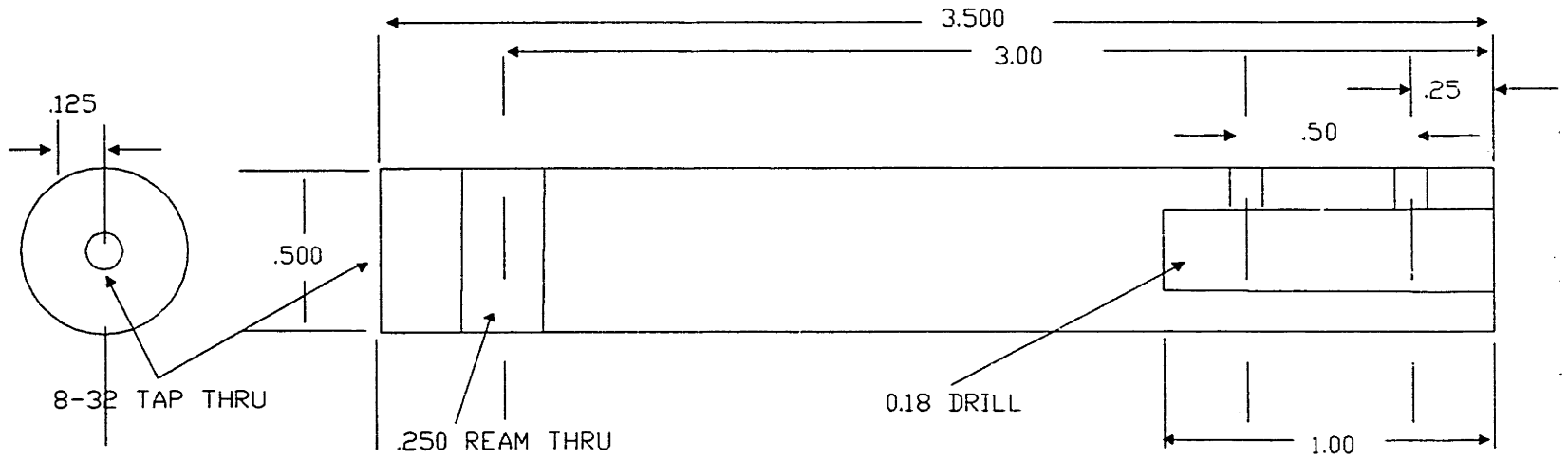

DESIGNER: D. GRAY H.SAWIN
CONTRACTOR: LNS MACHINE SHOP

COMMENTS:

REVISION 4/25/89

DWG SCALE: 2" = 1"
QUANTITY: 1 OF EA.

MATERIAL: .50 O.D. ALUMINUM ROD

1 OF 1

TOLERANCES:
X.X = +/-.050
X.XX = +/-.010
X.XXX = +/-.002

MIT DEPT. OF CHEMICAL ENGINEERING

PART: FARADAY CUP SUPPORT RODS

CODE: 3B.15B FILE NO: 3-BEAM

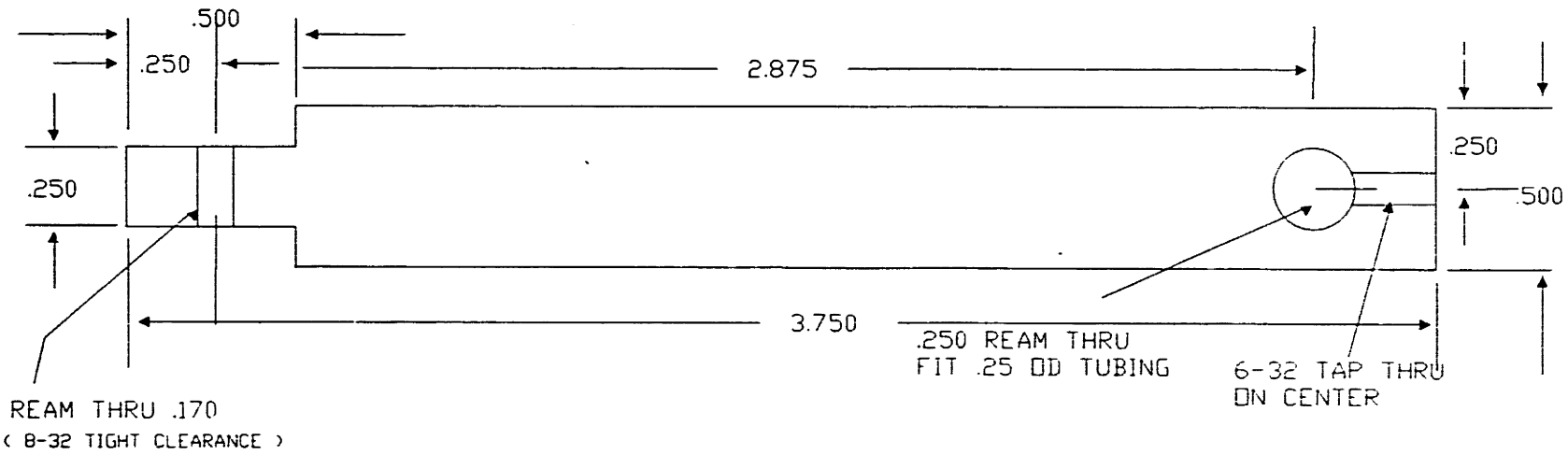

DESIGNER: D.GRAY H.SAWIN
CONTRACTOR: LNS MACHINE SHOP

COMMENTS:

REVISION 4/25/89

DWG SCALE: 2" = 1"
QUANTITY: 1 OF EA

MATERIAL: .50 O.D. ALUMINUM ROD

TOLERANCES

MIT DEPT. OF CHEMICAL ENGINEERING

PART: FARADAY CUP SLIDING BASE

CODE: 3B.16 FILE NO: 3-BEAM

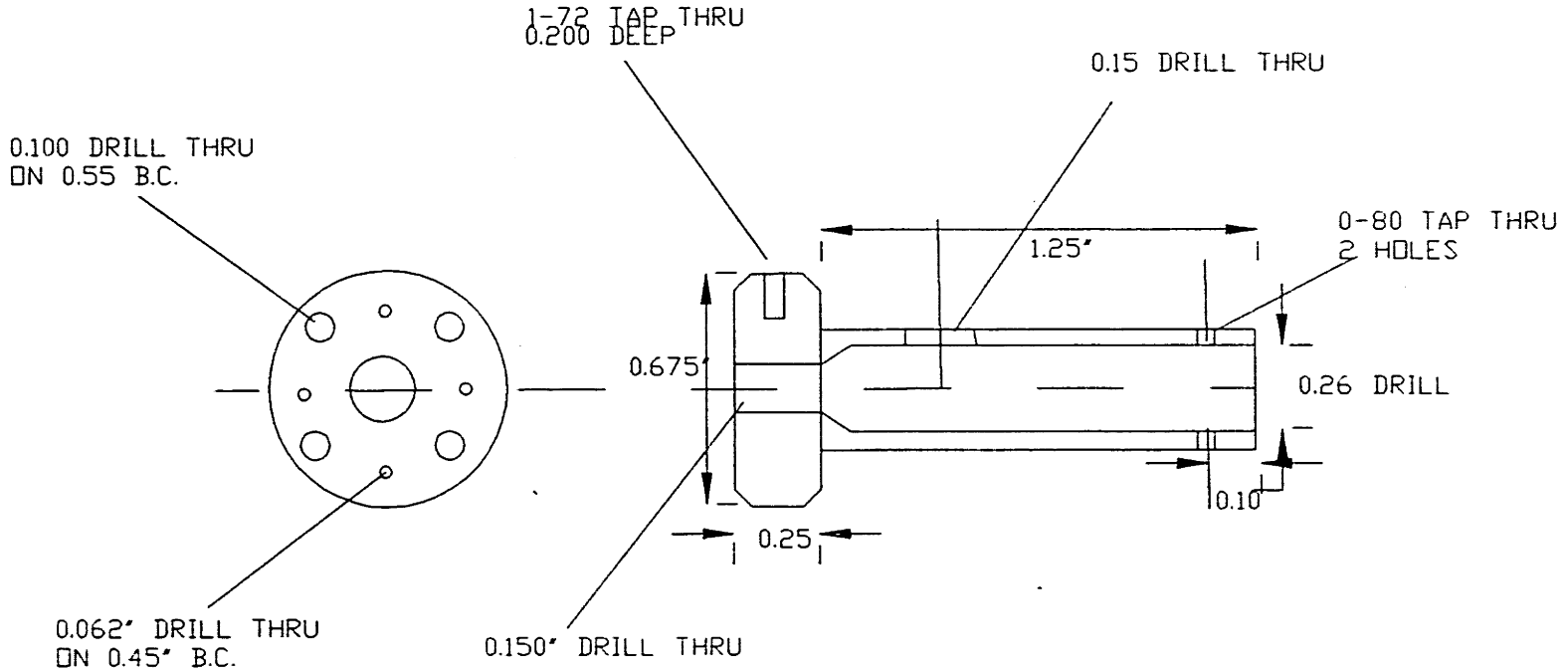

DESIGNER: D.GRAY
CONTRACTOR:

COMMENTS:

REVISION 4/25/89

DWG SCALE: 2" = 1"
QUANTITY: ABOVE

MATERIAL: 6061 Al

1 OF 1

TOLERANCES:

MIT DEPT. OF CHEMICAL ENGINEERING
CAMBRIDGE, MASSACHUSETTS 02139
Bldg. 66-221 METL LAB (617) 253-6587

PART: FARADAY CUP FACE SEAT

CODE: 3B.16B REVISION: 1/90

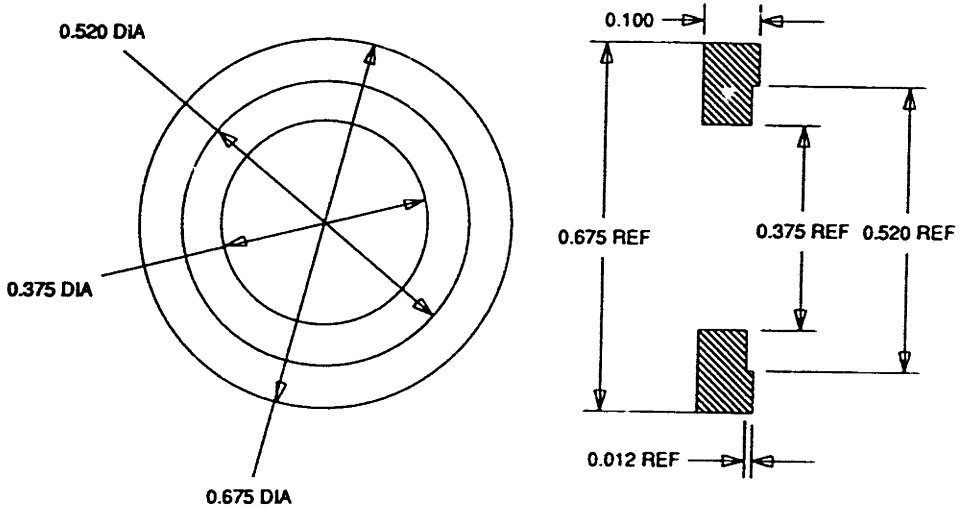

DESIGNER: D.C. GRAY
CONTRACTOR:

COMMENT:

DWG SCALE:
QUANTITY:

MIT DEPT. OF CHEMICAL ENGINEERING

PART: FARADAY CUP ASSEMBLY

CODE: 3B.17 FILE NO: 3-BEAM

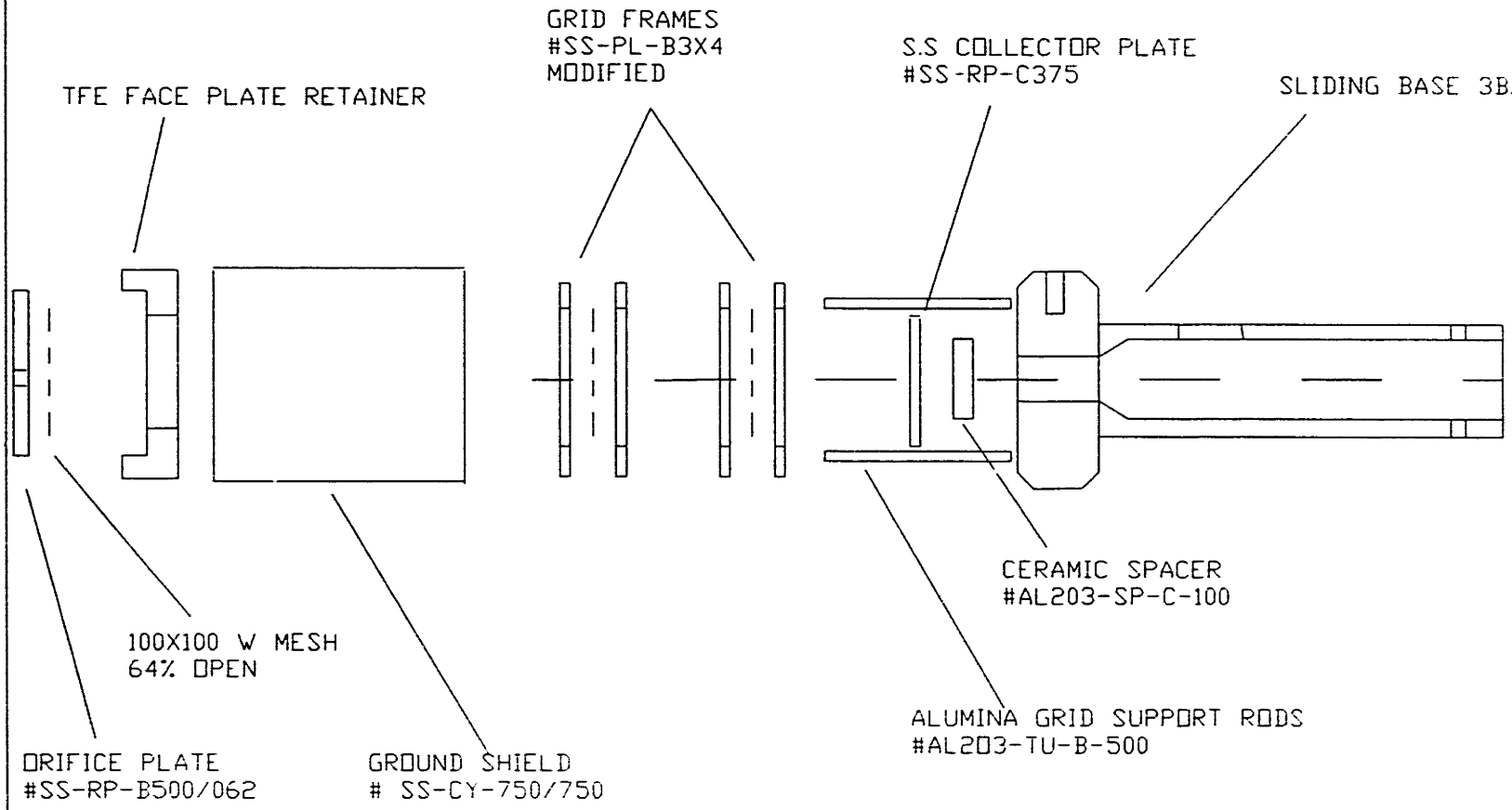

DESIGNER: D.GRAY
CONTRACTOR:

COMMENTS: ALL PART REFERENCES ARE TO KIMBALL PHYSICS STOCK PARTS

REVISION 4/25/89

DWG SCALE: 2" = 1"
QUANTITY: ABOVE

MATERIAL:

1 OF 1

TOLERANCES:
XX = +/- 050
XXX = +/- 010
XXXX = +/- 002

MIT DEPT. OF CHEMICAL ENGINEERING

PART: 4.62" FORMED BELLOWS ADAPTER

CODE: 3B.19 FILE NO: 3-BEAM

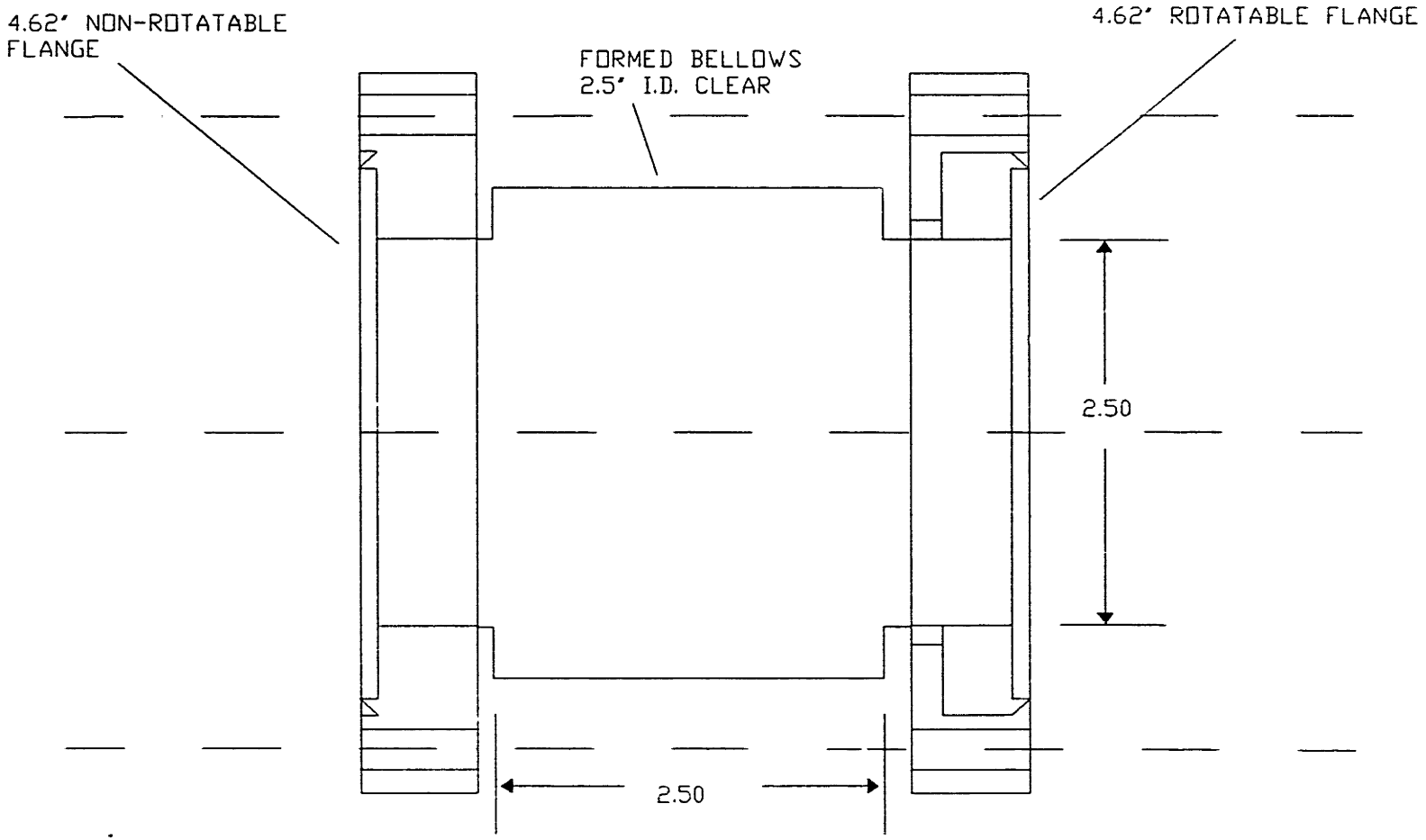

DESIGNER: D.C. GRAY
CONTRACTOR: MDC

COMMENTS:

REVISION 4/25/89

DWG SCALE: 1" = 1"
QUANTITY: 1

MATERIAL: MDC STOCK PARTS

1 OF 1

TOLERANCES:
XX = +/-.050
XXX = +/-.010
XXXX = +/-.002

MIT DEPT. OF CHEMICAL ENGINEERING

PART: DISCHARGE NOZZLE FLANGE

CODE: 3B.22 FILE NO: 3-BEAM

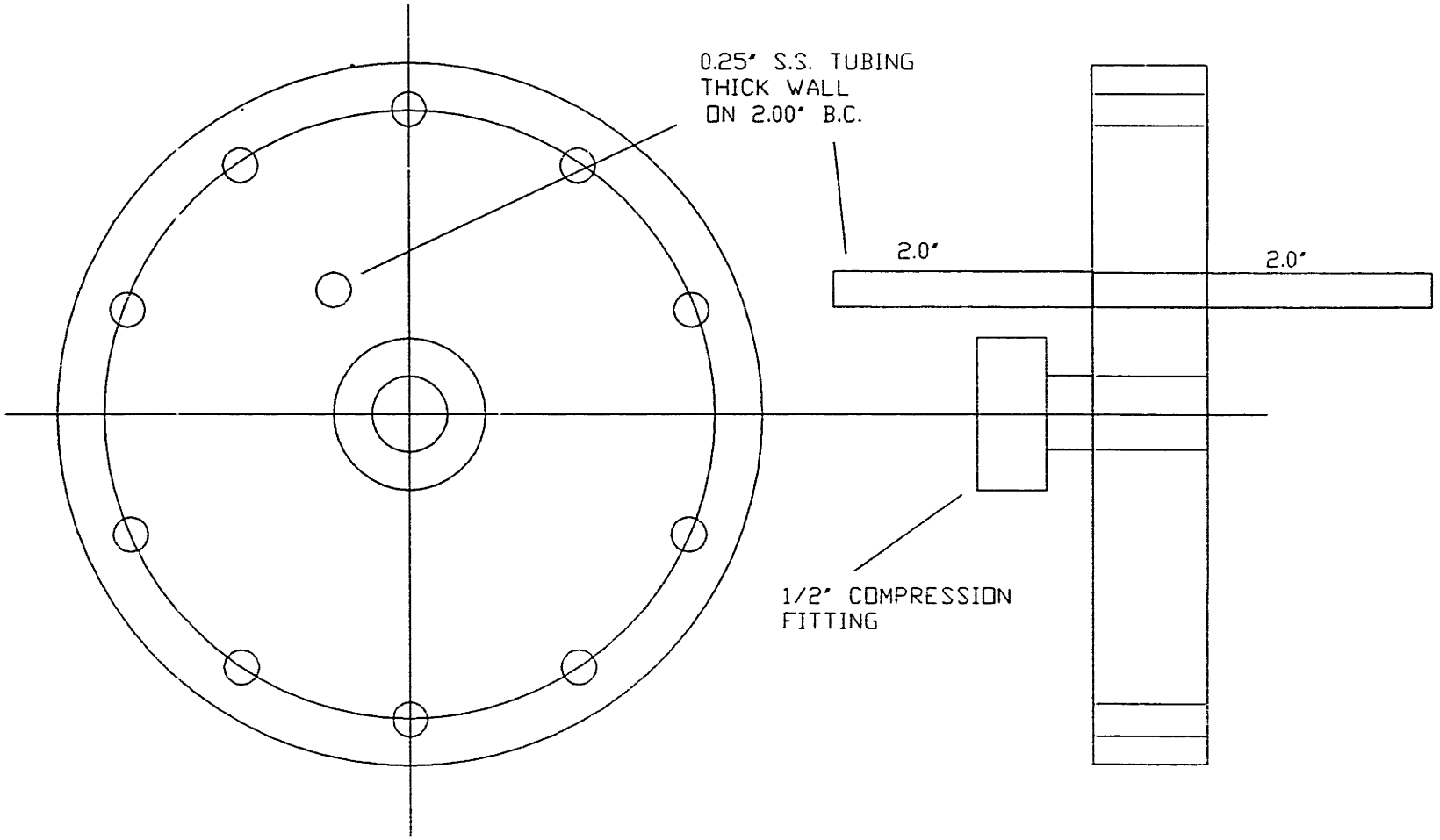

DESIGNER: D.C.GRAY
CONTRACTOR: MDC

COMMENTS:

REVISION 4/25/89

DWG SCALE: 1" = 1"
QUANTITY: 1

MATERIAL: MDC STOCK PARTS

1 OF 1

TOLERANCES:
X.X = ±.050
X.XX = ±.010
X.XXX = ±.001

MIT DEPT. OF CHEMICAL ENGINEERING

PART: PYROLYSIS NOZZLE FLANGE

CODE: 3B.23 FILE NO: 3-BEAM

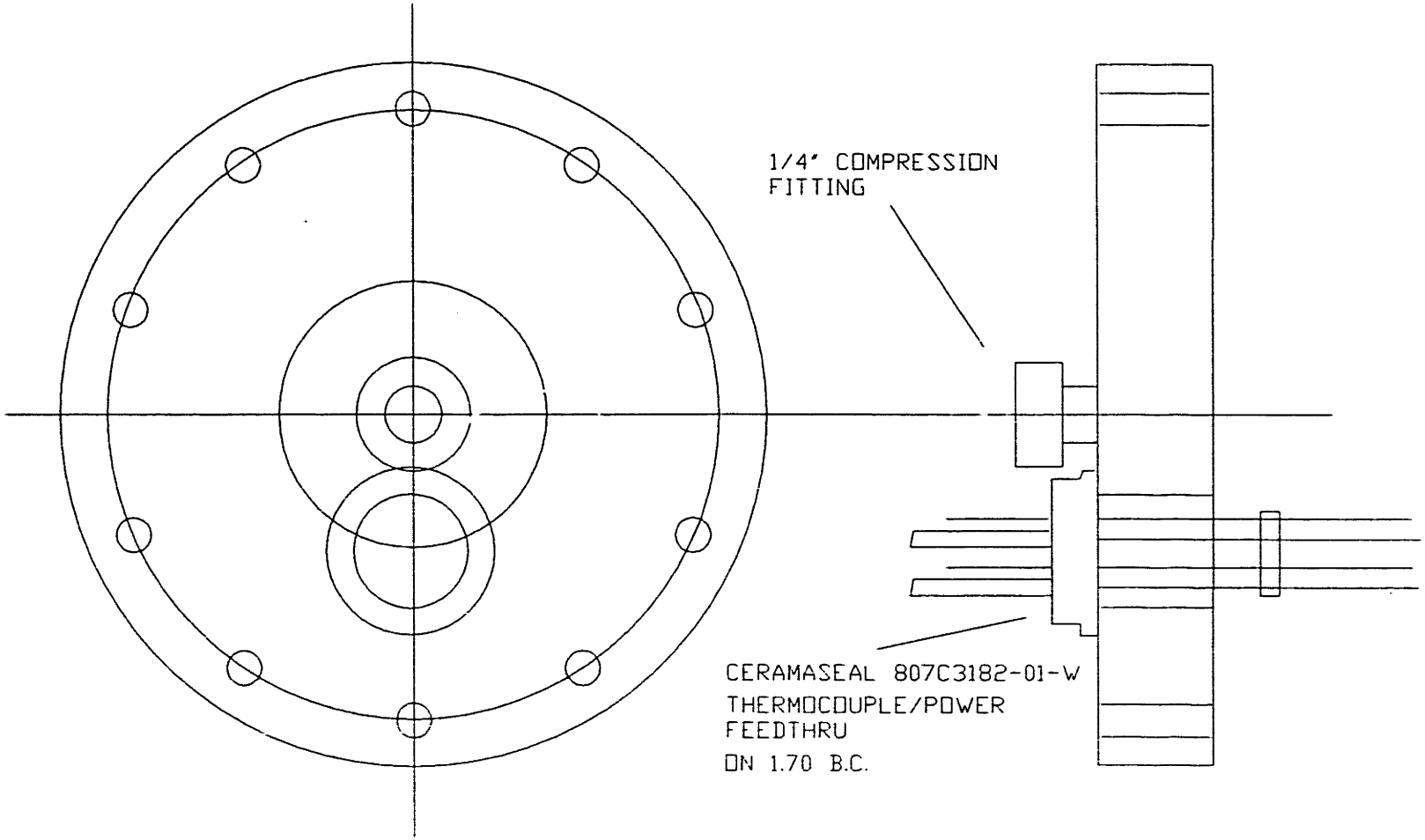

DESIGNER: D.C.GRAY
CONTRACTOR: MDC

COMMENTS:

REVISION 4/25/89

DWG SCALE: 1" = 1"
QUANTITY: 1

MATERIAL: MDC STOCK PARTS

1 OF 1

TOLERANCES:
X.X = ±.050
X.XX = ±.010
X.XXX = ±.001

MIT DEPT. OF CHEMICAL ENGINEERING
CAMBRIDGE, MASSACHUSETTS 02139
Bldg. 66-219, (617) 253-6587

PART: KAUFMAN GUN RADIATION SHIELD

CODE: 3B.50 REVISION: 3/14/90

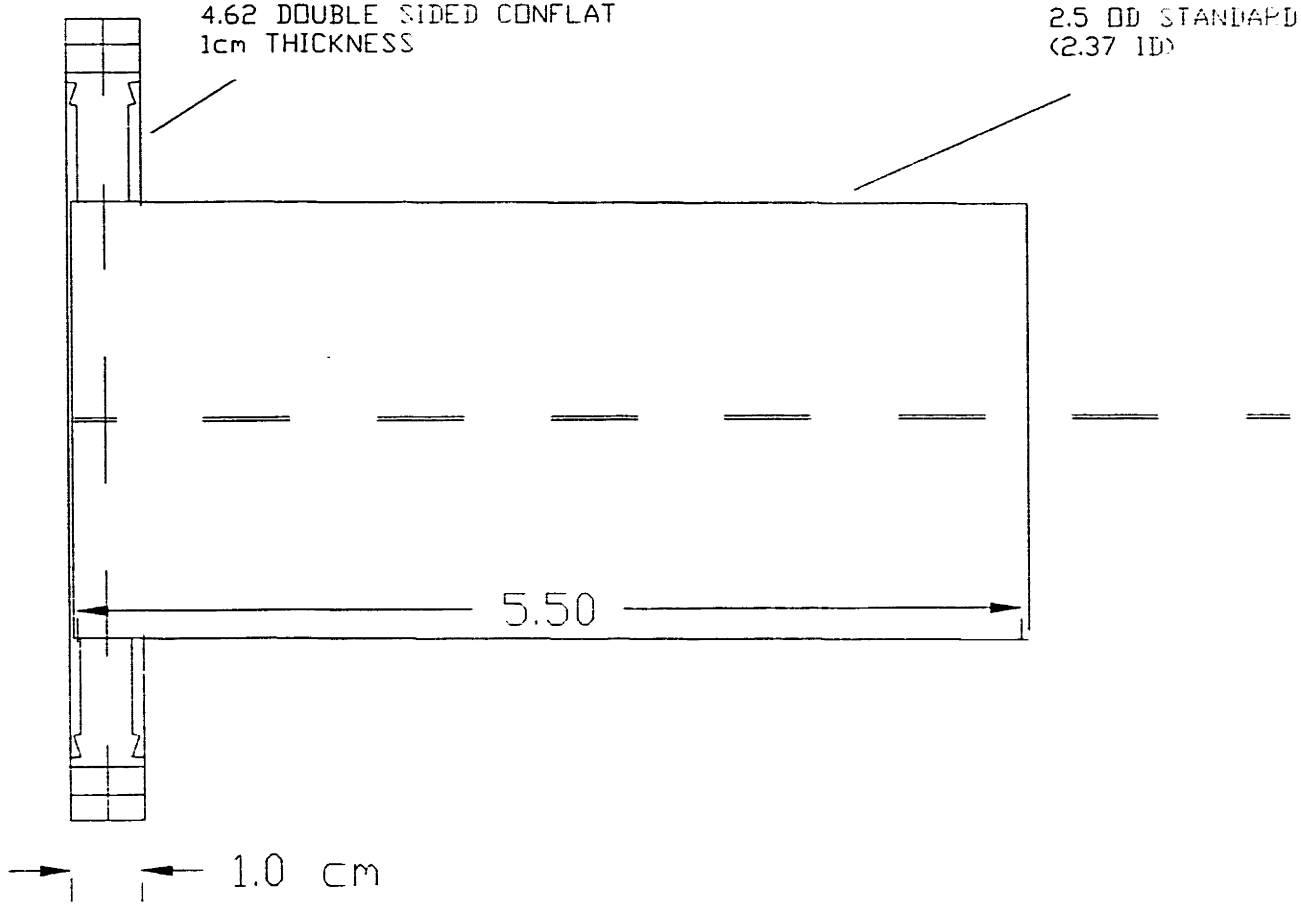

DESIGNER: D.C. GRAY
CONTRACTOR: MDC

COMMENTS: PERPENDICULARITY OF WELD IS CRITICAL

DWG SCALE: 1" = 1"
QUANTITY: 1 REQUIRED

MATERIAL: 4.62" FLANGE BLANK
2.5" OD SS TUBING

1 OF 1

TOLERANCES:
X.X = +/- 050
X.XX = +/- 010
X.XXX = +/- 002

MIT DEPT. OF CHEMICAL ENGINEERING
CAMBRIDGE, MASSACHUSETTS 02139
Bldg. 66-221 METL LAB (617) 253-6587

PART: ION GUN SHIELD CAP

CODE: 3B.51 REVISION: 6/20/91

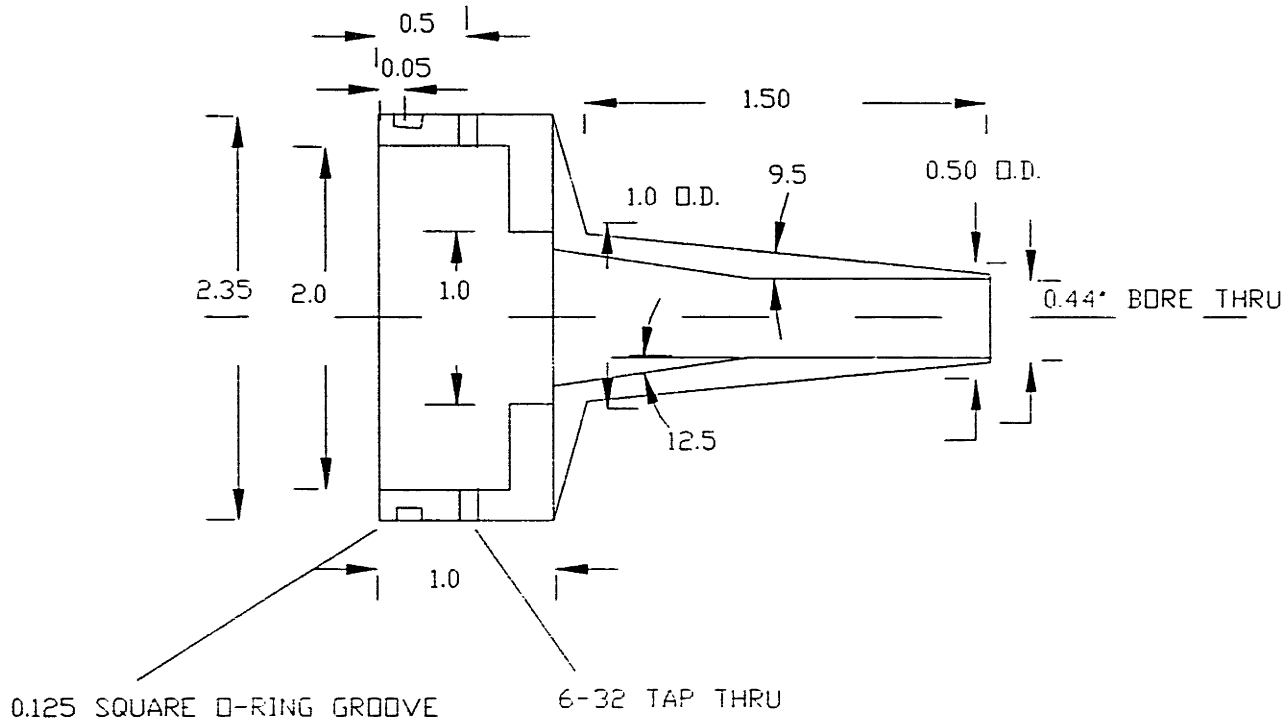

DESIGNER: D.C. GRAY
CONTRACTOR:

COMMENTS:

DWG SCALE: 1" = 1"
QUANTITY: 1 REQUIRED

MATERIAL: 6061 AL

1 OF 1

TOLERANCES:
X.X = +/-.050
X.XX = +/-.010
X.XXX = +/-.002

458

MIT DEPT. OF CHEMICAL ENGINEERING

CAMBRIDGE, MASSACHUSETTS 02139
Bldg. 66-221 METL LAB (617) 253-6587

PART: ECT ADAPTER ASSEMBLY

CODE: 3B.61 REVISION: 11/9/90 FINAL

CROSS SECTION A-A'

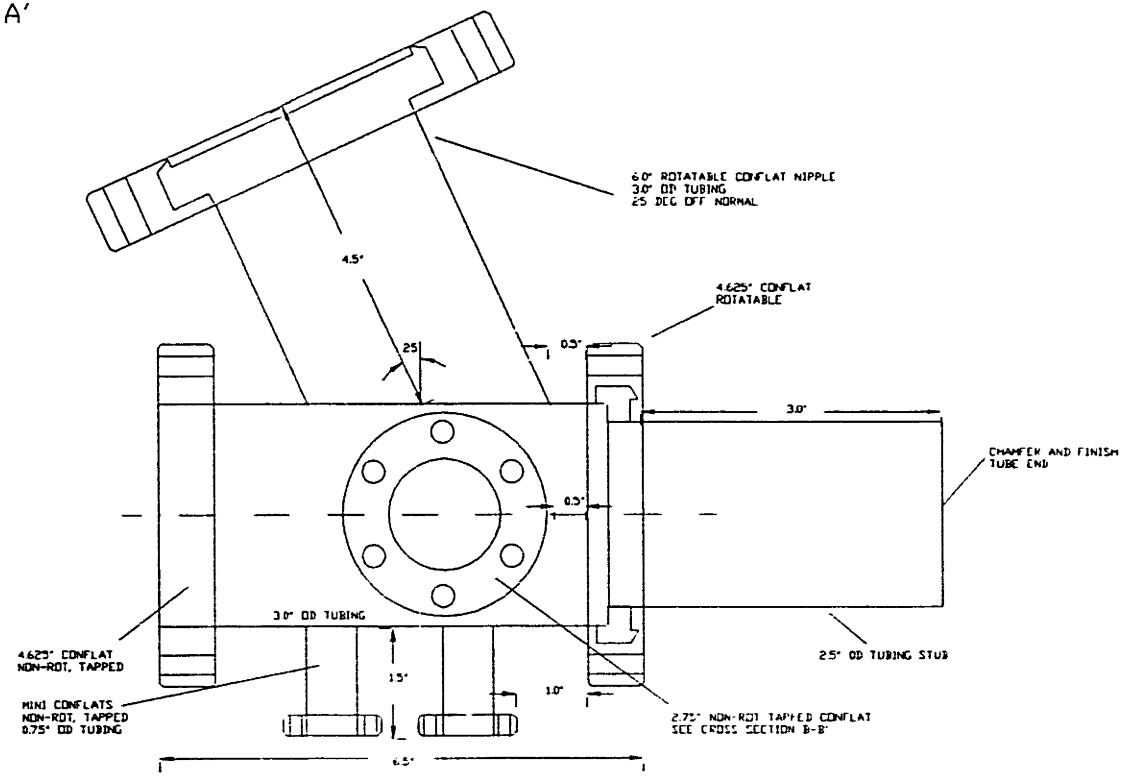

DESIGNER: D.C. GRAY
CONTRACTOR: MDC

COMMENTS:

DWG SCALE:
QUANTITY: 1

MATERIAL:

1 OF 3

TOLERANCES:
X.X = +/-.050
X.XX = +/-.010
X.XXX = +/-.002

MIT DEPT. OF CHEMICAL ENGINEERING CAMBRIDGE, MASSACHUSETTS 02139 Bldg. 66-221 METL LAB (617) 253-6587	PART: ECR ADAPTER ASSEMBLY CODE: 3B.62 REVISION: 11/9/90 FINAL

CROSS-SECTION B-B'

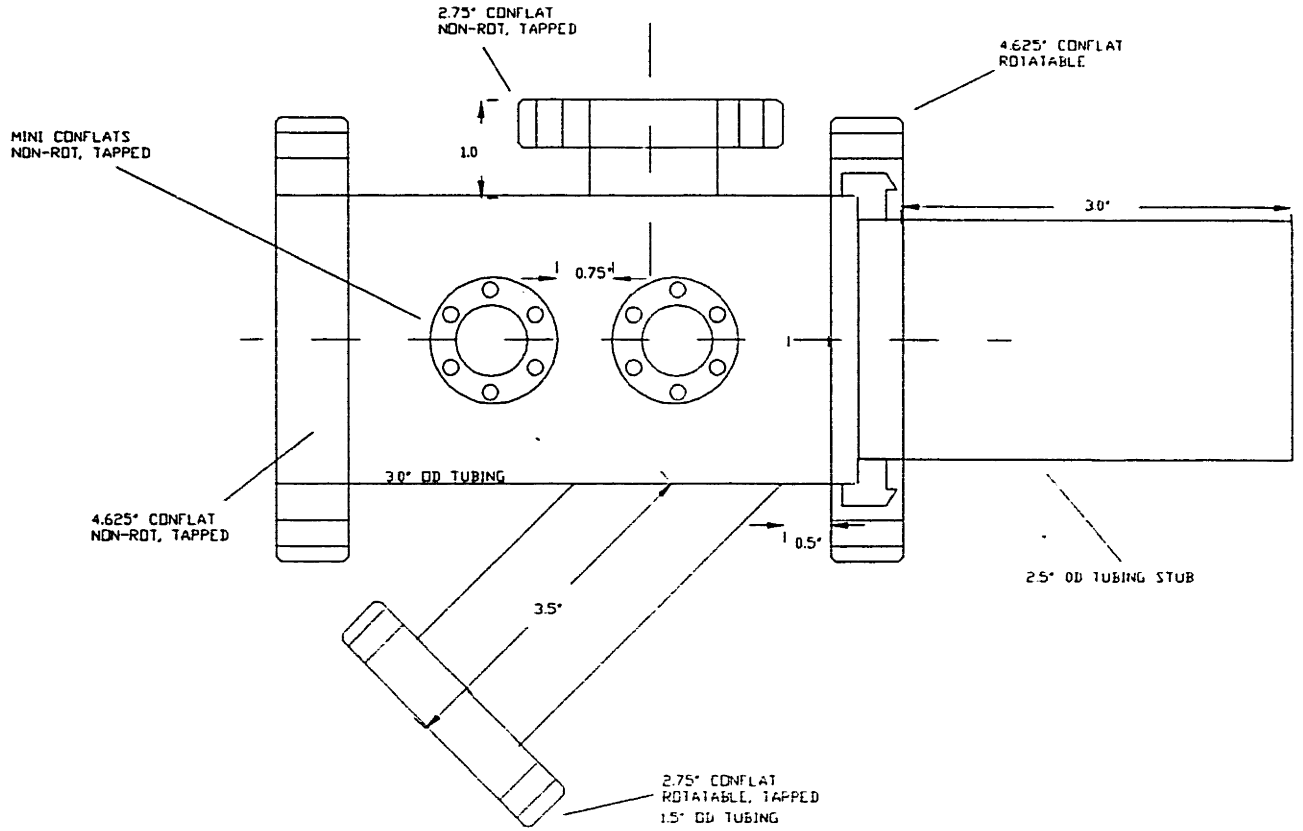

DESIGNER: D.C. GRAY CONTRACTOR: MDC COMMENTS:	DWG SCALE: QUANTITY: 1 MATERIAL:	2 OF 3 TOLERANCES: X.X = +/- 050 X.XX = +/- 010 X.XXX = +/- 002

MIT DEPT. OF CHEMICAL ENGINEERING

CAMBRIDGE, MASSACHUSETTS 02139
Bldg. 66-221 METL LAB (617) 253-6587

PART: ECR ADAPTER ASSEMBLY

CODE: 3B.64 REVISION: 11/9/90 FINAL

VIEW END ON
FROM NON-ROT SIDE

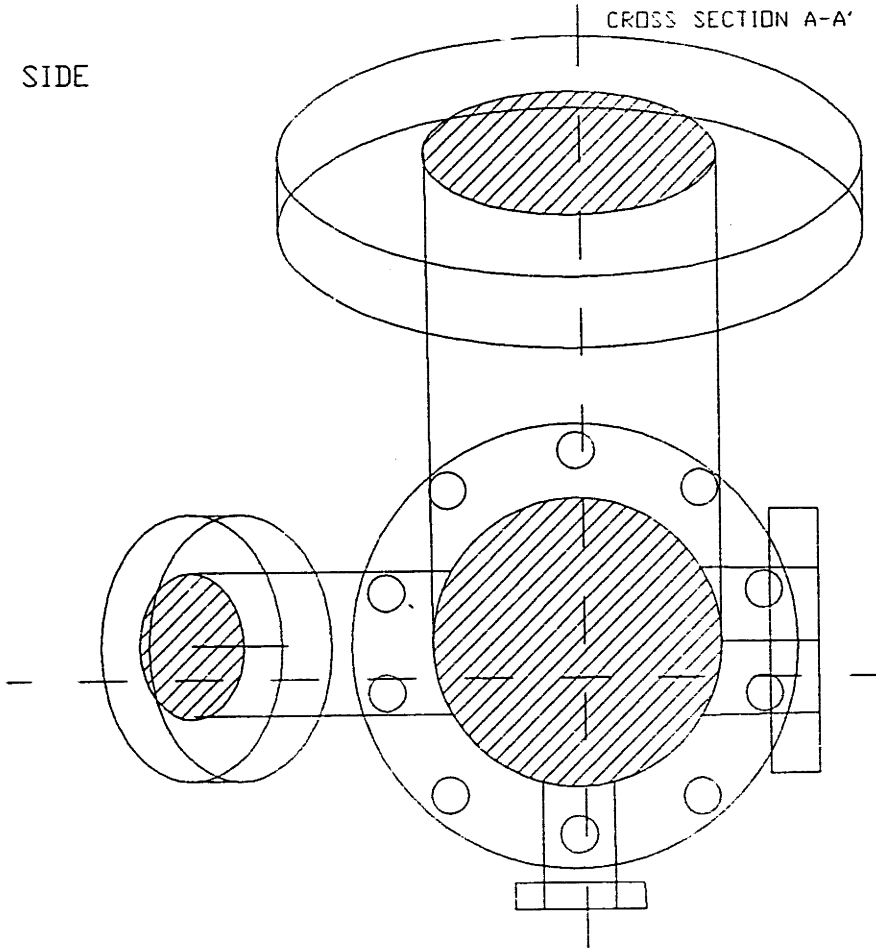

DESIGNER: D.C. GRAY
CONTRACTOR: MDC

COMMENTS:

DWG SCALE:
QUANTITY: 1

MATERIAL:

3 OF 3

TOLERANCES:
X.X = +/-.050
X.XX = +/-.010
X.XXX = +/-.002

MIT DEPT. OF CHEMICAL ENGINEERING CAMBRIDGE, MASSACHUSETTS 02139 Bldg. 66-221 METL LAB (617) 253-6587	PART: ECR ADAPTER NIPPLE CODE: 3B.65 REVISION: 11/9/90 FINAL

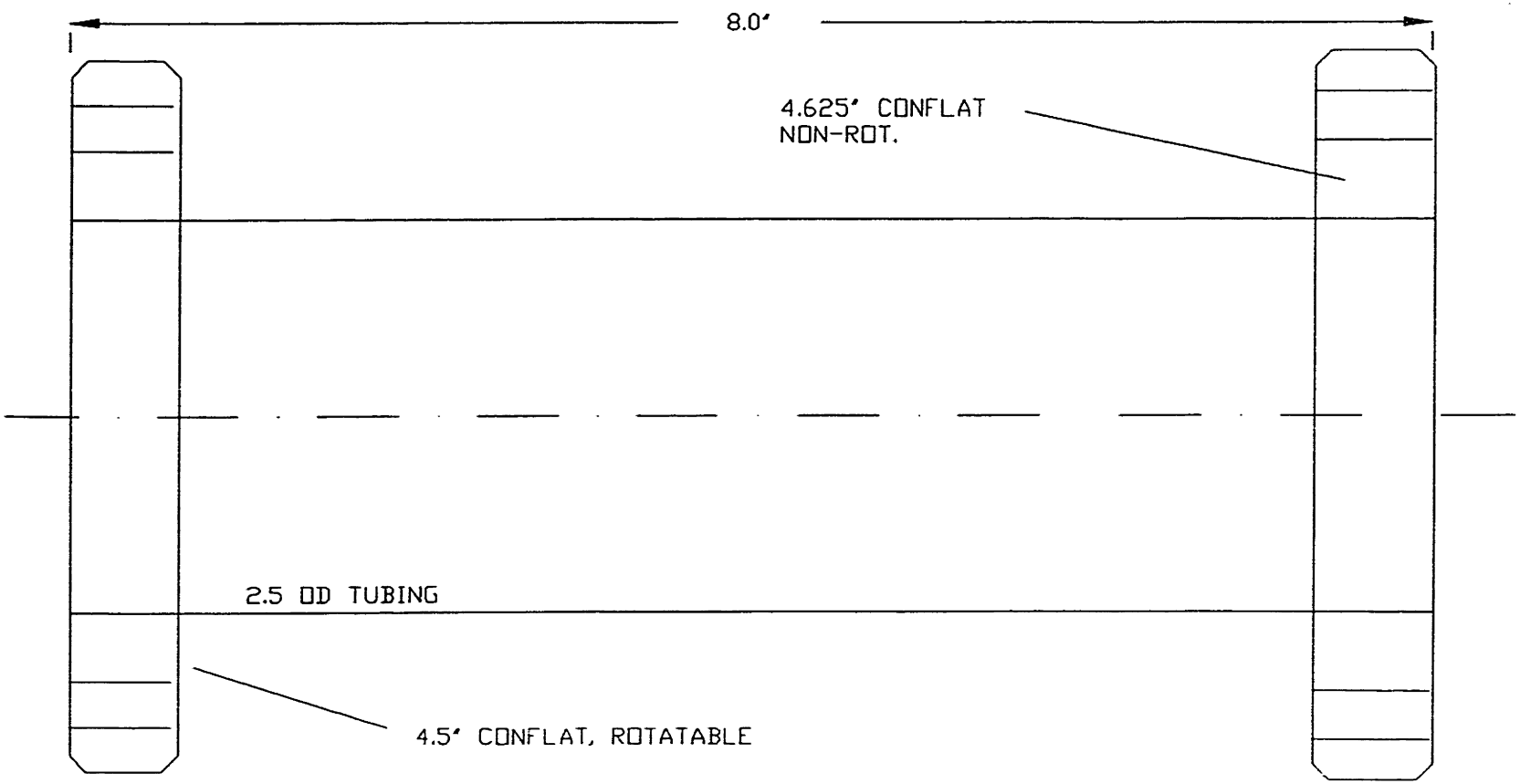

DESIGNER: D.C. GRAY CONTRACTOR: MDC COMMENTS:	DWG SCALE: QUANTITY: MATERIAL:	1 OF 1 TOLERANCES: X.X +/-.05 X.XX +/-.010 X.XXX +/-.00

MIT DEPT. OF CHEMICAL ENGINEERING
CAMBRIDGE, MASSACHUSETTS 02139
Bldg. 66-221 METL LAB (617) 253-6587

PART: KAUFMAN GUN EXTENSION RODS

CODE: 3B.66 REVISION: 6/20/91

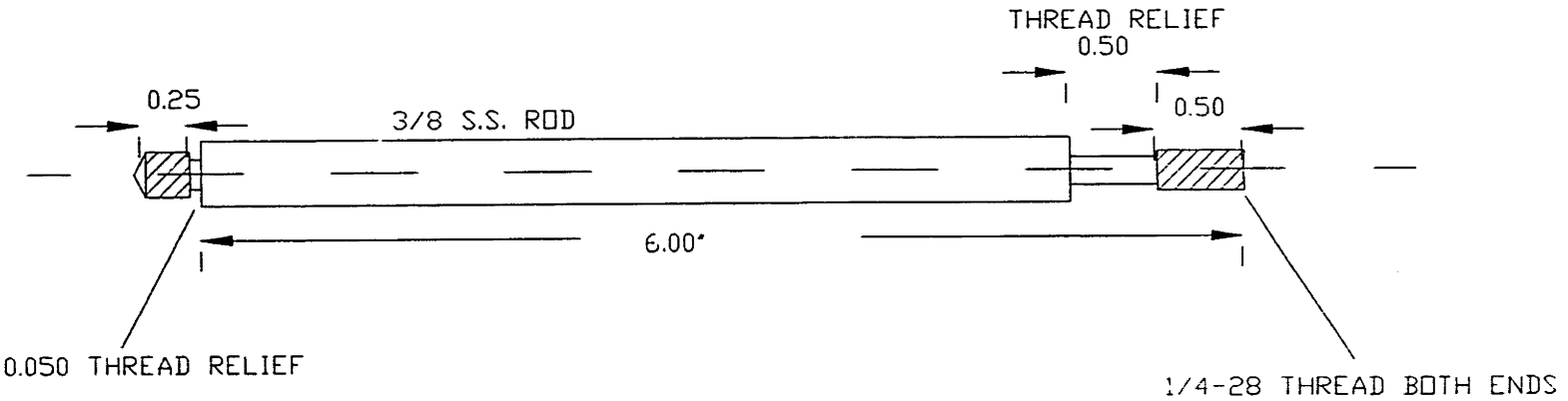

DESIGNER: D.C. GRAY
CONTRACTOR: MIT CHEM.E. SHOP

COMMENTS:

DWG SCALE: 1" = 1"
QUANTITY: 3 REQUIRED

MATERIAL: 3/8 S.S. ROD STOCK

1 OF 1

TOLERANCES:
X.X = +/- 050
X.XX = +/- 010
X.XXX = +/- 002

MIT DEPT. OF CHEMICAL ENGINEERING CAMBRIDGE, MASSACHUSETTS 02139 Bldg. 66-221 METL LAB (617) 253-6587	PART: KAUFMAN GUN EXTENSION MOUNT CODE: 3B.67 REVISION: 6/20/91

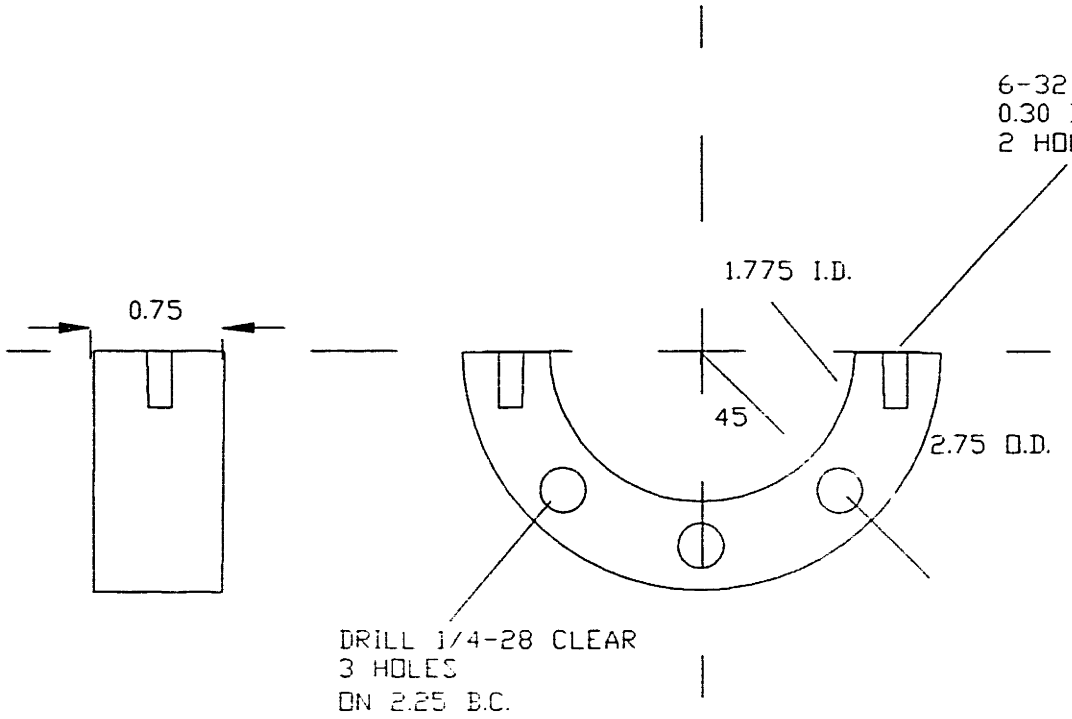

DESIGNER: D.C. GRAY CONTRACTOR: MIT CHEM.E. SHOP COMMENTS:	DWG SCALE: 1" = 1" QUANTITY: 1 REQUIRED MATERIAL: 6061 AL	1 OF 1 TOLERANCES: X.X = +/-.050 X.XX = +/-.010 X.XXX = +/-.002

MIT DEPT. OF CHEMICAL ENGINEERING

PART: SPECIAL GV2500V AND GV3000V GATE VALVES

CODE: 38.68 FILE NO: 3-BEAM

SPECIAL GV2500V

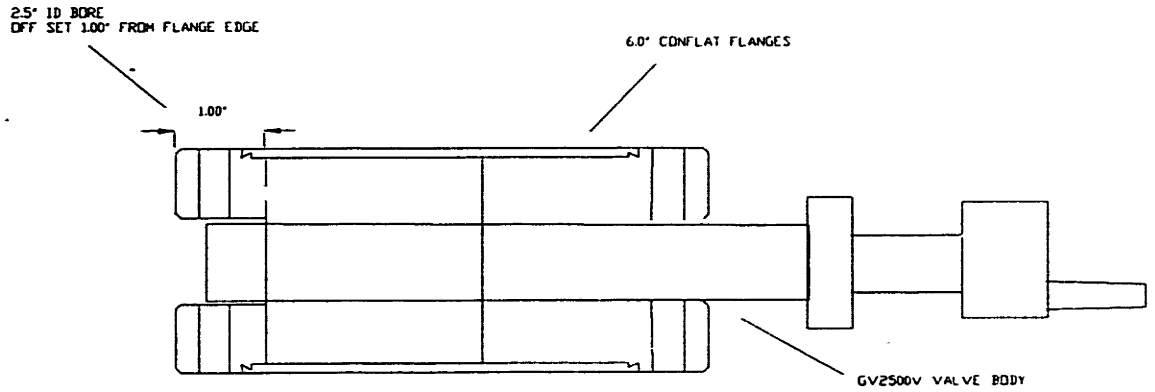

SPECIAL GV3000V

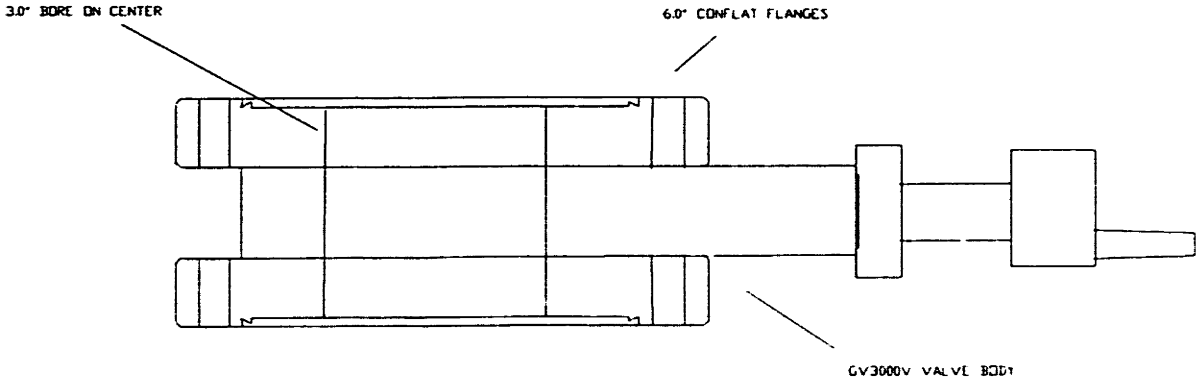

DESIGNER: D.C. GRAY

CONTRACTOR: MDC

COMMENTS:

DWG SCALE: SCALE

QUANTITY: 1

MATERIAL

TOLERANCES:

MIT DEPT. OF CHEMICAL ENGINEERING
CAMBRIDGE, MASSACHUSETTS 02139
Bldg. 66-221 METL LAB (617) 253-6587

PART: SHORT ECR ADAPTER

CODE: 3B.69 REVISION: 7/15/91

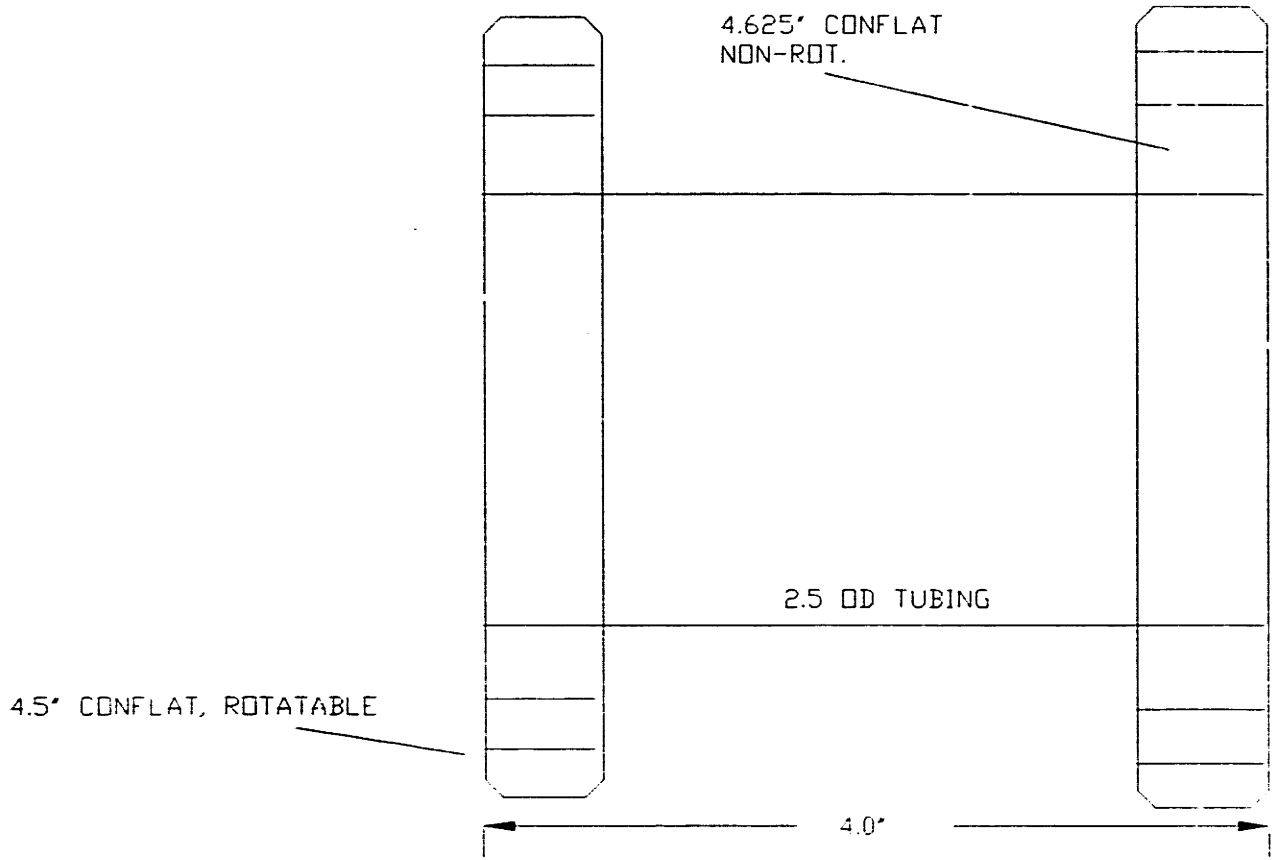

DESIGNER: D.C. GRAY
CONTRACTOR: SHARON VACUUM

COMMENTS:

DWG SCALE:
QUANTITY: 1 REQUIRED

MATERIAL: MODIFY CURRENT ADAPTER

1 OF 1

TOLERANCES
XX = +/- .050
XXX = +/- .010
XXXX = +/- .002

MIT DEPT. OF CHEMICAL ENGINEERING

PART: QCMB MOUNT

CODE: 3B.24 FILE NO: 3-BEAM

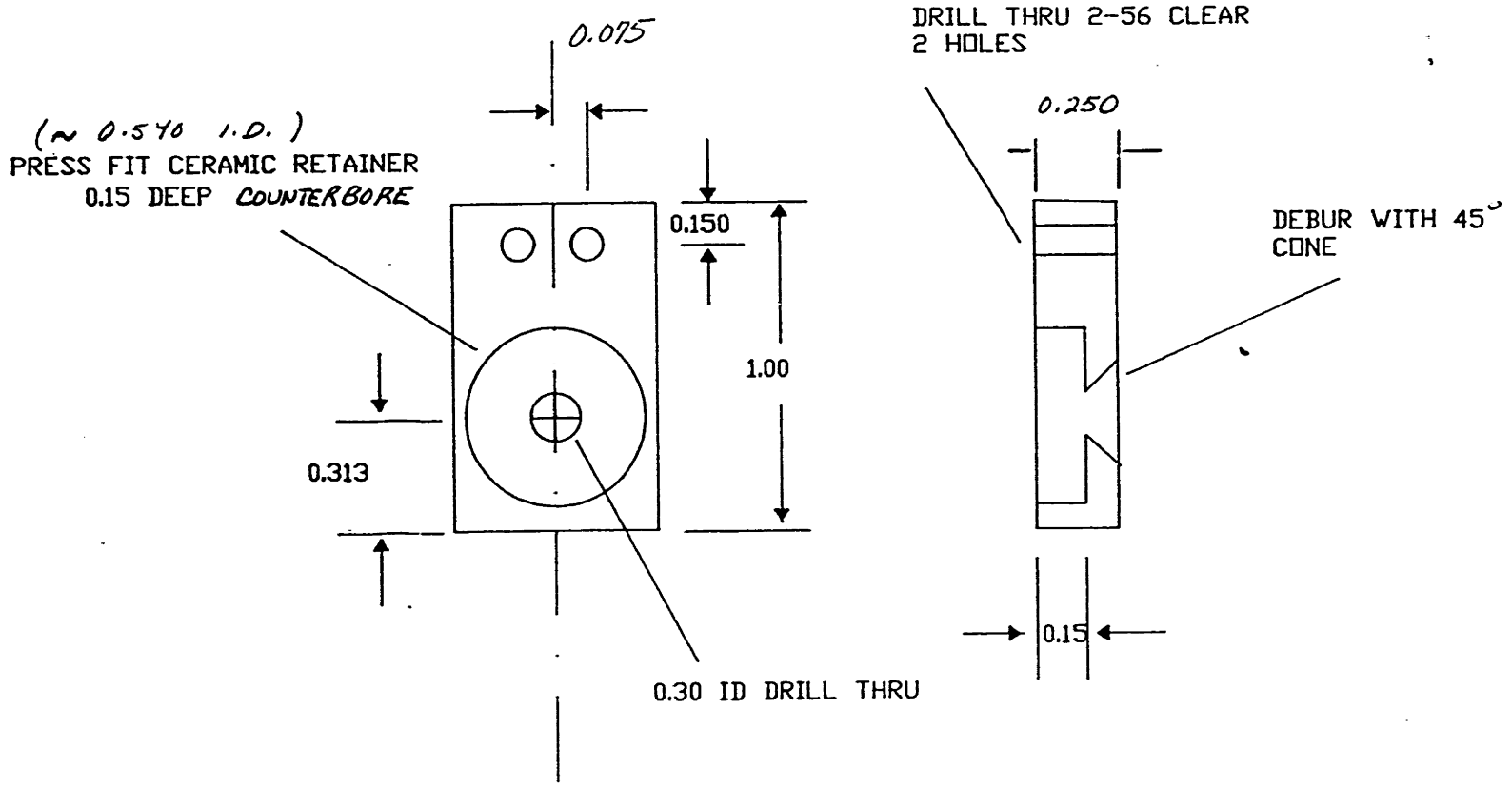

DESIGNER: D.C. GRAY
CONTRACTOR: REACTOR SHOP

COMMENTS: ALL SURFACES AND EDGES FINISHED AND DEBURRED

DWG SCALE: 2" = 1"
QUANTITY: 1

MATERIAL: 6061 ALUMINUM 0.25" PLATE

1 OF 1

TOLERANCES:
X.X = +/-.050
X.XX = +/-.010
X.XXX = +/-.002

MIT DEPT. OF CHEMICAL ENGINEERING

PART: QCMB MOUNTING ROD

CODE: 3B.25 FILE NO: 3-BEAM

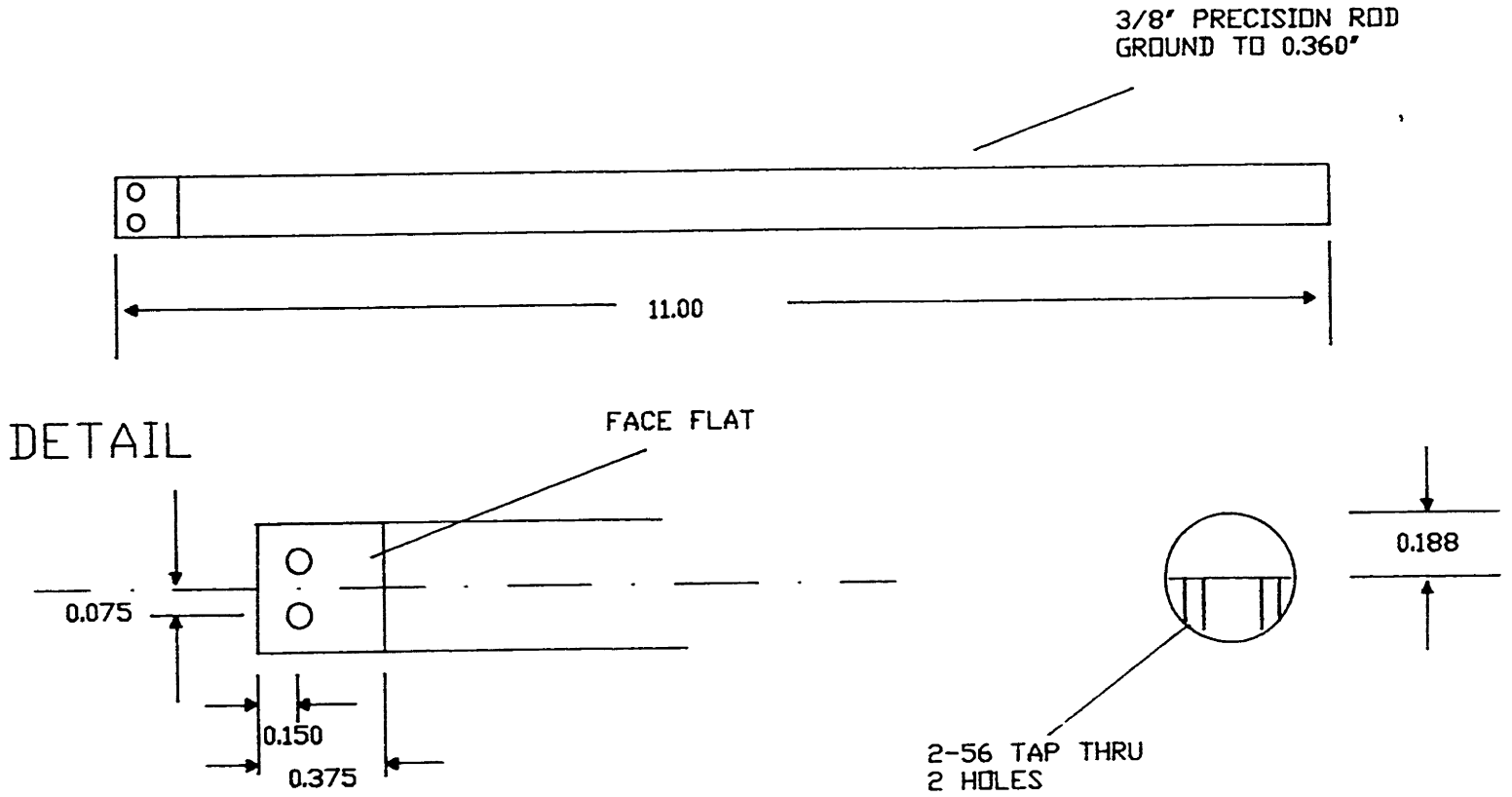

DESIGNER: DAVID C. GRAY
CONTRACTOR: REACTOR SHOP

COMMENTS:

DWG SCALE: NTS
QUANTITY: 1 REQUIRED

MATERIAL: 3/8" SS PRECISION GROUND ROD

1 OF 1

TOLERANCES:
X.X = +/-.050
X.XX = +/-.010
X.XXX = +/-.002

MIT DEPT. OF CHEMICAL ENGINEERING
CAMBRIDGE, MASSACHUSETTS 02139
Bldg. 66-221 METL LAB (617) 253-6587

PART: QCM MOUNTING PIN

CODE: 3B.72 REVISION: 9/1/91

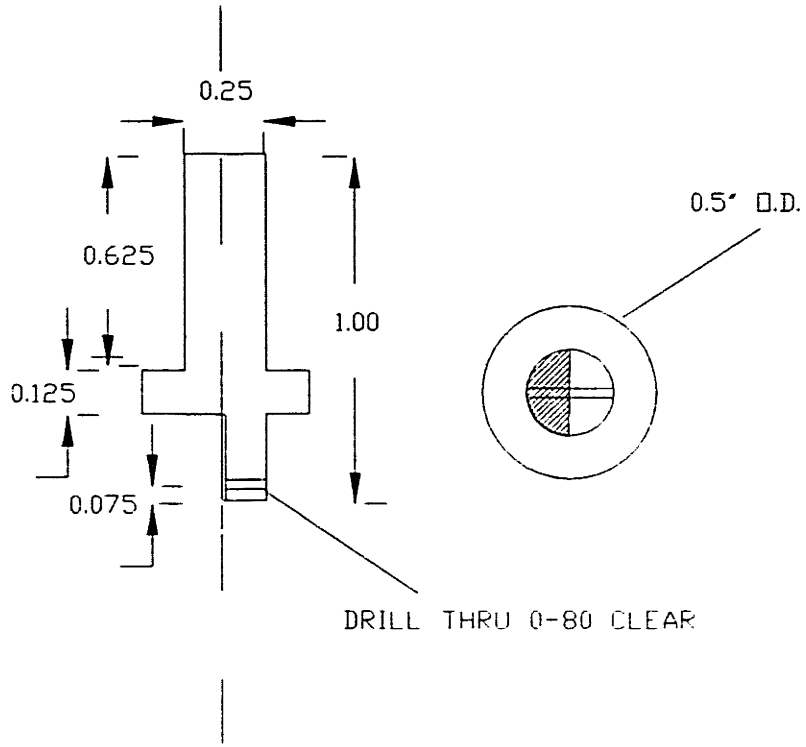

DESIGNER: D.C. GRAY
CONTRACTOR: CHEM ENG MACHINE SHOP

COMMENTS:

DWG SCALE: 2" = 1"
QUANTITY: 1

MATERIAL: STAINLESS STEEL

1 OF 1

TOLERANCES:
XX = +/- 050
XXX = +/- 010
XXXX = +/- 002

MIT DEPT. OF CHEMICAL ENGINEERING
CAMBRIDGE, MASSACHUSETTS 02139
Bldg. 66-221 METL LAB (617) 253-6587

PART: QCM MOUNTING BRACKET

CODE: 3B.73 REVISION: 9/1/91

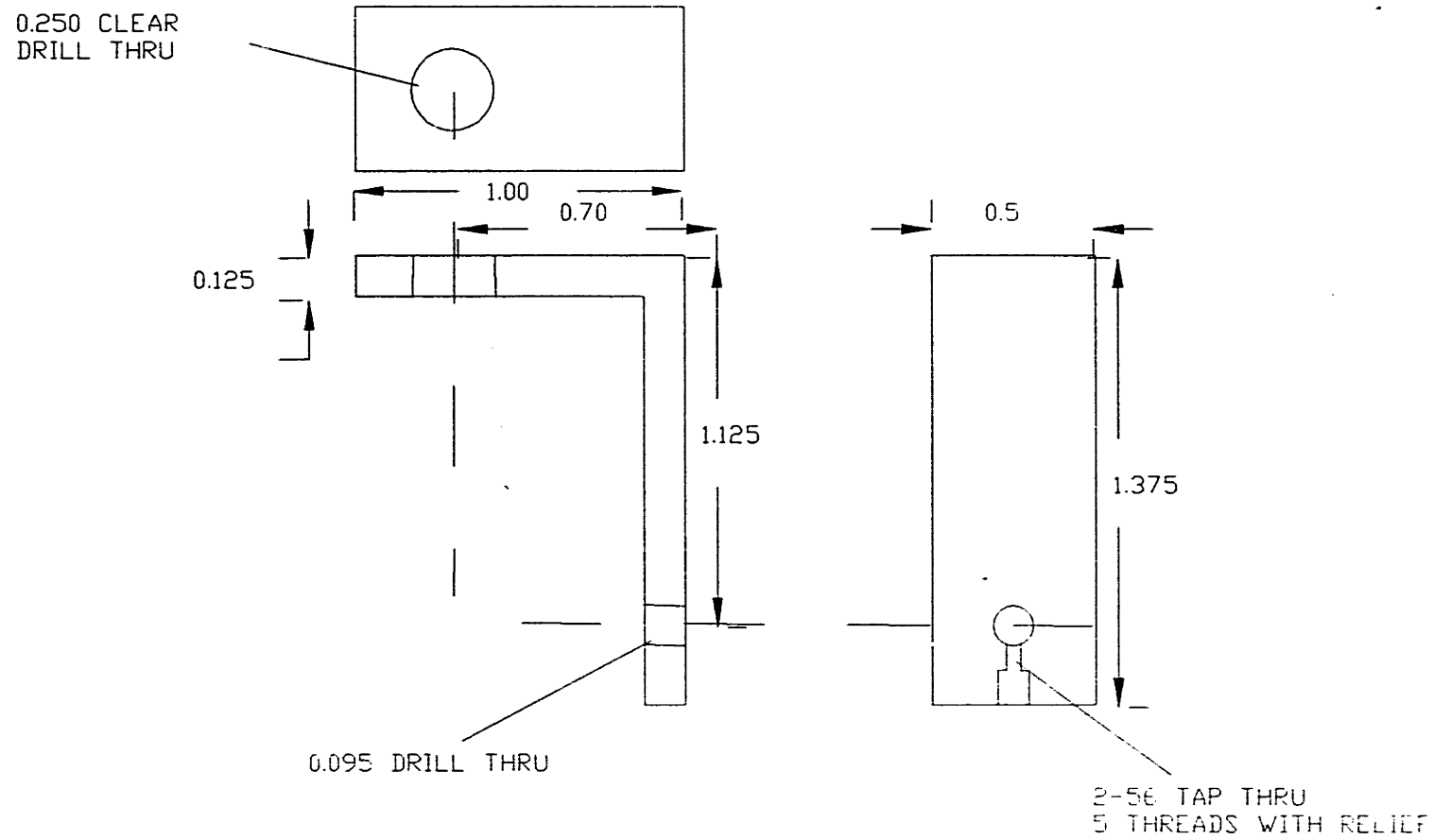

DESIGNER: D.C. GRAY
CONTRACTOR: CHEM ENG SHOP

COMMENTS:

DWG SCALE: 2" = 1"
QUANTITY: 1

MATERIAL: STAINLESS STEEL

1 OF 1

TOLERANCES:
X.X = +/-.050
X.XX = +/-.020
X.XXX = +/-.002

MIT DEPT. OF CHEMICAL ENGINEERING CAMBRIDGE, MASSACHUSETTS 02139 Bldg. 66-221 METL LAB (617) 253-6587	PART: QCM PIN RETAINER CODE: 3B.74 REVISION: 9/1/91

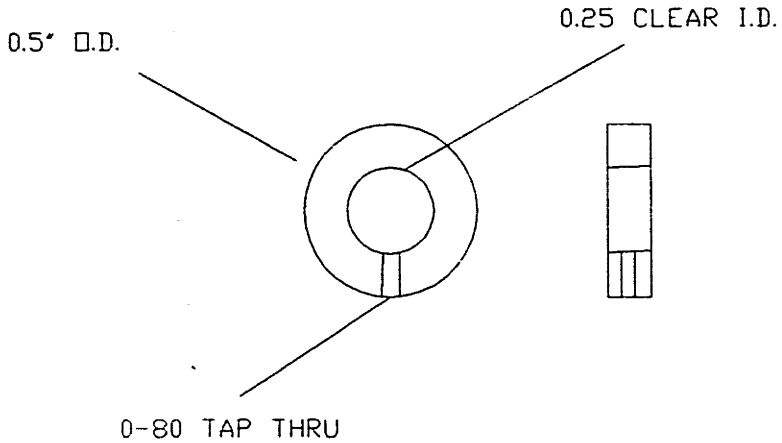

DESIGNER: D.C. GRAY CONTRACTOR: CHEM ENG SHOP COMMENTS:	DWG SCALE: 2"=1" QUANTITY: 1 MATERIAL: 6061 AL	1 OF 1 TOLERANCES: X.X = +/-.050 X.XX = +/-.010 X.XXX = +/-.002

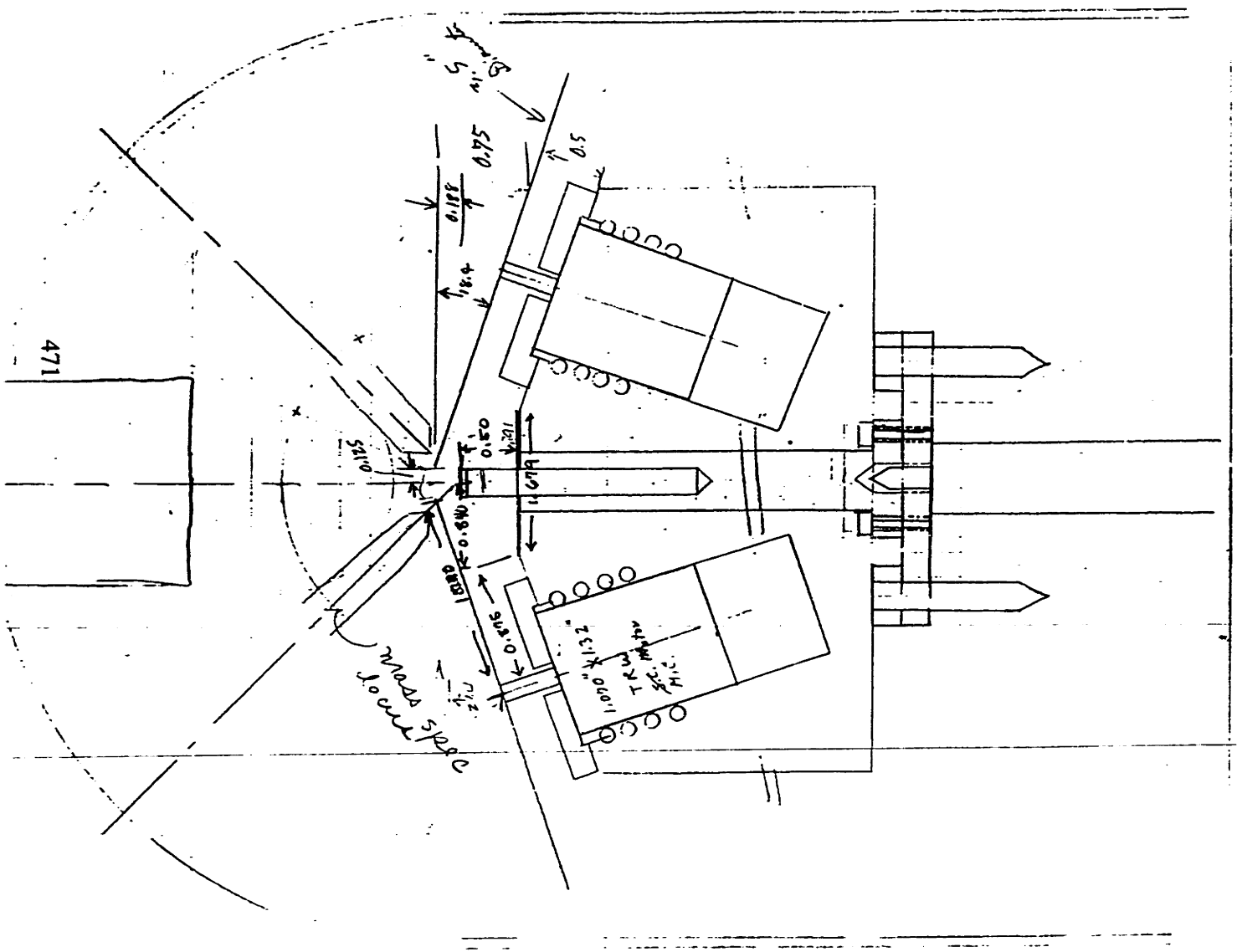

MIT CHEMICAL ENGINEERING

GENERAL INFORMATION

SCALE:

SHEET 1 OF 1

DIMENSIONS ARE IN INCHES

REVISION NO: 10

DESIGNED BY: DAVID C. GRAY
DRAFTED BY: DAVID C. GRAY

PRIMARY ASSEMBLY: 3-BEAM REACTOR
SECONDARY ASSEMBLY:

DRAWING TYPE: STANDARD MACHINE

MTL:

ITEM IDENTIFICATION

NAME: CHAMBER ORIGINALS
CODE:

FILE:

DESCRIPTION:

TOLERANCE SPECIFICATIONS

X	+/- .05	XX	+/- .02
XXX	+/- .005	XXXX	+/- .0005
X/XX	+/- 1/64	ANGULAR	+/- 1°

FLATNESS: .010 TOTAL
PERPENDICULARITY: .001 PER INCH
PARALLELISM: .005 TOTAL

I.D.'S TO BE WITHIN .002 T.I.R.

1) FINISHING MARKS CONFORM TO AMERICAN STANDARD CONVENTIONS.
2) BREAK ALL SHARP EDGES: .005 - .015
3) REMOVE ALL BURRS. LEAVE NO HEAVY ROLL, FILE, TOOL OR CHATTER MARKS.

LEGAL NOTES:

CONTRACTOR INFORMATION:

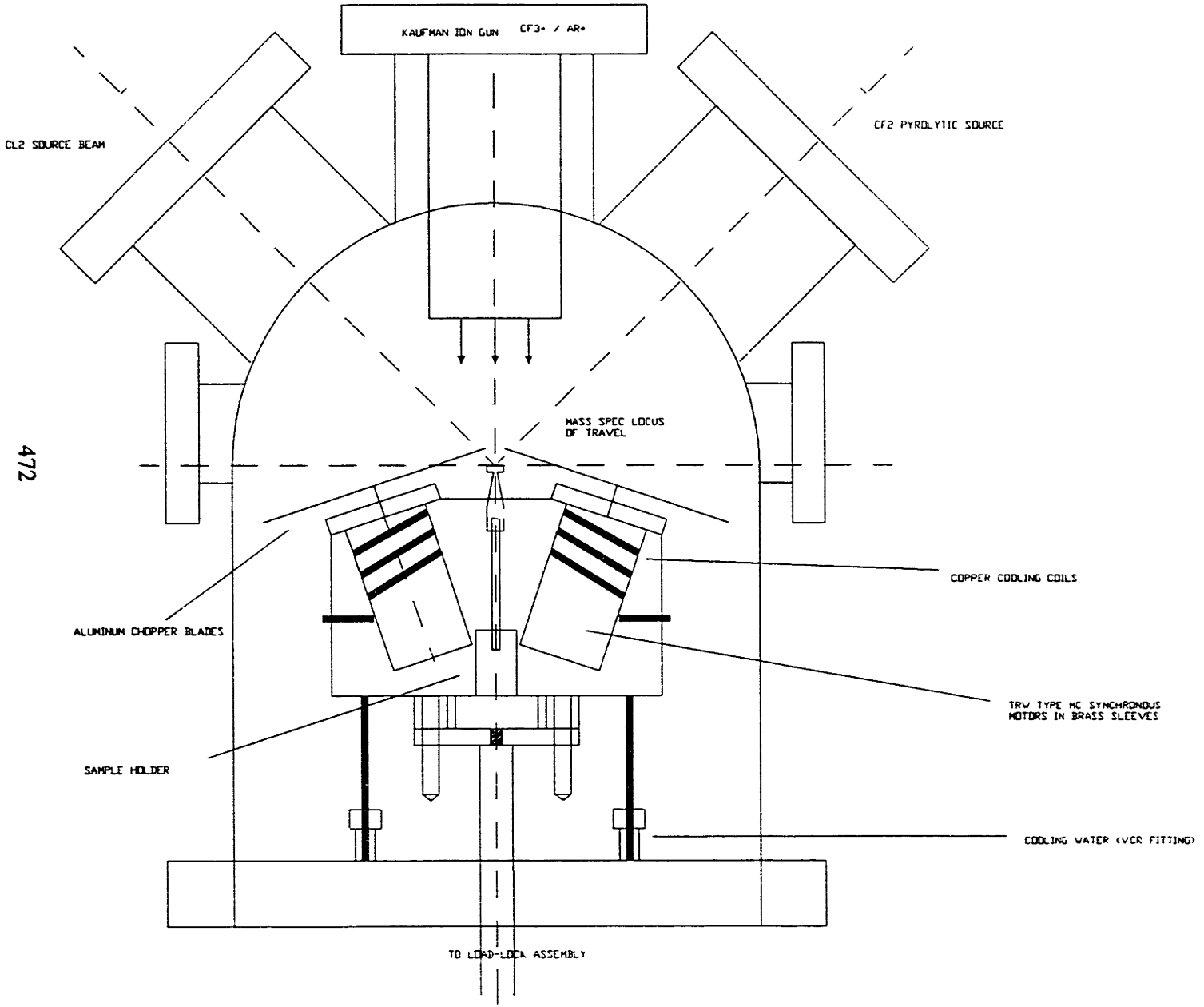

472

MIT CHEMICAL ENGINEERING

GENERAL INFORMATION

SCALE:

SHEET 1 OF 1

DIMENSIONS ARE IN INCHES

REVISION NO: 15

DESIGNED BY: DAVID C. GRAY
DRAFTED BY: DAVID C. GRAY

PRIMARY ASSEMBLY: 3-BEAM REACTOR
SECONDARY ASSEMBLY:

DRAWING TYPE: STANDARD MACHINE

ITEM IDENTIFICATION

NAME: CHOPPER MOTOR ASSEMBLY
CODE: COMP5.DWG

FILE: 3-BEAM

DESCRIPTION:

TOLERANCE SPECIFICATIONS

X	+/- .05	XX	+/- .02
XXX	+/- .005	XXXX	+/- .0005
X/XX	+/- 1/64	ANGULAR	+/- 1°

FLATNESS: .010 TOTAL
PERPENDICULARITY: .001 PER INCH
PARALLELISM: .005 TOTAL

I.D.'S TO BE WITHIN .002 TLR

1) FINISHING MARKS CONFORM TO AMERICAN STANDARD CONVENTIONS
2) BREAK ALL SHARP EDGES: .003 - .015
3) REMOVE ALL BURRS LEAVE NO HEAVY MILL FILE TOOL OR CHATTER MARKS

LEGAL NOTES:

CONTRACTOR INFORMATION:

MIT DEPT. OF CHEMICAL ENGINEERING

PART: CHOPPER MOTOR MOUNTS

CODE: 3B.9 FILE NO: 3-BEAM

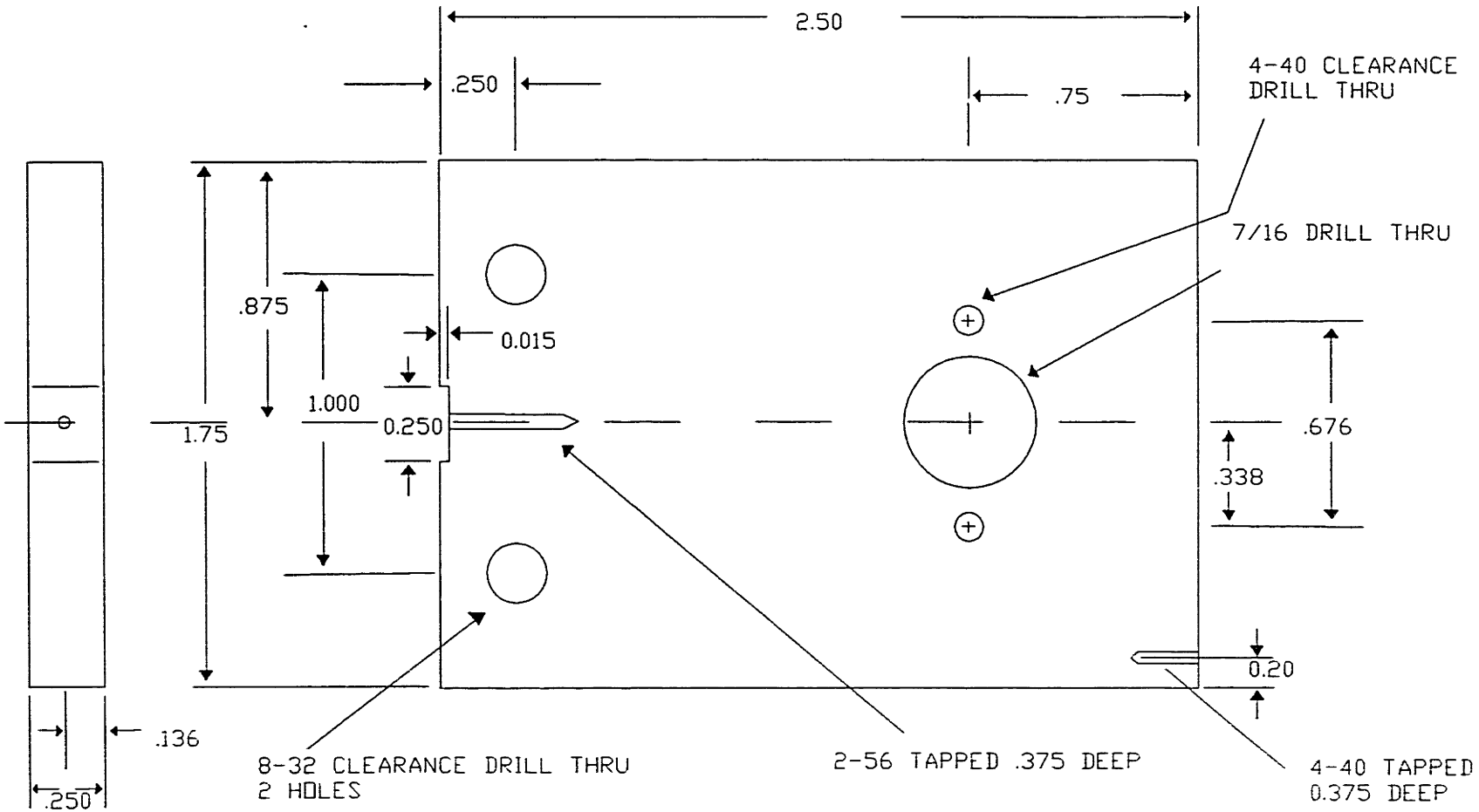

DESIGNER: D.GRAY H.SAWIN
CONTRACTOR: LNS MACHINE SHOP

COMMENTS:

REVISION 4/25/89

DWG SCALE: 2" = 1"
QUANTITY: 2

MATERIAL: .25 ALUMINUM PLATE
6061

1 OF 1

TOLERANCES:
X.X = ±.050
X.XX = ±.010
X.XXX = ±.001

MIT DEPT. OF CHEMICAL ENGINEERING

PART: CHOPPER BLADE 50% DUTY CYCLE

CODE: 3B.11 FILE NO: 3-BEAM

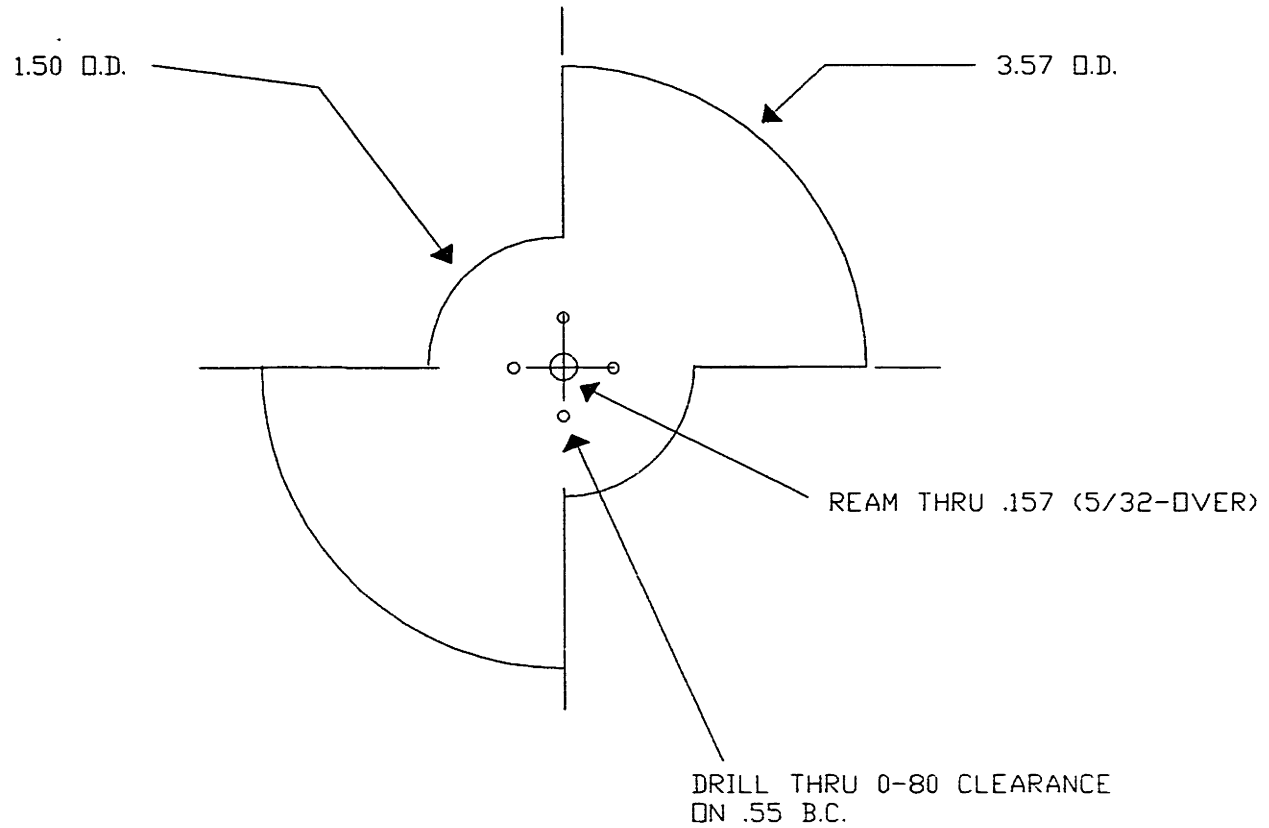

DESIGNER: D.GRAY H.SAWIN
CONTRACTOR: CHEM. ENG. MACHINE SHOP

COMMENTS:

REVISION 4/25/89

DWG SCALE: 1" = 1"
QUANTITY: 2

MATERIAL: 1/32 ALUMINUM PLATE
6061

1 OF 1

TOLERANCES:
X.X = ± .50
X.XX = ± .010
X.XXX = ± .001

MIT DEPT. OF CHEMICAL ENGINEERING

PART: CHOPPER BLADE COLLAR

CODE: 3B.12 FILE NO: 3-BEAM

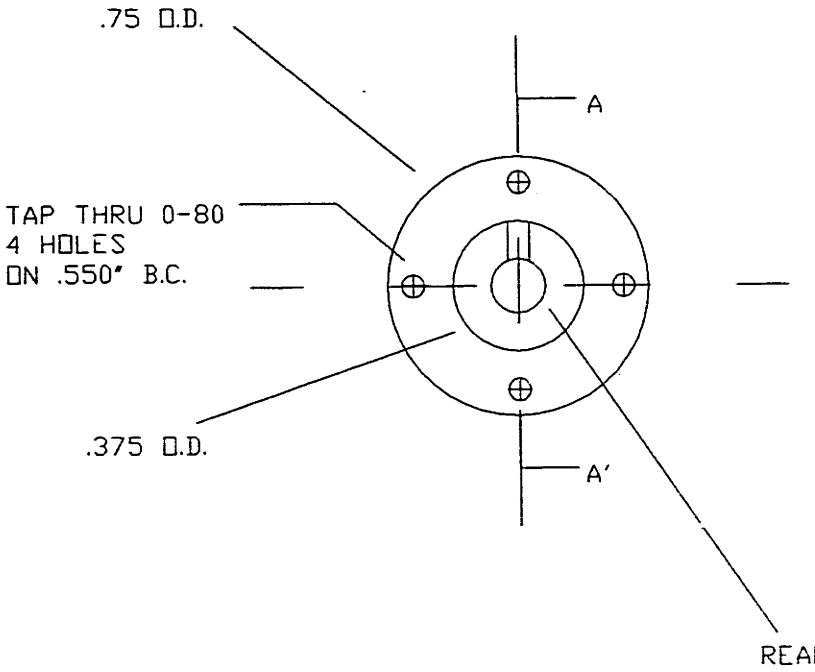

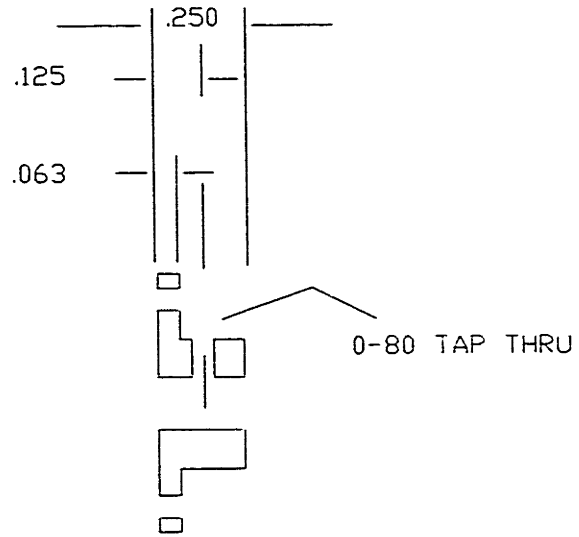

CROSS SECTION A-A'

DESIGNER: D.GRAY H.SAWIN

CONTRACTOR: LNS MACHINE SHOP

COMMENTS:

REVISION 4/25/89

DWG SCALE: 2" = 1"

QUANTITY: 2

MATERIAL: .125 AL PLATE 6061

1 OF 1

TOLERANCES:

X.X = ±.050

X.XX = ±.010

X.XXX = ±.001

MIT DEPT. OF CHEMICAL ENGINEERING

CAMBRIDGE, MASSACHUSETTS 02139
Bldg. 66-221 METL LAB (617) 253-6587

PART: CHOPPER MOTOR COOLING SLEAVE

CODE: 3B.79 REVISION: 1/90

476

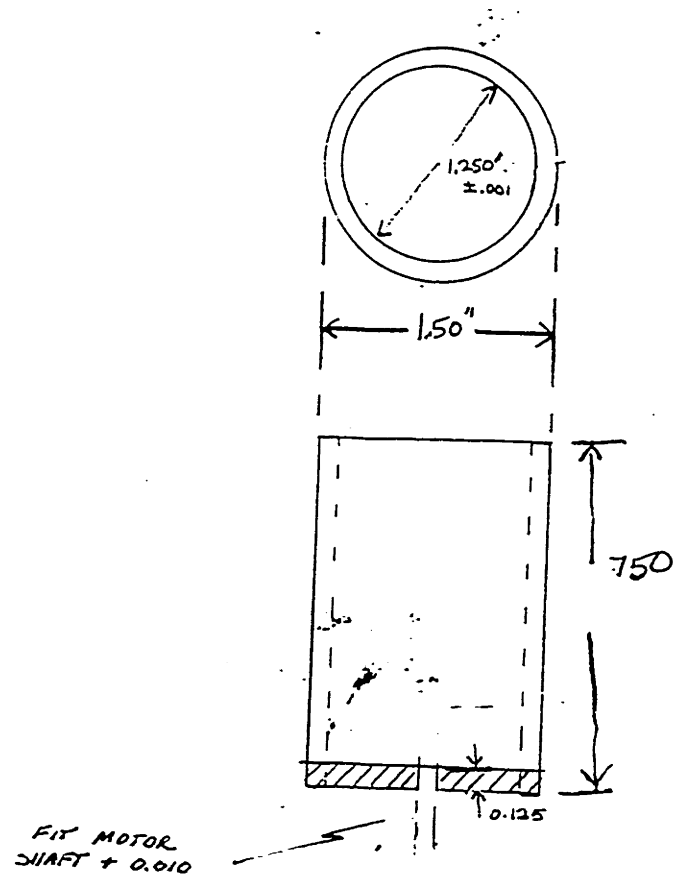

DESIGNER: D.C. GRAY
CONTRACTOR:

COMMENTS:

DWG SCALE:
QUANTITY: 2 REQUIRED

MATERIAL: BRASS

MIT DEPT. OF CHEMICAL ENGINEERING
CAMBRIDGE, MASSACHUSETTS 02139
Bldg. 66-221 METL LAB (617) 253-6587

PART: MOTOR DEPOSITION SHIELD

CODE: 3B.80 REVISION: 1/90

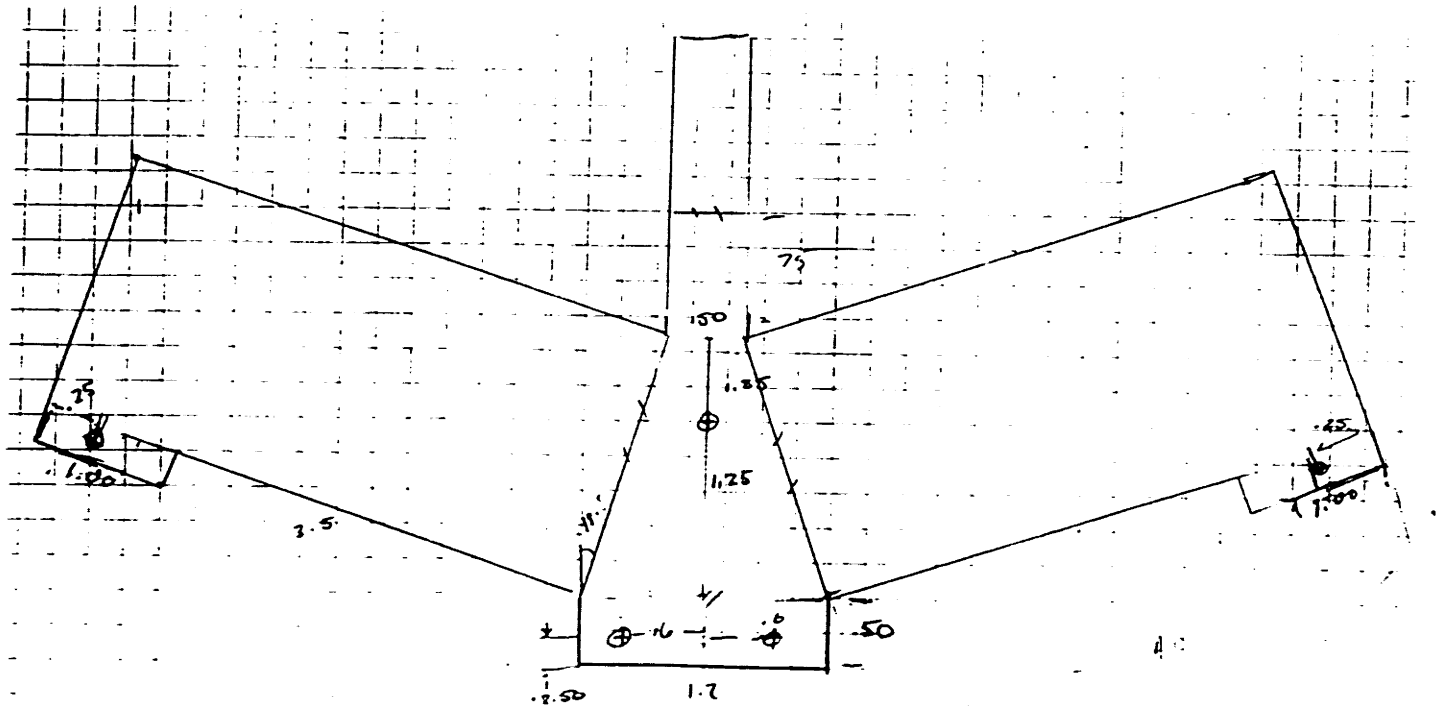

DESIGNER
CONTRACTOR

MIT DEPT. OF CHEMICAL ENGINEERING

PART: BREWSTER WINDOW FLANGES

CODE: 3B.21 FILE NO: 3-BEAM

2.75" ROTATABLE CONFLAT

1.50" O.D. STAINLESS STELL TUBING

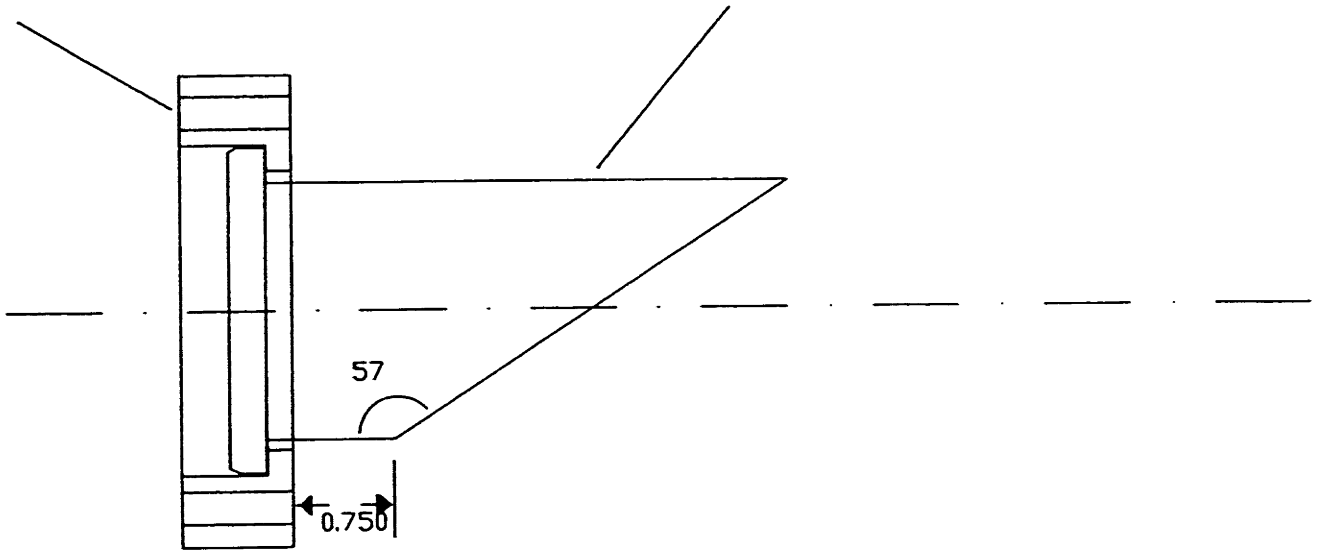

DESIGNER: DAVID C. GRAY
CONTRACTOR:

COMMENTS:

DWG SCALE: 1" = 1"
QUANTITY: 2 REQUIRED

MATERIAL: 1.5" S.S. TUBING
2.75" ROTATABLE CONFLAT

1 OF 1

TOLERANCES:
X.X = +/-.050
X.XX = +/-.010
X.XXX = +/-.002

Appendix B: Reactor Electrical Systems

In this appendix are included detailed schematics for all the major multibeam electrical systems.

Drawings appear in the following order:

B.1 Chamber Connections

B.1-1 Ion Analyzer Power Supply Connectors
B.1-2 Internal Faraday Cup Connector
B.1-3 Sample Mount Electrical Connector
B.1-4 Internal Sample Mount Connector

B.2 Ion Analyzer Power Supply

B.2-1 Power Supply Interconnections
B.2-2 Grid Power Supplies
B.2-3 Digital Panel Meter Voltage Dividers
B.2-4 IBEA- Vector Board Layout
B.2-5 IBEA- Terminal Strip Interconnections
B.2-6 IBEA- Box Layout

B.3 Kaufman Gun Power Supplies

B.3-1 Power Supply Interconnections
B.3-2 Filament Power Supply (FPS)
B.3-3 FPS- Vector Board Layout
B.3-4 FPS- Terminal Strip Interconnections
B.3-5 FPS- Box Layout

B.4 Data Acquisition Interface

B.4-1 Instrument I/O Requirements
B.4-2 Analog Filter Designs
B.4-3 DT2811 50 Pin interface
B.4-4 DAI- Vector Board Layout
B.4-5 DAI- Terminal Strip Interconnections
B.4-6 DAI- Box Layout

ten pin connector (air side)

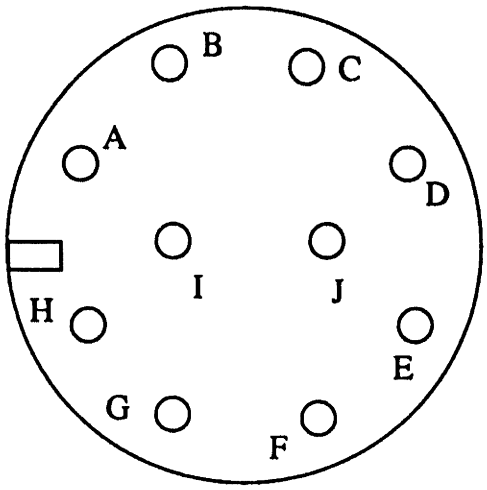

A:
B: G1 (probe face)
C:
D: G2 (ion retard)
E:
F: G3 (electron repeller)
G: (spare)
H:
I: (ion current)
J: (ground)

hexagonal connector to power supply

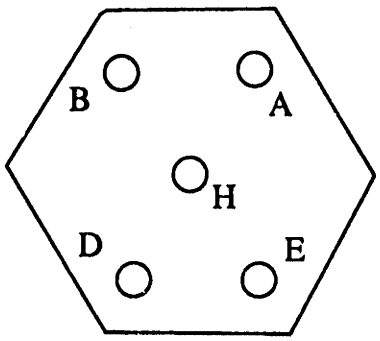

A: G1
B: gnd
H: spare
D: G2
E: G3

B.1-1 Ion Analyzer Power Supply Connectors.

probe side

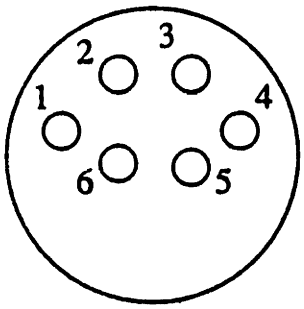

1: G1 (face plate)
2: G2 (retard)
3: spare
4: ion current
5: gnd
6: G3 (repeller)

B.1-2 Internal Faraday Cup Connector

ten pin connector (air side)

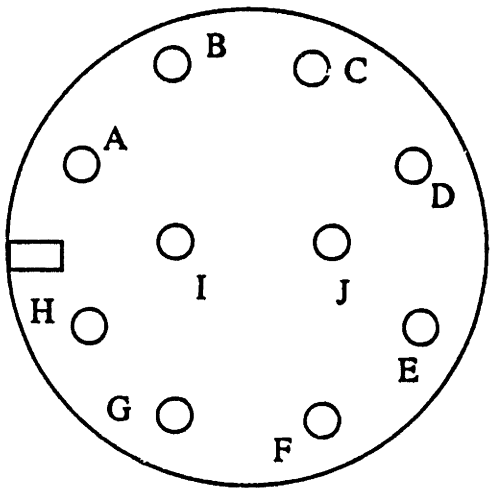

A: DC+ (heater)
B: (spare)
C: (gnd)
D:
E:
F: DC-
G:
H:
I: TC+ (chromel)
J: TC- (alumel)

B.1-3 Sample Mount Electrical Connector.

custom plug-in connector (female side)

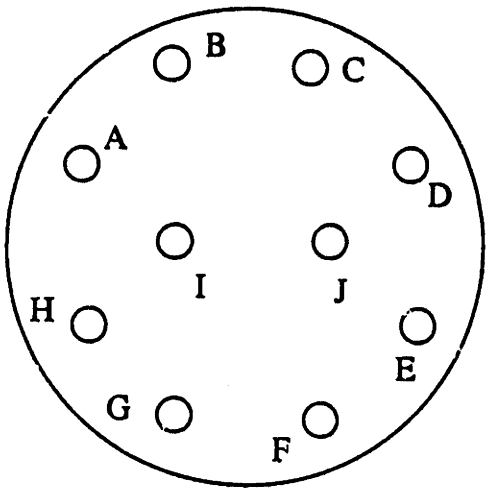

A:
B:
C:
D:
E:
F: DC-
G:
H: DC +
I: TC+ (chromel)
J: TC- (alumel)

B.1-4 Internal Sample Mount Electrical Connector.

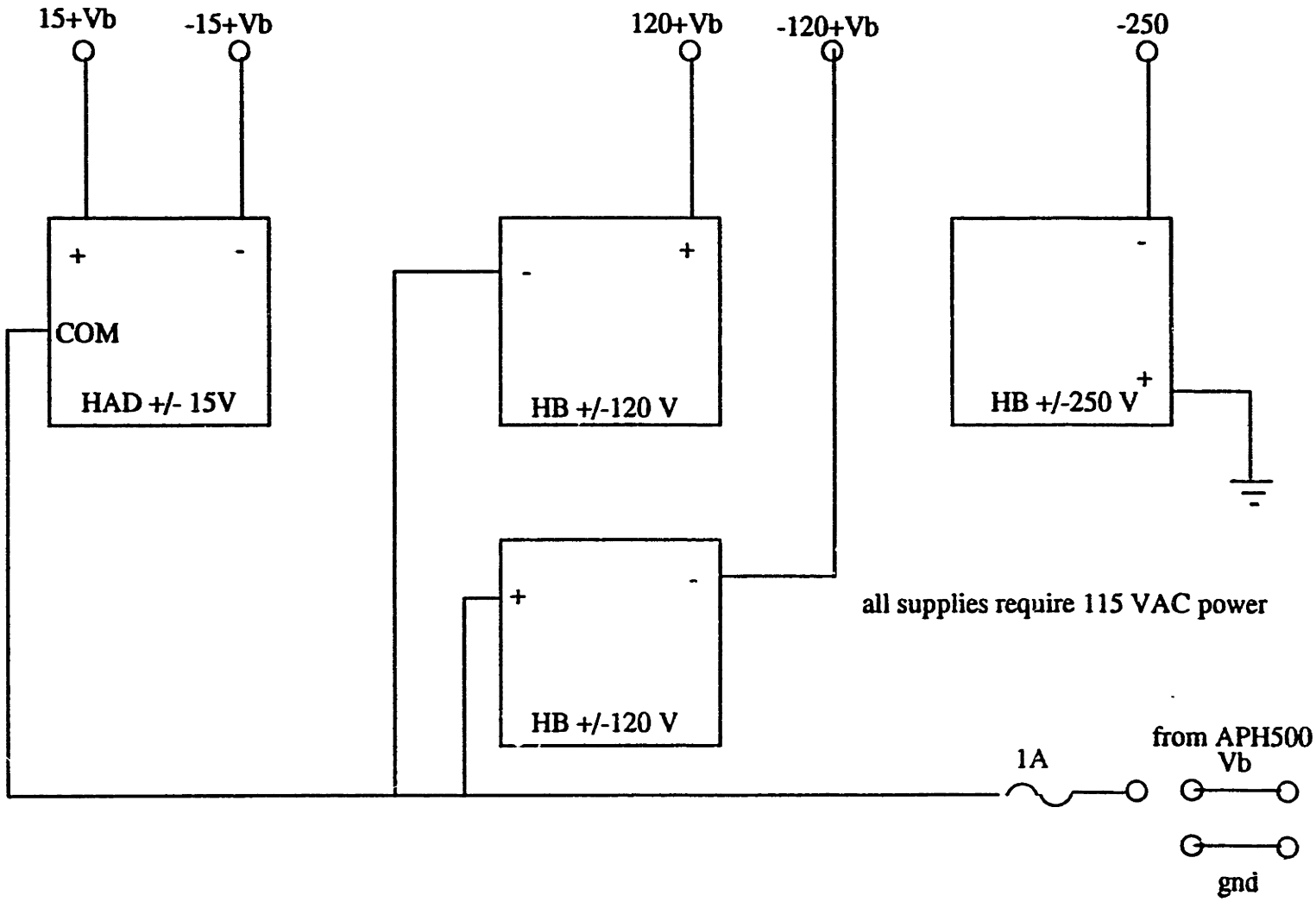

B.2-1 Power Supply Interconnections

G2 (ion retarding grid)

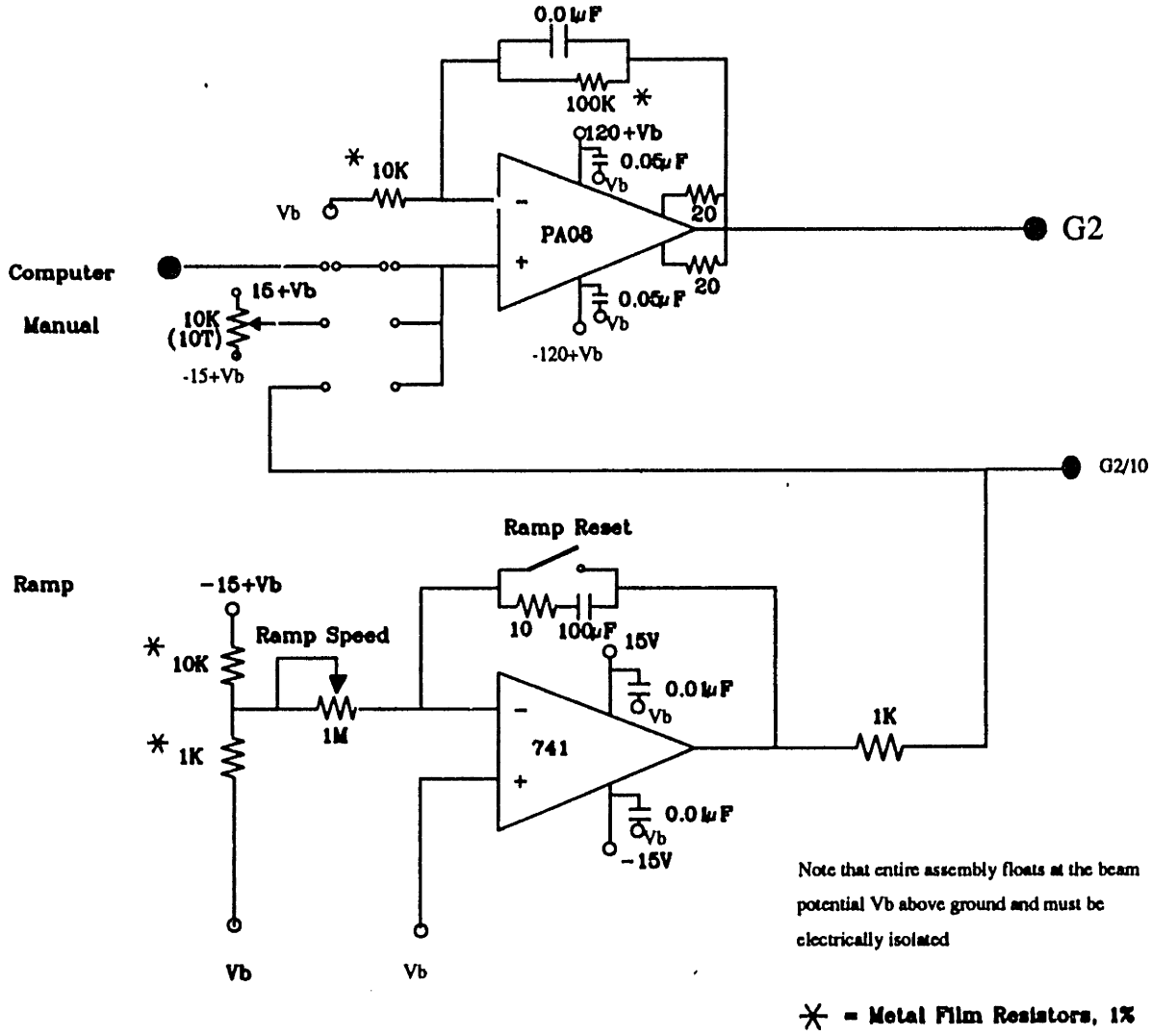

G1 (face grid)

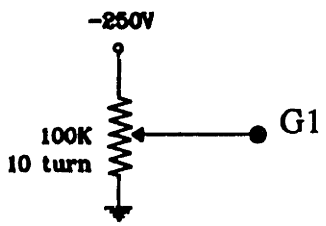

G3 (electron repeller grid)

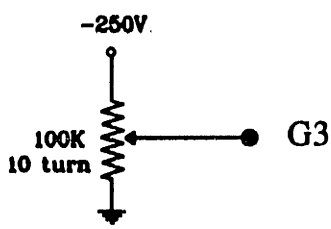

B.2-2 Grid Power Supplies.

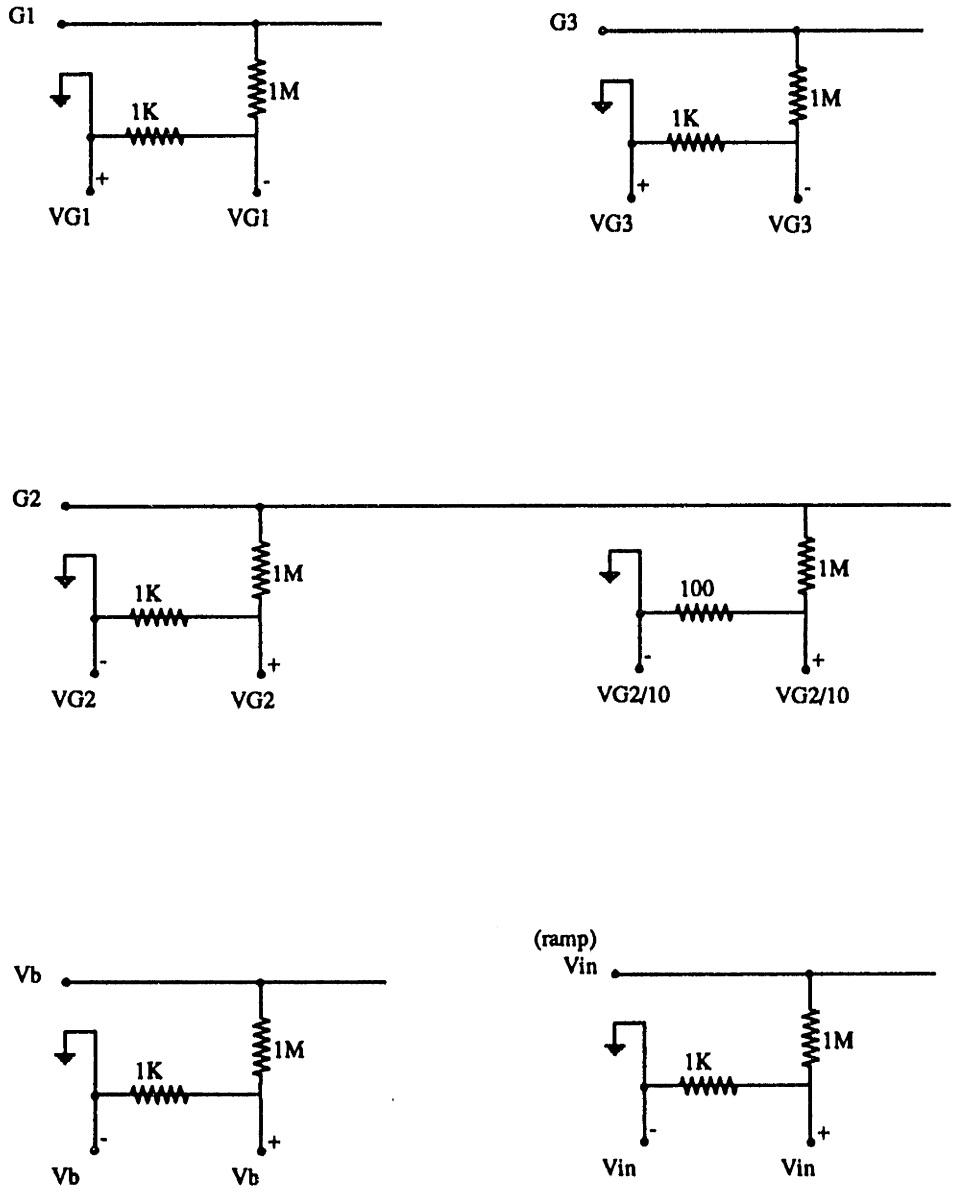

B.2-3 Digital Panel Meter Voltage Dividers.

EDGE CONNECTIONS

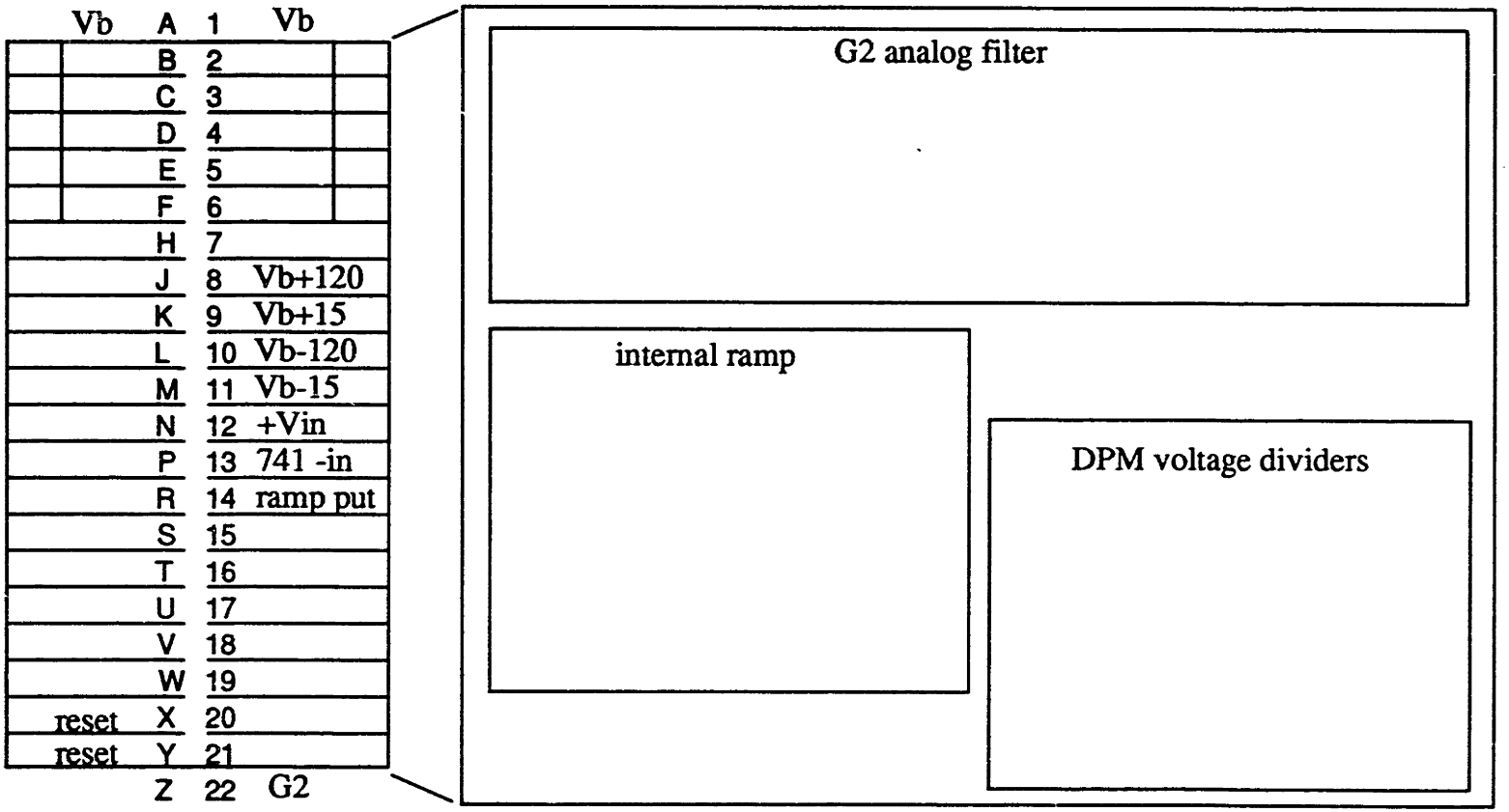

B.2-4 IBEA- Vector Board Layout.

Power Terminal

1		(green)	com gnd
2		(white)	AC+
3		(black)	AC-
4			
5		(orange/gr)	Vb/ com
6			
7		(brown)	-250
8		(red)	Vb-120
9		(yellow)	Vb-15
10		(purple)	Vb+15
11		(blue)	Vb+120

B.2-5 IBEA- Terminal Strip Interconnections.

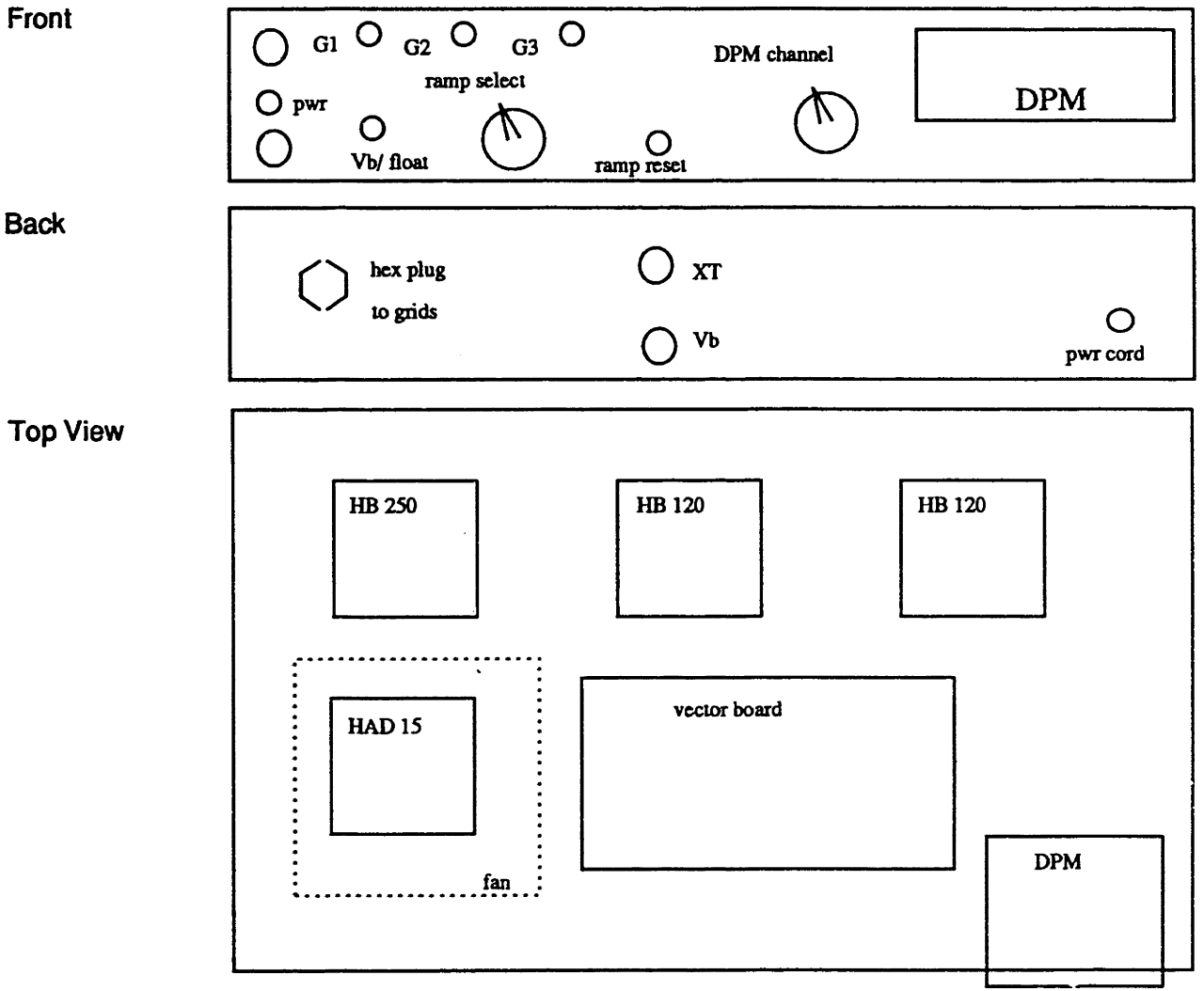

B.2-6 IBEA- Box Layout.

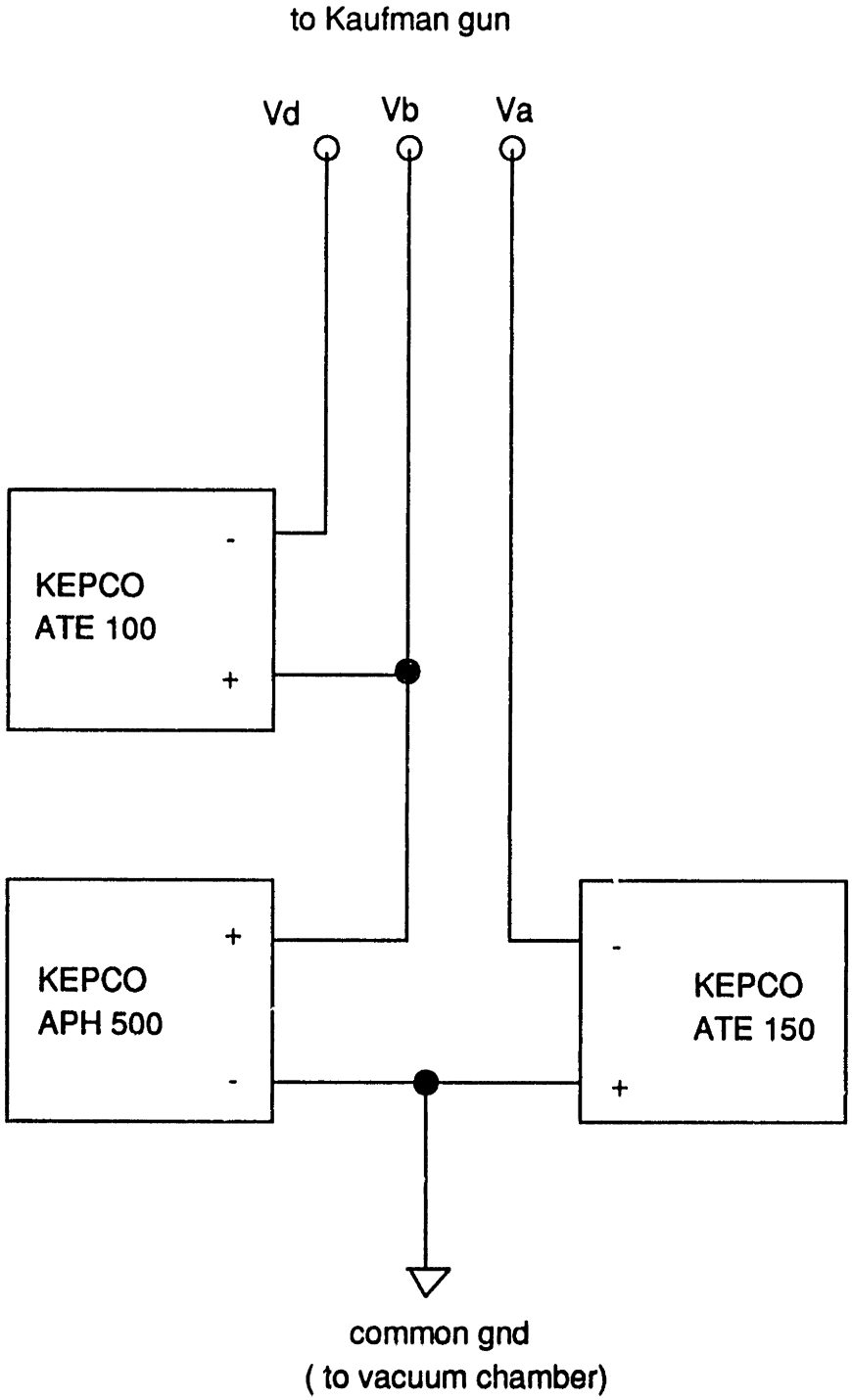

B.3-1 Power Supply Interconnections.

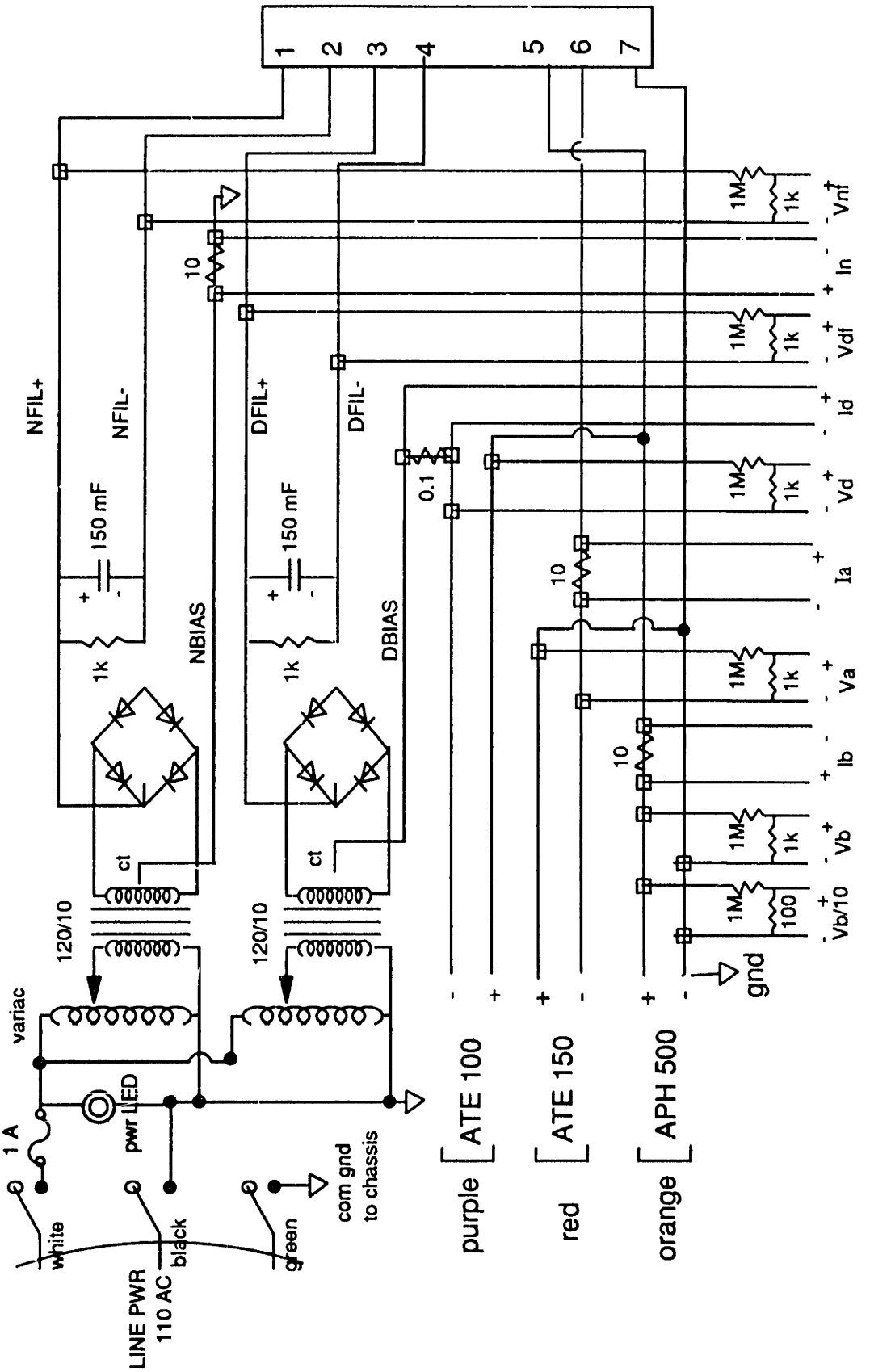

B.3-2 Filament Power Supply (FPS)

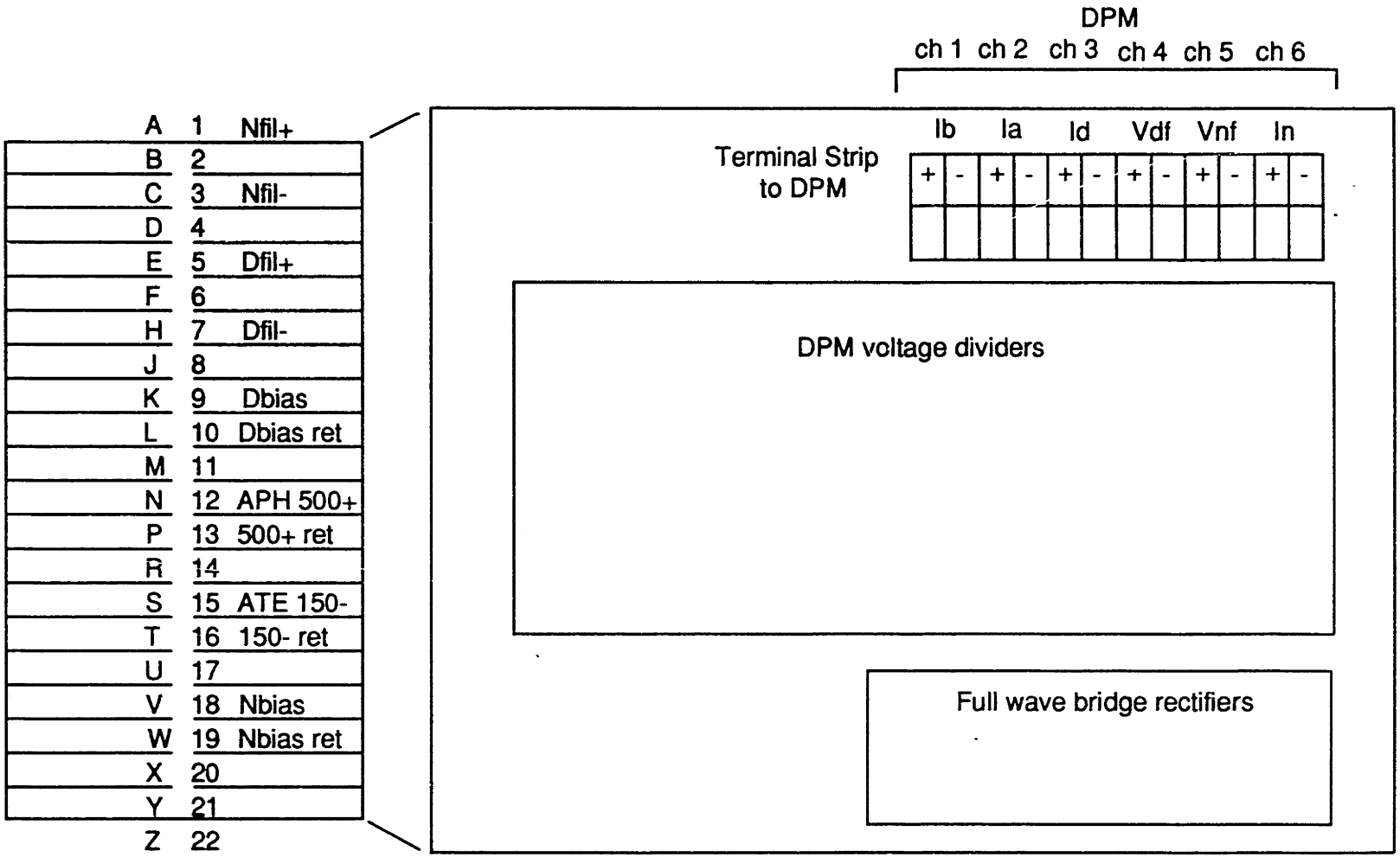

B.3-3 FPS- Vector Board Layout.

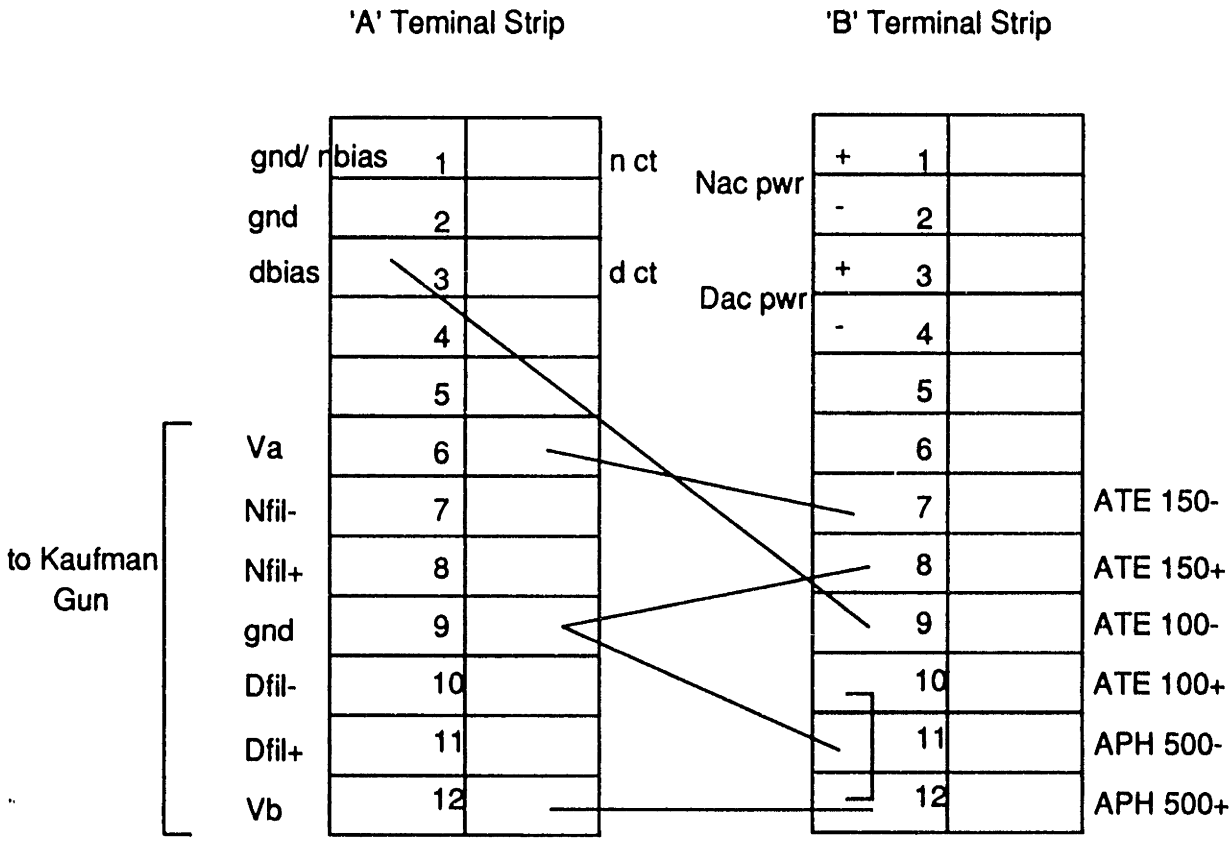

B.3-4 FPS- Terminal Strip Interconnections.

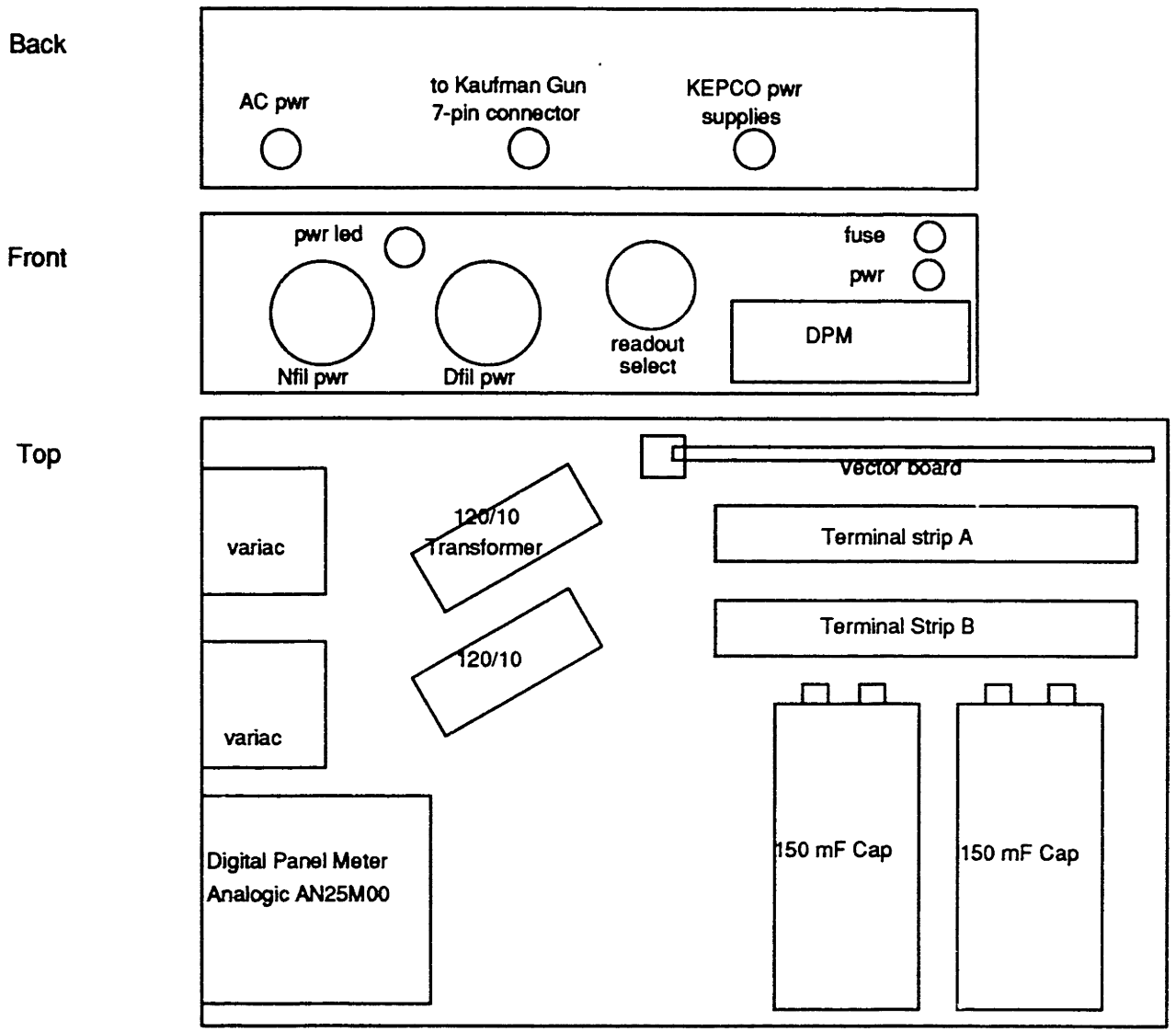

B.3-5 FPS- Box Layout.

A/D Conversions

DESCRIPTION	VOLTAGE RANGE (RAW)	ANALOG FILTER	VOLTAGE RANGE (FILTERED)	DT2811 CHANNEL
UTI-100C Mass Signal	0-10V	x0.5	0-5.0V	0
Interferometry Signal (Metrologic Photometer)	0-1.0V	x5.0	0-5.0V	1
Ion Current Signal	0-200mV	x10.0	0-2.0V	2
QCM Signal				3

D/A Conversions

UTI-100C Scan Ramp				DAC 1
High Mass Range	0-5.0V	x2.0	0-10 V	
Medium Mass Range	0-5.0V	none	0-5 V	
Low Mass Range	0-5.0V	x0.5	0-2.5 V	
Ion Beam Energy Analyzer Scan Ramp	0-5.0V	x2.0	0-10.0V	DAC 0

B.4-1 Instrument I/O Requirements.

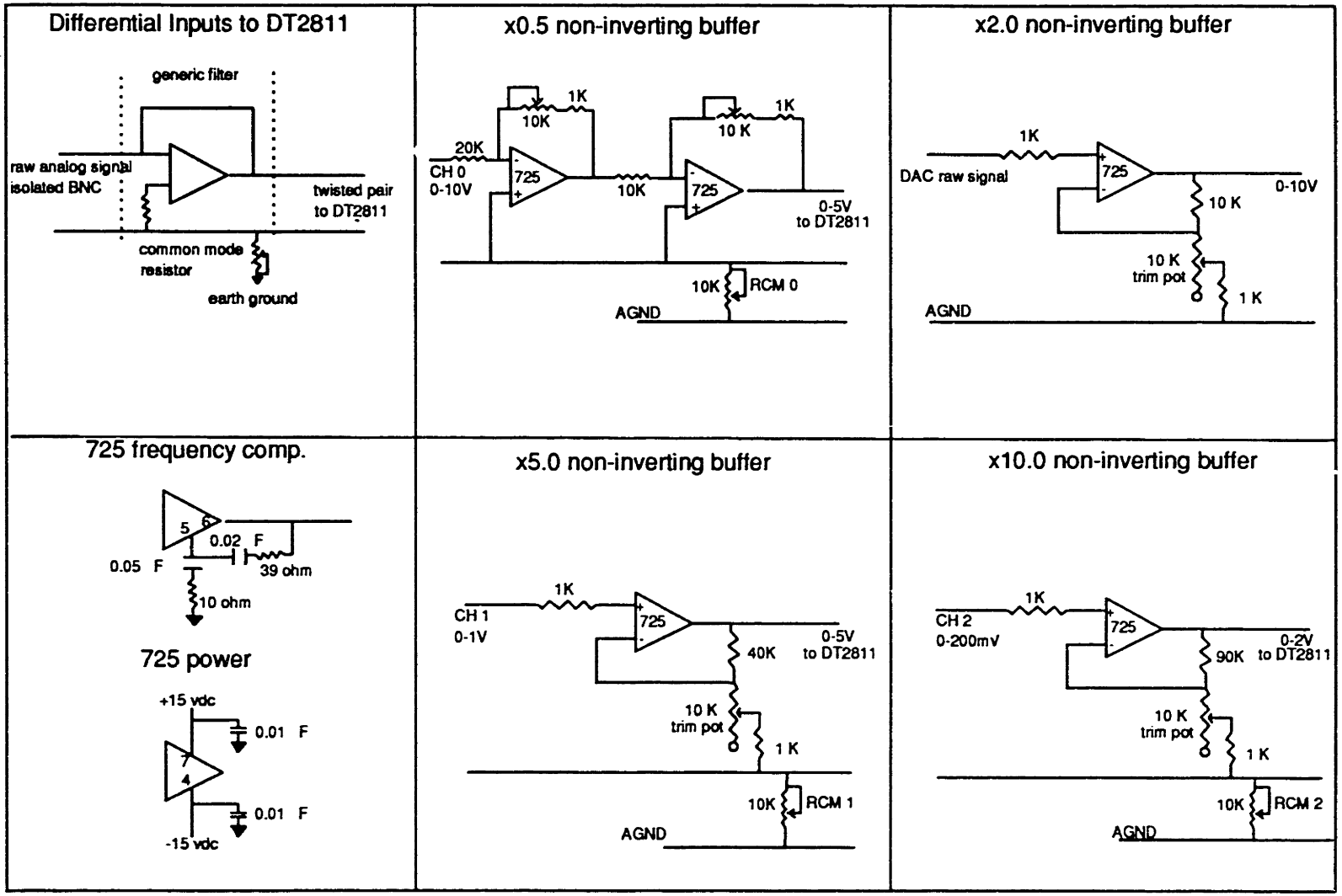

B.4-2 Analog Filter designs.

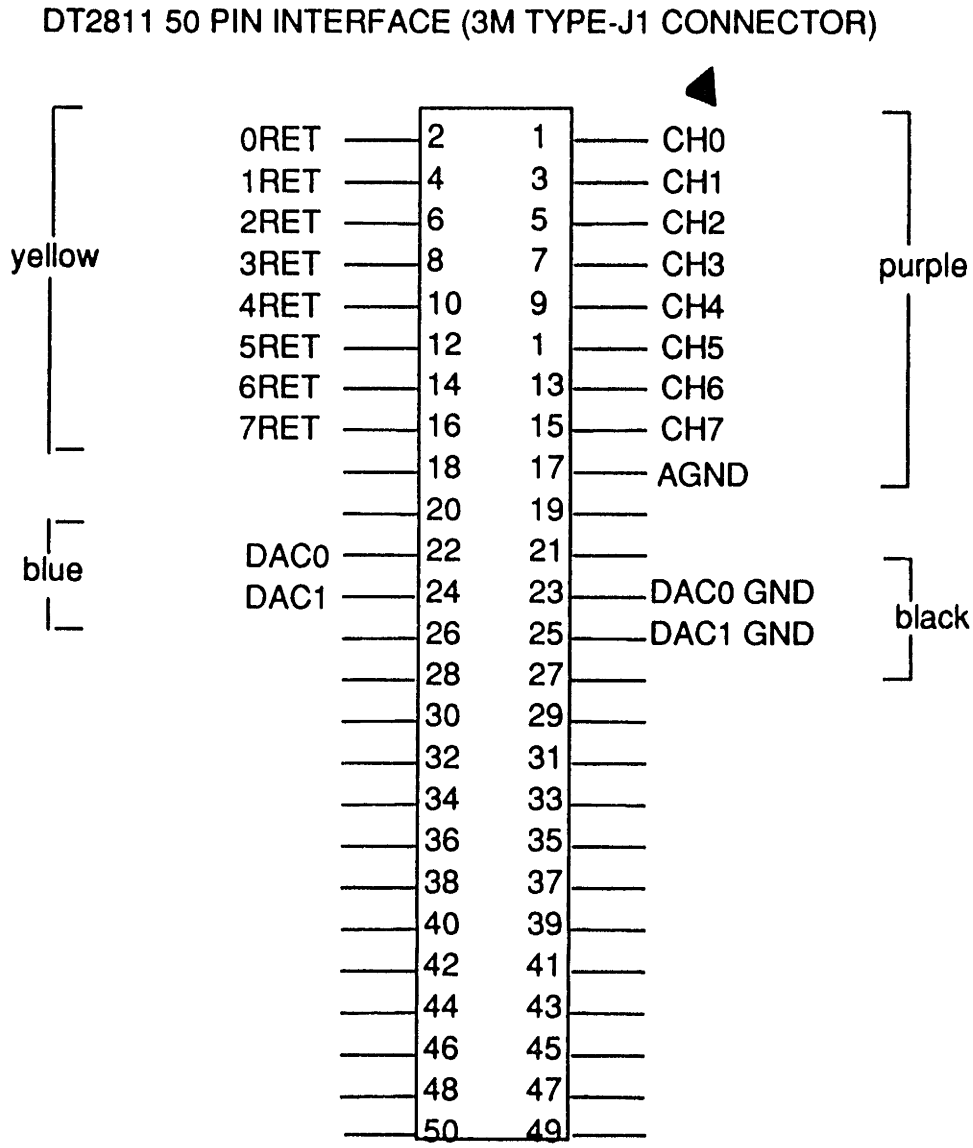

B.4-3 DT2811 50 Pin Interface.

EDGE CONNECTIONS

* #1 pin of 725 op amps face the edge connector
* frequency compensation is tied to agnd at 5 and 18

brown	AGND 0	A	1	+15 VDC	yellow
brown	AGND1	B	2	AGND	green
brown	AGND2	C	3	-15VDC	blue
brown	DAC0 RET	D	4	AGND	green
brown	DAC1 RET	E	5	AGND	green
		F	6		
		H	7		
		J	8		
gray	DAC1 OUT	K	9		
blue	DAC1IN	L	10		
gray	DAC0 OUT	M	11		
blue	DAC0 IN	N	12		
		P	13		
white	OUT 2	R	14		
green	2 RET	S	15		
red	IN 2	T	16		
white	OUT 1	U	17		
green	1 RET	V	18	AGND	green
red	IN 1	W	19	AGND	green
white	OUT 0	X	20	-15VDC	blue
green	0 RET	Y	21	AGND	green
red	IN 0	Z	22	+15VDC	yellow

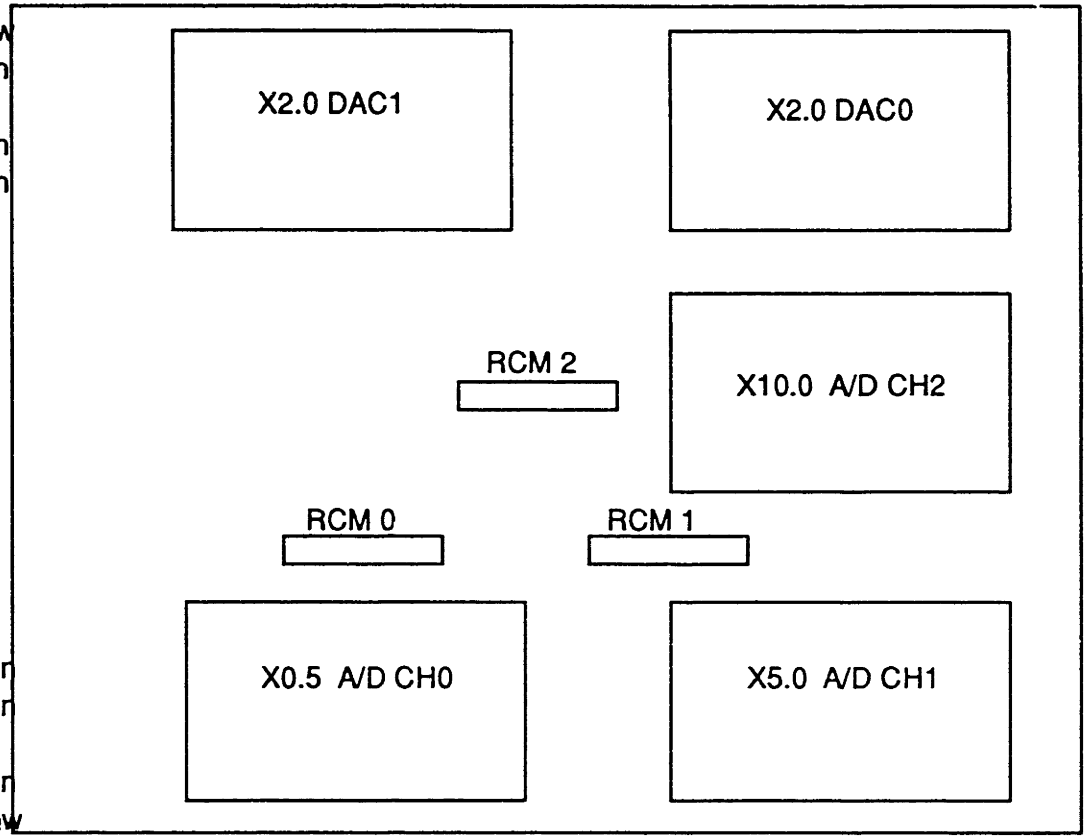

B.4-4 DAI- Vector Board Layout.

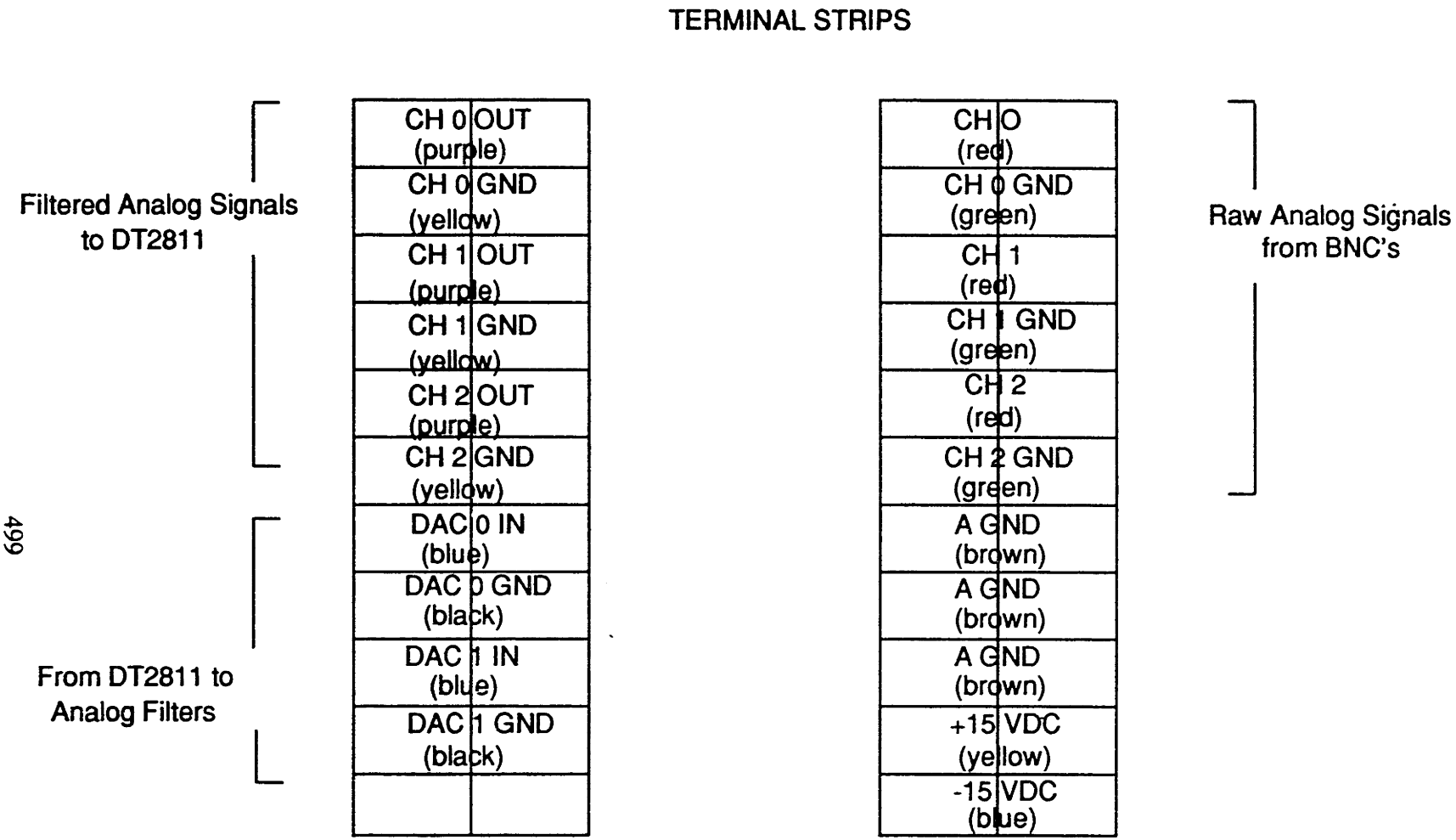

B.4-5 DAI- Terminal Strip Interconnections.

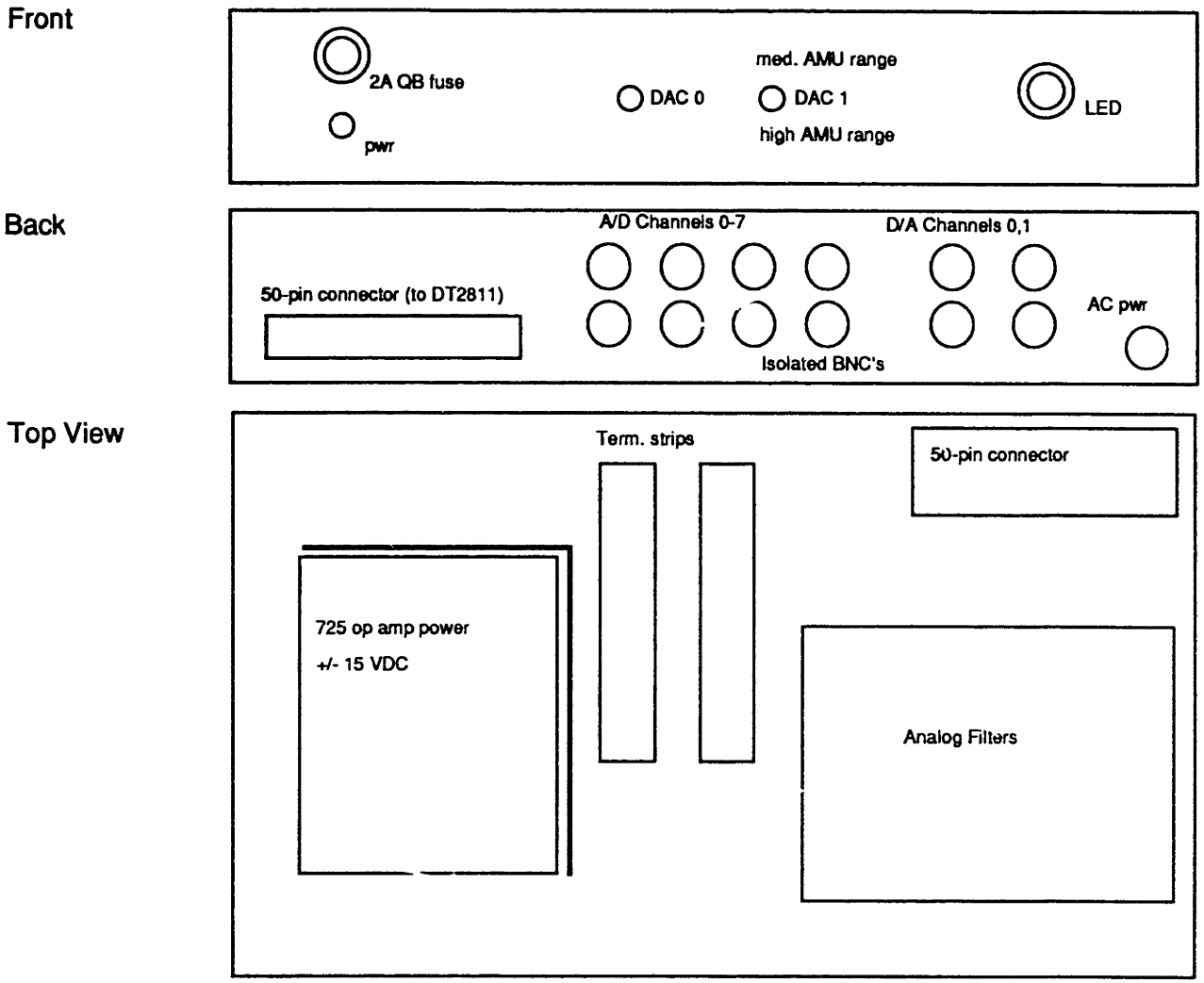

B.4-6 DAI- Box Layout.

Appendix C

Acquisition Code

This appendix contains the source code for the data acquisition and massage programs used in conjunction with the multibeam reactor experiments. The code compiles under Borland Turbopascal 4.0, however, problems were encountered in attaining upward compatibility of the linked-list data structures when we attempted upgrade to Turbopascal 5.0. The upgrade problem appears to be the result of a compiler bug in Turbo 5.0. Many of these routines were originally written by Igor Tepermeister [1992] for use with the XPS system under control of a Data Translations DT2811 card, and were subsequently modified for use in the multibeam system.

The main data acquisition program is entitled "3BACQ.PAS". Various program "tools" utilized by the main driver program are defined in the Turbopascal UNITS: ACQT3B.PAS, AMS3B.PAS, AAUX3B.PAS, PLTT3B.PAS, FILET3B.PAS, ZOOMT3B.PAS, and MSCRT3B.PAS. Mass spectral data, interferometry data, and QCM data are currently stored as Turbopascal records to the appropriate sub-directory under C:\EXPERIME\. on the Sargon lab XT computer. The massage program "MS3B.PAS" is subsequently required to read the data structures and to plot the data to the postscript printer.

```
PROGRAM ACQ3B;

USES DOS, Crt, GDriver, GKernel, GWindow,
    AcqT3B, AMs3B, AAux3B, PltT3B, FileT3B;

VAR
  IsExitProgram : boolean;
  FuncKey  : integer;
  Initial, Answer : str8;

  ExitSave : pointer;

  DirInfo  : SearchRec;

  OutInt : integer;
  OutHigh, OutLow : byte;


{$F+}
PROCEDURE MyExit; {$F-}
{Enable pointer disposal in case of a hard crash}

var
  CurrentPoint : DataPointer;

begin
 {Print exit code}
  ClearScreen;
  if (ExitCode <> 0) then begin
    GotoXY (10,10);
    Write ('Exit Code is: ', ExitCode);
    Sound (1200);
    Delay (5000);
    NoSound;
  end;

 {Terminate graphics}
  ClearScreen;
  LeaveGraphic;
  ClrScr;

 {Erase all the pointer lists}
  if (MsData.FirstPoint <> nil)  then EraseData (MsData);
  if (SmCurrData.FirstPoint <> nil)  then EraseData (SmCurrData);
  if (InterferData.FirstPoint <> nil) then EraseData (InterferData);

 {Set all DA to zero}

{DAC0 and and A/D's}
  Port[$21A] := 0;
  Port[$21B] := 0;

{DAC1 low and high byte}
  Port[$21C] := 0;
  Port[$21D] := 0;

 {Set all Digital lines to zero}
  Port[$21E] := 0;

 {Terminate comunication with IEEE GPIB}
```

```
  Writeln (IeeeOut, 'RESET');
  Close (IeeeOut);
  Close (IeeeIn);

 {Return to system termination routine}
  ExitProc := ExitSave;
end;


PROCEDURE InitCommun;

var
  GateString : string[3];
  Response : str255;

begin
  Assign (IeeeOut, 'IeeeOut');
  Rewrite (IeeeOut);
  Assign (IeeeIn, 'IeeeIn');
  Reset (IeeeIn);
  GotoXY (2,10);
  Write ('Testing Communication:');
  Writeln (IeeeOut, 'RESET');
  Writeln (IeeeOut, 'HELLO');
  Readln (IeeeIN, Response);
  GotoXY (2,11);
  Write (Response);

  Writeln (IeeeOut, 'OUTPUT 03;ID');
  Writeln (IeeeOut, 'ENTER 03');
  Readln (IeeeIn, Response);
  Response := RemoveSpaces(Response);
  GotoXY (2,12);
  Write ('  Device --- ', Response, '  OK');
  Writeln (IeeeOut, 'RESET');


 {Reset IEEE interface}
  Writeln (IeeeOut, 'RESET');            {Reset the connected devices}
  Writeln (IeeeOut, 'REMOTE');      {Enable computer control of all devices}
  Writeln (IeeeOut, 'LOCAL LOCKOUT');     {Lock out all devices}
  Writeln (IeeeOut, 'ARM SRQ');     {Enable SRQ to set light-pen interupt}

 {Determine the string for gate time}
  GateString := 'GA1';

              {Send the following commands to the HP5384A:
                 IN  : initialize
                 DN  : display all digits
                 DD  : decriment digit display by one
                 FI0 : Disable 100kHz filter
                 ML0 : disable manual level control
                 SM5 : set SRQ mask for Data ready and Error
                 WA1 : Enable wait-to-send data mode
                 GateString : appropriate gate}
  Writeln (IeeeOut, 'OUTPUT 03;IN,DN,FI0,ML0,SM5,WA1,',GateString);
  Writeln (IeeeOut, 'OUTPUT 03;FU1');

end;

PROCEDURE InitScreen;
```

```
begin
 {Clear the current screen}
   SelectScreen (1);
   ClearScreen;
 {Clear the Ramscreen}
   SelectScreen (2);
   ClearScreen;

   SetHeaderOn;

   SelectScreen (1);
   DefineWindow (1,0,0,XMaxGlb,YMaxGlb);              {System window}
   SelectWindow (1);
   DrawBorder;
   SetWindowModeOff;
   DrawLine (0,TextUp(24,2),XMaxGlb*8+7,TextUp(24,2));  {Command section}
   SetWindowModeOn;

   GotoXY (30,5);
   Write ('3-BEAM ACQUISITON PROGRAM');
   GotoXY (20,6);
   Write ('Written by: D. Gray and I. Teppermeister');
   GotoXY (33,7);
   Write ('Version ', Status.Version:3:1);
end;



PROCEDURE WriteMainRunScreen;

begin
   ClearScreen;
   DefineWindow (1,0,0,XMaxGlb,YMaxGlb);              {System window}
   SelectWindow (1);
   DrawBorder;
   SetWindowModeOff;
   DrawLine (0,TextUp(24,2),XMaxGlb*8+7,TextUp(24,2));  {Command section}
   SetWindowModeOn;

   DefineWindow (3,TextLeft (42,0), TextUp(3,0),
                 TextRight (75,0), TextDown(9,0));  {work window}
   SelectWindow (3);
   DrawBorder;
   DefineWindow (4,TextLeft (6,0), TextUp(11,0),
                 TextRight (37,0), TextDown(16,0));  {work window}
   SelectWindow (4);
   if (Status.IsSmCurrSpectraON) then DefineHeader (4, 'SAMPLE CURRENT ON')
                                 else DefineHeader (4, 'SAMPLE CURRENT OFF');
   DrawBorder;
   DefineWindow (5,TextLeft (42,0), TextUp(11,0),
                 TextRight (73,0), TextDown(16,0));  {work window}
   SelectWindow (5);
   if (Status.IsInterferSpectraON) then DefineHeader (5, 'INTERFEROMETRY ON')
                                   else DefineHeader (5, 'INTERFEROMETRY OFF');
   DrawBorder;

   SelectWindow (1);
   GotoXY (2,1);    Write (' RUN ');
   GotoXY (69,1);   Write (' ', Status.FileName, ' ');
   GotoXY (2,24);   Write ('F1=New File    F2=Ms    F3=Auxilary');
   GotoXY (72,24);  Write ('Esc=Exit');
```

```
  GotoXY (44,2);  Write ('MASS SPEC');
  GotoXY (57,2);  Write ('Spectra ', Status.MsNumber:1);
  GotoXY (69,2);  if (Status.IsMsSaved) then Write (' SAVED ')
                                  else Write (' ');

  GotoXY (5,22);  Write ('COMMENT:    ', Status.Description);
end;




BEGIN
 {Set version number in status record}
  Status.Version := 1.0;

 {Insert custom termination routine before system termination routine}
  ExitSave := ExitProc;
  ExitProc := @MyExit;

 {Enter graphics mode and set up the screen}
  ClrScr;
  InitGraphic;
  InitScreen;

{initialize communication with IEEE GPIB}
  InitCommun;

 {Zero all AD}
  Port[$21A] := 0;
  Port[$21B] := 0;
  OutInt  := Round(0.0);
  OutLow  := Lo (OutInt);
  OutHigh := Hi (OutInt);
  Port[$21C] := OutLow;
  Port[$21D] := OutHigh;

 {Set all Digital lines to zero}
  Port[$21E] := 0;

 {Obtain the path, default set to C:\experime}
  repeat
    Path := 'C:\experime';
    GotoXY (5,19);
    Write ('Input the path: (', Path, ')                              ');
    GetDescription (Path, 2, 20);
    Path := Path + '\';
  {Check if the specified path is valid}
    FindFirst (Path+'info', Directory, DirInfo);
    if (DosError > 0) then begin
      GotoXY (5,21); Write ('ERROR -- INVALID PATH');
      Sound (300);
      Delay (1000);
      NoSound;
      GotoXY (5,21); Write ('                    ');
    end;
  until (DosError = 0);

{Generate today's file code name}
  FileNameGen (Status.FileName);

 {Write the run screen}
```

```
 WriteMainRunScreen;

{Start main program loop, action chosen by function key}
 IsExitProgram := false;

 repeat

   DisplayTime;

  {Obtain the desired function}
   FuncKey := 1;
   if keypressed then GetFuncKey (FuncKey);

   Case FuncKey of
    {Obtain a new file saving the old data if required, F1=New File}
     59:begin

        {Check whether there are any spectra to save}
         if (  (Status.MsNumber  > 0   )
            or (Status.IsSmCurrSpectra )
            or (Status.IsInterferSpectra) ) then
              SaveRun (MsParam,
                       AuxParam);
        {Start new run file with next run file character}
         StatusReset;
         FileNameGen (Status.FileName);

         FuncKey := 2;
       end;

    {Take Mass Spectra, F2=MS}
     60:begin
         MsSection (MsParam, AuxParam);
         FuncKey := 2;
       end;

    {F3=Auxilary}
     61:begin
         AuxSection (AuxParam);
         FuncKey := 2;
       end;

    {Exit the program, ESC=Exit}
     150:begin
         GotoXY (2,25);
         Write ('EXIT -- are you sure ? (y or n)');
         repeat
           Answer := UpCase(readkey);
         until ((Answer = 'Y') or (Answer = 'N'));
         Erase25;
         if (Answer = 'Y') then begin
           IsExitProgram := true;
           if (  (Status.MsNumber  > 0   )
              or (Status.IsSmCurrSpectra )
              or (Status.IsInterferSpectra) ) then begin
             GotoXY (2,25);
             Write ('WARNING -- Run NOT SAVED      Save ? (y or n)');
             repeat
               Answer := UpCase(readkey);
             until ((Answer = 'Y') or (Answer = 'N'));
             if (Answer = 'Y') then
               SaveRun (MsParam,
```

```
                    AuxParam);
            end;
          end;

          Erase25;
          FuncKey := 1;
        end;

    end; {case}

{Continue to take strip charts while in mainrunscreen}

    if (Status.IsSmCurrSpectraON) then begin
      GetSmCurrDataPoint (AuxParam, true);
    end;
    if (Status.IsInterferSpectraON) then begin
      GetInterferDataPoint (AuxParam, true);
    end;

{After a spectra is executed, draw the spectra and stripchart data}
{after control is returned to main program loop}

    if (FuncKey = 2) then begin
      WriteMainRunScreen;
      if (Status.IsMsSpectra) then DrawSpectra (MsData.FirstPoint, true, 3);
      if (Status.IsSmCurrSpectra) then DrawSpectra (SmCurrData.FirstPoint, true, 4);
      if (Status.IsInterferSpectra) then DrawSpectra (InterferData.FirstPoint, true, 5);
    end;

  until (IsExitProgram);

END.



UNIT AcqT3B;
{Define system data structures and variables,  define procedures for}
{use by aquisition code, initialize all variables}

INTERFACE
uses DOS, Crt, GDriver, GKernel, GWindow;


TYPE
  str3   = string[3];
  str6   = string[6];
  str7   = string[7];
  str8   = string[8];
  str40  = string[40];
  str60  = string[60];
  str255 = string[255];
  StringKind = (Alfa, Numeric, Mix);

  StepType = (Fine, Course);

{Define a linked list structure for data storage}
  DataPointer = ^DataList;
  DataList = record
    Xvalue : real;
    Yvalue : real;
    NextPoint : DataPointer;
  end;
```

```
{Define system record structures}
  StatusRecord = record
    MsNumber     : integer;
    IsMsSaved    : boolean;
    IsMsSpectra  : boolean;

    MsSmallestStep : real;
    MsXSlope       : real;
    MsXIntercept   : real;

    IsSmCurrSpectra   : boolean;
    IsSmCurrSpectraON : boolean;

    IsInterferSpectra   : boolean;
    IsInterferSpectraON : boolean;

    IsGetDataContinuous : boolean;

    CurrentSpectraNumber : integer;

    BackSpectraFileName : str6;
    BackSpectraNumber   : integer;
    IsBackSubtructed    : boolean;

    UserInitial  : char;
    Version      : real;
    FileName     : str6;
    Description  : str60;
  end;

  SysRecord = record
    BasePress : real;

    SmFilm       : str8;
    SmAvgTemp    : real;
    SmCurr       : real;
    SmCurrScale  : integer;

    Isource   : str8;
    GasISName : str8;
    GasISPP   : real;
    Ipower    : real;
    Vion      : real;
    Vaccel    : real;

    Doser1    : str8;
    GasD1Name : str8;
    GasD1PP   : real;
    D1temp    : real;
    D1power   : real;

    Doser2    : str8;
    GasD2Name : str8;
    GasD2PP   : real;
    D2temp    : real;
    D2power   : real;
  end;

  MsRecord = record
    StartTime : real;

    StartMs     : real;
```

```
    EndMs       : real;
    StepMs      : real;
    NumberSteps : real;
    TimeDelay   : real;
    AmpScale    : integer;

    IsMsFlagOpen : boolean;
    MassRange    : string[8];
    IonId        : string[8];
    ChannVoltage : real;
    Resolution   : real;
    eCurrent     : real;
    eEnergy      : real;
    IonEnergy    : real;
    Focus        : real;
    Angle        : real;

    SysParam : SysRecord;
  end;

  AuxRecord = record
    SmCurrStartT      : real;
    SmCurrStepT       : real;
    SmCurrT0          : real;
    SmCurrNumberSteps : integer;
    SmCurrAmpScale    : integer;
    SmAvgCurr         : real;

    InterferStartT    : real;
    InterferStepT     : real;
    InterferT0        : real;
    InterferNumberSteps : integer;

    SysParam : SysRecord;
  end;

  DataRecord = record
    FirstPoint, LastPoint : DataPointer;
  end;



CONST
  MaxWorldsGlb  = 10;
  MaxWindowsGlb = 10;
  RamScreenGlb  = true;

  MixSet : Set of Char = ['A'..'Z', '0'..'9', '-'];

{0-75 AMU/4095, low range scan}
  SmallestStepLowMs    = 0.01831502;
  XSlopeLowMs          = 1.0; { 1.002805565;}
  XInterceptLowMs      = 0.0; {-0.292937036;}

{0-150 AMU/4095, med range scan}
  SmallestStepMedMs    = 0.03663004;
  XSlopeMedMs          = 1.0; {1.004552722;}
  XInterceptMedMs      = 0.0; {-0.666046909;}

{0-300 AMU/ 4095 steps, full range scan}
  SmallestStepHiMs     = 0.07326007;
  XSlopeHiMs           = 1.0;
```

```
  XInterceptHiMs      = 0.0;


VAR
  Regs : registers;

  Status      : StatusRecord;
  MsParam     : MsRecord;
  MsData      : DataRecord;
  AuxParam    : AuxRecord;
  SmCurrData  : DataRecord;
  InterferData : DataRecord;

  Path    : str60;
  IeeeIn, IeeeOut : text;

PROCEDURE DisplayTime;

PROCEDURE GetFuncKey (var FuncKey : integer);

PROCEDURE GetString (var InputString  : str8;
                     KindOfString : StringKind;
                     Xpos         : integer;
                     Ypos         : integer;
                     Field        : integer);

PROCEDURE GetReal (var Number : real;
                   Xpos   : integer;
                   Ypos   : integer;
                   Field  : integer;
                   DesPl  : integer);

PROCEDURE GetDouble (var Number : double;
                     Xpos   : integer;
                     Ypos   : integer;
                     Field  : integer;
                     DesPl  : integer);

PROCEDURE GetInteger (var Number : Integer;
                      Xpos   : integer;
                      Ypos   : integer;
                      Field  : integer);

PROCEDURE GetDescription (var InputString  : str60;
                          Xpos         : integer;
                          Ypos         : integer);

PROCEDURE Erase24;

PROCEDURE Erase25;

PROCEDURE Erase2425;

PROCEDURE WriteError (Error : str60);

PROCEDURE EraseInfoScreen;

PROCEDURE EraseData (var SpectraData : DataRecord);

FUNCTION Power (X, Y : double) : double;

FUNCTION RemoveSpaces (InString :  str255): str255;
```

```
IMPLEMENTATION
PROCEDURE DisplayTime;
   {Displays current time}

var
  Hour, Minute, Second, Sec100 : word;

begin
     GetTime (Hour, Minute, Second, Sec100);
     GotoXY (32,1);
     Write (' Time ',Hour:2,':',Minute:2,':',Second:2,' ');
end;



PROCEDURE GetFuncKey (var FuncKey : integer);

var
  Key : char;

begin
  Key := ReadKey;
  if (Key = #0) then begin
    Key := ReadKey;
    FuncKey := ord(Key);
  end
  else begin
    if (Key = chr(13)) then FuncKey := 13
    else begin
      if (Key = chr(27)) then FuncKey := 150
      else begin
        Sound (300); Delay (100); NoSound;
        FuncKey := 1;
      end;
    end;
  end;
end;



PROCEDURE GetString (var InputString  : str8;
                     KindOfString : StringKind;
                     Xpos         : integer;
                     Ypos         : integer;
                     Field        : integer);
      {The procedure obtains a string from the
       user.  The string is terminasted by a return.}

var
  CharValue, BoundLow, BoundHi, LetterCount : integer;
  CharIn : char;
  NewString : string[8];
  IsReturn : boolean;

  count : integer;

begin
  IsReturn := false;
  LetterCount := 0;
  NewString := '';
```

```
if (KindOfString = Alfa) then begin
   BoundLow := 64; BoundHi := 123; end;
if (KIndOfString = Numeric) then begin
   BoundLow := 44; BoundHi := 58; end;
if (KindOfString = Mix) then begin
   BoundLow := 44; BoundHi := 123; end;

repeat

 {Getting a proper later}
  repeat

   {Get a character}
    CharIn := readkey;

   {Check for special code and if true read the next character}
    if (CharIn = #0)
     then begin
       CharIn := readkey;
       CharValue := 0;
     end
     else begin
       CharValue := ord(CharIn);

     {Check for termination}
       if (CharIn = chr(13)) then IsReturn := true;

     {If not termination then erase the previous response}
       if ((LetterCount = 0) and not(IsReturn)) then begin
          for count := 1 to Field do begin
             GotoXY (Xpos+count-1,Ypos);
             Write (' ');
          end;
       end;

     {Check for backspace}
       if ((CharIn = chr(8)) and (LetterCount > 0)) then begin
          Delete (NewString, LetterCount, 1);
          LetterCount := LetterCount - 1;
          CharValue := 0;
          for count := 1 to Field do begin
             GotoXY (Xpos+count-1,Ypos);
             Write (' ');
          end;
          GotoXY (Xpos,Ypos);
          Write (NewString);
          Write ('_');
       end;
    end;

   {Inform of not acceptable character}
    if not ((((CharValue > BoundLow) and (CharValue < BoundHi))
       or IsReturn) or (CharValue = 32))  then begin
        Sound (300);
        Delay (200);
        NoSound;
    end;

  until (((CharValue > BoundLow) and (CharValue < BoundHi)) or IsReturn);

  if (CharIn <> chr(13)) then begin
     if ((LetterCount = 0) and (CharIn = '.')) then begin
```

```
          NewString := '0';
          LetterCount := 1;
          GotoXY (Xpos,Ypos);
          Write ('0');
        end;
        NewString := NewString+CharIn;
        LetterCount := LetterCount + 1;
        GotoXY (Xpos+LetterCount-1, Ypos);
        Write (CharIn);
        GotoXY (Xpos+LetterCount, Ypos);
        Write ('_');
      end;

  until (IsReturn or (LetterCount > Field));

  if (NewString <> '') then InputString := NewString;
end;



PROCEDURE GetReal (var Number : real;
                   Xpos   : integer;
                   Ypos   : integer;
                   Field  : integer;
                   DesPl  : integer);

var
  InputString : str8;
  code        : integer;
  count       : integer;

begin
  Str (Number:Field:DesPl, InputString);
  GotoXY (Xpos-1, Ypos);
  Write ('*');
  repeat
    GetString (InputString, Numeric, Xpos, Ypos, Field);
    Val (InputString, Number, code);
    if (code <> 0) then begin
      for count := 1 to Field do begin
        GotoXY (Xpos-1+count, Ypos);
        Write (' ');
      end;
    end;
  until (code = 0);
  for count := 1 to Field+2 do begin
    GotoXY (Xpos-2+count, Ypos);
    Write (' ');
  end;
end;



PROCEDURE GetDouble (var Number : double;
                     Xpos   : integer;
                     Ypos   : integer;
                     Field  : integer;
                     DesPl  : integer);

var
  InputString : str8;
  code        : integer;
```

```
  count       : integer;

begin
  Str (Number:Field:DesPl, InputString);
  GotoXY (Xpos-1, Ypos);
  Write ('*');
  repeat
    GetString (InputString, Numeric, Xpos, Ypos, Field);
    Val (InputString, Number, code);
    if (code <> 0) then begin
      for count := 1 to Field do begin
        GotoXY (Xpos-1+count, Ypos);
        Write (' ');
      end;
    end;
  until (code = 0);
  for count := 1 to Field+2 do begin
    GotoXY (Xpos-2+count, Ypos);
    Write (' ');
  end;
end;



PROCEDURE GetInteger (var Number : Integer;
                      Xpos   : integer;
                      Ypos   : integer;
                      Field  : integer);

var
  InputString : str8;
  code        : integer;
  count       : integer;

begin
  Str (Number:Field, InputString);
  GotoXY (Xpos-1, Ypos);
  Write ('*');
  repeat
    GetString (InputString, Numeric, Xpos, Ypos, Field);
    Val (InputString, Number, code);
    if (code <> 0) then begin
      for count := 1 to Field+1 do begin
        GotoXY (Xpos-1+count, Ypos);
        Write (' ');
      end;
    end;
  until (code = 0);
  for count := 1 to Field+2 do begin
    GotoXY (Xpos-2+count, Ypos);
    Write (' ');
  end;
end;



PROCEDURE GetDescription (var InputString  : str60;
                          Xpos         : integer;
                          Ypos         : integer);
 {The procedure obtains a string from the
  user.  The string is terminated by a return.}
```

```
var
  CharValue, LetterCount : integer;
  CharIn : char;
  NewString : str60;
  IsReturn : boolean;

begin
  IsReturn := false;
  LetterCount := 0;
  NewString := '';

  repeat

    repeat

     {Get a character}
      CharIn := readkey;

     {Check for special code and if true read the next character}
      if (CharIn = #0) then begin
        CharIn := readkey;
        CharValue := 0;
      end

      else begin
        CharValue := ord(CharIn);

       {Check for termination}
        if (CharIn = chr(13)) then IsReturn := true;

       {If the first input is not termination then erase}
       {the previous response from screen}
        if ((LetterCount = 0) and not(IsReturn)) then begin
          GotoXY (Xpos,Ypos);
          Write ('                              ',
                 '                             ');
        end;

       {Check for backspace}
        if ((CharIn = chr(8)) and (LetterCount > 0)) then begin
          Delete (NewString, LetterCount, 1);
          LetterCount := LetterCount - 1;
          CharValue := 0;
          GotoXY (Xpos,Ypos);
          Write ('                              ',
                 '                             ');
          GotoXY (Xpos,Ypos);
          Write (NewString);
          Write ('_');
        end;
      end;

     {If not acceptable character inform the user}
      if not (((CharValue > 31) and (CharValue < 123)) or IsReturn)
        then begin
         Sound (300);
         Delay (200);
         NoSound;
      end;

    until (((CharValue > 31) and (CharValue < 123)) or IsReturn);
```

```
      if not(IsReturn) then begin
        NewString := NewString+CharIn;
        LetterCount := LetterCount + 1;
        GotoXY (Xpos+LetterCount-1, Ypos);
        Write (CharIn);
        GotoXY (Xpos+LetterCount, Ypos);
        Write ('_');
      end;

    until IsReturn;

    if (NewString <> '') then InputString := NewString;
end;


PROCEDURE Erase24;

begin
    GotoXY (2,24);
    Write ('                                ',
           '                               ');
end;


PROCEDURE Erase25;

begin
    GotoXY (2,25);
    Write ('                                ',
           '                               ');
end;


PROCEDURE Erase2425;

begin
    GotoXY (2,24);
    Write ('                                ',
           '                               ');
    GotoXY (2,25);
    Write ('                                ',
           '                               ');
end;


PROCEDURE WriteError (Error : str60);
begin
    GotoXY (2,25);
    Write (Error);
    Delay (2000);
    Erase25;
end;


PROCEDURE EraseInfoScreen;

begin
```

```
  GotoXY (61,16);
  Write ('                ');
  GotoXY (61,17);
  Write ('                ');
  GotoXY (61,18);
  Write ('                ');
  GotoXY (61,19);
  Write ('                ');
  GotoXY (61,20);
  Write ('                ');
  GotoXY (61,21);
  Write ('                ');
  GotoXY (61,22);
  Write ('                ');
  GotoXY (61,23);
  Write ('                ');
end;


PROCEDURE EraseData (var SpectraData : DataRecord);

var
  CurrentPoint : DataPointer;

begin
  while (SpectraData.FirstPoint <> nil) do begin
    CurrentPoint := SpectraData.FirstPoint;
    SpectraData.FirstPoint := CurrentPoint^.NextPoint;
    dispose (CurrentPoint);
  end;
  SpectraData.FirstPoint := nil;
  SpectraData.LastPoint  := nil;
  SpectraData.LastPoint^.NextPoint := nil;
end;



FUNCTION Power (X, Y : double) : double;

begin
  Power := exp(Y*ln(X));
end;

FUNCTION RemoveSpaces (InString :  str255): str255;

begin
  while not( InString[1] in MixSet ) do
    Delete (InString, 1, 1);
  RemoveSpaces := InString;
end;

BEGIN
{Initialize all variables and linked lists}
  with Status do begin
    MsNumber    := 0;
    IsMsSaved   := false;
    IsMsSpectra := false;

    MsSmallestStep := SmallestStepHiMs;
    MsXSlope       := XSlopeHiMs;
```

```
  MsXIntercept   := XInterceptHiMs;

  IsSmCurrSpectra   := false;
  IsSmCurrSpectraON := false;

  IsInterferSpectra   := false;
  IsInterferSpectraON := false;

  IsGetDataContinuous := false;

  CurrentSpectraNumber := 0;

  IsGetDataContinuous := false;

  BackSpectraFileName  := 'None';
  BackSpectraNumber    := 0;
  IsBackSubtructed     := false;

  UserInitial  := 'D';
  Version      := 0.0;
  FileName     := ' ';
  Description  := 'no comments';
end;

with MsParam do begin
  StartTime      := 0.0;

  StartMs        := 0.0;
  EndMs          := 1.0;
  StepMs         := 1.0;
  NumberSteps    := 2;
  TimeDelay      := 0.001;
  AmpScale       := 8;
  IsMsFlagOpen   := TRUE;
  MassRange      := 'H';
  IonId          := 'n';
  ChannVoltage   := 0.0;
  Resolution     := 4.0;
  eCurrent       := 0.0;
  eEnergy        := 0.0;
  IonEnergy      := 0.0;
  Focus          := 0.0;
  Angle          := 0.0;

  with SysParam do begin
   {Initialize base pressure in microtorr}
    BasePress := 0.05;

    SmFilm       := 'polysi';
    SmAvgTemp    := 0.0;
    SmCurr       := 0.0;
   {Sample Current scale is number of decimals, 6=microamps}
    SmCurrScale  := 6;

    Isource   := 'KaufGun';
    GasISName := 'Argon';
   {Gas Partial Pressures are in microtorr}
    GasISPP   := 0.0;
    Ipower    := 0.0;
    Vion      := 0.0;
    Vaccel    := 0.0;
```

```
      Doser1    := ' ';
      GasD1Name := ' ';
      GasD1PP   := 0.0;
      D1temp    := 0.0;
      D1power   := 0.0;

      Doser2    := ' ';
      GasD2Name := ' ';
      GasD2PP   := 0.0;
      D2temp    := 0.0 ;
    {Forward power input in watts}
      D2power   := 0.0;
    end;
  end;

  with AuxParam do begin
    SmCurrStartT      := 0.0;
    SmCurrStepT       := 10.0;
    SmCurrT0          := 0.0;
    SmCurrNumberSteps := 2;
    SmCurrAmpScale    := 0;
    SmAvgCurr         := 0.0;

    InterferStartT    := 0.0;
    InterferStepT     := 10.0;
    InterferT0        := 0.0;
    InterferNumberSteps := 2;

    SysParam := MsParam.SysParam;
  end;

  with MsData do begin
    FirstPoint := nil;
    LastPoint  := nil;
    LastPoint^.NextPoint := nil;
  end;

  with SmCurrData do begin
    FirstPoint := nil;
    LastPoint  := nil;
    LastPoint^.NextPoint := nil;
  end;

  with InterferData do begin
    FirstPoint := nil;
    LastPoint  := nil;
    LastPoint^.NextPoint := nil;
  end;

END.


UNIT AMs3B;

INTERFACE
uses DOS, Crt, GDriver, GKernel, GWindow,
    AcqT3B, FileT3B, PltT3B, ZoomT3B, AAux3B;

PROCEDURE MsSection (var MsParam  : MsRecord;
                     var AuxParam : AuxRecord);
```

```
IMPLEMENTATION
procedure WriteMsScreen1 (var MsParam : MsRecord);

   {This procedure sets up the MS aquisition screen and writes all the
     acquisition parameters.}

begin
  SelectScreen (1);
  ClearScreen;

  DefineWindow (1,0,0,XMaxGlb,YMaxGlb);              {System window}
  SelectWindow (1);
  DrawBorder;
  SetWindowModeOff;
  DrawLine (0,TextUp(24,2),XMaxGlb*8+7,TextUp(24,2));  {Command section}
  SetWindowModeOn;
  DefineWindow (2, TextLeft (2,0), TextUp(2,-2),
              TextRight(59,0), TextDown(20,0));    {Closeup work window}
  SelectWindow (2);
  DrawBorder;

  SelectWindow (1);

  GotoXY (2,1);  Write (' MS ');
  GotoXY (62,1); Write (' ', Status.FileName, '  ', Status.MsNumber:1);
  GotoXY (73,1); if (Status.IsMsSaved) then Write (' SAVED ')
                              else Write ('       ');

  GotoXY (2,24);  Write ('F1=D-NEW  F2=D-SCALE    F3=Zoom  F4=Param    F10=Save');
  GotoXY (72,24); Write ('Esc=Exit');

  With MsParam do begin
    GotoXY (61,3); Write ('Starting Time:');
    GotoXY (62,4); Write (StartTime:7:2, '  (hhmm.ss)');
    GotoXY (65,5);
    if (Status.IsGetDataContinuous) then Write ('CONTINUOUS')
                              else Write ('  SINGLE  ');

    GotoXY (61,7); Write ('Starting Mass:');
    GotoXY (64,8); Write (StartMs:6:2, '  (amu)');

    GotoXY (61,9);  Write ('Ending Mass:');
    GotoXY (64,10); Write (EndMs:6:2, '  (amu)');

    GotoXY (61,11); Write ('Step Mass:');
    GotoXY (64,12); Write (StepMs:6:2, '  (amu)');

    GotoXY (61,13); Write ('Number of Steps:');
    GotoXY (64,14); Write (NumberSteps:4:0);

    GotoXY (61,15); Write ('Time Delay:');
    GotoXY (64,16); Write (TimeDelay:5:3, '  (s)');

    GotoXY (61,17); Write ('Current Scale:');
    GotoXY (64,18); Write ('10^- ', AmpScale:1, '  (A)');

    GotoXY (61,20); Write ('Mass Range: ', MassRange);
    if (Status.IsSmCurrSpectraON) then begin
      GotoXY (5,21);
      Write ('Sm Curr:  ', MsParam.SysParam.SmCurr:6:3);
    end;
```

```
  end;
end;


procedure WriteMsScreen2 (var MsParam : MsRecord);

   {This procedure sets up the MS parameter screen and writes all the
     system parameters to Ramscreen.}

begin
  GotoXY (2,25);  Write ('Setting up parameter screen.');

  SelectScreen (2);
  ClearScreen;

  DefineWindow (1,0,0,XMaxGlb,YMaxGlb);              {System window}
  SelectWindow (1);
  DrawBorder;
  SetWindowModeOff;
  DrawLine (0,TextUp(24,2),XMaxGlb*8+7,TextUp(24,2));  {Command section}
  SetWindowModeOn;

  GotoXY (2,1);    Write (' MS ');
  GotoXY (70,24);  Write ('Esc = Exit');

  with MsParam.SysParam do begin
    GotoXY (3,3);  Write ('SAMPLE PRARAMETERS');

    GotoXY (5,4);   Write ('Film:');
    GotoXY (20,4);  Write (SmFilm);

    GotoXY (5,5);   Write ('Avg. Temp.:');
    GotoXY (20,5);  Write (SmAvgTemp:3:0, '  (C)');

    GotoXY (40,4);  Write ('Samp. Current:');
    GotoXY (55,4);  Write (SmCurr:5:1, '  (uA)');

    GotoXY (40,5);  Write ('Curr. Scale:');
    GotoXY (55,5);  Write (SmCurrScale:2);


    GotoXY (3,8);  Write ('BEAM PRARAMETERS');

    GotoXY (5,9);    Write ('Ion Source:');
    GotoXY (20,9);   Write (Isource:8);

    GotoXY (5,10);   Write ('Source Gas:');
    GoToXY (20,10);  Write (GasISName:8);

    GotoXY (5,11);   Write ('Gas Press:');
    GoToXY (20,11);  Write (GasISpp:6:2, '  (E-6 t)');

    GotoXY (5,12);   Write ('For. Power:');
    GotoXY (20,12);  Write (Ipower:6:2, '  (w)');

    GotoXY (5,13);   Write ('Vion:');
    GotoXY (20,13);  Write (Vion:6:2, '  (V)');

    GotoXY (5,14);   Write ('Vaccel:');
    GotoXY (20,14);  Write (Vaccel:6:2, '  (V)');
```

```
    GotoXY (40,9);   Write ('Doser 1:');
    GotoXY (55,9);   Write (Doser1:8);

    GotoXY (40,10);   Write ('Source Gas:');
    GotoXY (55,10);   Write (GasD1Name:8);
    GoToXY (65,10);   Write (GasD1PP:4:1, '  (E-6 t)');

    GotoXY (40,11);  Write ('D1 Temp:');
    GotoXY (55,11);  Write (D1Temp:6:2, '  (C)');

    GotoXY (40,12);  Write ('Doser 2:');
    GotoXY (55,12);  Write (Doser2:8);

    GotoXY (40,13);  Write ('Source Gas:');
    GotoXY (55,13);  Write (GasD2Name:8);
    GotoXY (65,13);  Write (GasD2PP:4:1, '  (E-6 t)');

    GotoXY (40,14);  Write ('D2 Power:');
    GotoXY (55,14);  Write (D2Power:6:2, '  (w)');

  end;

  with MsParam do begin
    GotoXY (3,16);  Write ('MASS SPEC PARAMETERS');

    GotoXY (5,19);   Write ('MS Mode:');
    GotoXY (20,19);  if (IonId = 'p') then Write ('Positive')
                              else Write ('Neutral');

    GotoXY (5,20);   Write ('Channeltron:');
    GotoXY (20,20);  Write (ChannVoltage:5:0, '  (V)');

    GotoXY (5,21);   Write ('Resolution:');
    GotoXY (20,21);  Write (Resolution:5:2);

    GotoXY (5,22);   Write ('Mass Range:');
    GotoXY (20,22);  Write (MassRange);

    GotoXY (40,18);  Write ('MS Angle:');
    GotoXY (55,18);  Write (Angle:5:1,'  (deg)');

    GotoXY (40,19);  Write ('e- Current:');
    GotoXY (55,19);  Write (eCurrent:5:3, '  (mA)');

    GotoXY (40,20);  Write ('e- Energy:');
    GotoXY (55,20);  Write (eEnergy:5:1, '  (eV)');

    GotoXY (40,21);  Write ('Ion Energy:');
    GotoXY (55,21);  Write (IonEnergy:5:1, '  (eV)');

    GotoXY (40,22);  Write ('Focus:');
    GotoXY (55,22);  Write (Focus:5:1, '  (eV)');

    GotoXY (40,23);   Write ('Ms Flag:');
    GotoXY (55,23);  if (IsMsFlagOpen) then Write ('OPEN  ')
                              else Write ('CLOSED');

  end;

  SelectScreen (1);
  Erase25;
end;
```

```
procedure GetMsParam (var MsParam : MsRecord);

    {This procedure inputs the MS system parameters.  If <return> is
     entered as the first key, previous parameter settings are saved.}

var
  InputString : str8;
  IsYes : boolean;
  count : integer;

begin
  SwapScreen;

  IsYes := false;

  repeat
    with MsParam.SysParam do begin
      Erase2425;
      GotoXY (2,24);  Write ('Input SAMPLE parameters indicated by  *');

      InputString := SmFilm;
      GotoXY (19,4); Write ('*');
      GetString (InputString, Mix, 20, 4, 8);
      SmFilm := InputString;
      GotoXY (19,4);  Write ('         ');
      GotoXY (20,4);  Write (SmFilm);

      GetReal (SmAvgTemp, 20, 5, 7, 4);
      GotoXY (20,5);  Write (SmAvgTemp:3:0, '  (C)');

      GetReal (SmCurr, 55, 4, 5, 1);
      GotoXY (55,4);  Write (SmCurr:5:1, '  (uA)');

      GetInteger (SmCurrScale, 55, 5, 2);
      GotoXY (55,5);  Write (SmCurrScale:2);

      Erase2425;
      GotoXY (2,24);  Write ('Input BEAM parameters indicated by  *');


      Inp tString := Isource;
      GotoXY (19,9);  Write ('*');
      GetString (InputString, Mix, 20, 9, 8);
      Isource := InputString;
      GotoXY (19,9);  Write ('         ');
      GotoXY (20,9);  Write (Isource:8);

      InputString := GasISName;
      GotoXY (19,10);  Write ('*');
      GetString (InputString, Mix, 20, 10, 8);
      GasISName := InputString;
      GotoXY (19,10);  Write ('         ');
      GotoXY (20,10);  Write (GasISName:8);

      GetReal (GasISPP, 20, 11, 5, 1);
      GotoXY (20,11);  Write (GasISPP:6:2, '  (E-6 t)');

      GetReal (Ipower, 20, 12, 5, 1);
      GoToXY (20,12);  Write (Ipower:6:2, '  (w)');
```

```
    GetReal (Vion, 20, 13, 3, 0);
    GoToXY (20,13);  Write (Vion:6:2, '  (V)');

    GetReal (Vaccel, 20, 14, 3, 0);
    GoToXY (20,14);  Write (Vaccel:6:2, '  (V)');


    InputString := Doser1;
    GotoXY (54,9);  Write ('*');
    GetString (InputString, Mix, 54, 9, 8);
    Doser1 := InputString;
    GotoXY (54,9);  Write ('         ');
    GotoXY (55,9);  Write (Doser1:8);

    InputString := GasD1Name;
    GotoXY (54,10);  Write ('*');
    GetString (InputString, Mix, 54, 10, 8);
    GasD1Name := InputString;
    GotoXY (54,10);  Write ('         ');
    GotoXY (55,10);  Write (GasD1Name:8);

    GetReal (GasD1PP, 65, 10, 6, 2);
    GoToXY (65,10);  Write (GasD1PP:4:1, '  (E-6 t)');

    GetReal (D1Temp, 55, 11, 6, 2);
    GoToXY (55,11);  Write (D1Temp:6:2, '  (C)');


    InputString := Doser2;
    GotoXY (54,12);  Write ('*');
    GetString (InputString, Mix, 54, 12, 8);
    Doser2 := InputString;
    GotoXY (54,12);  Write ('         ');
    GotoXY (55,12);  Write (Doser2:8);

    InputString := GasD2Name;
    GotoXY (54,13); Write ('*');
    GetString (InputString, Mix, 54, 13, 8);
    GasD2Name := InputString;
    GotoXY (54,13);  Write ('         ');
    GotoXY (55,13);  Write (GasD2Name:8);

    GetReal (GasD2PP, 65, 13, 6, 2);
    GoToXY (65,13);  Write (GasD2PP:4:1, '  (E-6 t)');

    GetReal (D2Power, 55, 14, 6, 2);
    GoToXY (55,14);  Write (D2Power:6:2, '  (w)');

  end;

  with MsParam do begin
    Erase2425;
    GotoXY (2,24);  Write ('Input MASS SPEC parameters indicated by  *');

    repeat
      InputString := IonId;
      GotoXY (19, 19);  Write ('*');
      GetString (InputString, Alfa, 20, 19, 9);
    if ((InputString <> 'p') and (InputString <> 'n')) then begin
      Sound (300); Delay (200); NoSound;
      GotoXY (20,19); Write ('         ');
    end;
```

```
      until ((InputString = 'p') or (InputString = 'n'));
      IonId := InputString;
      GotoXY (19,19);  Write ('          ');
      GotoXY (20,19);
      if (IonId = 'p') then Write ('Positive')
                       else Write ('Neutral');

      GetReal (ChannVoltage, 20, 20, 5, 0);
      GotoXY (20,20);  Write (ChannVoltage:5:0, '  (V)');

      GetReal (Resolution, 20, 21, 5, 2);
      GoToXY (20,21); Write (Resolution:5:2);

      repeat
        InputString := MassRange;
        GotoXY (19, 22);  Write ('*');
        GetString (InputString, Alfa, 20, 22, 1);
      until ((InputString = 'H') or (InputString = 'M') or (InputString = 'L'));
      MassRange := InputString;
      GotoXY (19,22);  Write ('          ');
      GotoXY (20,22);  Write (MassRange);

      GetReal (Angle, 55, 18, 5, 1);
      GotoXY (55,18); Write (Angle:5:1, '  (deg)');

      GetReal (eCurrent, 55, 19, 5, 3);
      GoToXY (55,19); Write (eCurrent:5:3, '  (mA)');

      GetReal (eEnergy, 55, 20, 5, 1);
      GoToXY (55,20); Write (eEnergy:5:1, '  (eV)');

      GetReal (IonEnergy, 55, 21, 5, 1);
      GotoXY (55,21); Write (IonEnergy:5:1, '  (eV)');

      GetReal (Focus, 55, 22, 5, 1);
      GotoXY (55,22); Write (Focus:5:1, '  (eV)');

      if (IsMsFlagOpen) then InputString := 'o'
                        else InputString := 'c';
      GotoXY (54,23); Write ('*');
      GetString (InputString, Mix, 54, 23, 1);
      if (InputString = 'o') then IsMsFlagOpen := true
                             else IsMsFlagOpen := false;
      GotoXY (54,23);  Write ('          ');
      GotoXY (55,23);
      if (IsMsFlagOpen) then Write ('OPEN ')
                        else Write ('CLOSE');
  end;

    Erase2425;
    GotoXY (2,25);
    Write ('Are the parameters correct ? (y or n)');
    repeat
      InputString := UpCase(readkey);
      if (InputString = 'Y') then IsYes := true;
    until ((InputString = 'Y') or (InputString = 'N'));

  until (IsYes);
  Erase2425;

  SwapScreen;
end;
```

```
procedure GetMsAcqParam (var MsParam : MsRecord);

    {This procedure inputs the MS acquisition parameters.  If <return> is
     entered as the first key, previous parameter settings are saved.
     Since the AD/DA converters can only be incremented by discrete
     values, not all starting, ending, and step values are possible.
     The routine adjusts these values based on the fallowing:
       Total possible interger values for the 12 bit converter is 4096
       The range of a low scan is    0 -- 75 amu
       The range of a medium scan is 0 -- 150 amu
       The range of a high scan is   0 -- 300 amu
     The smallest possible steps are saved in constants
     SmallestStepLowMs, SmallestStepMedMs, SmallestStepHiMs
     and in the variable MsParam.SmaliestStepMs}

var
  InputString : str8;
  IsYes : boolean;

begin
  IsYes := false;

  repeat
    Erase2425;
    GotoXY (2,24);  Write ('Input MS Acquisition Parameters indicated by  *');

    with MsParam do begin

      if (MassRange = 'L') then begin;
        Status.MsSmallestStep := SmallestStepLowMs;
        Status.MsXSlope := XSlopeLowMs;
        Status.MsXIntercept := XInterceptLowMs;
      end;
      if (MassRange = 'M') then begin;
        Status.MsSmallestStep := SmallestStepMedMs;
        Status.MsXSlope := XSlopeMedMs;
        Status.MsXIntercept := XInterceptMedMs;
      end;
      if (MassRange = 'H') then begin;
        Status.MsSmallestStep := SmallestStepHiMs;
        Status.MsXSlope := XSlopeHiMs;
        Status.MsXIntercept := XInterceptHiMs;
      end;

      if (Status.IsGetDataContinuous) then InputString := 'c'
                                      else InputString := 's';
      GotoXY (65,5);  Write ('*');
      repeat
        GetString (InputString, Alfa, 65, 5, 1);
        if ((InputString <> 's') and (InputString <> 'c')) then begin
          Sound (300); Delay (200); NoSound;
          GotoXY (26,19); Write ('          ');
        end;
      until ((InputString = 's') or (InputString = 'c'));
      if (InputString = 's') then Status.IsGetDataContinuous := false
                             else Status.IsGetDataContinuous := true;
      GotoXY (65,5);  Write ('      ');
      GotoXY (66,5);
      if (Status.IsGetDataContinuous) then Write ('CONTINUOUS')
                                      else Write (' SINGLE  ');
```

```
        GetReal (StartMs, 64, 8, 6, 2);
        GotoXY (64,8); Write (StartMs:6:2, '  (amu)');


        GetReal (EndMs, 64, 10, 6, 2);
        if ((MassRange = 'L') and (EndMs > 75.0)) then EndMs := 75.0;
        if ((MassRange = 'M') and (EndMs > 150.0)) then EndMs := 150.0;
        if ((MassRange = 'L') and (EndMs > 300.0)) then EndMs := 300.0;
        if (EndMs <= StartMs) then EndMs := StartMs+0.1;
        GotoXY (64,10); Write (EndMs:6:2, '  (amu)');

        GetReal (StepMs, 64, 12, 6, 2);
        if (StepMs = 0.0) then StepMs := 0.1;
        GotoXY (64,12); Write (StepMs:6:2, '  (amu)');

        StartMs := Round(StartMs/Status.MsSmallestStep)*Status.MsSmallestStep;
        StepMs := Round(StepMs/Status.MsSmallestStep)*Status.MsSmallestStep;
        if (StepMs = 0.0) then StepMs := Status.MsSmallestStep;
        NumberSteps := Round((EndMs-StartMs)/StepMs)+1;
        if ((NumberSteps/2) <> Round(NumberSteps/2))
          then NumberSteps := NumberSteps + 1;
        EndMs := StartMs+((NumberSteps-1)*StepMs);

        GotoXY (64,8);   Write (StartMs:6:2, '  (amu)');
        GotoXY (64,10);  Write (EndMs:6:2,   '  (amu)');
        GotoXY (64,12);  Write (StepMs:6:2,  '  (amu)');
        GotoXY (64,14);  Write (NumberSteps:4:0);

        GetReal (TimeDelay, 64, 16, 5, 3);
        if (TimeDelay = 0.0) then TimeDelay := 0.0001;
        GotoXY (64,16); Write (TimeDelay:5:3, '  (s)');

        GetInteger (AmpScale, 69, 18, 1);
        GotoXY (64,18); Write ('10^- ', AmpScale:1, '  (A)');
      end;

      GotoXY (2,25);
      Write ('Are the parameters correct ? (y or n)');
      repeat
        InputString := UpCase(readkey);
        if (InputString = 'Y') then IsYes := true;
      until ((InputString = 'Y') or (InputString = 'N'));

    until (IsYes);

    Erase2425;
  end;


  procedure GetMsData (var MsParam : MsRecord);

      {The procedure obtains data from Mass Spectrometer connected to
       DT2811 acquisition card.  The acquired data is stored
       in a linked list.}

  type
    Bit16 = record
      Low, High : byte;
    end;

  var
```

```
  OutInt : integer;                {variables used by AD and DA}
  InStat, OutLow, OutHigh : byte;
  InValue : Bit16;

  X, XOld, Y, YOld : real;
  PointCount, count, code, FuncKey : integer;
  DelayTime : integer;
  IsADFinished, IsPauseFinished, IsSingleStep : boolean;
  Multiplier : real;

begin
  Erase2425;
  GotoXY (2,24);   Write ('F1 = Pause');
  GotoXY (70,24);  Write ('Esc = Exit');
  GotoXY (2,25);   Write ('Taking Ms Spectra');

  DisplayTime;

 {Parameter initialization}
  PointCount := 0;
  X := MsParam.StartMs;
  Multiplier := 1.0;
  for count := 1 to MsParam.AmpScale do Multiplier := Multiplier*10.0;
  DelayTime := Round(MsParam.TimeDelay*1000);

 {Screen initialization}
  DefineWorld (2, MsParam.StartMs, 2.50/Multiplier,
               MsParam.EndMs,  -0.01/Multiplier);
  SelectWorld (2);
  SelectWindow (2);

 {Set DAC1 to initial X position}
  Delay (30);
  OutInt  := Round((X*Status.MsXSlope+Status.MsXIntercept)
              /Status.MsSmallestStep);
  if (OutInt < 0) then OutInt := 0;
  OutLow  := Lo (OutInt);
  OutHigh := Hi (OutInt);
  Port[$21C] := OutLow;
  Port[$21D] := OutHigh;          {Start DA conversion}

 {Initialize AD channel 0, single conversion mode, no interrupts}
  OutLow := 0*128 + 0*64 + 0*32 + 0*16 + 0*8 + 0*4 + 0*2 + 0;
  Port[$218] := OutLow;           {Reset AD}
  OutLow := 0*128 + 0*64 + 0*32 + 0*16 + 0*8 + 0*4 + 0*2 + 0;
  Port[$219] := OutLow;           {Set gain = 1; set AD chan = 0}
  Delay (10);

 {Delay}
  Delay (3000);

 {Read the AD mass signal value}
  InValue.Low  := Port[$21A];
  InValue.High := Port[$21B];

 {Get initial auxilary data}
  if (Status.IsSmCurrSpectraON)  then  GetSmCurrDataPoint (AuxParam, false);

  if (Status.IsInterferSpectraON) then begin
    GetInterferDataPoint (AuxParam, false);
  end;
```

```
{Start mass scan acquisition loop}
 IsPauseFinished := true;
 IsSingleStep    := false;
 FuncKey := 1;

 repeat
  {Check for early termination or pause}
   if (keypressed or IsSingleStep) then begin

     DisplayTime;

     if (keypressed and not(IsSingleStep)) then GetFuncKey (FuncKey);

    {Pause}
     if ((FuncKey = 59) and (IsPauseFinished)) then begin
       IsPauseFinished := false;
       IsSingleStep := false;
       FuncKey := 1;
       if (Status.IsSmCurrSpectraON) then GetSmCurrDataPoint (AuxParam, true);
       if (Status.IsInterferSpectraON) then GetInterferDataPoint (AuxParam, true);
       GotoXY (2,24);
       Write ('F2 = Restart     F3 = Single Step                    ');
     end;

    {Restart}
     if ((FuncKey = 60) and not(IsPauseFinished)) then begin
       IsPauseFinished := true;
       IsSingleStep := false;
       FuncKey := 1;
       GotoXY (2,24);
       Write ('F1 = Pause                                          ');
     end;

    {Single step}
     if ((FuncKey = 61) and not(IsPauseFinished)) then begin
       IsPauseFinished := true;
       IsSingleStep    := true;
       FuncKey := 59;
     end;

    {Terminate}
     if (FuncKey = 150) then begin
      {Reset devices}
       Port[$21A] := 0;
       Port[$21B] := 0;
       Port[$21C] := 0;
       Port[$21D] := 0;

      {Get final auxilary data}
       if (Status.IsSmCurrSpectraON)  then  GetSmCurrDataPoint (AuxParam, false);
       if (Status.IsInterferSpectraON) then begin
         GetInterferDataPoint (AuxParam, false);
       end;

      {Set NumberSteps to actual number of points collected, and update}
      {the ending values}
       MsParam.NumberSteps := PointCount;
       MsParam.EndMs := MsParam.StartMs+
                        ((MsParam.NumberSteps-1)*MsParam.StepMs);
       Status.IsGetDataContinuous := false;
       EXIT;
     end;
```

```
  end;

{Set DA to X position}
  OutInt  := Round((X*Status.MsXSlope+Status.MsXIntercept)
                /Status.MsSmallestStep);
  if (OutInt < 0) then OutInt := 0;
  OutLow  := Lo (OutInt);
  OutHigh := Hi (OutInt);
  Port[$21C] := OutLow;
  Port[$21D] := OutHigh;          {Start DA conversion}

  Delay (DelayTime);

{Get Y value from the average of 10 consecutive readings}
  Y := 0.0;
  for count := 1 to 10 do begin
   {Start Data Acquisition (reset AD, set gain = 1, set AD Ch = 0)}
    OutLow := 0*128 + 0*64 + 0*32 + 0*16 + 0*8 + 0*4 + 0*2 + 0;
    Port[$218] := OutLow;
    OutLow := 0*128 + 0*64 + 0*32 + 0*16 + 0*8 + 0*4 + 0*2 + 0;
    Port[$219] := OutLow;

    IsADFinished := false;
    repeat
      InStat := Port[$218];
      if (InStat >= 128) then IsADFinished := true;
    until (IsADFinished);

   {Read the AD value}
    InValue.Low  := Port[$21A];
    InValue.High := Port[$21B];
  {convert Y to a digital value based on a peak voltage of 5.0V}
    Y := Y + ((integer(InValue)/4095)*5.0);
  end;
  Y := Y/10.0;          {Average}
  Y := Y/Multiplier;    {Store all data in Amp scale}

  GotoXY (25,25);
  Write ('X: ', X:8:3,'    Y: ', (Y*Multiplier):5:3);

  if (IsPauseFinished) then begin
   {Store data in linked list}
    with MsData do begin
      if FirstPoint = nil then begin          {Make new link}
        New (FirstPoint);
        LastPoint := FirstPoint;
        XOld := X;
        YOld := Y;
      end
      else begin
        New (LastPoint^.NextPoint);
        LastPoint := LastPoint^.NextPoint;
      end;
      LastPoint^.NextPoint := nil;            {Store data}
      LastPoint^.Xvalue := X;
      LastPoint^.Yvalue := Y;
      PointCount := PointCount + 1;
    end;

   {Plot data on screen}
    DrawLine (XOld, YOld, X ,Y);
```

```
      {Set next X position}
        XOld := X;
        YOld := Y;
        X := X + MsParam.StepMs;

      end;

  until (X > MsParam.EndMs);              {Terminate data acquisition}

 {Reset devices}
  Port[$21A] := 0;
  Port[$21B] := 0;
  Port[$21C] := 0;
  Port[$21D] := 0;

 {Get final auxilary data}
  if (Status.IsSmCurrSpectraON) then GetSmCurrDataPoint (AuxParam, false);
  if (Status.IsInterferSpectraON) then begin
    GetInterferDataPoint (AuxParam, false);
  end;

end;


PROCEDURE MsSection (var MsParam  : MsRecord;
                     var AuxParam : AuxRecord);

    {This procedure contains all the procedures used solely by the
     MS method analysis. These procedures obtain required system
     and acquisition parameters, and take data from the UTI100C system.}

VAR
  Multiplier : real;
  count : integer;

  Hour, Minute, Second, Sec100 : word;

  IsExitMs : boolean;
  FuncKey  : integer;
  Answer   : str8;

BEGIN
  WriteMsScreen1 (MsParam);
  WriteMsScreen2 (MsParam);
  if (Status.IsMsSpectra) then DrawSpectra (MsData.FirstPoint, true, 2);
  IsExitMs := false;

 {Ms section main loop}
  repeat

    DisplayTime;

    FuncKey := 1;
    if keypressed then GetFuncKey (FuncKey);
    Case FuncKey of

     {Take data -- new main parameter}
      59:begin
           if (Status.IsMsSpectra and not(Status.IsMsSaved)) then begin
             GotoXY (2,25);
             Write ('WARNING -- Spectra not saved     Save ? (y or n)');
             repeat
```

```
      Answer := UpCase(readkey);
    until ((Answer = 'Y') or (Answer = 'N'));
    if (Answer = 'Y') then begin
      Erase25;
      SaveMs (MsParam, Status.FileName, Status.MsNumber);
      Status.IsMsSaved := true;
    end;
  end;

{Remove old data}
  EraseData (MsData);
  MsParam.StartTime := 0.0;

{Update the spectra counters}
  if (Status.IsMsSaved or (Status.MsNumber = 0)) then begin
    Status.MsNumber  := Status.MsNumber + 1;
    Status.CurrentSpectraNumber  := Status.MsNumber;
    Status.IsMsSpectra := false;
    Status.IsMsSaved := false;
  end;
{Set limit on #spectra taken in a run}
  if (Status.MsNumber = 100) then IsExitMs := true;

  if not(IsExitMs) then begin
    MsParam.SysParam.SmCurr      := 0.0;

    ClearScreen;
    GetMsParam (MsParam);
    WriteMsScreen1 (MsParam);
    GetMsAcqParam (MsParam);

    Erase2425;
    GotoXY (2,25);  Write ('Start?  (y or n)');
    repeat
      Answer := ' ';
      if keypressed then Answer := UpCase(readkey);
      DisplayTime;
      if (Status.IsSmCurrSpectraON) then  GetSmCurrDataPoint (AuxParam, true);
      if (Status.IsInterferSpectraON) then GetInterferDataPoint (AuxParam, true);
    until ((Answer = 'Y') or (Answer = 'N'));

    if (Answer = 'Y') then begin
      GetTime (Hour, Minute, Second, Sec100);
      MsParam.StartTime := int(Hour)*100.0+int(Minute)+int(Second)/100.0;
      GotoXY (62,4);  Write (MsParam.StartTime:7:2, '  (hhmm.ss)');

      GetMsData (MsParam);
    {monitor mass peaks continuously if desired}
      while (Status.IsGetDataContinuous) do begin
        EraseData (MsData);
        GetMsData (MsParam);
      end;

      WriteMsScreen1 (MsParam);
      DrawSpectra (MsData.FirstPoint, true, 2);

      Status.IsMsSpectra := true;
    end
    else begin
      WriteMsScreen1 (MsParam);
    end;
  end;
```

```
    end;

{Take data -- new  scale only}
 60:begin
      if (Status.IsMsSpectra and not(Status.IsMsSaved)) then begin
        GotoXY (2,25);
        Write ('WARNING -- Spectra not saved     Save ? (y or n)');
        repeat
          Answer := UpCase(readkey);
        until ((Answer = 'Y') or (Answer = 'N'));
        if (Answer = 'Y') then begin
          Erase25;
          SaveMs (MsParam, Status.FileName, Status.MsNumber);
          Status.IsMsSaved := true;
        end;
      end;

     {Remove old data}
      EraseData (MsData);
      MsParam.StartTime := 0.0;

     {Update the spectra counters}
      if (Status.IsMsSaved or (Status.MsNumber = 0)) then begin
        Status.MsNumber  := Status.MsNumber + 1;
        Status.CurrentSpectraNumber  := Status.MsNumber;
        Status.IsMsSpectra := false;
        Status.IsMsSaved := false;
      end;
      if (Status.MsNumber = 100) then IsExitMs := true;

      if not(IsExitMs) then begin
        MsParam.SysParam.SmCurr      := 0.0;

        ClearScreen;
        WriteMsScreen1 (MsParam);
        Erase2425;
        GotoXY (2,24);  Write ('Input Amp Scale');
        GetInteger (MsParam.AmpScale, 69, 18, 1);
        GotoXY (64,18); Write ('10^- ', MsParam.AmpScale:1, '  (A)');

        Erase2425;
        GotoXY (2,25);  Write ('Start?  (y or n)');
        repeat
          Answer := ' ';
          if keypressed then Answer := UpCase(readkey);
          DisplayTime;
          if (Status.IsSmCurrSpectraON) then  GetSmCurrDataPoint (AuxParam, true);
          if (Status.IsInterferSpectraON) then GetInterferDataPoint (AuxParam, true);
        until ((Answer = 'Y') or (Answer = 'N'));

        if (Answer = 'Y') then begin
          GetTime (Hour, Minute, Second, Sec100);
          MsParam.StartTime := int(Hour)*100.0+int(Minute)+int(Second)/100.0;
          GotoXY (62,4);  Write (MsParam.StartTime:7:2, '  (hhmm.ss)');

          GetMsData (MsParam);

          WriteMsScreen1 (MsParam);
          DrawSpectra (MsData.FirstPoint, true, 2);

          Status.IsMsSpectra := true;
        end
```

```
            else begin
              WriteMsScreen1 (MsParam);
            end;
          end;
        end;

    {Analyze data}
     61:begin
          if (Status.IsMsSpectra) then begin;
            Multiplier := 1.0;
            for count := 1 to MsParam.AmpScale do
              Multiplier := Multiplier*10.0;
            ZoomSection (MsData.FirstPoint, Multiplier,
                         MsParam.StartMs, MsParam.EndMs,
                         MsParam.StartMs, 1.0,
                         Status.FileName);
            WriteMsScreen1 (MsParam);
            DrawSpectra (MsData.FirstPoint, true, 2);
          end
          else begin
            GotoXY (2,25);
            Write ('No Data to Analyze');
          end;
        end;

    {Display parameter screen}
     62:begin
          SwapScreen;
          repeat
            GetFuncKey (FuncKey);
          until (FuncKey = 150);
          SwapScreen;
        end;

    {Save Data with current run}
     68:begin
          if not(Status.IsMsSaved) then begin
             SaveMs (MsParam, Status.FileName, Status.MsNumber);
           end;

          Status.IsMsSaved := true;

         {Update the spectra status}
          GotoXY (73,1);  Write (' SAVED ');
        end;

    {Exit}
     150:begin
          IsExitMs := true;
        end;

    end;  {case}

    if (Status.IsSmCurrSpectraON) then begin
      GetSmCurrDataPoint (AuxParam, true);
    end;
    if (Status.IsInterferSpectraON) then begin
      GetInterferDataPoint (AuxParam, true);
    end;

  until (IsExitMs);
end;
```

```
END.


UNIT AAux3B;

INTERFACE
uses DOS, Crt, GDriver, GKernel, GWindow,
    AcqT3B, PltT3B;

PROCEDURE AuxSection (var AuxParam : AuxRecord);

PROCEDURE GetSmCurrDataPoint (var AuxParam : AuxRecord;
                              IsTimed  : boolean);

PROCEDURE GetInterferDataPoint (var AuxParam : AuxRecord;
                                IsTimed  : boolean);



IMPLEMENTATION
procedure WriteAuxScreen (var AuxParam : AuxRecord);

   {This procedure sets up the AUXILARY DIAGNOSTICS screen
    and writes all parameters.}

begin
  ClearScreen;

  DefineWindow (1,0,0,XMaxGlb,YMaxGlb);              {System window}
  SelectWindow (1);
  DrawBorder;
  SetWindowModeOff;
  DrawLine (0,TextUp(24,2),XMaxGlb*8+7,TextUp(24,2));  {Command section}
  SetWindowModeOn;
  DrawBorder;

  DefineWindow (2,2,TextUp(3,-2),(XMaxGlb div 2)+20,
          Textdown(8,2));
  SelectWindow (2);
  if (Status.IsSmCurrSpectraON) then DefineHeader (2, 'SAMPLE CURRENT ON')
                        else DefineHeader (2, 'SAMPLE CURRENT OFF');
  DrawBorder;

  DefineWindow (3,2,TextUp(12,-2),(XMaxGlb div 2)+20,
          Textdown(17,2));
  SelectWindow (3);
  if (Status.IsInterferSpectraON) then DefineHeader (3, 'INTERFEROMETRY ON')
                        else DefineHeader (3, 'INTERFEROMETRY OFF');
  DrawBorder;

  SelectWindow (1);
  GotoXY (2,1);  Write (' AUXILARY DIAGNOSTICS ');
  GotoXY (70,1);  Write (' ', Status.FileName, ' ');

 {Print permitted options}
  GotoXY (2,24);
  Write ('F1/F2=SmCurr  F3/F4=Interfer  F5/F6=Redep  F9=Redraw');
  GotoXY (70,24);  Write ('Esc = Exit');

  with AuxParam do begin
    GotoXY (61,3); Write ('Start Time');
    GotoXY (62,4); Write (SmCurrStartT:6:2, ' (hhmm.ss)');
```

```
    GotoXY (61,5); Write ('Time Step');
    GotoXY (64,6); Write (SmCurrStepT:6:0, '  (sec)');

    GotoXY (61,7); Write ('Sm Amp Scale');
    GotoXY (64,8); Write ('10^- ', SmCurrAmpScale:1, '  (A)');

    GotoXY (5,10);  Write ('Avg. Sample Current:');

    GotoXY (61,12); Write ('Start Time');
    GotoXY (62,13); Write (InterferStartT:6:2, ' (hhmm.ss)');

    GotoXY (61,14); Write ('Time Step');
    GotoXY (64,15); Write (InterferStepT:6:0, '  (sec)');
  end;

  if (Status.IsSmCurrSpectra)   then DrawSpectra (SmCurrData.FirstPoint, true, 2);
  if (Status.IsInterferSpectra) then DrawSpectra (InterferData.FirstPoint, true, 3);
end;



procedure GetSmCurrAcqParam (var AuxParam : AuxRecord);

    {This procedure inputs the SAMPLE acquisition parameters. If <return> is
     entered as the first key, previous parameter settings are saved.}

var
  InputString : str8;
  IsYes : boolean;

begin
  IsYes := false;

  repeat
    Erase2425;
    GotoXY (2,24);
    Write ('Input SAMPLE Acquisition Parameters indicated by  *');

    with AuxParam do begin
      GetReal (SmCurrStepT, 64, 6, 6, 0);
      if (SmCurrStepT < 1.0) then SmCurrStepT := 1.0;
      GotoXY (64,6); Write (SmCurrStepT:6:0, '  (sec)');

      GetInteger (SmCurrAmpScale, 69, 8, 1);
      GotoXY (64,8); Write ('10^- ', SmCurrAmpScale:1, '  (A)');
    end;

    GotoXY (2,25);
    Write ('Are the parameters correct ? (y or n)');
    repeat
      InputString := UpCase(readkey);
      if (InputString = 'Y') then IsYes := true;
    until ((InputString = 'Y') or (InputString = 'N'));

  until (IsYes);

  Erase2425;
  GotoXY (2,24);
  Write ('F1/F2=SmCurr   F3/F4=Interfer   F9=Redraw');
  GotoXY (70,24);  Write ('Esc = Exit');

end;
```

```
procedure GetInterferAcqParam (var AuxParam : AuxRecord);

    {This procedure inputs the INTEFER acquisition parameters. If <return> is
     entered as the first key, previous parameter settings are saved.}

var
  InputString : str8;
  IsYes : boolean;

begin
  IsYes := false;

  repeat
    Erase2425;
    GotoXY (2,24); Write ('Input INTERFER Acquisition Parameters indicated by *');

    with AuxParam do begin
      GetReal (InterferStepT, 64, 15, 6, 0);
      if (InterferStepT < 0.05) then InterferStepT := 0.05;
      GotoXY (64,15); Write (InterferStepT:6:0, '  (sec)');
   end;

    GotoXY (2,25); Write ('Are the parameters correct ? (y or n)');
    repeat
      InputString := UpCase(readkey);
      if (InputString = 'Y') then IsYes := true;
    until ((InputString = 'Y') or (InputString = 'N'));

  until (IsYes);

  Erase2425;
  GotoXY (2,24);
  Write ('F1/F2=SmCurr  F3/F4=Interfer  F9=Redraw');
  GotoXY (70,24); Write ('Esc = Exit');

end;



PROCEDURE GetSmCurrDataPoint (var AuxParam : AuxRecord;
                              IsTimed  : boolean);

    {The procedure obtains data from the IEEE 488 card connected to
     the HP5384A frequency counter. The acquired data is stored
     in a linked list.}


var
  GateString : string[3];      { variables used for IEEE bus communication}
  st5384A    : integer;
  Response   : str255;

  Hour, Minute, Second, Sec100 : word;

  T, SmC, Multiplier, Freq : real;

  count, code, FuncKey : integer;
  IsInterrupt : boolean;

begin
```

```
{Exit if too early to take data point}
 if (IsTimed) then begin
   GetTime (Hour, Minute, Second, Sec100);
   T := int(Hour)*3600.0+int(Minute)*60.0+int(Second) - AuxParam.SmCurrT0;
   if ((AuxParam.SmCurrNumberSteps > 1) and ((T-SmCurrData.LastPoint^.Xvalue)
    < AuxParam.SmCurrStepT)) then EXIT;
 end;

{Set multiplier}
 Multiplier := 1.0;
 for count := 1 to AuxParam.SmCurrAmpScale do Multiplier := Multiplier*10.0;

{Get Y value}
 SmC := 0.0;

  {Start data collection}
   Writeln (IeeeOut, 'OUTPUT 03;RE');

  {Check for interrupt and determine the cause}
   IsInterrupt := false;
   repeat
     Regs.AX := $0400;                    {Check for SRQ interrupt}
     Intr($10,Regs);
     While (Regs.AH <> 0) do begin        {If interrupt ...}
       Writeln (IeeeOut, 'SPOLL 03');
       Readln (IeeeIn,st5384A);
       if (st5384A and 64) <> 0 then begin
         if (st5384A and 1) <> 0 then IsInterrupt := true;          {Data Ready}
         if (st5384A and 4) <> 0 then begin          {Error}
           Writeln (IeeeOut, 'OUTPUT 03;SE');      {Get error code}
           Writeln (IeeeOut, 'ENTER 03');
           Readln (IeeeIn, Response);
           Response := RemoveSpaces(Response);
           GotoXY (2,25);
           Write ('ERROR #: ', Response, '                    ');
         end;
       end;
       Regs.AX := $0400;                  {Check for another interrupt}
       Intr($10,Regs);
     end;
   until (IsInterrupt);

  {Get data}
   Writeln (IeeeOut, 'ENTER 03');
   Readln (IeeeIn, Response);

  {Determine the real value of the data from the response}
   Delete (Response, 1, 128);
   Val (Response, Freq, code);
   SmC := Freq;

{Read the time}
 GetTime (Hour, Minute, Second, Sec100);
 T := int(Hour)*3600.0+int(Minute)*60.0+int(Second) - AuxParam.SmCurrT0;

 SmC := SmC/(Multiplier);   {Incorporate the multiplier}

 AuxParam.SmAvgCurr := SmC;

{Store data in linked list}
 with SmCurrData do begin
   if FirstPoint = nil then begin          {Make new link}
```

```
      New (FirstPoint);
      LastPoint := FirstPoint;
    end
    else begin
      New (LastPoint^.NextPoint);
      LastPoint := LastPoint^.NextPoint;
    end;
    LastPoint^.NextPoint := nil;          {Store data}
    LastPoint^.Xvalue := T;
    LastPoint^.Yvalue := SmC;
    AuxParam.SmCurrNumberSteps := AuxParam.SmCurrNumberSteps + 1;
  end;

end;



PROCEDURE GetInterferDataPoint (var AuxParam : AuxRecord;
                                IsTimed  : boolean);

    {The procedure obtains interferometry data from photometer thru the
     AD/DA data acquisition card.  The acquired data is stored
     in a linked list.}

type
  Bit16 = record
    Low, High : byte;
  end;

var
  InStat, OutLow, OutHigh : byte;
  InValue : Bit16;

  Hour, Minute, Second, Sec100 : word;

  T, PIP : real;
  count, code, FuncKey : integer;
  IsADFinished : boolean;

begin
 {Exit if too early to take data point}
  if (IsTimed) then begin
    GetTime (Hour, Minute, Second, Sec100);
    T := int(Hour)*3600.0+int(Minute)*60.0+int(Second) - AuxParam.InterferT0;
    if ((AuxParam.InterferNumberSteps > 1) and ((T-InterferData.LastPoint^.Xvalue)
      < AuxParam.InterferStepT)) then EXIT;
  end;

 {Get Y value from the average of 5 consecutive readings}
  PIP := 0.0;

  for count := 1 to 5 do begin
   {Start Data Acquisition (reset AD, set gain = 1, set AD Ch = 3)}
    OutLow := 0*128 + 0*64 + 0*32 + 0*16 + 0*8 + 0*4 + 0*2 + 0;
    Port[$218] := OutLow;
    OutLow := 0*128 + 0*64 + 0*32 + 0*16 + 0*8 + 0*4 + 1*2 + 1;
    Port[$219] := OutLow;

    IsADFinished := false;
    repeat
      InStat := Port[$218];
      if (InStat >= 128) then IsADFinished := true;
```

```
    until (IsADFinished);

   {Read the AD value}
    InValue.Low  := Port[$21A];
    InValue.High := Port[$21B];
    PIP := PIP + ((integer(InValue)/4095)*5.0);
gotoXY (2,3);
write (integer(InValue):4);
  end;

 {Read the time}
  GetTime (Hour, Minute, Second, Sec100);
  T := int(Hour)*3600.0+int(Minute)*60.0+int(Second) - AuxParam.InterferT0;

  PIP := PIP/5.0;       {Average}

 {Store data in linked list}
  with InterferData do begin
    if FirstPoint = nil then begin          {Make new link}
      New (FirstPoint);
      LastPoint := FirstPoint;
    end
    else begin
      New (LastPoint^.NextPoint);
      LastPoint := LastPoint^.NextPoint;
    end;
    LastPoint^.NextPoint := nil;            {Store data}
    LastPoint^.Xvalue := T;
    LastPoint^.Yvalue := PIP;
    AuxParam.InterferNumberSteps := AuxParam.InterferNumberSteps + 1;
  end;

end;



PROCEDURE AuxSection (var AuxParam : AuxRecord);

    {This procedure sets up procedures for monitoring AUXILARY data.
     Currently monitored: Sample Current, Inteferometry.}

TYPE
  Bit16 = record
    Low, High : byte;
  end;

VAR
  IsExitAux : boolean;
  FuncKey   : integer;
  Answer    : str8;

  Hour, Minute, Second, Sec100 : word;
  Time, TimeOld : real;

  OutLow, OutHigh : byte;
  InValue : Bit16;

BEGIN
  WriteAuxScreen (AuxParam);
  IsExitAux := false;
  GetTime (Hour, Minute, Second, Sec100);
  TimeOld := int(Hour)*3600.0+int(Minute)*60.0+int(Second);
```

```
{Repeat the Aux section}
 repeat

   DisplayTime;

   FuncKey := 1;
   if keypressed then GetFuncKey (FuncKey);

  {Automatic redraw at one minute intervals}
   GetTime (Hour, Minute, Second, Sec100);
   Time := int(Hour)*3600.0+int(Minute)*60.0+int(Second);
   if ((Time-TimeOld) > 60.0) then begin
         FuncKey := 67;
         TimeOld := Time;
   end;

   Case FuncKey of

    {Start taking Sample Current data}
     59:begin
         if (Status.IsSmCurrSpectra) then begin
           GotoXY (2,25);
           Write ('WARNING -- Sample Current data exists!     Continue ? (y or n)');
           repeat
             Answer := UpCase(readkey);
           until ((Answer = 'Y') or (Answer = 'N'));
           if (Answer = 'N') then begin
            {Remove old data}
             EraseData (SmCurrData);
             Status.IsSmCurrSpectra := false;
             GetTime (Hour, Minute, Second, Sec100);
             AuxParam.SmCurrStartT := int(Hour)*100.0+int(Minute)+int(Second)/100.0;
             GotoXY (62,4); Write (AuxParam.SmCurrStartT:6:2, ' (hhmm.ss)');
             AuxParam.SmCurrT0 := int(Hour)*3600.0+int(Minute)*60.0+int(Second);
             AuxParam.SmAvgCurr := 0.0;
             AuxParam.SmCurrNumberSteps := 0;
             WriteAuxScreen (AuxParam);
           end;
         end
         else begin
           GetTime (Hour, Minute, Second, Sec100);
           AuxParam.SmCurrStartT := int(Hour)*100.0+int(Minute)+int(Second)/100.0;
           GotoXY (62,4); Write (AuxParam.SmCurrStartT:6:2, ' (hhmm.ss)');
           AuxParam.SmCurrT0 := int(Hour)*3600.0+int(Minute)*60.0+int(Second);
           AuxParam.SmAvgCurr := 0.0;
           AuxParam.SmCurrNumberSteps := 0;
         end;

         GetSmCurrAcqParam (AuxParam);
         Status.IsSmCurrSpectra   := true;
         Status.IsSmCurrSpectraON := true;

         SelectWindow (2);
         DefineHeader (2, 'SAMPLE CURRENT ON');
         DrawBorder;

         repeat
           Delay (1000);
           GetSmCurrDataPoint (AuxParam, false);
         until (AuxParam.SmCurrNumberSteps > 2);
       end;
```

```
{Stop taking Sample Current data}
 60:begin
      GetSmCurrDataPoint (AuxParam, false);
      Status.IsSmCurrSpectraON := false;
      WriteAuxScreen (AuxParam);
    end;

{Start taking Interferometry data}
 61:begin
      if (Status.IsInterferSpectra) then begin
        GotoXY (2,25);
        Write ('WARNING -- Interferometry data exists!     Continue ? (y or n)');
        repeat
          Answer := UpCase(readkey);
        until ((Answer = 'Y') or (Answer = 'N'));
        if (Answer = 'N') then begin
         {Remove old data}
          EraseData (InterferData);
          Status.IsInterferSpectra := false;
          GetTime (Hour, Minute, Second, Sec100);
          AuxParam.InterferStartT := int(Hour)*100.0+int(Minute)+int(Second)/100.0;
          GotoXY (62,13); Write (AuxParam.InterferStartT:6:2, ' (hhmm.ss)');
          AuxParam.InterferT0 := int(Hour)*3600.0+int(Minute)*60.0+int(Second);
          AuxParam.InterferNumberSteps := 0;
          WriteAuxScreen (AuxParam);
        end;
      end
      else begin
        GetTime (Hour, Minute, Second, Sec100);
        AuxParam.InterferStartT := int(Hour)*100.0+int(Minute)+int(Second)/100.0;
        GotoXY (62,13); Write (AuxParam.InterferStartT:6:2, ' (hhmm.ss)');
        AuxParam.InterferT0 := int(Hour)*3600.0+int(Minute)*60.0+int(Second);
        AuxParam.InterferNumberSteps := 0;
      end;

      GetInterferAcqParam (AuxParam);
      Status.IsInterferSpectra   := true;
      Status.IsInterferSpectraON := true;

      SelectWindow (3);
      DefineHeader (3, 'INTERFEROMETRY ON');
      DrawBorder;

      repeat
        Delay (1000);
        GetInterferDataPoint (AuxParam, false);
      until (AuxParam.InterferNumberSteps > 2);
    end;

{Stop taking interferometry data}
 62:begin
      GetInterferDataPoint (AuxParam, false);
      Status.IsInterferSpectraON := false;
      WriteAuxScreen (AuxParam);
    end;

{Redraw}
 67:begin
      WriteAuxScreen (AuxParam);
      TimeOld := Time;
    end;
```

```
      {Exit}
       150:begin
             IsExitAux := true;
           end;

    end; {case}

    if (Status.IsSmCurrSpectraON) then begin
      GetSmCurrDataPoint (AuxParam, true);
      GotoXY (28,10); Write (AuxParam.SmAvgCurr, '  (A)');
    end;
    if (Status.IsInterferSpectraON) then begin
      GetInterferDataPoint (AuxParam, true);
    end;

  until (IsExitAux);
end;

END.
```

```
UNIT PltT3B;

INTERFACE
uses DOS, Crt, GDriver, GKernel, GWindow,
    AcqT3B, AnlT3B;

PROCEDURE DrawSpectra (FirstPoint : DataPointer;
                       IsConnect  : boolean;
                       Window     : integer);

PROCEDURE ScreenPlot (FirstPoint  : DataPointer;
                      Multiplier  : real;
                      XStart      : real;
                      XEnd        : real;
                      Max         : real;
                      Min         : real;
                      StartAssign : real;
                      ScanDirec   : real;
                      IsAxis      : boolean);

Procedure ProPlotMsSummary (    DataFirstPoint : DataPointer;
                            var MsPeakData     : MsPeakArray;
                            var MsParam        : MsRecord;
                                Path           : str60);

Procedure ProPlotAuxSummary (    SmCurrDataFirstPoint  : DataPointer;
                                 InterferDataFirstPoint : DataPointer;
                             var AuxParam               : AuxRecord);



IMPLEMENTATION
PROCEDURE DrawSpectra (FirstPoint : DataPointer;
                       IsConnect  : boolean;
                       Window     : integer);

var
  CurrentPoint : DataPointer;
  XStart, XEnd, Max, Min : real;
  X, XOld, Y, YOld : real;
```

```
begin
 {Find Start, End, Max, Min}
  CurrentPoint := FirstPoint;
  XStart := CurrentPoint^.Xvalue;
  Max := CurrentPoint^.Yvalue;
  Min := Max;
  while (CurrentPoint^.NextPoint <> nil) do begin
    if (Max < CurrentPoint^.Yvalue) then Max := CurrentPoint^.Yvalue;
    if (Min > CurrentPoint^.Yvalue) then Min := CurrentPoint^.Yvalue;
    CurrentPoint := CurrentPoint^.NextPoint;
  end;
  if (Max < CurrentPoint^.Yvalue) then Max := CurrentPoint^.Yvalue;
  if (Min > CurrentPoint^.Yvalue) then Min := CurrentPoint^.Yvalue;
  XEnd := CurrentPoint^.Xvalue;

 {Protect against false data}
  if ((Max = Min) and (Max <> 0.0)) then Min := Max-Max*0.95;
  if ((Max = Min) and (Max = 0.0))  then begin
    Max :=  0.1;
    Min := -0.1;
  end;
  if (FirstPoint = nil)
    then begin
      XStart := 1.0;
      XEnd   := 2.0;
    end;
  if (XStart >= XEnd) then XEnd := XStart+1.0;

  DefineWorld (Window, XStart, Max+(Max-Min)*0.05, XEnd, Min-(Max-Min)*0.05);
  SelectWorld (Window);
  SelectWindow (Window);

 {Plot data}
  CurrentPoint := FirstPoint;
  XOld := CurrentPoint^.Xvalue;
  YOld := CurrentPoint^.Yvalue;
  CurrentPoint := CurrentPoint^.NextPoint;
  while (CurrentPoint <> nil) do begin
    X := CurrentPoint^.Xvalue;
    Y := CurrentPoint^.Yvalue;
    if (IsConnect) then DrawLine (XOld, YOld, X, Y)
                   else DrawPoint (X, Y);
    CurrentPoint := CurrentPoint^.NextPoint;
    XOld := X;
    YOld := Y;
  end;
end;



PROCEDURE ScreenPlot (FirstPoint  : DataPointer;
                      Multiplier  : real;
                      XStart      : real;
                      XEnd        : real;
                      Max         : real;
                      Min         : real;
                      StartAssign : real;
                      ScanDirec   : real;
                      IsAxis      : boolean);

var
  TL, TR, TU, TD : integer;
```

```
  TickMark : real;
  count : integer;

  ValueString6 : string[6];
  ValueString9 : string[9];

  CurrentPoint : DataPointer;
  X, XOld, Y, YOld : real;

begin
  DefineWorld (1, 0, 0, XMaxGlb, YMaxGlb);
  SelectWorld (1);
  SelectWindow (1);

  TL := TextLeft (8,1)*8;
  TR := TextRight (76,1)*8;
  TU := TextUp (2,1);
  TD := TextDown (21,2);

  if (IsAxis) then begin
    SetWindowModeOff;
    DrawLine (TL, TD, TR, TD);
    DrawLine (TL, TD, TL, TU);

    TickMark := (TR-TL)/10;
    for count := 1 to 11 do begin
      DrawLine (Round(TL+TickMark*(count-1)), TD,
            Round(TL+TickMark*(count-1)), TD+5);
      Str ((StartAssign+ScanDirec*((XEnd-XStart)/10.0)*(count-1)):6:1,
          ValueString6);
      DrawText (Round(TL+TickMark*(count-1)), TD+10, 1, ValueString6);
    end;

    TickMark := (TU-TD)/10;
    for count := 1 to 11 do begin
      DrawLine (TL-5, Round(TD+TickMark*(count-1)),
            TL,   Round(TD+TickMark*(count-1)));
      Str ( ((Min + ((Max-Min)/10)*(count-1))*Multiplier):9:1, ValueString9 );
      DrawText (3, Round(TD+TickMark*(count-1))+5, 1, ValueString9);
    end;

    SetWindowModeOn;

  end;

  DefineWindow (2, (TL div 8), TU, (TR div 8), TD);
  DefineWorld (2, XStart, Max, XEnd, Min);
  SelectScreen (1);
  SelectWorld (2);
  SelectWindow (2);

  CurrentPoint := FirstPoint;
  XOld := CurrentPoint^.Xvalue;
  YOld := CurrentPoint^.Yvalue;
  while (CurrentPoint <> nil) do begin
    X := CurrentPoint^.Xvalue;
    Y := CurrentPoint^.Yvalue;
    DrawLine (XOld, YOld, X, Y);
    CurrentPoint := CurrentPoint^.NextPoint;
    XOld := X;
    YOld := Y;
  end;
```

```
end;


Procedure ProPlotMsSummary (    DataFirstPoint : DataPointer;
                        var MsPeakData     : MsPeakArray;
                        var MsParam        : MsRecord;
                           Path            : str60);

var
  Quote : string[1];
  NumStr : string[2];
  ProPlotFile : text;

  X, Y, YOld, YNext : double;
  Multiplier : real;
  PeakCount, count1, count2 : integer;

  CurrentPoint : DataPointer;

begin
  Quote := chr(39);
  GotoXY (2,25); Write ('Writing MS ProPLot File');

  Multiplier := 1.0;
  for count1 := 1 to MsParam.AmpScale do Multiplier := Multiplier*10.0;

  Str (Status.CurrentSpectraNumber, NumStr);
  if (Length(NumStr) = 1) then NumStr := '0'+ NumStr;

  assign  (ProPlotFile,
        Path+'\'+Status.FileName+NumStr+'.M');
  rewrite (ProPlotFile);

  Writeln (ProPlotFile, 'SET LEGEND SIZE= 2.0  FONT= PB');
  Writeln (ProPlotFile, 'SET LEGEND JUSTIFY= CENTER');
  Writeln (ProPlotFile, 'LEGEND 5.5, 7.87 ', Quote, 'MASS  SPECTROMETRY     File: ',
                    Status.FileName, '  ', Status.CurrentSpectraNumber,
                    ' of ', Status.MsNumber, Quote);

  Writeln (ProPlotFile, 'SET WINDOW X FROM 1.0 TO 8.0  Y FROM 2.25 TO 7.75  RESCALE ON');

  Writeln (ProPlotFile, 'SET TYPE BOX');
  Writeln (ProPlotFile, 'SET SYMBOL 9N SIZE= 0.1 ');
  Writeln (ProPlotFile, 'SET AXIS ALL INTENSITY= 1.1 ');
  Writeln (ProPlotFile, 'SET LABELS ALL SIZE= 1.25 ');
  Writeln (ProPlotFile, 'SET LABELS LEFT FORMAT EXP ');
  Writeln (ProPlotFile, 'SET TICKS TOP OFF');
  Writeln (ProPlotFile, 'SET TICKS BOTTOM SIZE=-0.8');
  Writeln (ProPlotFile, 'SET GRID X ON  STYLE DOTS  INTENSITY 0.005  RATIO 1.0');

  Writeln (ProPlotFile, 'SET TITLE TOP    SIZE= 2.25 OFFSET= 0.75');
  Writeln (ProPlotFile, 'SET TITLE LEFT   SIZE= 1.50 OFFSET= 0.90');
  Writeln (ProPlotFile, 'SET TITLE BOTTOM SIZE= 1.50 OFFSET= 0.25');

  Writeln (ProPlotFile, 'TITLE TOP ', Quote, ' ', Quote);
  Writeln (ProPlotFile, 'TITLE BOTTOM ', Quote, 'Mass Number  (amu)', Quote);
  Writeln (ProPlotFile, 'TITLE LEFT ', Quote, 'Channeltron Current  (A)', Quote);
  Writeln (ProPlotFile, ' ');

  Writeln (ProPlotFile, 'SET ORDER X Y');
```

```
CurrentPoint := DataFirstPoint;
YOld := -1.0;
Y := CurrentPoint^.Yvalue;
while (CurrentPoint <> nil) do begin
  X := CurrentPoint^.Xvalue;
  if (CurrentPoint^.NextPoint <> nil)
    then YNext := CurrentPoint^.NextPoint^.Yvalue
    else YNext := -3.0;
  if (abs(YNext) < 0.01/Multiplier) then YNext := 0.0;
  if not ((Y = YOld) and (Y = YNext)) then
    Writeln (ProPlotFile, X, ' ', Y);
  CurrentPoint := CurrentPoint^.NextPoint;
  YOld := Y;
  Y := YNext;
end;

Writeln (ProPlotFile, 'SET JOIN METHOD= LINEAR  INTENSITY= 1.0');
Writeln (ProPlotFile, 'JOIN');
Writeln (ProPlotFile, ' ');

Writeln (ProPlotFile, 'SET LEGEND SIZE= 1.0 SPACING= 1.25 FONT= C');
Writeln (ProPlotFile, 'SET LEGEND JUSTIFY= LEFT');

Writeln (ProPlotFile, 'LEGEND 8.5, 7.8 ', Quote, 'Start Time: ',
                      MsParam.StartTime:7:2, '  (hhmm.ss)', Quote);

Writeln (ProPlotFile, 'LEGEND 8.5, 7.5 ', Quote, '  ', Quote);
with MsParam do begin
  Writeln (ProPlotFile, 'LEGEND ', Quote, '  ACQUISITION PARAMETERS', Quote);
  Writeln (ProPlotFile, 'LEGEND ', Quote, 'Starting amu:    ',
                                  StartMs:6:2, '  (amu)', Quote);

  Writeln (ProPlotFile, 'LEGEND ', Quote, 'Ending amu:      ',
                                  EndMs:6:2, '  (amu)', Quote);

  Writeln (ProPlotFile, 'LEGEND ', Quote, 'Step amu:        ',
                                  StepMs:6:2, '  (amu)', Quote);

  Writeln (ProPlotFile, 'LEGEND ', Quote, 'Number of Steps: ',
                                  NumberSteps:4:0, Quote);

  Writeln (ProPlotFile, 'LEGEND ', Quote, 'Time Delay:      ',
                                  TimeDelay:5:3, '  (s)', Quote);

  Writeln (ProPlotFile, 'LEGEND ', Quote, 'Amp Sample:      ',
                                 '10^ -', AmpScale:1, '  (A)', Quote);


  Writeln (ProPlotFile, 'LEGEND ', Quote, '  ', Quote);
  Writeln (ProPlotFile, 'LEGEND ', Quote, '  ', Quote);
  Writeln (ProPlotFile, 'LEGEND ', Quote, '  ', Quote);


  Writeln (ProPlotFile, 'LEGEND ', Quote, '  MS PARAMETERS', Quote);

  Write   (ProPlotFile, 'LEGEND ', Quote, 'Ion ID:              ');
  if (IonID = 'p')
    then Writeln (ProPlotFile, 'POSITIVE', Quote)
    else Writeln (ProPlotFile, 'NEGATIVE', Quote);

  Writeln (ProPlotFile, 'LEGEND ', Quote, 'Channeltron Voltage:',
                   ChannVoltage:5:0, '  (V)', Quote);
```

```
  Writeln (ProPlotFile, 'LEGEND ', Quote, 'Resolution:          ',
                   Resolution:5:2, '      ', Quote);

  Writeln (ProPlotFile, 'LEGEND ', Qu ite, 'Mass Range:          ',
                   MassRange, Quote);

  Writeln (ProPlotFile, 'LEGEND ', Quote, 'e Current:          ',
                   eCurrent:5:3, '  (mA)', Quote);

  Writeln (ProPlotFile, 'LEGEND ', Quote, 'e Energy:          ',
                   eEnergy:5:1, '  (eV)', Quote);

  Writeln (ProPlotFile, 'LEGEND ', Quote, 'Ion Energy:          ',
                   IonEnergy:5:1, '  (eV)', Quote);

  Writeln (ProPlotFile, 'LEGEND ', Quote, 'Focus:          ',
                   Focus:5:1, '  (V)', Quote);

  Write   (ProPlotFile, 'LEGEND ', Quote, 'Ms Flag:          ');
  if (IsMsFlagOpen) then Writeln (ProPlotFile, 'OPEN  ', Quote)
                else Writeln (ProPlotFile, 'CLOSED', Quote);

  Writeln (ProPlotFile, 'LEGEND ', Quote, 'Angle:          ',
                   Angle:5:1, '  (deg)', Quote);

end;

with MsParam.SysParam do begin
  Writeln (ProPlotFile, 'LEGEND 0.5, 1.75 ', Quote, '  ', Quote);
  Writeln (ProPlotFile, 'LEGEND ', Quote, '   SAMPLE PARAMETERS', Quote);

  Writeln (ProPlotFile, 'LEGEND ', Quote, 'Film Identity:   ',
                   SmFilm, Quote);

  Writeln (ProplotFile, Quote);

  Writeln (ProPlotFile, 'LEGEND ', Quote, 'Sample Temp:     ',
                   SmAvgTemp:3:0,  '  (C)', Quote);

  Writeln (ProPlotFile, 'LEGEND ', Quote, 'Samp. Current:   ',
                   SmCurr:5:1, Quote);

  Writeln (ProPlotFile, 'LEGEND ', Quote, 'Curr Scale:   ',
                   SmCurrScale:2, Quote);

  Writeln (ProPlotFile, 'LEGEND 2.5, 1.75 ', Quote, '  ', Quote);
  Writeln (ProPlotFile, 'LEGEND ', Quote, '   BEAM PARAMETERS', Quote);

  Writeln (ProPlotFile, 'LEGEND ', Quote, 'Ion Source:    ',
                   Isource:8, Quote);

  Writeln (ProPlotFile, 'LEGEND ', Quote, 'Source Gas:     ',
                   GasISName:8, Quote);

  Writeln (ProPlotFile, 'LEGEND ', Quote, 'Source Press.:   ',
                   GasISPP:5:3, '  (E-6 t)', Quote);

  Writeln (ProPlotFile, 'LEGEND ', Quote, 'Ion Energy:    ',
                   Vion:3:0, '  (v)', Quote);

  Writeln (ProPlotFile, 'LEGEND ', Quote, 'Vaccel.:    ',
                   Vaccel:6:3, '  (v)', Quote);
```

```
    Writeln (ProPlotFile, 'LEGEND 5.0, 1.75 ', Quote, '  ', Quote);
    Writeln (ProPlotFile, 'LEGEND ', Quote, '  ', Quote);
    Writeln (ProPlotFile, 'LEGEND ', Quote, 'Neutral 1:     ',
                    GasD1Name:8, '     ', GasD1PP:6:2, '  (E-6 t)', Quote);

    Writeln (ProPlotFile, 'LEGEND ', Quote, 'Neutral 2:     ',
                    GasD2Name:8, '     ', GasD2PP:6:2, '  (E-6 t)', Quote);
  end;

  Writeln (ProPlotFile, 'SET LEGEND SIZE= 1.25 SPACING= 1.25 FONT= PB');
  Writeln (ProPlotFile, 'LEGEND 1.5, 0.75 ', Quote,
                  'Comments:   ',Status.Description, Quote);


  Writeln (ProPlotFile, 'SET LEGEND SIZE= 1.0 SPACING= 1.25 FONT= C');
  Writeln (ProPlotFile, 'LEGEND 8.5, 4.5 ', Quote, '  ', Quote);
  Writeln (ProPlotFile, 'LEGEND ', Quote, '  PEAK LOCATIONS', Quote);

 {Write peak locations}
  Writeln (ProPlotFile, 'SET LEGEND SIZE= .75 SPACING= 1.1 FONT= C');
  Writeln (ProPlotFile, 'LEGEND ', Quote,
        '    Amp Scale:  10^ -', MsParam.AmpScale:1, Quote);

  Writeln (ProPlotFile, 'LEGEND 8.25, 4.125 ', Quote, '  ', Quote);
  count1 := 1;
  count2 := 1;
  for PeakCount := 0 to 99 do begin
    if (MsPeakData[PeakCount] <> 0.0) then begin
      Writeln (ProPlotFile, 'LEGEND ', Quote,
            PeakCount:2, '  ',
           (MsPeakData[PeakCount]*Multiplier):5:3, Quote);
      count1 := count1 + 1;
      if (count1 > 40) then begin
        Writeln (ProPlotFile, 'LEGEND ', (8.25+0.75*count2):5:2, ' 4.125 ', Quote, '  ', Quote);
        count1 := 1;
        count2 := count2 + 1
      end;
    end;
  end;

  Close (ProPlotFile);
  Erase25;
end;



Procedure ProPlotAuxSummary (   SmCurrDataFirstPoint  : DataPointer;
                        InterferDataFirstPoint : DataPointer;
                      var AuxParam             : AuxRecord);

var
  Quote : string[1];
  ProPlotFile : text;

  X, Y, YOld, YNext : double;
  count1, count2 : integer;

  CurrentPoint : DataPointer;

begin
  Quote := chr(39);
  GotoXY (2,25); Write ('Writing AUXILARY ProPlot File');
```

```
assign  (ProPlotFile,
        Path+'PLOT\'+Status.FileName+'.A');
rewrite (ProPlotFile);

Writeln (ProPlotFile, 'SET LEGEND SIZE= 2.0 SPACING= 1.25 FONT= PB');
Writeln (ProPlotFile, 'SET LEGEND JUSTIFY= CENTER');
Writeln (ProPlotFile, 'LEGEND 5.5, 7.50 ', Quote, 'AUXILARY SPECTRA      File: ',
                Status.FileName, Quote);

Writeln (ProPlotFile, 'SET TYPE BOX');
Writeln (ProPlotFile, 'SET SYMBOL 9N SIZE= 0.1 ');
Writeln (ProPlotFile, 'SET AXIS ALL INTENSITY= 1.1 ');
Writeln (ProPlotFile, 'SET LABELS ALL SIZE= 1.25 ');
Writeln (ProPlotFile, 'SET LABELS LEFT FORMAT EXP ');
Writeln (ProPlotFile, 'SET TICKS TOP OFF');
Writeln (ProPlotFile, 'SET TICKS BOTTOM SIZE=-1.0');
Writeln (ProPlotFile, 'SET GRID X MAJOR  STYLE DOTS  INTENSITY 0.1');

Writeln (ProPlotFile, 'SET TITLE TOP    SIZE= 1.75 OFFSET= 1.0');
Writeln (ProPlotFile, 'SET TITLE LEFT   SIZE= 1.5  OFFSET= 1.0');
Writeln (ProPlotFile, 'SET TITLE BOTTOM SIZE= 1.5  OFFSET= 0.25');

if (Status.IsSmCurrSpectra) then begin
  Writeln (ProPlotFile, 'SET WINDOW X FROM 1.5 TO 8.0  Y FROM 4.75 TO 7.0  RESCALE OFF');

  Writeln (ProPlotFile, 'TITLE TOP ', Quote, 'SAMPLE CURRENT', Quote);
  Writeln (ProPlotFile, 'TITLE BOTTOM ', Quote, 'Run Time  (s)', Quote);
  Writeln (ProPlotFile, 'TITLE LEFT ', Quote, 'Current  (A)', Quote);
  Writeln (ProPlotFile, ' ');

  Writeln (ProPlotFile, 'SET ORDER X Y');

  CurrentPoint := SmCurrDataFirstPoint;
  YOld := -1.0;
  Y := CurrentPoint^.Yvalue;
  while (CurrentPoint <> nil) do begin
    X := CurrentPoint^.Xvalue;
    if (CurrentPoint^.NextPoint <> nil)
      then YNext := CurrentPoint^.NextPoint^.Yvalue
      else YNext := -1.0;
    if not ((Y = YOld) and (Y = YNext)) then
      Writeln (ProPlotFile, X, ' ', Y);
    CurrentPoint := CurrentPoint^.NextPoint;
    YOld := Y;
    Y := YNext;
  end;

  Writeln (ProPlotFile, 'SET JOIN METHOD= LINEAR  INTENSITY= 1.0');
  Writeln (ProPlotFile, 'JOIN');
  Writeln (ProPlotFile, ' ');
end;

if (Status.IsInterferSpectra) then begin
  Writeln (ProPlotFile, 'SET WINDOW X FROM 1.5 TO 8.0  Y FROM 1.25 TO 3.5  RESCALE OFF');

  Writeln (ProPlotFile, 'TITLE TOP ', Quote, 'INTERFEROMETRY', Quote);
  Writeln (ProPlotFile, 'TITLE BOTTOM ', Quote, 'Run Time  (s)', Quote);
  Writeln (ProPlotFile, 'TITLE LEFT ', Quote, 'Intensity  ', Quote);
  Writeln (ProPlotFile, ' ');

  Writeln (ProPlotFile, 'SET ORDER X Y');
```

```
    CurrentPoint := InterferDataFirstPoint;
    YOld := -1.0;
    Y := CurrentPoint^.Yvalue;
      while (CurrentPoint <> nil) do begin
      X := CurrentPoint^.Xvalue;
      if (CurrentPoint^.NextPoint <> nil)
        then YNext := CurrentPoint^.NextPoint^.Yvalue
        else YNext := -1.0;
      if not ((Y = YOld) and (Y = YNext)) then
        Writeln (ProPlotFile, X, ' ', Y);
      CurrentPoint := CurrentPoint^.NextPoint;
      YOld := Y;
      Y := YNext;
    end;

    Writeln (ProPlotFile, 'SET JOIN METHOD= LINEAR  INTENSITY= 1.0');
    Writeln (ProPlotFile, 'JOIN');
    Writeln (ProPlotFile, ' ');
  end;

  Writeln (ProPlotFile, 'SET LEGEND SIZE= 1.0 SPACING= 1.25 FONT= C');
  Writeln (ProPlotFile, 'SET LEGEND JUSTIFY= LEFT');

  with AuxParam do begin
    Writeln (ProPlotFile, 'LEGEND 8.5, 6.75 ', Quote, '  ', Quote);
    Writeln (ProPlotFile, 'LEGEND ', Quote, 'Start Time.:   ',
                    SmCurrStartT:6:2, '  (hhmm.ss)', Quote);

    Writeln (ProPlotFile, 'LEGEND ', Quote, 'Time Step:     ',
                    SmCurrStepT:6:0, '  (sec)', Quote);

    Writeln (ProPlotFile, 'LEGEND ', Quote, 'Sm Amp Scale:  ',
                    '10^- ', SmCurrAmpScale:1, '  (A)', Quote);

    Writeln (ProPlotFile, 'LEGEND ', Quote, '  ', Quote);
    Writeln (ProPlotFile, 'LEGEND ', Quote, 'Avg. Sample Current:  ', Quote);
    Writeln (ProPlotFile, 'LEGEND ', Quote, '    ',
                  SmAvgCurr:5:3, ' x 10^-', SmCurrAmpScale:1, '  (A)',
                  Quote);


    Writeln (ProPlotFile, 'LEGEND 8.5, 3.25 ', Quote, '  ', Quote);
    Writeln (ProPlotFile, 'LEGEND ', Quote, 'Start Time.:   ',
                    InterferStartT:6:2, '  (hhmm.ss)', Quote);

    Writeln (ProPlotFile, 'LEGEND ', Quote, 'Time Step:     ',
                    InterferStepT:6:0, '  (sec)', Quote);

  end;

  Close (ProPlotFile);
  Erase25;
end;



END.


UNIT FileT3B;

INTERFACE
```

```
uses DOS, Crt, GDriver, CKernel, GWindow,
    AcqT3B, AnlT3B;


PROCEDURE RetrieveData (var SData       : DataRecord;
                        RecordNumber : real;
                        LocalPath    : str40);

PROCEDURE SaveMs (var MsParam       : MsRecord;
                  FileName      : str6;
                  SpectraNumber : integer);

PROCEDURE RetrieveMsP (var MsParam       : MsRecord;
                       FileName      : str6;
                       SpectraNumber : integer);

PROCEDURE SaveAux (var AuxParam : AuxRecord;
                   FileName : str6);

PROCEDURE RetrieveAux (var AuxParam : AuxRecord;
                       FileName : str6);

PROCEDURE SaveRun (var MsParam   : MsRecord;
                var AuxParam  : AuxRecord);

PROCEDURE RetrieveRun;

PROCEDURE SaveMsPeakData (var MsPeakData    : MsPeakArray;
                          Multiplier    : real;
                          FileName      : str6;
                          SpectraNumber : integer);

PROCEDURE StatusReset;

PROCEDURE FindSpectraRelation (    FileName : str6;
                           var KeyCount : integer);

PROCEDURE CountSpectraRelation (    FileName : str6;
                            var KeyCount : integer);

PROCEDURE FileNameGen (var FileName : str6);

PROCEDURE GetFileName (var FileName : str6);

PROCEDURE GetSpectraNumber (    FileName      : str6;
                            LocalPath     : str40;
                        var SpectraNumber : integer);



IMPLEMENTATION
Procedure SaveData (FirstPoint   : DataPointer;
                    LocalPath    : str40);

type
  OutDataRecord = record
    Xvalue : real;
    Yvalue : real;
  end;

var
  PointCount : real;
```

```
  Data : OutDataRecord;
  DataFile : File of OutDataRecord;

  CurrentPoint : DataPointer;

begin
  GotoXY (2,25);
  Write ('Saving Data file');

  assign (DataFile, Path+LocalPath);
  rewrite (DataFile);

  CurrentPoint := FirstPoint;
  while (CurrentPoint <> nil) do begin
    Data.Xvalue := CurrentPoint^.Xvalue;
    Data.Yvalue := CurrentPoint^.Yvalue;
    write (DataFile, Data);
    CurrentPoint := CurrentPoint^.NextPoint;
  end;

  close (Datafile);
  Erase25;
end;



PROCEDURE RetrieveData (var SData        : DataRecord;
                        RecordNumber : real;
                        LocalPath    : str40);

type
  InDataRecord = record
    Xvalue : real;
    Yvalue : real;
  end;

var
  PointCount : real;

  Data : InDataRecord;
  DataFile : File of InDataRecord;

  CurrentPoint : DataPointer;

begin
  GotoXY (2,25);
  Write ('Retrieving Data file');

  assign (DataFile, Path+LocalPath);
  reset (DataFile);

  with SData do begin
    PointCount := 1;
    while (PointCount <= RecordNumber) do begin
      read (DataFile, Data);

      if FirstPoint = nil then begin          {Make new link}
        New (FirstPoint);
        LastPoint := FirstPoint;
      end
      else begin
        New (LastPoint^.NextPoint);
```

```
        LastPoint := LastPoint^.NextPoint;
      end;
      LastPoint^.NextPoint := nil;          {Store data}
      LastPoint^.Xvalue := Data.Xvalue;
      LastPoint^.Yvalue := Data.Yvalue;
      PointCount := PointCount + 1;
    end;
  end;

  close (Datafile);
  Erase25;
end;


PROCEDURE SaveMs (var MsParam      : MsRecord;
                  FileName     : str6;
                  SpectraNumber : integer);

var
  MsFile : File of MsRecord;

  SpectraNumberString : string[2];

begin
  GotoXY (2,25);
  Write ('Saving MS Parameters');

  Str (SpectraNumber, SpectraNumberString);
  if (Length(SpectraNumberString) = 1) then SpectraNumberString := '0'+SpectraNumberString;

  assign (MsFile, Path+'MS\'+FileName+SpectraNumberString+'.MP');
  rewrite (MsFile);
  write (MsFile, MsParam);
  close (MsFile);

  Erase25;

  SaveData (MsData.FirstPoint, 'MS\'+FileName+SpectraNumberString+'.MD');
end;


PROCEDURE RetrieveMsP (var MsParam      : MsRecord;
                       FileName     : str6;
                       SpectraNumber : integer);

var
  MsFile    : File of MsRecord;

  SpectraNumberString : string[2];


  TempFile : Text;

begin
  Str (SpectraNumber, SpectraNumberString);
  if (Length(SpectraNumberString) = 1) then SpectraNumberString := '0'+ SpectraNumberString;

  GotoXY (2,25);
  Write ('Retrieving MS Parameters for file: ', FileName+SpectraNumberString);
```

```
  assign (MsFile, Path+'MS\'+FileName+SpectraNumberString+'.MP');
  Assign(TempFile, 'shit.dat');
  rewrite(TempFile);
  writeln(tempfile, Path+'MS\'+FileName+SpectraNumberString+'.MP');
  Close(TempFile);
  reset (MsFile);
  read (MsFile, MsParam);
  close (MsFile);

  Erase25;
end;



PROCEDURE SaveAux (var AuxParam : AuxRecord;
                   FileName : str6);

var
  AuxFile : File of AuxRecord;

begin
  GotoXY (2,25);
  Write ('Saving AUXILARY Parameters');

  assign (AuxFile, Path+'AUXIL\'+FileName+'.AP');
  rewrite (AuxFile);
  write (AuxFile, AuxParam);
  close (AuxFile);
  Erase2425;

  if (SmCurrData.FirstPoint <> nil) then
    SaveData (SmCurrData.FirstPoint,
            'AUXIL\SAMPLE\'+FileName+'.SCD');
  if (InterferData.FirstPoint <> nil) then
    SaveData (InterferData.FirstPoint,
            'AUXIL\PLASMA\'+FileName+'.PPD');

  Erase25;
end;



PROCEDURE RetrieveAux (var AuxParam     : AuxRecord;
                       FileName     : str6);

var
  AuxFile : File of AuxRecord;

begin
  GotoXY (2,25);
  Write ('Retrieving AUXILARY Parameters for file: ', FileName);

  assign (AuxFile, Path+'AUXIL\'+FileName+'.AP');
  reset (AuxFile);
  read (AuxFile, AuxParam);
  close (AuxFile);

  Erase25;

  if (Status.IsSmCurrSpectra) then
    RetrieveData (SmCurrData,  AuxParam.SmCurrNumberSteps,
                'AUXIL\SAMPLE\'+FileName+'.SCD');
```

```
  if (Status.IsInterferSpectra) then
    RetrieveData (InterferData, AuxParam.InterferNumberSteps,
                  'AUXIL\PLASMA\'+FileName+'.PPD');
end;



PROCEDURE SaveRun (var MsParam   : MsRecord;
                   var AuxParam  : AuxRecord);

var
  RunFile : text;
  Answer : str8;
  IsSaveAuxil : boolean;
  count : integer;

begin
 {Determine if the not saved spectras are to be saved}
  Erase2425;

  if (not(Status.IsMsSaved) and (Status.MsNumber > 0)) then begin
    GotoXY (2,24);
    Write ('Latest MS spectra not saved --- save ? (y/n) : ');
    repeat Answer := readkey;
    until ((Answer = 'y') or (Answer = 'n'));
    if (Answer = 'y') then begin
      SaveMs (MsParam, Status.FileName, Status.MsNumber);
      Status.IsMsSaved := true;
    end
    else begin
      Status.MsNumber  := Status.MsNumber - 1;
      Status.IsMsSaved := true;
    end;
  end;
  Erase2425;

  IsSaveAuxil := false;
  if (Status.IsSmCurrSpectra or Status.IsInterferSpectra) then begin
    GotoXY (2,24);
    Write ('Latest AUXILARY spectra not saved --- save ? (y/n) : ');
    repeat Answer := readkey;
    until ((Answer = 'y') or (Answer = 'n'));
    if (Answer = 'y') then begin
      IsSaveAuxil := true;
      SaveAux (AuxParam, Status.FileName);
    end;
  end;
  Erase2425;

 {Check whether there are any spectra to save}
  if (  (Status.MsNumber > 0 )
     or (Status.IsSmCurrSpectra)
     or (Status.IsInterferSpectra) ) then begin

    GotoXY (2,24);
    Write ('Input Description');
    GotoXY (15,22);
    Write ('*');
    GetDescription (Status.Description,17,22);
    GotoXY (15,22);
    Write ('  ', Status.Description);
```

```
    GotoXY (2,25);
    Write ('Saving Run: ', Status.FileName);

    assign (RunFile, Path+'INFO\'+Status.FileName+'.RUN');
    rewrite (RunFile);
    writeln (RunFile, Status.Version:4:1);
    writeln (RunFile, Status.MsNumber);
    if IsSaveAuxil then begin
      writeln (RunFile, Status.IsSmCurrSpectra);
      writeln (RunFile, Status.IsInterferSpectra);
    end
    else begin
      writeln (RunFile, 'FALSE');
      writeln (RunFile, 'FALSE');
    end;
    writeln (RunFile, Status.Description);
    close (RunFile);

    Erase2425;
  end;
end;



PROCEDURE RetrieveRun;

var
  RunFile : text;
  Answer : str8;
  count : integer;

begin
  GotoXY (2,25);
  Write ('Retrieving Run: ', Status.FileName);

  assign (RunFile, Path+'INFO\'+Status.FileName+'.RUN');
  reset (RunFile);
  readln (RunFile, Status.Version);
  readln (RunFile, Status.MsNumber);
  readln (RunFile, Answer);
    if (Answer = 'TRUE') then Status.IsSmCurrSpectra := true
                         else Status.IsSmCurrSpectra := false;
  readln (RunFile, Answer);
    if (Answer = 'TRUE') then Status.IsInterferSpectra := true
                         else Status.IsInterferSpectra := false;
  readln (RunFile, Status.Description);
  close (RunFile);

  Erase2425;
end;



PROCEDURE SaveMsPeakData (var MsPeakData    : MsPeakArray;
                          Multiplier    : real;
                          FileName      : str6;
                          SpectraNumber : integer);

var
  OutPeak : Text;
  SpectraNumberString : string[2];
  count : integer;
```

```
begin
  GotoXY (2,25);
  Write ('Writing MS peak values');

  Str (SpectraNumber, SpectraNumberString);
  if (Length(SpectraNumberString) = 1)
    then SpectraNumberString := '0'+ SpectraNumberString;

  assign (OutPeak, Path+'MS\PEAKS\'+FileName+SpectraNumberString+'.MPD');
  rewrite (OutPeak);

  for count := 1 to 99 do begin
    Writeln (OutPeak, (MsPeakData[count]*Multiplier):7:3);
  end;

  Close (OutPeak);
  Erase25;
end;



PROCEDURE StatusReset;

begin
 {Reset all Status parameters}
  while (MsData.FirstPoint <> nil) do  EraseData (MsData);
  Status.MsNumber    := 0;
  Status.IsMsSpectra := false;
  Status.IsMsSaved   := false;

  if not(Status.IsSmCurrSpectraOn) then begin
    while (SmCurrData.FirstPoint <> nil) do EraseData (SmCurrData);
    Status.IsSmCurrSpectra := false;
  end;

  if not(Status.IsInterferSpectraOn) then begin
    while (InterferData.FirstPoint <> nil) do EraseData (InterferData);
    Status.IsInterferSpectra := false;
  end;

  Status.Description := ' ';
end;



PROCEDURE FileNameGen (var FileName : str6);

    {The procedure determines the first 6
     characters of the file name following a
     designated code:  User initial (1 char.)
     Year (1 char.), Month (1 Hex.Char.), Day (2 char.),
     and Run Number (1 char.)}

var
  Year, Month, Day, DayOfWeek : word;
  MonthCh, DayCh, YearCh : string[2];
  counter1Ch : char;
  counter1 : integer;
  DirInfo : SearchRec;
  TempFileName : str6;

begin
```

```
  GetDate (Year, Month, Day, DayOfWeek);

  Str (Month, MonthCh);
  if (Length(MonthCh) > 1) then MonthCh := char(Month-9+63);

  Str (Day, DayCh);
  if (Length(DayCh) = 1) then DayCh := '0'+DayCh;

  Year := Year-(Year div 10)*10;
  Str (Year, YearCh);

  FileName := Status.UserInitial+YearCh+MonthCh+DayCh;

  counter1 := 64;
  repeat
    counter1 := counter1 + 1;
    if (counter1 = 91) then begin
      GotoXY (2,25);
      Write ('Run Sequence FULL -- Restart with new initial          ');
      EXIT;
    end;
    counter1Ch := chr(counter1);
    TempFileName := FileName + counter1Ch;
    FindFirst (Path+'INFO\'+TempFileName+'.*', AnyFile, DirInfo);
  until (DosError <> 0);

  FileName := TempFileName;     {assign latest file to FileName}

end;



PROCEDURE GetFileName (var FileName : str6);

var
  IsStopRetrieval : boolean;
  FileCount, CurrentFile : integer;

  DirInfo  : SearchRec;
  FuncKey, count : integer;

begin
 {Set-up the screen}
  ClearScreen;
  DefineWindow (1,0,0,XMaxGlb,YMaxGlb);          {System window}
  SelectWindow (1);
  DrawBorder;
  SetWindowModeOff;
  DrawLine (0,TextUp(24,2),XMaxGlb*8+7,TextUp(24,2));  {Command section}
  SetWindowModeOn;

  SelectWindow (1);
  GotoXY (2,1);
  Write (' RUN RETRIEVE ');

 {Obtain the path}
  repeat
    Path := 'E:\dave\experime';
    GotoXY (2,24);
    Write ('Input the path: (', Path, ')');
    GetDescription (Path, 18, 24);
    Path := Path + '\';
```

```
    FindFirst (Path+'info/*.RUN', AnyFile, DirInfo);
    if (DosError > 0) then begin
      GotoXY (20,25); Write ('ERROR -- INVALID PATH or NO FILES');
      Sound (300);
      Delay (1000);
      NoSound;
      GotoXY (20,25); Write ('                                    ');
    end;
  until (DosError = 0);
  Erase24;

  {Reset all the parameters and erase all data prior to retrieval}
  {of new data}
  FileCount := 0;
  IsStopRetrieval := false;

  {Obtain and display all the file names available for retrieval}
  GotoXY (5,5);
  Write ('Files available for retrieval  (Path = ', Path, ')  :');

  {Find the first file}
  FindFirst (Path+'info\*.RUN', AnyFile, DirInfo);

  if (DosError = 0) then begin
   {if the first file exists, find the rest of the file names}
    FileCount := FileCount + 1;
    GotoXY (10+(trunc((FileCount-1)/15)*15),
          7+(FileCount-1)-(trunc((FileCount-1)/15)*15));
    Write (DirInfo.Name);
    repeat
      FindNext (DirInfo);
      if (DosError = 0) then begin
        FileCount := FileCount + 1;
        GotoXY (10+(trunc((FileCount-1)/15)*15),
              7+(FileCount-1)-(trunc((FileCount-1)/15)*15));
        Write (DirInfo.Name);
      end;
    until (DosError <> 0);
  end
  else IsStopRetrieval := true;

  {Retrieve the files for analysis}
  CurrentFile := 1;
  GotoXY (2,25);
  Write ('Hit RETURN to choose a run and terminate retrieval');

  while not(IsStopRetrieval) do begin;
    GotoXY (9+(trunc((CurrentFile-1)/15)*15),
          7+(CurrentFile-1)-(trunc((CurrentFile-1)/15)*15));
    Write ('>');

    GetFuncKey (FuncKey);

    GotoXY (9+(trunc((CurrentFile-1)/15)*15),
          7+(CurrentFile-1)-(trunc((CurrentFile-1)/15)*15));
    Write (' ');

    Case FuncKey of
      13 : begin
           {Find the first file}
            FindFirst (Path+'info\*.RUN', AnyFile, DirInfo);
```

```
            {Advance through the file names to the current file}
              for count := 2 to CurrentFile do FindNext (DirInfo);

            {Store it}
              FileName := DirInfo.Name;
              IsStopRetrieval := true;
            end;

        72 : CurrentFile := CurrentFile - 1;
        75 : CurrentFile := CurrentFile - 15;
        80 : CurrentFile := CurrentFile + 1;
        77 : CurrentFile := CurrentFile + 15;
      end;

      if (CurrentFile < 1) then CurrentFile := 1;
      if (CurrentFile > FileCount) then CurrentFile := FileCount;
    end;
    Erase25;
end;



PROCEDURE GetSpectraNumber (    FileName      : str6;
                                LocalPath     : str40;
                            var SpectraNumber : integer);

var
    DirInfo  : SearchRec;
    TotalSpectraNumber, SpectraCount : integer;
    SpectraCountString : string[2];

begin
    ClearScreen;
    DefineWindow (1,0,0,XMaxGlb,YMaxGlb);              {System window}
    SelectWindow (1);
    DrawBorder;
    SetWindowModeOff;
    DrawLine (0,TextUp(24,2),XMaxGlb*8+7,TextUp(24,2));   {Command section}
    SetWindowModeOn;

    SelectWindow (1);
    GotoXY (2,1);
    Write (' SPECTRA RETRIEVE ');

    GotoXY (57,1);
    Write ('Current File : ', FileName);

  {Find the first file}
    TotalSpectraNumber := 0;
    FindFirst (Path+LocalPath, AnyFile, DirInfo);

    if (DosError = 0) then begin
     {if the first file exists, find the rest of the file names}
      TotalSpectraNumber := TotalSpectraNumber + 1;
      repeat
        FindNext (DirInfo);
        if (DosError = 0) then begin
          TotalSpectraNumber := TotalSpectraNumber + 1;
        end;
      until (DosError <> 0);
    end;
```

```
  GotoXY (2,5); Write ('#    Spectra    Pr ');
  GotoXY (2,6); Write ('  Start   End    ');
  GotoXY (30,5); Write ('#    Spectra    PP');
  GotoXY (30,6); Write ('  Start   End    ');
  GotoXY (58,5); Write ('#    Spectra    PP');
  GotoXY (58,6); Write ('  Start   End    ');

  for SpectraCount := 1 to TotalSpectraNumber do begin
    RetrieveMsP (MsParam, FileName, SpectraCount);

    GotoXY (2+(trunc((SpectraCount-1)/15)*28),
          7+(SpectraCount-1)-(trunc((SpectraCount-1)/15)*15));
    Write (SpectraCount:2);
    GotoXY (5+(trunc((SpectraCount-1)/15)*28),
          7+(SpectraCount-1)-(trunc((SpectraCount-1)/15)*15));
    Write (MsParam.StartMs:6:1);
    GotoXY (13+(trunc((SpectraCount-1)/15)*28),
          7+(SpectraCount-1)-(trunc((SpectraCount-1)/15)*15));
    Write (MsParam.EndMs:6:1);

    Str (SpectraCount, SpectraCountString);
    if (Length(SpectraCountString) = 1)
      then SpectraCountString := '0'+SpectraCountString;
    FindFirst (Path+'PLOT\'+FileName+SpectraCountString+'.M', AnyFile, DirInfo);
    if (DosError = 0) then begin
      GotoXY (21+(trunc((SpectraCount-1)/15)*28),
            7+(SpectraCount-1)-(trunc((SpectraCount-1)/15)*15));
      Write ('Y');
    end;

    if ((keypressed) or (SpectraCount = TotalSpectraNumber)) then begin
      if (SpectraCount <> TotalSpectraNumber) then begin
        GotoXY (2+(trunc(SpectraCount/15)*28+4),
              7+SpectraCount-(trunc(SpectraCount/15)*15));
        Write ('-- MORE --');
      end;
      repeat
        GotoXY (2,24);
        Write ('Input Spectra Number (1 to ',
              TotalSpectraNumber:2, ') : ');
        GetInteger (SpectraNumber, 35, 24, 2);
      until ((SpectraNumber <= TotalSpectraNumber) and (SpectraNumber > 0));
      EXIT;
    end;
  end;
end;



PROCEDURE FindSpectraRelation (   FileName : str6;
                        var KeyCount : integer);

var
  MsParam1, MsParam2 : MsRecord;
  SpectraRelation : SpectraRelationArray;

  IsKeyParamChange : boolean;
  IsFlagChange     : boolean;

  OutFile : text;

  Data1Count, Data2Count, count : integer;
```

```
  MainSpectraNumber, SearchSpectraNumber : integer;

begin
  GotoXY (2,3);
  Write ('Determining spectra relations');

  {$I-}
  ChDir (Path+'MS\PEAKS\'+FileName);
  {$I+}
  if (IOResult <> 0) then MkDir (Path+'MS\PEAKS\'+FileName);
  ChDir ('C:\TURBO');

  assign (OutFile, Path+'MS\PEAKS\'+FileName+'\'+FileName+'.MSR');
  rewrite (OutFile);

  KeyCount := 0;
  Data1Count := 1;
  Data2Count := 5;

  MainSpectraNumber := 1;
  while (MainSpectraNumber <= Status.MsNumber) do begin;
    GotoXY (2,24);
    Write ('Main FIle: ', MainSpectraNumber:2);

    RetrieveMsP (MsParam1, FileName, MainSpectraNumber);

   {Zerro relation array}
    for count := 1 to 10 do SpectraRelation[count] := 0;

    SpectraRelation[1] := MainSpectraNumber;
    SearchSpectraNumber := MainSpectraNumber + 1;

    while (SearchSpectraNumber <= Status.MsNumber) do begin;
      GotoXY (20,24);
      Write ('Search File: ', SearchSpectraNumber:2);

      RetrieveMsP (MsParam2, FileName, SearchSpectraNumber);

     {Check for change in key BEAM parameters}
      IsKeyParamChange := false;
      if (MsParam1.SysParam.SmFilm <> MsParam2.SysParam.SmFilm)
        then IsKeyParamChange := true;
      if (MsParam1.SysParam.SmCurr <> MsParam2.SysParam.SmCurr)
        then IsKeyParamChange := true;
      if (MsParam1.SysParam.SmAvgTemp <> MsParam2.SysParam.SmAvgTemp)
        then IsKeyParamChange := true;
      if (MsParam1.SysParam.Vion <> MsParam2.SysParam.Vion)
        then IsKeyParamChange := true;
      if (MsParam1.SysParam.GasD1PP <> MsParam2.SysParam.GasD1PP)
        then IsKeyParamChange := true;
      if (MsParam1.SysParam.GasD2PP <> MsParam2 SysParam.GasD2PP)
        then IsKeyParamChange := true;

     {Changes in mass scan parameters}
      if (MsParam1.IonId <> MsParam2.IonId)
        then IsKeyParamChange := true;
      if (MsParam1.ChannVoltage <> MsParam2.ChannVoltage)
        then IsKeyParamChange := true;
      if (MsParam1.Resolution <> MsParam2.Resolution)
        then IsKeyParamChange := true;
      if (MsParam1.eCurrent <> MsParam2.eCurrent)
        then IsKeyParamChange := true;
```

```
        if (MsParam1.eEnergy <> MsParam2.eEnergy)
          then IsKeyParamChange := true;
        if (MsParam1.Angle <> MsParam2.Angle)
          then IsKeyParamChange := true;

      {Check for change in flag}
        IsFlagChange := false;
        if (MsParam1.IsMsFlagOpen <> MsParam2.IsMsFlagOpen)
          then IsFlagChange := true;

      {Determine the spectra relation}
        if not(IsKeyParamChange or IsFlagChange) then begin
          Data1Count := Data1Count + 1;
          SpectraRelation[Data1Count] := SearchSpectraNumber;
          SearchSpectraNumber := SearchSpectraNumber + 1;
        end;

        if IsFlagChange and not(IsKeyParamChange) then begin
          Data2Count := Data2Count + 1;
          SpectraRelation[Data2Count] := SearchSpectraNumber;
          SearchSpectraNumber := SearchSpectraNumber + 1;
        end;

        if (IsKeyParamChange) then begin
          MainSpectraNumber := SearchSpectraNumber;
          SearchSpectraNumber := Status.MsNumber + 2;
        end;

      end;

      KeyCount := KeyCount + 1;
      Data1Count := 1;
      Data2Count := 5;
      for count := 1 to 10 do
        Write (OutFile, SpectraRelation[count], ' ');
      Writeln (OutFile, ' ');

      if (SearchSpectraNumber = Status.MsNumber+1)
        then MainSpectraNumber := Status.MsNumber + 1;

    end;

    Close (OutFile);
    GotoXY (2,3);    Write ('                                    ');
    Erase24;
  end;



PROCEDURE CountSpectraRelation (    FileName : str6;
                                    var KeyCount : integer);

var
  InFile : text;
  Dummy : integer;

begin
  {$I-}
  assign (InFile, Path+'MS\PEAKS\'+FileName+'\'+FileName+'.MSR');
  reset (InFile);
  {$I+}
  if (IOResult <> 0) then begin
```

```
    GotoXY (2,24);
    Write ('ERROR -- File does NOT exist.  Creating file shell for modification');
    MkDir (Path+'MS\PEAKS\'+FileName);
    assign (InFile, Path+'MS\PEAKS\'+FileName+'\'+FileName+'.MSR');
    rewrite (InFile);
    WriteLN (InFIle, '0');
    Close (InFile);
    Delay (2000);
    KeyCount := 0;
  end
  else begin
    KeyCount := 0;
    repeat
      Readln (InFile, Dummy);
      KeyCount := KeyCount + 1;
    until SeekEof(InFile);
    Close (InFile);
  end;
  Erase2425;
end;

END.



UNIT ZoomT3B;

INTERFACE
uses DOS, Crt, GDriver, GKernel, GWindow,
    AcqT3B, PltT3B;


PROCEDURE ZoomSection (var FirstPoint  : DataPointer;
                       Multiplier  : real;
                       Start       : real;
                       Finish      : real;
                       StartAssign : real;
                       ScanDirec   : real;
                       FileName    : str8);




IMPLEMENTATION
Procedure FindMaxMin (var FirstPoint    : DataPointer;
                      Start, Finish : real;
                    var Max, Min      : real);

var
  CurrentPoint : DataPointer;

begin
  Max := -1.0;
  Min := 100000000;

  CurrentPoint := FirstPoint;
  while ((CurrentPoint <> nil) and (CurrentPoint^.Xvalue < Start)) do
    CurrentPoint := CurrentPoint^.NextPoint;

  while ((CurrentPoint <> nil) and (CurrentPoint^.Xvalue <= Finish)) do begin
    if (CurrentPoint^.Yvalue > Max) then Max := CurrentPoint^.Yvalue;
    if (CurrentPoint^.Yvalue < Min) then Min := CurrentPoint^.Yvalue;
```

```
    CurrentPoint := CurrentPoint^.NextPoint;
  end;

  if (Max <= Min) then Max := Min + 1.0;

end;



procedure Walk (var FirstPoint  : DataPointer;
                Multiplier  : real;
                Start       : real;
                Finish      : real;
                StartAssign : real;
                ScanDirec   : real);

var
  X, Y : real;
  FuncKey, counter : integer;
  PositionCounter, PositionMove, PositionStart, PositionEnd : integer;
  CurrentPoint : DataPointer;

begin
  SelectWorld (2);
  SelectWindow (2);

  Erase2425;
  GotoXY (2,25);
  Write ('Walking:    <-- left,   --> right,   PgUp, PgDn');

 {Find the start, end, and number of positions}
  CurrentPoint := FirstPoint;
  PositionStart := 1;
  PositionEnd   := 1;
  X := CurrentPoint^.Xvalue;

  while (X < Start) do begin
    X := CurrentPoint^.Xvalue;
    PositionStart := PositionStart + 1;
    PositionEnd   := PositionEnd + 1;
    CurrentPoint := CurrentPoint^.NextPoint;
  end;
  while ((X < Finish) and (CurrentPoint <> nil)) do begin
    PositionEnd   := PositionEnd + 1;
    CurrentPoint := CurrentPoint^.NextPoint;
    X := CurrentPoint^.Xvalue;
  end;
  PositionEnd   := PositionEnd - 1;

  PositionCounter := PositionStart;
  PositionMove := 1;

  CurrentPoint := FirstPoint;
  X := CurrentPoint^.Xvalue;
  Y := CurrentPoint^.Yvalue;
  while (X < Start) do begin
    X := CurrentPoint^.Xvalue;
    Y := CurrentPoint^.Yvalue;
    CurrentPoint := CurrentPoint^.NextPoint;
  end;

  DrawLine (X, 0.0, X, Y);
```

```
GotoXY (2,24);
    Write ('Step:', PositionMove:3,
          '   X: ', (StartAssign+ScanDirec*(X-Start)):8:3,
          '   Y: ', (Y*Multiplier):12:4);

repeat
  FuncKey := 1;
  if keypressed then GetFuncKey (FuncKey);

  if (FuncKey = 75) then begin
    SetColorBlack;
    DrawLine (X, 0.0, X, Y);
    SetColorWhite;
    DrawPoint (X, Y);

   {Go to the begining -- PositionCounter equals PositionStart}
    CurrentPoint := FirstPoint;
    X := CurrentPoint^.Xvalue;
    Y := CurrentPoint^.Yvalue;

   {Advance to one point behind the current position}
    PositionCounter := PositionCounter - PositionMove;
    if (PositionCounter < PositionStart) then PositionCounter := PositionStart;
    for counter := 2 to PositionCounter do
      CurrentPoint := CurrentPoint^.NextPoint;

    X := CurrentPoint^.Xvalue;
    Y := CurrentPoint^.Yvalue;

    DrawLine (X, 0.0, X, Y);
    GotoXY (2,24);
    Write ('Step:', PositionMove:3,
          '   X: ', (StartAssign+ScanDirec*(X-Start)):8:3,
          '   Y: ', (Y*Multiplier):12:4);
  end;

  if (FuncKey = 77) then begin
    if (CurrentPoint <> FirstPoint) then begin
      SetColorBlack;
      DrawLine (X, 0.0, X, Y);
    end;
    SetColorWhite;
    DrawPoint (X, Y);

    counter := PositionCounter + PositionMove;
    if (counter > PositionEnd) then counter := PositionEnd;
    while (PositionCounter < counter) do begin
      PositionCounter := PositionCounter + 1;
      CurrentPoint := CurrentPoint^.NextPoint;
    end;
    X := CurrentPoint^.Xvalue;
    Y := CurrentPoint^.Yvalue;

    DrawLine (X, 0.0, X, Y);
    GotoXY (2,24);
    Write ('Step:', PositionMove:3,
          '   X: ', (StartAssign+ScanDirec*(X-Start)):8:3,
          '   Y: ', (Y*Multiplier):12:4);
  end;

  if (FuncKey = 73) then begin
    PositionMove := PositionMove * 2;
```

```
        if (PositionMove > 512) then PositionMove := 512;
        GotoXY (2,24);
        Write ('Step:', PositionMove:3,
              '   X: ', (StartAssign+ScanDirec*(X-Start)):8:3,
              '   Y: ', (Y*Multiplier):12:4);
      end;

      if (FuncKey = 81) then begin
        PositionMove := PositionMove div 2;
        if (PositionMove < 1) then PositionMove := 1;
        GotoXY (2,24);
        Write ('Step:', PositionMove:3,
              '   X: ', (StartAssign+ScanDirec*(X-Start)):8:3,
              '   Y: ', (Y*Multiplier):12:4);
      end;

    until (FuncKey = 150);

    Erase2425;
end;



PROCEDURE ZoomSection (var FirstPoint  : DataPointer;
                       Multiplier  : real;
                       Start       : real;
                       Finish      : real;
                       StartAssign : real;
                       ScanDirec   : real;
                       FileName    : str8);

var
  NewStart, NewFinish : real;
  NewStartAssign, NewFinishAssign : real;
  Max, Min : real;

  IsExit : boolean;

  FuncKey : integer;
  InputString : str8;
  code : integer;



procedure WriteZoomScreen;

begin
  ClearScreen;

  DefineWindow (1,0,0,XMaxGlb,YMaxGlb);          {System window}
  SelectWindow (1);
  DrawBorder;
  SetWindowModeOff;
  DrawLine (0,TextUp(24,2),XMaxGlb*8+7,TextUp(24,2));  {Command section}
  SetWindowModeOn;

  GotoXY (2,24);
  Write ('F1=Start-End     F2=Spectra Walk');
  GotoXY (70,24);
  Write ('Esc = Exit');
end;
```

```
BEGIN
  WriteZoomScreen;

  NewStart := Start;
  NewFinish := Finish;
  NewStartAssign := StartAssign;

  FindMaxMin (FirstPoint, Start, Finish, Max, Min);
  ScreenPlot (FirstPoint, Multiplier,
           Start, Finish, Max, Min,
           StartAssign, ScanDirec, true);

  IsExit := false,
  repeat
    FuncKey := 1;
    if keypressed then GetFuncKey (FuncKey);
    Case Funckey of
      59:begin
           GotoXY (2,25);
           Write ('Input Starting Value: ');
           GetReal (NewStartAssign, 24, 25, 6, 1);
           if ((ScanDirec*NewStartAssign < ScanDirec*StartAssign)
            or (ScanDirec*NewStartAssign > ScanDirec*(StartAssign+ScanDirec*(Finish-Start))))
             then begin
               NewStartAssign := StartAssign;
               NewStart := Start;
             end
             else begin
               NewStart := Start+ScanDirec*(NewStartAssign-StartAssign);
             end;
           Erase25;

           GotoXY (2,25);
           Write ('Input Ending Value: ');
           GetReal (NewFinishAssign, 22, 25, 6, 1);
           NewFinish := (Start-StartAssign)+NewFinish;
           if ((ScanDirec*NewFinishAssign > ScanDirec*(StartAssign+ScanDirec*(Finish-Start)))
            or (ScanDirec*NewFinishAssign < ScanDirec*NewStartAssign))
             then begin
               NewFinish := Finish;
             end
             else begin
               NewFinish := Start+ScanDirec*(NewFinishAssign-StartAssign);
             end;
           Erase25;

           WriteZoomScreen;
           FindMaxMin (FirstPoint, Start, Finish, Max, Min);
           ScreenPlot (FirstPoint, Multiplier,
                    NewStart, NewFinish, Max, Min,
                    NewStartAssign, ScanDirec, true);
      end;

     60:begin
          Walk (FirstPoint, Multiplier, NewStart, NewFinish,
              NewStartAssign, ScanDirec);

        {Reset to original parameters}
          NewStart := Start;
          NewFinish := Finish;
          NewStartAssign := StartAssign;
```

```
            WriteZoomScreen;
            FindMaxMin (FirstPoint, Start, Finish, Max, Min);
            ScreenPlot (FirstPoint, Multiplier,
                        NewStart, NewFinish, Max, Min,
                        NewStartAssign, ScanDirec, true);
          end;

      {Exit}
        150:begin
            IsExit := true;
          end;
      end;

  until (IsExit);
end;

END.


Unit MScrt3b;

INTERFACE
uses DOS, Crt, GDriver, GKernel, GWindow,
    AcqT3B, PltT3B, Anlt3b;


PROCEDURE WriteMainScreen;

PROCEDURE WriteMainChoiceScreen;

PROCEDURE WriteFixChoiceScreen;

PROCEDURE WriteCorrectChoiceScreen;

PROCEDURE WriteAutomaticChoiceScreen;

PROCEDURE WriteMsPeakSummaryScreen (MsPeakData : MsPeakArray;
                                    AmpScale   : real);

PROCEDURE WritePeakProcessScreen (   FileName          : str6;
                                 var IsGenerateRelation : boolean;
                                 var NormPeak           : integer;
                                 var IsNormAverage      : boolean;
                                 var Direction          : integer);

PROCEDURE WriteMsSummaryScreen1 (FirstPoint : DataPointer;
                                 MsParam    : MsRecord);

PROCEDURE WriteMsSummaryScreen2 (MsParam : MsRecord);

PROCEDURE WriteAuxScreen (AuxParam : AuxRecord);

PROCEDURE GetMsParam (var MsParam : MsRecord);


IMPLEMENTATION
PROCEDURE WriteMainScreen;

var
  TempStr1 : str6;
  TempStr2 : str6;
```

```
begin
  ClearScreen;
  SetHeaderON;

  DefineWindow (1,TextLeft(1,0),TextUp(1,0),TextRight(58,0),TextDown(15,-5));
  SelectWindow (1);
  Str (Status.CurrentSpectraNumber, TempStr1);
  Str (Status.MsNumber, TempStr2);
  DefineHeader (1, 'DATA:   '+Status.FileName+' '+TempStr1+' of '+TempStr2);
  DrawBorder;

  DefineWindow (2,TextLeft(1,0),TextUp(16,2),TextRight(58,0),TextDown(24,-3));
  SelectWindow (2);
  if (Status.IsBackSubtructed) then begin
    Str (Status.BackSpectraNumber, TempStr1);
    DefineHeader (2, 'BACKGROUND  SUBTRACTED:   '+Status.BackSpectraFileName+' '+TempStr1);
  end
  else begin
    Str (Status.BackSpectraNumber, TempStr1);
    DefineHeader (2, 'BACKGROUND:   '+Status.BackSpectraFileName+' '+TempStr1);
  end;
  DrawBorder;

  DefineWindow (3,TextLeft(60,0),TextUp(1,0),TextRight(80,0),TextDown(15,-5));
  SelectWindow (3);
  DrawBorder;

  DefineWindow (4,TextLeft(60,0),TextUp(16,2),TextRight(80,0),TextDown(24,-3));
  SelectWindow (4);
  DrawBorder;

  GotoXY (68,1);  Write (' MS ');
end;


PROCEDURE WriteMainChoiceScreen;

begin
  GotoXY (61,4);  Write ('F1  - Retrieve Run ');
  GotoXY (61,5);  Write ('F2  - Choose Spec. ');
  GotoXY (61,6);  Write ('F3  - Aux. Scans   ');
  GotoXY (61,7);  Write ('F4  - Fix Data     ');
  GotoXY (61,8);  Write ('F5  - Correct Data ');
  GotoXY (61,9);  Write ('F6  - Manual Locate');
  GotoXY (61,10); Write ('F7  - Auto Locate  ');
  GotoXY (61,11); Write ('F8  - ProPlot Aux  ');
  GotoXY (61,12); Write ('F9  - ProPlot MS   ');
  GotoXY (61,13); Write ('F10 - Automatic    ');
  GotoXY (61,14); Write ('Alt-F1, -F2  Sum. ');
end;



PROCEDURE WriteFixChoiceScreen;

begin
  GotoXY (61,4);  Write ('F1  - Data Trim    ');
  GotoXY (61,5);  Write ('F2  - Min = 0.0    ');
  GotoXY (61,6);  Write ('F3  - Scale Data   ');
  GotoXY (61,7);  Write ('F4  -              ');
  GotoXY (61,8);  Write ('F5  -              ');
  GotoXY (61,9);  Write ('F6  -              ');
```

```
  GotoXY (61,10); Write ('F7  -              ');
  GotoXY (61,11); Write ('F8  -              ');
  GotoXY (61,12); Write ('F9  - Change Scale ');
  GotoXY (61,13); Write ('F10 - Change Param ');
  GotoXY (61,14); Write ('Esc - EXIT         ');
end;



PROCEDURE WriteCorrectChoiceScreen;

begin
  GotoXY (61,4);  Write ('F1  -              ');
  GotoXY (61,5);  Write ('F2  -              ');
  GotoXY (61,6);  Write ('F3  -              ');
  GotoXY (61,7);  Write ('F4  -              ');
  GotoXY (61,8);  Write ('F5  -              ');
  GotoXY (61,9);  Write ('F6  -              ');
  GotoXY (61,10); Write ('F7  -              ');
  GotoXY (61,11); Write ('F8  -              ');
  GotoXY (61,12); Write ('F9  - Choose Back. ');
  GotoXY (61,13); Write ('F10 - Back  Subt.  ');
  GotoXY (61,14); Write ('Esc - EXIT         ');
end;



PROCEDURE WriteAutomaticChoiceScreen;

begin
  GotoXY (61,4);  Write ('F1  - All Print    ');
  GotoXY (61,5);  Write ('F2  - Peak Process ');
  GotoXY (61,6);  Write ('F3  -              ');
  GotoXY (61,7);  Write ('F4  -              ');
  GotoXY (61,8);  Write ('F5  -              ');
  GotoXY (61,9);  Write ('F6  -              ');
  GotoXY (61,10); Write ('F7  -              ');
  GotoXY (61,11); Write ('F8  -              ');
  GotoXY (61,12); Write ('F9  -              ');
  GotoXY (61,13); Write ('F10 -              ');
  GotoXY (61,14); Write ('Esc - EXIT         ');
end;



PROCEDURE WriteMsPeakSummaryScreen (MsPeakData : MsPeakArray;
                                    AmpScale   : real);

var
  Multiplier : real;
  MassCount, count, FuncKey : integer;

begin
  ClearScreen;
  DefineWindow (1,0,0,XMaxGlb,YMaxGlb);              {System window}
  SelectWindow (1);
  DrawBorder;
  SetWindowModeOff;
  DrawLine (0,TextUp(24,2),XMaxGlb*8+7,TextUp(24,2));  {Command section}
  SetWindowModeOn;
  GotoXY (2,1);
  Write (' PEAK LOCATE ');
```

```
  GotoXY (70,24);
  Write ('Esc=EXIT');


 {Calculate multiplier}
  Multiplier := 1.0;
  for MassCount := 1 to round(AmpScale) do Multiplier := Multiplier*10.0;

  GotoXY (31,2);
  Write ('Amp Scale:  10^ -', AmpScale:1:0);

  MassCount := 1;
  for count := 0 to 99 do begin
    if (MsPeakData[count] <> 0.0) then begin
      GotoXY (5+(trunc((MassCount-1)/20)*20),
            4+(MassCount-1)-(trunc((MassCount-1)/20)*20));
      Write (count:2, '  ', (MsPeakData[count]*Multiplier):5:3);
      MassCount := MassCount + 1;
    end;
  end;

  repeat
    GetFuncKey (FuncKey);
  until (FunCkey = 150);
end;



PROCEDURE WritePeakProcessScreen (   FileName          : str6;
                          var IsGenerateRelation : boolean;
                          var NormPeak           : integer;
                          var IsNormAverage      : boolean;
                          var Direction          : integer);

var
  InputString : str6;
  IsYes : boolean;

begin
  ClearScreen;
  DefineWindow (1,0,0,XMaxGlb,YMaxGlb);              {System window}
  SelectWindow (1);
  DrawBorder;
  SetWindowModeOff;
  DrawLine (0,TextUp(24,2),XMaxGlb*8+7,TextUp(24,2));   {Command section}
  SetWindowModeOn;

  GotoXY (3,1);
  Write (' MS Peak Processing ');
  GotoXY (70,1);
  Write (' ', FileName, ' ');
  GotoXY (2,3);
  Write ('PROCESSING PARAMETERS:');

  repeat
    GotoXY (5,5);
    Write ('Relationship Matrix:  N');
    GotoXY (2,6);
    Write ('(N)ew,  (O)ld');
    repeat
      InputString := 'n';
      GotoXY (26, 5);  Write ('*');
```

```
  GetString (InputString, Alfa, 26, 5, 1);
  if ((InputString <> 'n') and (InputString <> 'o')) then begin
    Sound (300); Delay (200); NoSound;
    GotoXY (25,5); Write ('        ');
  end;
until ((InputString = 'n') or (InputString = 'o'));
GotoXY (2,6);
Write ('                                        ');
if (InputString = 'n') then begin
  GotoXY (5,5);
  Write ('Relationship Matrix:  New');
  IsGenerateRelation := true;
end
else begin
  GotoXY (5,5);
  Write ('Relationship Matrix:  Old');
  IsGenerateRelation := false;
end;

GotoXY (5,7);
Write ('Normalization:  N');
GotoXY (2,8);
Write ('(B)efore combining spectra,  (A)fter combining spectra,  (N)one');
repeat
  InputString := 'n';
  GotoXY (20, 7);  Write ('*');
  GetString (InputString, Alfa, 20, 7, 1);
  if ((InputString <> 'b') and (InputString <> 'a') and(InputString <> 'n')) then begin
    Sound (300); Delay (200); NoSound;
    GotoXY (21,7); Write ('        ');
  end;
until ((InputString = 'b') or (InputString = 'a') or (InputString = 'n'));
GotoXY (2,8);
Write ('                                                ');
NormPeak := 0;
if (InputString = 'b') then begin
  GotoXY (5,7);
  Write ('Normalization:  Before combining spectra');
  IsNormAverage := false;
  GotoXY (5,8);
  Write ('Normalization Peak:  ', NormPeak:2);
  GetInteger (NormPeak, 26, 8, 2);
  GotoXY (5,8);
  Write ('Normalization Peak:  ', NormPeak:2);
end;
if (InputString = 'a') then begin
  GotoXY (5,7);
  Write ('Normalization:  After combining spectra');
  IsNormAverage := true;
  GotoXY (5,8);
  Write ('Normalization Peak:  ', NormPeak:2);
  GetInteger (NormPeak, 26, 8, 2);
  GotoXY (5,8);
  Write ('Normalization Peak:  ', NormPeak:2);
end;
if (InputString = 'n') then begin
  GotoXY (5,7);
  Write ('Normalization:  None');
  IsNormAverage := true;
  NormPeak := -1;
end;
```

```
    GotoXY (5,10);
    Write ('Spectra Subtruction:  0');
    GotoXY (2,11);
    Write ('(1) 1-2,  (2) 2-1,  (0) None');
    GetInteger (Direction, 27, 10, 1);
    GotoXY (2,11);
    Write ('                              ');
    if (Direction = 1) then begin
      GotoXY (5,10);
      Write ('Spectra Subtruction:  1-2');
    end;
    if (Direction = 2) then begin
      GotoXY (5,10);
      Write ('Spectra Subtruction:  2-1');
      Direction := -1;
    end;
    if (Direction = 0) then begin
      GotoXY (5,10);
      Write ('Spectra Subtruction:  None');
    end;

    GotoXY (2,25);
    Write ('Are the parameters correct ? (y or n)');
    repeat
      InputString := UpCase(readkey);
      if (InputString = 'Y') then IsYes := true;
    until ((InputString = 'Y') or (InputString = 'N'));

  until (IsYes);
  Erase25;
end;



PROCEDURE WriteMsSummaryScreen1 (FirstPoint : DataPointer;
                          MsParam    : MsRecord);

begin
  GotoXY (2,25);
  Write ('Setting up Summary Screen');

  SelectScreen (2);
  ClearScreen;
  DefineWindow (1, TextLeft (2,0),  TextUp(2,-2),
              TextRight(59,0), TextDown(20,0));
  SelectWindow (1);
  DrawBorder;
  DrawSpectra (FirstPoint, true, 1);

  GotoXY (2,1);
  Write (' MS ');
  GotoXY (62,1);
  Write (' ', Status.FileName, '  ', Status.CurrentSpectraNumber,
       ' of ', Status.MsNumber, ' ');
  GotoXY (70,24);
  Write ('Esc = Exit');

  With MsParam do begin                    {Write parameters}
    GotoXY (61,3);  Write ('Starting Time:');
    GotoXY (62,4);  Write (StartTime:7:2, '  (hhmm.ss)');

    GotoXY (61,7);  Write ('Starting Mass:');
```

```
    GotoXY (64,8);  Write (StartMs:6:2, '  (amu)');

    GotoXY (61,9);   Write ('Ending Mass:');
    GotoXY (64,10);  Write (EndMs:6:2, '  (amu)');

    GotoXY (61,11);  Write ('Step Mass:');
    GotoXY (64,12);  Write (StepMs:6:2, '  (amu)');

    GotoXY (61,13);  Write ('Number of Steps:');
    GotoXY (64,14);  Write (NumberSteps:4:0);

    GotoXY (61,15);  Write ('Time Delay:');
    GotoXY (64,16);  Write (TimeDelay:5:3, '  (s)');

    GotoXY (61,17);  Write ('Current Scale:');
    GotoXY (64,18);  Write ('10^- ', AmpScale:1, '  (A)');

    GotoXY (61,20);  Write ('Mass Range: ', MassRange);

  end;

  SelectScreen (1);
  Erase25;
end;


procedure WriteMsSummaryScreen2 (MsParam : MsRecord);

   {This procedure sets up the MS screen and writes all the system
    and acquisition parameters.}

begin
  ClearScreen;

  DefineWindow (1,0,0,XMaxGlb,YMaxGlb);              {System window}
  SelectWindow (1);
  DrawBorder;
  SetWindowModeOff;
  DrawLine (0,TextUp(24,2),XMaxGlb*8+7,TextUp(24,2));  {Command section}
  SetWindowModeOn;

  GotoXY (2,1);
  Write (' MS ');
  GotoXY (62,1);
  Write (' ', Status.FileName, '  ', Status.CurrentSpectraNumber,
        ' of ', Status.MsNumber, ' ');

 {Print permitted options}
  GotoXY (70,24);
  Write ('Esc = Exit');

  with MsParam.SysParam do begin
    GotoXY (3,3);  Write ('SAMPLE PRARAMETERS');

    GotoXY (5,4);   Write ('Film:');
    GotoXY (20,4);  Write (SmFilm);

    GotoXY (5,5);   Write ('Avg. Temp.:');
    GotoXY (20,5);  Write (SmAvgTemp:3:0, '  (C)');

    GotoXY (40,4);  Write ('Samp. Current:');
```

```
  GotoXY (55,4);  Write (SmCurr:5:1, '  (uA)');

  GotoXY (40,5);  Write ('Curr. Scale:');
  GotoXY (55,5);  Write (SmCurrScale:2);


  GotoXY (3,8);  Write ('BEAM PRARAMETERS');

  GotoXY (5,9);    Write ('Ion Source:');
  GotoXY (20,9);   Write (Isource:8);

  GotoXY (5,10);   Write ('Source Gas:');
  GoToXY (20,10);  Write (GasISName:8);

  GotoXY (5,11);   Write ('Gas Press:');
  GoToXY (20,11);  Write (GasISpp:6:2, '  (E-6 t)');

  GotoXY (5,12);   Write ('For. Power:');
  GotoXY (20,12);  Write (Ipower:6:2, '  (w)');

  GotoXY (5,13);   Write ('Vion:');
  GotoXY (20,13);  Write (Vion:6:2, '  (V)');

  GotoXY (5,14);   Write ('Vaccel:');
  GotoXY (20,14);  Write (Vaccel:6:2, '  (V)');


  GotoXY (40,9);   Write ('Doser 1:');
  GotoXY (55,9);   Write (Doser1:8);

  GotoXY (40,10);   Write ('Source Gas:');
  GotoXY (55,10);   Write (GasD1Name:8);
  GoToXY (65,10);   Write (GasD1PP:4:1, '  (E-6 t)');

  GotoXY (40,11);  Write ('D1 Temp:');
  GotoXY (55,11);  Write (D1Temp:6:2, '  (C)');

  GotoXY (40,12);  Write ('Doser 2:');
  GotoX / (55,12);  Write (Doser2:8);

  GotoXY (40,13);  Write ('Source Gas:');
  GotoXY (55,13);  Write (GasD2Name:8);
  GotoXY (65,13);  Write (GasD2PF.4:1, '  (E-6 t)');

  GotoXY (40,14);  Write ('D2 Power:');
  GotoXY (55,14);  Write (D2Power:6:2, '  (w)');

end;

with MsParam do begin
  GotoXY (3,16);  Write ('MASS SPEC PARAMETERS');

  GotoXY (5,19);   Write ('MS Mode:');
  GotoXY (20,19);  if (IonId = 'p') then Write ('Positive')
                           else Write ('Neutral');

  GotoXY (5,20);   Write ('Channeltron:');
  GotoXY (20,20);  Write (ChannVoltage:5:0, '  (V)');

  GotoXY (5,21);   Write ('Resolution:');
  GotoXY (20,21);  Write (Resolution:5:2);
```

```
    GotoXY (5,22);   Write ('Mass Range:');
    GotoXY (20,22);  Write (MassRange);

    GotoXY (40,18);  Write ('MS Angle:');
    GotoXY (55,18);  Write (Angle:5:1, ' (deg)');

    GotoXY (40,19);  Write ('e- Current:');
    GotoXY (55,19);  Write (eCurrent:5:3, ' (mA)');

    GotoXY (40,20);  Write ('e- Energy:');
    GotoXY (55,20);  Write (eEnergy:5:1, ' (eV)');

    GotoXY (40,21);  Write ('Ion Energy:');
    GotoXY (55,21);  Write (IonEnergy:5:1, ' (eV)');

    GotoXY (40,22);  Write ('Focus:');
    GotoXY (55,22);  Write (Focus:5:1, ' (eV)');

    GotoXY (40,23);   Write ('Ms Flag:');
    GotoXY (55,23);  if (IsMsFlagOpen) then Write ('OPEN  ')
                              else Write ('CLOSED');

  end;
end;



PROCEDURE WriteAuxScreen (AuxParam  : AuxRecord);

   {This procedure sets up the AUXILARY DIAGNOSTICS screen
    and writes all parameters.}

begin
  ClearScreen;

  DefineWindow (1,0,0,XMaxGlb,YMaxGlb);          {System window}
  SelectWindow (1);
  DrawBorder;
  SetWindowModeOff;
  DrawLine (0,TextUp(24,2),XMaxGlb*8+7,TextUp(24,2));  {Command section}
  SetWindowModeOn;
  DrawBorder;

  SetHeaderOn;
  DefineWindow (2,2,TextUp(3,-2),(XMaxGlb div 2)+20,
           Textdown(9,2));
  DefineHeader (2, 'SAMPLE CURRENT');
  SelectWindow (2);
  DrawBorder;

  DefineWindow (3,2,TextUp(13,-2),(XMaxGlb div 2)+20,
           Textdown(19,2));
  DefineHeader (3, 'INTERFEROMETRY');
  SelectWindow (3);
  DrawBorder;

  SelectWindow (1);
  GotoXY (2,1);
  Write (' AUXILARY DIAGNOSTICS '),
  GotoXY (70,1);
  Write (' ', Status.FileName, ' ');
```

```
{Print permitted options}
  GotoXY (70,24);
  Write ('Esc = Exit');
  GotoXY (5,24);
  Write ('Walk = Alt-F1');
  GotoXY (25,24);
  Write ('IFR ascii line = Alt-F2');

  with AuxParam do begin
    GotoXY (61,3); Write ('Start Time');
    GotoXY (62,4); Write (SmCurrStartT:6:2, ' (hhmm.ss)');

    GotoXY (61,5); Write ('Time Step');
    GotoXY (64,6); Write (SmCurrStepT:6:0, '  (sec)');

    GotoXY (61,7); Write ('Sm Amp Scale');
    GotoXY (64,8); Write ('10^- ', SmCurrAmpScale:1, '  (A)');

    GotoXY (5,11);  Write ('Avg. Sample Current:');
    GotoXY (28,11); Write (SmAvgCurr:5:2,
                    ' x 10^-', SmCurrAmpScale:1, '  (A)');


    GotoXY (61,13); Write ('Start Time');
    GotoXY (62,14); Write (InterferStartT:6:2, ' (hhmm.ss)');

    GotoXY (61,15); Write ('Time Step');
    GotoXY (64,16); Write (InterferStepT:6:0, '  (sec)');

  end;

end;



PROCEDURE GetMsParam (var MsParam : MsRecord);

    {This procedure inputs the MS system parameters.  If <return> is
     entered as the first key, previous parameter settings are saved.}

var
  InputString : str8;
  IsYes : boolean;
  count : integer;

begin
  IsYes := false;

  repeat
    with MsParam.SysParam do begin
      Erase2425;
      GotoXY (2,24);  Write ('Input SAMPLE parameters indicated by  *');

      InputString := SmFilm;
      GotoXY (19,4); Write ('*');
      GetString (InputString, Mix, 20, 4, 8);
      SmFilm := InputString;
      GotoXY (19,4);  Write ('         ');
      GotoXY (20,4);  Write (SmFilm);

      GetReal (SmAvgTemp, 20, 5, 7, 4);
      GotoXY (20,5);  Write (SmAvgTemp:3:0, '  (C)');
```

```
GetReal (SmCurr, 55, 4, 5, 1);
GotoXY (55,4);  Write (SmCurr:5:1, '  (uA)');

GetInteger (SmCurrScale, 55, 5, 2);
GotoXY (55,5);  Write (SmCurrScale:2);

Erase2425;
GotoXY (2,24);  Write ('Input BEAM parameters indicated by  *');


InputString := Isource;
GotoXY (19,9);  Write ('*');
GetString (InputString, Mix, 20, 9, 8);
Isource := InputString;
GotoXY (19,9);  Write ('         ');
GotoXY (20,9);  Write (Isource:8);

InputString := GasISName;
GotoXY (19,10);  Write ('*');
GetString (InputString, Mix, 20, 10, 8);
GasISName := InputString;
GotoXY (19,10);  Write ('         ');
GotoXY (20,10);  Write (GasISName:8);

GetReal (GasISPP, 20, 11, 5, 1);
GotoXY (20,11);  Write (GasISPP:6:2, '  (E-6 t)');

GetReal (Ipower, 20, 12, 5, 1);
GoToXY (20,12);  Write (Ipower:6:2, '  (w)');

GetReal (Vion, 20, 13, 3, 0);
GoToXY (20,13);  Write (Vion:6:2, '  (V)');

GetReal (Vaccel, 20, 14, 3, 0);
GoToXY (20,14);  Write (Vaccel:6:2, '  (V)');


InputString := Doser1;
GotoXY (54,9);  Write ('*');
GetString (InputString, Mix, 54, 9, 8);
Doser1 := InputString;
GotoXY (54,9);  Write ('         ');
GotoXY (55,9);  Write (Doser1:8);

InputString := GasD1Name;
GotoXY (54,10);  Write ('*');
GetString (InputString, Mix, 54, 10, 8);
GasD1Name := InputString;
GotoXY (54,10);  Write ('         ');
GotoXY (55,10);  Write (GasD1Name:8);

GetReal (GasD1PP, 65, 10, 6, 2);
GoToXY (65,10);  Write (GasD1PP:4:1, '  (E-6 t)');

GetReal (D1Temp, 55, 11, 6, 2);
GoToXY (55,11);  Write (D1Temp:6:2, '  (C)');


InputString := Doser2;
GotoXY (54,12);  Write ('*');
GetString (InputString, Mix, 54, 12, 8);
Doser2 := InputString;
```

```
  GotoXY (54,12);  Write ('          ');
  GotoXY (55,12);  Write (Doser2:8);

  InputString := GasD2Name;
  GotoXY (54,13); Write ('*');
  GetString (InputString, Mix, 54, 13, 8);
  GasD2Name := InputString;
  GotoXY (54,13);  Write ('          ');
  GotoXY (55,13);  Write (GasD2Name:8);

  GetReal (GasD2PP, 65, 13, 6, 2);
  GoToXY (65,13);  Write (GasD2PP:4:1, '  (E-6 t)');

  GetReal (D2Power, 55, 14, 6, 2);
  GoToXY (55,14);  Write (D2Power:6:2, '  (w)');

end;

with MsParam do begin
  Erase2425;
  GotoXY (2,24);  Write ('Input MASS SPEC parameters indicated by  *');

  repeat
    InputString := IonId;
    GotoXY (19, 19);  Write ('*');
    GetString (InputString, Alfa, 20, 19, 9);
  if ((InputString <> 'p') and (InputString <> 'n')) then begin
    Sound (300); Delay (200); NoSound;
    GotoXY (20,19); Write ('          ');
  end;
  until ((InputString = 'p') or (InputString = 'n'));
  IonId := InputString;
  GotoXY (19,19);  Write ('          ');
  GotoXY (20,19);
  if (IonId = 'p') then Write ('Positive')
                   else Write ('Neutral');

  GetReal (ChannVoltage, 20, 20, 5, 0);
  GotoXY (20,20);  Write (ChannVoltage:5:0, '  (V)');

  GetReal (Resolution, 20, 21, 5, 2);
  GoToXY (20,21); Write (Resolution:5:2);

  repeat
    InputString := MassRange;
    GotoXY (19, 22);  Write ('*');
    GetString (InputString, Alfa, 20, 22, 1);
  until ((InputString = 'H') or (InputString = 'M') or (InputString = 'L'));
  MassRange := InputString;
  GotoXY (19,22);  Write ('          ');
  GotoXY (20,22);  Write (MassRange);

  GetReal (Angle, 55, 18, 5, 1);
  GotoXY (55,18); Write (Angle:5:1, '  (deg)');

  GetReal (eCurrent, 55, 19, 5, 3);
  GoToXY (55,19); Write (eCurrent:5:3, '  (mA)');

  GetReal (eEnergy, 55, 20, 5, 1);
  GoToXY (55,20); Write (eEnergy:5:1, '  (eV)');

  GetReal (IonEnergy, 55, 21, 5, 1);
```

```
      GotoXY (55,21); Write (IonEnergy:5:1, '  (eV)');

      GetReal (Focus, 55, 22, 5, 1);
      GotoXY (55,22); Write (Focus:5:1, '  (eV)');

      if (IsMsFlagOpen) then InputString := 'o'
                  else InputString := 'c';
      GotoXY (54,23); Write ('*');
      GetString (InputString, Mix, 54, 23, 1);
      if (InputString = 'o') then IsMsFlagOpen := true
                        else IsMsFlagOpen := false;
      GotoXY (54,23);  Write ('        ');
      GotoXY (55,23);
      if (IsMsFlagOpen) then Write ('OPEN ')
                  else Write ('CLOSE');
    end;


    Erase2425;
    GotoXY (2,25);
    Write ('Are the parameters correct ? (y or n)');
    repeat
      InputString := UpCase(readkey);
      if (InputString = 'Y') then IsYes := true;
    until ((InputString = 'Y') or (InputString = 'N'));

  until (IsYes);

  Erase2425;
end;

END.


PROGRAM MS3B;

USES DOS, Crt, GDriver, GKernel, GWindow,
   AcqT3B, MScn3B, FileT3B, AnlT3B, PltT3B;

VAR
  ExitSave  : pointer;

  IsExit            : boolean;
  IsRunRetrieved    : boolean;
  IsSpectraChosen   : boolean;
  IsPeakLocated     : boolean;
  IsBackSpectraChosen : boolean;

  MsPeakData : MsPeakArray;
  NumKeyParamChanges, NormPeak, Direction : integer;
  IsNormAverage, IsGenerateRelation : boolean;

  Multiplier : real;
  SpectraNumberString : string[2];
  InputString : str8;
  count, FuncKey : integer;

{$F+}
PROCEDURE MyExit; {$F-}

var
  CurrentPoint : DataPointer;
```

```
begin

 {Print exit code}
   ClearScreen;
   if (ExitCode <> 0) then begin
     GotoXY (10,10);
     Write ('Exit Code is: ', ExitCode);
     Sound (1200);
     Delay (100);
     NoSound;
   end;

 {Terminate graphics}
   ClearScreen;
   LeaveGraphic;
   ClrScr;

 {Erase all the pointer lists}
   EraseData (MsData);
   EraseData (SmCurrData);
   EraseData (InterferData);
   ErasePeak (MSPeakData);

 {Return to system termination routine}
   ExitProc := ExitSave;
end;



{$F+}
Function HeapExit (Size : word) : integer; {$F-}

var
   FuncKey : integer;

begin
   ClearScreen;
   GotoXY (5,10);
   Write ('Out of MEMORY for size ', Size);
   GotoXY (5,13);
   Write ('Hit RETURN to continue');
   GetFuncKey (FuncKey);

   HeapExit := 1;
end;

PROCEDURE CalcKeyParamFile (FileName      : str6;
                            KeyNumber     : integer;
                            NormPeak      : integer;
                            IsNormAverage : boolean;
                            Direction     : integer);

{This procedure creates data tables of peak heights/positions versus some
major system parameter such as ion energy, flux, etc. The data table can
be imported to 123 for systematic analysis of the variable's effect}

const
   M2 = 1E9;

type
   AverageArray = array [0..99] of integer;
```

```
var
  SpectraRelation : SpectraRelationArray;
  NormPeakValue : real;
  KeyMsPeakData1, KeyMsPeakData2, MsPeakData : MsPeakArray;
  AverageData : AverageArray;

  InFile, OutFile : text;

  Multiplier : real;
  SpectraNumberString : string[2];
  SpectraNumber, SpectraRelationCount, KeyCount : integer;
  count : integer;

begin
  GotoXY (2,3);
  Write ('Determining key parameter peak files');

  assign (InFile, Path+'MS\PEAKS\'+FileName+'\'+FileName+'.MSR');
  reset (InFile);

  for KeyCount := 1 to KeyNumber do begin
    GotoXY (10,20);
    Write ('Key parameter #: ', KeyCount:2);

   {Read in spectra relation for current key parameter}
    for SpectraRelationCount := 1 to 10 do
      Read (InFile, SpectraRelation[SpectraRelationCount]);
    ReadLn (inFile);

   {Zero arrays}
    for count := 0 to 99 do begin
      KeyMsPeakData1[count] := 0.0;
      AverageData[count] := 0;
    end;

   {Determine composit data e.g. add scans taken at various scales}
    SpectraRelationCount := 1;
    SpectraNumber := SpectraRelation[SpectraRelationCount];
    while (SpectraNumber <> 0) do begin
      SpectraNumber := SpectraRelation[SpectraRelationCount];
      GotoXY (5,21);
      Write ('Spectra1 #:');
      GotoXY (15+SpectraRelationCount*5,21);
      Write (SpectraNumber:2);

      EraseData (MsData);
      ErasePeak (MsPeakData);

      if (SpectraNumber <> 0) then begin
        RetrieveMsP (MsParam, FileName, SpectraNumber);
        Str (SpectraNumber, SpectraNumberString);
        if (Length(SpectraNumberString) = 1)
          then SpectraNumberString := '0'+ SpectraNumberString;
        RetrieveData (MsData, MsParam.NumberSteps,
                  'MS\'+Status.FileName+SpectraNumberString+'.MD');

        Multiplier := 1.0;
        for count := 1 to round(MsParam.AmpScale) do Multiplier := Multiplier*10.0;

        FindMsPeak (MsData.FirstPoint,
                  0.005, MsParam.AmpScale,
                  MsPeakData);
```

```
    {Determine normalization value if normalizing before combining}
     if not(IsNormAverage)
       then begin
         if (NormPeak >= 0) then NormPeakValue := MsPeakData[NormPeak]
                        else NormPeakValue := 1.0E-9;
         if (NormPeakValue = 0.0) then NormPeakValue := 1.0E-9;
       end
       else NormPeakValue := 1.0;

    {Normalize and combine}
     for count := 0 to 99 do begin
       if ((MsPeakData[count] <> 0.0) and (MsPeakData[count]*Multiplier < 2.49)) then begin
         KeyMsPeakData1[count] := KeyMsPeakData1[count] +
                          (MsPeakData[count] / NormPeakValue);
         AverageData[count] := AverageData[count] + 1;
       end;
     end;
   end;
   SpectraRelationCount := SpectraRelationCount + 1;
 end;

{Determine normalization value if normalizing after combining}
 if (IsNormAverage)
   then begin
     if ((NormPeak >= 0) and  (AverageData[NormPeak] <> 0))
       then  NormPeakValue :=  KeyMsPeakData1[NormPeak] / AverageData[NormPeak]
       else NormPeakValue := 1.0E-9;
     if (NormPeakValue = 0.0) then NormPeakValue := 1.0E-9;
   end
   else NormPeakValue := 1.0;

{Average}
 for count := 0 to 99 do begin
   if (AverageData[count] <> 0) then
     KeyMsPeakData1[count] := KeyMsPeakData1[count] /
                    (int(AverageData[count]) * NormPeakValue);
 end;

{Zero all arrays}
 for count := 0 to 99 do begin
   KeyMsPeakData2[count] := 0.0;
   AverageData[count] := 0;
 end;

{Determine composit background data}
 SpectraRelationCount := 6;
 SpectraNumber := SpectraRelation[SpectraRelationCount];
 while (SpectraNumber <> 0) do begin
   SpectraNumber := SpectraRelation[SpectraRelationCount];
   GotoXY (5,22);
   Write ('Spectra2 #:');
   GotoXY (15+(SpectraRelationCount-5)*5,22);
   Write (SpectraNumber:2);

   EraseData (MsData);
   ErasePeak (MsPeakData);

   if (SpectraNumber <> 0) then begin
     RetrieveMsP (MsParam, FileName, SpectraNumber);
     Str (SpectraNumber, SpectraNumberString);
     if (Length(SpectraNumberString) = 1)
       then SpectraNumberString := '0'+ SpectraNumberString;
```

```
      RetrieveData (MsData, MsParam.NumberSteps,
                'MS\'+Status.FileName+SpectraNumberString+'.MD');

      Multiplier := 1.0;
      for count := 1 to round(MsParam.AmpScale) do Multiplier := Multiplier*10.0;

      FindMsPeak (MsData.FirstPoint,
                0.005, MsParam.AmpScale,
                MsPeakData);

     {Determine normalization value if normalizing before combining}
      if not(IsNormAverage)
        then begin
          if (NormPeak >= 0) then NormPeakValue := MsPeakData[NormPeak]
                        else NormPeakValue := 1.0E-9;
          if (NormPeakValue = 0) then NormPeakValue := 1.0E-9;
        end
        else NormPeakValue := 1.0;

     {Normalize and combine}
      for count := 0 to 99 do begin
        if ((MsPeakData[count] <> 0.0) and (MsPeakData[count]*Multiplier < 2.49)) then begin
          KeyMsPeakData2[count] := KeyMsPeakData2[count] +
                          (MsPeakData[count] / NormPeakValue);
          AverageData[count] := AverageData[count] + 1;
        end;
      end;
    end;
    SpectraRelationCount := SpectraRelationCount + 1;
  end;

 {Determine normalization value if normalizing after combining}
  if (IsNormAverage)
    then begin
      if ((NormPeak >= 0) and  (AverageData[NormPeak] <> 0))
        then  NormPeakValue :=  KeyMsPeakData2[NormPeak] / AverageData[NormPeak]
        else NormPeakValue := 1.0E-9;
      if (NormPeakValue = 0.0) then NormPeakValue := 1.0E-9;
    end
    else NormPeakValue := 1.0;

 {Average}
  for count := 0 to 99 do begin
    if (AverageData[count] <> 0) then
      KeyMsPeakData2[count] := KeyMsPeakData2[count] /
                        (int(AverageData[count]) * NormPeakValue);
  end;

 {Subtract spectras and write to file}
  SpectraNumberString := chr(KeyCount+64);
  assign (OutFile, Path+'MS\PEAKS\'+FileName+'\'
                +FileName+SpectraNumberString+'.MK1');
  rewrite (OutFile);
  Writeln (OutFile, ' ');
  for count := 0 to 99 do  Writeln (OutFile, KeyMsPeakData1[count]);
  close (OutFile);

  assign (OutFile, Path+'MS\PEAKS\'+FileName+'\'
                +FileName+SpectraNumberString+'.MK2');
  rewrite (OutFile);
  Writeln (OutFile, ' ');
  for count := 0 to 99 do Writeln (OutFile, KeyMsPeakData2[count]);
```

```
    close (OutFile);

    if (Direction <> 0) then begin
      SpectraNumberString := chr(KeyCount+64);
      assign (OutFile, Path+'MS\PEAKS\'+FileName+'\'
                +FileName+SpectraNumberString+'.MKD');
      rewrite (OutFile);
      for count := 0 to 99 do begin
        if (Direction > 0)
          then KeyMsPeakData1[count] := KeyMsPeakData1[count] - KeyMsPeakData2[count]
          else KeyMsPeakData1[count] := KeyMsPeakData2[count] - KeyMsPeakData1[count];
        Writeln (OutFile, KeyMsPeakData1[count]);
      end;
      close (OutFile);
    end;

    GotoXY (2,20);  Write ('                                        ');
    GotoXY (2,21);  Write ('                                        ');
    GotoXY (2,22);  Write ('                                        ');
  end;
  Close (InFile);

end;



BEGIN
 {Insert custom termination routine before system termination routine}
  ExitSave := ExitProc;
  ExitProc := @MyExit;
  HeapError := @HeapExit;

 {Enter graphics and set up the screen}
  ClrScr;
  InitGraphic;
  GotoXY (31,10);
  Write (' MS Massage Program ');
  GotoXY (27,11);
  Write ('Written by: Igor Tepermeister');
  GotoXY (36,12);
  Write ('Version 1.0');

  IsRunRetrieved     := false;
  IsSpectraChosen    := false;
  IsPeakLocated      := false;
  IsBackSpectraChosen := false;

  WriteMainScreen;
  WriteMainChoiceScreen;

  FuncKey := 1;
  IsExit := false;
  repeat
    if keypressed then begin
      GetFuncKey (FuncKey);
      Erase25;
    end;

    Case FuncKey of

     {Obtain file for retrieval}
      59:begin
```

```
      GetFileName (Status.FileName);

      EraseData (MsData);
      EraseData (SmCurrData);
      EraseData (InterferData);
      ErasePeak (MSPeakData);

      RetrieveRun;

      if (Status.IsSmCurrSpectra or Status.IsInterferSpectra) then begin
        RetrieveAux (AuxParam, Status.FileName);

      end;

      Status.CurrentSpectraNumber := 0;

      IsRunRetrieved      := true;
      IsSpectraChosen     := false;
      IsPeakLocated       := false;
      IsBackSpectraChosen := false;

      FuncKey := 2;
    end;

{Choose spectra}
 60:begin
      if (IsRunRetrieved and (Status.MsNumber>0)) then begin
        GetSpectraNumber (Status.FileName,
                          'MS\'+Status.FileName+'*.MP',
                          Status.CurrentSpectraNumber);
        Erase25;

        EraseData (MsData);
        EraseData (BackData);
        ErasePeak (MSPeakData);

       {Retrieve background spectra}
        if (IsBackSpectraChosen) then begin
          RetrieveMsP (MsParam,
                       Status.BackSpectraFileName,
                       Status.BackSpectraNumber);
          Str (Status.BackSpectraNumber, SpectraNumberString);
          if (Length(SpectraNumberString) = 1)
            then SpectraNumberString := '0'+SpectraNumberString;
          RetrieveData (BackData, MsParam.NumberSteps,
                       'MS\'+Status.BackSpectraFileName+SpectraNumberString+'.MD');
        end;

       {Retrieve main spectra}
        RetrieveMsP (MsParam,
                     Status.FileName,
                     Status.CurrentSpectraNumber);
        Str (Status.CurrentSpectraNumber, SpectraNumberString);
        if (Length(SpectraNumberString) = 1)
          then SpectraNumberString := '0'+ SpectraNumberString;
        RetrieveData (MsData, MsParam.NumberSteps,
                     'MS\'+Status.FileName+SpectraNumberString+'.MD');

        Multiplier := 1.0;
        for count := 1 to round(MsParam.AmpScale) do
          Multiplier := Multiplier*10.0;
```

```
        WriteMsSummaryScreen1 (MsData.FirstPoint,
                               MsParam);

        IsSpectraChosen := true;
        IsPeakLocated   := false;
        Status.IsBackSubtracted := false;
      end
      else begin
        if (Status.MsNumber <= 0) then
          WriteError ('ERROR -- NO Ms SPECTRA')
        else WriteError ('ERROR -- NO RUN RETRIVED');
      end;
      FuncKey := 2;
    end;

{Show auxilary scans}
 61:begin
      if (IsRunRetrieved) then begin
        WriteAuxScreen (AuxParam);
        if (Status.IsSmCurrSpectra)
          then DrawSpectra (SmCurrData.FirstPoint, true, 2)
          else begin
            GotoXY (24,6);  Write ('NO DATA TAKEN');
          end;
        if (Status.IsInterferSpectra)
          then DrawSpectra (InterferData.FirstPoint, true, 3)
          else begin
            GotoXY (24,16);  Write ('NO DATA TAKEN');
          end;

        repeat
          GetFuncKey (FuncKey);
          if (FuncKey = 104) then
            Walk (InterferData.FirstPoint, 1.0, 3);
        until (FuncKey = 150);
        FuncKey := 61;
      end
      else WriteError ('ERROR -- NO RUN RETRIVED');

      FuncKey := 2;
    end;

{Fix data}
 62:begin
      if (IsSpectraChosen) then begin
        WriteFixChoiceScreen;
        repeat
          GetFuncKey (FuncKey);
        until (((FuncKey >= 59) and (FuncKey <= 68)) or (FuncKey = 150));

        Case FuncKey of

         {Start-End trim}
          59:begin
               TrimStartEnd (MsData, Multiplier, 1);
             end;

         {Set minimum to 0.0}
          60:begin
               Min0 (MsData.FirstPoint);
             end;
```

```
        {Scale Data}
          61:begin
              ScaleData (MsData.FirstPoint);
            end;

        {Change Amp Scale}
          67:begin
              ChangeAmpScale (MsData.FirstPoint, MsParam.AmpScale);
            end;

        {Parameter modify}
          68:begin
              WriteMsSummaryScreen2 (MsParam);
              GetMsParam (MsParam);
              WriteMsSummaryScreen2 (MsParam);
              GotoXY (2,25);
            end;
        end;

        if (FuncKey <> 150) then begin
          GotoXY (2,25);
          Write ('Save changes: (y/n) ');
          repeat
            InputString := UpCase(readkey);
          until ((InputString = 'Y') or (InputString = 'N'));
          if (InputString = 'Y')
            then begin
              Erase25;
              SaveMs (MsParam, Status.FileName,
                    Status.CurrentSpectraNumber);
            end;
        end;

      end
      else  WriteError ('ERROR -- NO RUN RETRIVED or SPECTRA CHOSEN');

      FuncKey := 2;
    end;

{Data Correct}
  63:begin
      if (IsSpectraChosen) then begin
        WriteCorrectChoiceScreen;
        repeat
          GetFuncKey (FuncKey);
        until (((FuncKey >= 59) and (FuncKey <= 68)) or (FuncKey = 150));

        Case FuncKey of

        {Retrieve background spectra}
          67:begin
              GetFileName (Status.BackSpectraFileName);
              GetSpectraNumber (Status.BackSpectraFileName,
                          'MS\'+Status.BackSpectraFileName+'*.MP ',
                          Status.BackSpectraNumber);
              IsBackSpectraChosen := true;

              EraseData (BackData);
              RetrieveMsP (MsParam,
                        Status.BackSpectraFileName,
                        Status.BackSpectraNumber);
              Str (Status.BackSpectraNumber, SpectraNumberString);
```

```
            if (Length(SpectraNumberString) = 1)
              then SpectraNumberString := '0'+SpectraNumberString;
            RetrieveData (BackData, MsParam.NumberSteps,
                    'MS\'+Status.BackSpectraFileName+SpectraNumberString+'.MD');
            RetrieveMsP (MsParam,
                    Status.FileName,
                    Status.CurrentSpectraNumber);

          end;

        {Spectra subtruct}
         68:begin
            if not(Status.IsBackSubtructed) then begin
              SpectraSubtruct (MsData, BackData);
              Status.IsBackSubtructed := true;
            end
            else WriteError ('ERROR -- BACKGROUND ALREADY SUBTRUCTED');
          end;

      end;
    end
    else WriteError ('ERROR -- NO SPECTRA CHOSEN or RUN RETRIVED');

    FuncKey := 2;
  end;

{Manual scan}
 64:begin
    if (IsSpectraChosen) then begin
      Walk (MsData.FirstPoint, Multiplier, 1);
    end
    else WriteError ('ERROR -- NO SPECTRA CHOSEN or RUN RETRIVED');

    FuncKey := 2;
  end;

{Peak locate}
 65:begin
    if (IsSpectraChosen) then begin
      ErasePeak (MsPeakData);
      FindMsPeak (MsData.FirstPoint,
              0.01, MsParam.AmpScale,
              MsPeakData);
      WriteMsPeakSummaryScreen (MsPeakData, MsParam.AmpScale);
      IsPeakLocated := true;
    end
    else WriteError ('ERROR -- NO SPECTRA CHOSEN or RUN RETRIVED');

    FuncKey := 2;
  end;

{ProPlot Auxilary summary}
 66:begin
    if (Status.IsSmCurrSpectra or Status.IsInterferSpectra) then begin
      ProPlotAuxSummary (SmCurrData.FirstPoint,
                  InterferData.FirstPoint,
                  AuxParam);
    end;
    FuncKey :=2;
 end,
```

```
{ProPlot Ms summary}
 67:begin
     if (IsSpectraChosen) then begin
       ProPlotMsSummary (MsData.FirstPoint,
                         MsPeakData,
                         MsParam,
                         'e:\dave\experime\plot');
     end
     else WriteError ('ERROR -- NO RUN RETRIEVED or SPECTRA CHOSEN');

     FuncKey := 2;
   end;

{Automatic Massage}
 68:begin
     if (IsRunRetrieved) then begin
       WriteAutomaticChoiceScreen;
       repeat
         GetFuncKey (FuncKey);
       until (((FuncKey >= 59) and (FuncKey <= 68)) or (FuncKey = 150));

       Case FuncKey of

        {All spectra print}
         59:begin
              ClearScreen;
              for Status.CurrentSpectraNumber := 1 to Status.MsNumber do begin
                EraseData (MsData);
                ErasePeak (MSPeakData);

                RetrieveMsP (MsParam,
                             Status.FileName,
                             Status.CurrentSpectraNumber);
                Str (Status.CurrentSpectraNumber, SpectraNumberString);
                if (Length(SpectraNumberString) = 1)
                  then SpectraNumberString := '0'+ SpectraNumberString;
                RetrieveData (MsData, MsParam.NumberSteps,
                              'MS\'+Status.FileName+SpectraNumberString+'.MD');

                FindMsPeak (MsData.FirstPoint,
                            0.01, MsParam.AmpScale,
                            MsPeakData);

                ProPlotMsSummary (MsData.FirstPoint,
                                  MsPeakData,
                                  MsParam, 'e:\dave\experime\plot');
              end;
              Status.CurrentSpectraNumber := 0;
              IsSpectraChosen := false;
            end;

        {Peak process}
         60:begin
              NumKeyParamChanges := 0;
              NormPeak := 0;
              IsNormAverage := false;
              Direction := 0;
              WritePeakProcessScreen (Status.FileName,
                                      IsGenerateRelation,
                                      NormPeak,
                                      IsNormAverage,
                                      Direction);
```

```
                If (IsGenerateRelation)
                  then FindSpectraRelation (Status.FileName,
                                            NumKeyParamChanges)
                  else CountSpectraRelation (Status.FileName,
                                             NumKeyParamChanges);

                if (NumKeyParamChanges <> 0) then begin
                  GotoXY (23,13);
                  Write ('Number of Key Files:  ', NumKeyParamChanges:2);

                  CalcKeyParamFile (Status.FileName,
                                    NumKeyParamChanges,
                                    NormPeak,
                                    IsNormAverage,
                                    Direction);
                end;

                Status.CurrentSpectraNumber := 0;
                IsSpectraChosen := false;
              end;

          end;
        end
        else WriteError ('ERROR -- NO RUN RETRIVED');

        FuncKey := 2;
      end;

  {Display summary screen1}
   104:begin
        if (IsSpectraChosen) then begin
          SwapScreen;
          repeat
            GetFuncKey (FuncKey);
          until (FuncKey = 150);
          FuncKey := 1;
          SwapScreen;
        end
        else WriteError ('ERROR -- NO RUN RETRIEVED or SPECTRA CHOSEN');
      end;

  {Display summary screen2}
   105:begin
          WriteMsSummaryScreen2 (MsParam);
          repeat
            GetFuncKey (FuncKey);
          until (FuncKey = 150);
          FuncKey := 2;
      end;

  {Exit}
   150:begin
        Erase25;
        GotoXY (2,25);
        Write ('EXIT: (y/n) ');
        repeat
          InputString := UpCase(readkey);
        until ((InputString = 'Y') or (InputString = 'N'));
        if (InputString = 'Y') then IsExit := true
                               else Erase25;
      end;
  end;
```

```
    if (FuncKey = 2) then begin
      WriteMainScreen;
      WriteMainChoiceScreen;

      if (IsSpectraChosen) then begin
        DrawSpectra (MsData.FirstPoint, true, 1);
      end;
      if (IsBackSpectraChosen) then begin
        DrawSpectra (BackData.FirstPoint, true, 2);
      end;
    end;

    FuncKey := 1;
  until (IsExit);
END.
```

Appendix D: Doser Design Code

This appendix contains a version of the FORTRAN code "FLOWTYPE.FOR" used in the calculation of flux gradients and enhancement factors for opaque regime dosers as described in Chapter 3. The program currently runs under Microsoft FORTRAN 77 version 2.0 (1985), and requires the include files "FLUX.INC" and "GASPROPS.INC" for compilation. Data is input by the user in floating point format in response to screen prompts. Output is sent to the screen, as well as to the file "DSRPARAM.DAT" which contains the run parameters, and one of three beam shape files depending on the flow regime: "OSHAPE.DAT", "TSHAPE.DAT", or "CSHAPE.DAT".

The goals of this programming effort were to provide a useful tool to aid in the design of opaque regime dosers, and to facilitate their characterization based on impact tube characterization in the 3-beam reactor. User input is required in 3 main categories:

1) doser and system geometric parameters,

2) gas properties, and

3) measured system pressures.

Total gas flow from the doser is calculated based on peak beam intensity measured by the impact tube, and is compared to that predicted from chamber pressure rise and the gas pumping speed. Large discrepancy between these values indicates misalignment of the impact orifice and the beam peak. The doser gas flow regime and hydrodynamic parameters are then calculated to determine the appropriate angular flux distribution functions. The user the has the options to calculate the beam flux distributions (point source) and to calculate fractional interception and enhancement factor over the target solid angle.

```
      PROGRAM MAIN
$DEBUG
C
C     This program is the main driver which calculates the
C     appropriate gas flow regime given a straight tube doser
C     geometry and gas properties.  The critical length parameter
C     is calculated.  The user may calculate beam shape
C     profiles and fractional interception using the correct
C     angular distribution profiles.
C     Uses files:  FLUX.INC, GASPROPS.INC
C     Outfiles:    DSRPARAM.DAT
C

$INCLUDE: 'FLUX.INC'
$INCLUDE: 'GASPROPS.INC'

      REAL*8  N,C,PTIP,POLD,M,Q,F,NCH,VC
      CHARACTER*12  FLOWTYPE,ANS
      LOGICAL CPAS1,TPAS1,OPAS1

C     PTIP=      REFERENCE TIP PRESSURE FOR MFP CALCULATION [=] TORR
C     POLD=      HOLDER FOR OLD TIP REFERENCE PRESSURE [=] TORR
C     C=         MEAN GAS VELOCITY [=] CM/SEC
C     N=         GAS DENSITY BASED ON PTIP [=] CM-3
C     M=         GAS MOLECULAR MASS [=] G
C     F=         FRACTIONAL INTERCEPTION OF SAMPLE

      OPEN(5, FILE='DSRPARAM.DAT', STATUS='NEW')

C     INITIALIZE THE COMMON BLOCK DATA
      CALL INTITIALIZE

      CPAS1=.TRUE.
      TPAS1=.TRUE.
      OPAS1=.TRUE.

1     CONTINUE

C     PROMPT THE USER FOR DOSER GEOMETRIC PARAMETERS
      CALL DOSRINPUT

C     PROMPT THE USER FOR GAS PROPERTIES
      CALL GASINPUT

C     PROMPT THE USER FOR MEASURED SYSTEM PRESSURES
      CALL PINPUT

C     WRITE(*,2)
2     FORMAT(//1X,'***CALCULATING GAS FLOW REGIME.....')

C     APPROXIMATE THE INITIAL DOSER TIP PRESSURE

      PBE=PBM/4.0*(CALIB/DCOS(ANGLE*2*PI/360))
      PTIP=2.0*PBE

5     CONTINUE

C     CALCULATE AVERAGE MEAN FREE PATHS AND KNUDSEN NUMBERS
C     CURRENT ESTIMATE OF PTIP IS USED
```

```
10   N=PTIP/(KB*0.75D-3*T)
     M=MW/NA
     C=(8*KB*T/(PI*M))**0.5
     MFP=(2**0.5*PI*SIGMA**2*N)**(-1)

     KNA=MFP/A
     KNL=MFP/L

C    SPECIFY GAS FLOW REGIME

     IF((KNA.GT.1.0).AND.(KNL.GT.1.0)) THEN
        FLOWTYPE='TRANSPARENT'
          ELSE IF (KNA.GT.1.0) THEN
        FLOWTYPE='OPAQUEI'
          ELSE
        FLOWTYPE='OPAQUE II'
     ENDIF

C    CALCULATE TOTAL THROUGHPUT BASED ON BEAM PRESSURE
     CALL FLOWRATE(FLOWTYPE,C)

C    CALCULATE DOSER PRESSURE PROFILE, REVISE PTIP ESTIMATE
     POLD=PTIP
     CALL DOSRPZ(PTIP,C,N)

C    PERFORM AN ITERATION WITH NEW PTIP IF NECESSARY

     IF (ABS(POLD/PTIP-1.0).GT.0.10) THEN
        WRITE(*,20) POLD,PTIP
20       FORMAT(1X,'POLD= ',D9.2,5X,'PTIP= ',D9.2)
        WRITE(*,30)
30       FORMAT(1X,'ANOTHER ITERATION IS RECOMMENDED. ITERATE?
    *          [Y OR N]: ')
        READ(*,40) ANS
40       FORMAT(A12)
        IF ((ANS.EQ.'Y').OR.(ANS.EQ.'y')) THEN
          GOTO 10
        ENDIF

     ENDIF


C    WRITE THE CURRENT PARAMETERS TO SCREEN
     CALL WRITESC1(PTIP,FLOWTYPE)

C    PROMPT THE USER TO RESET PARAMETERS OR CONTINUE

C    WRITE A DOSR PARAMETER FILE
     CALL WRITEPG1(PTIP,FLOWTYPE)


C    EXECUTE BEAM SHAPE CALCULATIONS IF DESIRED

45   WRITE(*,50)
50   FORMAT(//1X,'DO YOU WISH TO MAKE BEAM SHAPE CALCULATIONS?')
     READ(*,60) ANS
60   FORMAT(A12)
     IF ((ANS.EQ.'Y').OR.(ANS.EQ.'y')) THEN
       WRITE(*,70) FLOWTYPE
70     FORMAT(1X,'CURRENT FLOWTYPE IS: ', A12)
75     WRITE(*,80)
80     FORMAT(1X,'SELECT A FLOW REGIME FOR SHAPE CALCULATIONS:'/,
```

```
     *        1X, 'COSINE [C], TRANSPARENT [T], OPAQUE [O]: ')
          READ(*,90) ANS
90         FORMAT(A12)
          IF((ANS.EQ.'C').OR.(ANS.EQ.'c')) THEN
            CALL CSHAPE(CPAS1)
            CPAS1=.FALSE.
          ENDIF
          IF((ANS.EQ.'T').OR.(ANS.EQ.'t')) THEN
            CALL TSHAPE(TPAS1)
            TPAS1=.FALSE.
          ENDIF
          IF((ANS.EQ.'O').OR.(ANS.EQ.'o')) THEN
            CALL OSHAPE(OPAS1)
            OPAS1=.FALSE.
          ENDIF
          WRITE(*,100)
100        FORMAT(1X,'MODIFY INPUT PARAMETERS TO CONTINUE?[Y OR N]: ')
          READ(*,110) ANS
110        FORMAT(A12)
          IF ((ANS.EQ.'Y').OR.(ANS.EQ.'y'))  THEN
            GOTO 1
          ENDIF
        ENDIF

C       EXECUTE FLUX INTERCEPTION CALCULATIONS IF DESIRED

        WRITE(*,120)
120     FORMAT(//1X,'DO YOU WISH TO CALCULATE FLUX INTERCEPTION ?')
        READ(*,130) ANS
130     FORMAT(A12)
        IF ((ANS.EQ.'Y').OR.(ANS.EQ.'y'))  THEN
          IF (.NOT.OPAS1) THEN
            CALL TDINT(F)
            WRITE(*,140) F
140           FORMAT(1X,'FLUX INTERCEPTED: ',F10.7//)
            WRITE(4,150) F
150           FORMAT(1X,'FLUX INTERCEPTED: ',F10.7//)
          ELSE
            WRITE(*,*) 'PLEASE EXECUTE THE OSHAPE SECTION FIRST'
            GOTO 45
          ENDIF
        ENDIF

C       CALCULATE ENHANCEMENT FACTOR OVER TARGET AREA
C       ASSUMING ZERO STICKING COEFFICIENT

        VC=(2*PI*M*KB*T*0.75E-3)**(-0.5)
        E=(1+F*S/(0.75E-3*KB*T*VC*PI*RT**2))

        WRITE(*,160) E
160     FORMAT(1X,'TARGET ENHANCEMENT FACTOR: ',F10.7/)
        WRITE(4,170) E
170     FORMAT(1X,'TARGET ENHANCEMENT FACTOR: ',F10.7/)

        END

**********

        SUBROUTINE INTITIALIZE

C
C       DAVID C. GRAY  8/27/89
```

```
C    DEFINE VARIBLES:
C
C
C    RS=   SOURCE RADIUS INTEGRATION VARIABLE [=] CM
C    RT=   TARGET RADIUS INTEGRATION VARIABLE [=] CM
C    PHI=  SOURCE AZIMUTHAL INTEGRATION VARIABLE [=] CM
C    A=    SOURCE CAPILLARY DIAMETER [=] CM
C    D=    DOSER-SAMPLE DISTANCE [=] CM
C    L=    CAPILLARY LENGTH [=] CM
C    LO=   TUBE DISTANCE AT MOLECULAR FLOW TRANSITION [=] CM
C    LCRIT= CAPILLARY CRITICAL LENGTH PARAMETER [=] CM
C    RSLIM= SOURCE INSIDE RADIUS [=] CM
C    RTLIM= TARGET INSIDE RADIUS [=] CM
C    PHILIM=PHI INTEGRATION LIMIT [=] RAD
C    MFP=  GAS MFP
C    KNA=  GAS KNUDSEN NUMBER RELATIVE TO CAPILLARY DIAM
C    KNL=  GAS KNUDSEN NUMBER RELATIVE TO CAPILLARY LENGTH
C    ANGLE= ANGLE OF DOSER TO SAMPLE NORMAL [=] RAD
C    CALIB= DOSER CALIBRATION FACTOR [=] 1
C    THETAMAX= MAXIMUM DOSER-SAMPE ANGLE SUBTENDED [DEG]
C    NTOT= TOTAL MOLECULAR FLOW [=] MOLS/S
C    KB= BOLTZMAN CONSTANT [=] ERGS/K

$INCLUDE: 'FLUX.INC'
$INCLUDE: 'GASPROPS.INC'

C    INTITIALIZE PHYSICAL CONSTANTS

     PI=4.0*ATAN(1.0)
     KB=1.38D-16
     NA=6.022D+23

C    INTITIALIZE DOSER GEOMETRIC PARAMETERS

     RS=0.0
     RT=0.0
     PHI=0.0
     A=0.4
     D=1.0
     L=5.0
     RSLIM=0.2
     RTLIM=0.5
     PHILIM=PI/2
     MFP=0.0
     KNA=0.0
     KNL=0.0
     LCRIT=0.0
     LO=0.0
     ANGLE=0.0
     CALIB=1.0
     NTOT=0.0
     THETAMAX=0.0

     DOSRNAME='1/4 NOMINAL'
     DOSRMTRL='STAINLESS STL'

C    INITILIZE GAS PROPERTY DATA
C
C    SIGMA  =  MEAN MOLECULAR DIAMETER [=] CM
C    GAMMA  =  THE THERMODYNAMIC RATIO CP/CV
C    CP     =  CONSTANT PRESSURE STANDARD HEAT CAPACITY
C    CV     =  CONSTANT VOLUME STANDAT HEAT CAPACITY
```

```
C     MW    = MOLECULAR WEIGHT OF THE GAS [=] AMU
C     PS    = GAS SOURCE RESERVIOUR [=] TORR
C     RGRAD = DOSER TIP PRESSURE GRADIENT [=] TORR/CM
C     PCH   = CHAMBER BACKGROUND PRESSURE [=] TORR
C     PBE   = BEAM PRESSURE AT TUBE EXIT [=] TORR
C     PBM   = PEAK BEAM PRESSURE MEASURED AT SAMPLE [=] TORR
C     PBASE = CHAMBER BASE PRESSURE [=] TORR
C     S= GAS PUMPING SPEED [=] TORR-L/S
C     T= EXIT GAS TEMPERATURE [=] K
C     ETA= OPAQUE FLOW DIMENSIONLESS PARAMTER [=] 1
C     E= ENHANCEMENT FACTOR OVER TARGET AREA [=] 1

      GASNAME='ARGON'
      GASTYPE='MONATOMIC'

      PS=1.0D-2
      PBE=1.0E-3
      PBM=1.0E-4
      PCH=1.0E-5
      PBASE=1.0E-8
      RGRAD=0.0
      T=300.0

      SIGMA=5.0D-8
      CP=5.0/2.0
      CV=3.0/2.0
      GAMMA=5.0/3.0
      MW=40.0
      S=1000.0
      ETA=1.0
      E=1.0

      RETURN
      END

*********************************

      SUBROUTINE DOSRINPUT
C
C     INPUT THE DOSER GEOMETRIC PARAMETERS
C
$INCLUDE: 'FLUX.INC'
$INCLUDE: 'GASPROPS.INC'

      WRITE(*,5)
5     FORMAT(/1X,'***INPUT THE DOSER GEOMETRIC PARAMETERS***'/)
      WRITE(*,10)
10    FORMAT(1X,'ENTER TUBE INNER DIAMETER [cm]:')
      READ(*,15) A
15    FORMAT(F4.2)
      RSLIM=A/2.0
      WRITE(*,20)
20    FORMAT(1X,'ENTER THE TUBE LENGTH [cm]:')
      READ(*,25) L
25    FORMAT(F5.2)
      WRITE(*,30)
30    FORMAT(1X,'ENTER THE TARGET EQUIVALENT RADIUS [cm]:')
      READ(*,35) RTLIM
35    FORMAT(F4.2)
      WRITE(*,40)
40    FORMAT(1X,'ENTER THE DOSER-TO-TARGET DISTANCE [cm]:')
      READ(*,45) D
```

```
45   FORMAT(F5.2)
     THETAMAX=ATAN(RTLIM/D)*360/(2*PI)
     WRITE(*,50)
50   FORMAT(1X,'ENTER THE DOSER-TARGET ANGLE [deg]:')
     READ(*,55) ANGLE
55   FORMAT(F6.2)

     WRITE(*,60)
60   FORMAT(/1X,'ENTER A 12 CHARACTER DOSER NAME:')
     READ(*,65) DOSRNAME
65   FORMAT(A12)
     WRITE(*,70)
70   FORMAT(1X,'ENTER DOSER WALL MATERIAL:')
     READ(*,75) DOSRMTRL
75   FORMAT(A12)


     RETURN
     END
**********************************

     SUBROUTINE GASINPUT
C
C    INPUT GAS PHYSICAL PROPERTIES
C
$INCLUDE: 'FLUX.INC'
$INCLUDE: 'GASPROPS.INC'

     WRITE(*,5)
5    FORMAT(/1X,'***INPUT THE GAS PHYSICAL PROPERTIES***'/)
     WRITE(*,10)
10   FORMAT(1X,'PLEASE INPUT THE GAS NAME:')
     READ(*,15) GASNAME
15   FORMAT(A12)
     WRITE(*,20)
20   FORMAT(1X,'ENTER THE GAS TYPE:')
     READ(*,25) GASTYPE
25   FORMAT(A12)
     WRITE(*,30)
30   FORMAT(1X,'ENTER THE MOLECULAR WEIGHT:')
     READ(*,35) MW
35   FORMAT(F6.2)
     WRITE(*,40)
40   FORMAT(1X,'ENTER THE MOLECULAR DIAMETER [cm]:')
     READ(*,45) SIGMA
45   FORMAT(D11.2)
     WRITE(*,50)
50   FORMAT(1X,'ENTER THE CP VALUE:')
     READ(*,55) CP
55   FORMAT(F8.4)
     WRITE(*,60)
60   FORMAT(1X,'ENTER THE CV VALUE:')
     READ(*,65) CV
65   FORMAT(F8.4)
     GAMMA=CP/CV

     WRITE(*,70)
70   FORMAT(/1X,'ENTER THE NOMINAL GAS PUMPING SPEED [L/S]:')
     READ(*,75) S
75   FORMAT(F8.2)

     RETURN
```

```
      END
**********************************

      SUBROUTINE PINPUT
C
C     INPUT THE EXPERIMENTAL SYSTEM PRESSURES
C
$INCLUDE: 'FLUX.INC'
$INCLUDE: 'GASPROPS.INC'

      WRITE(*,10)
10    FORMAT(/1X, '***ENTER THE EXPERIMENTAL SYSTEM PARAMETERS***'/)
      WRITE(*,15)
15    FORMAT(1X,'ENTER THE CHAMBER BASE PRESSURE [TORR]:')
      READ(*,20) PBASE
20    FORMAT(D11.2)
      WRITE(*,25)
25    FORMAT(1X,'ENTER THE MEASURED BEAM PRESSURE [TORR]: ')
      READ(*,30) PBM
30    FORMAT(D11.2)

      IF (INT(ANGLE).LT.45) THEN
        WRITE(*,32) ANGLE
32      FORMAT(1X, 'DOSER IS AT ',F8.4,'DEGREES TO TARGET',
     *         ' ENTER IMPACT ANGLE CALIBRATION FACTOR:')
        READ(*,34) CALIB
34      FORMAT(F8.4)
      ENDIF

      WRITE(*,35)
35    FORMAT(1X, 'ENTER THE CHAMBER BACKGROUND PRESSURE [TORR].')
      READ(*,40) PCH
40    FORMAT(D11.2)
      WRITE(*,45)
45    FORMAT(1X,'ENTER THE DOSER TIP TEMPERATURE [K]:')
      READ(*,50) T
50    FORMAT(F8.2)

      RETURN
      END


**********************************

      SUBROUTINE FLOWRATE(FLOWTYPE,C)
C
C     CACULATE THE TOTAL DOSER THROUGHPUT BASED ON:
C     1) BASE PRESSURE RISE EXPERIMENTS
C     2) MEASURE BEAM PEAK INTENSITIES
C

$INCLUDE: 'FLUX.INC'
$INCLUDE: 'GASPROPS.INC'

      CHARACTER*12 FLOWTYPE,ANS
      REAL*8 Q,C,IPEAK,NTOTPR,SR,DO

C     CALCULATE STERADIANS SUBTENDED BY DETECTOR AREA

      DO=0.158
      SR=PI*DO**2/(4*D**2)
```

```
C     CALCULATE FLOW RATE BASED ON PEAK BEAM INTENSITY
C     REF: GIORDMAINE AND WANG

      IPEAK=(PBM*3.52D+22/((T*MW)**0.5))*D**2.0
      NTOT=((IPEAK*SIGMA)/(0.103*C**0.5*RSLIM**0.5))**2.0
      NTOT=NTOT*CALIB/4.0

C     CALCULATE FLOW RATE BASED ON P RISE AND PUMPING SPEED

      Q=(PCH-PBASE)*S
      NTOTPR=Q*9.61D+21/T

      IF (ABS(NTOT/NTOTPR-1.0).GT.0.10) THEN
        WRITE(*,10)
10       FORMAT(1X,'GAS PUMPING SPEED PROVIDED IS INCONSISTENT. ')
        S=NTOT/((9.61D+21/T)*(PCH-PBASE))
        WRITE(*,20) S
20       FORMAT(1X,'MODIFIED PUMPING SPEED IS: ',F9.2/)
        WRITE(*,30)
30       FORMAT(1X,'CONTINUE?[Y OR N]: ')
        READ(*,40) ANS
40       FORMAT(A12)
        IF ((ANS.EQ.'Y').OR.(ANS.EQ.'y')) THEN
50         CONTINUE
        ELSE
          STOP
        ENDIF
      ENDIF

      RETURN
      END

.
**********

      SUBROUTINE DOSRPZ(PTIP,C,N)

C
C     This subroutine approximates the gas pressure gradient at the
C     doser tip based on the gas source pressure, the chamber background
C     pressure, and the tube geometry.
C     Current approximation is linear.
C

$INCLUDE: 'FLUX.INC'
$INCLUDE: 'GASPROPS.INC'

      REAL*8 PTIP,C,N,MFPO,NO,PO,Q,GRAD,RSUM
      EXTERNAL PTIPFUNC

C     CALCULATE THE DOSER TIP PRESSURE GRADIENT ([=] TORR/CM)
C     GRADIENT IN THE KNUDSEN REGIME AT THE TIP END

      GRAD=3*NTOT/(2*PI*C*RSLIM**3)
      RGRAD=GRAD*(KB*0.75E-3*T)

C     CALCULATE CRITICAL LENGTH PARAMETER

      LCRIT=2.427*(C**0.5*RSLIM**1.5/(SIGMA*NTOT**0.5))

C     CALCULATE THE KNUDSEN-VISCOUS FLOW TRANSITION LENGTH
      MFPO=0.1*A
```

```
      NO=(MFPO*2**0.5*PI*SIGMA**2)**(-1.0)
      PO=NO*KB*0.75D-3*T

      LO=(PO-PTIP)/RGRAD

C     ALTERNATE METHOD FOR PTIP CALCULATION

      IF(LO.GT.L) THEN
        PS=PBE+RGRAD*L
      ELSE

C     CONVERT TOTAL FLOW TO TORR-L/S, CALCULATE RESERVIOR PRESSURE
        Q=NTOT*T/9.61E+21
        PS=(Q*(L-LO)/(90.0*A**4.0)+PO**2.0)**0.5
      ENDIF

C     INTEGRATE OVER TUBE LENGTH TO FIND AVERAGE PTIP
C       M=6
C       DO 20 J=1,M+1
C         CALL TRAPPT(PTIPFUNC,LO,L,RSUM,J,Q,PO)
C       CONTINUE

C     CALCULATE PTIP BASED ON NTOT

        PTIP=NTOT*(4*KB*T*0.75D-3)/(C*PI*A**2)

C     CALCULATE ETA BASED ON NTOT

            ETA=5.657*SIGMA**2*NTOT/(C*A)



      RETURN
      END

************************************

      SUBROUTINE WRITESC1(PTIP,FLOWTYPE)
C
C     WRITE THE DOSER PARAMETER SUMMARY TO SCREEN
C

$INCLUDE: 'FLUX.INC'
$INCLUDE: 'GASPROPS.INC'

      REAL*8  PTIP
      CHARACTER*12  FLOWTYPE

      WRITE(*,5)
5     FORMAT(1X, '****DOSER GEOMETRIC PARAMETERS (CGS UNITS)****'/)
      WRITE(*,10) RSLIM,A,L
10    FORMAT(1X,'RSLIM= ',F8.4,5X,'A= ',F8.4,9X,'L= ',F8.4)
      WRITE(*,15) RTLIM,THETAMAX,D
15    FORMAT(1X,'RTLIM= ',F8.4,5X,'THETAMAX= ',F5.2,6X,'D= ',F8.4)
      WRITE(*,20) ANGLE,CALIB
20    FORMAT(1X,'DOSER ANGLE= ',F6.2,3X,'CALIBRATION FACTOR= ',F5.2)
      WRITE(*,22) DOSRNAME, DOSRMTRL
22    FORMAT(1X,'DOSRNAME= ',A12/,1X,'DOSRMTRL= ',A12//)

      WRITE(*,25)
25    FORMAT(1X,'****GAS PROPERTY INFORMATION*****'/)
      WRITE(*,30) GASNAME, GASTYPE
```

```
30   FORMAT(1X,'GASNAME= ',A12,19X,'GASTYPE= ',A12)
     WRITE(*,35) SIGMA,MW
35   FORMAT(1X,'SIGMA= ',D11.2,2X,'MW= ',F7.2)
     WRITE(*,40) GAMMA,CP,CV
40   FORMAT(1X,'GAMMA= ',F4.2,9X,'CP= ',F8.4,8X,'CV= ',F8.4)
     WRITE(*,42)
42   FORMAT(1X,'SYSTEM PRESSURES: ')
     WRITE(*,45) PS,PBE,PBM,PCH,PBASE
45   FORMAT(20X,'PSOURCE= ',D9.2/,20X,'PBEAM EXIT= ',D9.2/,20X,
    *     'PBEAM MEASURED= ',D9.2/,20X,'PCHAMBER BACKGROUND= ',D9.2/,
    *     20X,'PBASE= ',D9.2)
     WRITE(*,47) S
47   FORMAT(1X,'GAS PUMPING SPEED= ',F9.2//)

     WRITE(*,50) T
50   FORMAT(1X,'****CALCULATED*****',5X,'TBEAM (K)= ',F8.2/)
     WRITE(*,55) PTIP,FLOWTYPE
55   FORMAT(1X,'PTIP REFERENCE= ',D9.2,15X,'FLOWTYPE= ',A12)
     WRITE(*,60) MFP,KNA,KNL
60   FORMAT(1X,'MFP= ',F8.4,7X,'KNA= ',F8.4,7X,'KNL= ',F8.4)
     WRITE(*,65) NTOT,RGRAD
65   FORMAT(1X,'TOTAL FLOW= ',D11.2,17X,'RGRAD= ',D11.2)
     WRITE(*,70) LCRIT,LO,ETA
70   FORMAT(1X,'CRITICAL LENGTH= ',D11.4,12X,
    *        'TRANSITION LENGTH= ',D11.4/1X,'ETA= ',D11.4)

     RETURN
     END

**********************************

     SUBROUTINE WRITEPG1(PTIP,FLOWTYPE)
C
C    WRITE THE DOSER PARAMETER SUMMARY TO FILE
C    DSRPARAM.DAT.
C

$INCLUDE: 'FLUX.INC'
$INCLUDE: 'GASPROPS.INC'

     REAL*8  PTIP
     CHARACTER*12  FLOWTYPE


     WRITE(5,5)
5    FORMAT(1X, '****DOSER GEOMETRIC PARAMETERS (CGS UNITS)****'/)
     WRITE(5,10) RSLIM,A,L
10   FORMAT(1X,'RSLIM= ',F8.4,5X,'A= ',F8.4,9X,'L= ',F8.4)
     WRITE(5,15) RTLIM,THETAMAX,D
15   FORMAT(1X,'RTLIM= ',F8.4,5X,'THETAMAX= ',F5.2,6X,'D= ',F8.4)
     WRITE(5,20) ANGLE,CALIB
20   FORMAT(1X,'DOSER ANGLE= ',F6.2,3X,'CALIBRATION FACTOR= ',F5.2)
     WRITE(5,22) DOSRNAME, DOSRMTRL
22   FORMAT(1X,'DOSRNAME= ',A12/,1X,'DOSRMTRL= ',A12//)

     WRITE(5,25)
25   FORMAT(1X,'****GAS PROPERTY INFORMATION*****'/)
     WRITE(5,30) GASNAME, GASTYPE
30   FORMAT(1X,'GASNAME= ',A12,19X,'GASTYPE= ',A12)
     WRITE(5,35) SIGMA,MW
35   FORMAT(1X,'SIGMA= ',D11.2,2X,'MW= ',F7.2)
     WRITE(5,40) GAMMA,CP,CV
```

```
40   FORMAT(1X,'GAMMA= ',F4.2,9X,'CP= ',F8.4,8X,'CV= ',F8.4)
     WRITE(5,42)
42   FORMAT(1X,'SYSTEM PRESSURES: ')
     WRITE(5,45) PS,PBE,PBM,PCH,PBASE
45   FORMAT(20X,'PSOURCE= ',D9.2/,20X,'PBEAM EXIT= ',D9.2/,20X,
    *     'PBEAM MEASURED= ',D9.2/,20X,'PCHAMBER BACKGROUND= ',D9.2/,
    *     20X,'PBASE= ',D9.2)
     WRITE(5,47) S
47   FORMAT(1X,'GAS PUMPING SPEED= ',F9.2/)

     WRITE(5,50) T
50   FORMAT(1X,'****CALCULATED*****',5X,'TBEAM (K)= ',F8.2/)
     WRITE(5,55) PTIP,FLOWTYPE
55   FORMAT(1X,'PTIP REFERENCE= ',D9.2,15X,'FLOWTYPE= ',A12)
     WRITE(5,60) MFP,KNA,KNL
60   FORMAT(1X,'MFP= ',F8.4,7X,'KNA= ',F8.4,7X,'KNL= ',F8.4)
     WRITE(5,65) NTOT,RGRAD
65   FORMAT(1X,'TOTAL FLOW= ',D11.2,17X,'RGRAD= ',D11.2)
     WRITE(5,70) LCRIT,LO,ETA
70   FORMAT(1X,'CRITICAL LENGTH= ',D11.4,12X,
    *        'TRANSITION LENGTH= ',D11.4,/1X,'ETA= ',D11.4)

     RETURN
     END

*****************************************

     SUBROUTINE CSHAPE(CPAS1)
C
C    This program is a routine to display
C    normalized beam intensity variation across a
C    sample surface from an ideal point cosine emmitter.
C    OUTFILES: CSHAPE.DAT

     REAL*8 THETA,RTINC,DJNORM
     INTEGER M
     LOGICAL CPAS1

$INCLUDE: 'FLUX.INC'

     EXTERNAL DJCOS

     IF (CPAS1) THEN
       OPEN(4, FILE='CSHAPE.DAT',STATUS='NEW')
     ENDIF

     WRITE(4,10)
10   FORMAT(10X,'***FLUX VARIATION OF A COSINE DOSER***'//)

     WRITE(*,11)
11   FORMAT(1X,'***YOU ARE IN THE PROGRAM CSHAPE.FOR***'///)

     WRITE(4,20)
20   FORMAT(1X,'DOSER GEOMETRIC PARAMETERS (CGS UNITS):'/)
     WRITE(4,30) 2*RSLIM
30   FORMAT(20X,'DOSER INSIDE DIAMTER: ',F8.4)
     WRITE(4,40) 2*RTLIM
40   FORMAT(20X,'SAMPLE TARGET DIAMETER: ',F8.4)
     WRITE(4,50) D
50   FORMAT(20X,'DOSER-TO-SAMPLE DISTANCE: ',F8.4)
     WRITE(4,60) THETAMAX
60   FORMAT(20X,'THETAMAX: ',F8.4//)
```

```
      WRITE(4,65)
65    FORMAT(1X,'DISTANCE:',4X,'JCOS:'/)

      RTINC=RTLIM/20

      DO 80, M=0,20
        RT=0.0+RTINC*M
        THETA=ATAN(RT/D)
        DJNORM=DJCOS(THETA)/DJCOS(0.0)
        WRITE(4,70) RT, DJNORM
70      FORMAT(1X,F8.4,5X,F8.4)
80    CONTINUE

      RETURN
      END


      REAL*8 FUNCTION DJCOS(ANG)
C
C     NORMALIZED ANGULAR DISTIBUTION FUNCTION FOR COSINE DOSER
C
      REAL*8 ANG
$INCLUDE: 'FLUX.INC'

      DJCOS=DCOS(ANG)/PI

      RETURN
      END

*************************************

      SUBROUTINE TSHAPE(TPAS1)
C
C     CALCULATE BEAM SHAPES IN THE TRANSPARENT REGIME
C     OUTFILES: TSHAPE

      REAL*8 THETA,RTINC,DJNORM
      INTEGER M
      LOGICAL TPAS1

$INCLUDE: 'FLUX.INC'

      EXTERNAL DJTRANS

      IF (TPAS1) THEN
        OPEN(4, FILE='TSHAPE.DAT',STATUS='NEW')
      ENDIF

      WRITE(4,10)
10    FORMAT(10X,'***FLUX VARIATION OF A TRANSPARENT DOSER***'//)

      WRITE(*,11)
11    FORMAT(1X,'***YOU ARE IN THE PROGRAM TSHAPE.FOR***'///)

      WRITE(4,20)
20    FORMAT(1X,'DOSER GEOMETRIC PARAMETERS (CGS UNITS):'/)
      WRITE(4,30) 2*RSLIM
30    FORMAT(20X,'DOSER INSIDE DIAMTER: ',F8.4)
      WRITE(4,40) 2*RTLIM
40    FORMAT(20X,'SAMPLE TARGET DIAMETER: ',F8.4)
      WRITE(4,50) D
50    FORMAT(20X,'DOSER-TO-SAMPLE DISTANCE: ',F8.4)
```

```
      WRITE(4,60) THETAMAX
60    FORMAT(20X,'THETAMAX: ',F8.4//)
      WRITE(4,65)
65    FORMAT(1X,'DISTANCE:',4X,'JTRANS:'/)

      RTINC=RTLIM/20

      DO 80, M=0,20
        RT=0.0+RTINC*M
        THETA=ATAN(RT/D)
        DJNORM=DJTRANS(THETA)/1.0
        WRITE(4,70) RT, DJNORM
70      FORMAT(1X,F8.4,5X,F8.4)
80    CONTINUE

      RETURN
      END

*****************************************

      REAL*8 FUNCTION DJTRANS(ANG)
C
C     NORMALIZED ANGULAR DISTIBUTION FUNCTION FOR TRANSPARENT CHANNEL
C     This code segment describes a normalized angular flux
C     distribution for the transparent flow regime.  The formula
C     is derived by Olander J.A.P. 41, 2769 (1970).  Flux
C     distributions are shown by Campbell et. al.
C
      REAL*8 ANG,GAMMA,PSI,P,R,TSIN
$INCLUDE: 'FLUX.INC'


      GAMMA=2*RSLIM/L
      PSI=2*GAMMA/3
      P=DTAN(ANG)/GAMMA

      IF (ANG.LT.1.0E-6) THEN
        DJTRANS=1.0
        GOTO 100
      ENDIF

      IF (DTAN(ANG).GE.GAMMA) THEN

        TSIN=(1-(DCOS(ANG))**2)**0.5

        DJTRANS=PSI*(DCOS(ANG))+(4*GAMMA*(1-PSI)/(3*PI))*
     *((DCOS(ANG))**2/TSIN)

      ELSE

        R=DACOS(P)-P*(1-P**2)**0.5

        DJTRANS=PSI*(DCOS(ANG))+(2/PI)*(DCOS(ANG))*((1-PSI)*R+(2/3)*
     *(1-PSI)*(1-(1-P**2)**1.5)/P)

      ENDIF

      WRITE(4,70) ANG, DJTRANS
70    FORMAT(1X,F8.4,5X,F8.4)


100   CONTINUE
```

```
      RETURN
      END

*************************************

      SUBROUTINE OSHAPE(OPAS1)
C
C     CALCULATE BEAM SHAPES IN THE OPAQUE REGIME
C     OUTFILES: OSHAPE.DAT

      REAL*8 THETA,RTINC,DJNORM,JPEAK
      LOGICAL OPAS1,FLAG

$INCLUDE: 'FLUX.INC'
$INCLUDE: 'GASPROPS.INC'

      EXTERNAL DJOPAQ

      IF (OPAS1) THEN
        OPEN(4, FILE='OSHAPE.DAT',STATUS='NEW')
      ENDIF

      WRITE(4,10)
10    FORMAT(10X,'***FLUX VARIATION OF AN OPAQUE DOSER***'//)

      WRITE(*,11)
11    FORMAT(1X,'***YOU ARE IN THE PROGRAM OSHAPE.FOR***'///)

      WRITE(4,20)
20    FORMAT(1X,'DOSER GEOMETRIC PARAMETERS (CGS UNITS):'/)
      WRITE(4,30) 2*RSLIM
30    FORMAT(20X,'DOSER INSIDE DIAMTER: ',F8.4)
      WRITE(4,40) 2*RTLIM
40    FORMAT(20X,'SAMPLE TARGET DIAMETER: ',F8.4)
      WRITE(4,50) D
50    FORMAT(20X,'DOSER-TO-SAMPLE DISTANCE: ',F8.4)
      WRITE(4,60) THETAMAX
60    FORMAT(20X,'THETAMAX: ',F8.4//)

      FLAG=.TRUE.
      RTINC=RTLIM/20
      JPEAK=DJOPAQ(0.0,FLAG)
      FLAG=.FALSE.
      WRITE(4,65)
65    FORMAT(1X,'DISTANCE:',4X,'JOPAQ:'/)

      DO 80, M=0,20
        RT=0.0+RTINC*M
        THETA=ATAN(RT/D)
        DJNORM=DJOPAQ(THETA,FLAG)/JPEAK
        WRITE(4,70) RT, DJNORM
70      FORMAT(1X,F8.4,5X,F8.4)
80    CONTINUE

      RETURN
      END

************************************************

      REAL*8 FUNCTION DJOPAQ(ANG,FLAG)

      REAL*8 ANG,INORM,Q
```

```
      LOGICAL FLAG
$INCLUDE: 'FLUX.INC'
$INCLUDE: 'GASPROPS.INC'

      EXTERNAL SHAPE
      EXTERNAL FUNC2
C
C     CALCULATE THE NOMALIZATION CONSTANT IF FIRSTPASS
C

      PHILIM=0.9999*PI/2.0
      ZERO=0.0

      IF (FLAG) THEN
        M=7
        DO 20 J=1,M+1
          CALL TRAPZN(FUNC2,ZERO,PHILIM,Q,J,FLAG)
20      CONTINUE

        INORM=2.0*PI*Q
        WRITE(4,30) INORM
30      FORMAT(1X,'NORMALIZATION CONSTANT IS: ',F8.4//)
      ENDIF


      DJOPAQ=SHAPE(ANG,FLAG)/INORM

      RETURN
      END

************************************

      REAL*8 FUNCTION SHAPE(ANG,FLAG)
C
C     This subprogram calculates the flux distribution in Giordmaine
C     and Wang's opaque regime.  Constants have been dropped because
C     they cancel in the normalization
C
      REAL*8 ANG,KCONST,Q,THETA,LLIM,ULIM,R
      LOGICAL FLAG
$INCLUDE: 'FLUX.INC'
$INCLUDE: 'GASPROPS.INC'

      EXTERNAL FUNC

C     ENTER ALL REQUIRED PHYSICAL CONSTANTS FOR THE GAS(CGS)

      IF(FLAG) THEN

        WRITE(4,2)
2       FORMAT(1X,'***NORMALIZATION ROUTINE IN THE OPAQUE REGIME***'///)
        WRITE(4,4)RSLIM,RGRAD
4       FORMAT(1X,'DOSER PARAMETERS:  RADIUS:',F8.4,' FLUX GRAD:',E12.3)
        WRITE(4,6)SIGMA
6       FORMAT(1X,'MOLECULAR DIAMETER OF THE GAS: ',E12.3//)

        FLAG=.FALSE.
      ELSE
        CONTINUE
      ENDIF
```

```
C     EVALUATE THE FUNCTION KCONST

      R=RGRAD*(0.75E-3*KB*T)**(-1.0)

      IF (ANG.LT.1.0E-6) THEN
         KCONST=1.0E+6
      ELSE
         KCONST=(2*RSLIM/DTAN(ANG))*((PI*SIGMA**2*R)/
     *    (1.4142*DCOS(ANG)))**0.5
      ENDIF


      LLIM=0.0
      ULIM=1.0
      M=8

      DO 15  J=1,M+1
       CALL TRAPZS(FUNC,LLIM,ULIM,Q,J,KCONST)
15    CONTINUE

      SHAPE=Q*COS(ANG)**1.5


      RETURN
      END

*****************************************

      REAL*8 FUNCTION FUNC2(X,FLAG)

      REAL*8 X
      LOGICAL FLAG
      EXTERNAL SHAPE

      FUNC2=SHAPE(X,FLAG)*DSIN(X)

      RETURN
      END

*****************************************

      SUBROUTINE TRAPZN(FUNC2,A,B,S,N,FLAG)

      REAL*8 A,B,S,X,DEL,SUM
      LOGICAL FLAG

      IF (N.EQ.1) THEN
       S=0.5*(B-A)*(FUNC2(A,FLAG)+FUNC2(B,FLAG))
       IT=1
      ELSE
       TNM=IT
       DEL=(B-A)/TNM
       X=A+0.5*DEL
       SUM=0.
       DO 11 J=1,IT
        SUM=SUM+FUNC2(X,FLAG)
        X=X+DEL
11     CONTINUE
       S=0.5*(S+(B-A)*SUM/TNM)
       IT=2*IT
      ENDIF
      RETURN
```

```
      END

*****************************************

      SUBROUTINE TRAPZS(FUNC,A,B,S,N,K)

      REAL*8 A,B,S,K,X,DEL,SUM

      IF (N.EQ.1) THEN
        S=0.5*(B-A)*(FUNC(A,K)+FUNC(B,K))
        IT=1
      ELSE
        TNM=IT
        DEL=(B-A)/TNM
        X=A+0.5*DEL
        SUM=0.
        DO 11 J=1,IT
          SUM=SUM+FUNC(X,K)
          X=X+DEL
11      CONTINUE
        S=0.5*(S+(B-A)*SUM/TNM)
        IT=2*IT
      ENDIF
      RETURN
      END

*****************************************

      SUBROUTINE TRAPPT(FUNC,A,B,S,N,Q,PO)

      REAL*8 A,B,S,Q,PO,X,DEL,SUM

      IF (N.EQ.1) THEN
        S=0.5*(B-A)*(FUNC(A,Q,PO)+FUNC(B,Q,PO))
        IT=1
      ELSE
        TNM=IT
        DEL=(B-A)/TNM
        X=A+0.5*DEL
        SUM=0.
        DO 11 J=1,IT
          SUM=SUM+FUNC(X,Q,PO)
          X=X+DEL
11      CONTINUE
        S=0.5*(S+(B-A)*SUM/TNM)
        IT=2*IT
      ENDIF
      RETURN
      END


***********************************

      REAL*8 FUNCTION FUNC(X,K)

      REAL*8 X,K
      EXTERNAL AERF

      FUNC=(1-X**2)**0.5*AERF(2*K*X)

      RETURN
      END
```

```
*****************************************

      REAL*8 FUNCTION AERF(X)
C
C     POLYNOMIAL APPROXIMATION TO THE ERF FUNCTION (ABRAMOWITZ &
C     STEGUN 7.1.25. ERROR<2E-5.


      REAL*8 X,T,P,A1,A2,A3

      DATA P,A1,A2,A3/0.47047,0.34802,-0.09587,0.74785/

      T=1/(1+P*X)
      IF (X.LT.1.0E+2) THEN
        AERF=1-(A1*T+A2*(T**2)+A3*(T**3))*EXP(-1*X**2)
      ELSE
        AERF=1-(A1*T+A2*(T**2)+A3*(T**3))
      ENDIF

      RETURN
      END

*****************************************

      REAL*8 FUNCTION PTIPFUNC(X,Q,PO)
C
C     CALCULATE AVERAGE TIP PRESSURE IN THE VISCOUS TIP
C     REGION
$INCLUDE: 'FLUX.INC'

      REAL*8 Q,PO,X

      PTIPFUNC=(Q*(X-LO)/(90.0*A**4.0)+PO**2.0)**(-0.5)

      RETURN
      END

*****************************************

      SUBROUTINE TDINT(F)
C
C     DRIVER FOR THE 3-D FLUX INTEGRAL
C     3-D INTEGRATION VIA QGUASS
C     ALL VARIABLE AND FUNCTIONS ARE DOUBLE PRECISION
C     INTEGRAL IS DIVIDED IN UP TO TEN, TEN POINT
C     QUADRATURE SEGMENTS
C
$INCLUDE: 'FLUX.INC'
$INCLUDE: 'GASPROPS.INC'

      DOUBLE PRECISION Q,R,F

C     DEFINE COMMON BLOCK XYZ

      DOUBLE PRECISION X,Y,Z,XMIN,XMAX,YMIN,YMAX,ZMIN,ZMAX
      COMMON/XYZ/  X,Y,Z,XMIN,XMAX,YMIN,YMAX,ZMIN,ZMAX

C     SET OUTER INTEGRAL LIMITS

      XMIN=0.0
      XMAX=2.0*PI
      YMIN=0.0
```

```
      YMAX=RTLIM
      ZMIN=0.0
      ZMAX=RSLIM

C     CALL THE 3D INTEGRATION ROUTINE

      WRITE(*,*) 'IN 3-D INTEGRATION'
      CALL QUAD3D(XMIN,XMAX,Q)

C     WRITE PROGRAM OUTPUT TO TERMINAL


      WRITE(*,'(1X,D17.10)') Q
      F=(2/RSLIM**2.0)*Q

      RETURN
      END


************************************************************


      SUBROUTINE QUAD3D(X1,X2,SS)
C
C     DRIVER FOR 3-D INTEGRATION VIA 10PT GC
C
      EXTERNAL H
      DOUBLE PRECISION H,X1,X2,SS,PSUM(10),ULIM,LLIM,ACCUM


      N=1
      ACCUM=0.0
      ULIM=X1
      DO 10 I=1,N
        LLIM=ULIM
        ULIM=I*X2/N
        CALL QGAUSX(H,LLIM,ULIM,SS)
        PSUM(I)=SS
        ACCUM=ACCUM+SS
10    CONTINUE

      SS=ACCUM

      RETURN
      END

************************************************************

      DOUBLE PRECISION FUNCTION F(ZZ)

      EXTERNAL DJOPAQ

$INCLUDE: 'FLUX.INC'
$INCLUDE: 'GASPROPS.INC'

      DOUBLE PRECISION ZZ,THETA,YY

      DOUBLE PRECISION X,Y,Z,XMIN,XMAX,YMIN,YMAX,ZMIN,ZMAX
      COMMON/XYZ/  X,Y,Z,XMIN,XMAX,YMIN,YMAX,ZMIN,ZMAX

      Z=ZZ
```

```
      YY=(D**2.0+Y**2.0+Z**2.0-2*Y*Z*DCOS(X))**0.5
      THETA=DACOS(D/YY)
      F=(DJOPAQ(THETA,.FALSE.)*D*Y*Z)/YY**3.0

      RETURN
      END

*****************************************************************

      DOUBLE PRECISION FUNCTION G(YY)
      EXTERNAL F,Z1,Z2
      DOUBLE PRECISION F,Z1,Z2,YY,SS,PSUM(10),LLIM,ULIM,ACCUM

      DOUBLE PRECISION X,Y,Z,XMIN,XMAX,YMIN,YMAX,ZMIN,ZMAX
      COMMON/XYZ/  X,Y,Z,XMIN,XMAX,YMIN,YMAX,ZMIN,ZMAX

      Y=YY
      N=1
      ACCUM=0.0
      ULIM=Z1(X,Y)
      DO 10 I=1,N
        LLIM=ULIM
        ULIM=I*Z2(X,Y)/N
        CALL QGAUSZ(F,LLIM,ULIM,SS)
        PSUM(I)=SS
        ACCUM=ACCUM+SS
10    CONTINUE
      G=ACCUM

      RETURN
      END

*****************************************************************

      DOUBLE PRECISION FUNCTION H(XX)
      EXTERNAL G,Y1,Y2
      DOUBLE PRECISION G,Y1,Y2,XX,SS,PSUM(10),ULIM,LLIM,ACCUM

      DOUBLE PRECISION X,Y,Z,XMIN,XMAX,YMIN,YMAX,ZMIN,ZMAX
      COMMON/XYZ/  X,Y,Z,XMIN,XMAX,YMIN,YMAX,ZMIN,ZMAX

      X=XX
      N=1
      ACCUM=0.0
      ULIM=Y1(X)
      DO 10 I=1,N
        LLIM=ULIM
        ULIM=I*Y2(X)/N
        CALL QGAUSY(G,LLIM,ULIM,SS)
        PSUM(I)=SS
        ACCUM=ACCUM+SS
10    CONTINUE
      H=ACCUM

      RETURN
      END

*****************************************************************

      SUBROUTINE QGAUSX(FUNC,A,B,SS)
```

```
      DOUBLE PRECISION FUNC,X,W,XM,XR,DX,A,B,SS

      DIMENSION X(5),W(5)
      DATA X/.1488743389,.4333953941,.6794095682,.8650633666,.9739065285
     */
      DATA W/.2955242247,.2692667193,.2190863625,.1494513491,.0666713443
     */
      XM=0.5*(B+A)
      XR=0.5*(B-A)
      SS=0
      DO 11 J=1,5
        DX=XR*X(J)
        SS=SS+W(J)*(FUNC(XM+DX)+FUNC(XM-DX))
11    CONTINUE
      SS=XR*SS
      RETURN
      END

*************************************************************

      SUBROUTINE QGAUSY(FUNC,A,B,SS)

      DOUBLE PRECISION FUNC,X,W,XM,XR,DX,A,B,SS

      DIMENSION X(5),W(5)
      DATA X/.1488743389,.4333953941,.6794095682,.8650633666,.9739065285
     */
      DATA W/.2955242247,.2692667193,.2190863625,.1494513491,.0666713443
     */
      XM=0.5*(B+A)
      XR=0.5*(B-A)
      SS=0
      DO 11 J=1,5
        DX=XR*X(J)
        SS=SS+W(J)*(FUNC(XM+DX)+FUNC(XM-DX))
11    CONTINUE
      SS=XR*SS
      RETURN
      END

*************************************************************

      SUBROUTINE QGAUSZ(FUNC,A,B,SS)

      DOUBLE PRECISION FUNC,X,W,XM,XR,DX,A,B,SS

      DIMENSION X(5),W(5)
      DATA X/.1488743389,.4333953941,.6794095682,.8650633666,.9739065285
     */
      DATA W/.2955242247,.2692667193,.2190863625,.1494513491,.0666713443
     */
      XM=0.5*(B+A)
      XR=0.5*(B-A)
      SS=0
      DO 11 J=1,5
        DX=XR*X(J)
        SS=SS+W(J)*(FUNC(XM+DX)+FUNC(XM-DX))
11    CONTINUE
      SS=XR*SS
      RETURN
      END
```

```
*********************************************************

      DOUBLE PRECISION FUNCTION Z1(PX,PY)

      DOUBLE PRECISION PX,PY
      DOUBLE PRECISION X,Y,Z,XMIN,XMAX,YMIN,YMAX,ZMIN,ZMAX
      COMMON/XYZ/  X,Y,Z,XMIN,XMAX,YMIN,YMAX,ZMIN,ZMAX

      Z1=ZMIN

      RETURN
      END

*********************************************************

      DOUBLE PRECISION FUNCTION Z2(PX,PY)

      DOUBLE PRECISION PX,PY
      DOUBLE PRECISION X,Y,Z,XMIN,XMAX,YMIN,YMAX,ZMIN,ZMAX
      COMMON/XYZ/  X,Y,Z,XMIN,XMAX,YMIN,YMAX,ZMIN,ZMAX

      Z2=ZMAX

      RETURN
      END

*********************************************************

      DOUBLE PRECISION FUNCTION Y1(PX)

      DOUBLE PRECISION PX
      DOUBLE PRECISION X,Y,Z,XMIN,XMAX,YMIN,YMAX,ZMIN,ZMAX
      COMMON/XYZ/  X,Y,Z,XMIN,XMAX,YMIN,YMAX,ZMIN,ZMAX

      Y1=YMIN

      RETURN
      END

*********************************************************

      DOUBLE PRECISION FUNCTION Y2(PX)

      DOUBLE PRECISION PX
      DOUBLE PRECISION X,Y,Z,XMIN,XMAX,YMIN,YMAX,ZMIN,ZMAX
      COMMON/XYZ/  X,Y,Z,XMIN,XMAX,YMIN,YMAX,ZMIN,ZMAX

      Y2=YMAX
      RETURN
      END



C
C     FLUX.INC COMMON BLOCK DEFINED
C
      REAL*8 RS,RT,PHI,A,D,L,LO,RSLIM,RTLIM,PHILIM,NTOT,
     *       MFP,KNA,KNL,LCRIT,ANGLE,CALIB,THETAMAX
      REAL*8 PI,KB,NA
      CHARACTER*12 DOSRNAME, DOSRMTRL
```

```
      COMMON/FLUX/ RT,RS,PHI,A,D,L,LO,RSLIM,RTLIM,PHILIM,NTOT,
     *             MFP,KNA,KNL,LCRIT,ANGLE,CALIB,THETAMAX

      COMMON/CONST/ PI,KB,NA

      COMMON/DOSRID/ DOSRNAME,DOSRMTRL




C
C     GASPROPS.INC COMMON BLOCK DEFINED
C     D.C. GRAY 1/91
C

      REAL*8 SIGMA,GAMMA,CP,CV,MW,RGRAD,PS,PBE,PBM,PCH,PBASE,T,S
      REAL*8 ETA,E
      CHARACTER*12 GASNAME,GASTYPE

      COMMON/GASPROPS/SIGMA,GAMMA,CP,CV,MW,RGRAD,
     *             PS,PBE,PBM,PCH,PBASE,T,S,ETA,E
      COMMON/GASID/ GASNAME,GASTYPE
```